The Dissertation Committee for Andrew Kenneth Keene Certifies that this is the approved version of the following dissertation:

Next-Generation Equipment and Procedures for Combined Resonant Column and Torsional Shear Testing

Committee:

Kenneth H. Stokoe II, Supervisor

Brady R. Cox

Clark R. Wilson

Robert B. Gilbert

Ellen M. Rathje

Next-Generation Equipment and Procedures for Combined Resonant Column and Torsional Shear Testing

by

Andrew Kenneth Keene, B.S.C.E.; M.S.

Dissertation

Presented to the Faculty of the Graduate School of

The University of Texas at Austin

in Partial Fulfillment

of the Requirements

for the Degree of

Doctor of Philosophy

The University of Texas at Austin

May 2017

Dedication

To my mother, father, and brother for unconditional love and support

Acknowledgements

I am deeply grateful to my advisor, Dr. Kenneth H. Stokoe II for his guidance and mentorship through my Ph.D. studies at the University of Texas at Austin. I am indebted to my academic and research advisors, Drs. Brady R. Cox, Clark R. Wilson, Robert B. Gilbert, and Ellen M. Rathje for their support and advice during my graduate studies at the University of Texas at Austin.

During my Ph.D. studies, various graduate students and friends in the Civil, Architectural, and Environmental Engineering Department at the University of Texas at Austin have made valuable contribution to my personal and professional life. I give thanks to Julia Roberts, David Teague, Andrew Stolte, Jeremy Faker, Ivan Garcia, Olivia Deterling, Brianna Peterman, Jon Roebuck, Zach Bemis, Hande Gerkus, Ian McMillen, Sorin Secara, Onur Kacar, Booanm Shin, Yaning Wang, Steve Xu, Chris Armstrong, Gaston Quaglia, Kaleigh McLaughlin, Yuta Nakamura, James Munson, Jakob Walter, Jonas Bauer, and Chris Nelson. Additional friends and colleagues that were integral to my life and work activates at the University of Texas at Austin include Alicia Zapata, Farn-Yuh Menq, Andrew Valentine, Robert Kent, Cecil Hoffpauir, Federico Castro, and Danny Quiroz.

Friends, colleagues, and mentors from my time at the University of Wisconsin-Madison have provided continued to support to my professional career and include Dr. Tuncer Edil, Dr. Dante Fratta, Dr. James Tinjum, Dr. Craig Benson, Idil Akin, Ben Warren, Zhipeng Su, Dr. Gizem Bozkurt, Dr. Marcos Montoro, Ozlem Bozyurt, Vonmarie Martinez, Dr. Jongwan Eun, and Mandi Siebels. Dr. Ali Ebrahimi was a great mentor and friend throughout my engineering studies at the University of Wisconsin-Madison and my

path through graduate school would not have been possible without his advice and encouragement.

I am grateful for the friends I have had in Madison, Wisconsin and throughout my life who have always given me unconditional support and friendship, especially Stacie Reece, Paul Adsit, Florence Whitehead, Brett Stroud, Ian Schelly, Brad Schabel, Jay Janowski, and Jimmy Mack.

Finally, I am eternally grateful for the love and support from my family. My parents Dr. Cindy Ann Anderson-Keene and James S. Keene M.D. have been by my side at every turn throughout my life. My brother Jerod James Keene has always been there to motivate me to be a better version of myself. My late grandparents Bob and Blanch Anderson raised and cared for me much of my early life. Arloa, Becky, and Nicole Wiesenberger are an important part of my life and have always cared about my studies and career. Todd McGrath has been an important mentor and friend and has guided me through much of my professional experiences. I look forward to time spend with friends and family as we all journey forward, thank you!

Next-Generation Equipment and Procedures for Combined Resonant Column and Torsional Shear Testing

Andrew Kenneth Keene, Ph.D.

The University of Texas at Austin, 2017

Supervisor: Kenneth H. Stokoe, II

In this dissertation, work aimed at developing next-generation equipment and procedures for combined resonant column and torsional shear (RCTS) testing are detailed. The work in this dissertation covers three key areas of RCTS testing that need improvement to reach the next level of RCTS testing. The first area involved improvement in measurement resolution with modern control and monitoring equipment. Concurrently, original software was written to enhance the efficiency, accuracy, and repeatability of the test. The second area involved advancing concepts for evaluating and modeling nonlinear behavior of soil, which was done in part by using raw RCTS test data collected and stored from 2013-2017. The third area involved evaluating and modifying the design of the existing RCTS device to accommodate higher levels of shearing strain and provide higher loading capacity.

First, when testing at small shear strains (< 0.001%) within the linear-elastic range of soils, very small excitation voltages must be used and very small voltages are recorded from the RCTS sensors. Obtaining accurate measurements in the linear-elastic range is critically important when testing at low confining pressures (in the range of 0.1 to 1 atm). In traditional RCTS data acquisition systems, very small recorded voltages are lost due to limited resolution of the control and monitoring subsystems. Concurrently, the very small

recorded voltages are generally heavily contaminated by environmental background noise that invalidates the automated process for reducing raw data into engineering results. Control and monitoring equipment and software were developed that can enhance the measurement and data reduction process when making low-strain measurements.

Second, testing of soil in the nonlinear shear strain range (typically greater than 0.001%) is a complex process that departs from traditional dynamic models for single-degree-of-freedom (SDOF) systems. Traditionally, RCTS results from testing in the nonlinear shear strain range involve slight adaptation of traditional SDOF models to obtain nonlinear relationships. Nonlinear dynamics model concepts were taken from literature and adapted to better understand and model nonlinear behavior of soils in RCTS testing. Furthermore, development of nonlinear models at moderate strains help to bridge the spectrum of soil testing which tends to divide into evaluating soils at small to moderate strains ($< 0.2\%$) or at large strains ($\geq 0.2\%$).

Third, when testing soils at large shearing strains ($> 0.2\%$), traditional RCTS systems are physically or electronically limited. At higher confining pressures (> 2 atm) where soils become quite stiff, the traditional RCTS control equipment is electronically incapable of driving enough torque output to strain soils in shear above desired levels ($> 0.1\%$). At low confining pressures (< 1 atm) where soils are soft, the traditional RCTS device is physically constrained from achieving a degree of twist that generates strains above the moderate shear strain range ($> 0.5\%$). An RCTS testing device was designed that has a torque-output capacity at least three times greater than a traditional RCTS device and an allowable degree of twist that can generate shearing strains above 1%.

Table of Contents

List of Figures

List of Tables

Chapter 1

Dissertation Background, Research Significance, Objectives of Research, and Organization of Dissertation

1.1 BACKGROUND

Combined resonant column and torsional shear (RCTS) testing is used to evaluate the deformational characteristics of soil and rock for the purposes of understanding the geotechnical behavior of a site subjected to vibrations from sources such as machinery, heavy automobile or rail traffic, industrial mining operations, construction, etc. or from earthquake loading. RCTS testing is a specialized geotechnical laboratory testing method where the RC portion was developed in the 1960's and 1970's and was limitedly automated with available software and hardware in the 1980's and 1990's. The TS portion was developed at The University of Texas (UT) in the 1980's. The RCTS equipment was developed and has been evaluated at UT over the past four decades by Isenhower (1979), Lodde (1982), Ni (1987), Kim (1991), and Menq (2003). The thrust of the research in this dissertation involves development of the next-generation of automation and analysis. The quality and scope of this testing method improves as data acquisition technology and computerized automation continues to advance. Additional aspects of this dissertation offers ideas for extending the shear train range over which the RCTS test can be conducted.

Current RCTS testing is based on the software and hardware technology that has been available for over the past decade. In RCTS testing done over a decade ago, the resolution of data acquisition systems limited the quality of the signals that could be acquired from the sensors and created a threshold below which RCTS testing results could not be obtained. In effect, the threshold limited measurements from being accurate at shear

strains below 0.0005%, which is paramount when testing soils at confining pressures below 1 atmosphere. Furthermore, background noise was difficult to remove via electronic fileting or digital processing, which made taking accurate measurements challenging. Signal conditioning in the form of analog filtering was available, but expensive with limited versatility. Digital signal processing was minimal or difficult to implement because of the limited capability of computer hardware and the programmable software resources available. Significant advances have been made in the capabilities of data acquisition equipment to execute higher resolution sampling of signals, use of multiple channels to increase number of sensors used to test a specimen, reduce the influence of noise from electrical and background sources, and programmatically adjustable hardware to provide versatility for data acquisition. With modern computing power and memory, the wide selection of software programming platforms available, and digital signal processing techniques, many new possibilities exist to enhance data quality, streamline data processing, and further automate the RCTS test. Additional scopes of work that will be possible with this several order of magnitude increase in data acquisition resolution will include: (1) Improved data analysis techniques; (2) improved signal processing and more comprehensive property evaluation; (3) additional characterization of material properties such as modulus degradation during testing; and (4) improved monitoring and control of specimens tested in anisotropic test states.

Upon development of the next-generation RCTS equipment and procedures, the device has been used to evaluate solid and hollow specimens, materials under isotropic and anisotropic loading conditions, and triggering potential of soils susceptible to liquidation. The objective in this dissertation is to build a next-generation RCTS testing system that streamlines RCTS testing protocol and expands the usefulness of the results and availability of data for post-test analysis. This next-generation system will be used to

conduct leading-edge research such as: (1) evaluation of the dynamic properties of coarse grained material created from blasted and/or crushed rock used in construction of heap leach pads for metallic mining operations; (2) development of laboratory testing methods for evaluating liquefaction susceptibility of soils; and (3) develop constitutive relationships between liquefaction susceptibility and the engineering properties obtained in RCTS tests.

1.2 RESEARCH SIGNIFICANCE

A key contribution of next-generation RCTS testing to the body of geotechnical engineering is to create control and monitoring equipment, advanced software, and a RCTS device that can map mechanical behavior of soil from the linear-elastic strain range (< 0.0003%) to the nonlinear-plastic shear strain range (> 1%). A geotechnical engineering laboratory test that can effectively map the large shear strain range of soil behavior from 10^{-6} % to 1% does not currently exist. This range is achieved using a combination of geotechnical laboratory tests, that include, but are not limited to, traditional combined resonant column and torsional shear (RCTS, 10^{-4} % to 0.5%), cyclic triaxial (CTX, 0.001% to 2%), and cyclic simple shear (CSS, 0.5% to 2). A device and control and monitoring system that can accurately map 8 orders of magnitude of shear strain (i.e. 10^{-6} % to 1% or higher) was developed and is presented in this dissertation.

The RCTS data acquisition system and testing device developed in this dissertation are not generally capable of evaluating the deformational characteristics of soils at shear strains greater than 1%. The testing system and device advanced in this dissertation is capable of accurately testing soils over the large shear strain range of soil behavior, from 10^{-6} % to 1%, that is of interest for all displacement-based geotechnical engineering analysis. The limitations of the traditional RCTS data acquisition system and testing device and the objectives achieved in this dissertation can be best explained with a graphical

representation. A normalized shear modulus versus the logarithm of shear strain (G/G_{max} - log γ) plot and shear stress versus shear strain (τ - γ) plot are shown to present the limitations of the traditional RCTS device, areas for improvement desired, and areas of interest for aspects of engineering design (Figure 1.1 and Figure 1.2).

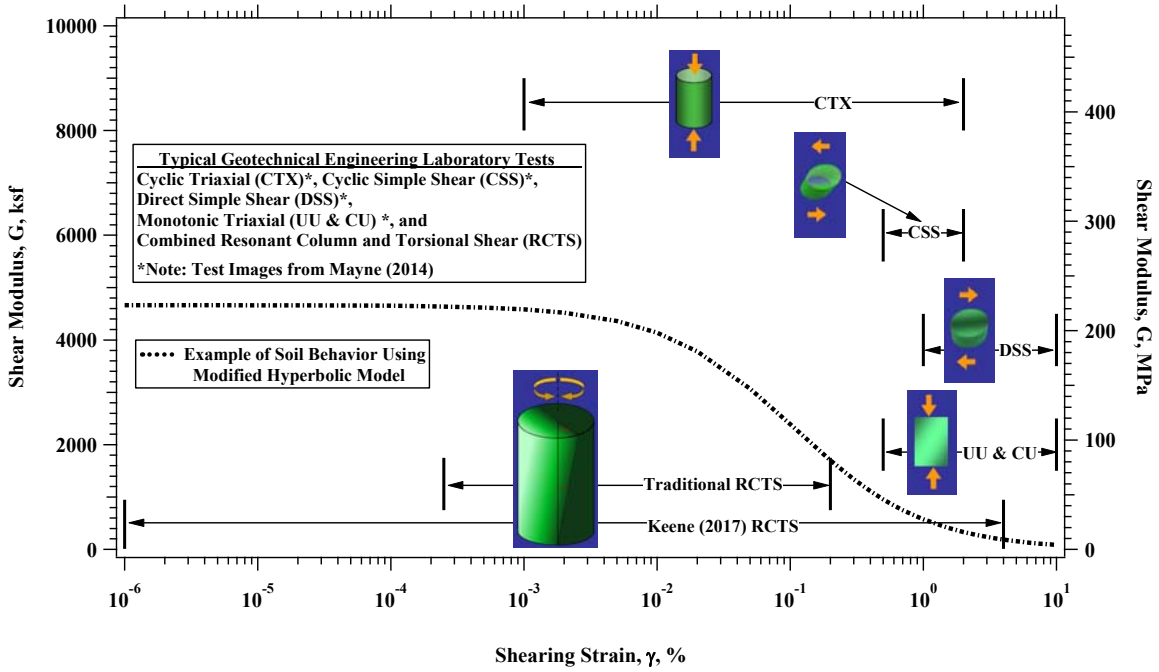

Figure 1.1: Range of Performance of Geotehcnical Laboratory Soil Tests as They Relate to Comparison of G/G_{max} with Shearing Strain.

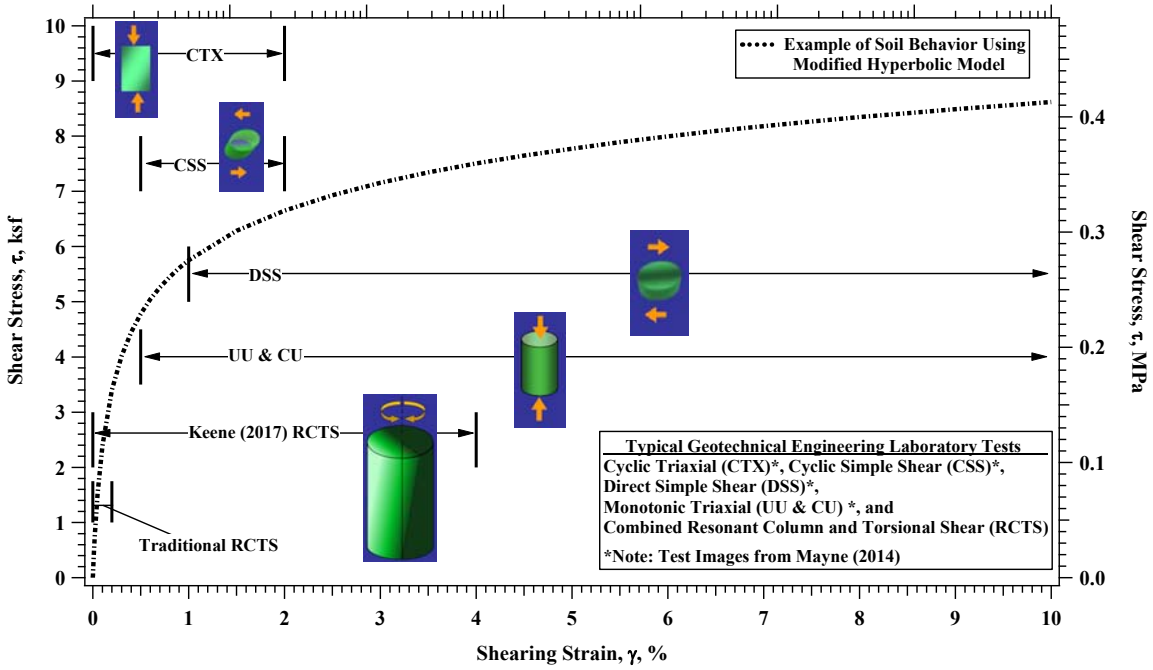

Figure 1.2 Range of Performance of Geotehcnical Laboratory Soil Tests as They Relate to Comparison of Shear Stress with Shearing Strain.

1.3 OBJECTIVES OF RESEARCH

1.3.1 Suggestions from Ni (1987) About Improving The RCTS Test Method and Analysis of Deformation-Based Behavior of Soils

1. The resonant column device should be further modified so that accurate measurements of volume change can be performed. Also, the device should be modified so that saturated specimens can be tested.
2. Sampling speed, resolution, sensitivity, and memory capacity are very critical in performing free vibration tests. This measurement method should be improved with new electronic equipment.
3. The drive mechanism should be improved so that larger strains can be generated in the specimen, and the dynamic behavior of soil under large strains should be

studied. Also, the central wire loading device should be redesigned so that larger axial loads can be applied to the top of the specimen.

4. The proximitor, which is used to measure specimen twist during torsional shear tests, should be replaced with a higher capacity proximitor so that larger torsional displacements can be measured.
5. Investigation of the high-amplitude behavior of soils and ability to test soils under true triaxial states of stress should be continued.
6. Alternate ways of performing true triaxial resonant column tests should be studied. Application of either a static torsional strain or stress before performing low-amplitude tests should be studied.
7. True nonlinear analysis of torsional vibration should be studied. A nonlinear dynamic analysis of the resonant column test should be developed in which both stiffness and damping vary nonlinearly. Dynamic properties from both resonant column and torsional shear tests should then be compared.

1.3.2 Scope of Research in this Dissertation

In this dissertation, work aimed at developing next-generation equipment and procedures for combined resonant column and torsional shear (RCTS) testing are detailed. The work in this dissertation covers three key areas of RCTS testing that need improvement to reach the next level of RCTS testing. The first area involved improvement in measurement resolution with modern control and monitoring equipment. Concurrently, original software was written to enhance the efficiency, accuracy, and repeatability of the test. The second area involved advancing concepts for evaluating and modeling nonlinear behavior of soil, which was done in part by using raw RCTS test data collected and stored from 2013-2017. The third area involved evaluating and modifying the design of the

existing RCTS device to accommodate higher levels of shearing strain and provide higher loading capacity.

First, when testing at small shear strains (< 0.001%) within the linear-elastic range of soils, very small excitation voltages must be used and very small voltages are recorded from the RCTS sensors. Obtaining accurate measurements in the linear-elastic range is critically important when testing at low confining pressures (in the range of 0.1 to 1 atm). In traditional RCTS data acquisition systems, very small recorded voltages are lost due to limited resolution of the control and monitoring subsystems. Concurrently, the very small recorded voltages are generally heavily contaminated by environmental background noise that invalidates the automated process for reducing raw data into engineering results. Control and monitoring equipment and software were developed that can enhance the measurement and data reduction process when making low-strain measurements.

Second, testing of soil in the nonlinear shear strain range (typically greater than 0.001%) is a complex process that departs from traditional dynamic models for single-degree-of-freedom (SDOF) systems. Traditionally, RCTS results from testing in the nonlinear shear strain range involve slight adaptation of traditional SDOF models to obtain nonlinear relationships. Nonlinear dynamics model concepts were taken from literature and adapted to better understand and model nonlinear behavior of soils in RCTS testing. Furthermore, development of nonlinear models at moderate strains help to bridge the spectrum of soil testing which tends to divide into evaluating soils at small to moderate strains (< 0.2%) or at large strains (≥ 0.2%).

Third, when testing soils at large shearing strains (> 0.2%), traditional RCTS systems are physically or electronically limited. At higher confining pressures (> 2 atm) where soils become quite stiff, the traditional RCTS control equipment is electronically incapable of driving enough torque output to strain soils in shear above desired levels (>

0.1%). At low confining pressures (< 1 atm) where soils are soft, the traditional RCTS device is physically constrained from achieving a degree of twist that generates strains above the moderate shear strain range (> 0.5%). An RCTS testing device was designed that has a torque-output capacity at least three times greater than a traditional RCTS device and an allowable degree of twist that can generate shearing strains above 1%.

This dissertation reveals the steps and resulting designs that alleviate the limitations of traditional RCTS control and monitoring equipment and testing device. Finally, there is a large amount of material on investigations and recommendations that lead to a better understanding of RCTS testing and a more economized approach for automating and conducting RCTS tests.

1.4 ORGANIZATION OF DISSERTATION

This research consists of main topics: (1) construction of a next-generation control and monitoring system; (2) programming of next-generation software for improved RCTS testing, automation, and user operation; (3) enhancements in data collection, processing, and analysis techniques; (4) increased understanding of dynamic testing of single-degree-of-freedom systems; (5) insight into not previously seen nonlinear shear strain behavior and new modeling concepts; and (6) evaluation of the electromagnetic drive system used in the traditional RCTS device and a design of a higher capacity RCTS device. This dissertation contains 14 chapters as follows:

Chapter 1: Dissertation Background, Research Significance, Objectives of Research, and Organization of Dissertation.

Chapter 2: Background, Theory, and Basic Introduction for the Combined Resonant Column and Torsional Shear (RCTS) Testing Methods and Equipment

Chapter 3: Control and Monitoring Equipment and Enhancements

Chapter 2

Background, Theory, and Basic Introduction for the RCTS Testing Methodology and Equipment

2.1 INTRODUCTION: BACKGROUND ON COMBINED RESONANT COLUMN AND TORSIONAL SHEAR (RCTS) TESTING

Some of the text in this chapter was adapted from the University of Texas at Austin Geotechnical Engineering Report GR06-04 titled "Test Procedures and Calibration Documentation Associated with the RCTS and URC Tests at The University of Texas at Austin" written by Stokoe, Choi, Jeon, and Lee (2006). Primarily, the "Test Procedures" of GR06-04 were updated in a document written by Stokoe, K.H., Keene, A.K., Shin, B., and Wang, Y. (2016) University of Texas at Austin Geotechnical Engineering Report GR16-05, which is incorporated into this chapter. All of the figures used in GR16-05 were developed in conjunction with this dissertation.

Combined resonant column and torsional shear (RCTS) equipment is used to evaluate the deformational characteristics (shear modulus and material damping in shear) of soil and rock specimens. The generalized RCTS equipment was developed at The University of Texas at Austin over the past four decades (Isenhower, 1979; Lodde, 1982; Ni, 1987; Kim, 1991; Menq, 2003; and Keene, 2017). The equipment is of the fixed-free type, with the bottom of the specimen fixed and torsional excitation applied to the free top. Both resonant column (RC) and torsional shear (TS) tests can be performed in a sequential series on the same specimen over a shearing strain range from about 10^{-6} % to slightly more than 10^{-1} %. The primary difference between the two types of tests is the excitation frequency and method of analysis. In the RC test, frequencies generally above 20 Hz are required and inertia of the specimen and drive system are needed to analyze the

measurements. On the other hand, slow cyclic loading involving frequencies generally below 2 Hz is performed in the TS test and inertia does not enter the data analysis. The function of the RC test is to resonate a cylindrical specimen in torsion in a manner consistent with testing of a single-degree-of-freedom system to determine the dynamic material behavior. The resonant column test is based on the one-dimensional wave equation derived from the theory of elasticity. The shear modulus is obtained by measuring the first-mode resonant frequency while material damping is evaluated from either the free-vibration decay curve or from the width of the frequency response curve assuming viscous damping. Rather than measuring the dynamic response of the system, the function of the TS test is to measure the actual stress-strain hysteresis loop determined by means of measuring the torque-twist curve. This chapter presents the theoretical basis behind both the RC and TS tests and the control and monitoring systems used to conduct the testing. In total, two control and monitoring systems were constructed to simultaneously operate four RCTS testing devices.

2.2 OVERVIEW OF COMBINED RESONANT COLUMN AND TORSIONAL SHEAR (RCTS) EQUIPMENT

The RCTS device can be idealized as a fixed-free system as shown in Figure 2.1. The bottom end of the specimen is fixed against rotation at the base pedestal, and top end of the specimen is excited by a non-contacting driving system. The driving system, which consists of a top cap and drive plate, can rotate freely to excite the specimen in cyclic torsion.

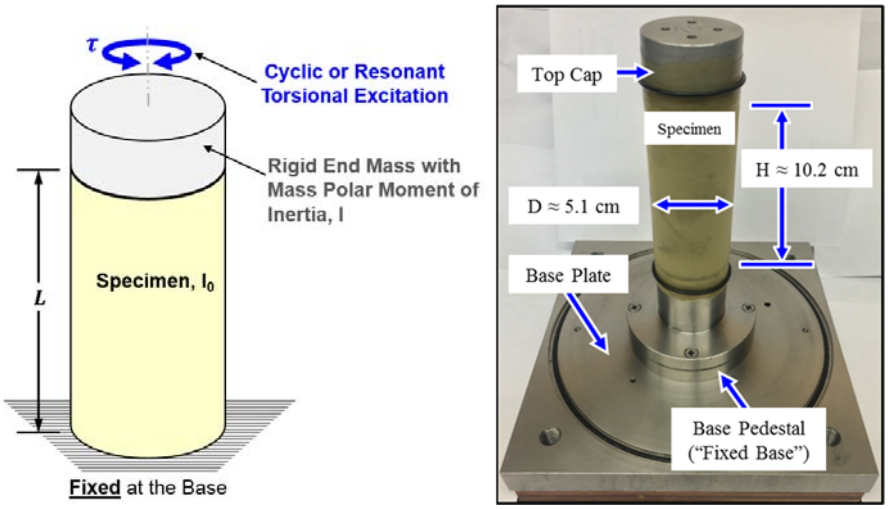

Figure 2.1: Generalized Fixed-Free RCTS Equipment with a Solid Specimen.

The basic operational principle is to vibrate the cylindrical specimen in first-mode torsional motion. Sinusoidal torsional excitation is applied to the top of the specimen over a range in frequencies, and the variation of the acceleration amplitude of the specimen with frequency is obtained. Once first-mode resonance is established, measurements of the resonant frequency and amplitude of vibration are made. These measurements are then combined with equipment characteristics and specimen characteristics to calculate shear wave velocity and shear modulus based on elastic wave propagation as illustrated in Figure 2.4 on page 16. Material damping is determined either from the width of the frequency response curve or from the free-vibration decay curve or both. These measurements are discussed in detail in section 2.3.3 starting on 28.

The torsional shear (TS) test is another method of determining shear modulus and material damping using the same RCTS equipment but operating it in a different manner. The simplified configuration of the torsional shear test is shown Figure 2.5. A cyclic torsional force with a given frequency, generally below 5 Hz, is applied at the top of the specimen. Instead of determining the resonant frequency, the stress-strain hysteresis loop is determined from measuring the torque-twist response of the specimen. Proximitors are

used to measure the angle of twist while the voltage applied to the coil is calibrated to yield torque. Shear modulus is calculated from the slope of a line through the end points of the hysteresis loop, and material damping is obtained from the area of the hysteresis loop as shown in Figure 2.5.

The RCTS device used in this study has three advantages. First, both resonant column and torsional shear tests can be performed with the same set-up simply by changing (outside the confining chamber) the frequency of the forcing function. Variability due to preparing "identical" samples is eliminated so that both test results can be compared effectively. Second, the torsional shear test can be performed over a shearing strain range between 1 $x10^{-5}$ % and about 10^{-1} %, depending upon specimen stiffness. Common types of torsional shear tests, which generate torque by a mechanical motor outside of the confining chamber, are usually performed at strains above 0.01 % because of system compliance. However, the RCTS device used in this study generates torque with an electrical coil-magnet system inside the confining chamber, thus eliminating the problem with an external motor. The torsional shear test can be performed at the same low-strain amplitudes as the resonant column test, and results between torsional shear and resonant column testing can be easily compared over a wide range of strains. Third, the loading frequency in the torsional shear test can be changed easily from 0.01 Hz to 5 Hz. Therefore, the effect of frequency on deformational characteristics can be conveniently investigated using this device.

The RCTS device consists of four basic subsystems which are: (1) a confinement system, (2) a drive system, (3) a height-change measurement system, and (4) a motion monitoring system. The general configuration of the RCTS device (without the confinement system) is shown in Figure 2.6. The RCTS device was automated using National Instruments (NI) data acquisition (DAQ) equipment and a LabVIEW based

software platform so that a computer and DAQ system controls the RC and TS tests, collects the data, reduces the data to material parameters, and generates graphical and tabular presentations. The DAQ equipment consists of a NI PXI-2566 High-Current General-Purpose Relay Switch board, NI PXI-6251 M Series DAQ, and NI PXI-4461 Dynamic Signal Analyzer (DSA) modules. These modules are housed in a NI PXI-1033 Chassis that interfaces with a Dell OptiPlex 9020 Minitower computer through an MXI-Express Controller. Computer-aided subsystems are discussed in the following sections. The configuration of the computerized system is shown in Figure 2.7. In total, two control and monitoring systems were constructed to simultaneously operate four RCTS testing devices.

2.2.1 RCTS Confinement System

The confining chamber is made of stainless steel. A thin-walled (0.6 cm in thickness) hollow cylinder fits into circular grooves machined into a 2.5-cm thick base and top plates. Four stainless steel connecting rods (1.28 cm in diameter) are used to secure the base and top plates to the hollow cylinder, and O-rings in the circular grooves are used to seal the chamber. In this configuration, the chamber has been designed to withstand a maximum air pressure of about 200 psi (1379 kPa). To safely test samples at higher confining pressures (pressures on the order of 350 psi ~ 2413 kPa), the confinement system is modified by adding additional stainless steel rods to secure the cylinder to reinforced top and base plates.

Compressed air is used to confine isotopically the specimen in the RCTS device. The air pressure to the chamber is generally regulated by a Fairchild M 30 regulator and air supplied to the regulator is filtered. At high confining pressures, additional regulators are used. The soil specimen is sealed in either one or two membranes and pore pressure in the specimen is vented to atmospheric pressure so that drained testing is performed.

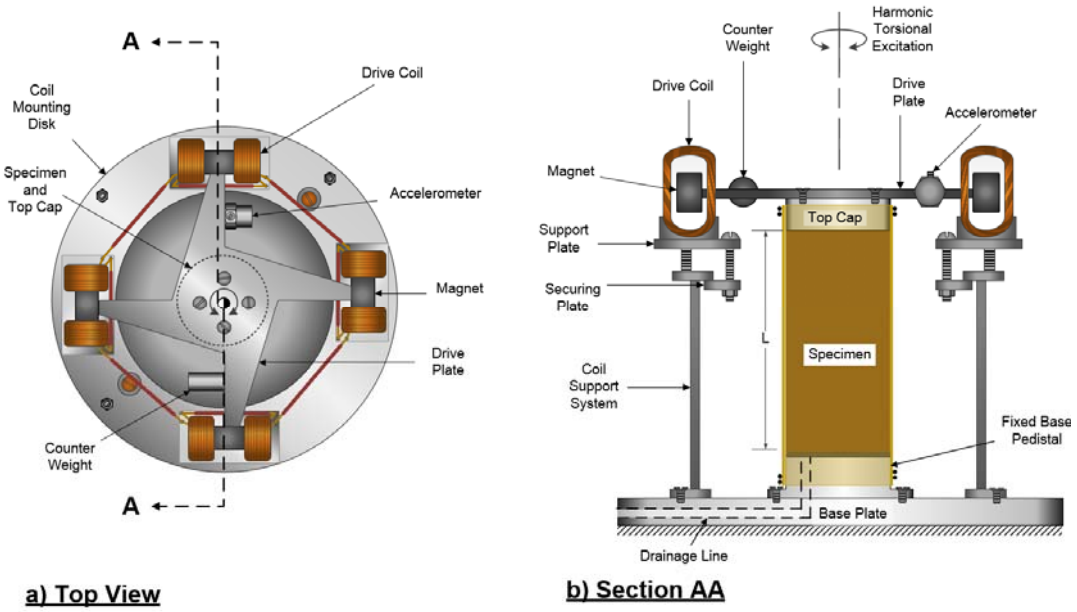

Figure 2.2: Soil Specimen in the RCTS Device; Resonant Column Portions with Accelerometer Measurements Highlighted (Confinement Chamber Not Shown).

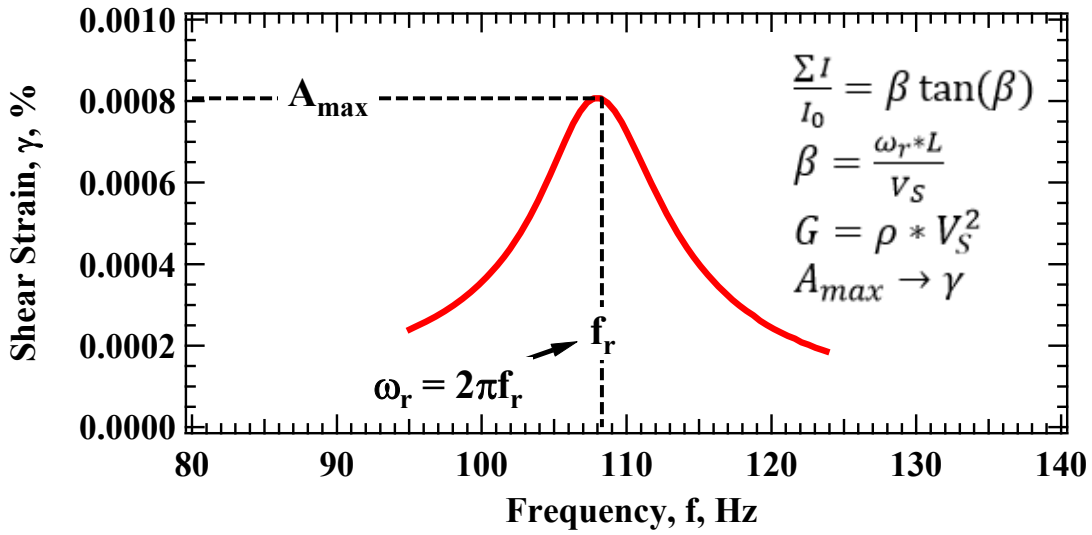

Figure 2.3: Example Frequency Response Curve Measured in the Fixed-Free Resonant Column Device from which Shear Modulus (G), Shear Strain (γ), and half-power damping ratio (D) are Determined.

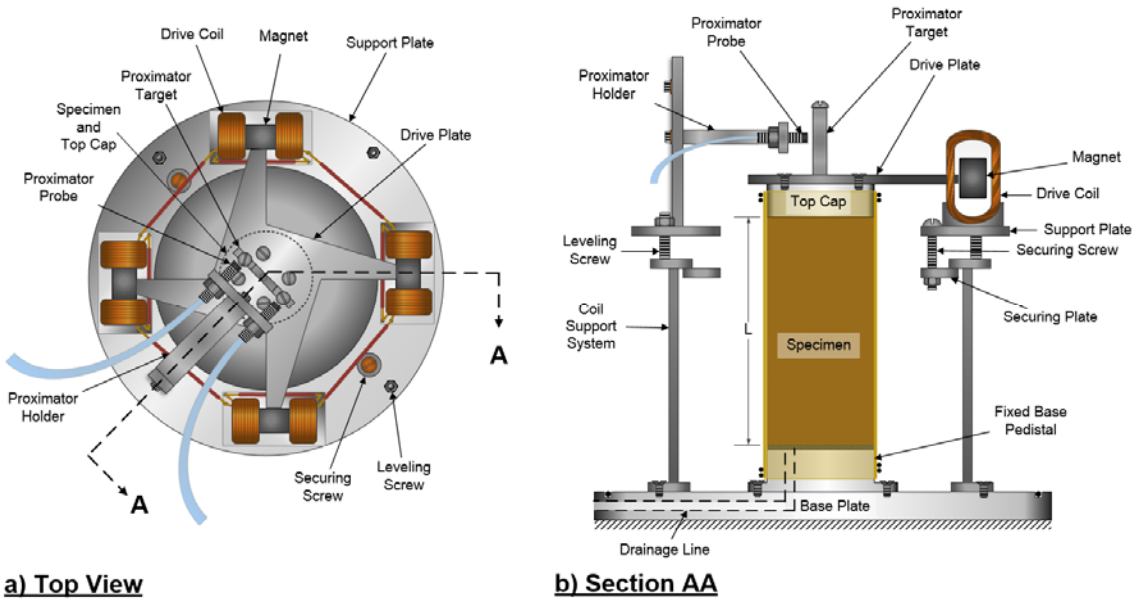

Figure 2.4: Soil Specimen in the RCTS Device; Torsional Shear Portion with Proximitor Measurements Highlighted (Confinement Chamber Not Shown).

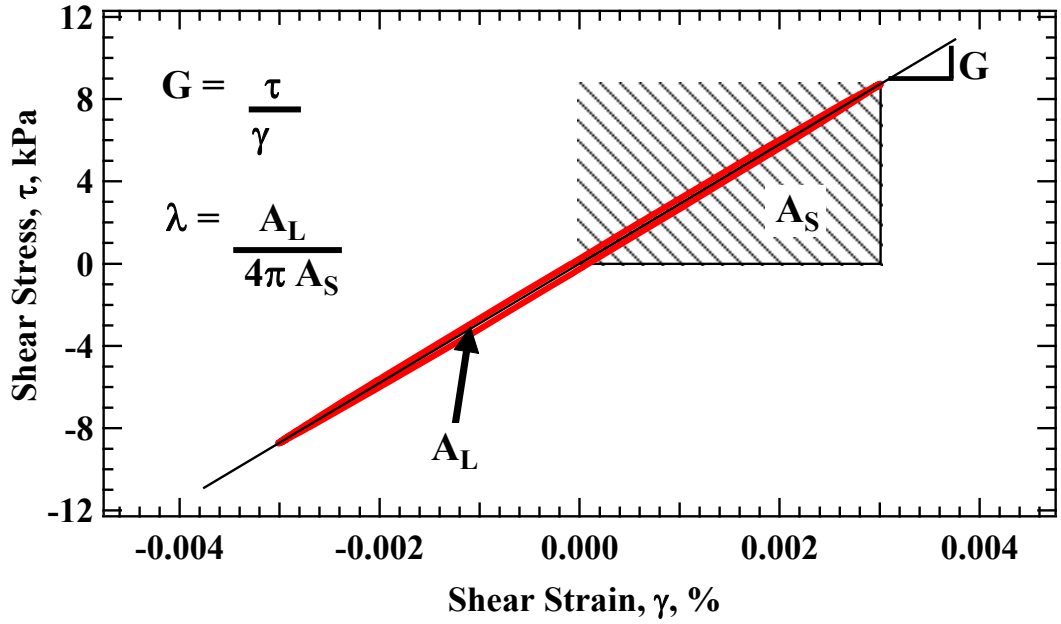

Figure 2.5: Configuration of a Torsional Shear Test and Evaluation of Shear Modulus and Material Damping Ratio from Measurement of the Stress-Strain Hysteresis Loop.

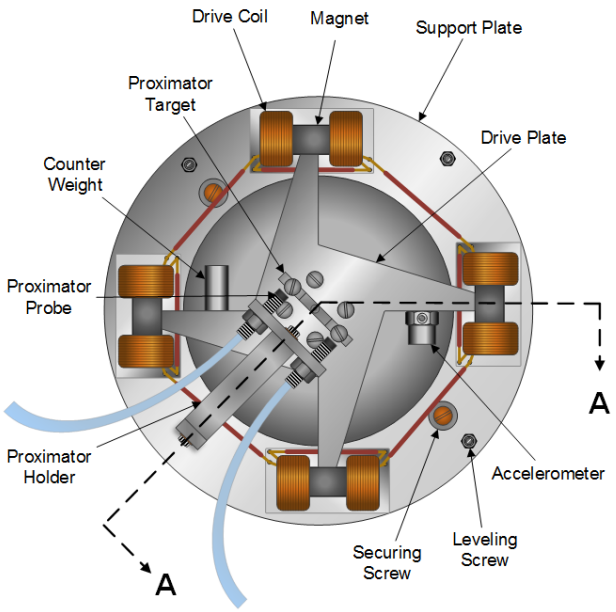

a) Top View of Drive and Monitoring Systems (LVDT is Removed for Clarity)

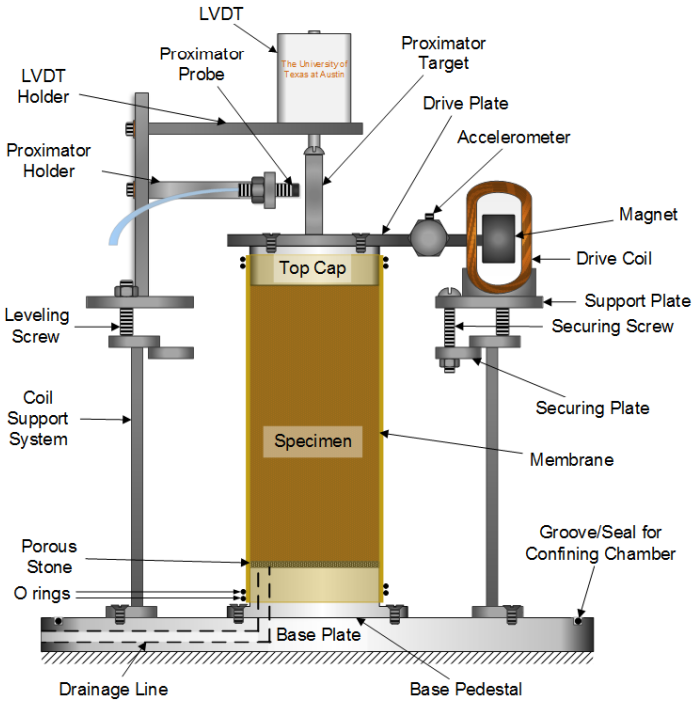

b) Section AA Showing Soil Specimen in RCTS Set-Up

Figure 2.6: General Configuration of RCTS Equipment.

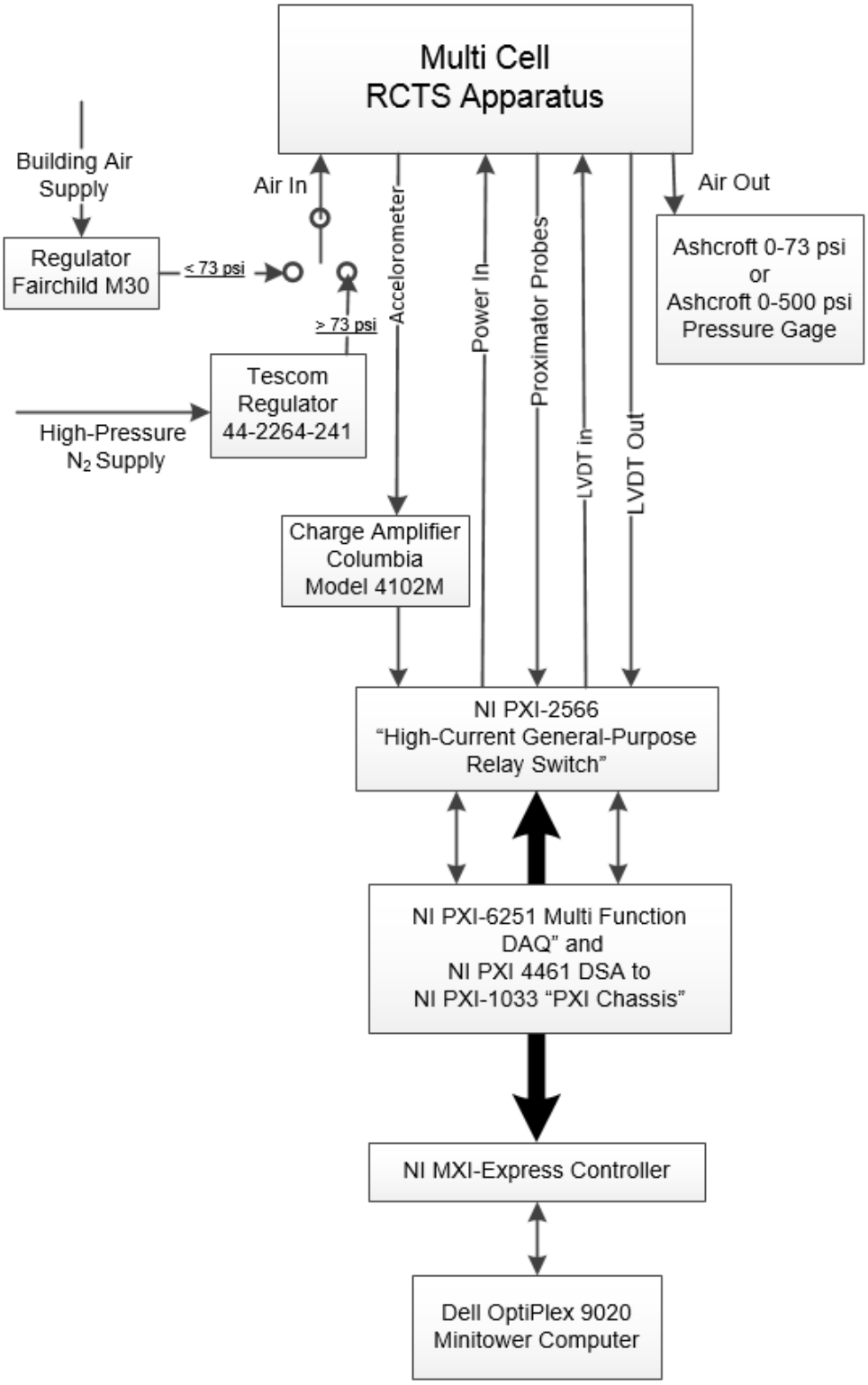

Figure 2.7: Configuration of Computerized RCTS Test Equipment.

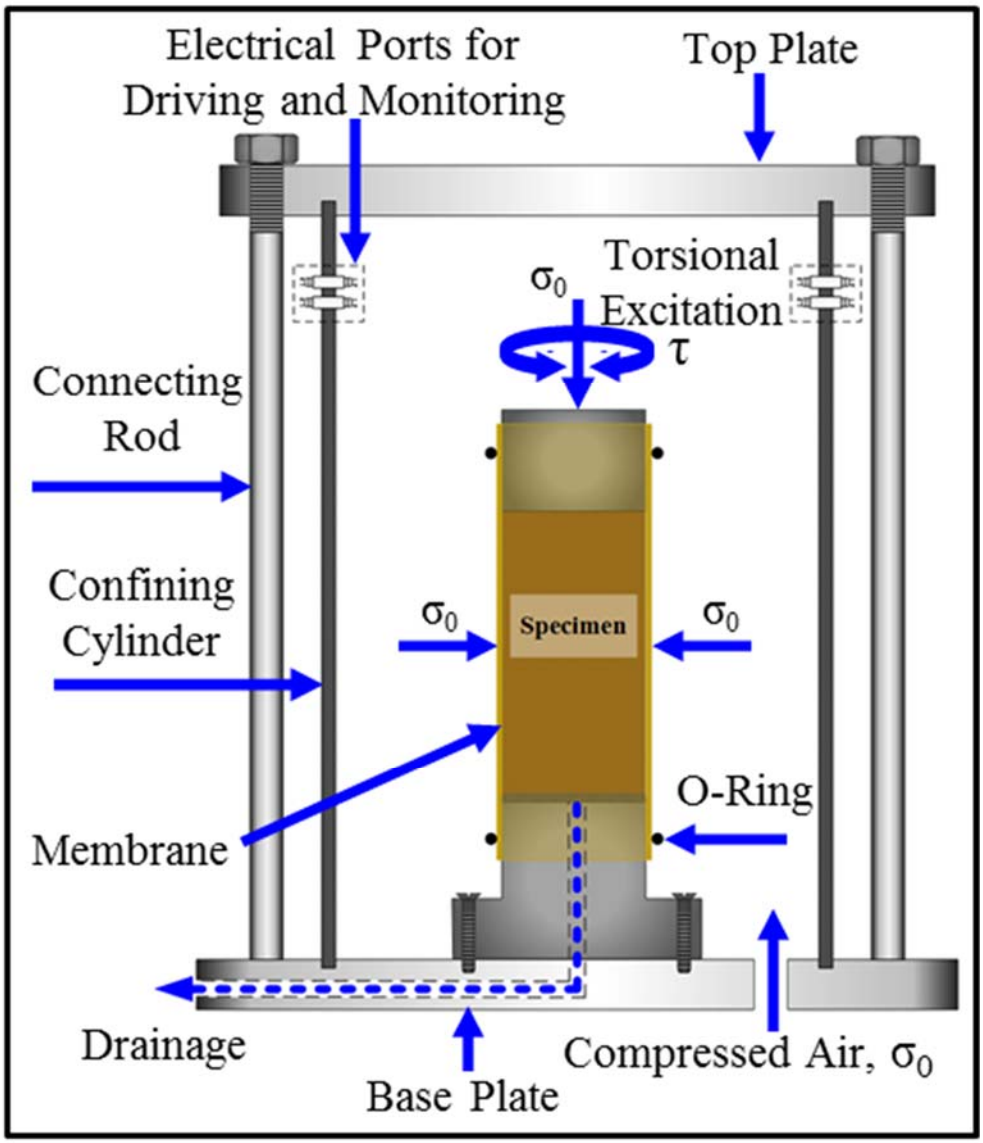

Figure 2.8: Simplified Configuration of Confinement System.

Inside the confining chamber, the air pressure acts upon the membrane(s) containing the specimen. Figure 2.8 shows the simplified configuration of the confinement system. The only calibrated portions of the confinement system are the pressure gauges which are used to read the cell air pressure. These gauges are calibrated every six months against reference gauges and electrical pressure transducers.

2.2.2 Drive System

The drive system consists of a four-armed drive plate, four magnets, eight drive coils, a power amplifier, and a function generator. Each magnet is rigidly attached to the end of one arm of the drive plate as shown in Figure 2.6. Eight drive coils encircle the ends of the four magnets so that the drive plate excites the soil specimen in torsional motion when a current is passed through the coils. The maximum torque that the drive system can develop depends on the strength of the magnets, size of the drive coils, resistance of the drive coils, size of the space between the magnets and drive coils, length of the arms of the drive plate, and the electrical characteristics of the function generator and power amplifier. For the three drive systems generally used in testing (dives systems Nos. 4, 5, and 8), the maximum torque was about 0.60 lb-ft (82 N-cm).

A schematic diagram of the drive system is shown in Figure 2.9. The computer controls the NI PXI-6251 DAQ system to input sinusoidal voltage to the drive coils. In the resonant column (RC) test, the NI PXI-6251 DAQ module performs frequency sweeps with a constant amplitude while in the torsional shear test, a fixed-frequency N-cycle mode is used. For high-amplitude resonant column and torsional shear (TS) tests, the sinusoidal input current is switched to and amplified by a power amplifier (HP 6824A) before going to the drive coils.

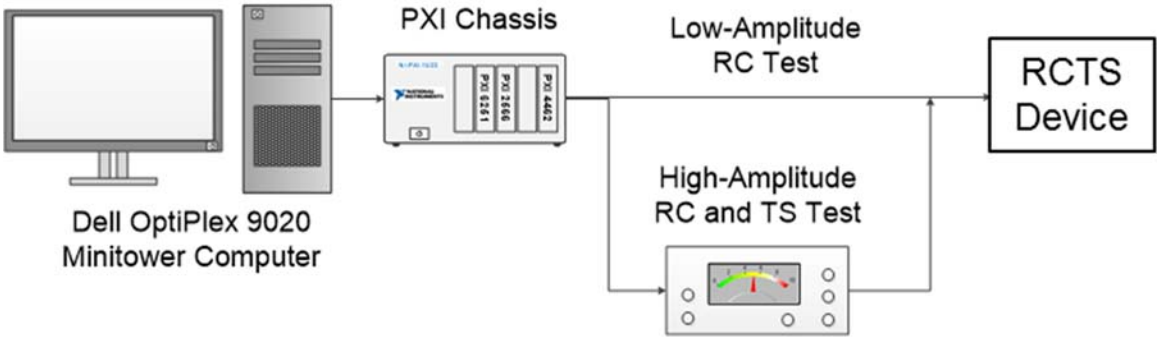

Figure 2.9: Schematic Diagram of the Drive System.

2.2.3 Height-Change Measurement System

The height change of the specimen is measured to account for the changes in the length and mass of the specimen during consolidation or swell. This measurement is also used to calculate changes in the mass moment of inertia, mass density, and void ratio of the specimen during testing (by assuming isotropic strain under isotropic confinement and constant degree of saturation). The height change is measured by a linear variable differential transformer (LVDT). The height change measurement system consists of an LVDT (Columbia Model SH-200-53R), and the NI PXI-4461 and NI PXI-6251 DAQ modules. The LVDT core is not in contact with the LVDT coil housing so that no friction occurs during RCTS testing.

The output and calibration factor of an LVDT depend on both the frequency and magnitude of the excitation voltage. The LVDT's are calibrated yearly using micrometers as discussed by Lodde (1982). In this system, the NI PXI-4461 generates the input signal in the LVDT coil at a frequency of 500 Hz and a voltage level of 4.77 RMS volts. The output from the LVDT is read simultaneously with the NI PXI-6251 DAQ module. The height change is calculated from the output voltage combined with the calibration factor. The schematic diagram of the height change measuring system is shown in Figure 2.10.

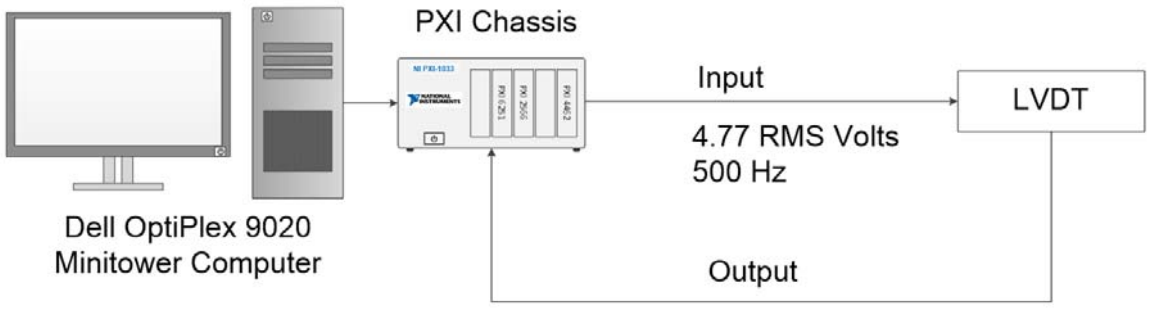

Figure 2.10: Schematic Diagram of the Height-Change Measurement System in the RCTS System.

Two aspects of the drive system in the RCTS equipment system have to be calibrated. First, the mass polar moment of the inertia, I_0, of each drive plate and top cap must be determined. This is done using specimens made of metal rods which are used as fixed-free torsional pendulums as discussed by Isenhower (1979) and Lodde (1982). The second aspect consists of determining the torque-current calibration factor for each drive plate. This process also involves use of the metal rods as discussed by Isenhower and Lodde. These calibrations are performed on an annual basis.

2.2.4 Motion Monitoring System

Dynamic soil and rock properties are obtained in the RC test at the resonant frequency which is usually above 20 Hz while torsional shear testing is used to measure the low-frequency (below 5 Hz) cyclic stress-strain relationship of soil and rock specimens. Because of the different frequencies applied in the resonant column and torsional shear tests, different motion monitoring systems are used.

2.2.4.1 Resonant Column (RC) Test

The motion monitoring system in the RC test is designed to measure the resonant frequencies, dynamic response curves around the resonant frequencies, and free-vibration decay curves. This system consists of an accelerometer (Columbia Research Laboratory Model 302-6), a charge amplifier (Columbia Research Laboratory Model 4102M) and NI PXI-6251 DAQ module. The entire system is calibrated yearly using a reference accelerometer (traceable to NIST) and shake table as discussed in Isenhower (1979) and Lodde (1982).

The accelerometer is oriented to be sensitive to torsional vibrations of the drive plate. The charge amplifier conditions the accelerometer output to be linear for all levels of acceleration in the test. The data acquisition system reads the output voltage from the accelerometer at each frequency. The resonant frequency (f_r) is obtained from the

frequency response curve as shown in Figure 2.3. Once the resonant frequency is obtained, the computer activates the data acquisition system to excite the specimen at the resonant frequency and then suddenly stops the current so that the free-vibration decay curve is recorded by the NI PXI-6251 DAQ module. The schematic diagram of the motion monitoring system involving the accelerometer is shown in Figure 2.11.

The resonant frequency of a soil or rock specimen is generally in the range of 20 Hz to 300 Hz with this equipment. To test soil or rock specimens effectively over a wide range of stiffness, the search for the resonant frequency is performed in two stages, first a rough sweep and then a fine sweep. During the rough sweep, a fast stepped-sine frequency sweep (0.25 Hz step) is used. Based on the estimated dynamic properties of the system, a fine sweep, with appropriate step rate and number of cycles per step, is then performed to determine an accurate resonant frequency in the neighborhood where the resonant frequency was found in the rough sweep.

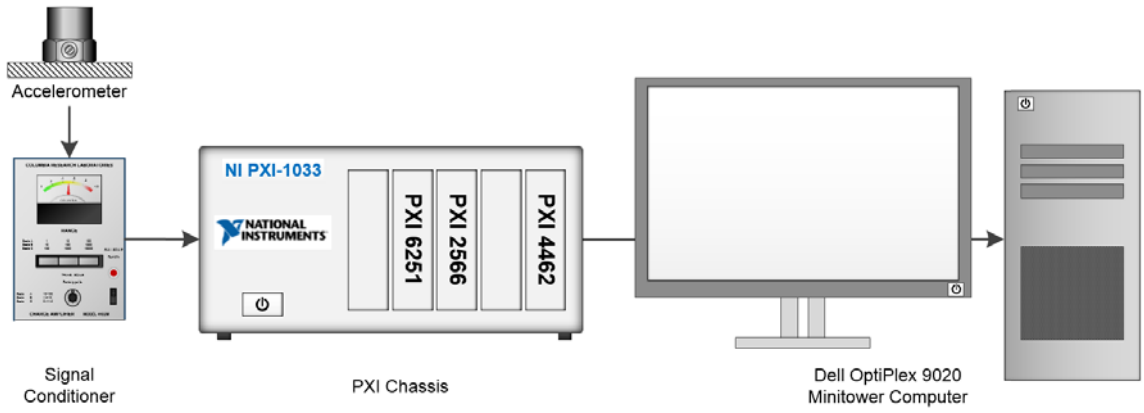

Figure 2.11: Schematic Diagram of the Dynamic Motion Monitoring System in the RC Test.

2.2.4.2 Torsional Shear (TS) Test

The motion monitoring system in the TS test (3300 Proximitor System) is used to monitor torque-twist hysteresis loops of the specimen as illustrated in Figure 2.5. This system consists of two proximitors (Bently Nevada 330100-50-05), two proximitor probes (Bently Nevada M 300-00), a DC power supply (Lambda LL-903), a U-shaped target, and the NI PXI-4461. The U-shaped target is secured to the top of the drive plate, and the two proximitor probes are rigidly attached to the support stand (see Figure 2.4). The entire system is calibrated yearly using a micrometer as discussed in Kim (1991).

A schematic diagram of the motion monitoring system in the torsional shear test is shown in Figure 2.12. The function of the proximitor probes is to measure the width of the air gap between the target and the probe tip. Because the proximitor probes do not touch the drive plate, no compliance problems are introduced into the measurement. Two probes are used and the operational amplifier subtracts the signal of one probe from the other so that the effect of any bending in the specimen toward the probes can be eliminated. The proximitor system is a very effective low-frequency motion monitoring system which does not introduce any compliance problems into the measurement. With the simultaneous measurement of torque, load-displacement hysteresis loops can be determined.

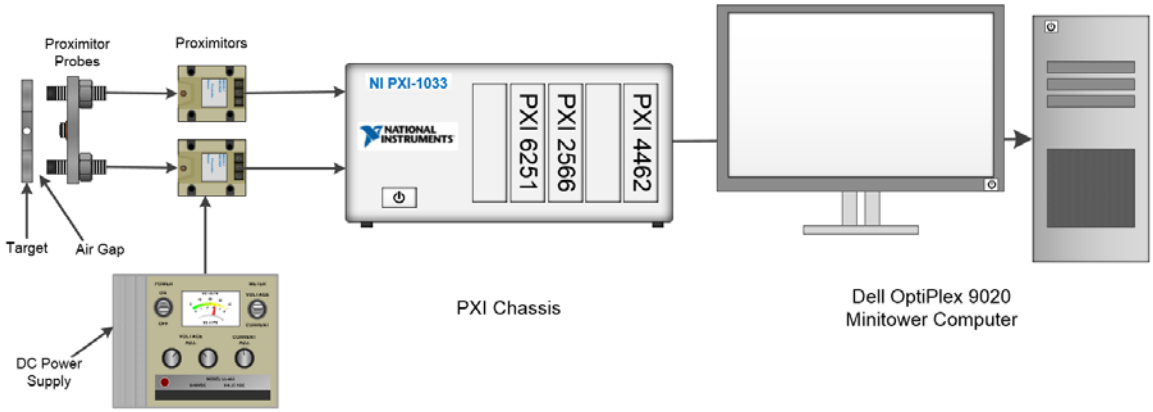

Figure 2.12: Schematic Diagram of the Motion Monitoring System in the Torsional Shear Test (3300 Proximitor System).

2.3 RESONANT COLUMN (RC) PORTION OF THE COMBINED RCTS SYSTEM

The resonant column test is based on the one-dimensional wave equation derived from the theory of elasticity. The shear modulus is obtained by measuring the first-mode resonant frequency while material damping is evaluated from either the free-vibration decay curve or from the width of the frequency response curve assuming viscous damping.

2.3.1 Shear Modulus

The governing equation of motion for the fixed-free torsional resonant column test is:

$$\frac{\sum I}{I_0} = \frac{\omega_r \cdot L}{V_S} \cdot \tan\left(\frac{\omega_r \cdot L}{V_S}\right) \qquad (2.1)$$

where $\Sigma I = I_s + I_m + \text{---}$

I_s = mass polar moment of inertia of the specimens,

I_m = mass polar moment of inertia of membrane(s),

I_0 = mass polar moment of inertia of rigid end mass at the top of the specimen,

L = length of the specimen,

V_S = shear wave velocity of the specimen, and

ω_r = first-mode resonant circular frequency of the system (used to approximate ω_n).

The value of I_0 is known from the calibration of the drive plate. The values of I_s and L are easily determined from the specimen size and weight. The value of I_m is determined from the relative lengths of the membrane on the specimens. Once the first-mode resonant frequency is determined, the shear wave velocity can be calculated from Eq. 3.1 by assuming that the resonant circular frequency (ω_r) and ω_n are equal.

As noted above and shown in Figure 2.3 the resonant circular frequency, ω_r, is measured instead of natural frequency, ω_n, and ω_r is used to calculate shear wave velocity.

If the damping in the system is zero, ω_r and ω_n are equal. The relationship between ω_r and ω_n is:

$$\omega_r = \omega_n\sqrt{1 - 2D^2} \tag{2.2}$$

A typical damping ratio at γ~0.1% encountered in the resonant column test is less than 10 percent, which corresponds to a difference of less than 1 percent between ω_r and ω_n. The values of γ~0.1% is quite large. Most RC measurements are performed at smaller γs so that D < 7% and the difference between ω_r and ω_n is less than 0.05%.

Once the shear wave velocity is determined, shear modulus is calculated from the relationship:

$$G = \rho \cdot V_S^2 \tag{2.3}$$

where ρ is the total mass density of the specimens (total unit weight divided by gravity).

2.3.2 Shearing Strain

The shearing strain varies radially within the specimen and may be expressed as a function of the distance from the longitudinal axis as illustrated in Figure 2.13. The equivalent shearing strain, γ_{eq} or γ, is represented by:

$$\gamma = r_{eq} * {}^{\theta_{max}}/_{L} \tag{2.4}$$

where r_{eq} = equivalent radius,

θ_{max} = angle of twist at the top of the specimen, and

L = length of the specimen.

Chen and Stokoe (1979) studied the radial distribution in shearing strain to find a value of r_{eq} for the specimen tested in the RCTS equipment to evaluate an effective strain. They found that the value of req varied from 0.82*r_0 for a peak shearing strain amplitude

below 0.001 % to 0.79*r_0 for a peak shearing strain of 0.1 % for a solid specimen. These values of r_{eq} have been adopted in this study.

In the resonant column test, the resonant period (T_r, seconds), and output voltage of accelerometer (A_c, volts) at resonance are measured. Accelerometer output is changed to the displacement by using the accelerometer calibration factor (CF, volts/in./sec^2) assuming harmonic motion. The accelerometer displacement is divided by the distance (D_{ac}, inches) between the location of accelerometer and the axis of the specimen to calculate the angle of twist at the top of the specimen (θ_{max}). The shearing strain is then calculated by:

$$\gamma = r_{eq} \frac{A_c \cdot T_r^2}{4\pi^2 \cdot CF} \cdot \frac{1}{D_{ac}} \cdot \frac{1}{L} \qquad (2.5)$$

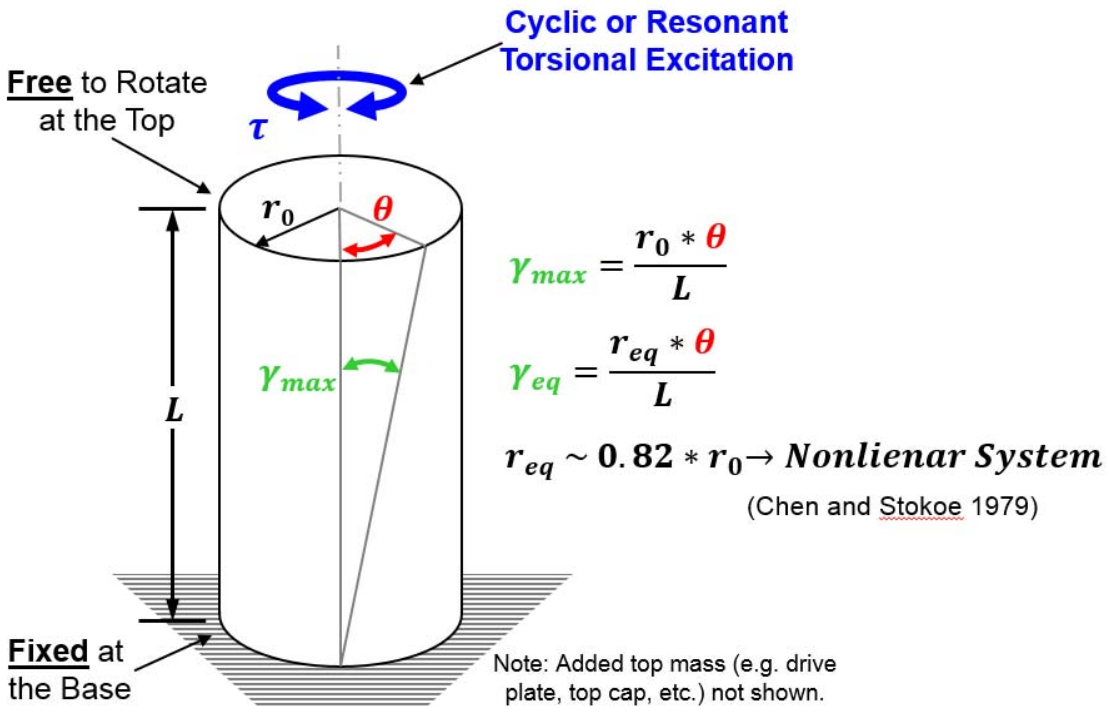

Figure 2.13: Shearing Strain in RCTS Specimen Column.

2.3.3 Material Damping

In the resonant column test, the material damping ratio can be evaluated from either the free-vibration decay method or from the half-power bandwidth method. Each of these methods is discussed below. It is important to note that, in these measurements, the damping measurement includes material damping in the specimen plus any damping in the equipment. Calibration of equipment-generated damping is discussed in Chapter 4.

2.3.3.1 Free-Vibration Decay Method

Material damping in soil and rock specimens can be quite complex to define. However, the theory for a single-degree-of-freedom system with viscous damping is a useful framework for describing the effect of material damping which occurs in soil and rock (Richart et al. 1970). The decay of free vibrations of a single-degree-of-freedom system with viscous damping is described by the logarithmic decrement, δ, which is the ratio of the natural logarithm of two successive amplitudes of motion as:

$$\delta = \ln\left(\frac{Z_1}{Z_2}\right) = \frac{2\pi D}{\sqrt{1-D^2}} \qquad (2.6)$$

where Z_1 and Z_2 = two successive strain amplitudes of motion, and

D = material damping ratio.

The free-vibration decay curve is recorded using the data acquisition system by shutting off the driving force while the specimen is vibrating at the resonant frequency. The amplitude of each cycle is measured from the decay curve, and the logarithmic decrement is then calculated.

Data points other than the peak amplitude of each cycle can also be used from the free-vibration decay curve for calculating logarithmic decrement. Both the peak and trough of each cycle can be used to double the amount of points used to analyze the free-vibration decay curve for damping ratio, this method will be termed the half-cycle peak-to-peak

method. The theoretical framework for a single-degree-of-freedom system with viscous damping is expanded to include a signal processing method known as the Hilbert Transform (Feldman 2011). The Hilbert Transform provides the instantaneous amplitude of the signal, which is used to calculate logarithmic decrement as:

$$\delta = \frac{\ln\left(\frac{Z_1}{Z_2}\right)}{F_s/f_d} = \frac{2\pi D}{\sqrt{1-D^2}} \tag{2.7}$$

where Z_1 and Z_2 = two successive instantaneous strain amplitudes of motion,

F_S = sampling rate,

f_d = the damped natural frequency, and

D = material damping ratio.

Material damping ratio is calculated from logarithmic decrement according to:

$$D = \sqrt{\frac{\delta^2}{4\pi^2+\delta^2}} \tag{2.8}$$

A typical damping measurement from a free-vibration decay curve (from a metal calibration specimen) is shown in Figure 2.14. In this method, it is not certain which strain amplitude is a representative strain for damping ratio because strain amplitude decreases during free-vibration decay. In this dissertation, a representative strain amplitude was used as the peak strain amplitude during steady-state vibration for shearing strains below 0.001% which are assumed to be in the linear range where G equals G_{max}. However, at larger strains, the representative strain is smaller than the peak strain, and the average strain determined for the first three cycles of free vibration are used.

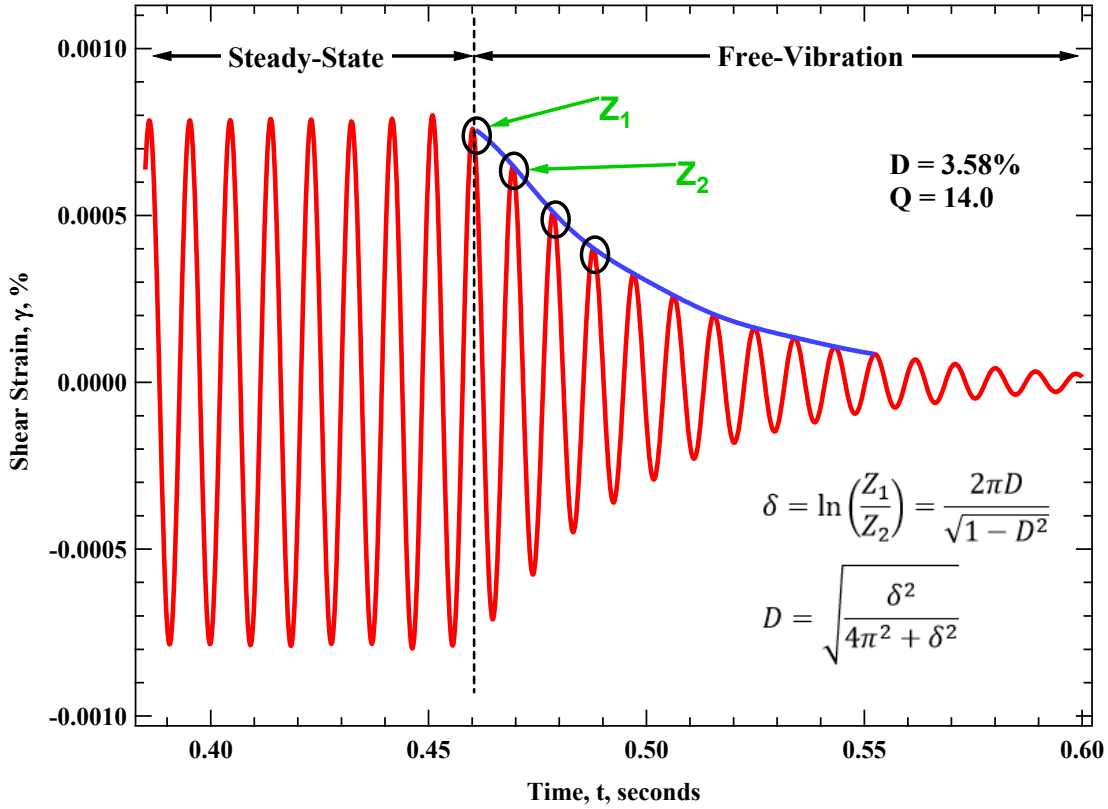

Figure 2.14: Determination of Material Damping Ratio from the Free-Vibration Decay Curve Using a Metal Specimen.

2.3.3.2 Half-Power Bandwidth Method

Another method of measuring damping in the resonant column test is the half-power bandwidth method, which is based on measurement of the width of the frequency response curve near resonance. From the frequency response curve, the logarithmic decrement can be calculated from (Richart et al. 1970):

$$\delta = \frac{\pi}{2} \cdot \frac{f_2^2 - f_1^2}{f_r^2} \cdot \sqrt{\frac{A^2}{A_{max}^2 + A^2}} \cdot \frac{\sqrt{1-2D^2}}{1-2D^2} \qquad (2.9)$$

where f_1 is the frequency below the resonance where the strain amplitude is A, f_2 is the frequency above the resonance where the strain amplitude is A, fr is the resonant frequency, and D is the material damping ratio.

If the damping ratio is small and A is chosen as $0.707*A_{max}$, which is called the half-power point, the logarithmic decrement can be simplified as:

$$\delta = \pi \cdot \frac{f_2 - f_1}{f_r} \tag{2.10}$$

Therefore, the damping ratio can be expressed as:

$$D = \frac{f_2 - f_1}{2f_r} \tag{2.11}$$

A typical damping measurement by the half-power bandwidth method (for a metal calibration specimen) is shown in Figure 2.15.

Another method of measuring damping in the resonant column test is involves using a least-mean-squares fit of the theoretical response curve equation for a single-degree-of-freedom system to the measured response curve. The theoretical response curve for a single-degree-of-freedom system from Richart et al. (1970) is given by:

$$M = \frac{1}{\sqrt{[1-(\omega/\omega_n)^2]^2+[2D(\omega/\omega_n)]^2}} \tag{2.12}$$

where M is the displacement response factor, ω is the input frequency, ω_n is the circular natural frequency, and D is the material damping ratio.

This method is more reliable when significant levels of background noise are present. This method serves as an "averaging" technique to lessen complications from background noise.

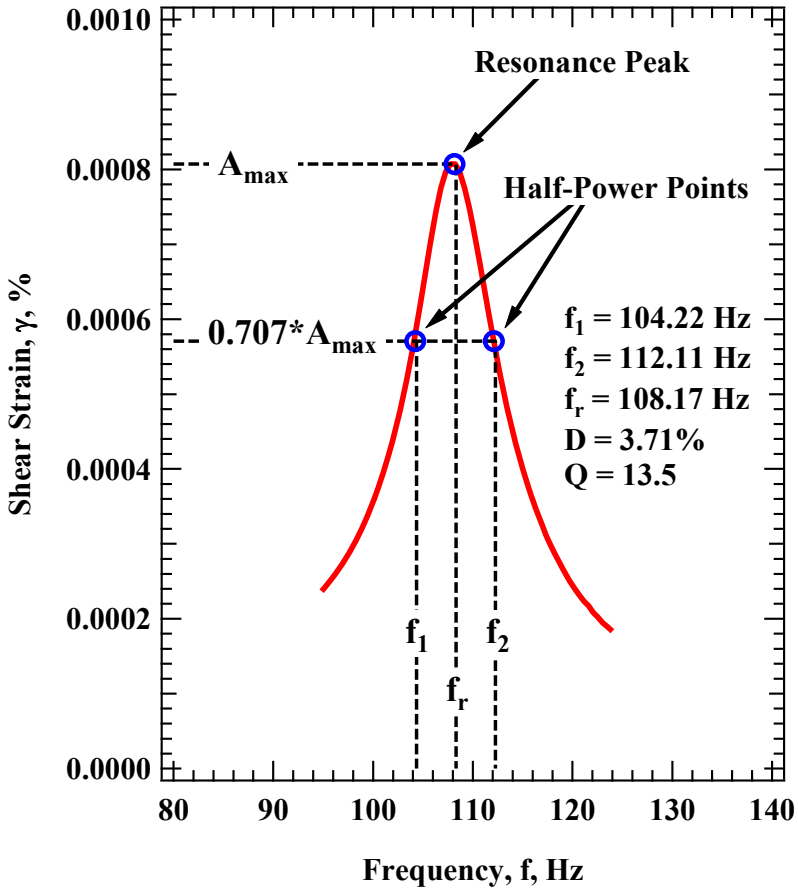

Figure 2.15: Determination of Material Damping from the Half-Power Bandwidth Method Using a Soil Specimen.

Traditionally, background noise can be a problem in measuring material damping using the free-vibration decay method at very small strains, strains less than about 0.0003%. On the other hand, background noise generally has a smaller effect on the frequency response curve at strains below even 0.0003%. Therefore, the half-power bandwidth method is often preferred to the free-vibration decay method for making small-strain damping measurements. However, at larges strains, symmetry in the frequency response curve is no longer maintained, and a serious error can be introduced in the half-power bandwidth method (Ni, 1987).

In this report, higher data acquisition resolution, modern data and signal processing techniques, and additional testing methods developed herein were employed to make damping measurements using both methods at strains as low as 10^{-6} %. Both types of damping measurements were made at small-strains in an attempt to obtain good data sets while only the free-vibration decay method was used at larger strains (above 0.001%).

2.4 TORSIONAL SHEAR (TS) PORTION OF THE COMBINED RCTS SYSTEM

The torsional shear test is another method of determining the deformational characteristics (modulus and damping) of soil or rock specimens using the same RCTS equipment. Rather than measuring the dynamic response of the specimen, the actual stress-strain hysteresis loop is determined by means of measuring the torque-twist curve. Shear modulus is calculated from the slope of the hysteresis loop, and the hysteretic damping ratio is calculated using the area of the hysteresis loop.

2.4.1 Shear Modulus

Because shear modulus is calculated from the stress-strain hysteresis loop, shearing stress and shearing strain in the torsional shear test need to be defined.

2.4.2 Shearing Stress

Determination of shearing stress in the torsional shear test is based on the theory of elasticity for circular or tubular rods in pure torsion. Assume that pure torque, T, is applied to the top of the specimen. The torque can be calculated from:

$$T = \int_{r_i}^{r_o} \tau_r (2\pi r) r \, dr \qquad (2.13)$$

where τ_r is the shearing stress at a distance r from the axis of specimen and, r_0 and r_i are outside and inside radii, respectively. If the shearing stress is assumed to vary linearly across the radius:

$$\tau_r = \tau_m \cdot (r/r_0) \tag{2.14}$$

where τ_m is the maximum shearing stress at $r = r_0$. Eq. 4.2 can be rewritten as:

$$T = \frac{\tau_m}{r_0} \cdot \frac{\pi}{2} \cdot (r_0^4 - r_i^4) = \frac{\tau_m}{r_0} \cdot J_p \tag{2.15}$$

where J_p is the area polar moment of inertia. From Eq. 4.3, one can write:

$$\tau_m = r_0 \cdot \frac{T}{J_p} \tag{2.16}$$

Because shearing stress is assumed to vary linearly across the radius, the average torsional shearing stress is defined as:

$$\tau_{avg} = r_{eq} \cdot \frac{T}{J_p} \tag{2.17}$$

The value of r_{eq} is the same value as used in the resonant column analysis for calculation of shearing strain (Section 2.3.2).

The value of applied torque, T, is calculated from the input voltage applied to the drive system, V_T (volts), and the torque calibration factor, K_T (torque / volts). Thus, average shearing stress becomes:

$$\tau_{avg} = \tau_{eq} \cdot K_T \cdot V_T / J_p \tag{2.18}$$

2.4.3 Shearing Strain

Calculation of shearing strain in the torsional shear test follows the same procedure used in the resonant column test. The proximitor system directly measures the displacement

(instead of acceleration measured in the resonant test). Hence, the angle of twist (θ) is calculated from the proximitor output voltage, V_P (volts), and the proximitor calibration factor, K_P (rad / volt). Shearing strain, γ, is then calculated from:

$$\gamma = r_{eq} \cdot K_P \cdot V_P / L \tag{2.19}$$

2.4.4 Shear Modulus

Once the stress-strain hysteresis loop is measured, the shear modulus, G, is calculated from the slope of a line through the end points of the hysteresis loop as shown in Figure 2.16. Thus, the shear modulus is calculated from:

$$G = \tau / \gamma \tag{2.20}$$

where τ is peak shearing stress and γ is peak shearing strain.

2.4.5 Hysteretic Damping Ratio

Hysteretic damping ratio in the torsional shear test is measured using the amount of energy dissipated in one complete cycle of loading, unloading, and reloading and the peak strain energy stored in the specimen during the cycle. In the torsional shear test, the dissipated energy is measured from the area of the stress-strain hysteresis loop. The energy per cycle, W_d, due to a viscous damping force, F_d, is:

$$W_d = \int_0^T F_d \cdot \dot{x}\, dt \tag{2.21}$$

where $\dot{x}$ is a velocity and T is a period. For simple harmonic motion with frequency of ω, i.e. $x = A\,Cos(\omega t - \varphi)$, W_d becomes:

$$W_d = \pi c \omega A^2 \tag{2.22}$$

From the Eq. 4.10, the viscous damping coefficient can be expressed as:

$$c = W_d/(\pi\omega A^2) \tag{2.23}$$

The peak strain energy, W_s, stored by the spring is equal to the area under the secant modulus line in Figure 2.16 and can be written as:

$$W_s = kA^2/2 \tag{2.24}$$

The critical damping coefficient, c_c, is:

$$c_c = 2 \cdot \sqrt{k\,m} = 2\,k/\omega_n \tag{2.25}$$

where k is an elastic spring constant, m is a mass, and ω_n, is a natural frequency of system. Using Eq. 4.12, Eq. 4.13 can be rewritten as:

$$c_c = 4W_s/(\omega_n A^2) \tag{2.26}$$

Therefore, the damping ratio, D, can be expressed as:

$$D = c/c_c = W_d/(4\pi W_s) \cdot (\omega_n/\omega) \tag{2.27}$$

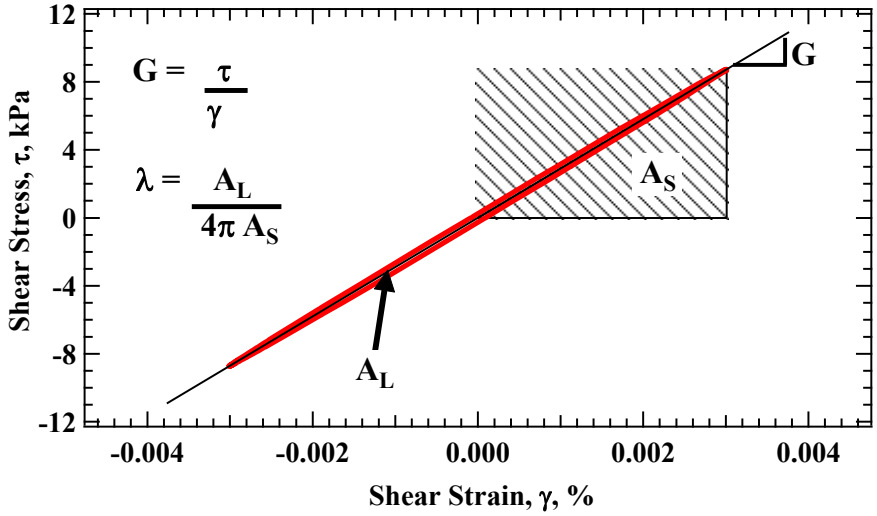

Figure 2.16: Determination of Shear Modulus and Material Damping Ratio in the Torsional Shear Test.

For soil or rock materials, damping is often assumed to be frequency independent. Therefore, ω_n/ω is ignored and hysteretic damping is written as:

$$D = \frac{1}{4\pi} \cdot \frac{W_d}{W_s} \tag{2.28}$$

where W_d is the area of the hysteresis loop and W_s is the area of the triangle as shown in Figure 2.16.

2.5 SUMMARY

Combined resonant column and torsional shear (RCTS) equipment is used to evaluate the deformational characteristics (shear modulus and material damping in shear) of soil and rock specimens. The RCTS device can be idealized as a fixed-free system. The bottom end of the specimen is fixed against rotation at the base pedestal, and top end of the specimen is excited by a non-contacting driving system. The driving system, which consists of a top cap and drive plate, can rotate freely to excite the specimen in cyclic torsion. The resonant column test is based on the one-dimensional wave equation derived from the theory of elasticity. The shear modulus is obtained by measuring the first-mode resonant frequency while material damping is evaluated from either the free-vibration decay curve or from the width of the frequency response curve assuming viscous damping. The torsional shear test is another method of determining the deformational characteristics (modulus and damping) of soil or rock specimens using the same RCTS equipment. Rather than measuring the dynamic response of the specimen, the actual stress-strain hysteresis loop is determined by means of measuring the torque-twist curve. Shear modulus is calculated from the slope of the hysteresis loop, and the hysteretic damping ratio is calculated using the area of the hysteresis loop. This chapter presented the theoretical basis behind both the RC and TS tests. The information about the testing equipment and test

procedures presented in this chapter was written in conjunction with The University of Texas at Austin Geotechnical Engineering Report GR16-05 (Stokoe, K.H., Keene, A.K., Shin, B., and Wang, Y., 2016).

Chapter 3

Control and Monitoring Equipment and Enhancements

3.1 Introduction: Details of Control and Monitoring Equipment

As discussed in Chapter 2, the RCTS device was automated using National Instruments (NI) data acquisition (DAQ) equipment and LabVIEW based software so that the software and DAQ system control the RC and TS tests, collect the data, reduce the data to mechanical and material parameters, and generate graphical and tabular presentations. The DAQ equipment consists of a NI PXI-6251 M Series DAQ, NI PXI-4461 Dynamic Signal Analyzer (DSA), and NI PXI-2566 High-Current General-Purpose Relay Switch board. These modules are housed in a NI PXI-1033 Chassis that interfaces with a Dell OptiPlex 9020 Minitower computer through an MXI-Express Controller. Computer-aided subsystems are discussed in the following subsections.

The NI PXI-1033 Chassis has 5 slots and supplies cooling and power demands to modules housed in the unit. The NI PXI-1033 integrates the various controllers that can be housed in the unit, which can be synchronized on an independent 10 MHz reference clock. The unit achieves up to 110 MB/s sustained throughput to the computer via PCIe card slot.

The NI PXI-6251 M Series DAQ is used to drive the RCTS device and acquire signals from the accelerometer, LVDT, pressure transducers, and a return from the output channel to verity that the output and DAQ is functioning properly. There are additional channels that can be used if additional sensors are added to the current configuration. The NI PXI-4461 Dynamic Signal Analyzer is used primarily for acquisition from the proximitor probes and excitation of the LVDT. The NI PXI-2566 High-Current General-Purpose Relay Switch board is used to switch all of the data acquisition channels between two sets of cables. Switching between two sets of cables allows two RCTS devices to be

operated by the same system without having to physically switch the connections between RCTS devices. The NI PXI-2566 is also used to switch between different output configurations to enhance resolution of or amplify the output signal driving the RCTS device. The current configuration and synchronization of the modules housed in the NI PXI-1033 Chassis, along with the enhancements discussed in this chapter, allow for enhanced efficiency of RCTS testing and simultaneous, real-time, and highly accurate monitoring during RCTS testing. In this chapter, the capabilities of the components used for RCTS testing are discussed along with some enhancements added to expand these capabilities.

3.1.1 Basics of Data Acquisition (DAQ) Resolution

Minimum voltage resolution represents the lowest voltage that can be either driven or acquired by a DAQ over a preselected voltage range. The minimum voltage, V_{min} is based on the digital resolution of the DAQ and is calculated by:

$$V_{min} = \frac{V}{2^{n-1}} \tag{3.1}$$

where n is the vertical digital resolution in units of bits.

Commonly, the V_{min} coincides with the noise floor of the system and thus will introduce noise into the system at a level of V_{min}. To conduct resonant column and torsional shear tests at the lowest measureable shear strains, a voltage range must be selected for each channel that is relevant to the driven signal or sensor signal being acquired. The of DAQ systems for resonant column/torsional shear (RCTS) testing requires a thorough understanding of the capabilities of the DAQ system.

3.1.2 National Instruments NI PXI-6251 16 Channel M Series DAQ

One of the data acquisition system (DAQ) used in this study is a National Instruments (NI) PXI-6251 16 channel M Series DAQ for driving and acquiring signals. The NI PXI-6251 has 16-bits of resolution with a minimum voltage resolution of $3.05 \cdot 10^{-5}$ V (i.e. for a ± 1 V range). The DAQ system is comprised of 2 analog outputs with ±10 V and ±5 V software programmable ranges and 16 analog input channels with ± 10, 5, 2, 1, 0.2, and 0.1 V software programmable ranges. In the case of sensor signals with no DC offset, selecting a narrow analog voltage range in needed to achieve adequate resolution. Some sensors in RCTS testing may contain a DC offset (e.g., charge amplification of accelerometers, proximitors probes, pressure transducers, etc.) and acquiring a signal with a significant DC offset (e.g. 0.05 V and larger) can lead to selecting a voltage range that is too large for the resolution needed to gather adequate information of interest. Several customizations are discussed in the subsequent sections that were built to acquire signals while maximizing the resolution of the NI PXI-6251.

The NI PXI-6251 has a single channel maximum 1.25 MS/s sampling rate and a 1.00 MS/s multichannel aggregate sampling rate that is divided amongst the channels that are activated during data acquisition. If all 16 analog input and 2 analog output channels are activated during testing, the effective sampling rate is thus 55,555 samples per second. Since the excitation frequency used in RC testing rarely exceeds 500 Hz, a minimum sampling rate of over 100 times the expected testing frequency far exceeds any foreseeable testing needs. For practical application of the RC software and data acquisition, a sampling rate of 10 kHz is used.

The NI PXI-6251 has a limitation on the amperage that can be generated by the analog output channels. The analog output is limited to 5 mA and the RCTS device has a resistive impedance of approximately 40 Ohms, thus the output voltage limitation of the

NI PXI-6251 is below 200 mV. Due to this limitation, for practical purposes, the output to the drive coils of the RCTS device is routed through an amplifier when an excitation above 150 mV. Similarly, the impedance of the LVDT (Columbia Model SH-200-53R) is approximately 60 Ohms (based on the 4 currently in use), which is too great to use the NI PXI-6251 and thus the NI PXI-4461 is used for supplying power to the LVDT.

The channels connected the NI PXI-6251 are wired to a NI TB-2706 terminal block. All of the connections to this module are single-ended with the sensor inputs and outputs wired to the corresponding channel pinout. The negative analog output and input channels have separate ground pinouts on the terminal block. Each of the channels connected to the NI TB-2706 are separated in twisted, shielded, and jacketed cable pairs with separate grounding terminals for the shielding. The paired cables are then routed to the NI PXI-2566 High-Current General-Purpose Relay Switch board. A photograph of the cables wired to the NI TB-2706 are shown in Figure 3.1.

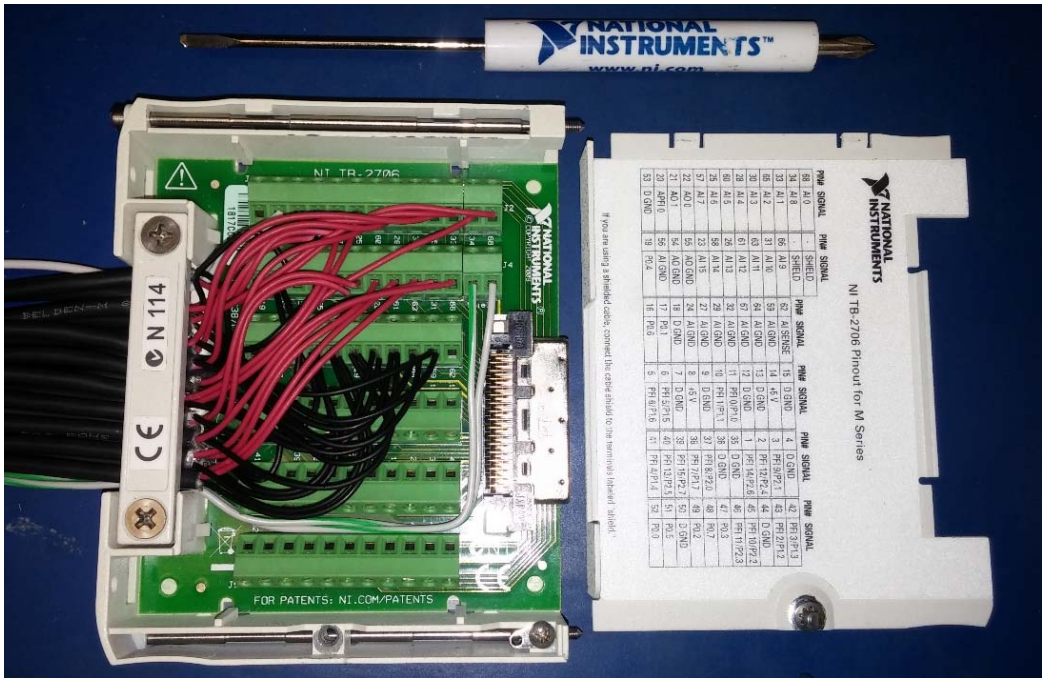

Figure 3.1: Wiring and Pinout Diagram for TB-2706 Servicing the NI PXI-6251 Module.

3.1.3 National Instruments NI PXI-4461 Dynamic Signal Analyzer

The NI PXI-4461 Dynamic Signal Analyzer is a higher-end module with built-in programmable analog AC Coupling and anti-aliasing filtering, simultaneous sampling, input channels with voltage ranges up to ± 42.4 V with 24-bits of resolution, and 204.8 kS/s per channel. The minimum voltage resolution of this module is $1.2 \cdot 10^{-7}$ V (i.e. for a ± 1 V range). The DAQ system is comprised of 2 analog outputs with ± 10, 1, and 0.1 V software programmable ranges and 2 analog input channels with ± 42.4, 31.6, 10.0, 3.16, 1.00, and 0.316 V software programmable ranges.

The primary use of the NI PXI-4461 is for acquisition of the proximitors and excitation of the LVDT. The proximitor probes (Bently Nevada M 300-00) possess a DC offset that corresponds to the distance of the probe from the target fixed to the drive plate. The functional range of these sensors is 1 to 100 mils (250 to 2500 μm), which corresponds to an output voltage of approximately 0 to -24 V. The acquisition of signals from these sensors done in one of two ways: (1) the DAQ module can be set to a range of 0 to -31.6 V and the DC offset of the sensors can be removed digitally during software analysis, and (2) the AC couple configuration can be activated programmatically, where the DC offset is removed electronically and a narrower voltage range is selected. The difference between these two acquisition options depends on the expected frequencies acquired during the test. The AC coupler analog filter has a highpass cutoff frequency of 3.4 Hz corresponding to a -3 dB gain and at 22.6 Hz at a -0.1 dB gain. Therefore, this analog filter cannot be used for TS testing where the frequencies of excitation range from 0.1 to 2 Hz. However, activation of this filter is useful for RC testing when test frequencies are above 22.6 Hz. For practical purposes, the lower end frequency limit for using this analog filter during RC testing is limited to 30 Hz, where the signal amplitude reduction is less than 0.1%. The characteristics of this filter are shown in Figure 3.2.

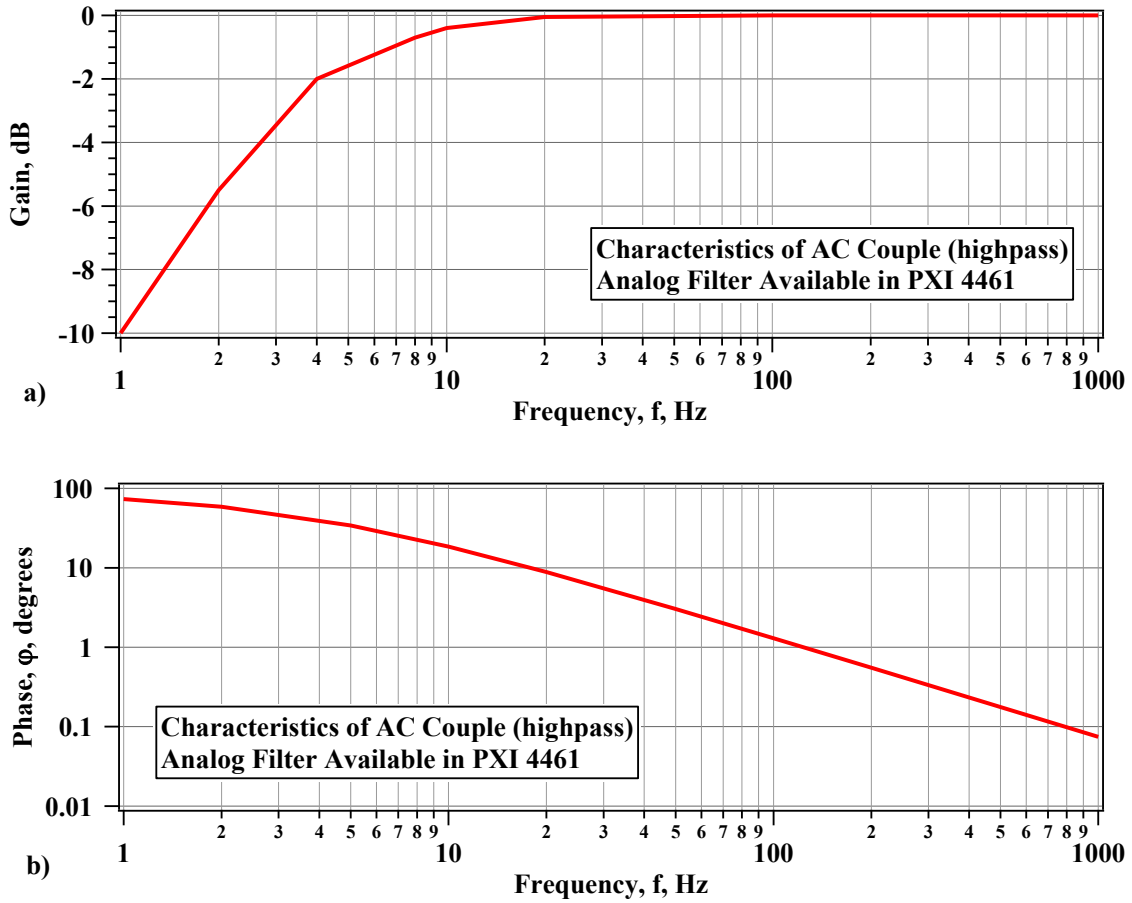

Figure 3.2: Characteristics of the NI PXI-4461 AC Couple (highpass) Filter for a) Frequency versus Gain and b) Frequency versus Phase.

During RC tests, the filter is programmatically activated when test frequencies are above 30 Hz and deactivated when tests frequencies are below 30 Hz. The phase of the dynamic response relative to the excitation function is measured and plotted during the test. Currently, this is used for observation and quality control. A correction for the phase shift caused by the AC couple filter is needed if using the phase from the proximitors for analysis of the dynamic response of the system being tested.

The NI PXI-4461 is also equipped with an adjustable anti-aliasing (lowpass) filter that is activated based on the sampling rate selected before signal input or output. The adjustable setting of the anti-aliasing filter is partitioned based on the range of the sampling

rate selected. The anti-aliasing filter setting introduces a sampling delay based on the sampling rate selected. The online manual can be consulted for the various delay attributes, but for use of this equipment for RCTS testing, the sampling rate is fixed at 10 kHz, which corresponds to a 40 sample delay. This delay introduces a phase shift that does not enter into analysis during RC testing (i.e. for the proximitors), but is corrected for during TS testing.

The LVDT sensor requires an excitation voltage of 6.75 V at 500 Hz. The ± 10.0 V range is used for this excitation signal and the sampling rate used is the same as the sampling rate already found to be suitable for RC testing, i.e. 10 kHz.

The NI PXI-4461 is more than capable for signal acquisition from the proximitor sensors and for excitation of the LVDT sensor. The NI PXI-1033 Chassis is designed for, and more than capable of, synchronizing the NI PXI-4461 and the NI PXI-6251 for simultaneously driving the RCTS device, providing excitation to the LVDT sensor, and acquiring signals from the accelerometer, proximitors, LVDT, and additional sensors (e.g. pore-pressure transducers, piezoelectric elements, etc.).

Cables from the RCTS device can be connected to the NI PXI-4461 module using standard BNC connectors. All of the connections to this module can be single-ended, pseudo-differential, or differential, each of which can be programmatically activated. The connections are then routed to the NI PXI-2566 High-Current General-Purpose Relay Switch board. A photograph of a NI PXI-4461 module is shown in Figure 3.3.

Figure 3.3: Photograph of a NI PXI-4461 Module without Mounting in the NI PXI-1033 Chassis.

3.1.4 National Instruments NI PXI-2566 High-Current General-Purpose Relay Switch

The NI PXI-2566 High-Current General-Purpose Relay Switch board is used to provide switching for all of the output and data acquisition channels coming from the NI PXI-6251 and NI PXI-4461 modules. The switching enables all of the output and measurement channels to route to two sets of cables. Switching between two sets of cables allows two RCTS devices to be operated by the same system without having to physically switch the connections between RCTS devices. In cases where the output must be reduced to allow for higher resolution excitation or to amplify the output signal driving the RCTS device, the NI PXI-2566 also routes the excitation channel through a voltage attenuator or the HP 6824A power supply amplifier, respectively.

The NI PXI-2566 has 16 single-pull double-through (SPDT) relay switches. The switches can operate at 115 cycles per second and switch while carrying up to 2 amps AC or DC. The switching speed and electrical capacity is well beyond any functional requirements for RCTS testing. The channels connected to the NI PXI-2566 have the positive sensor wires fixed in a NI TB-2666 terminal block. All of the negative or grounding cables are routed directly to the NI PXI-4461 and NI PXI-6251 modules. The sensor wires connected to the NI TB-2666 are combined into pairs, each twisted and shielded, and are contained separately into 3 groups within one jacketed cable. Each of the SPDT relay switches are connected though a total of 8 jacketed cables. A photograph of the cables wired to the NI TB-2666 are shown in Figure 3.4. The Wiring diagram of the NI PXI-4461 and NI PXI-6251 routing through the NI PXI-2566 is shown in Figure 3.16.

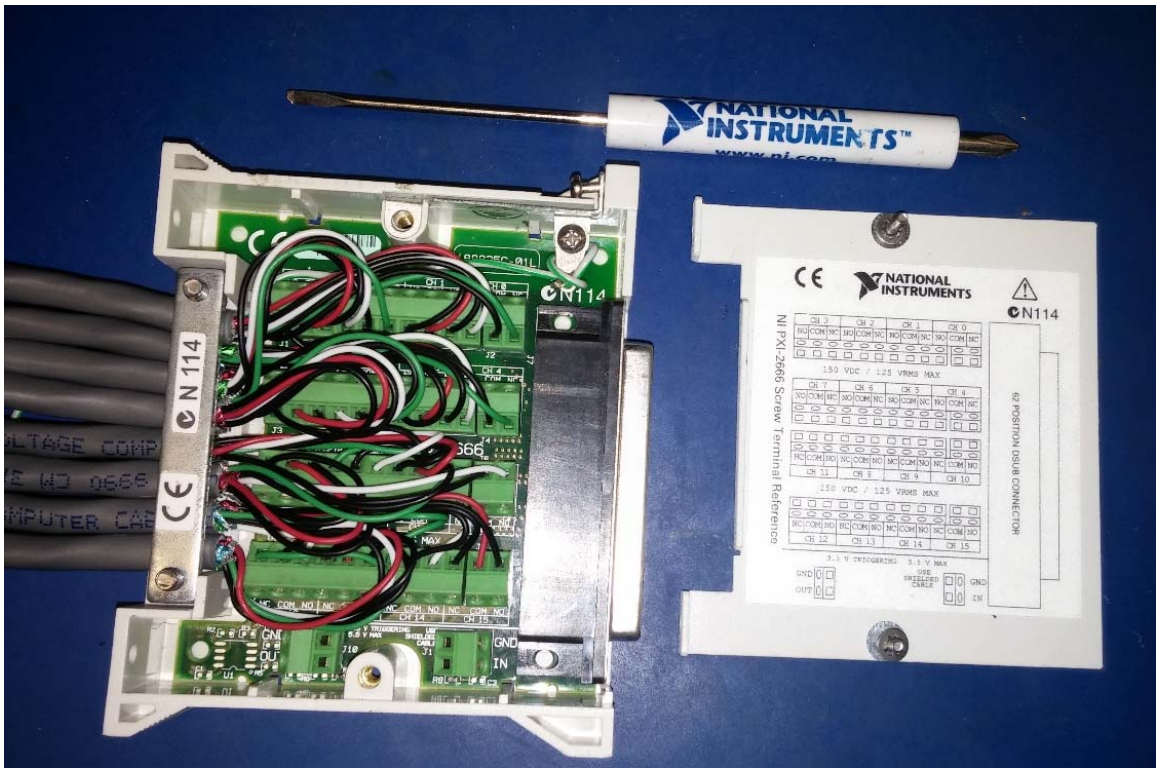

Figure 3.4: Wiring and Pinout Diagram for NI TB-2666 Servicing the NI PXI 2256 Module.

3.2 EQUIPMENT ENHANCEMENTS

3.2.1 Voltage Attenuation for Very Small-Strain RC Testing

Since low driving voltages are needed for very small-strain RC testing, V_{min} of the DAQ can limit the resolution of the signal being sent to the drive coils. For instance, a driving voltage of 0.5 to 5 mV (approximately $5x10^{-6}$ % to $5x10^{-4}$ % shear strain) is preferred for obtaining the maximum shear modulus (G_{max}) in low-amplitude RC testing and, for 16-bit resolution, an input voltage of 1 mV would induce noise at a level 1.5% of the maximum amplitude. As this noise level is sent to the drive coils, unintended excitation of the system occurs and is recorded by the sensors.

A method for utilizing the full range of the DAQ system and sending a clearer signal to the drive coils was used that involved a voltage attenuator. An analog voltage attenuator is comprised of two or more resistors, with resistors in series and in parallel to the analog output path. The configuration of an analog voltage attenuator is shown in Figure 3.5.

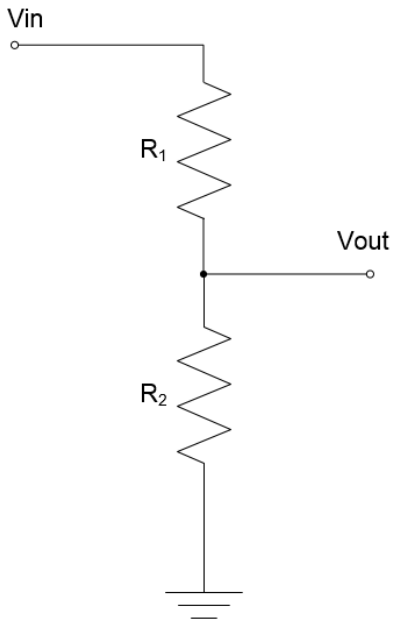

Figure 3.5: Circuitry of an Analog Voltage Attenuator.

The voltage attenuation from V_{in} to V_{out} can be calculated by:

$$V_{out} = V_{in} \cdot \frac{R_2}{(R_1+R_2)} \tag{3.2}$$

where R_1 and R_2 are resistors in units of Ohms. For example, with V_{in} of 10 V, R_1 of 126 Ohm, and R_2 of 1.4 Ohm, V_{out} would be 0.1 V or 1/100. This type of circuit enables full use of ±10 V and ±5 V analog output voltage ranges of the NI PXI-6251 and provides high resolution of the output signals at low excitation voltages. A photograph of a built voltage attenuator is shown in Figure 3.6. An example of the increase in excitation resolution by using voltage division, where in one case the DAQ system drove a 1 mV with no voltage division and the other case where the DAQ system drove 100 mV with 1/100 voltage division, is shown in Figure 3.7.

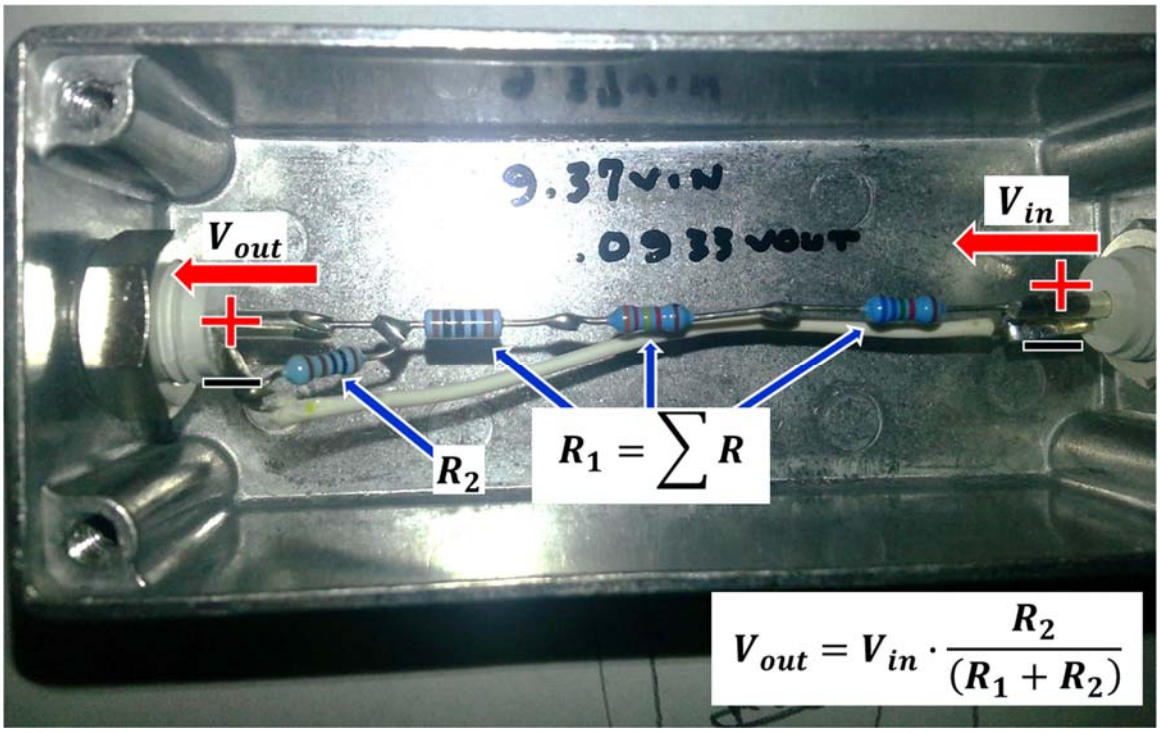

Figure 3.6: Photograph (from Robert Kent) of a Typical Voltage Attenuator Circuit.

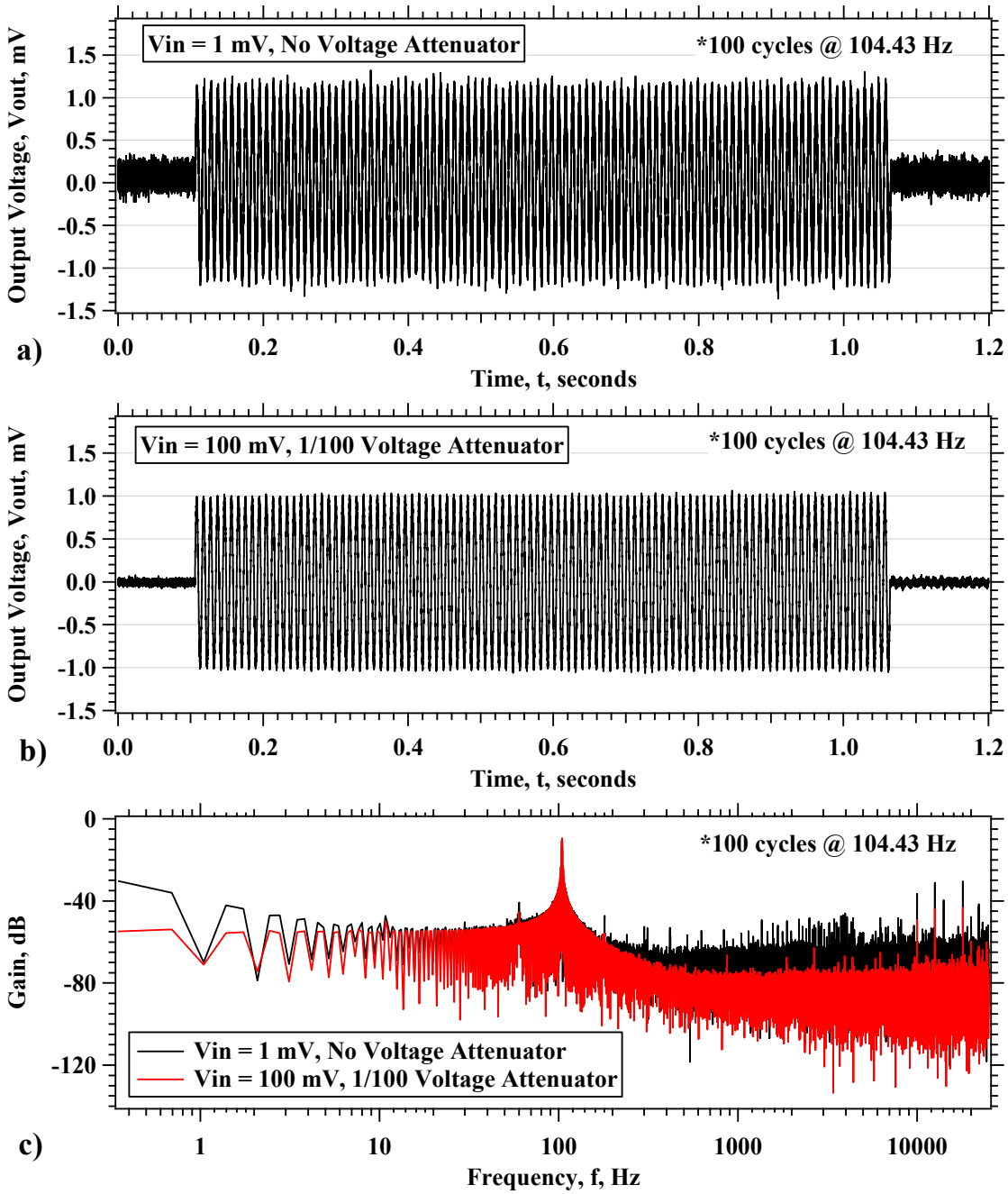

Figure 3.7: a) Measurement of 1 mV Input with +/- 5 V Analog Output Range, b) Measurement of 100 mV Input Voltage with 1/100 Voltage Attenuator and +/- 5 V Analog Output Range, and c) Spectral Gains of Signals with and without Voltage Attenuator.

When observing the spectral response of the signals (as shown in Figure 3.7) with and without the voltage attenuator, considerable improvement is seen when using the voltage attenuator at frequencies both above and below the frequency of excitation (i.e. frequency of interest). Consideration must be made for the increase in RCTS equipment damping (F_{EMF} = equipment-generated back ("resisting") electromagnetic force) that is a function of the impedance of the drive coils and any connected analog circuitry. Thus, low-resistance resistors are selected for voltage division to limit the introduction of resistance along this circuit. Further details regarding the calculation and influence of equipment damping is discussed in preceding chapters.

3.2.2 Passive AC Coupling (Highpass) Filtering

When a charge amplifier (Columbia Research Laboratory Model 4102M) is used to convert charge from an accelerometer (Columbia Research Laboratory Model 302-6), to a recordable voltage, a DC offset has been found to be introduced by the charge amplifier unit. The presence of this DC voltage may require increasing the voltage range of the channel and consequently reducing resolution of the recorded signal. If measurements are performed with AC Coupling/Highpass filtering capabilities, the DC offset can be removed and allows selecting of one of the smaller ± 10, 5, 2, 1, 0.2, or 0.1 V software programmable ranges for the analog input channels of the NI PXI-6251. As discussed herein, inexpensive construction of a circuit that acts as a highpass filter is a reliable and cheap alternative to expensive DSA equipment. More importantly, the highpass filter circuit can be customized to the specific sensor or application of interest.

A typical first-order, passive, high-pass analog filter can be constructed with circuitry comprising of a capacitor and a resistor. With a highpass filter, a cutoff frequency can be calculated using the values of capacitance (C) in the capacitor and resistance (R) in the resistor. The capacitor possesses high reactance at low frequencies acting as an open

circuit for frequency content of the signal at very low AC frequencies or with DC, i.e. attenuating low analog frequency content. Above the cutoff frequency the reactance of the capacitor is sufficiently reduced and acts more as a short circuit allowing the input signal to pass directly through the circuit. The configuration of a high-pass filter is shown in Figure 3.8.

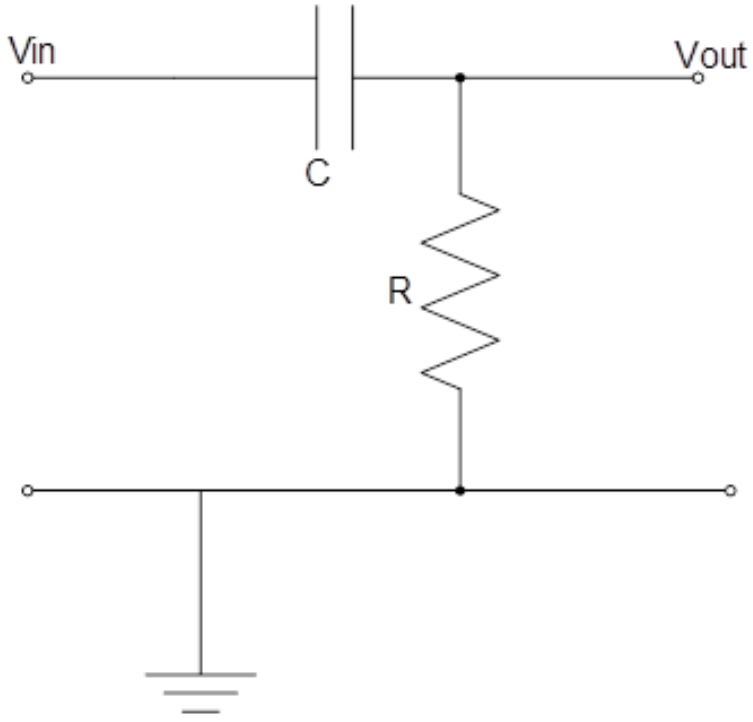

Figure 3.8: Circuitry of a First-Order High-Pass Analog Filter.

The characteristics of a highpass filter can be determined using several expressions for calculating the cutoff frequency, f_C, phase shift, φ (introduced by the filter), and attenuation (Gain) of the signal over the frequency range of interest. The cutoff frequency is given by:

$$f_c = \frac{1}{2\pi RC} \tag{3.3}$$

where R is resistance in units of Ohms of the resistor and C is capacitance in units of Farads (F). The phase shift of the signal is a function of frequency and is found using:

$$\varphi(f) = \tan^{-1}\left(\frac{1}{2\pi fRC}\right) \tag{3.4}$$

where f is frequency in units of Hertz (Hz). The Gain of the signal is found by conducting intermediate calculations of impedance of the capacitor, X_C, and impedance of the circuit, Z, which are found by:

$$X_c = \frac{1}{2\pi fC} \tag{3.5}$$

$$Z = \sqrt{R^2 + X^2} \tag{3.6}$$

$$\text{Gain} = 20 * \log\left(\frac{R}{Z}\right) \tag{3.7}$$

where the Gain is in units of decibels (dB).

One of the circuits designed as an AC Coupler for use in resonant column testing (of the two RCTS testing systems developed) has a capacitance of 15,000 nF and a resistance of 98,900 Ohms. The theoretical phase shift and gain vs. frequency of this filter was calculated and measured to ensure proper characteristics and minimal interference with signals acquired in RC testing. The characteristics of the highpass analog filter is shown in Figure 3.9.

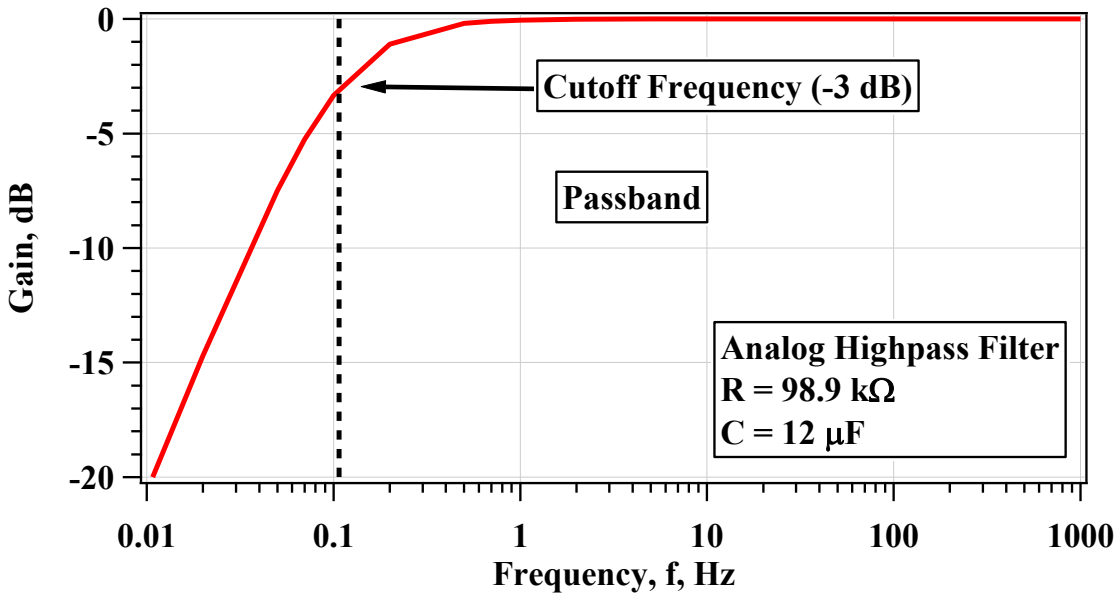

a) Comparison of Gain with Frequency of a Theoretical High-Pass Filter.

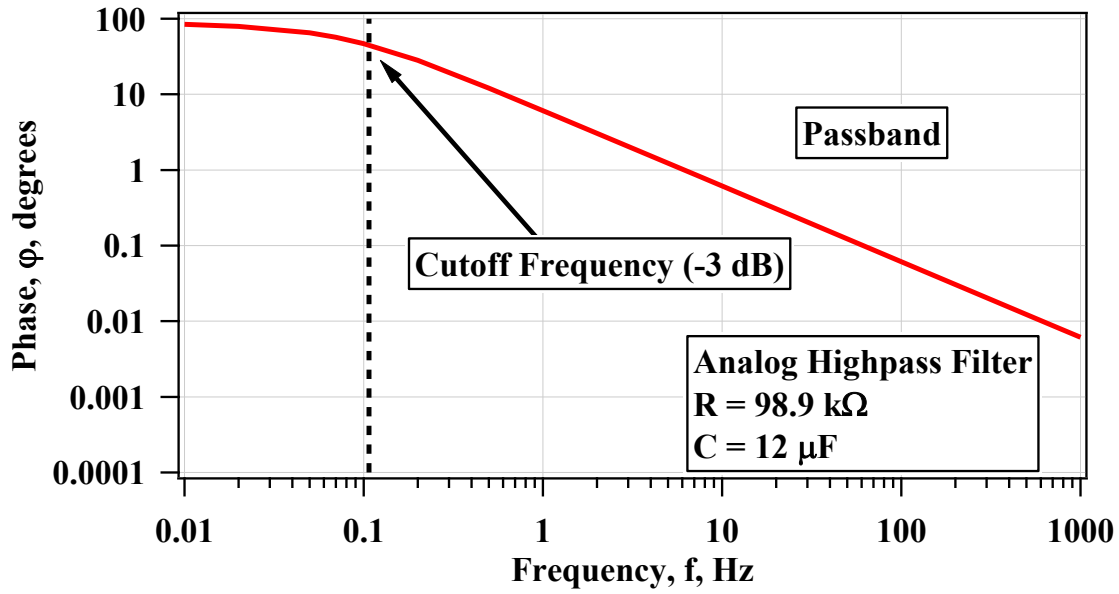

b) Comparison of Phase Shift with Frequency of a Theoretical High-Pass Filter.

Figure 3.9: Theoretical Gain and Phase Shift Characteristics of a 15,000 nF and of 98,900 Ω Highpass Filter.

The AC coupler circuit can be easily constructed and evaluated. A photograph of one of the AC coupler circuits employed in this study in shown in Figure 3.10. In addition, an experiment was conducted to provide a demonstration of one of the AC coupler analog circuits for conditioning a signal acquired from an accelerometer. In the experimental demonstration, an accelerometer was excited using an electrodynamic shaker. The shaker was powered to excite at 200 Hz with an acceleration of 0.168 g. Signals acquired directly from the charge amplifier unit and through the AC coupler circuit are presented in Figure 3.11.

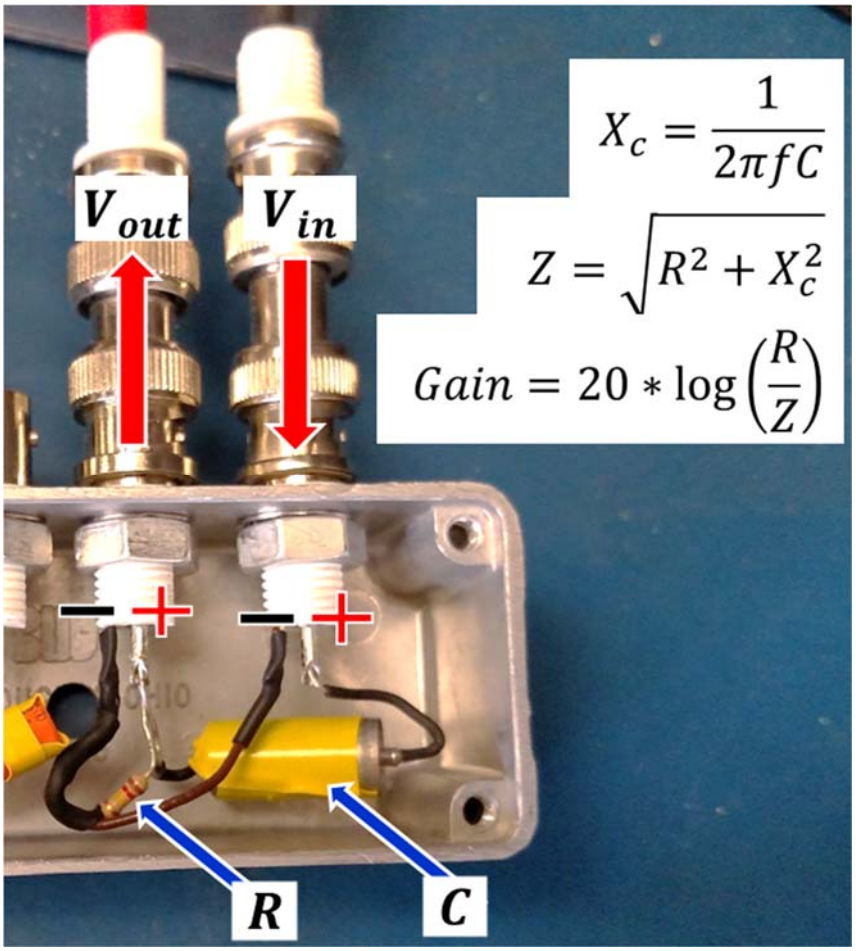

Figure 3.10: Photograph of one of the AC coupler circuits employed in this study

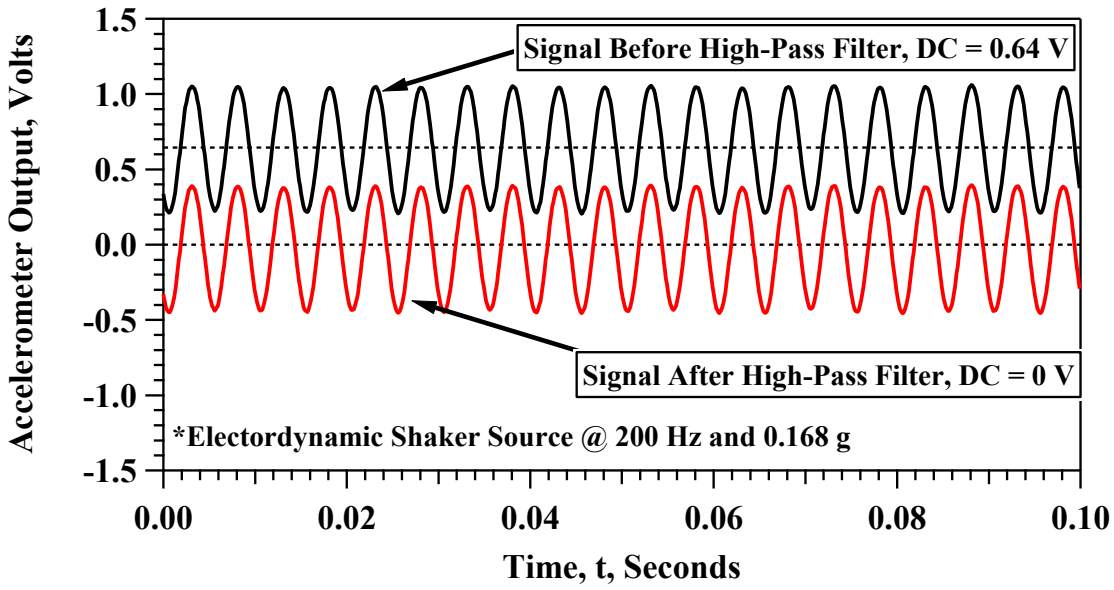

Figure 3.11: Electrodynamic shaker powered to excite at 200 Hz with an acceleration of 0.168 g. Signals are acquired directly from the charge amplifier unit and through the AC coupler circuit.

3.3 ADDITIONAL SENSOR SIGNAL ACQUISITION

In previously built RCTS testing systems, different motion sensors were used for the RC test and the TS test. An accelerometer was exclusively used in the RC test, while proximitors were exclusively used in the TS test. The accelerometer is not a preferred sensor to use in TS testing because the signal output from the sensor is considerably small, relative to the proximitors, at the low frequencies used in TS testing (< 2 Hz). Furthermore, because of configuring permanent AC coupling circuits for the accelerometer sensors, the accelerometer cannot be used in the range of frequencies at which TS testing is conducted (below 2 Hz). An electrodynamic shaker was used to test the proximitor and accelerometer sensors at the same peak harmonic displacement, but over the range of frequencies that are potentially used in the RC test. A graphical presentation of the electrodynamic shaker experiment is provided to show the voltage outputs from the proximitor and accelerometer sensors over a range of frequencies that may occur in the RC test (Figure 3.12).

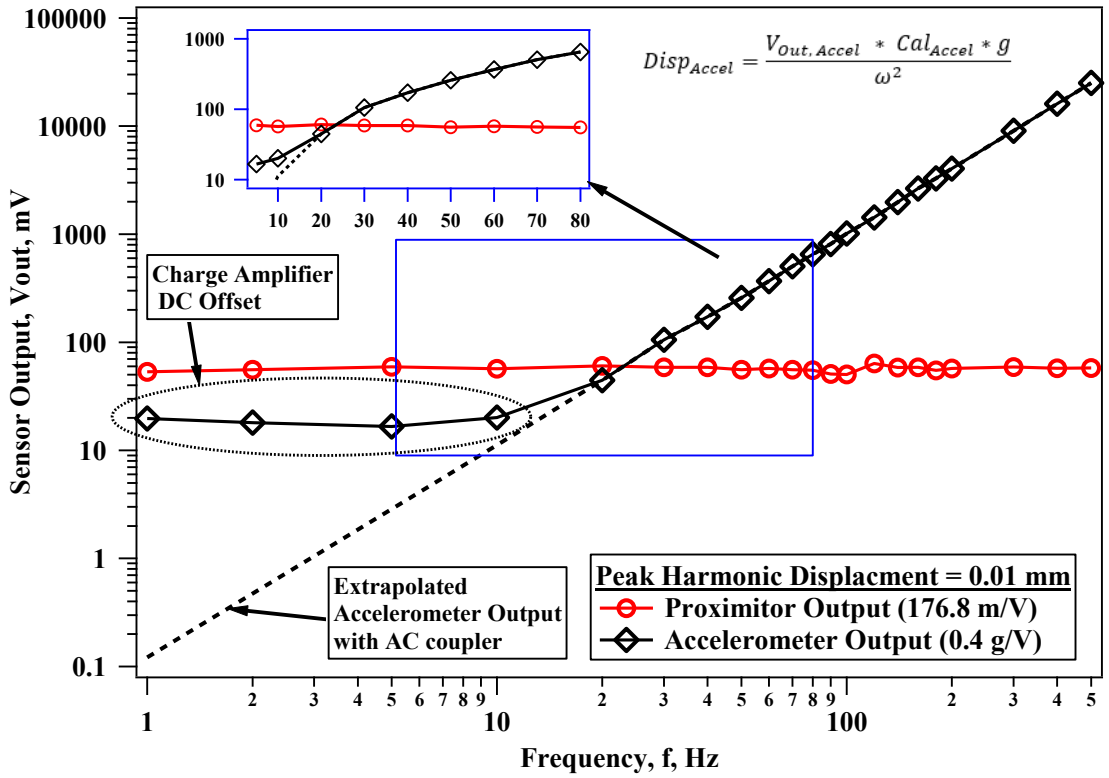

Figure 3.12: An electrodynamic shaker used to excite proximitor and accelerometer sensors at the same peak sinusoidal displacement, over the range of frequencies, and the outputs from each sensor are plotted.

The increased voltage output of the accelerometer at higher frequencies relative to the proximitors causes a reduction in the influence of background noise at higher frequencies. However, in RCTS testing, two proximitors are used which helps to cancel out background noise that is equally present in both of the sensor outputs. Electrical background noise at 60 Hz is more effectively removed by the proximitors, but is prevalent in the accelerometer output. Thus, the proximitors are the preferred sensors when RC testing contains testing frequencies that are at or below 60 Hz. Results from RC testing on a poorly-graded sand with clay (SP-SC) specimen is shown for three confining pressures, where two of the pressures resulted in the specimen possessing resonance near 60 Hz, and the third pressure resulted in the specimen possessing resonance around 110 Hz, as shown

in Figure 3.13, Figure 3.14, and Figure 3.15, respectively. The proximitors effectively remove 60 Hz background noise when RC testing contains excitation frequencies near 60 Hz. The accelerometer possesses much less background noise relative to the proximitors at excitation frequencies greater than 60 Hz. Both the results from the accelerometer and proximitors are provided during RC testing and the operator can select the more accurate data when reducing RC testing results.

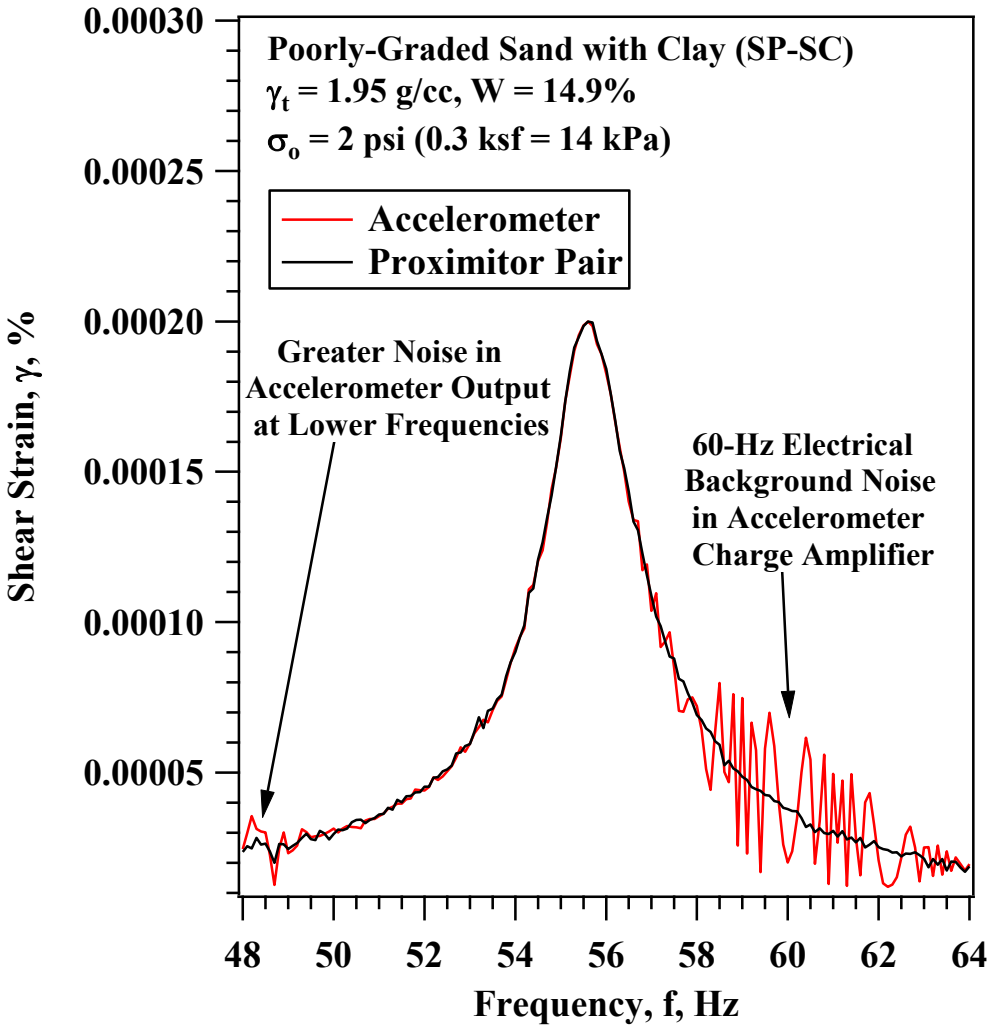

Figure 3.13: Results from RC Testing on a Poorly-Graded Sand with Clay Specimen (SP-SC) at a Confining Pressure of 0.14 atm; Showing the Influence of 60-Hz Background Noise of the Accelerometer Output.

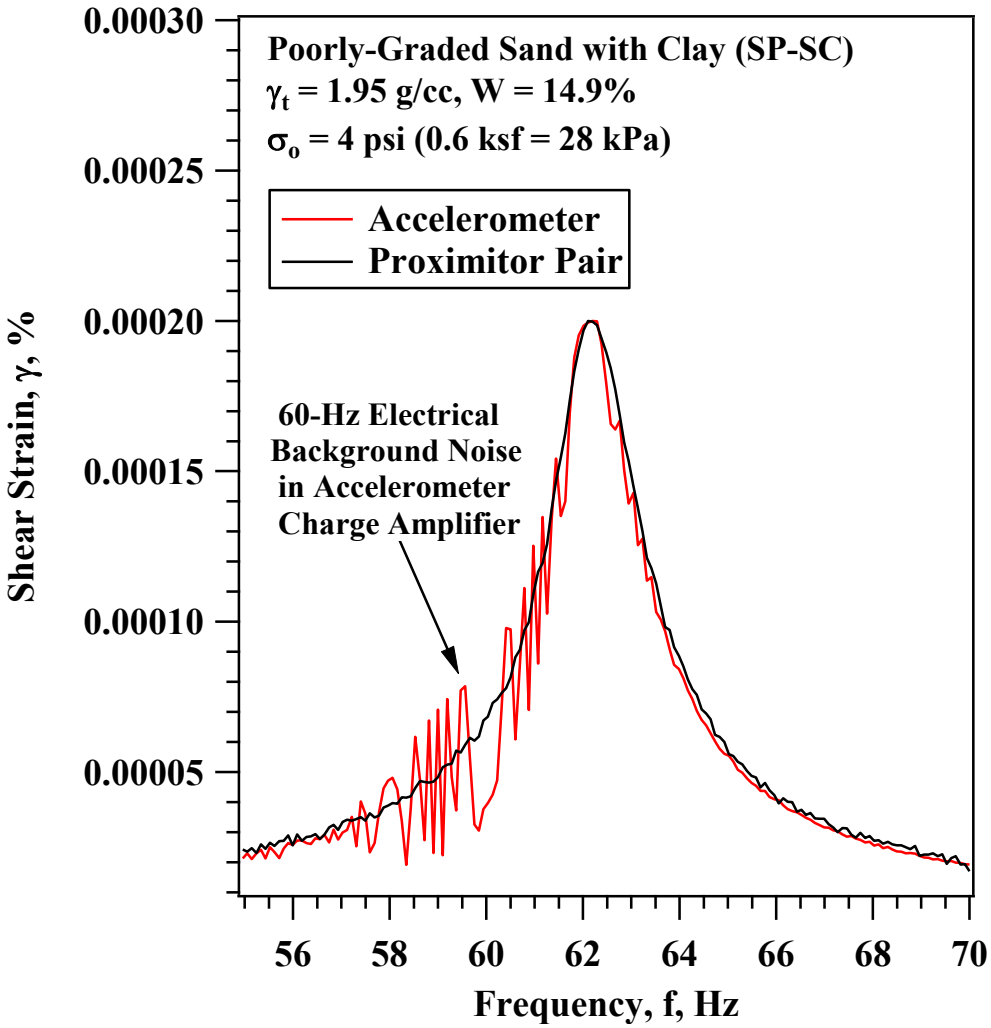

Figure 3.14: Results from RC Testing on a Poorly-Graded Sand with Clay Specimen (SP-SC) at a Confining Pressure of 0.27 atm; Showing the Influence of 60-Hz Background Noise of the Accelerometer Output.

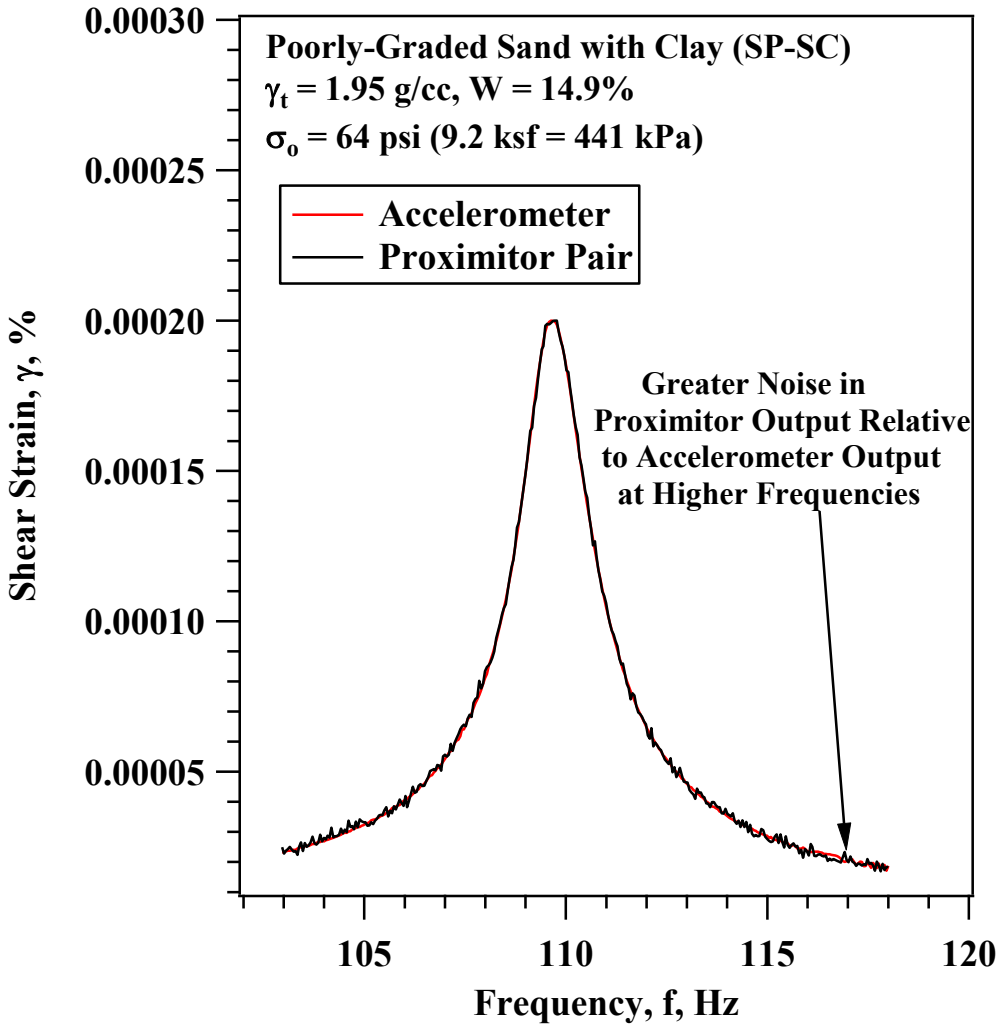

Figure 3.15: Results from RC Testing on a Poorly-Graded Sand with Clay Specimen (SP-SC) at a Confining Pressure of 4.35 atm; Showing the Influence of Background Noise on the Proximitor Output Relative to the Accelerometer Output at Higher Frequencies.

3.4 FULL SYSTEM CONFIGURATION

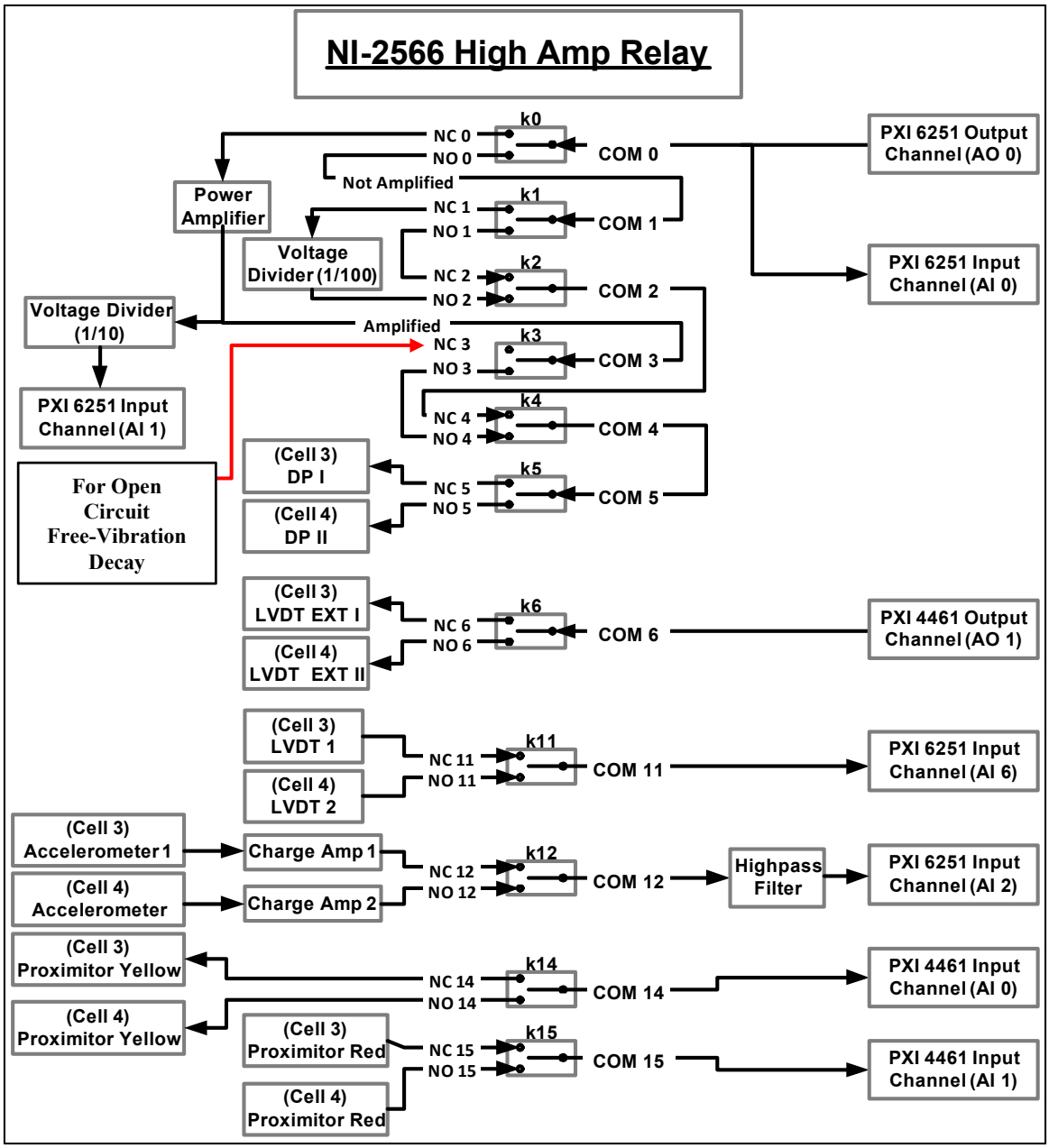

Figure 3.16: Wiring diagram of the NI PXI-4461 and NI PXI-6251 routing to the NI PXI-2566.

Figure 3.17: NI PXI-6251, NI PXI-2256, and NI PXI-4461 Housed within the NI PXI-1033 Chassis with and Connected Through a Custom Made Circuit Board.

3.5 SUMMARY

The configuration and synchronization of the modules housed in the NI PXI-1033 Chassis, along with the enhancements discussed in this chapter, allow increased efficiency in RCTS testing and simultaneous, real-time, and highly accurate monitoring during RCTS testing. The capabilities and combinations of components discussed in this chapter, for the most part eliminate the need for peripheral equipment allowing a “single unit” system for control and monitoring of at least two RCTS devices. In addition to the testing capabilities employed in the control and monitoring systems discussed herein, each of the modules

used possess state-of-the-art resolution, sampling rates, synchronization, and customizability.

Enhancements were added to the control and monitoring system include a voltage attenuator and AC coupling circuit. The voltage attenuator was added to allow to send a clearer signal to the drive coils during testing. When observing the spectral response of the signals with and without the voltage attenuator, considerable improvement is seen when using the voltage attenuator at frequencies both above and below the frequency of excitation (i.e. frequency of interest). The AC coupling circuit was added to remove the DC offset produced by the accelerometer charge amplifier, which allows a smaller analog voltage range to be selected. The AC coupling circuit is inexpensive to construct can be customized to the specific sensor or application of interest. These enhancements also allow RCTS tests to be conducted at lower shearing strains and with a high degree of proficiency than have been achieved in past systems or other studies.

In previously built RCTS testing systems, different motion sensors were used for the RC test and the TS test. The accelerometer is not a preferred sensor to use in TS testing because the signal output from the sensor is considerably small, relative to the proximitors, at the low frequencies used in TS testing (< 2 Hz). The increased voltage output of the accelerometer at higher frequencies relative to the proximitors causes a reduction in the influence of background noise at higher frequencies. However, in RC testing, using two proximitors help to cancel out background noise that is equally present in both of the sensor outputs. The usefulness of either sensor depends on the frequencies excited during the test. The system discussed in this dissertation acquires signals from both the accelerometer and proximitor sensors during RC testing. The operator can select the more accurate data when reducing RC testing results.

Chapter 4

Studies of the RCTS Device Characteristics Involving Electronic Circuitry and Equipment-Generated Damping

4.1 INTRODUCTION

When sending a current through a coil of wire, a magnetic field is generated due to Ampere's Law (Serway and Jewett, 2003). This magnetic field becomes concentrated when wire is wound into the shape of a coil. In the RCTS device, a series of eight wire coils are configured at a constant radial distance symmetrically around the circumference of a stainless steel support plate as shown in Figure 4.1. The coils are glued into mounting brackets, which are secured to the stainless steel support plate. Four magnets that are secured to arms of a drive plate are positioned within the eight coils so that one coil is around each end of the magnet. The magnets are positioned within the coils in such a way that an electromagnetic solenoid is formed. When current is passed through the coils, a magnetic field is generated that shares the same orientation as the magnetic poles of the permanent magnets. The interacting magnetic fields of the coils and the magnets generate a force based on the rules of electromagnetism. The solenoids are configured radially from the central axis of the drive plate, which forms an electromagnetic toque motor. The drive plate is mounted on and secured to the top cap which is placed on top of a cylindrical test specimen. This arrangement allows torque to be applied along the central axis of a cylindrical specimen once a confining pressure has been applied. The electromagnetic toque motor is controlled using an excitation voltage from a control system that can supply static, slow cyclic, or higher frequency torsional loads over a large range of force levels (10^{-6} to 0.7 ft-lbs) and excitation frequencies (0 to 500 Hz). A conceptual schematic of the torsional driving system is shown in Figure 4.2.

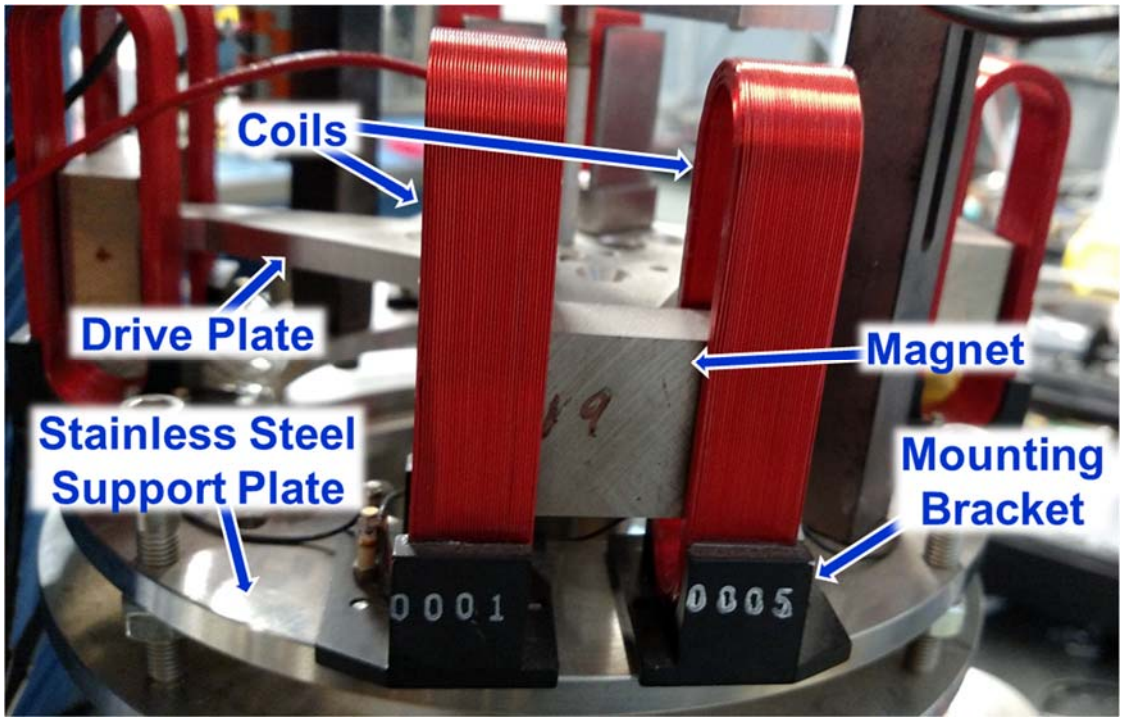

Figure 4.1: Photograph of a Side View of The Torsional Driving System.

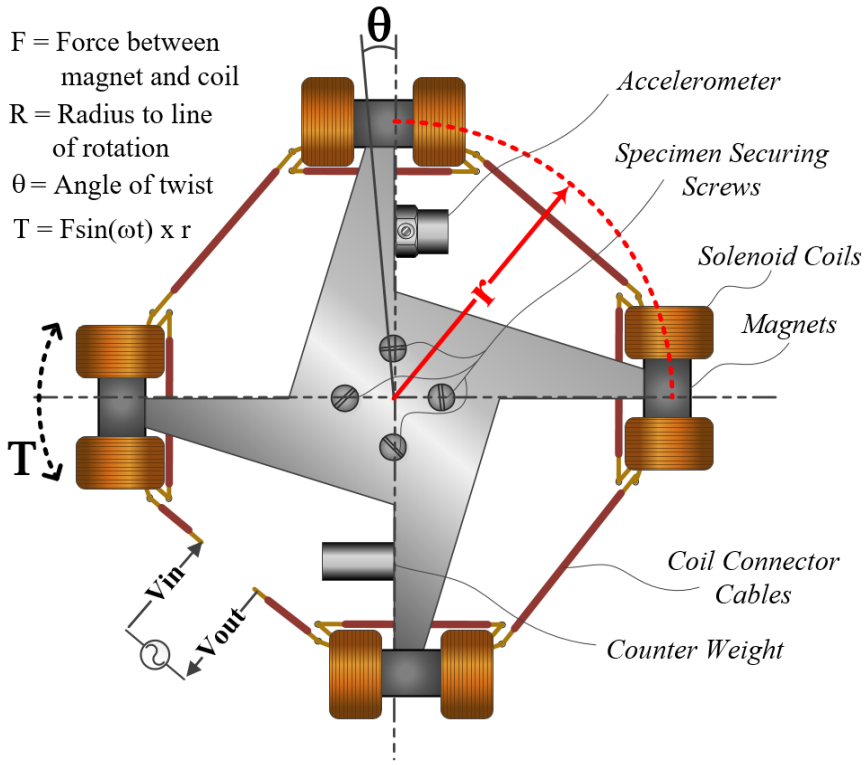

Figure 4.2: Conceptual schematic of The Torsional Driving System.

Several electrical characteristics of the toque motor are important to understand when conducting RCTS testing. Based on Ohm's law (Serway and Jewett, 2003), the circuitry of the RCTS coils causes a reduction in the electromagnetic toque as a function of frequency when voltage is used to control the excitation. Furthermore, a phase shift is introduced as a function of frequency between the excitation voltage and current within the coils. These electronic characteristics exist because the series of coils contain a net static electrical resistance and the coils themselves act as inductors, which introduces a net frequency dependent resistance (i.e. impedance). The electronic characteristics of the electromagnetic toque motor have implications for both RC and TS testing, which are evaluated and presented in section 4.2. The primary effect of the phase shift brought on by the circuitry torque motor is equipment-generated damping in the TS test, which is discussed and evaluated in section 4.3.

Several of the electromagnetic characteristics of the toque motor that are also important to understand when conducting RCTS testing. Because the magnetic solenoids that make up the electromagnetic toque motor operate over a large range of frequencies, the magnetic flux created by the permanent magnets is constantly changing relative to the coils. Based on Faraday's law (Serway and Jewett, 2003) of electromagnetic induction, changing magnetic flux through a conductor generates an electric current in that conductor. As characterized by Lenz's law (Serway and Jewett, 2003), this induced current (i.e. eddy currents) generates a magnetic field that opposes the source that created the changing magnetic flux. In effect, the movement of the permanent magnets through the coils creates a force that resists the movement of the magnets. Since electromagnetic induction is rate dependent, the force that repels the movement of the magnets within the solenoids is proportional to the rate of that movement, i.e. proportional to the velocity of the magnets. Due to the radial movement of the drive plate, the velocity in the solenoids is an angular

velocity and thus is proportional to the angular frequency of the electromagnetic toque motor. The primary effect of the rate dependent electromagnetic induction is equipment-generated damping in the RC test, which is discussed and evaluated in section 4.4 and section 4.5.

4.2 ELECTRICAL SYSTEM CHARACTERISTICS

4.2.1 Circuity of the RCTS Drive Coils

Comprising the complete circuit used in the RCTS system, the drive coils consists of several in-series coils of wire. The coils themselves act as resistors, due to the long length of the wires used to make up the coils, and impose impedance on the circuit. With the use of alternating current (AC), the coils act as inductors, imposing additional impedance on the circuit. Since the impedance of an inductor increases with frequency, as the frequency increases the current carried at a constant voltage decreases. Consequently, in the RCTS system, the ratio of current to voltage decreases as frequency increases and a phase shift, between the excitation voltage and the current in the coils, is induced.

The relationship between the excitation voltage, V, and the input current, I, sent through the drive coils is given by:

$$\mathrm{I} = \frac{\mathrm{V}}{\mathrm{R}+\mathrm{j}\omega\mathrm{L}} \tag{4.1}$$

where R is the equivalent resistance of the drive coils, j is the complex operator $\sqrt{-1}$, ω is the circular frequency of the driving voltage, and L is the equivalent inductance of the coils. The phase shift, φ, between the excitation current and voltage is found by:

$$\varphi = \tan^{-1}\left(\frac{\omega\mathrm{L}}{\mathrm{R}}\right) \tag{4.2}$$

and the absolute magnitude of the current, $|I|$, is calculated by:

$$|I| = \frac{|V|}{\sqrt{R^2+(\omega L)^2}} \tag{4.3}$$

where the denominator represents the overall impedance, Z, of the system and the numerator is the absolute value of the excitation voltage sent through the dive coils.

4.2.2 Evaluating Circuity of the RCTS Drive Coils

The RCTS drive coils need to be evaluated to understand the characteristics of the electrical circuits that they form and the effects that these characteristics have on the performance of the RCTS testing device. First, a single coil was evaluated for the value of resistance and inductive impedance, a photograph of the coil and conceptual schematic are shown in Figure 4.3. The coil was evaluated using an AC voltage input from an Agilent 33120A Waveform Generator at 1 V with frequencies ranging from 10 to 1000 Hz. The output voltage and current were measured using two separate Agilent 34411A Multimeters and confirmed using a Wavetek Meterman 37XR. The value of resistance, R, was found to be 5.9 Ohm and the inductance, L, was found to be 2.97 mH. The coils in the RCTS device are wired in series and thus the total resistance and total inductance are the sum of the coil resistances and inductances, respectively based on Ohm's Law (Serway and Jewett, 2003). There are 8 coils in the RCTS device and thus the total resistance and total inductance, based on the single coil evaluated, are expected to be 47.2 Ohm and 23.75 mH, respectively. A photograph and circuitry concept for a RCTS drive plate is shown in Figure 4.4. The values of R and L for a UT drive plate were measured and reported in Menq (2003) to be 48 Ω and 23.6 mH, respectively. The results of the experiment on a single coil, the theorized 8 coil configuration, and results from Menq (2003) are shown as relationships between the excitation voltage, V, and the input current, I, and the phase, φ, between the current and the excitation voltage as seen in Figure 4.5 and Figure 4.6, respectively.

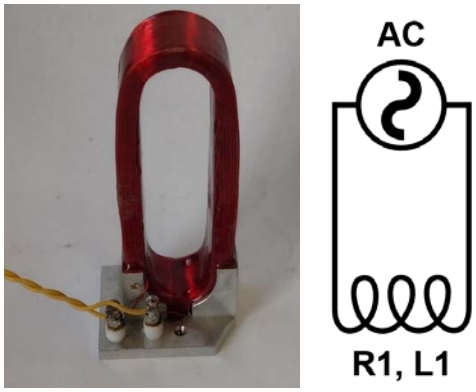

Figure 4.3: Photograph of a single RCTS coil and conceptual circuit schematic.

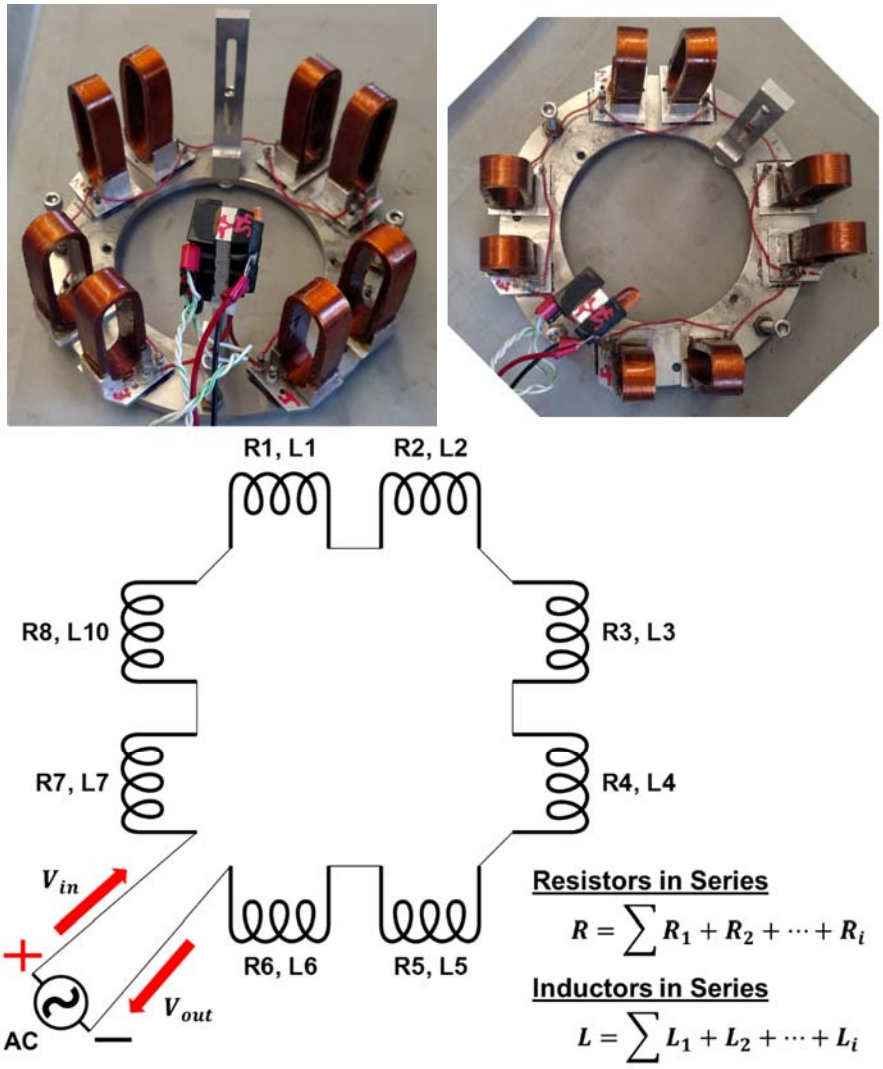

Figure 4.4: Photograph of a RCTS coils and conceptual circuit schematic.

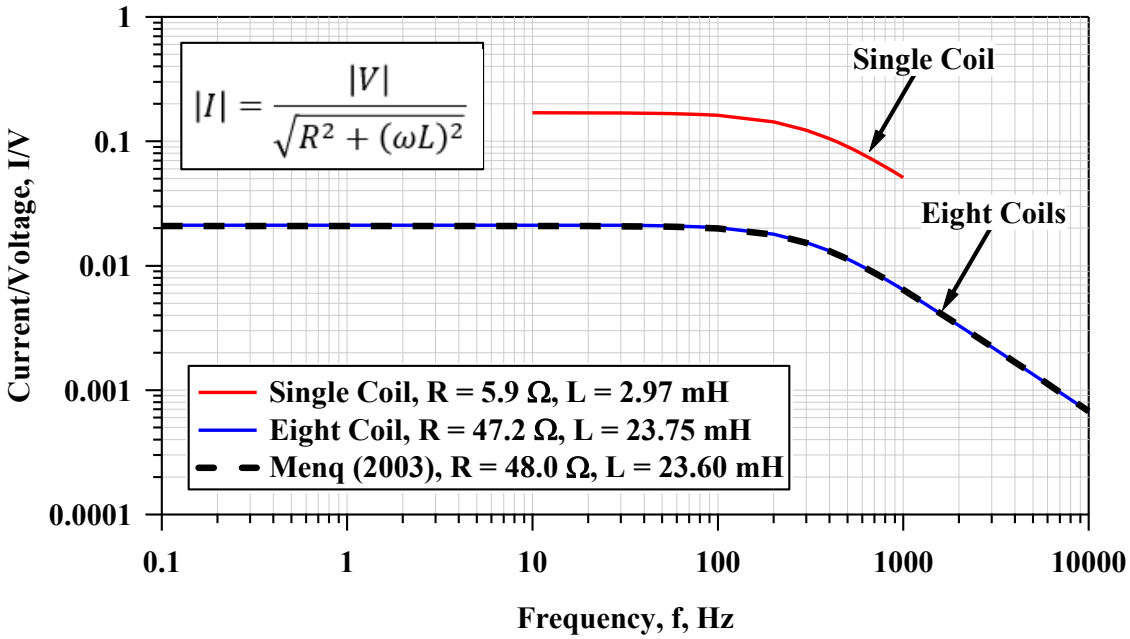

Figure 4.5: Variation of Current/Voltage with Excitation Frequency.

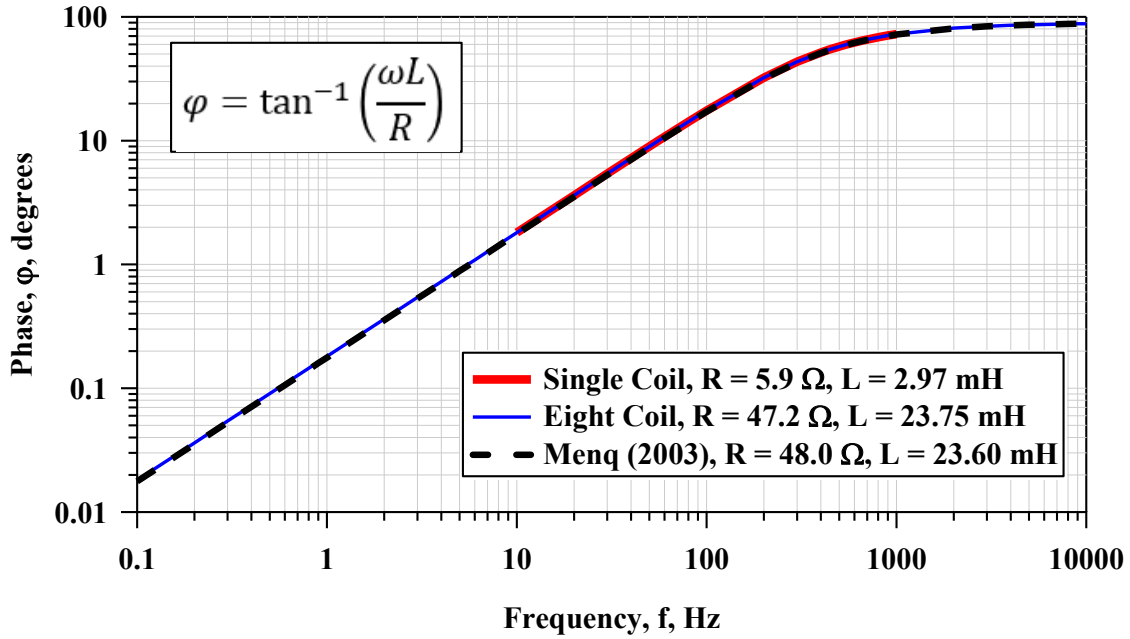

Figure 4.6: Variation of Phase Shift with Excitation Frequency.

The importance of knowing the drive plate circuitry and electrical characteristics pertain to the equipment-generated damping and reduction of the input current relative to the excitation voltage. In TS testing, the phase between the input shear stress and corresponding shear strain is responsible for the area of the hysteresis loop. The phase introduced by the drive plate circuitry is traditionally calibrated for by testing a metal specimen at several excitation frequencies ranging from 0.1 to 5 Hz. The hysteretic damping of the metal specimen is assumed to be negligible and the resulting damping that is measured is used to develop a frequency dependent calibration factor. In TS testing, the frequency dependent calibration factor is used to subtract the equipment-generated damping at the corresponding excitation frequency.

The reduction of the input current relative to the excitation voltage becomes important for more advanced analysis in RC testing and is most important at higher frequencies (> 50 Hz). In the advanced analysis of RC testing results, a torque calibration factor is used to determine the level of torque applied to a specimen based on the excitation voltage. Thus, the calibration factor is given in units of torque per peak excitation voltage (e.g. ft-lb/V). Since the current is the electrical component that is directly related to the toque generated by the drive plate, a correction is needed to account for the reduction in the current relative to the excitation voltage with increasing frequency of excitation. The correction is relatively small, but is important for an increasingly accurate analysis of nonlinear soil and rock dynamic behavior.

4.3 EQUIPMENT-GENERATED DAMPING IN TS TESTING

During TS testing, a phase shift is introduced because the signal used in the analysis of the hysteresis loop corresponds to the excitation voltage, and the current, which is directly proportional to the torque driven by the drive plate, lags the excitation voltage. Thus, the actual torqueing motion has a phase delay and the function used for analysis of the hysteresis loop does not. In traditional TS testing, the phase introduced by the drive plate circuitry is calibrated for by testing a metal specimen at several excitation frequencies ranging from 0.1 to 5 Hz. The hysteretic damping of the metal specimen is assumed to be negligible and the resulting damping that is measured is used to develop a frequency dependent calibration factor.

To demonstrate that the TS equipment-generated damping is caused by the drive plate circuitry, two sinusoids are theoretically created where one has a phase shift equal to the phase shift brought on by impedance as discussed in the previous section. The phase shift, φ, between the current and excitation voltage is given by:

$$\varphi = \tan^{-1}\left(\frac{\omega L}{R}\right) \tag{4.4}$$

where ω is the excitation frequency in radians/second, L is the inductance of the drive coils which was 23.75 mH, and R is the resistance of the drive coils which was 47.2 Ohms. The two theoretically simulated sinusoids are:

$$\text{Stimulus} = \sin(\omega t) \tag{4.5}$$

$$\text{Response} = \sin(\omega t - \varphi) \tag{4.6}$$

where φ is the phase shift introduced by the drive coil circuitry as shown in Figure 4.6. Using the stimulus and response sinusoids, the calculation for hysteretic damping ratio, D, from the hysteretic loop is calculated as:

$$D = \frac{W_d}{(4\pi \times W_s)} \tag{4.7}$$

where W_d is the energy dissipated in one cycle of loading and W_s is the peak strain energy stored in the specimen.

The results of the calibration, where hysteretic damping is measured with the metal specimen, are compared with the hysteretic damping theorized using the drive coil phase shift, as shown in Figure 4.7. The hysteretic damping theorized using the drive coil phase shift is essentially the same as the hysteretic damping measured with the metal specimen, which was originally known as the TS equipment-generated damping. Furthermore, the range of excitation frequencies that are calibrated for are from 0.01 to 20 Hz, which is a larger range than the range used in TS testing (i.e. 0.1 to 5 Hz). The hysteretic damping theorized using the drive coil phase shift shows nearly perfect agreement with the hysteretic damping measured with the metal specimen as seen in Figure 4.7. For practical purposes, the traditional calibration procedure using the metal specimens to develop a calibration factor to correct for the drive coil phase shift is a simpler process then evaluating the electrical characteristics of the drive coil circuitry. Furthermore, the traditional method is shown to ascertain the same results as the more complex analysis of evaluating the electrical characteristics of the drive coil circuitry. Understanding the electrical characteristics of the drive coils becomes important for a more advanced analysis in RC testing.

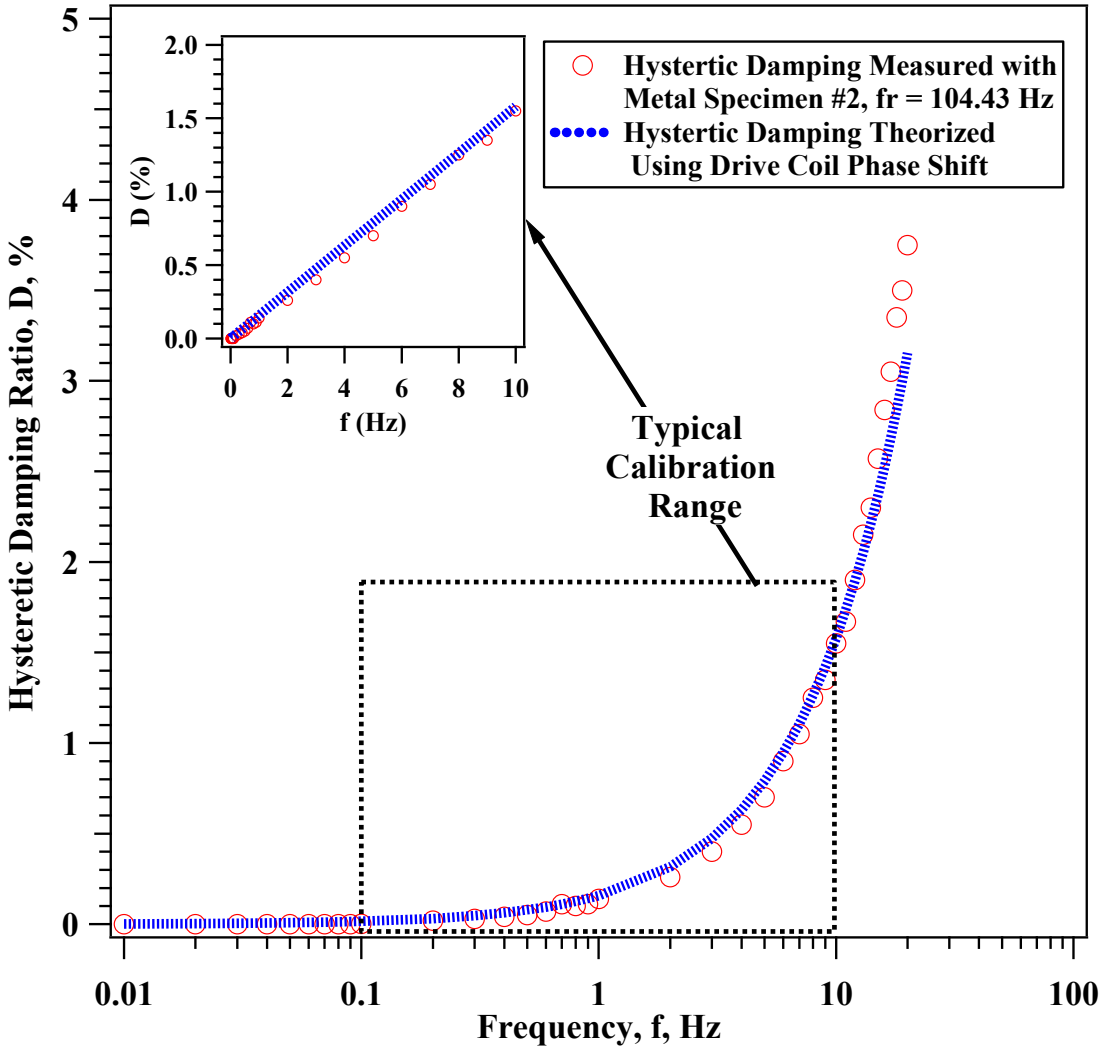

Figure 4.7: Results of the Calibration Showing Hysteretic Damping Measured with Metal Specimen #2 Compared with the Hysteretic Damping Theorized using the Drive-Coil System Phase Shift Associated with the Eight Drive Coils.

4.4 EQUIPMENT-GENERATED DAMPING IN RC TESTING

As discussed earlier, equipment-generated damping is caused by the drive coils of the RC system in combination with the magnets moving through the coils at a certain velocity. The magnets moving through the coils creates eddy currents i.e. back-generated current that is proportional to the velocity at which the magnets are travelling through the coils. The eddy currents generated in the coils due to the velocity of the magnets is referred to as the back generated electromagnetic force (back EMF) in Menq, F.Y (2003), Menq, J. and Rix (2003), Cascante et al. (2003), Wang et al. (2003), and Sasanakul (2005). There are many approaches discussed in these studies for understanding and correcting for back EMF. In this section several experiments are conducted to provide a better understanding of back EMF, the effect of Back EMF when performing RC tests, and a practical approach to correct for Back EMF.

4.4.1 Open-Relay Free-Vibration Damping Method

The dynamic magnetic interactions that produce back EMF are dependent on the drive coils forming a closed circuit. Once the circuit is opened, back EMF no longer occurs because an open circuit has a resistance approaching infinity and, with I=V/R, the back EMF is zero. This effectively eliminates the presence of back EMF and the true material damping ratio of the specimen can be measured. In this section, zero back EMF is accomplished by using a programmable mechanical relay that opens at a specified time increment after the driving force is shut off after exciting the specimen at the resonant frequency and reaching steady-state vibration.

The device used is the NI PXI-2566 High-Current General-Purpose Relay Switch which has a maximum operating time rated at 4.4 ms. An operating time of 4.4 ms would be one full cycle at a frequency of 227 Hz and a half-cycle at 114 Hz. However, the typical operating time in the NI PXI-2566 is rated at 2 ms, which greatly improves these

characteristics and, in this study, the relay operation time does little to limit measurements that can be taken from a free-vibration decay test where equipment-generated damping has been eliminated by using a relay switch.

4.4.2 Open-Relay Used for Drive Plate Calibration Methods

Traditionally, equipment-generated damping was determined by measuring half-power damping and free-vibration decay damping of several metal specimens, where the material damping was assumed to be zero. Each of the metal specimens was manufactured with different inner and outer diameters. There are a total of eighteen metal specimens, one approximately 5 in. tall, eleven approximately 7 in. tall, and six approximately 8.5 in. tall. The varying dimensions and distribution of mass of the metal specimens give each a unique resonant frequency and material damping ratios; however, the material damping values are very small relative to soils and rock and the back EMF of the RCTS device.

A calibration program was created that would determine the resonant frequency and half-power damping from the sweep test. The resonant frequency and half-power damping was then used to excite the specimen at resonance at a number of cycles commensurate with the material damping ratio. Once steady-state vibration is reached the excitation is abruptly suspended and free-vibration occurs. Based on the half-power damping ratio measured from the sweep test, the system was allowed to undergo free-vibration decay to approximately 50% of the steady-state shear strain level, at which point the relay was opened and the system continued to attenuate in free-vibration without the influence of equipment-generated damping. Since a minor delay occurs due to the relay operation, the cycle before and after the relay operation is removed from the analysis. This type of test was done for several of the metal specimens to determine the true material damping ratio of the metal specimens and actual back EMF. Three of these tests are

presented for Metal Specimens 2, 6, and 8 shown in Figure 4.8, Figure 4.9, and Figure 4.10, respectively.

The process of using a relay switch to measure free-vibration decay damping of the metal specimens without the influence of back EMF does so accurately and is repeatable. This process was done with ten of the metal specimens and the true back EMF was calculated from the difference between the damping measured from the system (i.e., sum of the back EMF and metal specimen damping) and the damping measured from the metal specimen. This calibration experiment was done with UT drive plates #4 and #9 and the results of which are shown in Figure 4.11 and Figure 4.12, respectively.

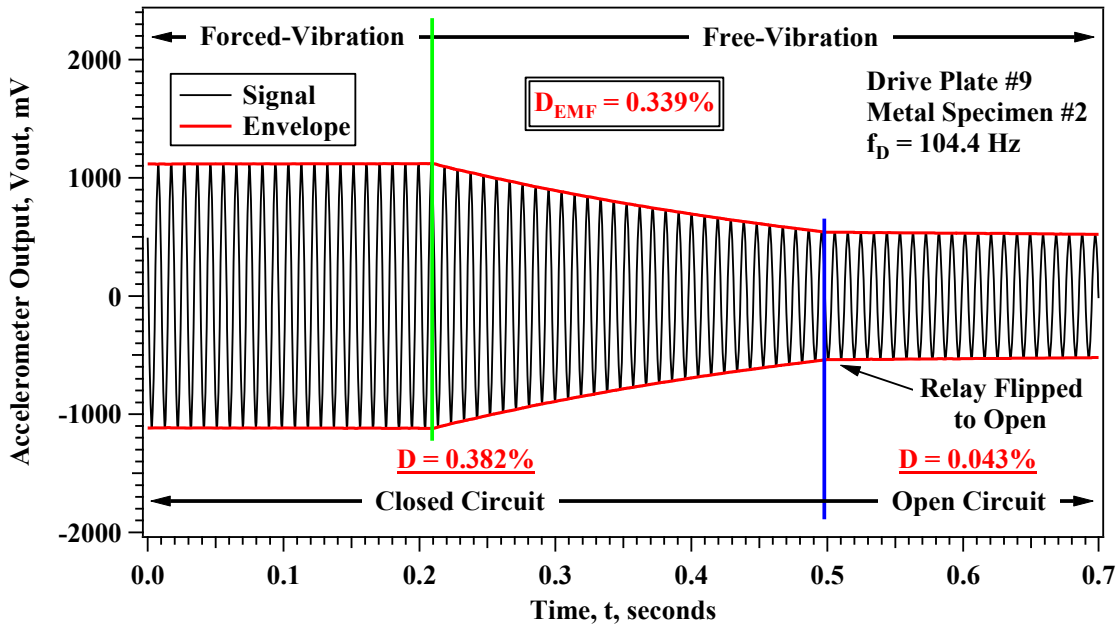

Figure 4.8: Free-Vibration Decay of Metal Specimen #2 with and without the Influence of Back EMF of Drive Plate #9.

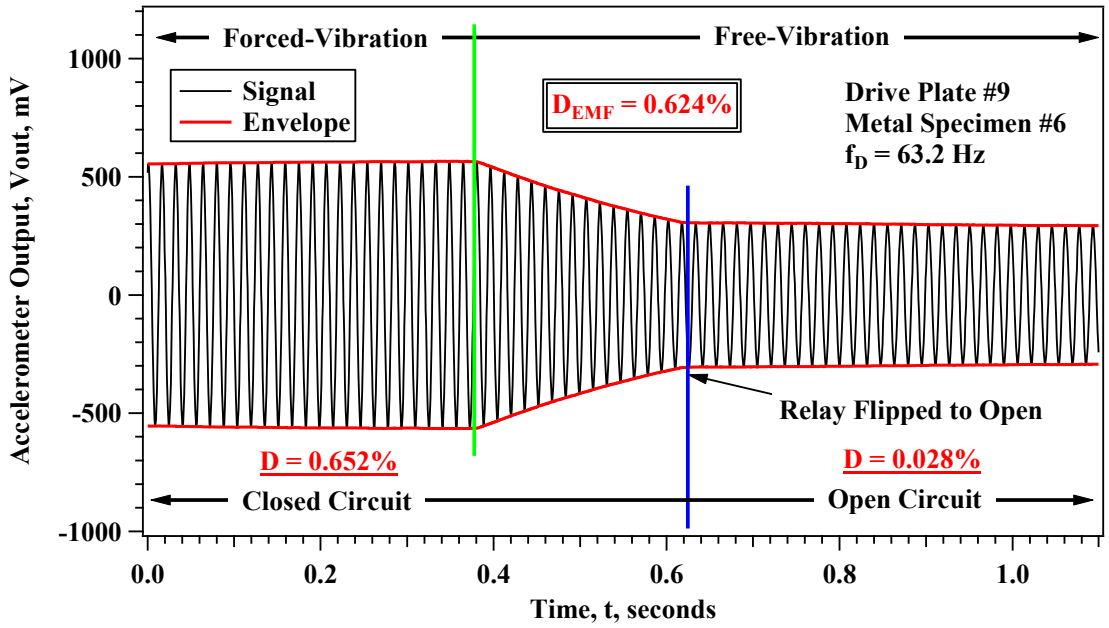

Figure 4.9: Free-Vibration Decay of Metal Specimen #6 with and without Influence of Back EMF of Drive Plate #9.

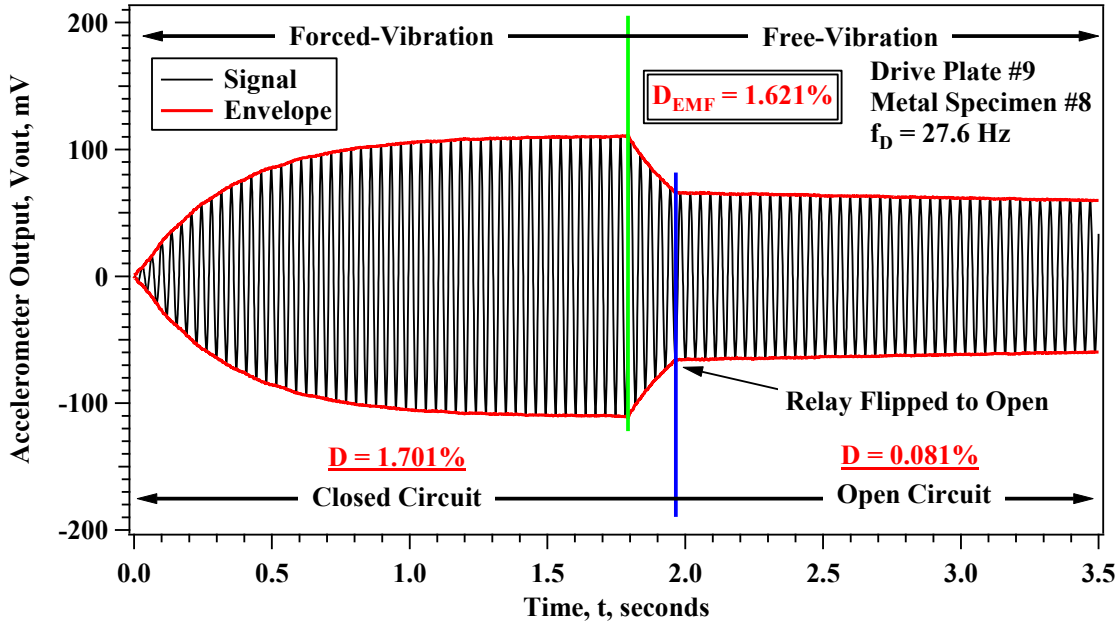

Figure 4.10: Free-Vibration Decay of Metal Specimen #8 with and without Influence of Back EMF of Drive Plate #9.

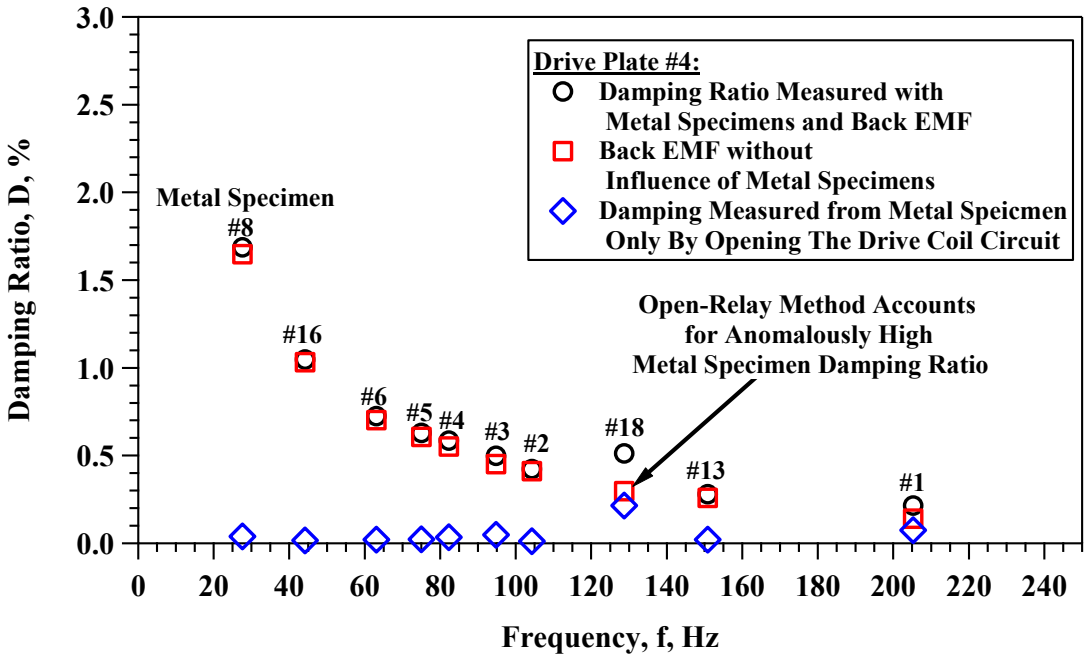

Figure 4.11: Free-Vibration Decay of Ten Metal Specimens with and without Influence of Back EMF of Drive Plate #4.

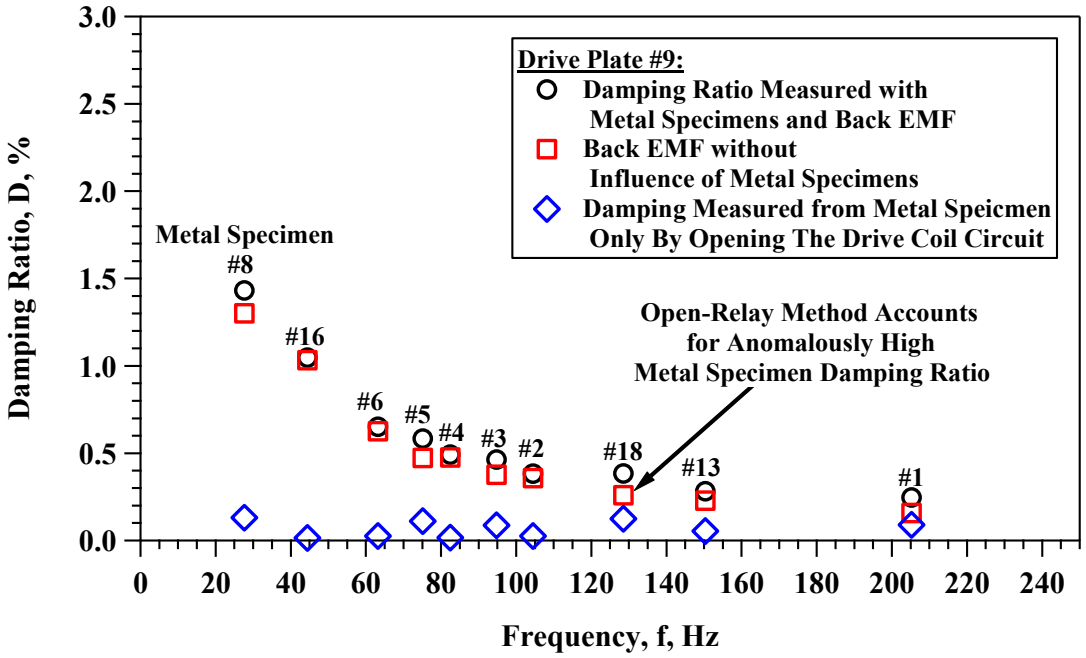

Figure 4.12: Free-Vibration Decay of Ten Metal Specimens with and without Influence of Back EMF of Drive Plate #9.

4.4.3 Differences between Calibration Factors for Equipment-Generated Damping Measured with and Without Metal Specimens

For many years, the back EMF calibration at UT has been done by measuring damping with three metal specimens and assuming the damping of the metal specimens was negligible. The three metal specimens typically used are #2, 6, and 8. The back EMF calibration factor, for the free-vibration decay damping calibration factor (FVD_{eq}), was calculated as:

$$FVD_{eq} = FVD_{eq,cal} * f^{-1} \quad (4.8)$$

where $FVD_{eq,cal}$ is the calibration factor sought in the procedure and f is the resonant frequency of the specimen being tested. Using the data presented for UT Drive Plate #4 in the previous section, the calibration factor is $FVD_{eq,cal}$ = 47.4. The calibration factor is determined based on testing metal specimens #2, 6, and 8, which have resonant frequencies of 104.3, 63.1, and 27.6 Hz, respectively.

The same function is used to determine the calibration factor for the ten metal specimens that were evaluated using the processes involving the open relay to determine the actual back EMF. Using the same data presented for UT Drive Plate #4 in the previous section, but for the actual back EMF, the calibration factor is $FVD_{eq,cal}$ = 47.6. A comparison between the two methods is shown in Figure 4.13. Based on the comparison from the original and open relay calibration methods, there is little difference between the methods. The original method overestimates the back EMF by 0.28% for Drive Plate #4 (0.83% for Drive Plate #9), which is generally negligible during RC testing. When testing materials with material damping ratios below 0.1%, this slight overestimation should be considered. The original method is far simpler to perform and is recommended for general equipment-generated damping calibration and corrections to damping ratios measured during RC testing.

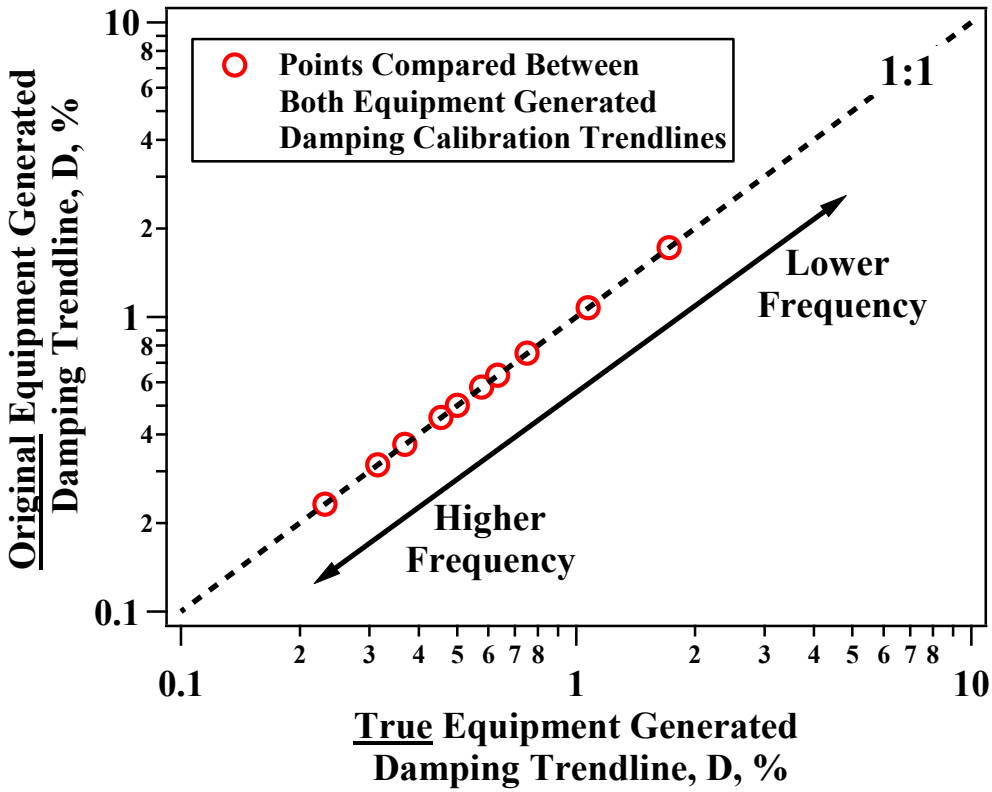

Figure 4.13: Comparison Between Original and True Equipment-Generated Damping Calibration Trendlines.

4.5 METHODS FOR DETERMINING THE EQUIPMENT-GENERATED DAMPING COEFFICIENT, C_{EQ}

Traditional correction for equipment-generated damping has been done by correcting the damping ratio measured during RC tests, as opposed to the damping coefficient. Another approach involves correcting the damping coefficient within the damping ratio measured during the test. This method is much more complicated when testing soil specimens, but is necessary for a more fundamental understanding of equipment-generated damping and for advanced analysis of RC test results. In this section, the equipment-generated damping coefficient is determined using several experimental approaches to demonstrate that equipment-generated damping is purely velocity dependent

and behaves as a viscous dashpot in a single-degree-of-freedom (SDOF) system. The first approach involves measuring the total system damping (i.e. including back EMF) using the metal specimens, determining their individual torsional spring constants and mass-polar moment of inertias, and back calculating to get the damping coefficient for each test. The second approach involves using the amplitude of the torsional excitation and the magnitude of the response curve to determine the overall damping ratio and then using the individual torsional spring constants and mass-polar moment of inertias to back calculate the damping coefficient from each test. The third approach involves isolating the experiment from the RCTS drive system to simply using one of the RCTS coils and an electrodynamic shaker to control the velocity and displacement of the magnet within the coil. Each of these methods converges on the same result showing that equipment-generated damping in the RCTS device is purely velocity dependent and can be accurately represented by a viscous damping coefficient. Furthermore, that the traditional methods of calibrating and correcting for equipment-generated damping are suitable for standard RCTS testing applications. The more detailed aspects of this evaluation are important for more advanced analysis of nonlinear dynamic RC test results.

4.5.1 Equipment-Generated Damping Coefficient: via Torsional Spring Constants

The excitation system and dynamic response of the cylindrical specimens are equivalent to a single-degree-of-freedom (SDOF) system vibrating in torsion, which is defined as:

$$J_o\ddot{\theta} + c_t\dot{\theta} + k_t\theta = T\sin(\omega * t) \tag{4.9}$$

where J_0 is the mass polar moment of inertia of the specimen, c_t is the torsional damping coefficient, k_t is the torsional spring constant, T is the torque applied to the specimen, ω is the angular frequency of the torqueing function, t is time, and $\ddot{\theta}$, $\dot{\theta}$, and θ are angular

acceleration, angular velocity, and angle of twist, respectively. In the case of RC testing on the metal specimens, the mass polar moment of inertia, J_o, is the sum of the mass polar moments of inertia of the drive plate, J_{DP}, the fastening disc on top of the metal specimen, J_{TC}, and the stem of the metal specimen, J_{spec}. Using a formulation from Richart, Hall, and Woods (1970), the undamped natural frequency, ω_n, is given by:

$$\omega_n = \sqrt{\frac{k_t}{J_o}} \text{ and } k_t = \omega_n^2 * J_o \tag{4.10}$$

where as defined earlier, k_t is the torsional spring constant and J_o is the sum of the mass polar moment of inertia. The torsional damping ratio is given by:

$$D = \frac{c_t}{c_c} \tag{4.11}$$

where c_t is the torsional damping coefficient and c_c is the critical damping coefficient in torsion. The critical damping coefficient in torsion is given by:

$$c_c = 2\sqrt{k_t * J_o} \tag{4.12}$$

The dimensions and masses of the metal specimens are known and the circular resonant frequencies, ω_n, are determined from RC testing. The undamped circular natural frequency given in Richart, Hall, and Woods (1970) and is related to the circular resonant frequency as:

$$\omega_r = \omega_n\sqrt{1 - 2D^2} \tag{4.13}$$

where because the damping ratio measured in RC testing on the metal specimens is below 2%, the difference between ω_n and ω_r is less than 0.04% and thus $\omega_n \approx \omega_r$. Therefore, the torsional spring constant for each of the metal specimens can be determined and the

torsional damping coefficient can be back calculated using the formulations presented above, which can be reduced by the following:

$$c_t = D * c_c = D * 2\sqrt{k_t * J_o} = D * 2\sqrt{(\omega_n^2 * J_o) * J_o} = 2D\omega_n J_o \qquad (4.14)$$

where c_t is the damping coefficient caused by the "back EMF".

The damping coefficient determined in this method includes the damping coefficient of the metal specimens themselves, which may lead to a slight overestimation of the damping coefficient brought on by the equipment-generated damping (back EMF). To correct for the damping coefficient of the metal specimens, the damping ratios determined by the open-relay free-vibration method presented in Section 4.4 can be used to eliminate damping of the metal specimens. The results of these two methods are presented together and along with the methods discussed in the following two subsections, as seen in Figure 4.19.

4.5.2 Equipment-Generated Damping Coefficient: via Magnitude Response Factor

The damping coefficient brought on by the equipment-generated damping can also be determined by knowing the torque, T, excited on the specimen and the magnitude response factor, M, measured during RC testing on the metal specimens. In Richart, Hall, and Woods (1970), M is given as:

$$M = \frac{A}{\frac{Q_o}{k}} = \frac{1}{\sqrt{\left[1-\left(\frac{\omega}{\omega_n}\right)^2\right]^2+\left[2D\left(\frac{\omega}{\omega_n}\right)\right]^2}} \qquad (4.15)$$

where in the case of a torsional system, A is the angle of twist, θ, Q_o is the torqueing function, T, and k is the torsional spring constant k_t. This equation can be simplified to relate the damping ratio to the maximum magnitude response factor, M_{max} as:

$$M_{max} = \frac{\theta_{max}}{\frac{T}{k_t}} = \frac{1}{2D\sqrt{1-2D^2}} \approx \frac{1}{2D} \tag{4.16}$$

where D can be solved directly as a function of M_{max} using the quadratic formula. However, the difference between the direct solution and the approximate solution of $M_{max} = 1/2D$ is negligible for the damping ratios found in RC testing. The angle of twist is determined in the RC test using an accelerometer with calibration factor, F_{cal}, of 2.48 pk-V/g and is located 2 in. (0.1667 ft) from the center of rotation. Therefore the angle of twist can be determined using the peak output voltage of the accelerometer, V_{accel}, and is calculated by:

$$\theta = \tan^{-1}\left[\frac{\left(V_{accel} * 32.174\ ^{ft}/_{sec^2}\right)/(F_{cal}*\omega^2)}{0.1667\ ft}\right] \tag{4.17}$$

The torque, T, applied comes from a calibration factor that is based on the excitation voltage sent to the electromagnetic torque motor and is in units of ft-lb/V. This torque calibration factor is adjusted for the current reduction caused by the circuitry of the drive coils as discussed in Section 0. Therefore, the damping coefficient brought on by equipment-generated damping can be found by:

$$C_t = D * C_c = \frac{T}{2*\theta_{max}*k_t} * 2\sqrt{k_t * J_o} = \frac{T*\omega_n*J_o}{\theta_{max}*\omega_n^2*J_o} = \frac{T}{\theta_{max}*\omega_n} \tag{4.18}$$

The result of this methods is presented along with the methods discussed in the subsequent section and preceding subsection, as seen in Figure 4.19.

4.5.3 Equipment-Generated Damping Coefficient: via One Coil Evaluation

An experiment was designed and constructed to move a magnet within a coil at a specified displacement and frequency while measuring the current and voltage generated in the coil due to eddy currents. The experiment was displacement controlled using an accelerometer and proximitor to verify the peak sinusoidal displacement. At each peak sinusoidal displacement, the excitation frequency was varied over a range of 10 to 300 Hz.

The experiment was repeated at five peak sinusoidal displacements of 0.01, 0.02, 0.05, 0.1, and 0.5 mm. Photographs of the experiment and annotations of the components involved in the experiment are presented in Figure 4.15 and Figure 4.15.

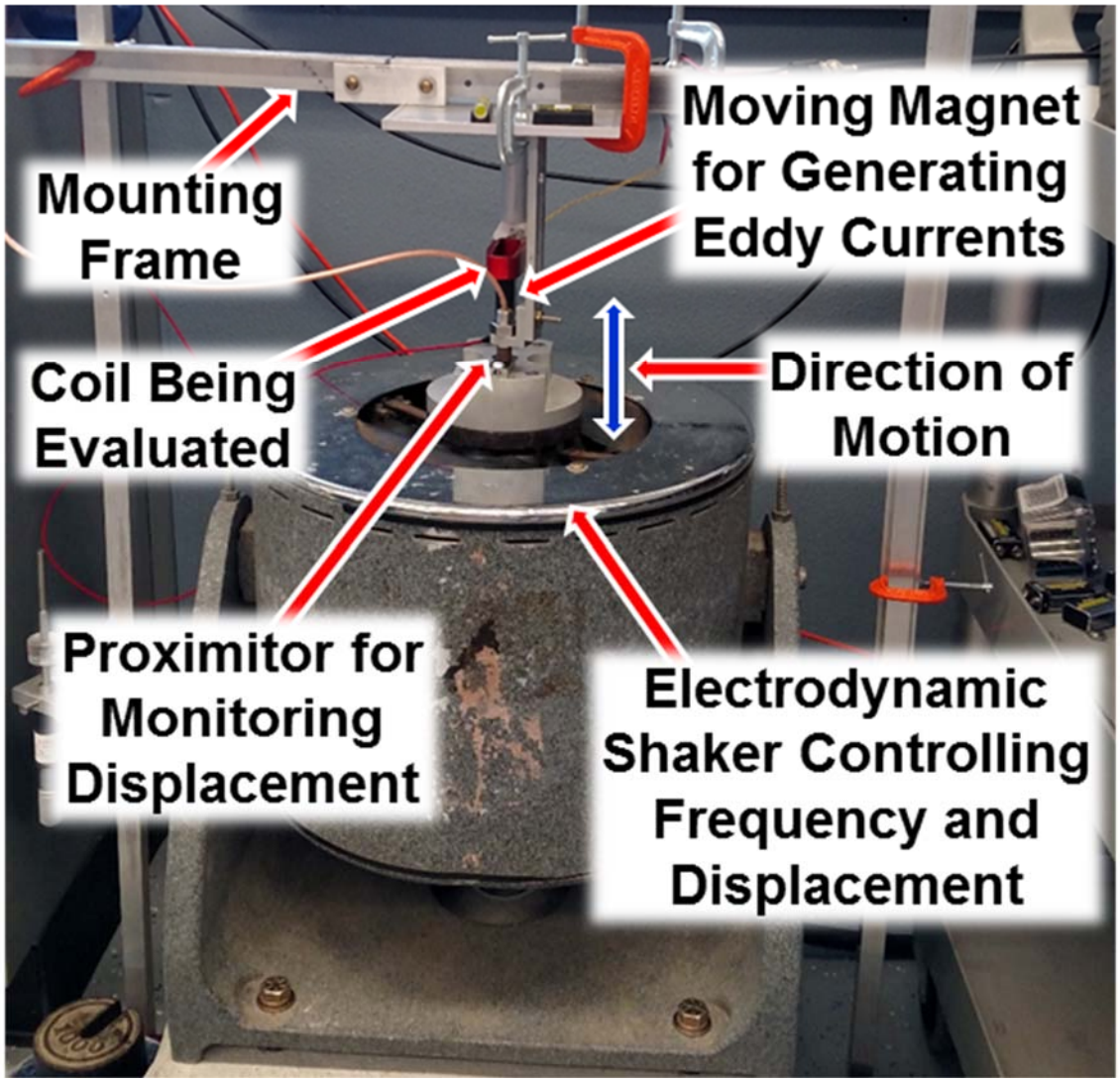

Figure 4.14: Experimental Setup of Electrodynamic Shaker used to Move a Magnet within a Coil at Specific Displacements and Frequencies (i.e. controlled velocity).

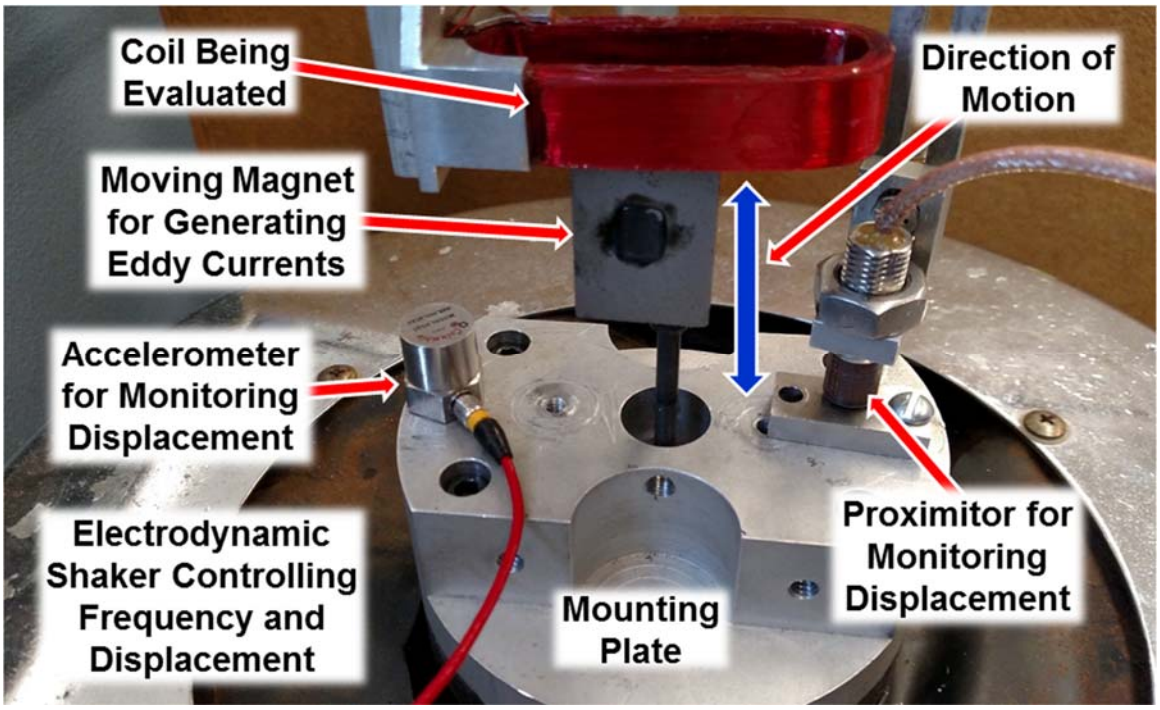

Figure 4.15: Details of Experimental Setup of Electrodynamic Shaker used to Move a Magnet within a Coil at Specific Displacements and Frequencies (i.e. controlled velocity) with Sensors Shown for Measuring Displacements.

The results of the experiment are first presented as a comparison of the generated eddy currents, I_{ec}, with peak sinusoidal displacement, d, at specific frequencies and a comparison of the generated eddy currents with frequency at specific peak sinusoidal displacements, which are presented in Figure 4.16 and Figure 4.17, respectively.

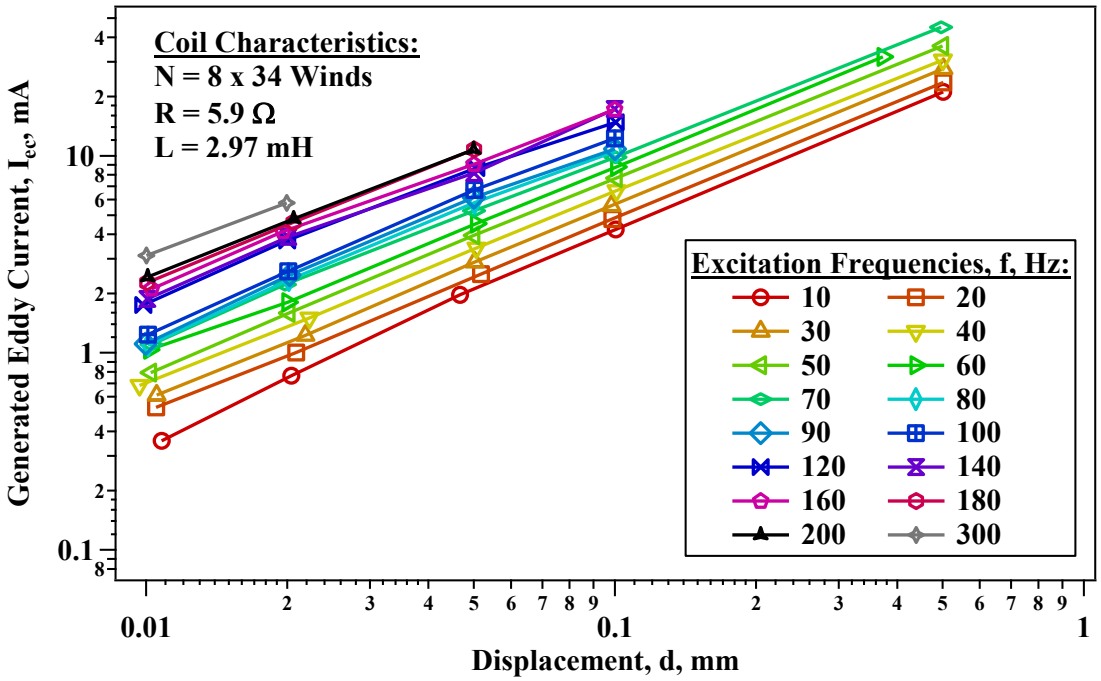

Figure 4.16: Comparison of Generated Eddy Currents with Peak Sinusoidal Displacement at Specific Frequencies.

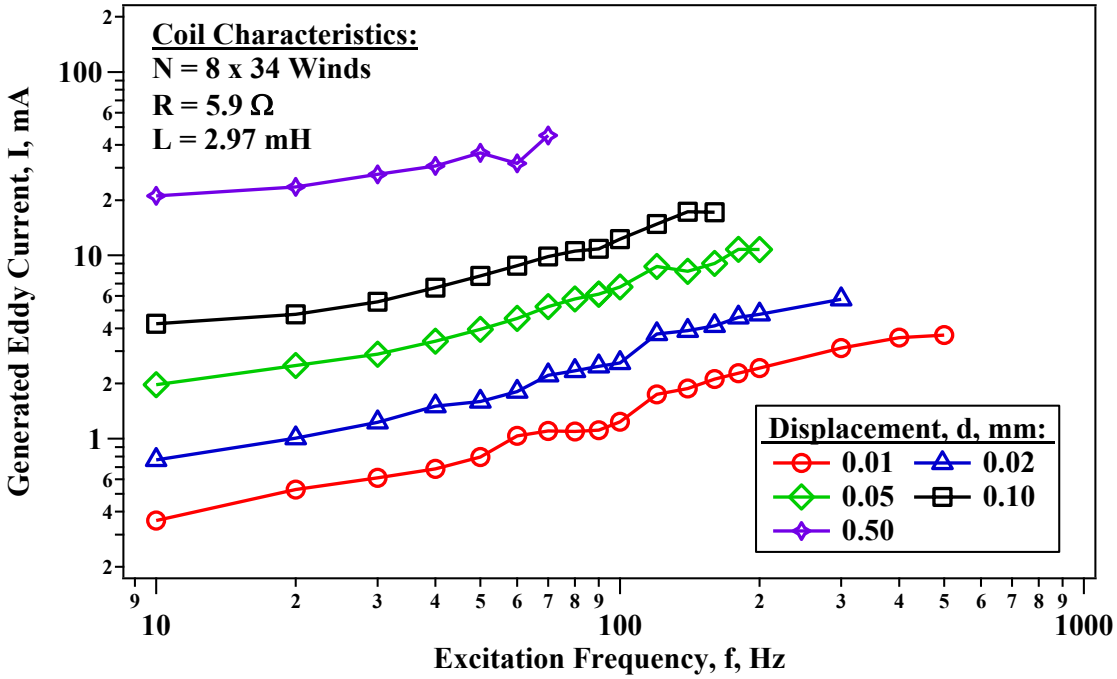

Figure 4.17: Comparison of Generated Eddy Currents with Frequency at Specific Peak Sinusoidal Displacements.

In Chapter 12, the force output versus input current was determined for the same coil used in this chapter for the study of eddy currents. The operating force per current, F/I, of the coil was determined to be 1.405 Newton/Ampere (N/A), more details for understanding the operating range of this factor are discussed in Chapter 12. The linear velocity, ν, from this eddy current experiment can be calculated by:

$$\nu = \omega * d \tag{4.19}$$

where ω is the circular frequency (2πf) excited in the electrodynamic shaker and d is the controlled peak sinusoidal displacement. The eddy currents, I_{ec}, generated in this experiment can be multiplied by the force per current factor (F/I = 1.405 N/A) to determine the generated eddy current force, F_{ec}, which is given by:

$$F_{ec} = I_{ec} * F/I \tag{4.20}$$

where F_{ec} is the generated eddy current force in units of N and this is compared with the ν in units of m/s. The slope of F_{ec} versus ν gives the linear equipment-generated damping coefficient, c_ν, for this system as 0.3382 N-sec/m. The results used to determine c_ν are presented as the comparison of generated eddy current and force with velocity, as seen in Figure 4.18.

Since the work in this dissertation regarding the factors in the torsional SDOF system are presented in standard units, c_ν can be converted from metric to standard units as:

$$c_{\nu,\text{standard}} = \frac{c_{\nu,\text{metric}}}{9.80665\ \text{m/sec}^2 * 0.45359\text{kg/lb} * 3.2808399\text{ft/m}} \tag{4.21}$$

where $c_{\nu,\text{standard}}$ is found to be 0.0232 lb-sec/ft. Since there are 8 coils in the RCTS device, the linear equipment-generated damping coefficient for the RCTS device is 0.1854 lb-

sec/ft. The linear force component of c_v must be converted to eddy current torque, T_{ec}, based on the distance to the center of rotation, r, which is given by:

$$T_{ec} = F_{ec} * r \tag{4.22}$$

The distance from the center of the magnets to the axis of rotation is 3.25 in., thus the torsional equipment-generated damping coefficient, c_t, is given by combining the previous two expressions as:

$$c_t = c_v * r^2 = 0.1854\,\text{lb} \cdot \text{sec/ft} * \left(\frac{3.25\text{ in.}}{12\text{ in./ft}}\right)^2 = 0.0136\ \text{ft} \cdot \text{lb} \cdot \text{sec/rad} \tag{4.23}$$

where c_t is given in the proper units for the damping coefficient in a torsional SDOF system. The result of this methods is presented along with the methods discussed in the subsequent sections, as seen in Figure 4.19.

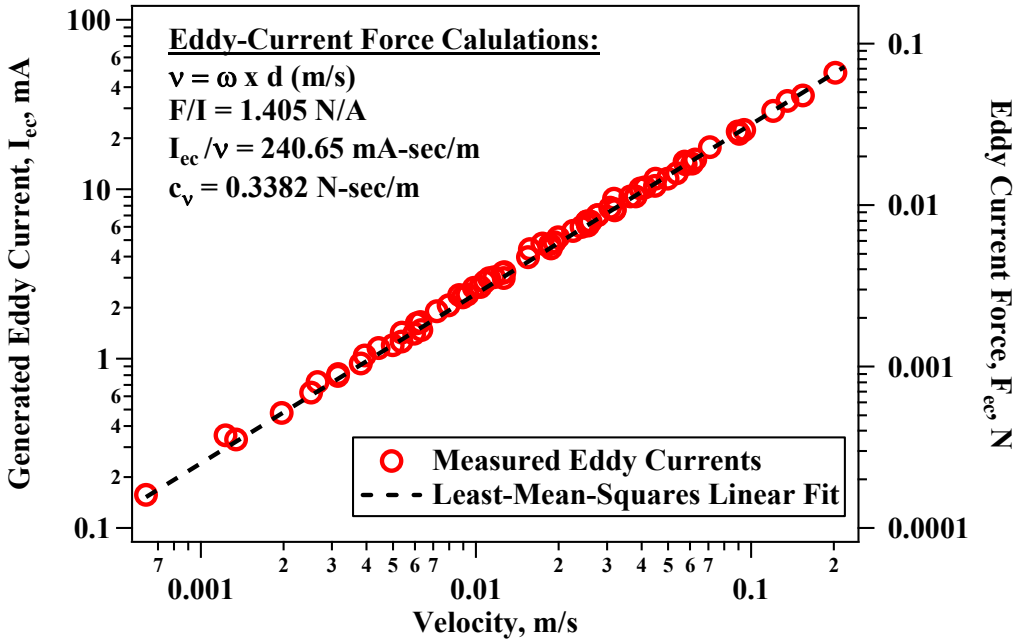

Figure 4.18: Comparison Generated Eddy Current and Force with Velocity.

4.5.4 Results of Equipment-Generated Damping Coefficient Evaluations

Several methods were used to evaluate the equipment-generated damping coefficient that utilizes several aspects of SDOF theory. An additional method was performed that involved an experiment to evaluate the equipment-generated damping coefficient that is isolated from the complex configuration of the RCTS electromagnetic torqueing motor. Concurrently, the isolated experiment does not involve the 8 coils that make up the RCTS electromagnetic torqueing motor or the numerous metal specimens used to evaluate the device. Each of these methods result in a relatively consistent value for the equipment-generated damping coefficient at seen in Figure 4.19.

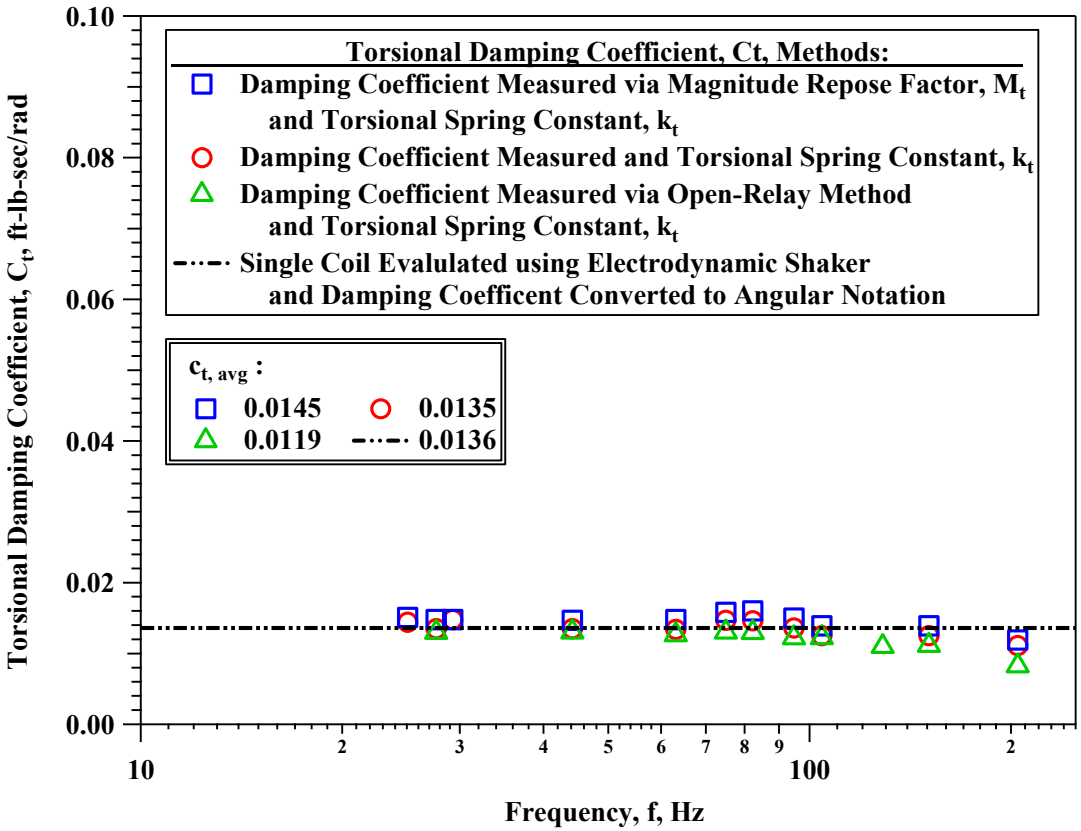

Figure 4.19: Comparison Generated Eddy Current and Force with Velocity.

4.6 SUMMARY

The results of the calibration, where hysteretic damping is measured with the metal specimen, are compared with the hysteretic damping theorized using the drive coil phase shift. The hysteretic damping theorized using the drive coil phase shift is essentially the same as the hysteretic damping measured with the metal specimen, which was originally known as the TS equipment-generated damping. For practical purposes, the traditional calibration procedure using the metal specimens to develop a calibration factor to correct for the drive coil phase shift is a simpler process then evaluating the electrical characteristics of the drive coil circuitry. Furthermore, the traditional method is shown to ascertain the same results as the more complex analysis of evaluating the electrical characteristics of the drive coil circuitry.

The original calibration procedure to for equipment-generated damping in the the free-vibration decay test was compared with a method where a relay switch is opened during free-vibration decay to eliminate equipment-generated damping. Based on the comparison from the original and open-relay calibration methods, there is little difference between the methods. The original method overestimates the back EMF by 0.28% for Drive Plate #4 (0.83% for Drive Plate #9), which is generally negligible during RC testing. When testing materials with material damping ratios below 0.1%, this slight overestimation should be considered. The original method is far simpler to perform and is recommended for general equipment-generated damping calibration and corrections to damping ratios measured during RC testing.

This chapter shows that equipment-generated damping in the RCTS device does not extend beyond basic electrical circuity principals and rules of electromagnetism. Equipment-generated damping has been shown to be purely velocity dependent and is thus represented as a viscous damping coefficient added into the differential equation for a

single-degree-of-freedom system. Numerous attempts have been made to understand and account for equipment-generated damping, but the traditional calibrations to correct for equipment-generated damping are not complex and are easily implemented. The more detailed variables that describe the complexities of the RCTS electromagnetic torqueing motor are easily calibrated for using traditional methods; however, these more detailed variables are useful for more complex analysis of the nonlinear dynamic behavior of soils, which is discussed in later chapters in this dissertation.

Chapter 5

Signal Processing Techniques for Enhancing Small-Strain Measurements during the Resonant Column Test

5.1 INTRODUCTION

With modern computer processing power, digital programming capacity, and digital filtering capabilities, many new capabilities for signal conditioning of sensor outputs have been made possible. In traditional RCTS testing, digital signal conditioning technology was limited or difficult to implement and significant noise at low voltage levels made high resolution measurements in RCTS testing challenging. Several digital filtering and signal processing techniques have been implemented and standardized for making reliable measurements at very-low to low shearing strains ($0.00003 < \gamma \leq 0.0003$) in RC testing.

During the frequency sweep portion of the RC test, a time-domain method called the wavelet integration method of analysis is used to eliminate background noise and reduce large volumes of signal data to generate a typical response curve. This method acts as a narrow bandpass filter that integrates a prescribed set of cycles at a specific excitation frequency and provides the amplitude response (i.e. shearing strain) and phase between the force excitation and system response. When the noise level is too great to be removed by the wavelet integration method of analysis, an additional method is used to eliminate the influence of background noise on the results obtained from the frequency sweep. This process involves the use of a least-mean squares fitting method that fits the response curve equation to the measured data to iteratively determine the results obtained from the frequency sweep.

Following the frequency sweep, the free-vibration decay test is conducted. During the free-vibration portion of the RC test, a step-by-step approach is used to obtain accurate results. First, free-vibration decay tests are repeated and the signals from the series of repeat tests are stacked to reduce "random" background noise. Second, targeted notch filtering is conducted to remove harmonic background noise (i.e., harmonic distortion). Third, the targeted notch filtering is followed by bandpass Butterworth filtering to reduce residual background noise. Fourth, the Hilbert Transform signal processing method is used to obtain a larger amount of data for evaluate the free-vibration decay damping ratio. In combination, the methods developed herein allow repeatable and accurate evaluations of signals from the free-vibration decay test.

5.2 Signal Processing Techniques For The Frequency Sweep In Noisy Environments

When conducting a frequency sweep on a specimen, having near real-time results plot, as the range of input frequencies is swept, are useful for presentation and quality control purposes. When observing the progression of the frequency sweep, one can confirm that the test is executing properly. Concurrently, when the results are plotted in near real-time, one can determine if any testing anomalies are present, such as the LVTD core coming into contact with the LVDT assembly, one of the magnets coming into contact with the drive coils, or other unexpected irregularities. Near real-time presentation of the results is obtained by using a time-domain filtering and signal processing method that is executed to streamline collection and presentation of the data. In order to observe results in near real-time with seemingly continuous execution during the frequency sweep, only finite segments of signals are processed. To have fast refresh rates for signals to present on screen and to maintain favorable sampling rates, the signal segment is short leading to a limited

number of samples that can be immediately analyzed. With a limited number of samples, and due to the computational cost of conducting frequency domain analysis operations, time-domain processing is more appropriate than using a frequency domain type of analysis (i.e. conducting a Fast-Fourier-Transform on each set of cycles in real-time). After the frequency sweep is conducted and the response curve is obtained, further data processing is used to improve accuracy of the results obtained from the test. The preceding sub-sections layout the computational methods performed during and after the frequency sweep test to increase precision and accuracy of the results.

5.2.1 Wavelet Integration Method Used for a Stepped-Sine Frequency Sweep in the Resonant Column Test

The real-time digital data processing conducted during the frequency sweep during RC testing is done using a program written in LabVIEW to excite a range of frequencies at a prescribed frequency step and number of cycles per frequency step. The following subsection explains the computational methods that are executed in that program. To preface the subsection, the frequency sweep comprises of a constant force type of excitation (the stimulus) to the system and the dynamic response (the response) of the system is measured. The digital signal processing of the stimulus and response is executed sequentially and is described step-by-step where: (Step 1) the response and stimulus waveforms are windowed using; (Step 2) an analytic signal is programmed at the frequency of interest and multiplied with the windowed stimulus and response waveforms; (Step 3) the product of the windowed waveforms and analytic signal are integrated; (Step 4a) single-valued magnitudes are calculated from the integrated stimulus and response waveforms; and (Step 4b) the magnitude and phase of the response relative to the stimulus are determined from the integrated stimulus and response waveforms. The first two steps construct a cascade of filters that form a complex-valued wavelet that is multiplied by, and

integrated with, the stimulus and response waveforms, which thus creates the time-domain digital processing method known at the wavelet integration method. Each of the steps used in the wavelet integration method involve principals and methods discussed in Feldman (2011), Santamarina and Fratta (2005), and Wilson (2013).

Step 1 of the wavelet integration method involves windowing the stimulus and response signals, which can reduce end effects in time-domain processing and further mitigate the presence of transient vibrations recorded in the signal. A preselected number of cycles are chosen and the segment of the signal, at a specific excitation frequency, is used for analysis. A Hanning window is applied to the signal consisting of the finite number of cycles. The general form of the Hanning window is presented in Santamarina and Fratta (2005) as:

$$w_i = \frac{1}{2} + \frac{1}{2}\cos\left[\frac{2\pi}{E}(i - M)\right] \quad |i - M| \leq \frac{E}{2} \tag{5.1}$$

where the window is centered around i=M and the time width of the window is E·Δt. The integration of this window extends from –E/2 to E/2, thus the integration of this window is then:

$$\int_{-E/2}^{E/2} w_i = \frac{1}{2} + \frac{1}{2}\cos\left[\frac{2\pi}{E}(i - M)\right] d(i - M) = \frac{1}{2} \tag{5.2}$$

The amplitude correction factor for this window is the reciprocal of the coherent gain (integral of w_i) of the Hanning window, which is 2. The window used in the LabVIEW program for the swept sine test is a steeper type of Hanning window and is defined as:

$$w_n = 1 - 1 \times \sin\left(\frac{2\pi * n}{N} + \frac{\pi}{2}\right) \tag{5.3}$$

where a +1 and phase (φ) of 90° are added so that the window begins and ends at zero, n is 1 sample, and N is found by:

$$N = \left(\frac{C_i}{f}\right) \times F_s \tag{5.4}$$

where C_i are the number of integration cycles, f is the excitation frequency (Hz), and Fs is the sampling rate (samples/sec). Thus, N is the total number of samples recorded over the specified number of integration cycles and is based on the current excitation frequency of the sweep and the sampling rate of the DAQ. When integrating this window the amplitude correction factor is 1. Therefore, the stimulus and response signals can be windowed by matrix multiplication and are, respectively:

$$w_n(\mathrm{Stim}) = w_n * \mathrm{Stim}_n \tag{5.5}$$

$$w_n(\mathrm{Resp}) = w_n * \mathrm{Resp}_n \tag{5.6}$$

Step 2 of the wavelet integration method involves creating the analytic signal at the frequency of interest and multiplied by the windowed signals. The analytic signal, b_t takes the form:

$$b_t = \cos(2\pi ft - \varphi) + i\sin(2\pi ft - \varphi) \tag{5.7}$$

where f is the excitation frequency (Hz), t is time, and φ is the end phase from the previously excited signal during the frequency sweep.

The stimulus and response signals are converted to complex notation as:

$$\mathrm{simulus} = x_t = \mathrm{Re[stimulus]} + \mathrm{Im[stimulus]} \tag{5.8}$$

$$\mathrm{response} = y_t = \mathrm{Re[response]} + \mathrm{Im[response]} \tag{5.9}$$

where x_t is the complex form of the stimulus signal, y_t is the complex form of the response signal, and Re and Im indicate the real and imaginary quantities, respectively.

Step 3 of the wavelet integration method involves integrating the product of the windowed waveforms and analytic signal. The magnitudes of the windowed stimulus and response waveforms are then found by multiplying them with the analytic signal and taking the sum of each array:

$$Z_{stim} = X_p = \sum_{t=0}^{N} b_t \times x_t \tag{5.10}$$

$$Z_{resp} = Y_p = \sum_{t=0}^{N} b_t \times y_t \tag{5.11}$$

where Z_{stim} and Z_{resp} are complex quantities of the sum of the analytic signal multiplied with the stimulus and response sinusoids, respectively. At this point, Step 4a involves converting X_p and Y_p into single-valued amplitudes of each signal which is given by:

$$x_p = 2 \times \frac{\sqrt{Re(X_p)^2 + Im(X_p)^2}}{N} \tag{5.12}$$

$$y_p = 2 \times \frac{\sqrt{Re(Y_p)^2 + Im(Y_p)^2}}{N} \tag{5.13}$$

where N is the total number of samples and each quantity is multiplied by 2 to correct for the magnitude of the cascaded Hanning window and analytic signal filters.

In Step 4b, the complex conjugate of Z_{resp} divided by Z_{stim} gives a complex quantity for the transfer function which is then used to find the amplification factor, M and phase, φ measured between signals. The correction for the cascaded filters can be ignored when finding the amplification factor directly, because the integrals of the cascaded filters cancel out. The amplification factor and phase are found by:

$$Z_{mag} = \left(\frac{Z_{resp}}{Z_{stim}}\right)^* \tag{5.14}$$

$$M = |Z_{mag}| = \sqrt{Re[Z_{mag}]^2 + Im[Z_{mag}]^2} \tag{5.15}$$

$$\varphi = \tan^{-1}\left(\frac{\mathrm{Im}[Z_{mag}]}{\mathrm{Re}[Z_{mag}]}\right) \tag{5.16}$$

where * indicates the complex conjugate (e.g., x+yi → x-yi) and || is the absolute value (i.e. square root of the sum of the squares). In the RC test, the phase (φ) measured by the DAQ system is not the same as the actual phase shift between excitation and system response because there are other equipment characteristics that need to be accounted for first.

To gain insight into the proficiency of this time-domain filtering method, a transfer function is generated using the cascade of the Hanning window and analytic signal filters from the wavelet integration method. The frequency of interest was selected to be 100 Hz and the transfer function generated from 1 Hz to 3,000 Hz. First, the cascade of the Hanning window and analytic signal filters is multiplied by sinusoids at numerous frequencies to build a transfer function as a function of frequency. Second, to present the effect of the Hanning winnow filter, the analytic signal filter was multiplied by sinusoids at numerous frequencies without cascading with the Hanning window. The plot of the transfer functions of these techniques versus frequency are shown in Figure 5.1. The Hanning window is used so that the signal segments analyzed are continuous (i.e. the beginning and end of the signals are approximately zero). By windowing to create continuous signals, the Gibbs Oscillations (Wilson 2013) that occur in the frequency-domain are reduced, as seen in Figure 5.1. Reduction of the Gibbs Oscillations allows for a cleaner frequency filtering process and results in more accurate solution.

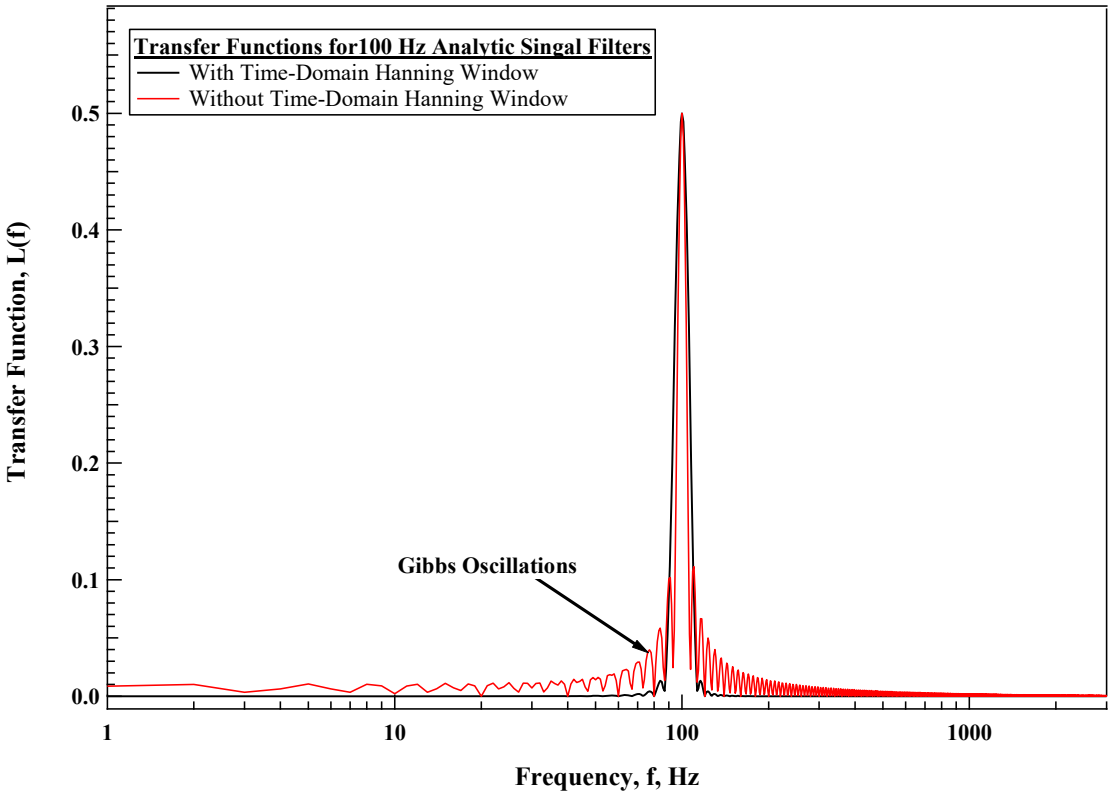

Figure 5.1: Transfer function of analytic signal filter plotted versus frequency.

5.2.2 Wavelet Integration Method: Example for a Stepped-Sine Sweep

An example of the digital data processing in the LabVIEW swept sine program is given where the response of a single-degree-of-freedom (SODF) oscillator is simulated. A conceptual diagram of a SDOF oscillator is shown in Figure 5.2. The dynamic response of the SDOF oscillator is modeled using:

$$\ddot{x}m + c\dot{x} + kx = Q_0 \sin(\omega t) \tag{5.17}$$

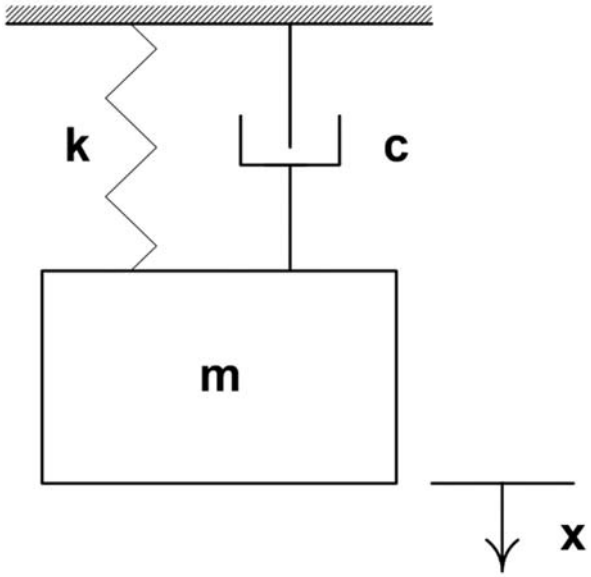

Figure 5.2: Conceptual diagram of a SDOF oscillator.

where $\ddot{x}$ is the acceleration of the mass, m is the mass of the system, $\dot{x}$ is the velocity of the mass, c is the damping coefficient of the dashpot, x is the vertical displacement of the mass, k is the spring constant of the spring, Q_0 is the amplitude of the constant force type of excitation, and sin(ωt) is the sinusoidal excitation function.

For the digital processing aspects, the number of integration cycles is 15 and the sampling rate is 10,000 samples/sec. The input properties of the SDOF oscillator are f_r = 10 Hz, D = 4%, m = 0.5 lb-sec^2/ft, and Q_0 = 100 lb. Based on these characteristics the stimulus and response signals can be simulated. The stimulus signal will have a frequency equal to the resonant frequency of the system and a magnitude of Q_0 (100 lb) and thus the response signal will have an amplitude equal to $A_{max} = M_{max}*Q_0/k$ (A_{max} = 0.63174 ft), where M_{max} and k is given by:

$$M_{max} = \frac{1}{2D\sqrt{1-D^2}} = \frac{1}{2*0.04\sqrt{1-0.04^2}} = 12.51 \qquad (5.18)$$

and

$$f_n = \frac{f_r}{\sqrt{1-2D^2}} = \frac{10\ \text{Hz}}{\sqrt{1-2*0.04^2}} = 10.016\ \text{Hz} \tag{5.19}$$

thus

$$k = (2\pi * f_n)^2 * m$$

$$= (2\pi * 10.016\ \text{Hz})^2 * 0.5\ \frac{\text{lb}-\text{sec}^2}{\text{ft}} = 1980.2577\ \text{lb/ft} \tag{5.20}$$

where k is the spring constant. The simulated stimulus and response signals are defined by:

$$\text{simulus} = Q_0 \sin(\omega t) \tag{5.21}$$

$$\text{response} = M_{max} \times \frac{Q_0}{k} \sin(\omega_r t - \varphi_r) = \frac{1}{2D\sqrt{1-D^2}} \times \frac{Q_0}{k} \sin(\omega_r t - \varphi_r) \tag{5.22}$$

where the excitation frequency equals the resonant frequency ($\omega=\omega_r$), t is the time is seconds, M_{max} is the maximum dynamic amplification of the system, which occurs at ω_r, and φ_r is the phase shift between the stimulus and the response signal occurring at the resonant frequency. The phase shift at the natural frequency is 90 degrees; however, do to the presence of damping, the resonant frequency is less than the natural frequency and the phase shift at the resonant frequency is less than at the phase shift at the natural frequency. This phase shift at the resonant frequency is given by:

$$\tan \varphi_r = \frac{2D \times {\omega_r}/{\omega_n}}{1-\left({\omega_r}/{\omega_n}\right)^2} \tag{5.23}$$

where:

$${\omega_r}/{\omega_n} = \sqrt{1-2D^2} \tag{5.24}$$

and:

$$\varphi_r = \tan^{-1}\left(\frac{\sqrt{1-2D^2}}{D}\right) \tag{5.25}$$

For the SDOF properties provided, φ_r is equal to 87.7057 degrees, which is the phase used to generate the response signal. The dynamic response curves for this SDOF is plotted in Figure 5.3.

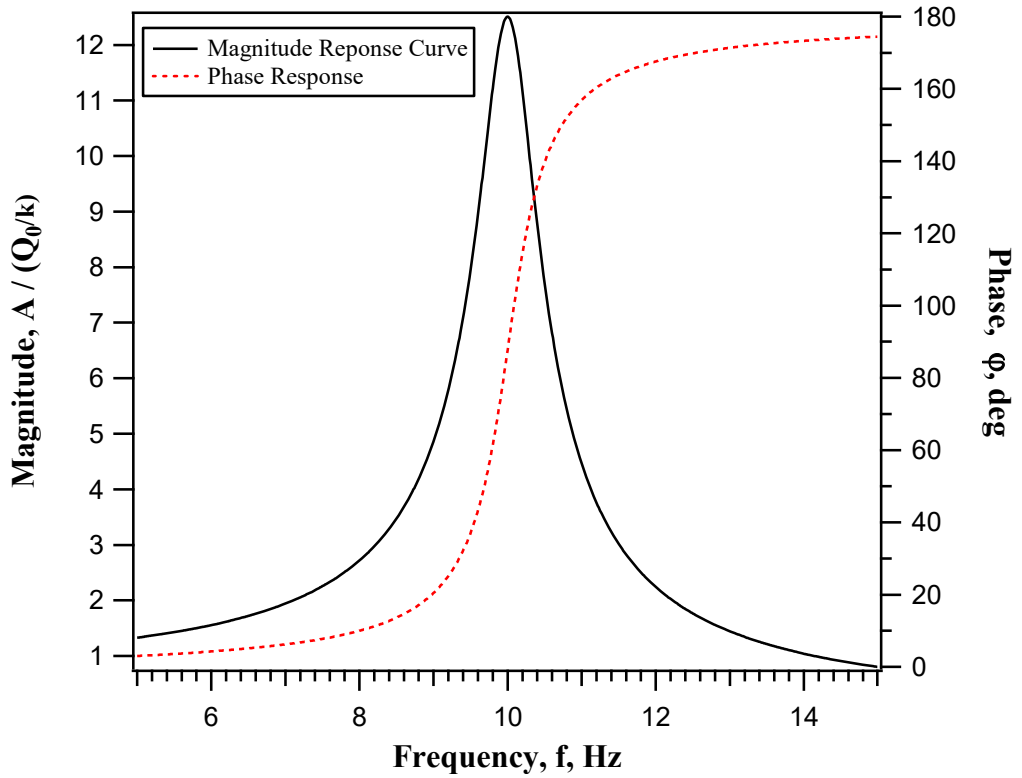

Figure 5.3: Response curves for SDOF oscillator with f_r = 10 Hz, D = 4%, m = 0.5 lb-sec^2/ft, and Q_0 = 10 lb.

The wavelet integration method of analysis discussed previously is evaluated based on signals simulated from the SDOF characteristics discussed in this section. The illustration shown in Figure 5.4 presents the step-by-step digital signal processing method and shows that the same results are obtained as the inputs used to create the stimulus and response signals.

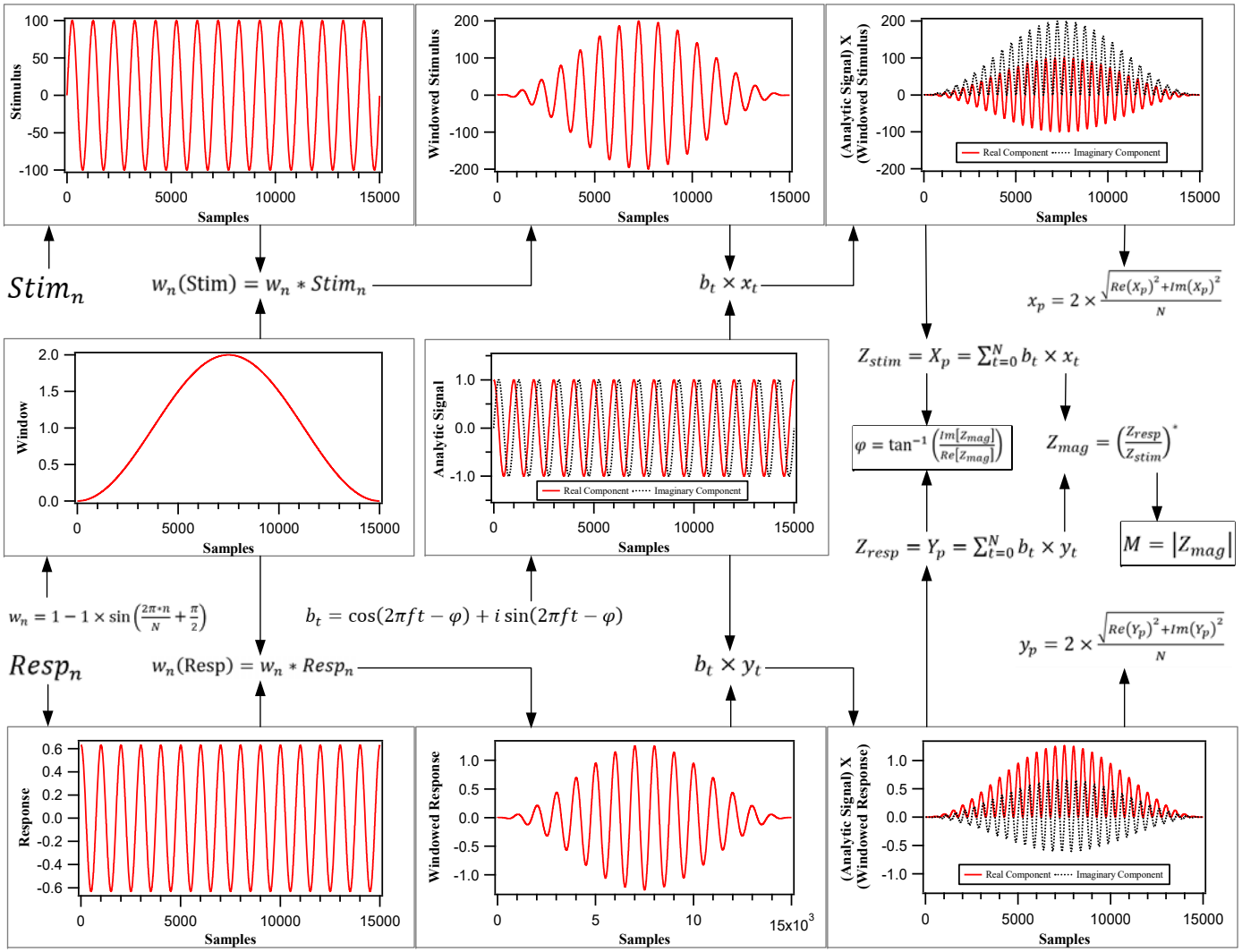

Figure 5.4: Step-by-step visualization of the Wavelet Integration Method of Analysis.

To complete the example, numerical values are shown after Step 1-3, where the products of the waveforms and cascaded filters are integrated. The calculations are continued as shown:

Step 4a

$$Z_{stim} = X_p = \sum_{t=0}^{N} b_t \times x_t = -1.308608 \cdot 10^{-9} + 750000.00i \quad (5.26)$$

$$Z_{resp} = Y_p = \sum_{t=0}^{N} b_t \times y_t = 4734.2262 + 189.67277i \quad (5.27)$$

$$x_p = 2 \times \frac{\sqrt{Re(X_p)^2 + Im(X_p)^2}}{N} = 2 \times \frac{\sqrt{(-1.308608 \cdot 10^{-9})^2 + (750000.00)^2}}{15000.000} = 100 \quad (5.28)$$

$$\varphi_{x_p} = \tan^{-1}\left(\frac{Im[x_p]}{Re[x_p]}\right) = \tan^{-1}\left(\frac{750000.00}{-1.308608 \cdot 10^{-9}}\right) = 90 \text{ deg} \quad (5.29)$$

$$y_p = 2 \times \frac{\sqrt{Re(Y_p)^2 + Im(Y_p)^2}}{N} = 2 \times \frac{\sqrt{(4734.2262)^2 + (189.67277)^2}}{15000.000}$$

$$= 0.63173657 \quad (5.30)$$

$$\varphi_{y_p} = \tan^{-1}\left(\frac{Im[y_p]}{Re[y_p]}\right) = \tan^{-1}\left(\frac{189.67277i}{4734.2262}\right) = 2.2942799 \text{ deg} \quad (5.31)$$

$$\varphi_{diff} = \varphi_{x_p} - \varphi_{y_p} = 87.7057 \text{ deg} \quad (5.32)$$

Step 4b

$$Z_{mag} = \left(\frac{Z_{resp}}{Z_{stim}}\right)^* = \left(\frac{4734.2262 + 189.67277i}{-1.308608 \cdot 10^{-9} + 750000.00}\right)^*$$

$$= 2.5289702 \cdot 10^{-4} + 6.3123016 \cdot 10^{-3}i \quad (5.33)$$

$$M = |Z_{mag}| = \sqrt{Re[Z_{mag}]^2 + Im[Z_{mag}]^2} =$$

$$\sqrt{(2.5289702 \cdot 10^{-4})^2 + (6.3123016 \cdot 10^{-3})^2} = 6.3173657 \cdot 10^{-3} \quad (5.34)$$

$$\varphi = \tan^{-1}\left(\frac{\mathrm{Im}[Z_{mag}]}{\mathrm{Re}[Z_{mag}]}\right) = \tan^{-1}\left(\frac{6.3123016\cdot10^{-3}}{2.5289702\cdot10^{-4}}\right)$$

$$= 1.5307536 \text{ rad} = 87.705721 \text{ deg} \quad (5.35)$$

The accuracy was taken to 8 significant digits to show that the hand calculations will match the results of the digital signal processing presented. As noted earlier, the phase used to simulate the response signal was 87.7057, thus the digital signal processing method used in the LabVIEW swept sine program returned almost to the same phase that was used to create the response signal. The stimulus signal was equal to Q_0, which was 100 lb, and the response signal was $M_{max}*Q_0/k$, which was 0.63174. The output from the digital processing method was $6.3174\cdot10^{-3}$ which is equivalent to:

$$\frac{A_{resp}}{A_{stim}} = \frac{M_{max}*Q_0/k}{Q_0} = \frac{M_{max}}{k} = \frac{12.51}{1980.2577} = 0.0063174 \quad (5.36)$$

where A_{resp} and A_{stim} are the amplitudes of the response and stimulus signals, respectively. Therefore, the digital processing method returned the exact transfer function that would be predicted from the input parameters of the SDOF oscillator.

5.2.3 Least-Mean-Squares Fitting to the Frequency Response Curve

The digital signal processing conducted during the frequency sweep allows more precise measurement of the dynamic response and phase shift of the system. However, when exciting at very small strains, environmental vibrations, electrical noise, or testing anomalies (e.g. acute vibrations from human activity), the quality of the response curve can still be limited. An additional approach to bypass the influence of background vibrations and electrical noise involves finding the characteristics of the response curve (i.e. fn and D) by determining the minimum least-mean-square between the SDOF response curve equation and the results measured from the frequency sweep. This method is more

robust for determining the resonant frequency and material damping ratio than the traditional half-power bandwidth approach.

As mentioned previously, there are two methods used to determine the response curve parameters from the frequency sweep. These include: (1) Using a half-power bandwidth method and interpolating between the local maxima and minima near the half-power points to make a more precise determination of the half-power frequencies, and (2) use of a least-mean squares fitting method that fits the response curve equation to the measured data to iteratively determine the values for the natural frequency and damping ratio.

When using the interpolation method, the half-power frequencies are determined by finding the local maximum and minimum amplitudes of the response curve for frequency segments above and below the resonant frequency. These local maxima and minima are recorded points of the response curve that are directly above and below $A_{max}/\sqrt{2}$ and interpolation between these points leads to a more accurate prediction of the half-power frequencies. If the data points used to populate the measured response curve are too few, this method allows more accurate determination of the half-power frequencies. In the analysis process, the frequency segment below the resonant frequency is evaluated as is and the frequency segment above the resonant frequency can be reversed so that the following equation can be used to evaluate both half-power frequencies:

$$f_{1,2} = f_L + (f_H - f_L) * \left(\frac{(A_i - A_L)}{(A_H - A_L)}\right) \tag{5.37}$$

where $f_{1,2}$ are the half-power frequencies, f_L is the frequency corresponding to the measured amplitude (A_L) below the half-power frequency being interpolated to, f_H is the frequency corresponding to the measured amplitude (A_H) above the half-power frequency being interpolated to, and A_i is the half-power amplitude (i.e. $A_{max}/\sqrt{2}$) from which the half-

power frequency is being interpolated to. This method will henceforth be called the half-power interpolation method.

The interpolation method leads to a prediction of the half-power frequencies, f_1 and f_2, that in combination with the measured resonant frequency, f_r, will lead to a calculation of the half-power damping ratio, which is given in the simplified form for low damping ratios (and linear dynamic behavior) as:

$$D_{HP} = \frac{f_2 - f_1}{2 * f_r} \tag{5.38}$$

where D_{HP} is the damping ratio.

The results from the frequency sweep are typically measured using an accelerometer and thus the response curve is acceleration-based. When using the least-mean-squares fitting approach, the acceleration-based response curve must be converted to a displacement-based response curve. The acceleration-based response curve, R_a, is converted to a displacement-based response curve, R_d, by:

$$R_d = R_a / \omega^2 \tag{5.39}$$

where ω is the excitation circular frequency of the sweep

The least-mean-squares fitting method uses the theoretical response curve for a single-degree-of-freedom (SDOF) system which is given in Richart et al. (1970) as:

$$M = \frac{1}{\sqrt{[1-(\omega/\omega_n)^2]^2 + [2D(\omega/\omega_n)]^2}} \tag{5.40}$$

where the dynamic magnification factor is M, ω is the input frequency, ω_n is the natural circular frequency, and D is the damping ratio. This method will henceforth be called the least-mean-squares fit method. To utilize this equation, the measured response curve is first normalized. In this study, the fitting algorithm was limited to 10,000 iterations and

tolerance for the fitting parameters of 1E-8. This method is only valid for linear behavior of a SDOF system, which has a symmetric response curve and cannot describe non-linear systems that have asymmetric response curves. Therefore, when RC testing progresses from a linear to a nonlinear dynamic response, the traditional half-power bandwidth method can be used; however, the half-power bandwidth method is also invalid for nonlinear dynamic response curves.

The robustness of the least-mean-squares method relative to the half-power bandwidth method is presented where several frequency sweep tests were conducted on a poorly graded sand specimen at very low shear strains. The resulting response curves are plotted with the theoretical response curves generated from least-mean-squares method as seen in Figure 5.5. From the tests shown in Figure 5.5, the resonant frequencies determined using the half-power bandwidth and least-mean-squares methods are plotted in Figure 5.6. The material damping ratio results using both methods are plotted together in Figure 5.7. The least-mean-squares method is shown to have far greater accuracy, especially when estimating the material damping ratio from the frequency sweep test.

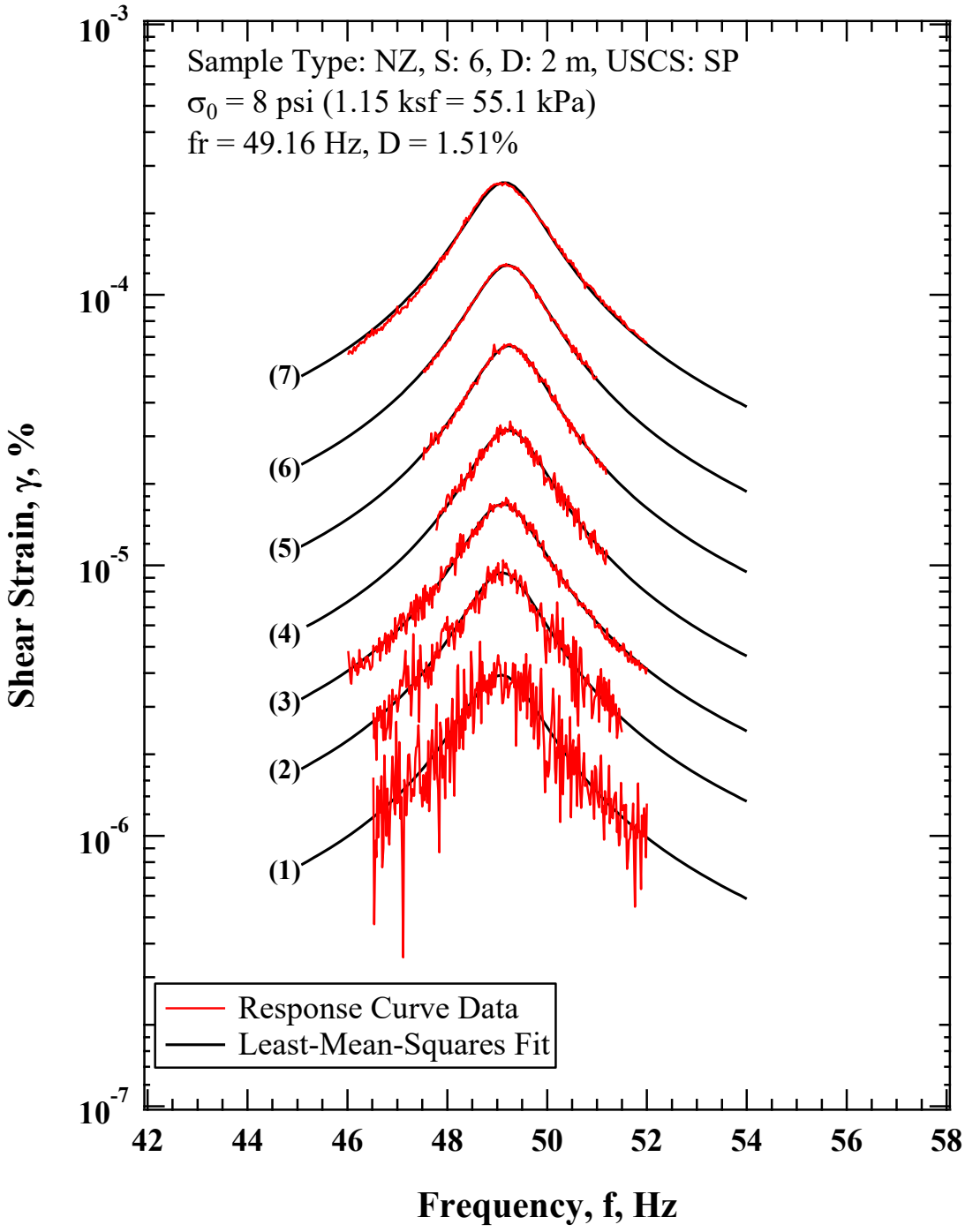

Figure 5.5: Comparison of the Variation in Shear Strain with Excitation Frequency from Response Curves Obtained from Frequency Sweep Tests on a USCS SP at an isotropic confining pressure of σ_o = 0.54 atm.

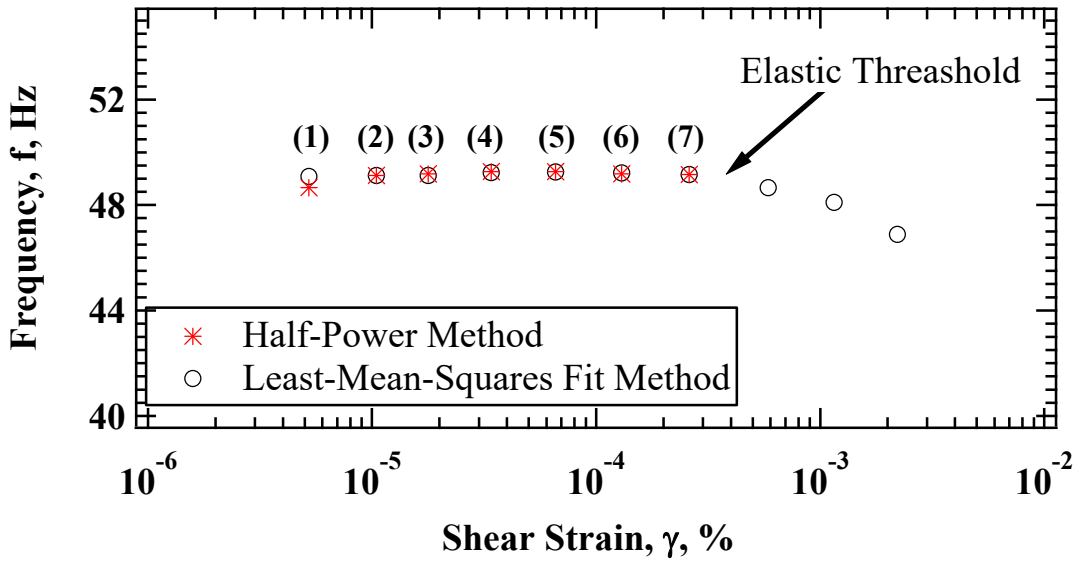

Figure 5.6: Comparison of the Variation in Resonant Frequency with Shear Strain from the Half-Power Bandwidth and Least-Mean-Squares Methods from Frequency Sweep Tests on a USCS SP at an isotropic confining pressure of σ_o = 0.54 atm.

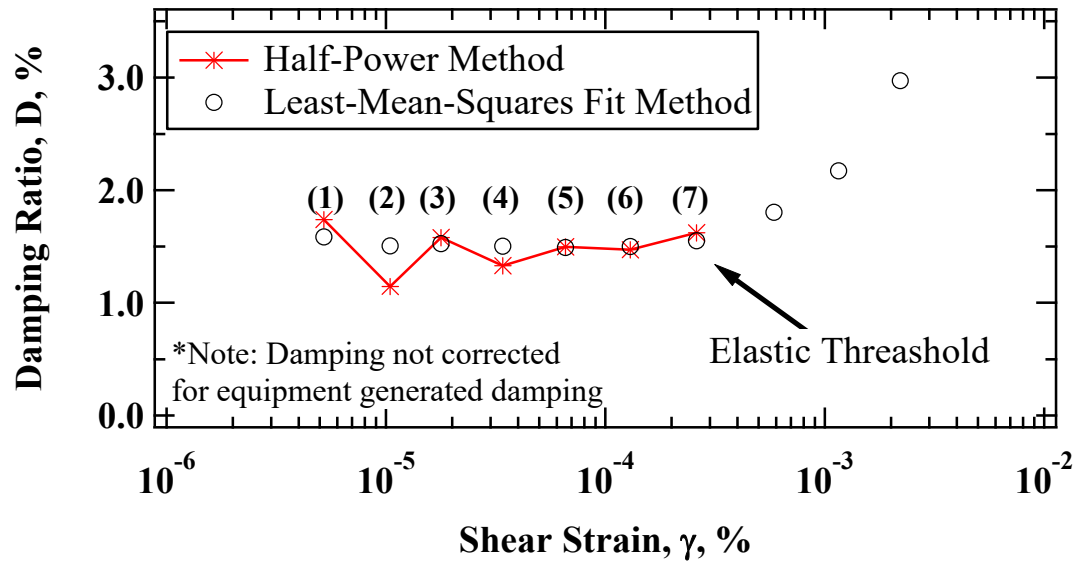

Figure 5.7: Comparison of the Variation in Material Damping Ratio with Shear Strain from the Half-Power Bandwidth and Least-Mean-Squares Methods from Frequency Sweep Tests on a USCS SP at an isotropic confining pressure of σ_o = 0.54 atm.

5.3 SIGNAL PROCESSING TECHNIQUES FOR FREE-VIBRATION DECAY IN NOISY ENVIRONMENTS AND LOW EXCITATION INPUTS

For measurements involving free-vibration decay curves at very low shear strains, the impact of background noise and environmental vibrations can range from detrimental to completely prohibitive. Environmental vibrations created by building machinery (e.g. mechanical, electrical, and plumbing systems) are included in the measured signal. Bending of the specimen, rather than perfect torsion, can also occur. As these cannot all be considered "random" background noise, targeted conditioning must be used so that the "true" signal is not corrupted.

To condition the signals for accurate measurement of material damping ratio, four steps are employed. The first step includes signal stacking to obtain a sufficient signal-to-noise ratio. Stacking of a signal involves conducting repeat tests and averaging each signal (Wilson 2013). The second step involves a process of targeted notch filtering, which is effective for removing high levels of noise at specific frequencies, which is described in Wilson (2013) as a narrow-band rejection filter. The third step involves bandpass filtering, which is effective for reducing all levels of background noise outside of the frequency range of interest. The fourth involves using the Hilbert Transform method to use the entire waveform for analysis rather than the peak and/or trough signal amplitudes. In combination the steps developed herein allow accurate and consistent measurement of the free-vibration decay signal.

5.3.1 Step 1: Signal Stacking and Signal-to-Noise ratio

If the noise content of the signal is considered to be Gaussian random noise, then the signal-to-noise ratio (SNR) can be used to understand the level of noise relative to the true signal and to ensure adequate stacking of the signal. The SNR is provided in Santamarina and Fratta (2005) as:

$$\mathrm{SNR} = \frac{V_S}{V_N} \tag{5.41}$$

where V_S is the maximum signal amplitude and V_N is the standard deviation of the noise.

As detailed in Santamarina and Fratta (2005) signal stacking is an effective approach for collecting clear signals and to reduce the influence of background noise. The nature of low amplitude free-vibration decay or torsional shear testing involves excitation of the system in the linear-elastic range, thus the "true" signal should not vary when consecutive tests are conducted. The number of signals to stack is calculated by choosing predetermined statistical parameters that define the probabilistic outcome that a true signal will result from signal stacking. For very low-amplitude excitations the number of signals to stack is calculated using:

$$M = \left(\frac{\alpha \cdot \sigma^{<noise>}}{\beta \cdot x^{<max>}}\right)^2 \tag{5.42}$$

where M is the number of signal to be stacked, $\sigma^{<noise>}$ is the standard deviation of the background noise, $x^{<max>}$ is the mean peak amplitude of the signal, α is a function of the probability that $x^{<max>}$ will not deviate from the true value within a selected range defined as β. Since the SNR is given as x<max> divided by σ<noise>, the number of signals needed to be stacked can also be given as:

$$M = \left(\frac{\alpha}{\beta \cdot \mathrm{SNR}}\right)^2 \tag{5.43}$$

When stacking signals, the resulting stacked signal takes the form:

$$x_i^{<avr>} = \frac{1}{M} \sum_k x_{i,k} \tag{5.44}$$

where $x_i^{<avr>}$ is the stacked average signal, M is the number of signals stacked, $x_{i,k}$ is the ith data point in the signal of the kth signal.

Signal stacking is a method that can only be employed when low amplitude resonant column or torsional shear tests are being conducted and only linear-elastic strains are excited into the system. Signal stacking cannot be used when higher strains are applied to a soil specimen, as the specimen is deforming plastically (non-linear range) and the response of the signal is not theoretically repeatable. The question may arise for when to stop signal stacking based on the where the transition between linear-elastic and non-linear strain occurs; however, the statistical calculation of M (number of signals to stack) becomes 1 within the linear-elastic strain range of typical materials tested in the resonant column or torsional shear tests. Time-domain and frequency-domain examples of signal stacking of 20 free-vibration decay signals from a poorly-graded sand specimen tested at σ_o = 0.46 atm are shown in Figure 5.8 and Figure 5.9, respectively. Considerable noise reduction occurs after stacking signals from 20 repeat free-vibration decay tests.

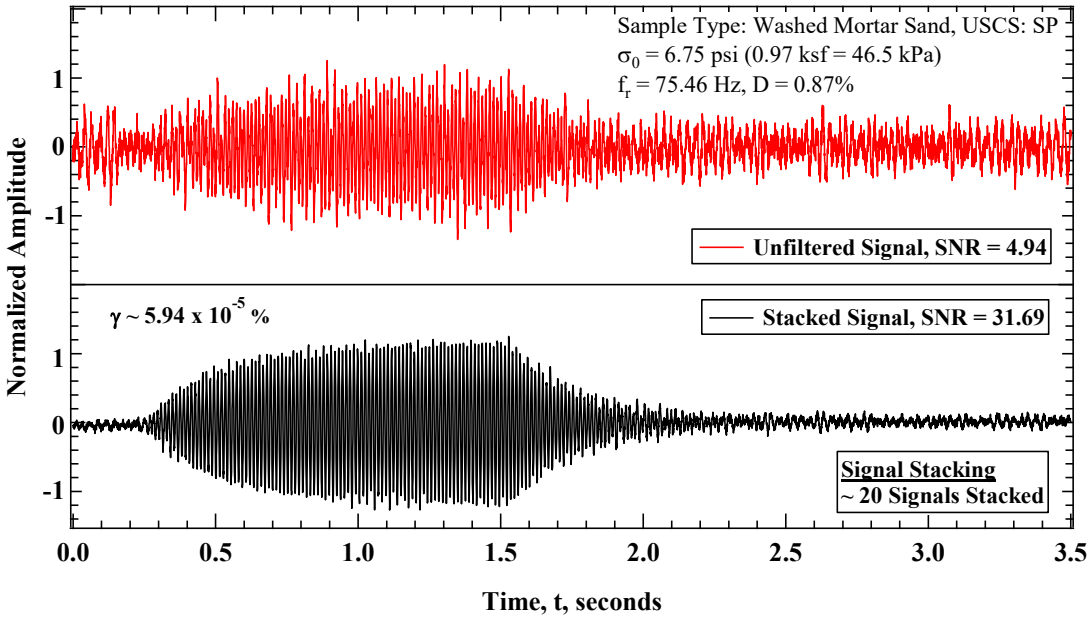

Figure 5.8: Time-Domain Example of Signal Stacking of 20 Free-Vibration Decay Signals from a Poorly-Graded Sand (Washed Mortar Sand) Specimen Tested at σ_o = 0.46 atm.

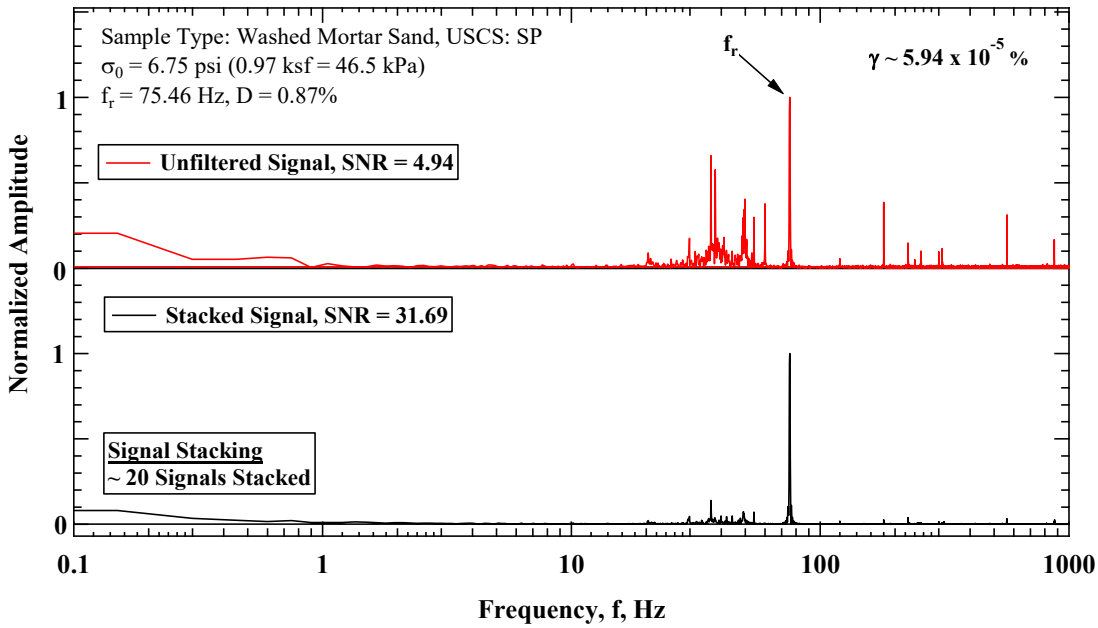

Figure 5.9: Frequency-Domain Example of Signal Stacking of 20 Free-Vibration Decay Signals from a Poorly-Graded Sand (Washed Mortar Sand) Specimen Tested at σ_o = 0.46 atm.

5.3.2 Step 2: Targeted Notch Filtering

One method to remove significant noise levels that occur at specific frequencies is apply frequency-targeted notch filters. Commonly 60-Hz electrical noise and other building vibrations are present in the recorded signal. Higher frequency noise can be found in the recorded system response that comes from various sources in a building due to vibrating mechanical systems (e.g., boiler system, HVAC components, rooftop units, etc.). These sources do not classify as Gaussian distributed random noise and my not be adequately removed by signal stacking. The only sure way these sources of vibration would cancel from stacking is that when stacking two signals the AC instances of these sources were exactly 180 degrees out of phase. However, tracking these sources and timing the RCTS tests to coincide where two instances are 180 degrees out of phase is not practical. Rather notching out these frequencies in the frequency-domain is done to remove this form of signal contamination. Time-domain and frequency-domain examples of targeted notch filtering on a free-vibration decay signal from a poorly-graded sand specimen tested at σ_o = 1.1 atm are shown in Figure 5.10 and Figure 5.11, respectively. Considerable noise reduction occurs after 10 successive notch filters are used on a free-vibration decay signal.

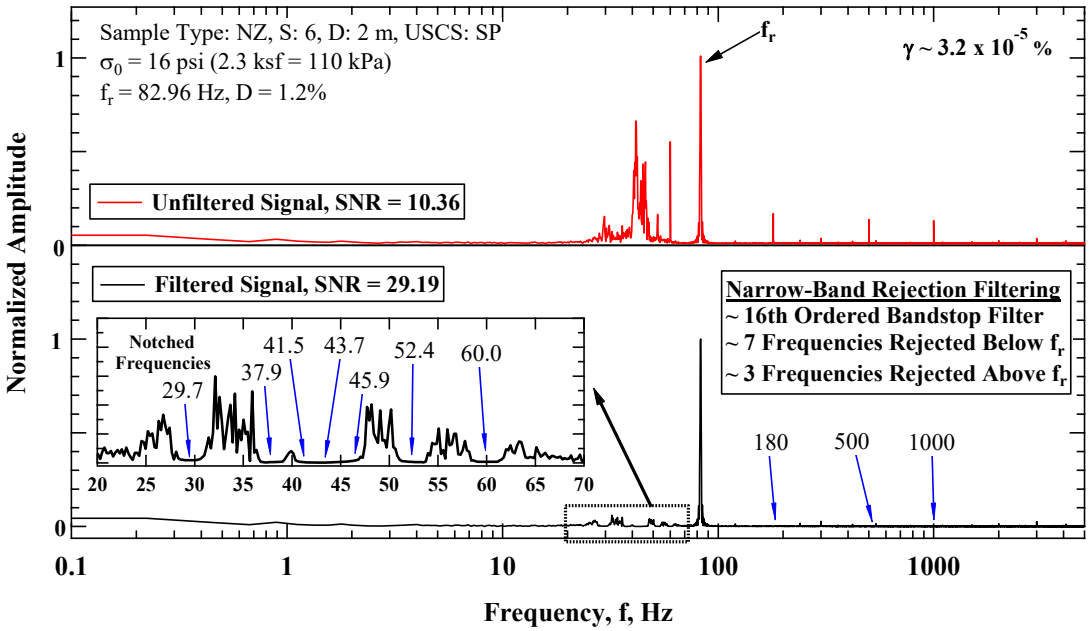

Figure 5.10: Time-Domain Example of Targeted Notch Filtering on a Free-Vibration Decay Signal from a Poorly-Graded Sand (from New Zealand) Specimen Tested at σ_o = 1.1 atm.

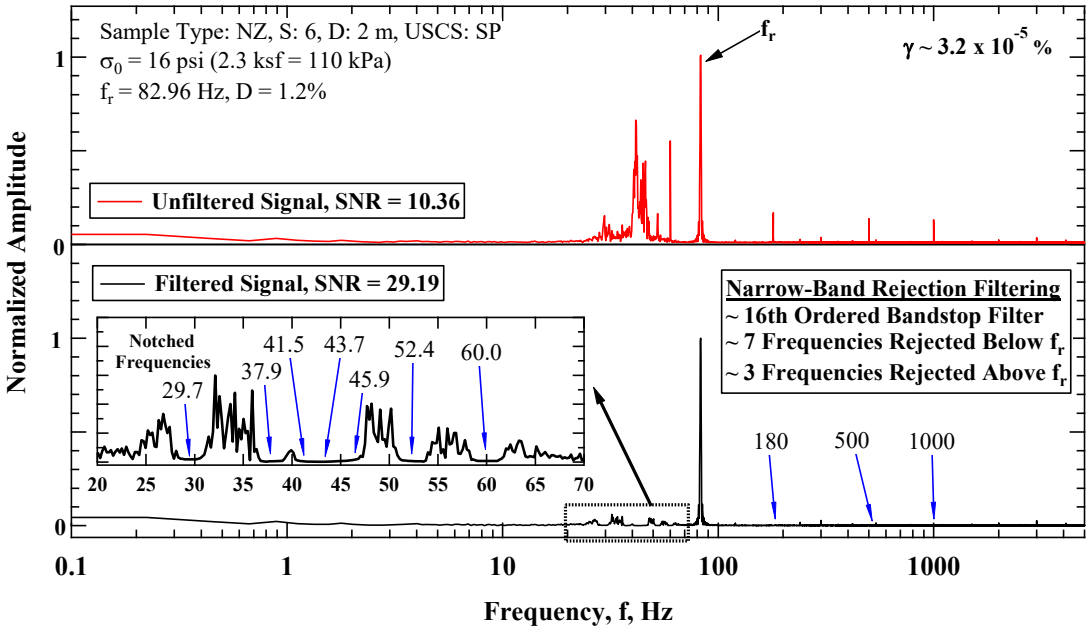

Figure 5.11: Frequency-Domain Example of Targeted Notch Filtering on a Free-Vibration Decay Signal from a Poorly-Graded Sand (from New Zealand) Specimen Tested at σ_o = 1.1 atm.

5.3.3 Step 3: Butterworth Bandpass Filtering

Commonly lowpass filter types are Chebyshev, Bessel, Butterworth, etc. Some filter types cause ripple in the passband frequencies and can also introduce unwanted phase shift. One of the more reliable types of filters is the Butterworth filter, also known as the maximum flatness filter because minimal Gibbs Oscillations (i.e. ripple) are introduced into the passband frequencies (Wilson 2013). In addition to the maximum flatness characteristic of a Butterworth filter, higher ordered Butterworth filters have a narrower transition band or faster roll-off, which increases the stopband frequencies by attenuating unwanted frequencies closer to the cutoff frequency. The cutoff frequency is selected when designing the filter and specifies the frequency where the spectral amplitude is reduced to 0.707 or -3 dB of the passband amplitudes.

A digital Butterworth can be designed to have a specified cutoff frequency and order that filters unwanted frequencies closer to the frequency of interest. The shape of a Butterworth filter is given by:

$$G(\omega) = \frac{1}{\sqrt{1+\omega^{2n}}} \tag{5.45}$$

where ω is the circular frequency and n is the order of the filter. An example of 1st, 3rd, and 8th ordered lowpass Butterworth filters with a cutoff frequency of 500 Hz is shown in Figure 5.12.

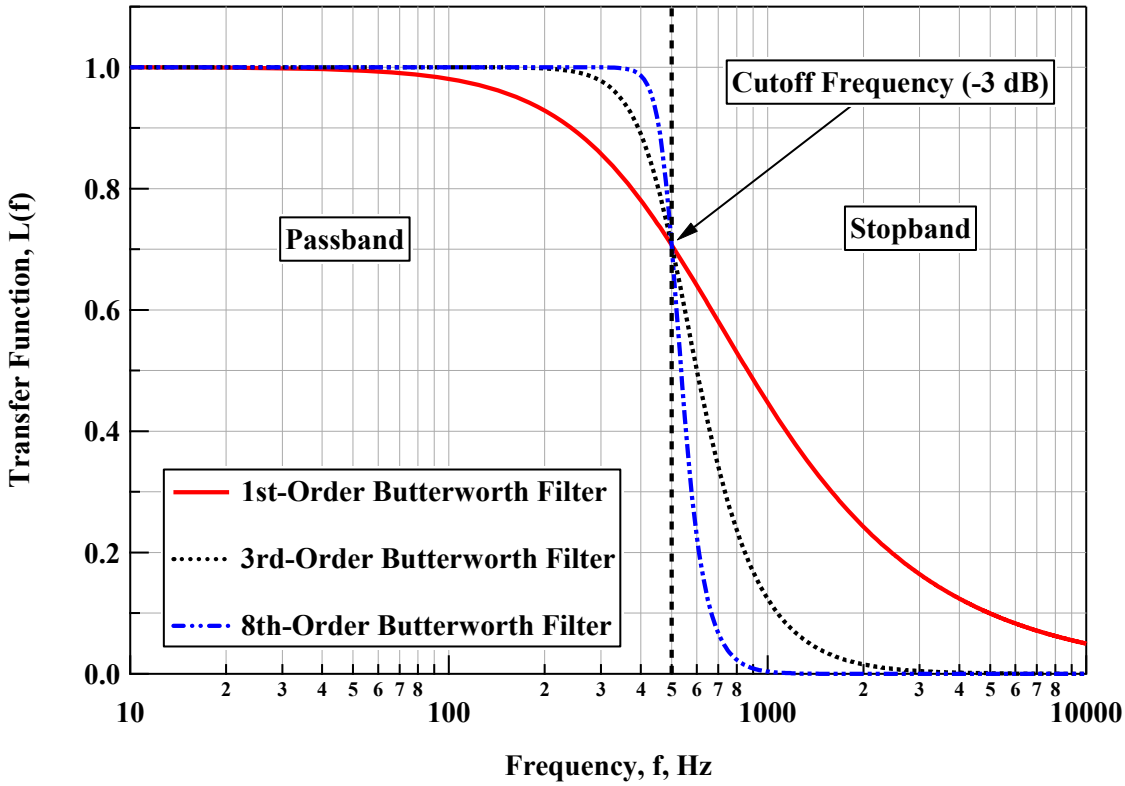

Figure 5.12: Example of 1st, 3rd, and 8th Ordered Lowpass Butterworth Filters with a Cutoff Frequency of 500 Hz.

Filtering a digital signal can be done using a lowpass 8th order Butterworth filter, the steps for which are described subsequently. The frequency-domain transfer function of the Butterworth filter can be produced by:

$$\omega_k = \left[\frac{0*f_s}{N}, \frac{1*f_s}{N}, \ldots, \frac{N/2*f_s}{N}\right] \tag{5.46}$$

$$G(\omega) = \frac{1}{\sqrt{1+\left(\frac{\omega_k}{\omega_c}\right)^{2n}}} \tag{5.47}$$

where ω_k is the frequency resolution, f_s is the sampling rate, N is the number of samples, ω_c is the cutoff frequency, and n is the order of the Butterworth filter. Note that ω_k stops at the Nyquist frequency, so that the transfer function filter is applied symmetrically about the Nyquist frequency and filters the positive and negative frequencies equally.

A bandpass filter can be constructed using two Butterworth filters, one configured as a lowpass filter and one configured as a highpass filter. The cutoff frequencies for each of these filters can be calculated so that a specific magnitude reduction occurs at the frequency of interest. If a magnitude reduction, G(ω), is selected, then the highpass and lowpass filter cutoff frequencies are respectively:

$$\omega_{c,high} = \frac{\omega}{\left(\frac{1}{(1-G(\omega))^2}-1\right)^{1/2n}} \tag{5.48}$$

$$\omega_{c,low} = \frac{\omega}{\left(\frac{1}{(G(\omega))^2}-1\right)^{1/2n}} \tag{5.49}$$

where ω is the frequency of interest and n is the order of the Butterworth filter that will be created. The lowpass and highpass Butterworth filters associated with the two cutoff frequencies are, respectively:

$$G(\omega)_{highpass} = 1 - \frac{1}{\sqrt{1+\left(\frac{\omega_k}{\omega_{c,high}}\right)^{2n}}} \tag{5.50}$$

$$G(\omega)_{lowpass} = \frac{1}{\sqrt{1+\left(\frac{\omega_k}{\omega_{c,low}}\right)^{2n}}} \tag{5.51}$$

The signal, x_n is converted to the frequency domain using a Discrete Fourier Transform:

$$x_n = [x_0, x_1, \dots, x_{N-1}] \tag{5.52}$$

$$X_k = \sum_{k=0}^{N-1} x_n e^{\left(-i2\pi\frac{n*k}{N}\right)} \tag{5.53}$$

where X_k is the complex frequency-domain representation of the signal.

The Butterworth filter can then be applied by multiplying the Butterworth transfer functions with the complex numbered frequency-domain representation of the signal which is:

$$\left(\prod_{k=0}^{\frac{k}{2}-1} X_k * G(\omega) \middle| \prod_{k=k/2}^{k} X_k * \overleftarrow{G(\omega)}\right) \tag{5.54}$$

where (|) indicates concatenating of the results of two arrays and $\overleftarrow{G(\omega)}$ indicates the reversing of the Butterworth transfer function. This equation can be used for both the highpass and lowpass filter transfer functions. The filtered frequency-domain signal is returned to the time domain by:

$$x_n = \frac{1}{N}\sum_{k=0}^{N-1} X_k e^{\left(i2\pi\frac{n*k}{N}\right)} \tag{5.55}$$

Since G(ω) is selected before configuring the filters, the amplitude reduction of the signal is known and is used to restore the amplitude of the signal. Restoring the "true" signal amplitude is important for determining the shear strain that was excited during the test. When multiplying the frequency domain signal by both the highpass and lowpass filter, after converting back to the time domain, the signal is divided by $G(\omega)^2$. Time-domain and frequency-domain examples of Butterworth bandpass filtering on a free-vibration decay signal from a poorly-graded sand specimen tested at σ_o = 1.1 atm are shown in Figure 5.13 and Figure 5.14, respectively. Considerable noise reduction occurs after an 8th ordered Butterworth filter is used on a free-vibration decay signal.

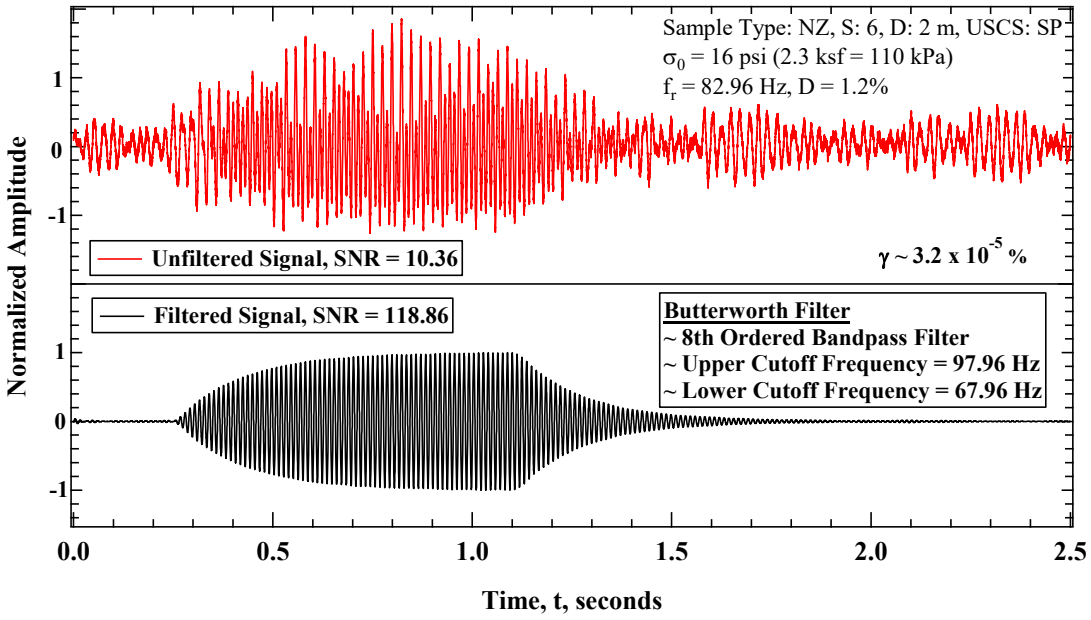

Figure 5.13: Time-Domain Example of Butterworth Bandpass Filtering on a Free-Vibration Decay Signal from a Poorly-Graded Sand (from New Zealand) Specimen Tested at σ_o = 1.1 atm.

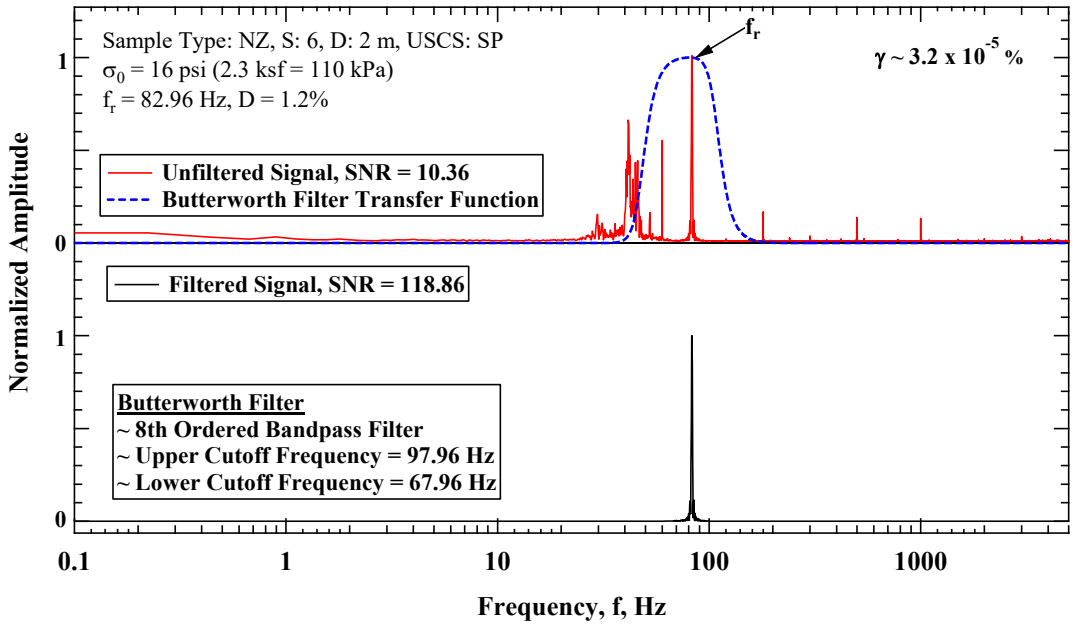

Figure 5.14: Frequency-Domain Example of Butterworth Bandpass Filtering on a Free-Vibration Decay Signal from a Poorly-Graded Sand (from New Zealand) Specimen Tested at σ_o = 1.1 atm.

5.3.4 Step 4: Hilbert Transform and Instantaneous Signal Parameters

After any necessary signal stacking or digital filtering is conducted, further signal processing techniques are used to conduct a more detailed and thorough analysis of the signal. The Hilbert transform is a useful and modern signal processing technique that is available due to higher sampling rates, finer voltage resolution of the acquired signals, and ample computer processing and memory. The Hilbert transform allows a large number of points that map the amplitude of the vibration well beyond the number of peak points of the signal. This allows use of statistical processing techniques that make vibration analysis more precise (Feldman 2011).

The formulation for the Hilbert transform is given in Feldman (2011) by:

$$H[x(t)] = \tilde{x}(t) = \pi^{-1} \int_{-\infty}^{\infty} \frac{x(\tau)}{t-\tau} d\tau \tag{5.56}$$

where the analytic signal is given as:

$$X(t) = x(t) + i\tilde{x}(t) \tag{5.57}$$

To return from complex form of analytic signal X(t) back to real function x(t) the following function is used:

$$x(t) = 0.5[X(t) + X^{*}(t)] \tag{5.58}$$

where X* is the complex conjugate of X(t).

In order to assess the detailed aspects of a signal, a method for finding instantaneous characteristics of the signal is employed. As discussed in Santamarina and Fratta (2005) a Hilbert transform is used to generate a signal with a -90° phase shift of the original signal. The new signal is assigned as imaginary values and the original signal assigned as real values, otherwise known as the analytic signal (Feldman 2011). The instantaneous

amplitude of the summed signal is the absolute value, which is presented in Santamarina and Fratta (2005) as:

$$amp_i = \sqrt{Im\left(x_i^{<A>}\right)^2 + Re\left(x_i^{<A>}\right)^2} \tag{5.59}$$

where amp_i is the instantaneous amplitude of the signal, i is the sample position of the signal and Im and Re are the imaginary and real components of the signal, respectively.

Additional characteristics of the signal that are of interest include the instantaneous phase, ϕ_i and instantaneous circular frequency, ω_i, which are respectively:

$$\varphi_i = \tan^{-1}\left(\frac{Im\left(x_i^{<A>}\right)}{Re\left(x_i^{<A>}\right)}\right) \tag{5.60}$$

$$\omega_i = \frac{\varphi_i - \varphi_{i+1}}{\Delta t} \tag{5.61}$$

where Δt is the inverse of the sampling rate.

An example is created to visualize in the usage of the Hilbert Transform complex coordinate space and in the time domain. The following plots were adapted from Feldman (2011), but the example is of a free vibration decay signal from a linear system with a damped natural frequency, f_D of 5.004 Hz, and a damping ratio, D of 4%. From the equations listed previously the signal characteristics of the free-vibration decay signal are plotted in Figure 5.15 through Figure 5.19.

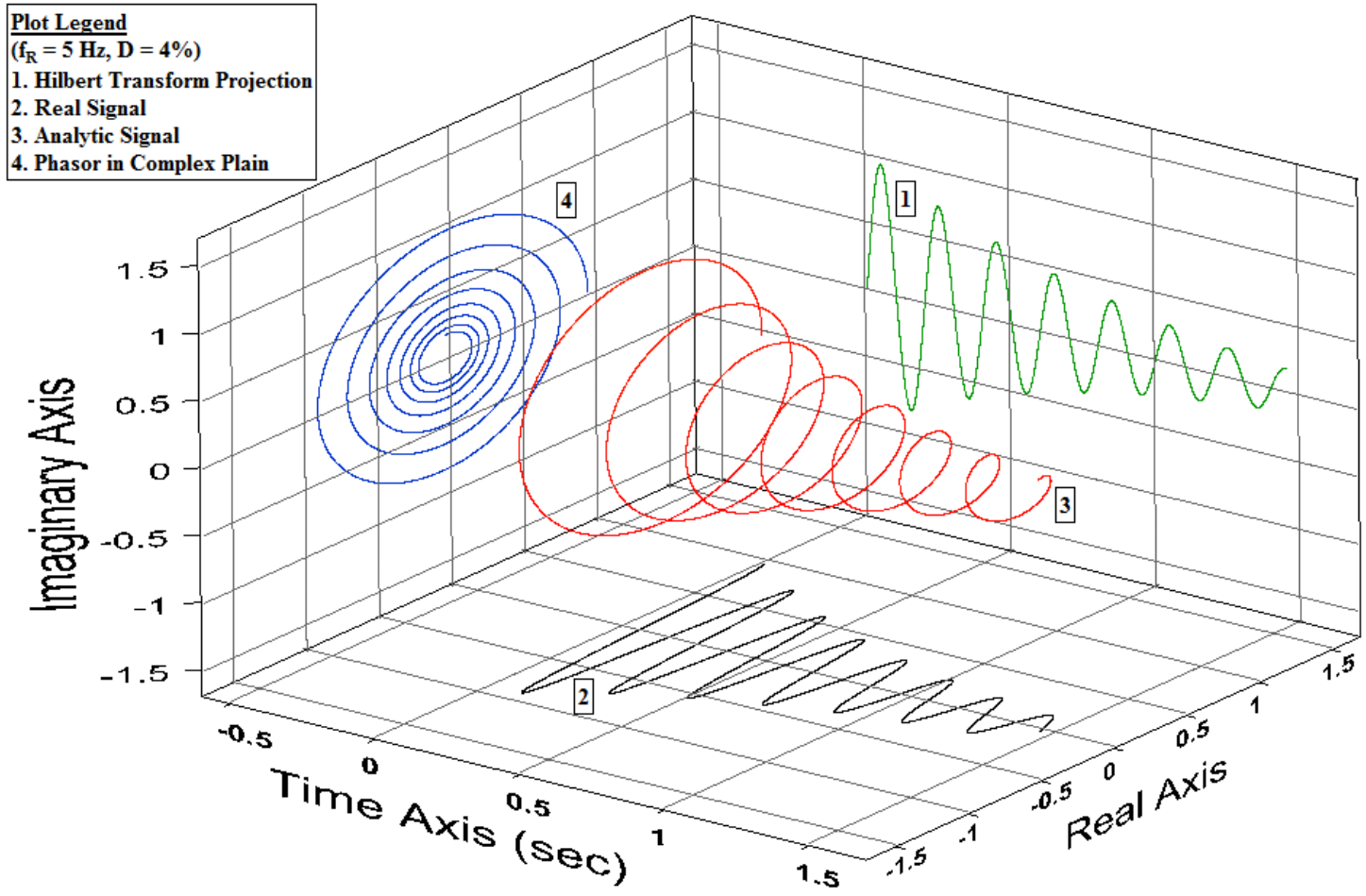

Figure 5.15: Analytic Signal Plotted in 3D, Real Signal Projected onto the Real Plane, Hilbert Transform Projected onto the Imaginary Plane, and Analytic Signal Projected onto the Complex Plane, adapted from Feldman (2011).

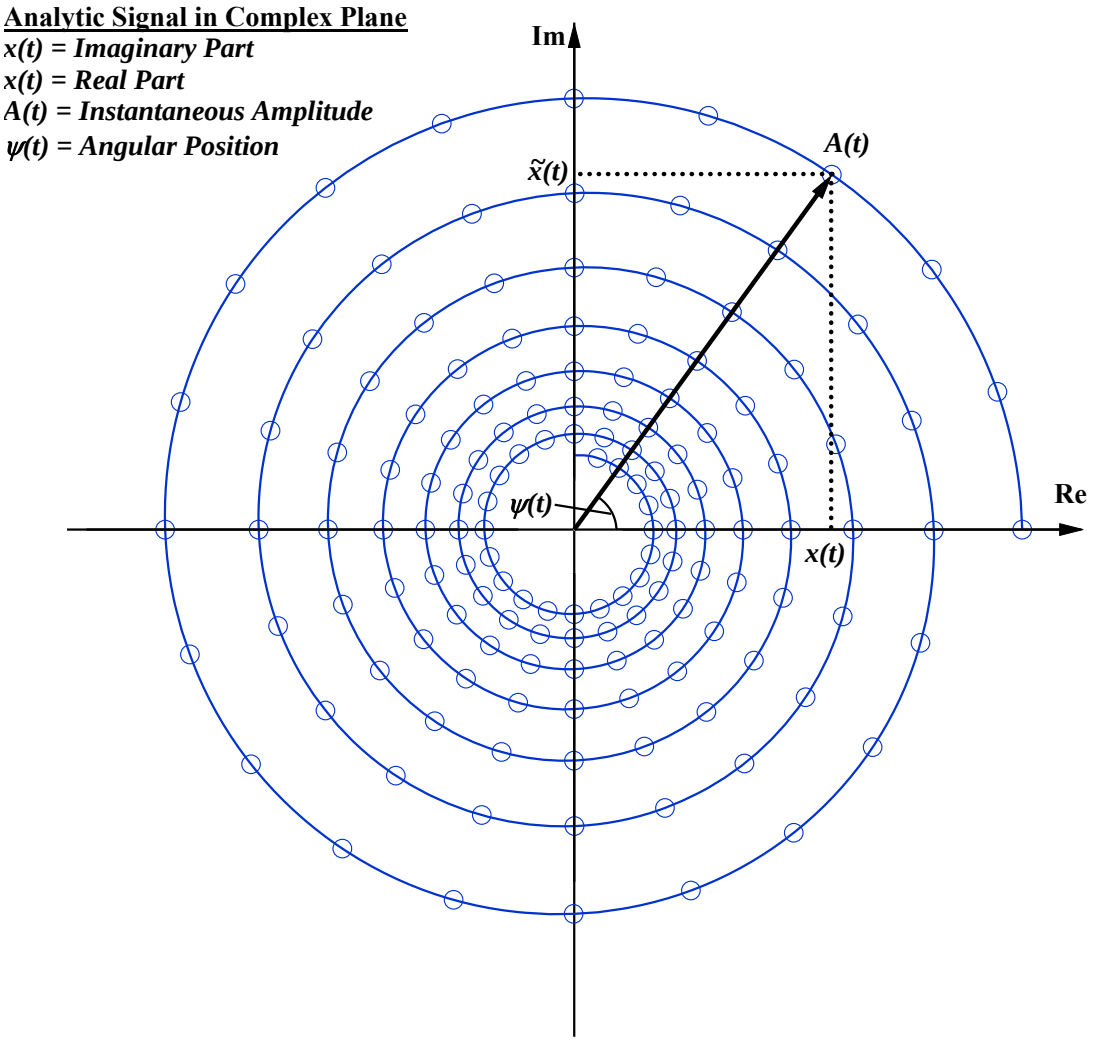

Figure 5.16: Analytic Signal Plotted in the Complex Plane with Analytic Signal Characteristics Shown, adapted from Feldman (2011).

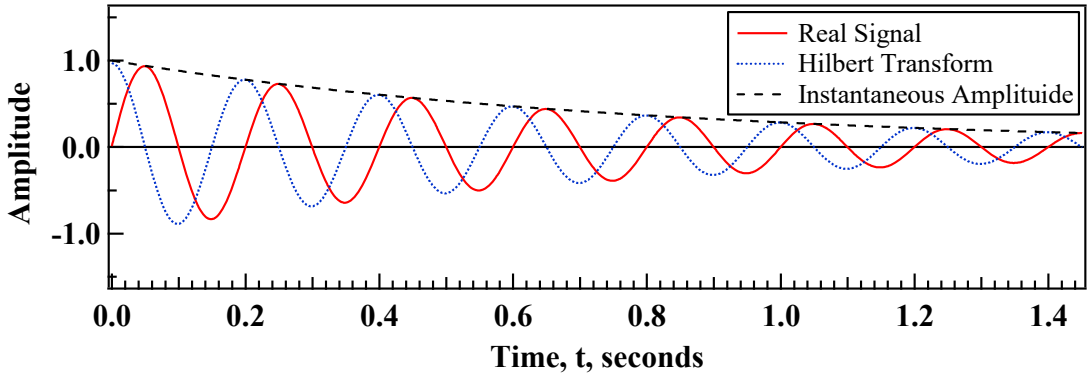

Figure 5.17: Plot of the Real Signal, Hilbert Transform, and Instantaneous Amplitude versus Time, adapted from Feldman (2011).

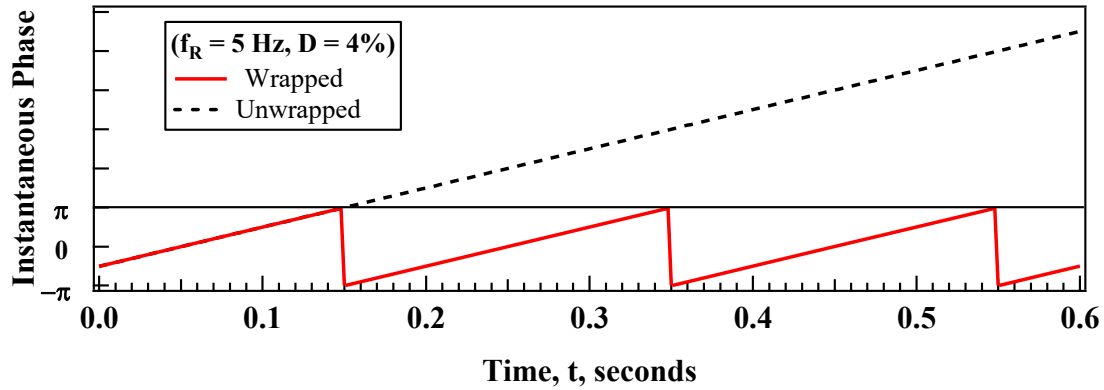

Figure 5.18: Plot of the Wrapped and Unwrapped Phase versus Time Determined Using the Hilbert Transform on a Free Vibration Decay Signal, adapted from Feldman (2011).

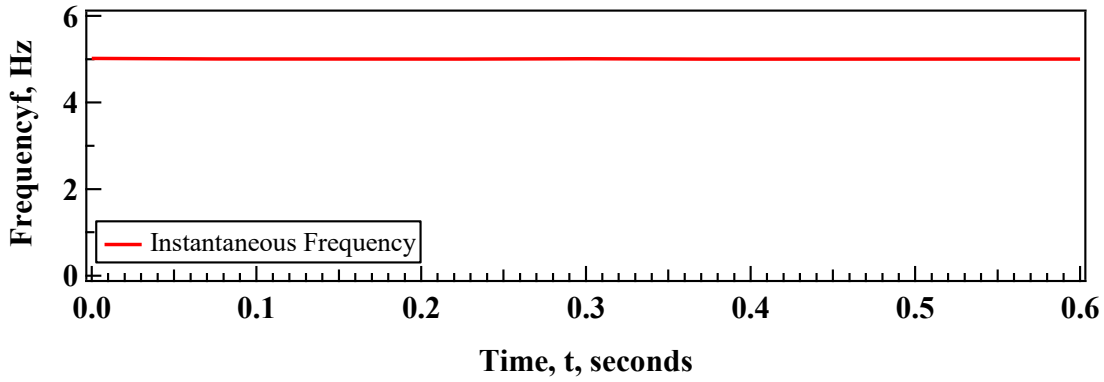

Figure 5.19: Plot of Instantaneous Frequency versus Time Determined Using the Hilbert Transform on a Free Vibration Decay Signal, adapted from Feldman (2011).

Since damping is primarily the characteristic of interest when evaluating the free-vibration decay test, the number of data points gained by the Hilbert transform method make calculation of the logarithmic decrement more robust. The theoretical framework for a single-degree-of-freedom system with viscous damping is expanded to include the Hilbert Transform method. The instantaneous amplitude of the signal is used to calculate logarithmic decrement as:

$$\delta = \frac{\ln\left(\frac{Z_1}{Z_2}\right)}{F_S/f_D} = \frac{2\pi D}{\sqrt{1-D^2}} \tag{5.62}$$

where Z_1 and Z_2 are two successive instantaneous strain amplitudes of motion, F_S is the sampling rate, f_D is the damped natural frequency, and D is the material damping ratio. Thus the material damping ratio is calculated from logarithmic decrement according to:

$$D = \sqrt{\frac{\delta^2}{4\pi^2+\delta^2}} \tag{5.63}$$

In the linear strain range damping is typically very small and the difference between the natural frequency, damped natural frequency, and resonant frequency is on the order of 0.001 Hz and thus the differences are negligible. Since the resonant frequency is known from the stepped sine sweep test, run subsequent to the steady-state decay, it is convenient to use the resonant frequency for simplicity in calculation of damping.

5.3.5 Combination of Stacking, Filtering, and Using the Hilbert Transform on Free-Vibration Decay Test Signals

On an individual basis, each of the stacking, targeted notch filtering, and bandpass filtering methods have been shown to greatly enhance the quality of the recorded signals. Signal stacking helps to mask any test anomalies, reduce random background noise, and increase the reliability of the measured response signal. Targeted notch filtering removes harmonic distortion that occurs consistently at specific frequencies and is not removed by signal stacking. Bandpass Butterworth filtering further reduces the impact of residual random or consistent background noise. When these methods are combined together, the impacts of testing anomalies, harmonic distortion, and random noise are greatly reduced; thus, higher signal quality and measurement repeatability are achieved.

A demonstration of the combined stacking and filtering methods is shown for free-vibration decay tests on a poorly-graded sand specimen tested at very low shear strains (~ 7×10^{-6} %) at a confining pressure of 0.46 atm (see Figure 5.20). The frequency-domain representation of the raw signal shows that the background noise had far greater amplitude than the measured system response. Even after conducting the test 20 times and stacking the results, the background noise had greater amplitude than the measured system response. When using combined targeted notch and bandpass Butterworth filtering on one raw signal, the measured system response has greater energy than the background noise; however, the level of the background noise is still detrimental. After combined signal stacking, targeted notch filtering, and bandpass Butterworth filtering, the amplitude of the measured system response relative to the background noise is sufficient to accurately calculate the material damping ratio from the free-vibration decay test. The final step (Step 4) involving the Hilbert Transform is shown in Figure 5.21.

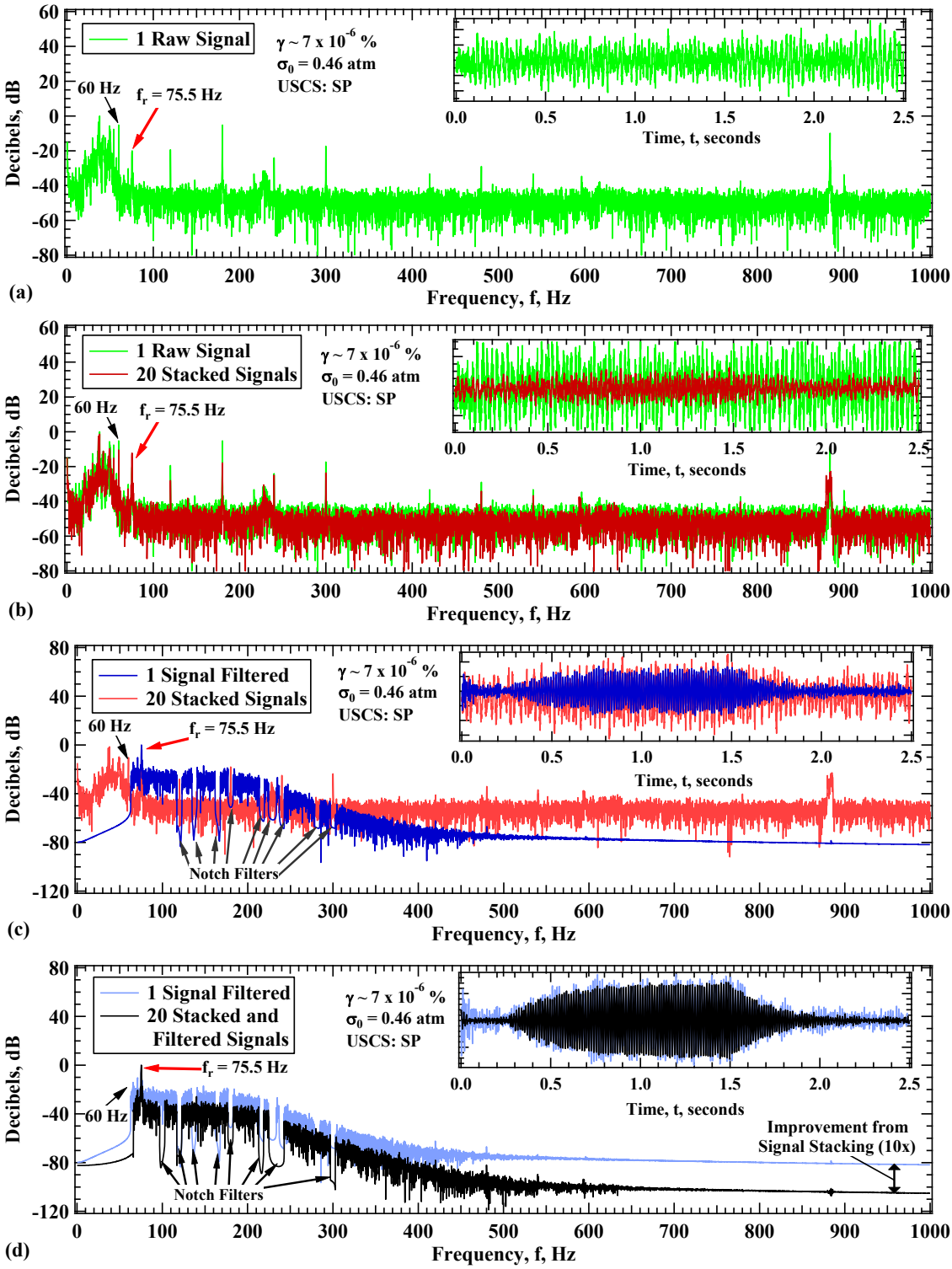

Figure 5.20: Free-Vibration Decay Measurements: Frequency- and Time-Domain Examples of Signal Stacking and Filtering.

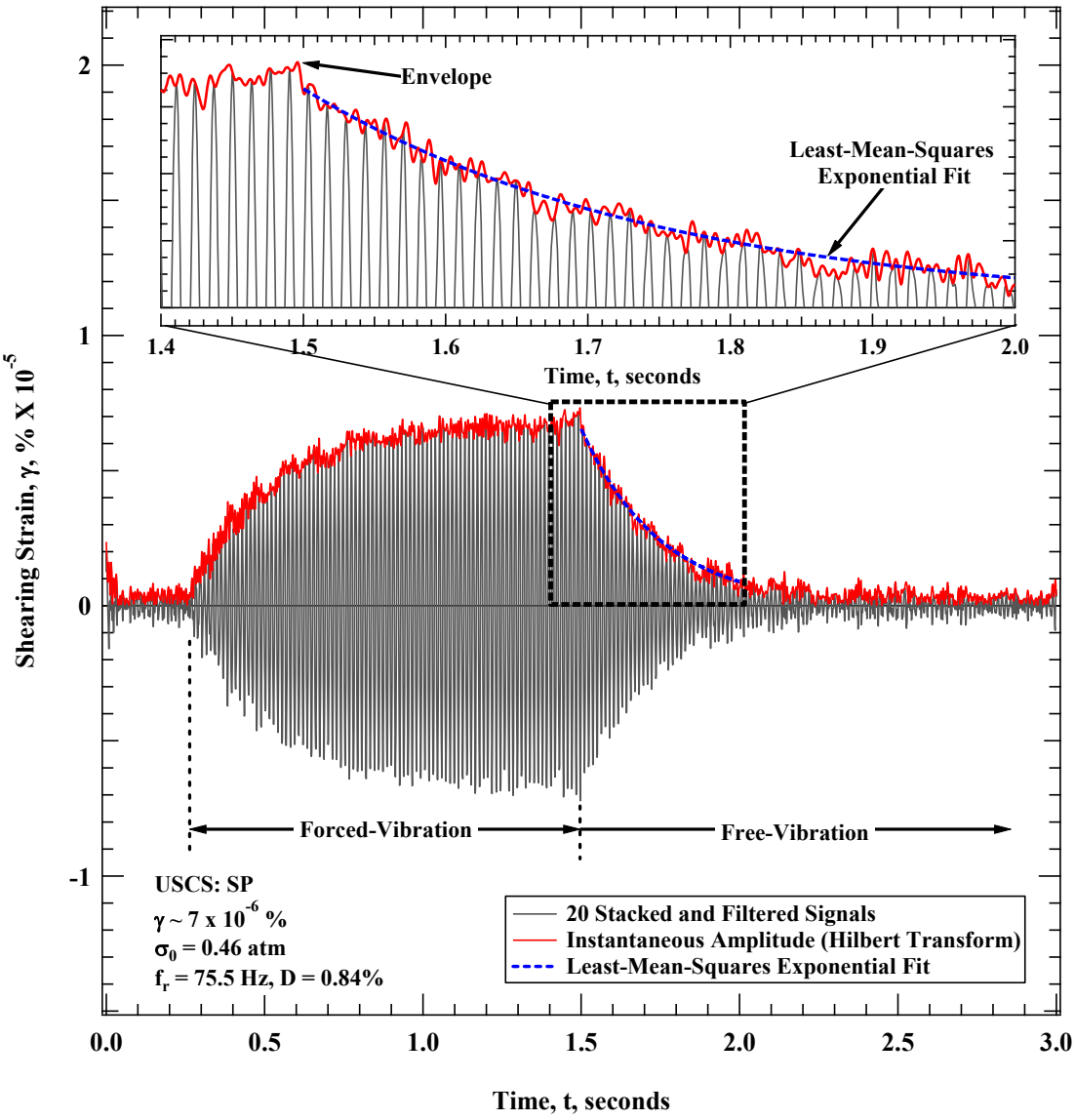

Figure 5.21: Time-Domain Example of Combined Signal Stacking, Filtering, and Hilbert Transform of Free-Vibration Decay Test Signals from a poorly-graded sand specimen tested at very low shear strains (~ 7 x 10^{-6} %) at a confining pressure of 0.46 atm.

5.4 VALIDATION OF SIGNAL PROCESSING METHODS AND COMPARISON WITH TRADITIONAL RC CONTROL SYSTEM

To validate the signal stacking and digital processing methods for taking measurements at very low strains, tests were conducted on a washed mortar sand specimen and Metal Specimen #2. From the tests conducted, data of a single raw signal, stacked signals, stacked signals with digital processing, and subsequent frequency sweep were recorded. The results of these experiments shown for a washed mortar sand in Figure 5.22. In general, the free-vibration decay results are shown to be unreliable at very low shear strains unless combined signal stacking and filtering are used. The reliability of the free-vibration decay results also depend on the frequency of excitation and the background noise present during testing, but in general combined signal stacking and filtering is needed when testing at shearing strains below 0.0003%.

The results of the experiments for Metal Specimen #2 are shown in Figure 5.23. Similar to the results for the washed mortar sand, the free-vibration decay results are shown to be unreliable below a shear strain of 0.0003%. The tests on the metal specimen were conducted over the full range of shear strains capable of the RCTS device for Metal Specimen #2. The results from testing the full range of shear strains capable in the RCTS device shows that there are no irregularities that arise from using combined signal stacking and filtering for free-vibration decay analysis when testing at higher shear strains. Thus, the methods are sound when testing a linear SDOF system.

Measurements with and without the techniques presented herein are shown to indicate that the techniques are needed and that there use does not distort the true values being measured. The new system is also compared with the traditional system by showing the variation in shear modulus with shearing strain for a washed mortar sand tested at 0.61,

1.22, 2.45, and 4.89 atm. The comparisons between the two systems are shown in Figure 5.24.

The new system has clearly enhanced resolution and the ability to tests soils at very low shear strains, which has not been achieved in other RCTS testing systems. The practical application of this enhanced resolution is important when testing test soft soils, where accurate measurements of the maximum shear modulus, G_{max}, and minimum material damping ratio, D_{min}, are difficult to obtain. This enhanced resolution becomes important when testing sands and gravels at confining pressures below 1 atm where the linear-elastic threshold can be as low as 0.0001%. Concurrently, when testing silts and clays, the excitation frequencies used for testing can be around or below 60 Hz, which was shown in Chapter 3 to be problematic. In situations where excitation frequencies used for testing are around or below 60 Hz, the digital processing methods presented herein are essential for taking accurate measurements. Though all of the examples shown in this chapter where demonstrated using accelerometer data, each of the processing routines presented are also used with the proximitor data, which is more robust when excitation frequencies are around or below 60 Hz. Both accelerometer and proximitor data are analyzed and provided to the operator to choose from when reducing RC test results.

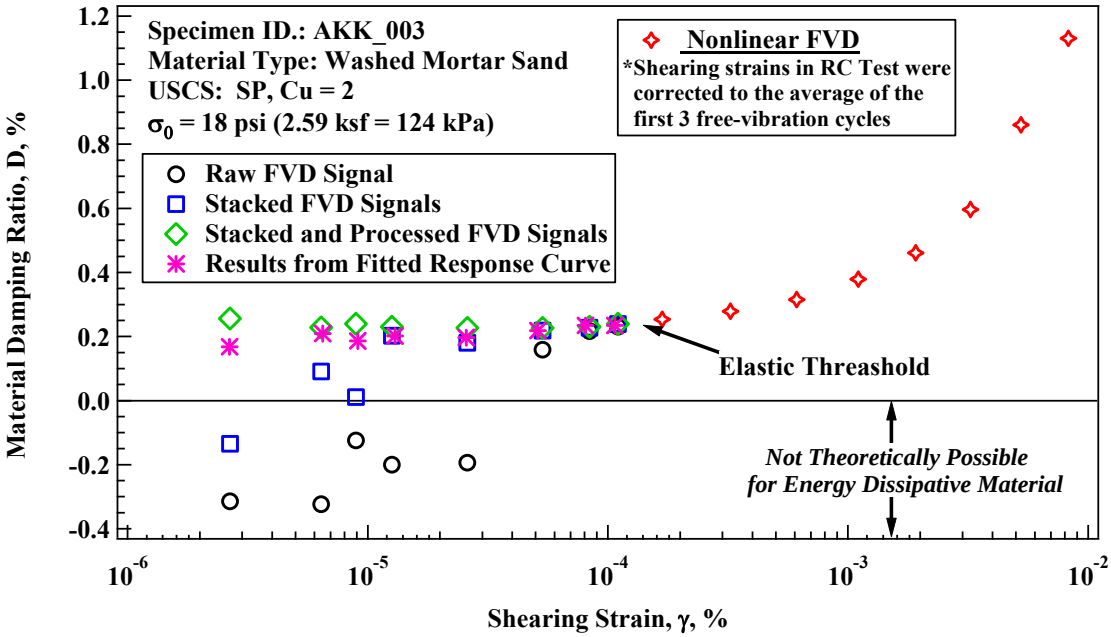

Figure 5.22: Comparison of the Variation in Material Damping Ratio with Shearing Strain from Frequency Sweep Tests and Free-Vibration Decay Tests on a Washed Mortar Sand Tested at σ_o = 1.27 atm.

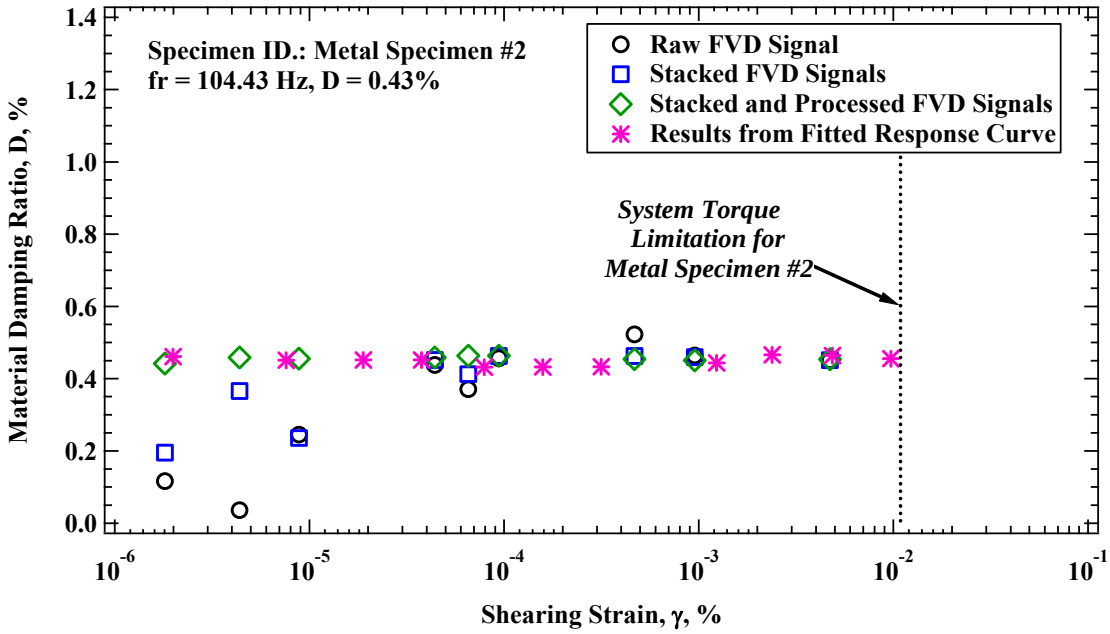

Figure 5.23: Comparison of the Variation in Material Damping Ratio with Shearing Strain from Frequency Sweep Tests and Free-Vibration Decay Tests on Metal Specimen #2.

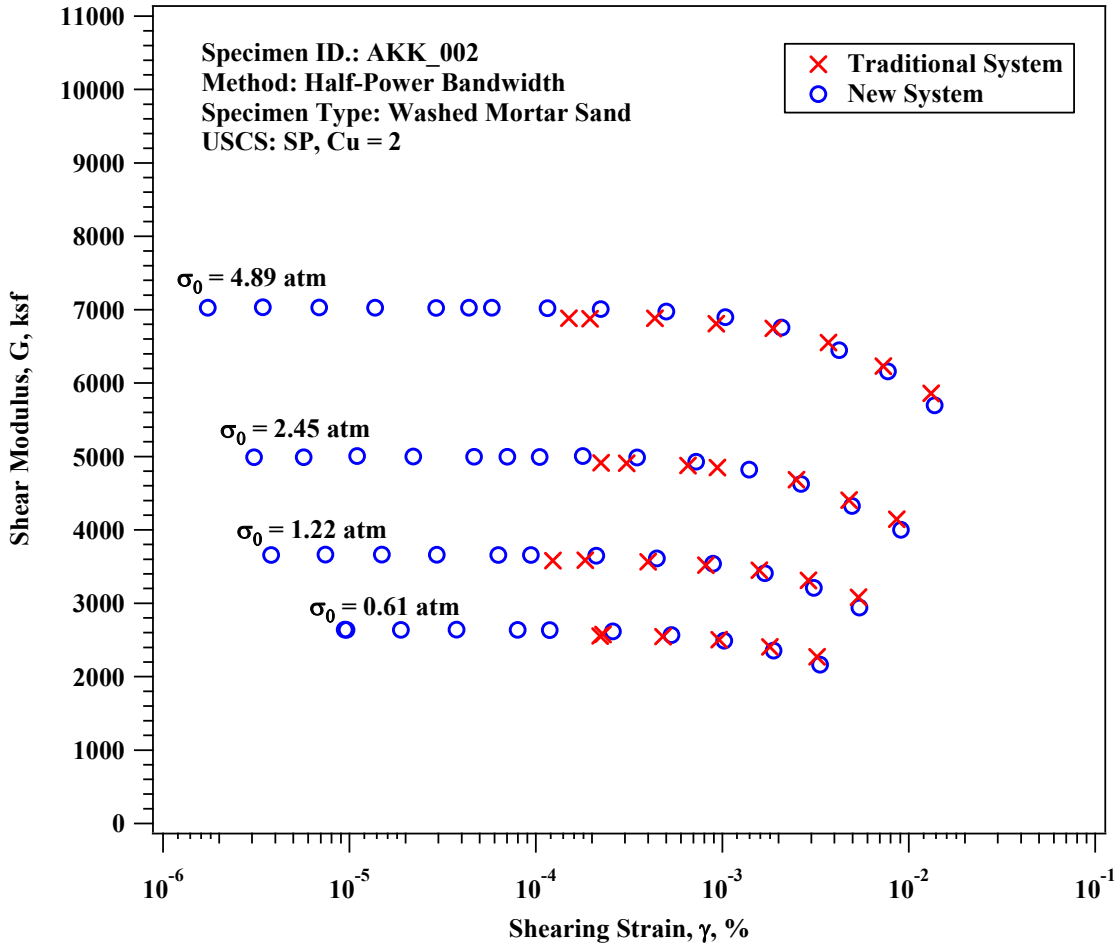

Figure 5.24: Comparison of Shear Modulus Measurements with Shearing Strain for New and Traditional RCTS Testing Systems.

5.5 SUMMARY

Higher data acquisition resolution, modern data and signal processing techniques, and additional testing methods developed herein were employed to make measurements of the resonant frequency and material damping ratio at strains as low as 10^{-6} %. The practical application of this enhanced resolution is important when testing test soft soils. Making accurate measurements at shear strains than range from 10^{-6} to 10^{-3} % is curtail for obtaining the maximum shear modulus, G_{max}, and minimum material damping ratio, D_{min}. Taking measurements at shear strains at or below 10^{-4} % are essential when testing sands and gravels at confining pressures below 1 atm where the linear-elastic threshold can be as low as 0.0001%. Concurrently, when testing silts and clays, the excitation frequencies used for testing can be around or below 60 Hz, which was shown in Chapter 3 to be problematic. In situations where excitation frequencies used for testing are around or below 60 Hz, the testing procedures and digital processing methods presented herein are essential for taking accurate measurements. Though all of the examples shown in this chapter where demonstrated using accelerometer data, each of the processing routines presented are also used with the proximitor data, which is more robust when excitation frequencies are around or below 60 Hz. Both accelerometer and proximitor data are analyzed and provided to the operator to choose from when reducing RC test results.

A time-domain digital signal subroutine was developed called the wavelet integration method that is highly proficient at reducing the influence of background noise. Following the frequency sweep tests where the wavelet integration method is employed, there are two methods used to determine the response curve characteristics (i.e. f_r & D) from the frequency sweep. These are: (1) Using an interpolation method between the local maxima and minima near the half-power points to make a more precise determination of the half-power frequencies, and (2) use of a least-mean squares fitting method that fits the

response curve equation to the measured data to iteratively determine the values for the natural frequency and material damping ratio. In general, the least-mean-squares fitting method much more robust when making small-strain measurements, where the SDOF system response is linear, but where significant levels of background noise may be present.

Signals from free-vibration decay tests are conditioned in four steps to make accurate measurements of material damping ratio and the damped natural frequency (when needed). The first step includes signal stacking to obtain a sufficient signal-to-noise ratio. The second step involves a process of targeted notch filtering, which is effective for removing high levels of noise at specific frequencies, which is described in Wilson (2013) as a narrow-band rejection filter. The third step involves bandpass filtering, which is effective for reducing all levels of background noise outside of the frequency range of interest. The fourth involves using the Hilbert Transform method to use the entire waveform for analysis rather than the peak and/or trough signal amplitudes. In combination, the steps developed herein allow accurate and consistent measurement of the free-vibration decay signal at shear strains as low as 10^{-6} %.

Traditionally, background noise is a problem when measuring material damping using the free-vibration decay method at very small strains (< 0.0003%). On the other hand, background noise generally has a smaller effect on the frequency response curve at strains below even 0.0003%. Therefore, the frequency sweep test results are often preferred to the free-vibration decay test results for making small-strain damping measurements. The methods discussed in this chapter are meant to make robust measurements in the linear-elastic strain range to shear strains as low as 10^{-6} %. The ability to accurately define the dynamic behavior in the linear-elastic strain range has been achieved for both the frequency sweep and free-vibration decay tests using both the accelerometer and proximitor data.

Chapter 6

Analytical Evaluation of the Methods of Analysis Used in the Resonant Column Test at Small Strains to Determine the Most Accurate Methods

6.1 INTRODUCTION

In resonant column (RC) testing, the accuracy of the measuring values for shear strain, γ, resonant frequency, r_r, half-power damping ratio, D_{HP}, and free-vibration decay damping ratio, D_{fv}, can be greatly affected by the level of background noise present. The influence of background noise on the accuracy of the measurements is primarily a concern when testing in the elastic shear strain range (i.e. $\gamma < 0.0008\%$). However, as discussed in Chapter 3, the influence of background is different depending on the sensors used and the frequency excited during the test. A typical resonant column test is composed of two parts. In the first part, a downgrade frequency sweep is used to determine the resonant frequency, half-power damping ratio, and maximum shear strain amplitude excited during the sweep. The second part begins by exciting the specimen at the resonant frequency determined in part 1. The downgrade sweep is followed by a free-vibration decay test where the specimen is excited at the resonant frequency. After reaching steady-state vibration (i.e. maximum shear strain measured during the downgrade frequency sweep), the excitation is abruptly suspended and the specimen is allowed to freely vibrate. The free-vibration test is used to determine the damped natural frequency and free-vibration damping ratio. The purpose of this chapter is to analytically evaluate some methods available to digitally process signals from the frequency sweep and free-vibration decay parts of the RC test.

The process for analytically evaluating the digital signal processing methods was done using Monte Carlo simulations. In each Monte Carlo simulation, theoretical signal responses were simulated based on dynamic theory of a viscously damped single-degree-

of-freedom (SDOF) system. Background noise was simulated using a random number generator and was added to the theoretically simulated response signal. The level of background noise selected was based on a prescribed signal-to-noise ratio (SNR). Once "noisy" signals were generated, the digital signal processing methods were used repeatedly over hundreds of Monte Carlo simulations. The results of the repeated evaluations of randomly noisy signals were used to develop statistics that describe the accuracy of each of the digital signal processing methods used. Each set of Monte Carlo simulations were conducted for specified SNRs and the statistics of each Monte Carlo set were used to compare the probabilistic accuracy of each digital signal processing method based on SNR. The results of these experiments provide insight into which digital signal processing methods yield the highest degree of accuracy based on the SNR present, which is discussed and presented herein. Using an experimental approach to this study instead of the analytical approach discussed in this chapter would not be meaningful because the characteristics of the background noise may not be random during each test, an incredibly large amount of test data would be required to generate the same number of evaluations, and the testing process would take far too long to conduct a timely parametric evaluation.

Noisy signals were simulated to represent the frequency sweep part of the RC test. The resulting response curves were determined by using a root-mean-squares (RMS) method and the wavelet integration method (WIM). The accuracy of the two methods was evaluated for determining γ, f_r, and D_{HP}. The WIM was found to be much more robust than the RMS method for reducing the influence of background noise on the resulting response curves. An additional method was employed to further reduce the influence of background noise which involved finding the characteristics of the response curve (i.e. γ, f_r, and D_{HP}) by determining the minimum least-mean-squares (LMS) difference between the SDOF response curve equation and the results measured from the frequency sweep. This method

is more robust for determining γ, f_r, and D_{HP} than the traditional half-power bandwidth approach. This chapter presents the results of analytically evaluating each of these methods.

Noisy signals were simulated to represent numerous free-vibration decay tests. In each set of Monte Carlo simulations, the percent of signal decay used to calculate the D_{FV} was changed. Furthermore, numerous SNRs were used to simulate the noisy signals. The results of the experiment were used to determine what percent of signal decay yields the most accurate D_{FV} result based on the SNR. In addition, the results of this experiment can be used to help guide the use of a weighted LMS fit of an exponential decay curve to the free-vibration decay envelope based the SNR present during the test. The results and recommendations from this experiment are presented herein.

6.2 DESCRIPTION OF THE MONTE CARLO SIMULATIONS

The process for analytically evaluating the digital signal processing methods was done using Monte Carlo simulations. The development of the Monte Carlo simulations were based off of notes provided in Wilson (2013) and Gilbert (2014). In each Monte Carlo simulation, theoretical signal responses were simulated based on dynamic theory of a viscously damped single-degree-of-freedom (SDOF) system as described in Richart, Hall and Woods (1970). Background noise was simulated using a LabVIEW random number generator and was added to the theoretically simulated response signal. The level of background noise selected was based on a prescribed signal-to-noise ratio (SNR). Once "noisy" signals were generated, the digital signal processing methods were used repeatedly over hundreds of Monte Carlo simulations. The results of the repeated evaluations of randomly noisy signals were used to develop statistics that describe the accuracy of each of the digital signal processing methods used. Each set of Monte Carlo simulations were

conducted for specified SNRs and the statistics of each Monte Carlo set were used to compare the probabilistic accuracy of each digital signal processing method based on SNR

The standard deviation used in the LabVIEW Gaussian Distributed random noise generator was determined by:

$$\sigma_{noise} = \frac{A_{max}}{SNR} \tag{6.1}$$

where σ_{noise} is the standard deviation of the noise input into the random number generator and A_{max} is the maximum amplitude of the simulated signal. A random number (i.e. realization) was generated for each sample in the response signal array. Each Monte Carlo set consisted of a total of number of N simulations. In each Monte Carlo set a different SNR is for simulated noisy signals.

The mean, μ, of each Monte Carlo set was calculated using:

$$\mu = \frac{\sum_{i=1}^{N} x_i}{N} \tag{6.2}$$

where μ is the mean, x_i is the magnitude response of a single Monte Carlo simulation, and N is the total number of simulations. The standard deviation, σ, of the Monte Carlo set was calculated using:

$$\sigma = \sqrt{\frac{\sum_{i=1}^{N}(\mu - x_i)^2}{N}} \tag{6.3}$$

As mentioned previously the μ and σ for each Monte Carlo set was calculated and each Monte Carlo set was conducted at a specific SNRs. From the statistical parameters determined from each set, the probability that the measured value is within a certain percent difference can be determined. Based on the simulations conducted, the statistical parameters describe a normal distribution N(μ, σ) and thus the probability distribution can be described as seen in Gilbert (2014) as:

$$F_X(x) = P(X \leq x) = \Phi\left(\frac{x-\mu}{\sigma}\right) \quad (6.4)$$

where F_X is the cumulative distribution function (CDF), P is the probability that $X \leq x$ given $N(\mu, \sigma)$, Φ represents the CDF operation, and x is the value being evaluated (Gilbert 2014). Based on the Monte Carlo results, the probability that a measured value is within plus/minus percent, δ, of the mean value is given by:

$$P(a < X \leq b) = F_X(b) - F_X(a) = \Phi\left(\frac{\mu*(1+\delta)}{\sigma}\right) - \Phi\left(\frac{\mu*(1-\delta)}{\sigma}\right) \quad (6.5)$$

where the value of the CDF from the side below the mean is subtracted from the side above the mean yielding the percent probability that a measured value is within a certain percent of the mean. A tolerance can be prescribed for a particular characteristic (e.g. γ, f_r, D, etc.) being measured that the measured value is within $\pm\delta\%$ of the expected value. The probability that the measured value is within $\pm\delta\%$ of the expected value is based on two criteria: (1) The measured value is within a tolerance of the expected value based on the standard deviation determined in the Monte Carlo simulation and (2) The mean value determined in a Monte Carlo set is within $\pm\delta\%$ of the value used to create the simulation. For example, the tolerance that a result is within ± 1% of the expected value would be described as:

$$P(a < X \leq b) = \Phi\left(\frac{\mu*1.01}{\sigma}\right) - \Phi\left(\frac{\mu*0.99}{\sigma}\right) \quad (6.6)$$

6.3 Analytical Evaluation: Accuracy of Shear Strain Measurements from The Frequency Sweep Test

In RC testing, the accuracy of the magnitude of the response signal is only important for determining the shear strain that was excited during the test. Thus, the introduction of noise, which would cause a deviation in the measured shear strain from the true shear stain, would only cause a shift in the documented shear strain value during the test. In the linear-elastic strain range this difference would have minimal influence on the appearance of the G/G_{max} curve that is of interest in RC testing. Therefore, the interest in this exercise is to identify the potential inaccuracy in the shear stain values that might occur. More importantly is how the presence of noise might affect the measurement of the maximum shear modulus and the material damping ratio. In this section the exercises are differentiated into separated examples, where first the presence of noise is used to evaluate the effect on the measured shear strain of the system. Then a separate simulation is used to determine the effect on the measurements of shear modulus and material damping ratio.

The basic processing techniques for evaluating signals in the free-vibration test were discussed previously, but there can be several limitations based on background noise and degree of nonlinearity present in the test result. In this subsection, the limitation of the methods for evaluating the free-vibration material damping ratio with the presence of background noise is quantified. The accuracy of signal processing in the free-vibration test is probabilistically defined based on the signal-to-noise ratio calculated from the result. Numerical simulations are used to determine the probability of obtaining an accurate result within a given confidence interval and based on the level of Gaussian distributed random noise present. The numerical simulations were used to refine the free-vibration signal processing technique so that the most probabilistically accurate result is obtained. Finally,

the results of the numerical simulation and analytical evaluations are compared with signals obtained experimentally.

6.3.1 Theoretically Created Signal at Resonance

This analytical evaluation of the stepped-sine sweep evaluation method was done based on the same example presented in Chapter 5. For the digital processing aspects, the number of integration cycles is 15 and the sampling rate is 10,000 samples/sec. The input properties of the SDOF oscillator are f_r = 10 Hz, D = 4%, m = 0.5 lb-sec^2/ft, and Q_0 = 100 lb. Based on these characteristics the stimulus and response signals can be simulated. The stimulus signal will have a frequency equal to the resonant frequency of the system and a magnitude of Q_0 (100 lb) and thus the response signal will have an amplitude equal to A_{max} = M_{max}*Q_0/k (A_{max} = 0.63174 ft). The phase shift at the natural frequency is 90 degrees; however, do to the presence of damping, the resonant frequency is less than the natural frequency and the phase shift at the resonant frequency is less than at the phase shift at the natural frequency. For the SDOF properties supplied, φ_r is equal to 87.7057 degrees, which is the phase used to generate the response signal. The signal was created using:

$$A = \sin(\omega * t - \varphi) \tag{6.7}$$

where A is the signal amplitude, ω is the circular frequency (rad/sec), t is the time (sec), and φ is the phase (rad).

6.3.2 Monte Carlo Simulation of Noise Effect on Calculated Shear Strain

Numerous Monte Carlo simulations were conducted while adjusting the signal-to-noise ratio (SNR) of the response signal to evaluate the accuracy of the Wavelet Integration method utilized in the LabVIEW swept sine program. In each Monte Carlo simulation, an array of random noise was added to the response signal and the standard deviation of the

noise was selected based on the SNR selected for the set. Each Monte Carlo set involved 10000 simulations and the magnitude and phase shift was calculated in each simulations. The Gaussian random noise generator in LabVIEW was used and seeded for each simulations with the seed applied consecutively from 1 to 10000 so that this simulation is repeatable and can be duplicated. The mean and standard deviation of the magnitude and phase for all of the 10000 iterations was calculated to determine the probability that a single test will yield a shear strain and phase shift that is within a certain percent difference of the true value. In addition, the Wavelet Integration is compared with a method used in traditional RC testing where the root-mean-squared (RMS) amplitude of the stimulus and response signal is calculated and the magnitude is found from the quotient of these two RMS values. This method was found to be superior to the Traditional RC method involving taking the RMS values for the stimulus and response signals. Finally, the experiment detailed herein provides some understanding to the experimental error of this test when evaluating the shear strain measured during the RC test and provides a minimum tolerance of SNR when measuring shearing strain in RC tests.

The stimulus and response signals were configured using the same SDOF oscillator described in the previous subsection. Thus, the standard deviation used in the LabVIEW Gaussian random noise generator was determined by:

$$\sigma_{noise} = \frac{M_{max} * Q_0/k}{SNR} = \frac{0.631737}{SNR} \tag{6.8}$$

where σ_{noise} is the standard deviation of the noise input into the random number generator. A random number was generated for each sample in the response signal array which amounted to 15000 Gaussian randomly distributed values. Each Monte Carlo set consisted of a different SNR with the full experiment ranging in SNR values from 0.001 to 10,000. The number of Monte Carlo simulations, N, conducted was 10000.

6.3.3 Results of the Analytical Evaluation: Shear Strain from Response Curve

As mentioned previously, two methods are used for determining the transfer function between the stimulus and noisy response signals for each individual Monte Carlo simulation. The Wavelet Integration method that has been discussed throughout this section and the RMS method mentioned before. From each Monte Carlo set based on SNR, statistical parameters were determined for each of these methods and used to determine probability that the measured value is within ± 1% of the expected value and also that the mean from each Monte Carlo set is within ± 1% of the simulation input value. The results are plotted in Figure 6.1 and Figure 6.2.

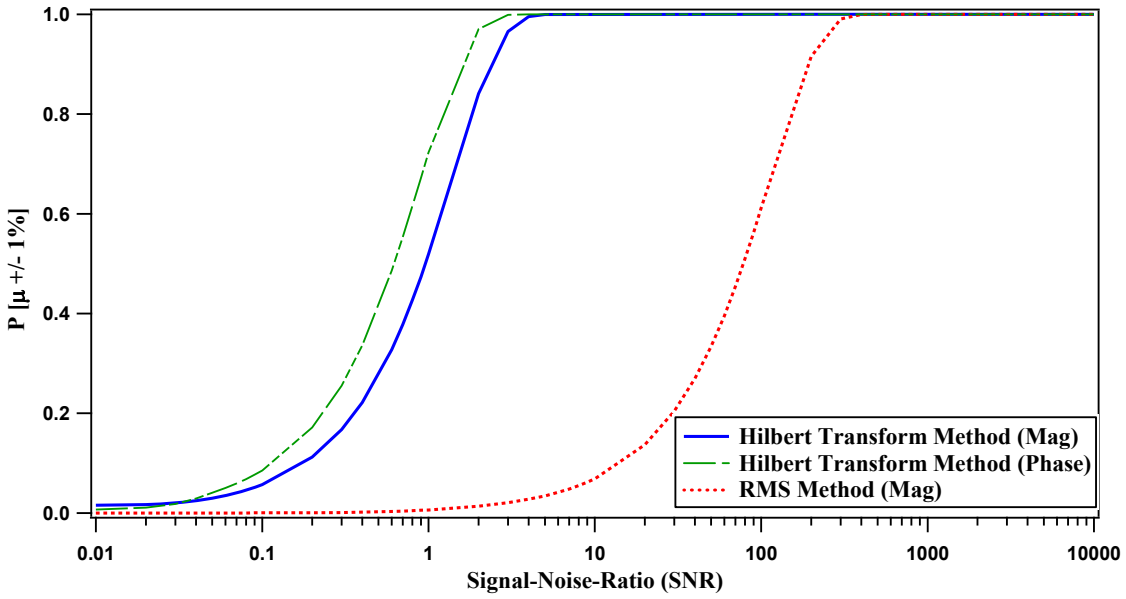

Figure 6.1: Comparison of the Probability of Obtaining a Result ± 1% of the Expected Value with Signal-to-Noise-Ratio (SNR) for the Magnitude found from Wavelet Integration Method, the Phase Found from the Wavelet Integration Method, and Magnitude Found from the Root-Mean-Squares (RMS) Method.

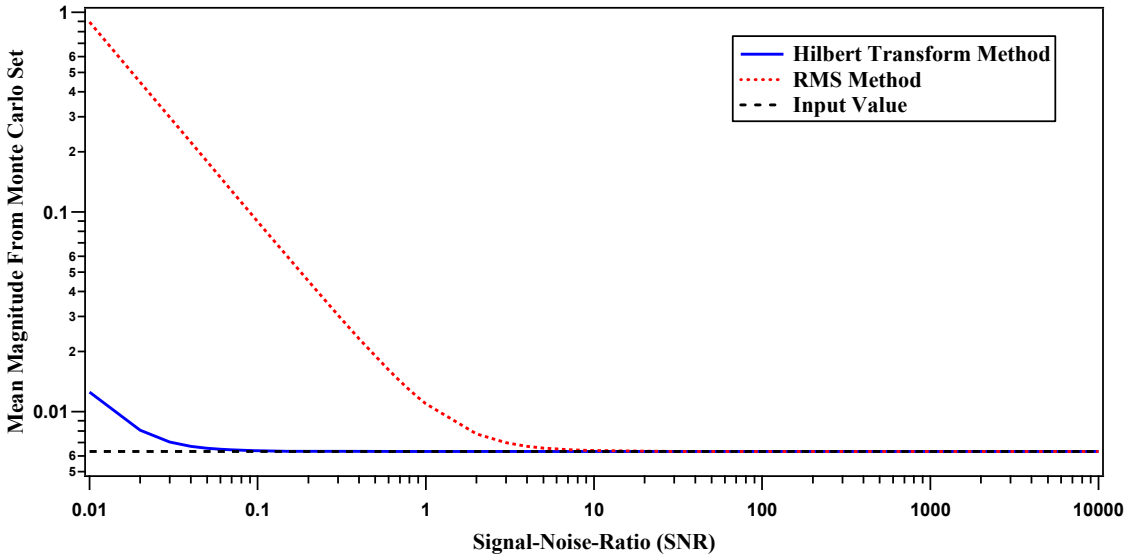

Figure 6.2: Comparison of the Mean Magnitude from the Monte Carlo Set with Signal-to-Noise-Ratio (SNR) for the Magnitude found from Wavelet Integration Method, the Magnitude Found from the Root-Mean-Squares (RMS) Method, and the Input Value used to Simulate the Analysis.

The probability that the measured value is within ± 1% of the expected value is significantly better for the Wavelet Integration Method than the RMS method. This can be attributed to the fact that the Wavelet Integration method employs a rigorous filter via multiplying both signals by the analytic signal. Since random noise generation creates noise across all frequencies, this filter removes much of the noise contamination, where the RMS method may lead to only some of the noise to subtract out; however, not uniformly across the stopband frequencies as the Wavelet Integration method does. The mean magnitude from the Monte Carlo sets for both the Wavelet Integration and the RMS methods do not converge with the expected value for very low SNR. However, the mean from the Hilbert method (SNR~0.1) converges much sooner with the expected value than the RMS method (SNR~10).

In the plot comparing standard deviation of the methods from each of Monte Carlo sets to the SNR, the RMS method has a standard deviation that equals the expected value

when the SNR is equal to 1. This confirms that no noise reduction occurs when using the RMS method. The Wavelet Integration method has a standard deviation that equals the expected value when the SNR is equal to 0.01, which indicates that this method reduces the level of noise by 2 orders of magnitude. The phase was also evaluated and shown to have less susceptibility to the random noise experiment than the measurement of the magnitude of the signals.

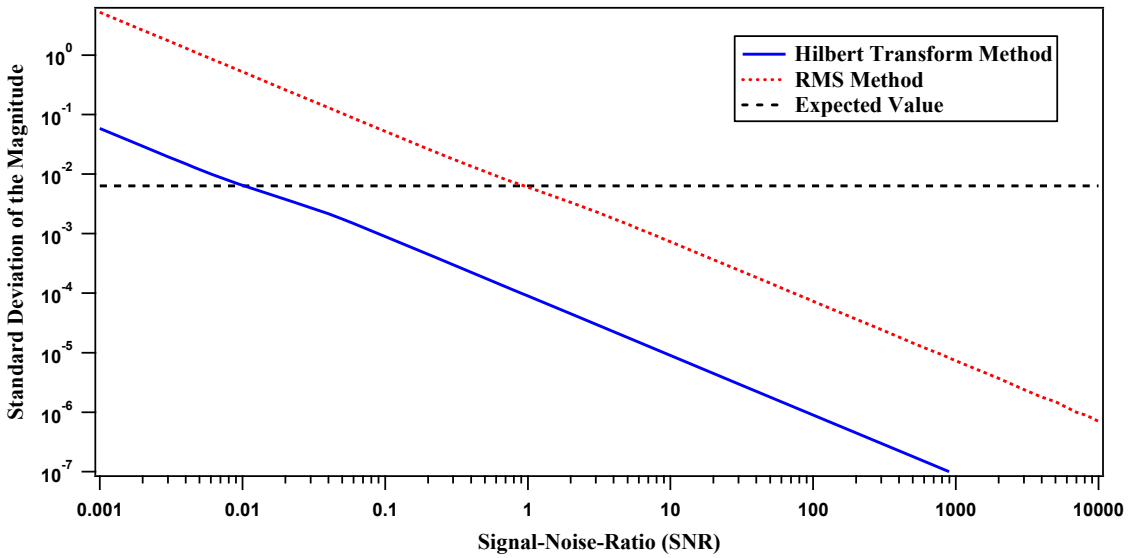

Figure 6.3: Comparison of the Standard Deviation from the Monte Carlo Set with Signal-to-Noise-Ratio (SNR) for the Magnitude found from Wavelet Integration Method, the Magnitude Found from the Root-Mean-Squares (RMS) Method, and the Input Value used to Simulate the Analysis.

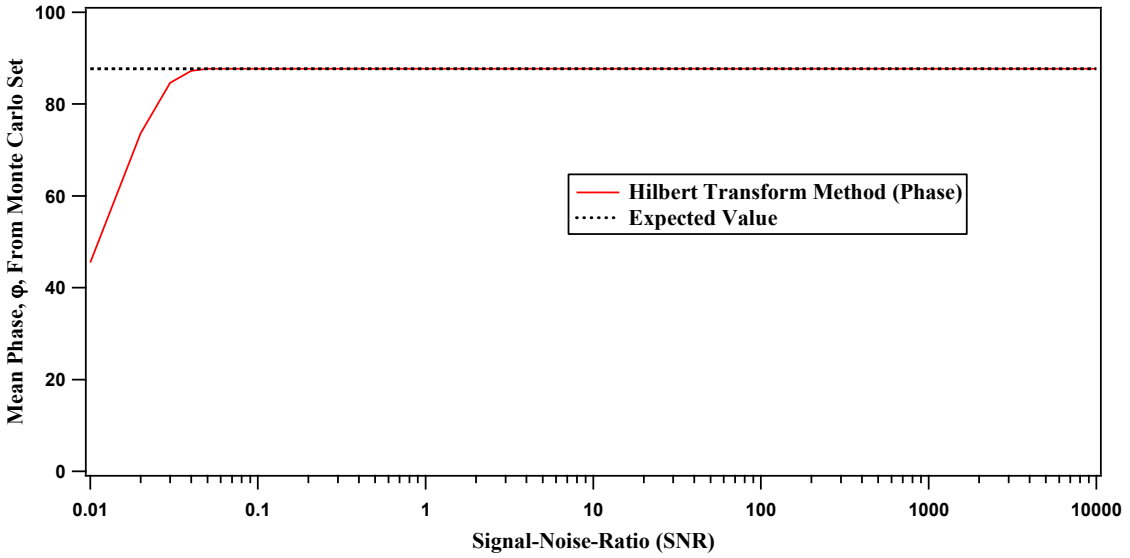

Figure 6.4: Comparison of the Mean Phase from the Monte Carlo Set with Signal-to-Noise-Ratio (SNR) for the Magnitude found from Wavelet Integration Method.

6.4 Analytical Evaluation: Accuracy of Resonant Frequency and Damping Measurements from The Frequency Sweep Test

6.4.1 Theoretically Created Response Curves, Signals, and Methods of Analysis

In this investigation, a response curve was created theoretically and sinusoids were created each with amplitudes matching amplitudes of the response curve. Noise was then added to each of the sinusoids where the noise was created using a Gaussian distributed random number generator. The level of the noise was programmed based on a selected noise standard deviation. The noise level chosen was based on the signal-to-noise ratio (SNR) where the signal level was selected as the peak of the response curve (i.e. amplitude at resonance. For the digital processing aspects, the number of cycles simulated at each frequency were 5, 10, 20, and 40. The input properties of the SDOF oscillator are f_r = 150 Hz and the damping ratios evaluated were 0.5, 1, 5, and 10%. The theoretically created response curves with noise were evaluated with four methods that have been subsequently

presented in this dissertation, which include: (1) Wavelet Integration digital signal processing method (WIM) combined with the half-power bandwidth approach (HPB); (2) Wavelet Integration digital signal processing method combined with least-mean-squares fitting (LMS) of the SDOF response curve equation to the response curve data; (3) Taking the root-mean-square (RMS) of the signal at each frequency combined with the half-power bandwidth approach; and (4) Taking the root-mean-square (RMS) of the signal at each frequency combined with least-mean-squares fitting of the SDOF response curve equation to the response curve data. An example a theoretically created noisy response curve with a 1% damping ratio and SNR of 4 and was evaluated with the WIM and RMS methods as shown in Figure 6.5. The theoretically created noisy single at the resonant frequency is shown in Figure 6.6. The preceding sections present the results of analytically evaluating each of these methods.

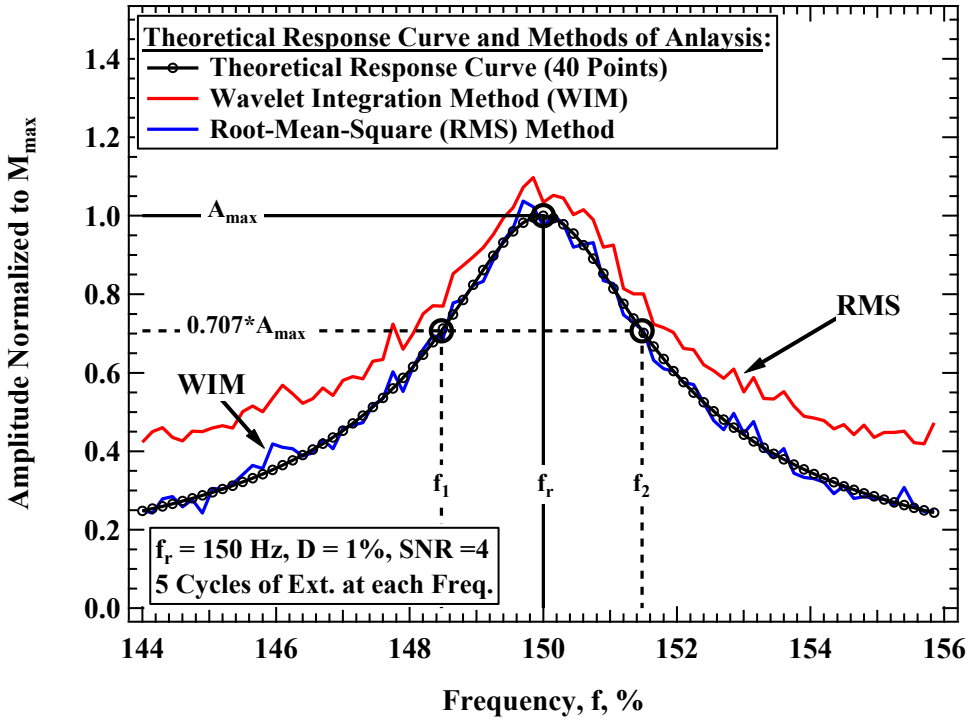

Figure 6.5: Theoretically Created Noisy Response Curve with a 1% Damping Ratio and SNR of 4 and was Evaluated with the WIM and RMS methods.

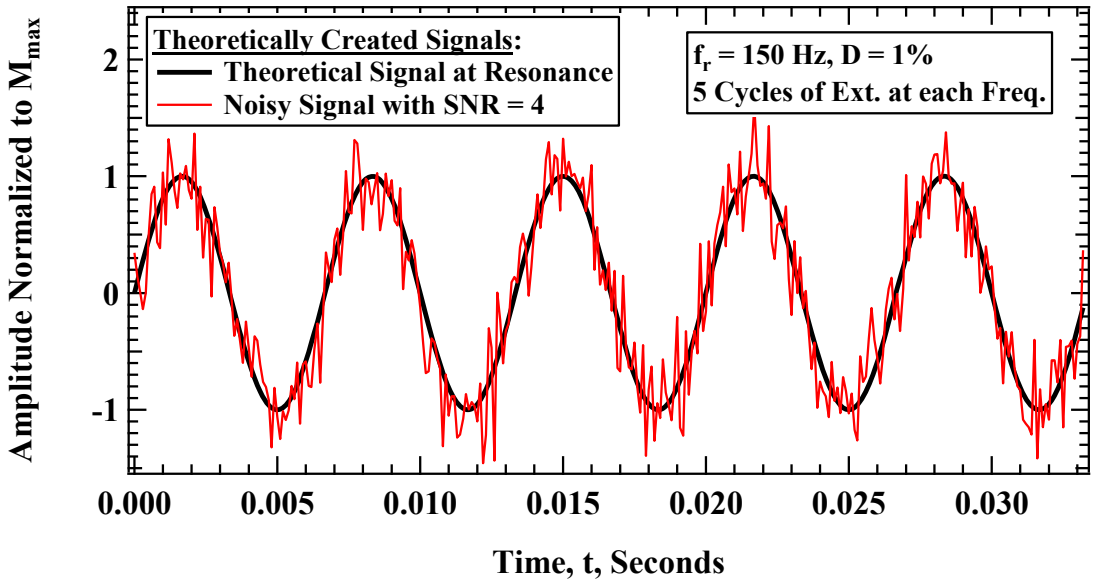

Figure 6.6: Theoretically Created Noisy Signal at Resonance with SNR of 4.

6.4.2 Monte Carlo Simulations of Noisy Response Curve Data

Numerous Monte Carlo simulations were conducted while adjusting the signal-to-noise ratio of the response signals to evaluate the accuracy of methods that can be utilized to evaluate response curve data from a frequency sweep test. In each Monte Carlo simulation an array of random noise was added to the response signal and the standard deviation of the noise was selected based on the signal-to-noise ratio (SNR) selected for the set. In this particular study, the SNRs evaluated ranged from 2 to 1000. The Monte Carlo sets for each SNR consisted of 300 trials. The response curves were simulated with 40 frequencies that had range defined by:

$$f_{low} = f_r - 2D \cdot f_r \tag{6.9}$$

$$f_{high} = f_r + 2D \cdot f_r \tag{6.10}$$

where f_r is the resonant frequency, D is the damping ratio, and f_{low} and f_{high} represent the start and end frequencies of the analysis, respectively. Thus, 40 signals are simulated for

each Monte Carlo trial. The number of samples used to simulate each signal were based on a sampling rate of 10,000 samples/sec and were dependent on the frequency used from the response curve and the number of cycles being evaluated. The range of samples used to simulate the response signal ranged from 200 to 4500 samples based on the parameters of the simulation, which is also the number of realizations to create random noise. A Gaussian random noise generator in LabVIEW was used and seeded for each iteration with the seed applied consecutively based on the product of the number of the sample within the simulated signal (out of 200 to 4500), the number of the simulated response curve signal (out of 40), and the number of the Monte Carlo trial (out of 300). Based on the numbers of simulated noise samples, response curve signals, and Monte Carlo trials, the number of realizations for each SNR evaluated ranges from 2.4×10^6 to 5.4×10^7. The Gaussian random noise generator in LabVIEW has up to 2^{90} samples before the pattern repeats itself, thus no realizations were repeated in this study. Based on this description, this analytical evaluation is repeatable and can be duplicated.

As mentioned in the previous section, four methods of analysis for processing response curve data were used. The mean and standard deviation of the resonant frequency and damping ratio for each of the four methods used and each of the SNRs simulated were calculated to determine the probability that a single test will yield a resonant frequency and damping ratio that is within a certain percent difference of the true value. The experiment detailed herein provides some understanding to the experimental error of these methods when measuring resonant frequency and damping ratio in noisy environments and which method of analysis is the most robust for making accurate and precise measurements. Furthermore, the results of this experiment can be used to establish a minimum tolerance for each method based on SNR when measuring resonant frequency and damping ratio from RC testing.

The response signals were configured using the same SDOF oscillator characteristics as discussed in the previous section. Thus, the standard deviation used in the LabVIEW Gaussian random noise generator was determined by:

$$\sigma_{noise} = \frac{M_{max}}{SNR} \tag{6.11}$$

where σ_{noise} is the standard deviation of the noise input into the random number generator. A random number (i.e. realization) was generated for each sample in the response signals, which as discussed previously amounts to 200 to 4500 Gaussian randomly distributed values. Each Monte Carlo trial consisted of a different SNR with the full experiment ranging in SNR values from 2 to 1000.

6.4.3 Results of the Analytical Evaluation: Resonant Frequency and Damping Ratio from Response Curve

As mentioned previously, four methods are used for determining the resonant frequency and damping ratio from noisy response signals for each individual Monte Carlo trial. These methods are (1) Wavelet Integration digital signal processing method (WIM) combined with the half-power bandwidth approach (HPB); (2) Wavelet Integration digital signal processing method combined with least-mean-squares fitting (LMS) of the SDOF response curve equation to the response curve data; (3) Taking the root-mean-square (RMS) of the signal at each frequency combined with the half-power bandwidth approach; and (4) Taking the root-mean-square (RMS) of the signal at each frequency combined with least-mean-squares fitting of the SDOF response curve equation to the response curve data.

From each Monte Carlo set, statistical parameters were determined for each of the four methods, which and were used to determine probability that the measured value is within ± δ% of the expected value (i.e. simulation input value). The mean and standard deviation for the simulations where D = 1% with 5 cycles at each frequency are shown in

Figure 6.7 and Figure 6.8, respectively. The probability that the measured damping ratio was within ± 1% of the expected value is shown in Figure 6.9.

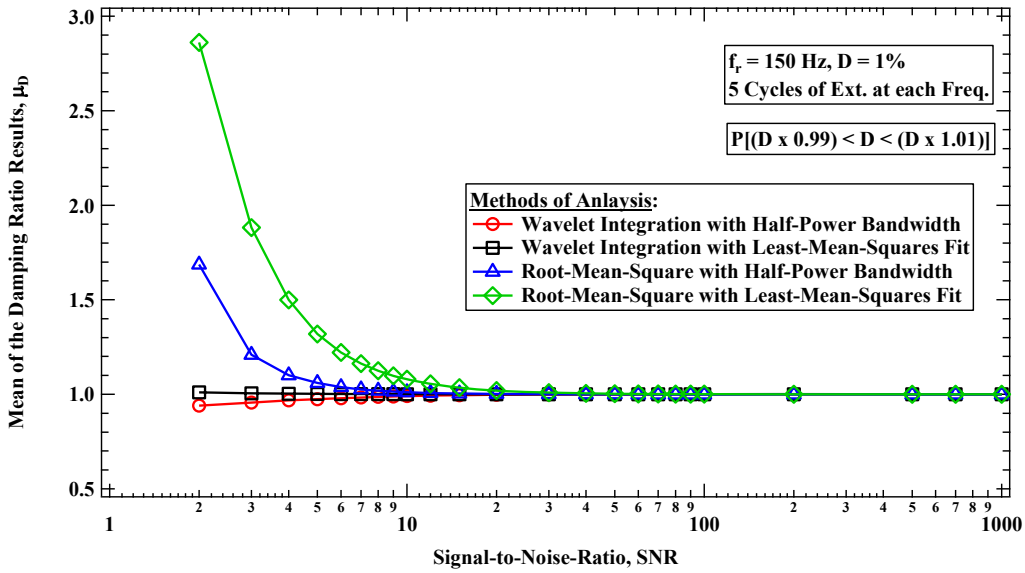

Figure 6.7: Comparison of the Mean Damping Ratio from the Monte Carlo Set with Signal-to-Noise-Ratio (SNR) for the Damping Ratio Found from Four Methods of Analysis.

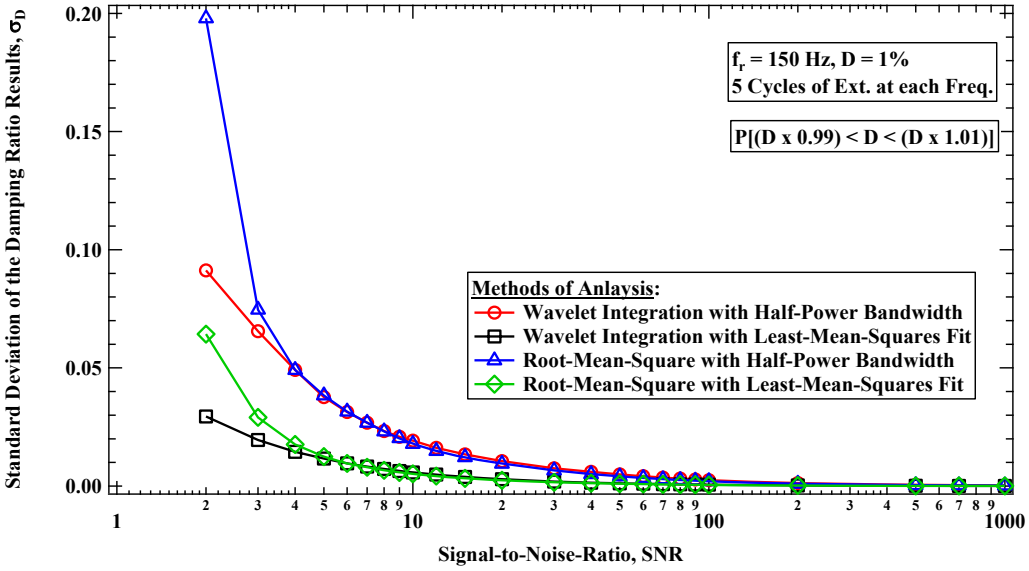

Figure 6.8: Comparison of the Standard Deviation Damping Ratio from the Monte Carlo Set with Signal-to-Noise-Ratio (SNR) for the Damping Ratio Found from Four Methods of Analysis.

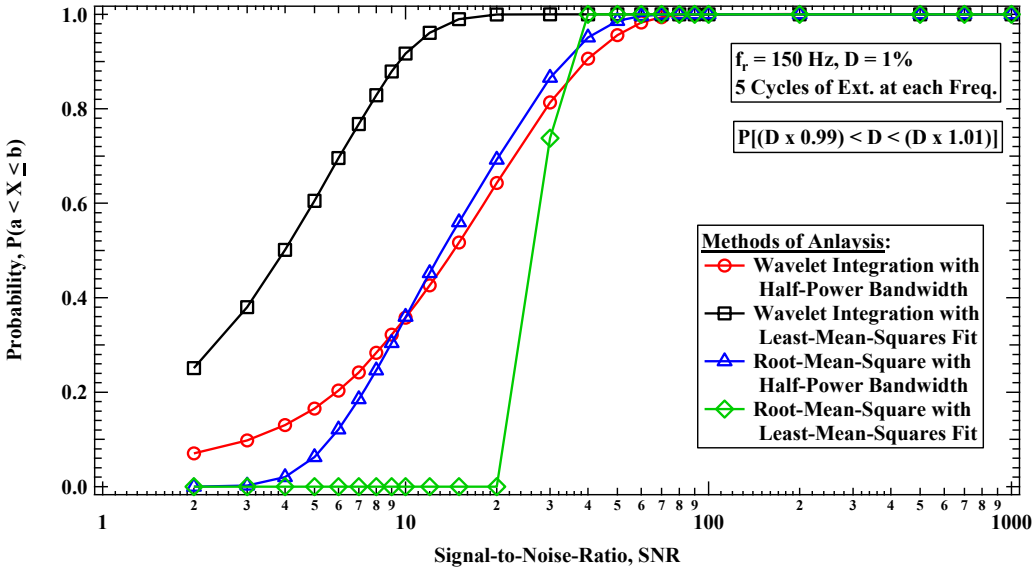

Figure 6.9: Comparison of the Probability of Obtaining a Result ± 1% of the Expected Value with Signal-to-Noise-Ratio (SNR) for the Damping Ratio found from Four Methods of Analysis.

The probability that the measured value is within ± 1% of the expected value is significantly better for the Wavelet Integration Method than the RMS method. This can be attributed to the fact that the Wavelet Integration method employs a rigorous filter via multiplying both signals by the analytic signal. Since random noise generation creates noise across all frequencies, this filter removes much of the noise contamination, where the RMS method may lead to only some of the noise to subtract out. Furthermore, the Wavelet Integration Method in combination with the least-mean-squares approach has much greater accuracy than the other three methods.

6.5 Analytical Evaluation: Accuracy of Methods Used to Evaluate Free-Vibration Decay Results

6.5.1 Theoretically Created Free-Vibration Test Signals

For each of the numerical simulations, a typical free-vibration test result was created artificially. The number of cycles needed to achieve a defined percent of steady-state vibration is given in Chopra (2001) by:

$$\frac{|u_j|}{u_0} = 1 - e^{-2\pi \cdot \varsigma \cdot j} \tag{6.12}$$

where u_j is the absolute value of the amplitude at cycle j, u_0 is the steady-state amplitude, and j is the number of input cycles. The theoretical decay curve is determined similar to the forced vibration envelope and is given by:

$$\frac{|u_j|}{u_0} = e^{-2\pi \cdot \varsigma \cdot j} \tag{6.13}$$

The simulation of a typical free-vibration test can be created by multiplying a continuous sinusoidal function by these force-vibration and steady-state vibration components. The quotient of $|u_j|/u_0$ represents a ratio of steady-state vibration over j number of cycles from initial conditions. This ratio can also be expressed as a percentage of steady-state vibration. With a damping ratio of 5% and a percentage of steady-state vibration of 99.5%, the number of cycles to reach steady-state is 16.87. To create an artificial signal representative of the test, the number of cycles calculated to reach 99.5% of steady-state vibration would be rounded up so that the forced-vibration stops at either zero displacement and peak velocity or peak displacement and zero velocity. For the free-vibration segment of the artificial signal, the number of cycles of decay are doubled leading to a percent decay of 0.0025%. This is done to evaluate further percentages of decay and to be more representative of an actual test where the decay does not seize. As will be proven

later on, the processing methods do not need to assess decay past 60% of the maximum amplitude.

Once artificial free-vibration test signals are created, a random number generator can be used to create Gaussian distributed random noise. The random number generator used was a subVI in LabVIEW called "Gaussian White Noise Generator.vi" An array of random numbers is created with a standard deviation based on a preselected signal-to-noise ratio, SNR, which is defined in this case as:

$$\text{SNR} = \frac{A_S}{\sigma_N} \tag{6.14}$$

where A_S is the maximum signal amplitude and σ_N is the standard deviation of the noise. The random noise is added to the signal array. Thus the maximum signal amplitude occurs at 99.5% steady-state and the standard deviation of the noise is this value divided by the chosen SNR. An example of an artificially created free-vibration test signal with a resonant frequency of 20 Hz, damping ratio of 5%, and a SNR of 10 is shown in Figure 6.10.

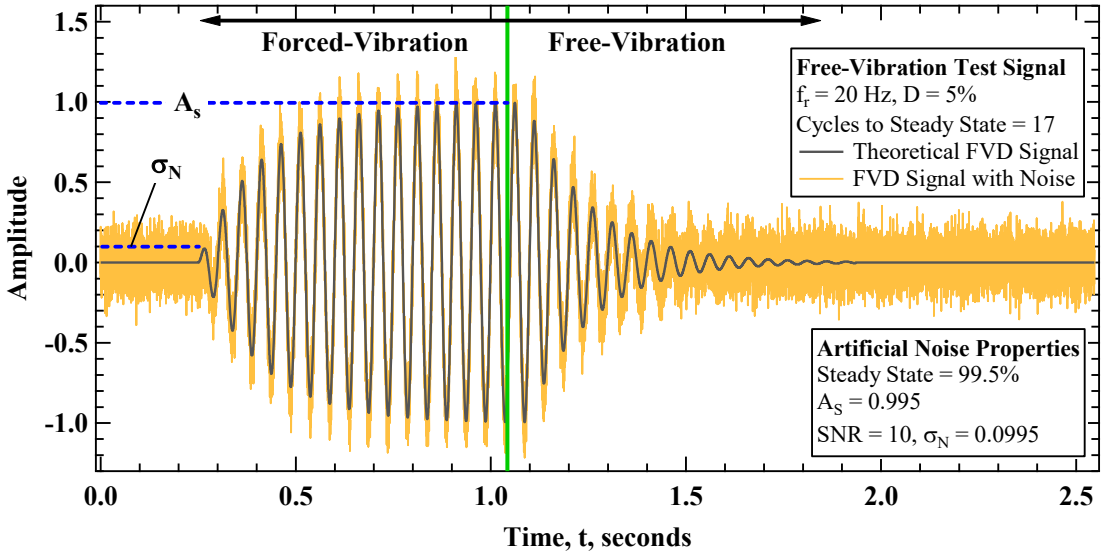

Figure 6.10: Example of Free-Vibration Decay Test Signal with Artificially Added Background Noise

When conducting the free-vibration test, the number of cycles used to excite the specimen are known and thus the specific data points that make up the free-vibration segment are known and can be evaluated. A segment of samples are recorded before the forcing function is applied and are used to measure the baseline standard deviation of the noise contaminating the signal.

6.5.2 Monte Carlo Simulation of Noise Effect on Calculated Free-Vibration Damping Ratio

Since damping is primarily the measurement of interest in free vibration decay, the number of data points gained by the Hilbert transform method make calculation of the logarithmic decrement more thorough. The theoretical framework for a single-degree-of-freedom system with viscous damping is expanded to include the Hilbert Transform method. The instantaneous amplitude of the signal is used to calculate logarithmic decrement as:

$$\delta = \frac{\ln\left(\frac{Z_1}{Z_2}\right)}{F_s/f_D} = \frac{2\pi D}{\sqrt{1-D^2}} \tag{6.15}$$

where Z_1 and Z_2 are two successive instantaneous strain amplitudes of motion, F_S is the sampling rate, f_D is the damped natural frequency (measured in the stepped sine sweep test), and D is the material damping ratio. Thus the material damping ratio is calculated from logarithmic decrement according to:

$$D = \sqrt{\frac{\delta^2}{4\pi^2+\delta^2}} \tag{6.16}$$

In the linear strain range damping is typically very small and the difference between the natural frequency, damped natural frequency, and resonant frequency is on the order of 0.001 Hz and thus the differences are negligible. Since the resonant frequency is known

from the stepped sine sweep test ran subsequent to the steady-state decay, it is convenient to use the resonant frequency for simplicity in calculation of damping.

The number of cycles used to reach steady-state vibration, which are used for excitation in the free-vibration test are calculated as shown previously and use the material damping ratio determined from the stepped sine sweep test. In general, the methods developed for determining the response curves parameters from stepped sine sweep test have more resolution and accuracy than the free-vibration test. Thus using the material damping ratio from the sweep test to define excitation cycles in the free-vibration test is assumed to be a reliable approach.

When evaluating the free-vibration segment with significant background noise present, the computational methods discussed previously begin to lose accuracy depending on how much of the free-vibration segment is used. The accuracy of the measured damping ratio decreases as more of the free-vibration segment is used because greater noise amplitudes contaminate the analysis. An example using the same signal presented in Figure 6.10 is used and the free-vibration segment is analyzed at 10%, 30%, and 60% levels of decay and the damping ratios measured are 4.84%, 4.69%, and 4.14%, respectively. Thus, the measured damping ratio is further underestimated from the true value of 5% as more of the segment is evaluated, these results are shown in Figure 6.11.

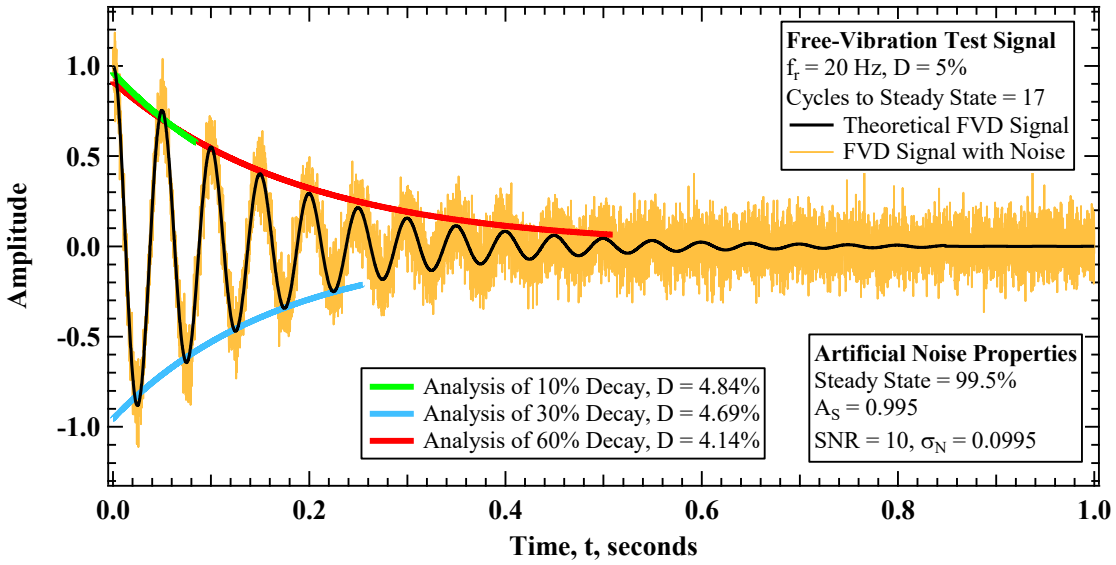

Figure 6.11: Example of Free-Vibration Decay Test Signal with Artificially Added Background Noise and Different Damping Ratios Recorded Depending on the Percent of the Decay Segment that Was Analyzed

In an actual free-vibration test, the signal is processed using bandpass and notch filtering that would significantly remove most of the noise present in a signal with an unfiltered SNR of 10. However, this example demonstrates that, when evaluating a signal with significant levels of noise present, using less of the free-vibration segment when predicting the material damping ratio is more accurate as less of the segment is used. Since a random number generator is used to simulate background noise, the damping ratios measured for each percent of signal decay used are non-unique and when averaged over numerous simulations will tend towards a normal distribution. Therefore, Monte Carlo simulations can be used to determine the normal distribution parameters based on SNR and percent of decay used in the damping ratio calculation.

6.5.3 Constructing the Monte Carlo Experiment to Evaluate Free-Vibration Damping Ratio Calculations

Numerous Monte Carlo simulations were conducted while adjusting the signal-to-noise ratio of the response signal to evaluate the accuracy of the free-vibration method based on the percent of signal decay used to calculate the free-vibration damping ratio. In each Monte Carlo simulation an array of random noise was added to the response signal and the standard deviation of the noise was selected based on the SNR selected for the set. In the Monte Carlo simulations bandpass filtering was also used since this will be implemented in experimental free-vibration tests.

The number of Monte Carlo simulations needed are based on the number of simulations needed to obtain stable normal distribution parameters from the set. Initially 500 simulations were conducted for background noise with an SNR of 1, which is the minimum SNR that could be evaluated. The normal distribution parameters were observed to become stable over 500 simulations. For each simulation, the free-vibration damping ratio was measured and the mean and standard deviation were recalculated for each additional simulation. The results for a single set of Monte Carlo simulations for a SNR of 2 and 10% of the signal decay used for analysis is presented in Figure 6.12 through Figure 6.14.

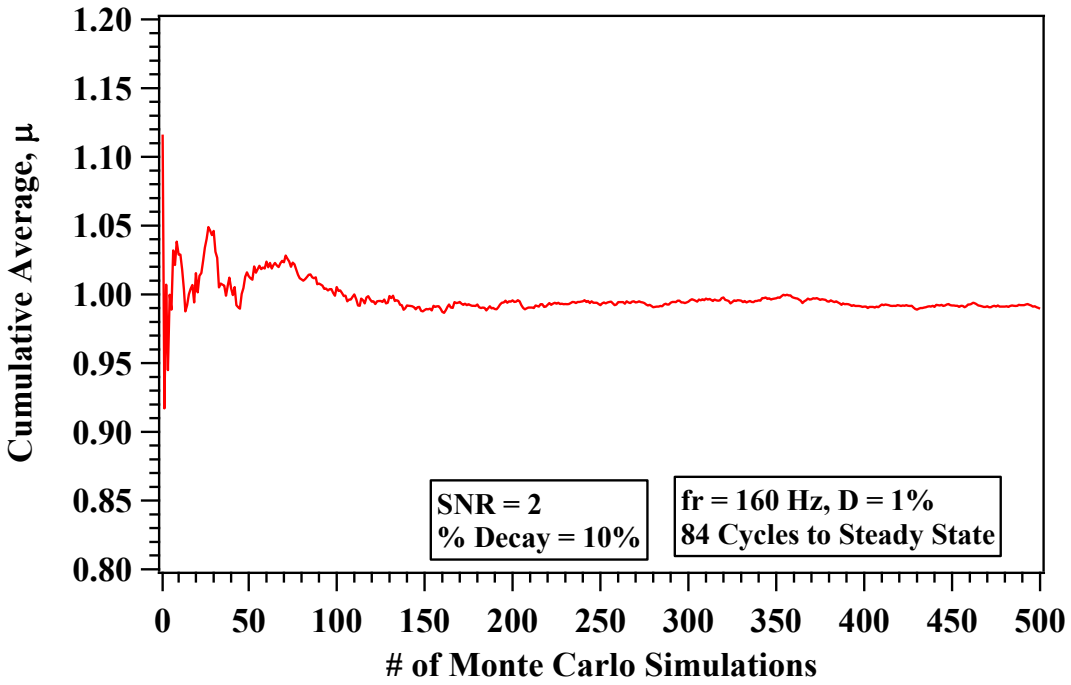

Figure 6.12: Cumulative Mean of the Calculated Damping Ratios Compared with Number of Monte Carlo Simulations Conducted

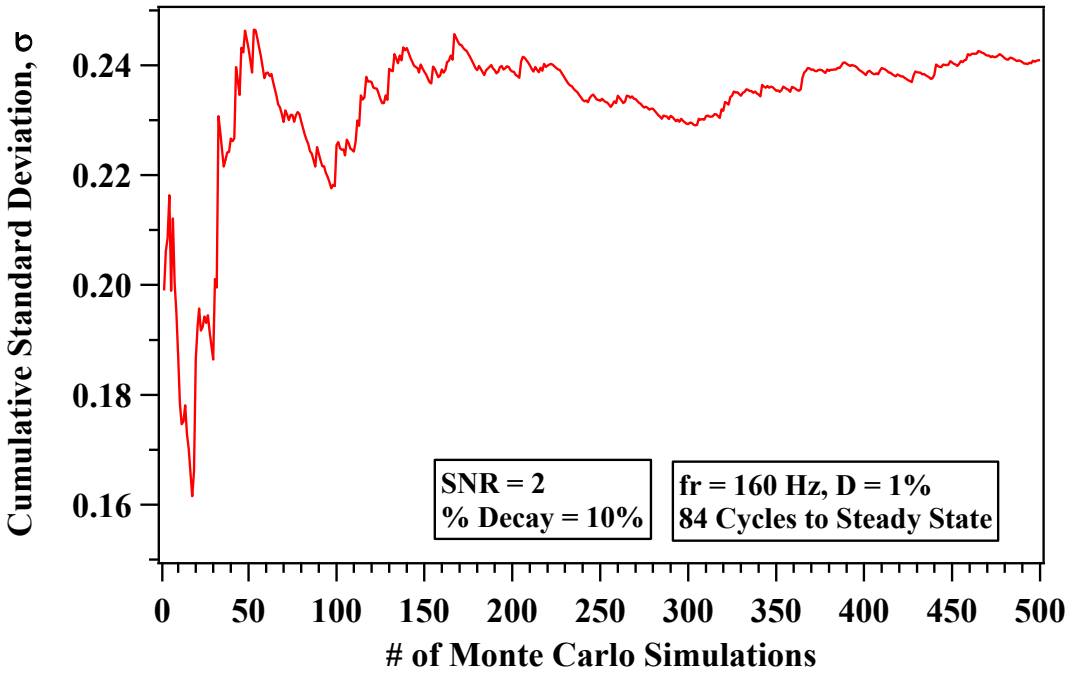

Figure 6.13: Cumulative Standard Deviation of the Calculated Damping Ratios Compared with Number of Monte Carlo Simulations Conducted.

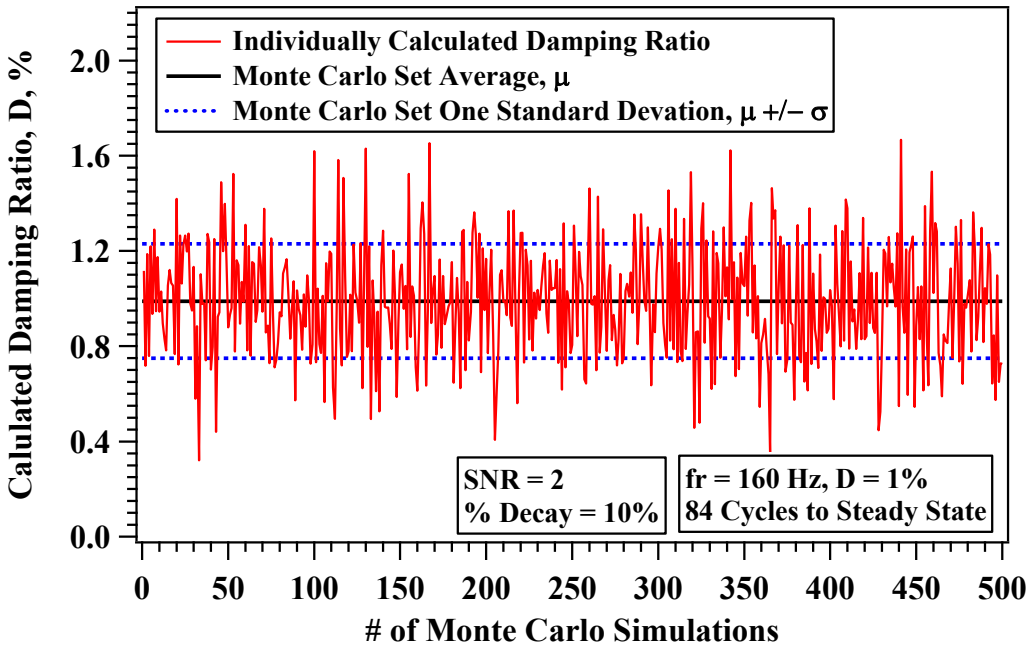

Figure 6.14: Calculated Damping Ratio of Each Monte Carlo Set Compared with Number of Monte Carlo Simulations Conducted.

6.5.4 Results of the Analytical Evaluation: Accuracy Based on Percent of Free-Vibration Decay and Signal-to-Noise Ratio

The cumulative mean and cumulative standard deviation were found for each Monte Carlo set that consisted of 500 simulations. The resulting cumulative mean and cumulative standard deviation are presented for a system with f_r = 150 Hz and D = 1% and were determined for Monte Carlo sets that consisted of percent of decay analyzed ranging from 1% to 99% and SNRs that tanged from 1 to 100. The variation in the cumulative mean of the calculated damping ratio result compared with the percentage of the decay signal used to calculate the material damping ratio is shown in Figure 6.15. The variation in the cumulative standard deviation of the calculated damping ratio result compared with the percentage of the decay signal used to calculate the material damping ratio is shown in Figure 6.16. Numerous relationships are plotted and each differ by the SNR used in the simulations.

The cumulative mean appears to converge around 10% of signal decay for low SNRs; however, the standard deviations are shown to be higher for lower percentages of signal decay analyzed. Thus, when assessing the probability distributions formed by the combination of these two statistics, contours are generated that present the uncertainty of obtaining an accurate result based on percentage of the free-vibration decay curve used for analysis and the SNR present during the test. The probability of the calculated damping ratio falling within ±0.1, 0.5, and 1% of the expected value based on SNR is compared with the percentage of the decay signal used to calculate the material damping ratio are shown in Figure 6.17, Figure 6.18, and Figure 6.19, respectively. In Figure 6.17, Figure 6.18, and Figure 6.19, a line of maximum probability based on SNR and percentage of the decay signal used in analysis is formed. Each of the lines of maximum probability are shown as that variation in percentage of free-vibration decay curve to use for analysis with SNR as seen in Figure 6.20.

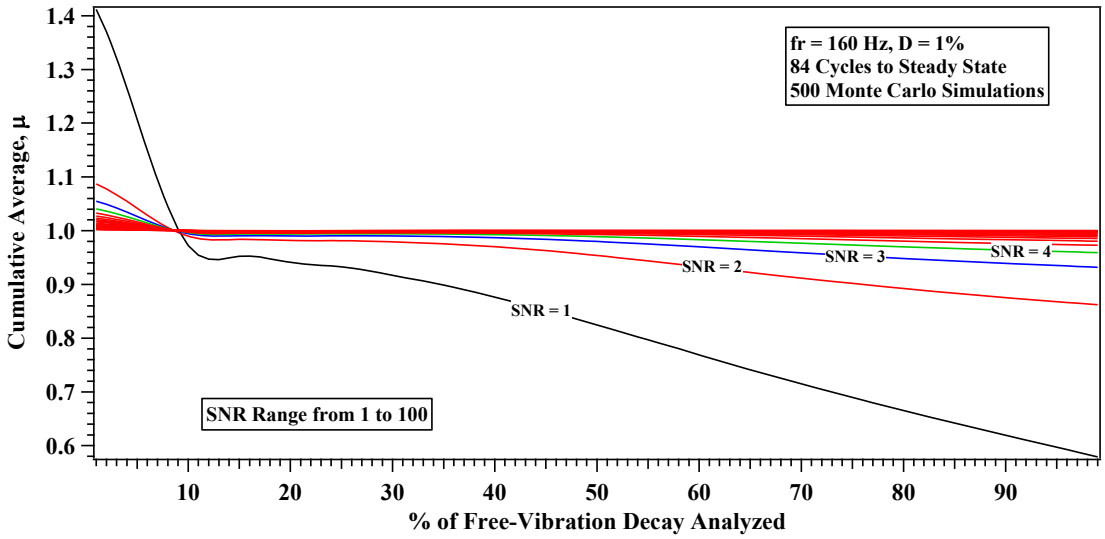

Figure 6.15: Variations in the Cumulative Mean of the Calculated Damping Ratio Result from 500 Monte Carlo Simulations with the Percentage of the Decay Signal Used to Calculate the Material Damping Ratio. Numerous Relationships are Plotted and Each Differ by the Signal-to-Noise-Ratio Used in the Simulations.

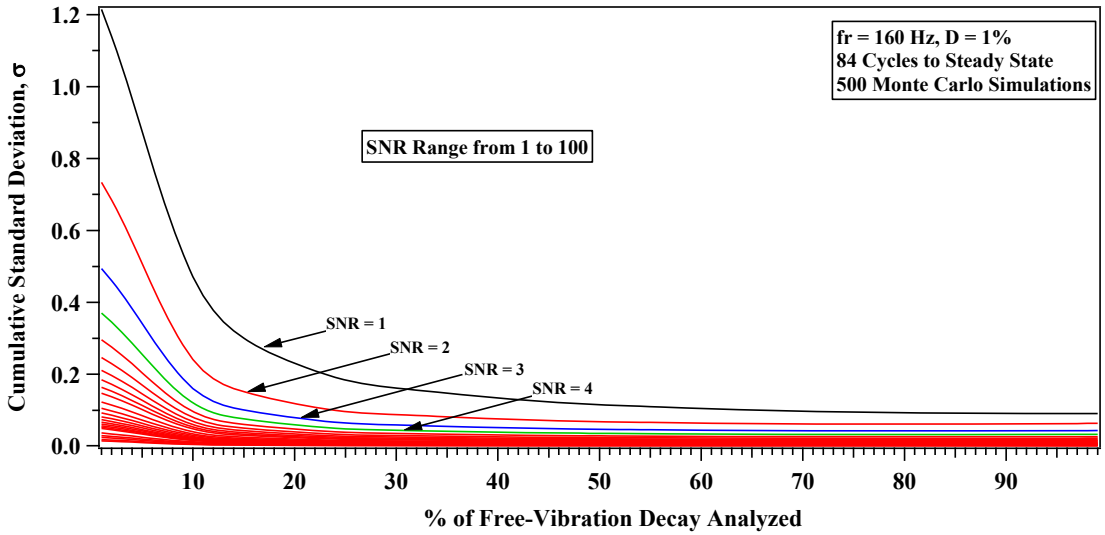

Figure 6.16: Variation in the Cumulative Standard Deviation of the Calculated Damping Ratio Result from 500 Monte Carlo Simulations with the Percentage of the Decay Signal Used to Calculate the Material Damping Ratio. Numerous Relationships are Plotted and Each Differ by the Signal-to-Noise-Ratio Used in the Simulations.

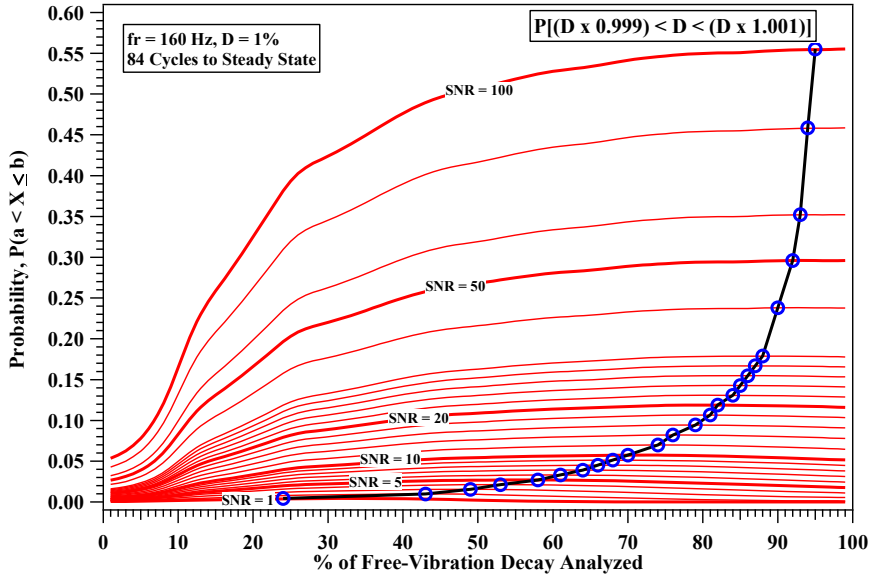

Figure 6.17: Probability of the Calculated Damping Ratio Falling within ±0.1% of the Expected Value Compared with the Percentage of the Decay Signal Used to Calculate the Material Damping Ratio. Numerous Relationships are Plotted and Each Differ by the Signal-to-Noise-Ratio Used in the Simulations.

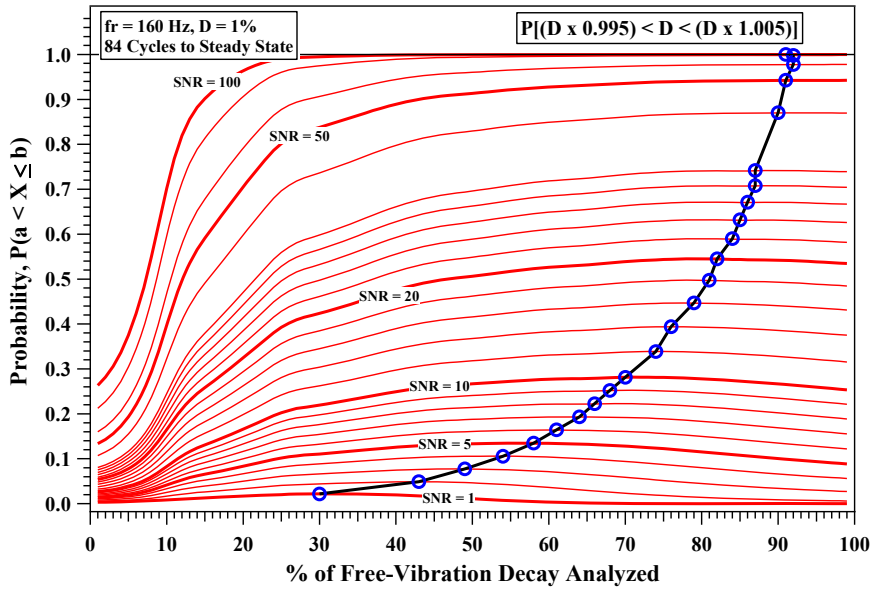

Figure 6.18: Probability of the Calculated Damping Ratio Falling within ±0.5% of the Expected Value Compared with the Percentage of the Decay Signal Used to Calculate the Material Damping Ratio. Numerous Relationships are Plotted and Each Differ by the Signal-to-Noise-Ratio Used in the Simulations.

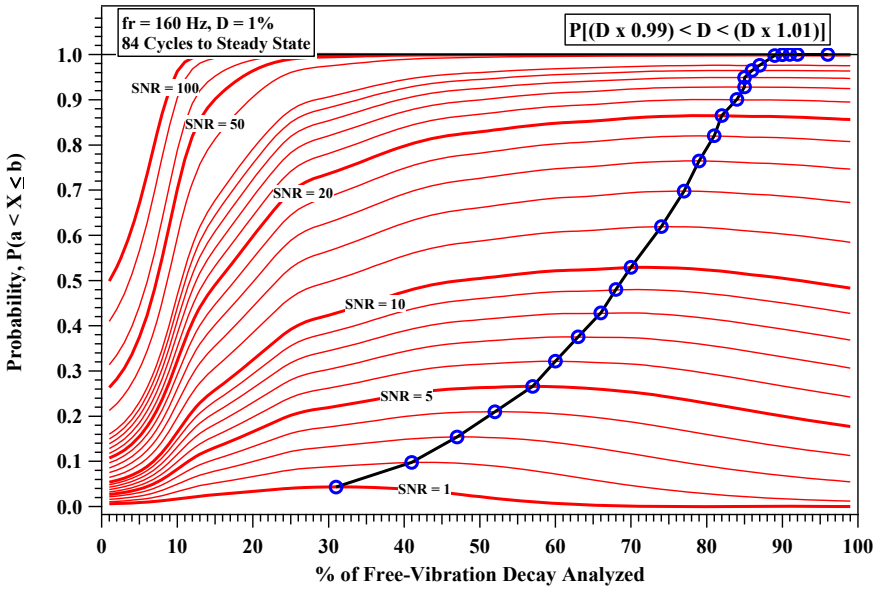

Figure 6.19: Probability of the Calculated Damping Ratio Falling within ±0.1% of the Expected Value Compared with the Percentage of the Decay Signal Used to Calculate the Material Damping Ratio. Numerous Relationships are Plotted and Each Differ by the Signal-to-Noise-Ratio Used in the Simulations.

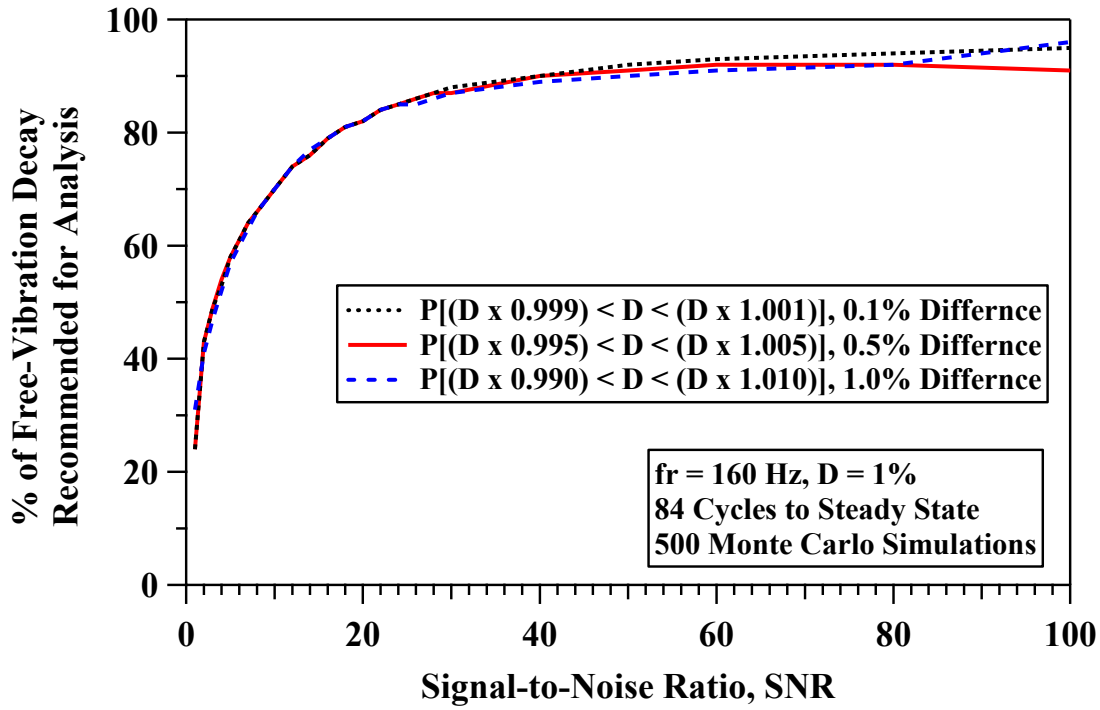

Figure 6.20: Variation in Percentage of Free-Vibration Decay Curve to Use for Analysis with Signal-to-Noise Ratio.

The line of maximum probability for percentage of free-vibration decay curve to use for analysis based on SNR does not change significantly based on the level of tolerance chosen as seen in Figure 6.20. Thus, the line of maximum probability serves as a recommendation for the percentage of free-vibration decay curve to use for analysis based on SNR. Furthermore, when configuring a weighted LMS fit of an exponential decay curve to the free-vibration decay envelope based the SNR present during the test, the contours presented in Figure 6.17, Figure 6.18, and Figure 6.19 can be normalized and used to create the values of the weighted array.

6.6 SUMMARY

In resonant column (RC) testing, the accuracy of the measuring values for shear strain, γ, resonant frequency, r_r, half-power damping ratio, D_{HP}, and free-vibration decay damping ratio, D_{fv}, can be greatly affected by the level of background noise present. The purpose of this chapter was to analytically evaluate some methods available to digitally process signals from the frequency sweep and free-vibration decay parts of the RC test.

The process for analytically evaluating the digital signal processing methods was done using Monte Carlo simulations. In each Monte Carlo simulation, theoretical signal responses were simulated based on dynamic theory of a viscously damped single-degree-of-freedom (SDOF) system. Background noise was simulated using a random number generator and was added to the theoretically simulated response signal. The level of background noise selected was based on a prescribed signal-to-noise ratio (SNR). Once "noisy" signals were generated, the digital signal processing methods were used repeatedly over hundreds of Monte Carlo simulations. The results of the repeated evaluations of randomly noisy signals were used to develop statistics that describe the accuracy of each of the digital signal processing methods used. Each set of Monte Carlo simulations were conducted for specified SNRs and the statistics of each Monte Carlo set were used to compare the probabilistic accuracy of each digital signal processing method based on SNR. In this chapter, the results of these experiments provide insight into which digital signal processing methods yield the highest degree of accuracy based on the SNR present.

Noisy signals were simulated to represent the frequency sweep part of the RC test. The resulting response curves were determined by using a root-mean-squares (RMS) method and the wavelet integration method (WIM). The accuracy of the two methods was evaluated for determining γ, f_r, and D_{HP}. The WIM was found to be much more robust than the RMS method for reducing the influence of background noise on the resulting response

curves. An additional method was employed to further reduce the influence of background noise which involved finding the characteristics of the response curve (i.e. γ, f_r, and D_{HP}) by determining the minimum least-mean-squares (LMS) difference between the SDOF response curve equation and the results measured from the frequency sweep. This method was found to be more robust for determining γ, f_r, and D_{HP} than the traditional half-power bandwidth approach.

Noisy signals were simulated to represent numerous free-vibration decay tests. In each set of Monte Carlo simulations, the percent of signal decay used to calculate the D_{FV} was changed. Furthermore, numerous SNRs were used to simulate the noisy signals. The results of the experiment were used to determine what percent of signal decay yields the most accurate D_{FV} result based on the SNR.

The probability of the calculated damping ratio falling within ±0.1, 0.5, and 1% of the expected value based on SNR was compared with the percentage of the decay signal used to calculate the material damping ratio. A line of maximum probability based on SNR and percentage of the decay signal used in analysis was formed and was found not change significantly based on the level of tolerance. Thus, the line of maximum probability serves as a recommendation for the percentage of free-vibration decay curve to use for analysis based on SNR. Furthermore, when configuring a weighted LMS fit of an exponential decay curve to the free-vibration decay envelope based the SNR present during the test, the contours presented in in this chapter can be normalized and used to create the values of the weighted array.

Chapter 7

Experimental Evaluation of the Methods of Analysis Used in the Torsional Shear Test at Small Strains to Determine the Most Accurate Methods

7.1 INTRODUCTION

With modern computer processing power, digital programming capacity, and digital filtering capabilities, many new capabilities for signal conditioning of sensor outputs have been made possible. In traditional combined resonant column (RC) and torsional shear (TS) testing, digital signal conditioning technology was limited or difficult to implement and significant noise at low voltage levels made high resolution measurements in RCTS testing challenging. Several digital filtering and signal processing techniques have been implemented and standardized for making reliable measurements at very-low to low shearing strains ($0.00005 < \gamma \leq 0.0005$) in TS testing.

Several data processing techniques can be utilized to obtain accurate results from torsion shear (TS) testing from low to moderate shearing strains. The basic equations for determining shearing stress, shearing strain, shear modulus, and hysteretic damping ratio from the TS test were shown in Chapter 2. During the TS test, a step-by-step approach is used to obtain accurate shearing stress, shearing strain, shear modulus, and hysteretic damping ratio results. First, TS tests are repeated and the signals from the series of repeat tests are stacked to reduce "random" background noise. The number of signals needed for stacking depends on the level of background noise present, where the larger the level of noise the greater the number of signals needed for stacking. Second, lowpass Butterworth filtering is conducted to reduce residual background noise. Third, a digital signal processing technique is used to reduce the signal data into results on a per-cycle basis or

from all cycles excited during the test. The per-cycle analysis is intended for nonlinear TS testing, where stiffness or damping characteristics can change based on the number of cycles of torsional loading. Analyzing all cycles during the test is useful at small strains, where the objective is to reduce the influence of background noise, which is more easily done when more cycles of loading are available for analysis.

In this chapter, several digital signal processing techniques are evaluated to determine which methods are most accurate for reducing the data recording from TS testing after signal stacking and digital filtering is performed. The details behind the signal stacking and digital filtering methods were covered in Chapter 5, thus in this chapter only examples of how these improve signals from TS testing are presented. There are four digital signal processing techniques that are evaluated in this chapter include. The first involves finding the maximum value and taking the quotient of the shearing stress and shearing strain to determine shear modulus and using the traditional area integration method for determining the hysteretic damping ratio. The second involves calculating the root-mean-squares (RMS) amplitudes and taking the quotient of the shearing stress and shearing strain to determine shear modulus and using the traditional area integration method for determining the hysteretic damping ratio. The third involves the use of a least-mean squares fitting method that fits a linear trend to the measured hysteresis loop to iteratively determine the slope of the hysteresis loop. The third technique is combined with the traditional area integration method for determining the hysteretic damping ratio. The fourth technique involves using the wavelet integration method that was discussed in Chapter 5, where the magnitude response, between the shear stress and the shear strain, is the shear modulus. The phase shift measured between the shear stress and shear strain is used to simulate a hysteresis loop from which the traditional area integration method is used to for determine the hysteretic damping ratio. Each of the digital processing techniques are

evaluated experimentally by conducting TS tests. The techniques presented in this section mainly apply to measurements taken at low shearing strains where the impact of background noise and environmental vibrations can range from detrimental to completely prohibitive.

7.2 DATA ACQUISITION PRINCIPALS AND PARAMETERIZATION FOR THE TS TEST

Depending on the type of the proximitor being used and the positon of the proximitors above the specimen, the amplitude of the signal coming from the sensors can differ greatly. First, the calibration factor of the proximitors are in units of volts per inch, thus the signal recorded from the sensors contain a DC offset depending on the distance from the proximitor target. In this study the proximitors used have an effective range of 0.005 in. to 0.075 in. which with signals that range from 1 to 25 volts. This DC offset can be handled in a couple ways: (1) A DC shifter can be used to counteract the magnitude of the DC offset, (2) A data acquisition system (DAQ) that can acquire signals above 25 volts, or (3) An analog attenuator (voltage divider) is used to reduce the signal to a level within the range of the DAQ. The method used herein involves use of a data acquisition system that can acquire signals up to 42 V foregoing the need for a DC shifter or attenuator.

The DAQ used is the NI PXI-4461, which has adjustable voltage ranges to make better use of the 24-bit resolution of the device, which are ± 0.316, 1.00, 3.16, 10.0, 31.6, 42.4 volts. The ranges can also be selected to have a maximum or minimum range of 0, which can more effectively use available voltage ranges. When setting up a specimen for RCTS testing, the proximitors are usually configured 0.035 in (~ 10 V) away from the proximitor target. Thus, based on the initial DC offset and the voltage output range of the proximitors, the 10.0 or 31.6 range are suitable for TS testing in this instance. Before

selecting one of these ranges the largest AC component of the signal should be determined. In TS testing the maximum shearing strain, γ_{max} is:

$$\gamma_{max} = r_{max} * {}^{\theta_{max}}/_{l} \tag{7.1}$$

where r_{max} is the equivalent radius, θ_{max} is the angle of twist at the top of the specimen, and

l is length of the specimen.

The largest AC component of the signal in RCTS testing can be determined by the following steps: (1) the ratio of the height-to-diameter is 2:1 ($l/r_{max} = 2$), (2) Shear strains excited in the specimen during RCTS are not expected to exceed a shearing strain of 1%, and (3) the mounting location of the proximitors are 0.71 in. from the center of the specimen. Reconfiguring the equation above gives:

$$\theta = 2 \times \gamma = \tan^{-1}\left(\frac{\delta}{d}\right) \tag{7.2}$$

where δ is the displacement measured by the proximitor and d is the position of the proximitor relative to the center of the specimen. Using an approximate proximitor calibration factor, F_{prox} of 0.0037 in./V for the proximitors, the maximum AC signal component in TS testing will be approximately:

$$\delta = \tan\left(\frac{\gamma * l}{r}\right) \times \frac{d}{F_{prox}} = \tan(.01 * 2) \times \frac{0.71\text{ in}}{0.0037\text{ in/V}} = 3.84\text{ V} \tag{7.3}$$

Given a preset DC component of 10 V and an AC component of 3.84 V, the ± 31.6 V range will be used in most instances. If in some cases the preset DC component is less than approximately 6 V, then the ± 10 V range should be used. Finally, this calculation must be redone if significant changes are made to the setup, namely the proximitor calibration factor and the proximitor mounting location.

Now that the typical voltage range used for TS testing in known, the shearing strain resolution is achievable based on the resolution of the DAQ and can also be approximated using a similar procedure. The minimum voltage, V_{min} is based on the digital resolution of the DAQ and is calculated by:

$$V_{min} = \frac{V}{2^n} = \frac{+31.6\ V}{2^{24}} = 1.88 \times 10^{-6}\ V \tag{7.4}$$

where n is the vertical digital resolution in units of bits. To determine the shear strain resolution, the previous equation is reconfigured as:

$$\gamma_{min} = \frac{r_{max} * \theta_{min}}{l} = 0.5 \times \tan^{-1}\left(\frac{V_{min} \times F_{prox}}{d}\right) \tag{7.5}$$

$$= 0.5 \times \tan^{-1}\left(\frac{1.88 \times 10^{-6}\ V \times 0.0037\ in./V}{0.71\ in}\right) = 4.91 \times 10^{-7}\% \tag{7.6}$$

However, this coincides with the noise floor of the device and additional background noise from external sources will also be present. To determine what a minimum measurement of shear strain might be in a TS test, the signal-to-noise-ratio is considered. The signal-to-noise-ratio (SNR) is given by:

$$SNR = \frac{A_S}{A_N} \tag{7.7}$$

where A_{signal} is the amplitude of the signal and A_{noise} is the amplitude of the noise. The amplitude of the signal should be 100 times (SNR=100) the amplitude of the noise floor. Thus, the minimum shear strain in a TS test for the configuration of this system should be $4.91 \times 10^{-5}\%$. Measurements at lower levels of shear strain can be obtained if signal stacking and digital signal processing are used during TS test, which is discussed later.

7.3 SENSOR CONFIGURATION IN TS TESTING

7.3.1 Use of Two Proximitors to Reduce Background Noise and Reduce the Influence of Bending on the Result of the TS Test

Several steps must be taken when converting signals recorded from the proximitors to shearing strains measured during the TS test. Each signal has a DC offset that must first be removed. The DC component of the signal can be removed by subtracting the mean of the signal. Since the AC component is a continuous sinusoid, the mean of the signal will precisely equal the value of the DC offset. The method for reducing background noise and ignoring bending involves subtracting one Proximitor signal from the other and dividing by 2. When bending occurs the signals recorded from the proximitors will be in phase and this component will cancel. Similarly if there is background noise that is assumed to be Gaussian random noise, then subtracting one signal from the other will reduce the amplitude of the noise present. With pure torsion, the two signals recorded are 180 degrees out of phase and subtracting one signal from the other will double the amplitude of the torsional displacement measured.

For this method to be accurate the voltage readings must be converted to displacements, because the calibration factors of these sensors slightly differ. Thus, the voltage readings from the proximitors will be different when the same amplitude of displacement is occurring. Converting to displacement first will also ensure that any bending measured will be eliminated. Therefore, the overall displacements measured during one TS test is found by:

$$\mathrm{d} = \frac{1}{2} * \left[(\mathrm{prox1} - \mathrm{avg(prox1)}) * \mathrm{F}_{\mathrm{prox,1}} - (\mathrm{prox2} - \mathrm{avg(prox2)}) * \mathrm{F}_{\mathrm{prox,2}}\right] \tag{7.8}$$

where d is the measured displacement, prox1 and prox2 are arrays containing the voltage readings taken during the test, avg indicates taking the average of the signal, $F_{prox,1}$ and $F_{prox,2}$ are the proximitor calibration factors for proximitors 1 and 2, respectively. Signals recorded at low and moderate shearing strain are shown in Figure 7.1 through Figure 7.4.

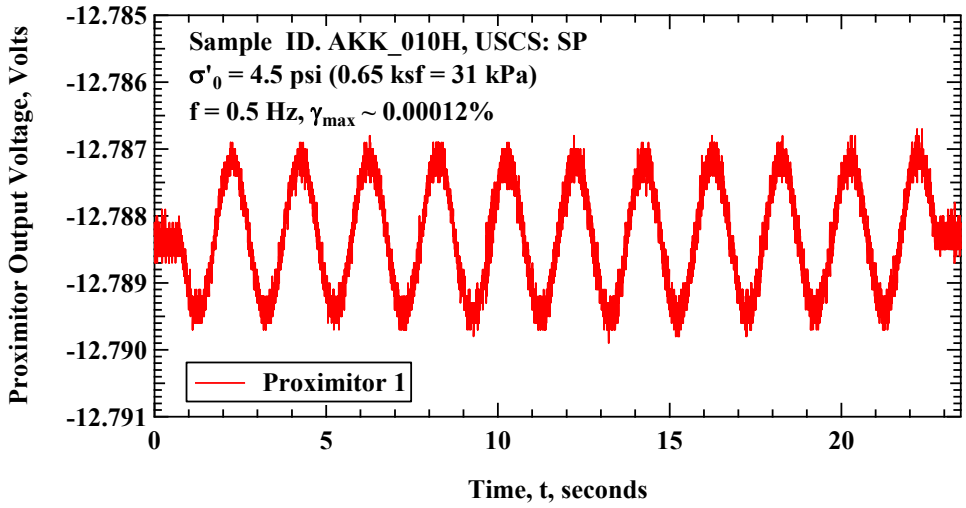

Figure 7.1: Raw Proximitor Signal Measured During TS Test with a Maximum Shearing Strain of 0.00012% for a Hollow Cylinder of Washed Mortar Sand Tested at σ'_o = 0.31 atm.

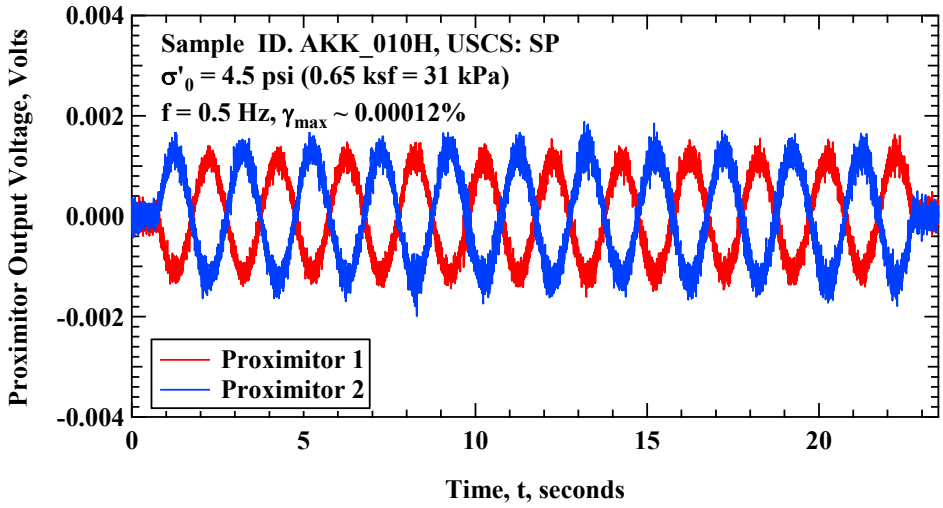

Figure 7.2: DC Offset Removed from Raw Proximitor Signals Measured During TS Test with a Maximum Shearing Strain of 0.00012% for a Hollow Cylinder of Washed Mortar Sand Tested at σ'_o = 0.31 atm.

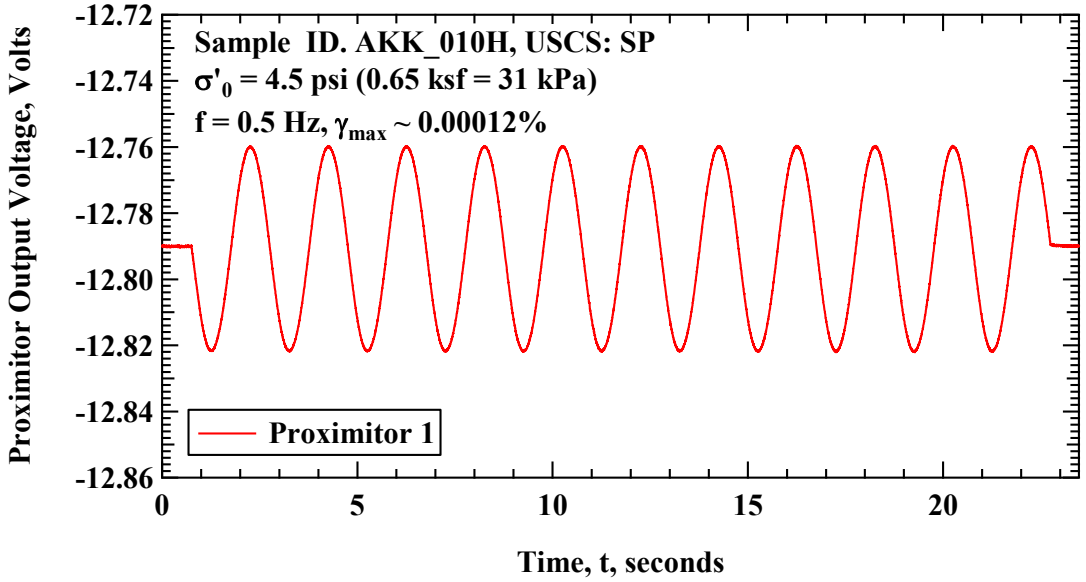

Figure 7.3: Raw Proximitor Signal Measured During TS Test with a Maximum Shearing Strain of 0.00315% for a Hollow Cylinder of Washed Mortar Sand Tested at σ'_o = 0.31 atm.

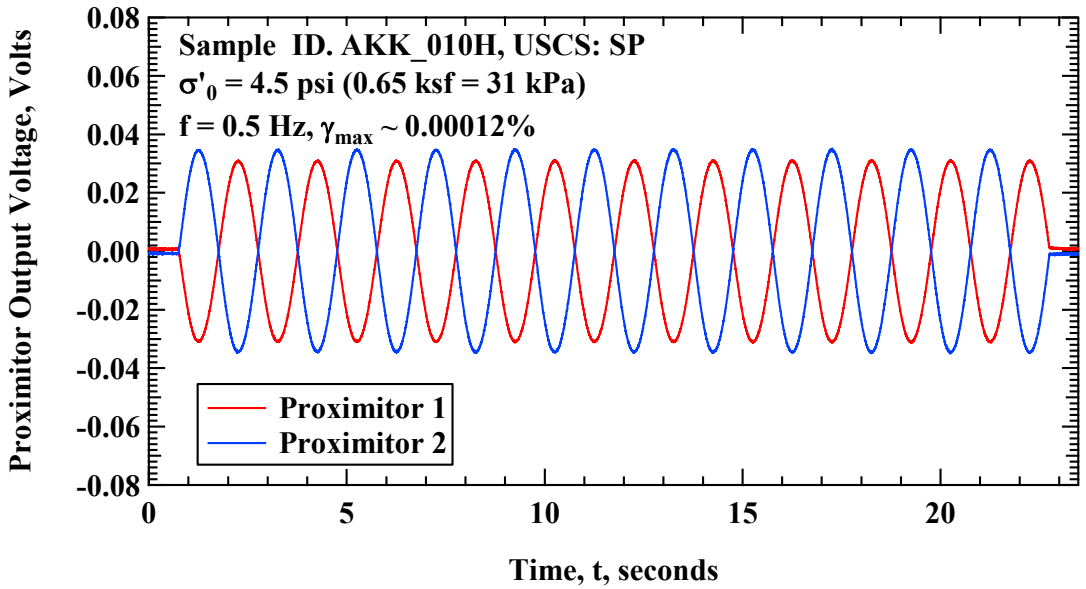

Figure 7.4: DC Offset Removed from Raw Proximitor Signals Measured During TS Test with a Maximum Shearing Strain of 0.00315% for a Hollow Cylinder of Washed Mortar Sand Tested at σ'_o = 0.31 atm.

7.4 SIGNAL STACKING AND DIGITAL FILTERING OF TS TEST SIGNALS

During the TS test, a step-by-step approach is used to obtain accurate shearing stress, shearing strain, shear modulus, and hysteretic damping ratio results. First, TS tests are repeated and the signals from the series of repeat tests are stacked to reduce "random" background noise. The number of signals needed for stacking depends on the level of background noise present, where the larger the level of noise the greater the number of signals needed for stacking. Second, lowpass Butterworth filtering is conducted to reduce residual background noise. The details behind the signal stacking and digital filtering methods were covered in Chapter 5. Some examples of how signal stacking and digital filtering reduces the influence of background noise is shown in Figure 7.6 and Figure 7.6.

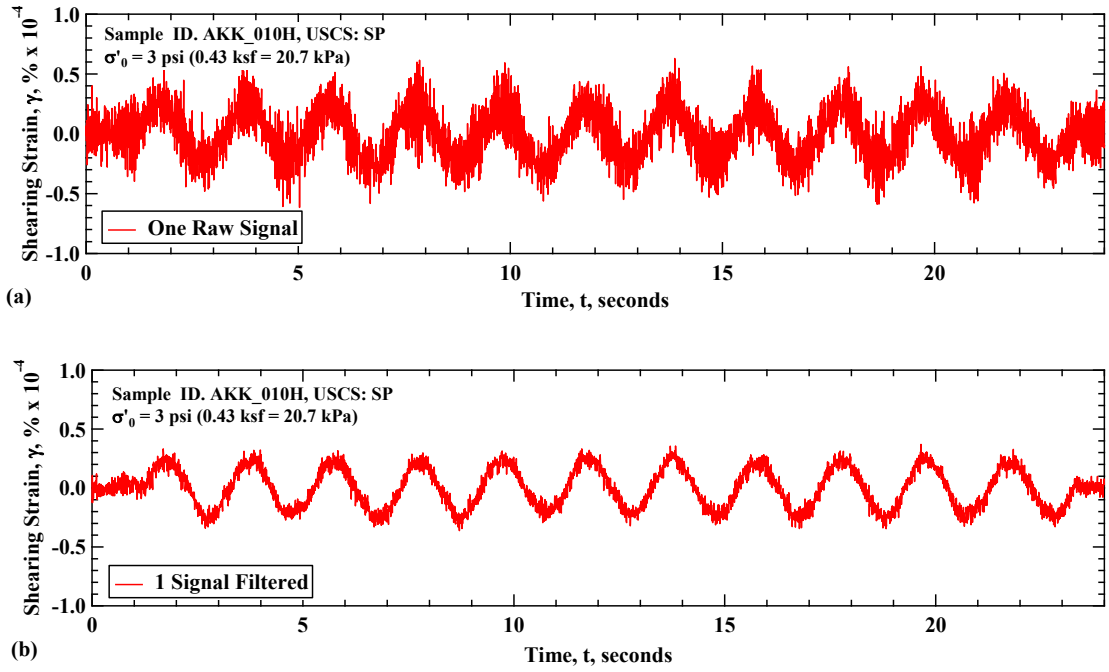

Figure 7.5: Shear Strain Response in the TS Test versus Time for (a) One Raw Signal, and (b) One Filtered Signal for a Hollow Cylinder of Washed Mortar Sand Tested at σ'_o = 0.2 atm.

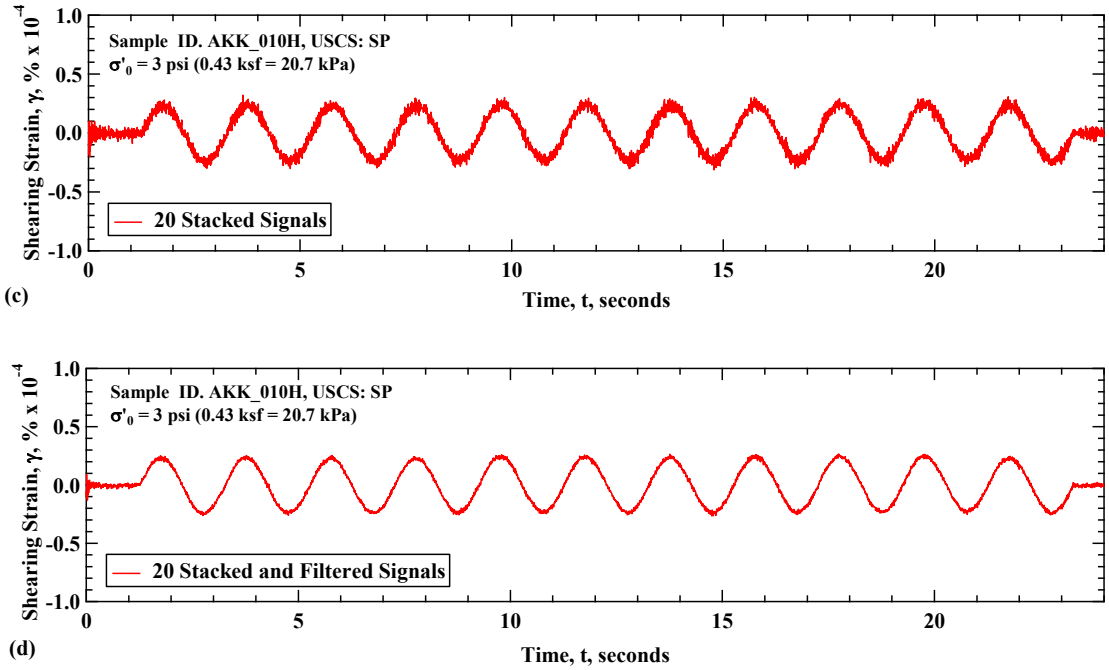

Figure 7.6: Shear Strain Response in the TS Test versus Time for (c) 20 Stacked Signals, and (d) 20 Stacked and Filtered Signals for a Hollow Cylinder of Washed Mortar Sand Tested at σ'_o = 0.2 atm.

7.5 DIGITAL SIGNAL PROCESSING TECHNIQUES

7.5.1 Max/Min Shearing Stress and Strain and Area Integration Method

The simplest way to determine the shear modulus is by dividing the maximum shearing stress, τ_{max}, by the maximum shearing strain, γ_{max}, of each cycle to obtain the shear modulus, G. Damping is found by comparing amount of energy dissipated in one complete cycle of loading and the peak strain energy stored in the specimen during the cycle.

The amount of energy dissipated in one complete cycle of loading, W_d is equal to the area of the hysteresis loop, which is found using an integrative approach which is simplified as:

$$W_d = \sum_{i=0}^{N} \left[\frac{1}{2}(y_{i+1} + y_i) * (x_{i+1} - x_i)\right] \quad (7.9)$$

where N is the number of samples per cycle, y is shear stress (τ), x is the shear strain (γ), and i is a single data point. The peak strain energy stored in the specimen during the cycle, W_s is area of the triangle which is found by multiplying the τ_{max} and γ_{max} and dividing by 2.

$$D = \frac{1}{4\pi} \cdot \frac{W_d}{W_s} \tag{7.10}$$

where D is the damping ratio.

When using this method, at low shearing strains significant background noise contaminates the signals recorded from the proximitors, which leads to an overestimation of shearing strain and an underestimation of the shear modulus. This inaccuracy is most prominent at low shear strains and dissipates as higher shear strains are excited in the specimen.

7.5.2 Root-Mean-Squared Method

The root-mean-squared (RMS) method is applied by measuring the root mean square of one cycle of both the stimulus and response signal. This method can be implemented after the stimulus signal has been converted to shearing stress and the response signal has been converted to shearing strain. The RMS of a signal is given by:

$$x_{rms} = \sqrt{\frac{1}{N} * \sum_{i=1}^{N} x_i^2} \tag{7.11}$$

where r_{rms} is the root mean square of the signal, N is the number of samples in one cycle, and x_i is the ith value of the signal. The RMS value of one cycle from the array of shearing stress data, τ_i can be divided by the RMS value of one cycle from the array of shearing strain data, γ_i; thus the shear modulus for a single cycle is calculated by:

$$G_{1cyc} = \frac{\sqrt{\frac{1}{N}*\sum_{i=1}^{N}\tau_i^2}}{\sqrt{\frac{1}{N}*\sum_{i=1}^{N}\gamma_i^2}} = \frac{\sqrt{\sum_{i=1}^{N}\tau_i^2}}{\sqrt{\sum_{i=1}^{N}\gamma_i^2}} = \frac{\tau_{rms}*\sqrt{2}}{\gamma_{rms}*\sqrt{2}} = \frac{\tau_{max}}{\gamma_{max}} \quad (7.12)$$

The value γ_{max} using the RMS method can be used for creating G-logγ and D-logγ plots. For calculating the material damping ratio, the area of the triangle, W_s is found by multiplying τ_{max} with γ_{max} and dividing by 2. The area of the loop, W_d is found the same way as in the area integration method.

7.5.3 Least-Mean-Squares Method

The least-mean-squares (LMS) method is applied by fitting a linear trend line to the shearing stress versus shearing strain using a least-mean-squares fit. The model for the least squared fit line is defined a slope parameter, G_i, which is iteratively determined by reducing the residual values, r_i between the slope parameter multiplied by the shearing strain array, γ_i subtracted by the shearing stress array, τ_i. This is found by:

$$r_i = \tau_i - \sum_{j=1}^{N}\gamma_{ij} * G_i \quad (7.13)$$

where i is the ith residual, j is the index of the data point, N is the number of samples in a cycle, and G_i is the tested model parameter which is equivalent to the shear modulus. The residual values are minimized by finding the minima of the quantity S which is defined by:

$$S = \sum_{i=1}^{m} r_i^2 \quad (7.14)$$

The iterations are concluded when the gradient vector or the derivative of S with respect to G_i is less than or equal to a tolerance value of 0.0001. Examples of the LMS method predicting shear modulus is show in Figure 7.8 and Figure 7.8. The area of the loop, and subsequently the damping ratio, can be calculated using the values of the residual array; however, the result would be quantitatively equal to the area integration method.

Alternatively, damping is calculated using the area of the loop, W_d divided 4π*Ws. W_s is area of the triangle, which in this case is defined as, $\tau_{max}^2/2G$. Where τ_{max} is the shear stress applied during the test and G is the shear modulus determined using the LMS method. The LMS method may be proficient in reducing the influence of background noise if the noise tends to be randomly distributed. If the noise is randomly distributed, then the least-mean-fit will iterate to find the most accurate solution that would tend to cancel out the randomness of the noise.

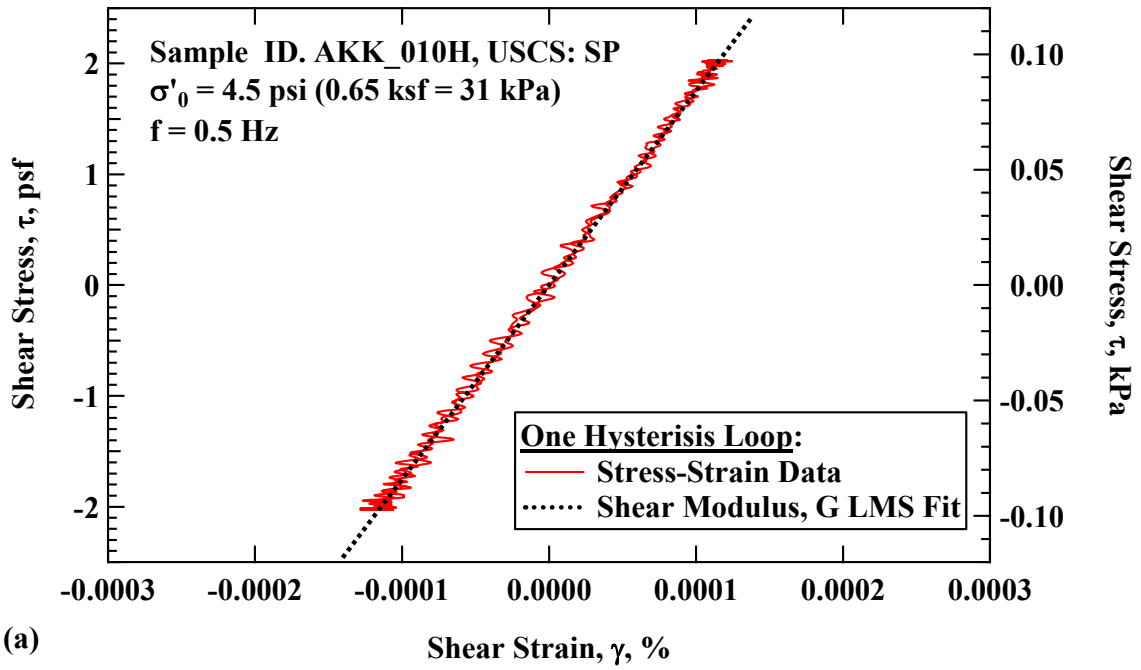

Figure 7.7: (a) Least-Mean-Squares Fit Through Stress-Strain Hysteresis Loop at a Lower Shear Strain for a Hollow Cylinder of Washed Mortar Sand Tested at σ'_o = 0.31 atm.

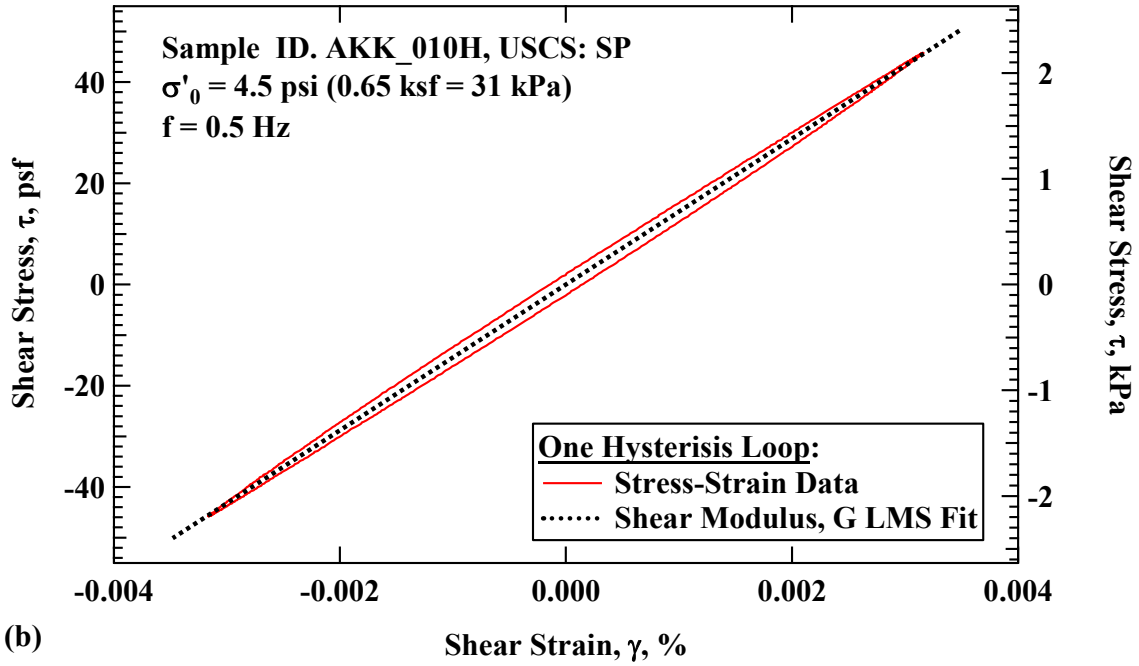

Figure 7.8: (b) Least-Mean-Squares Fit Through Stress-Strain Hysteresis Loop at a Higher Shear Strain for a Hollow Cylinder of Washed Mortar Sand Tested at σ'_o = 0.31 atm.

7.5.4 Wavelet Integration Method

The details of the wavelet integration method was discussed in Chapter 5, where the method results in a magnitude response, M, and phase shift, φ, measured between the stimulus and response signals. If the stimulus signal is the shear stress applied during the test and the response signal is resulting shearing strain, then the M is the shear modulus, G. The phase shift between the two signals can be used to find the amount of energy dissipated in one complete cycle of loading. This is done by creating two arbitrary sinusoids, one that includes the phase shift that was measured between the two signals, which is given as:

$$\text{simulus} = y_i = A * \sin(\omega t) \tag{7.15}$$

$$\text{response} = x_i = A * \sin(\omega t - \varphi) \tag{7.16}$$

where ω is the circular frequency of excitation, t is the time, and A is 1.

The area of the loop, W_d is found using:

$$W_d = \sum_{i=0}^{N} \left[\frac{1}{2}(y_{i+1} + y_i) * (x_{i+1} - x_i)\right] \tag{7.17}$$

where N is the number of samples per cycle. Ws is area of the triangle which is $A^2/2 = 1/2$.

$$D = \frac{W_d}{2\pi} \tag{7.18}$$

where D is the damping ratio. The final step in this computational method is similar to the area integration method, except the area of the loop is based on the phase measured between the two signals using the wavelet integration method rather than integrating the loop directly with the two time domain signals. As discussed in Chapter 5, the wavelet integration method acts as a narrow bandpass filter and thus is proficient at reducing the influence of background noise.

7.6 COMPARISON OF DATA PROCESSING TECHNIQUES ALONG WITH THE USE OF SIGNAL STACKING

Each of the data processing techniques described in the previous subsection were evaluated using experimental results that came from TS tests conducted on a hollow cylindrical poorly-graded sand specimen. Washed mortar sand was the type of poorly-graded sand tested and the TS tests were conducted at a confining pressure of 0.2 atm. The Max/Min, Root-Mean-Squares, Least-Mean-Squares, and Wavelet Integrations Methods were compared at the 10^{th} cycle of each TS test. Each data processing technique was used

to show the variation in shear strain, shear modulus, and hysteretic damping ratio with number of singles stacked. Each data processing technique was also used before and after digital filtering was used. The variation in shearing strain with number of signals stacked for the max/min, root-mean-squares, least-mean-squares, and wavelet integrations methods, before and after digital filtering, are shown in Figure 7.9. The wavelet integration method converges on a stable value with fewer number of signals stacked, with or without digital filtering, than the other methods. The max/min method is shown to be the least accurate.

The variation in shear modulus and hysteretic damping ratio with number of signals stacked is shown in Figure 7.10 and Figure 7.11, respectively, for the max/min, root-mean-squares, least-mean-squares, and wavelet integrations methods, before and after digital filtering. Similar conclusions can be drawn, where the wavelet integration method is more robust that the other methods and the max/min method is the least useful. When comparing the results of TS tests, the hysteretic damping ratio appears to be the most sensitive parameter to signal stacking, digital filtering, and the data processing method chosen. In general, the wavelet integration is found to be the most stable method.

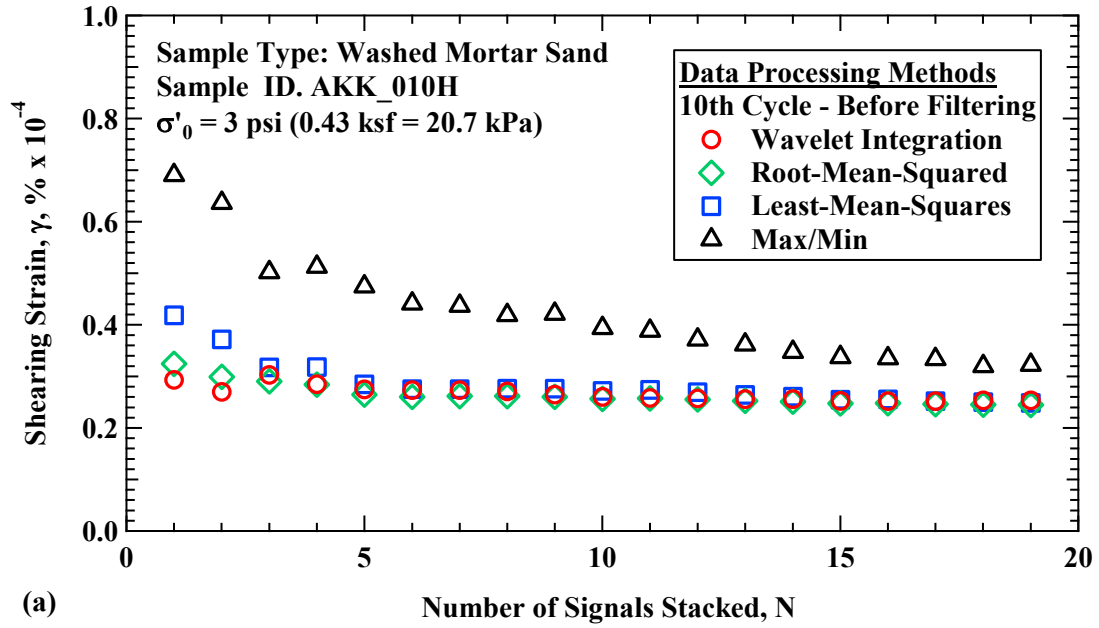

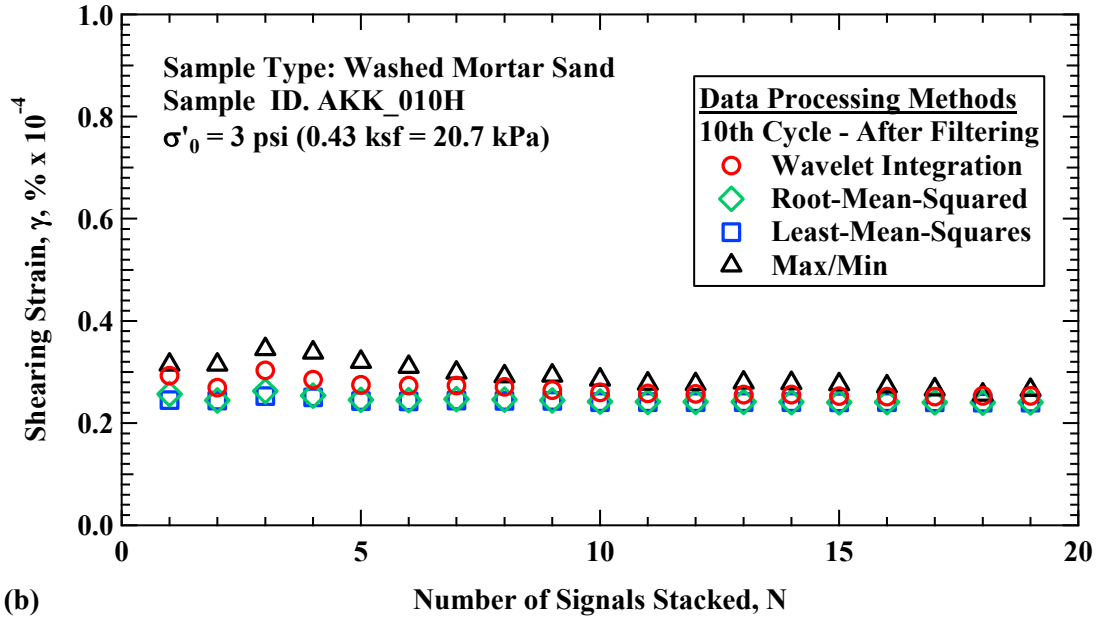

Figure 7.9: Variation in Shearing Strain with Number of Signals Stacked for the Max/Min, Root-Mean-Squares, Least-Mean-Squares, and Wavelet Integrations Methods (a) Before Digital Filtering and (b) After Digital Filtering for a Hollow Cylinder of Washed Mortar Sand Tested at σ'_o = 0.2 atm.

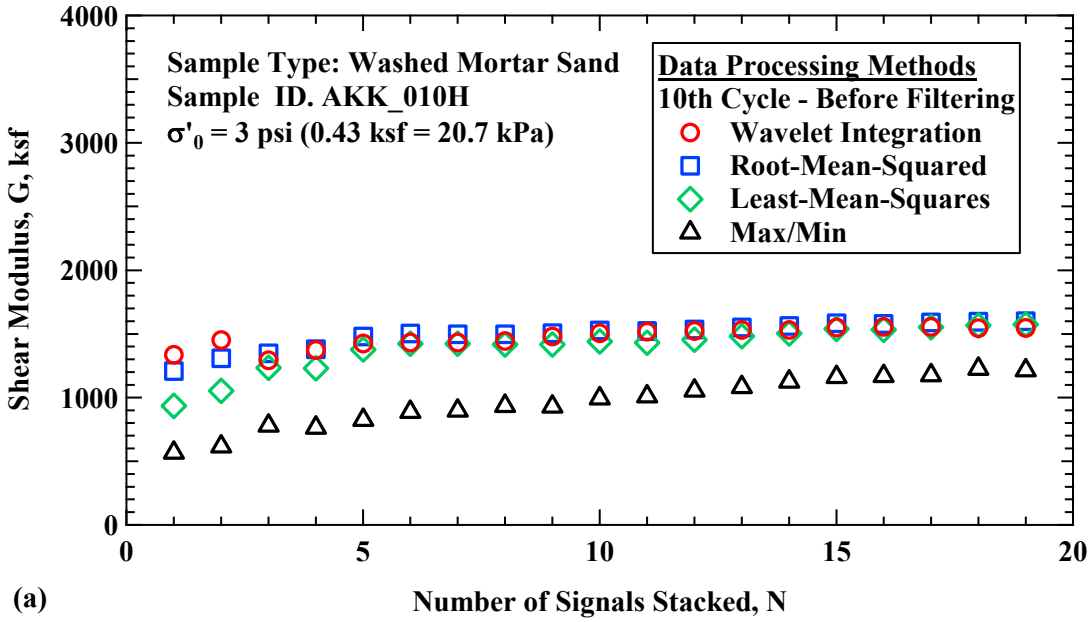

(a)

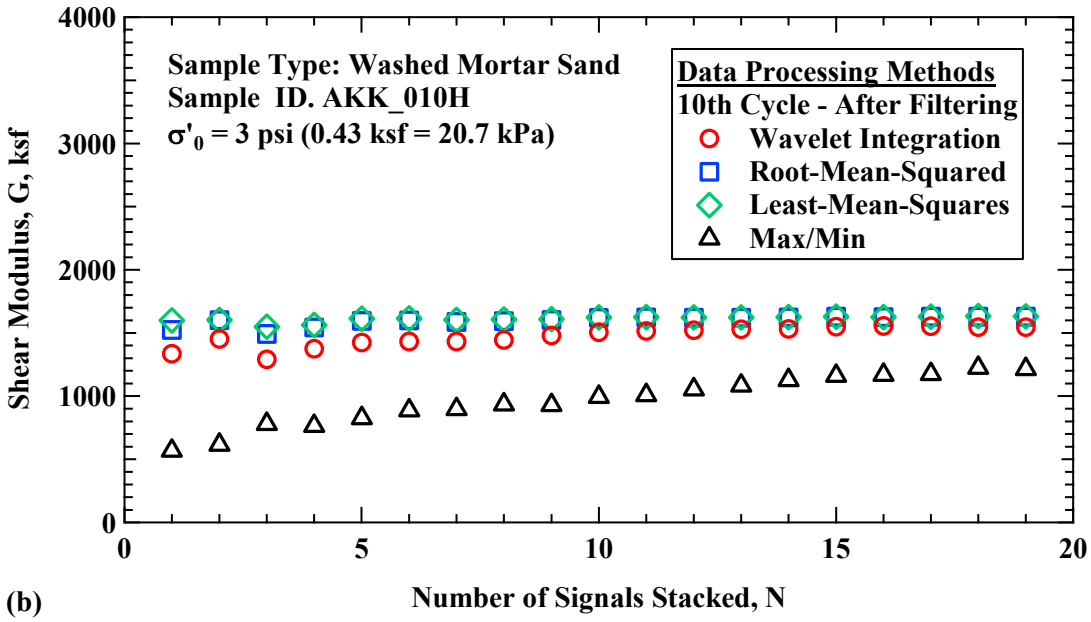

(b)

Figure 7.10: Variation in Shear Modulus with Number of Signals Stacked for the Max/Min, Root-Mean-Squares, Least-Mean-Squares, and Wavelet Integrations Methods (a) Before Digital Filtering and (b) After Digital Filtering for a Hollow Cylinder of Washed Mortar Sand Tested at σ'_o = 0.2 atm.

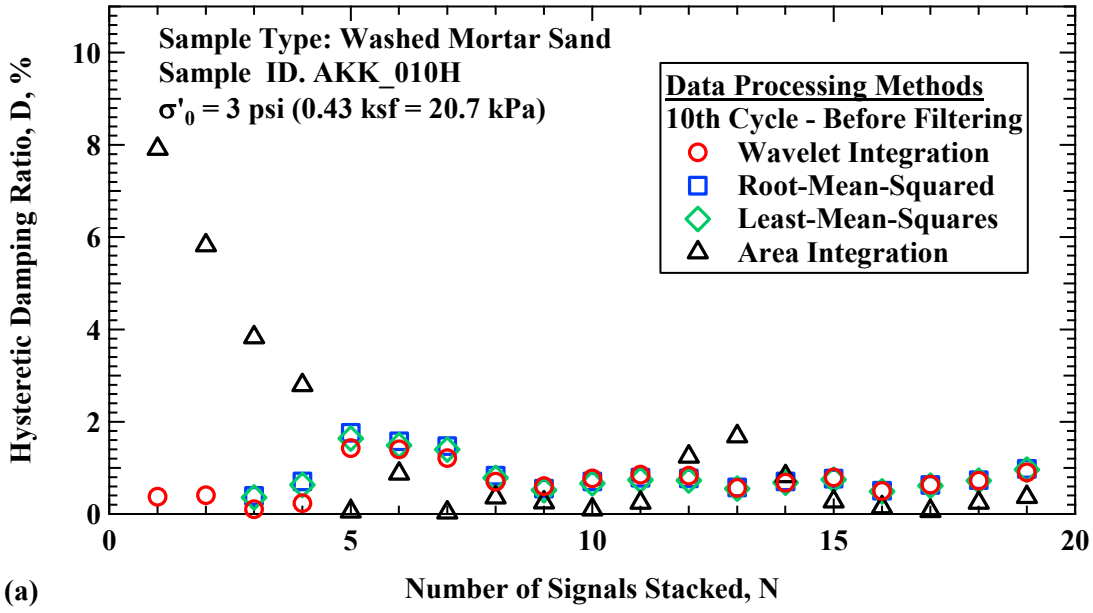

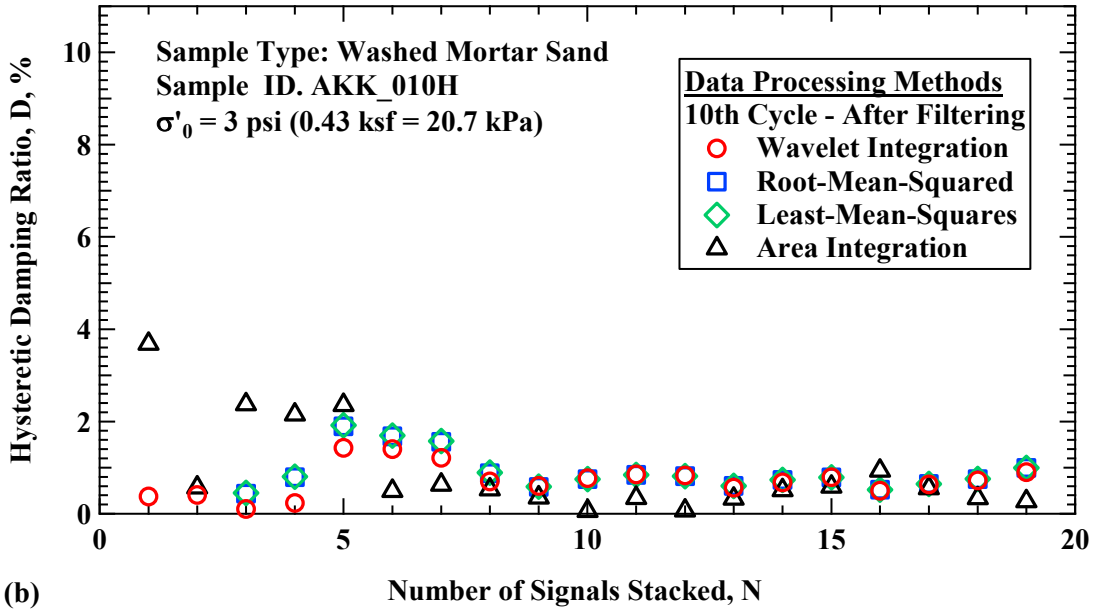

Figure 7.11: Variation in Hysteretic Damping Ratio with Number of Signals Stacked for the Max/Min, Root-Mean-Squares, Least-Mean-Squares, and Wavelet Integrations Methods (a) Before Digital Filtering and (b) After Digital Filtering for a Hollow Cylinder of Washed Mortar Sand Tested at σ'_o = 0.2 atm.

7.7 SUMMARY

Several data processing techniques can be utilized to obtain accurate results from torsion shear (TS) testing from low to moderate shearing strains. During the TS test, a step-by-step approach is used to obtain accurate shearing stress, shearing strain, shear modulus, and hysteretic damping ratio results. First, TS tests are repeated and the signals from the series of repeat tests are stacked to reduce "random" background noise. The number of signals needed for stacking depends on the level of background noise present, where the larger the level of noise the greater the number of signals needed for stacking. Second, lowpass Butterworth filtering is conducted to reduce residual background noise. Third, a digital signal processing technique is used to reduce the signal data into results on a per-cycle basis or from all cycles excited during the test. The per-cycle analysis is intended for nonlinear TS testing, where stiffness or damping characteristics can change based on the number of cycles of torsional loading. Analyzing all cycles during the test is useful at small strains, where the objective is to reduce the influence of background noise, which is more easily done when more cycles of loading are available for analysis.

In this chapter, several digital signal processing techniques were evaluated to determine which methods are most accurate for reducing the data recording from TS testing after signal stacking and digital filtering is performed. There are four digital signal processing techniques that are evaluated in this chapter include. The first involves finding the maximum value and taking the quotient of the shearing stress and shearing strain to determine shear modulus and using the traditional area integration method for determining the hysteretic damping ratio. The second involves calculating the root-mean-squares (RMS) amplitudes and taking the quotient of the shearing stress and shearing strain to determine shear modulus and using the traditional area integration method for determining the hysteretic damping ratio. The third involves the use of a least-mean squares (LMS)

fitting method that fits a linear trend to the measured hysteresis loop to iteratively determine the slope of the hysteresis loop. The third technique is combined with the traditional area integration method for determining the hysteretic damping ratio. The fourth technique involves using the wavelet integration method, where the magnitude response, between the shear stress and the shear strain, is the shear modulus. The phase shift measured between the shear stress and shear strain is used to simulate a hysteresis loop from which the traditional area integration method is used to for determine the hysteretic damping ratio. Each of the digital processing techniques were evaluated experimentally by conducting TS tests at very low shear strains. The wavelet integration method is more robust that the RMS and LMS methods and the max/min method is the least accurate. When comparing the results of TS tests, the hysteretic damping ratio appears to be the most sensitive parameter to signal stacking, digital filtering, and the data processing method chosen. In general, the wavelet integration is found to be the most stable method. The techniques presented in this section mainly apply to measurements taken at low shearing strains where the impact of background noise and environmental vibrations can range from detrimental to completely prohibitive.

Chapter 8

Experimental Testing and Numerical Modeling Used to Evaluate the Effects of Frequency Sweep Rate When Using a Stepped-Sine Sweep in Resonant Column Testing

8.1 INTRODUCTION

Resonant column testing is used to determine the dynamic properties of soil and rock specimens. The dynamic behavior of these materials are determined by exciting cylindrical specimens in torsion in a manner consistent with testing of a damped single-degree-of-freedom system (SDOF). A typical resonant column test is composed of two parts. In the first part, a downgrade frequency sweep is used to determine the resonant frequency, half-power damping ratio, and maximum shear strain amplitude excited during the sweep. The second part begins by exciting the specimen at the resonant frequency determined in part 1. The downgrade sweep is followed by a free-vibration decay test where the specimen is excited at the resonant frequency. After reaching steady-state vibration (i.e. maximum shear strain measured during the downgrade frequency sweep), the excitation is abruptly suspended and the specimen is allowed to freely vibrate. The free-vibration test is used to determine the damped natural frequency and free-vibration damping ratio. Also, the steady-state shear strain amplitude is measured just before the power is abruptly suspended to check that the strain amplitude in the free-vibration decay test matches the peak amplitude at resonance from the downgrade frequency sweep. For this sequence of two-part tests to be accurate, the sweep rate used must be suitable to obtain the correct dynamic characteristics of the specimen in both parts. Sweeping too fast may lead to an incorrect prediction of the dynamic properties from the sweep test and would also result in using the wrong frequency for the free-vibration test.

Configuring sweep rates are different depending on the type of sweep method used. Three common sweeps used for testing SDOF systems are stepped-sine sweep, linear chirp, and exponential chirp. Each of these sweep types involve incremental or constant changes in frequency linearly or nonlinearly with time, and can either be upgrade or downgrade. This study investigates the effects that choosing different sweep rates and sweep types have when testing SDOF systems, mainly for the purpose of testing soil and rock specimens in the resonant column device. The sweep types used were downgrade stepped-sine and downgrade linear chirp. The evaluation of sweep rate and sweep type involved experimental tests on metal calibration specimens and one soil specimen, followed by numerical simulations used to model the dynamic behavior as was observed in the experimental tests.

8.2 EXAMPLE OF PROPER AND IMPROPER SWEEP RATE

An example of two stepped-sine sweeps conducted on the same damped SDOF system, but with two different sweep rates, is shown in Figure 8.1. In one sweep, the frequency was swept too fast because too few cycles of excitation were used at each frequency step. An adequate number of cycles are needed to obtain a maximum amplitude response at each corresponding excitation frequency. Sweeping too fast also led to high harmonic distortion. In another sweep, the frequency was swept at a suitable step rate to obtain the true dynamic characteristics of the system. This example demonstrates the large range of dynamic behavior that will occur when using sweep rates that are faster than a nominal sweep rate for a particular SDOF system.

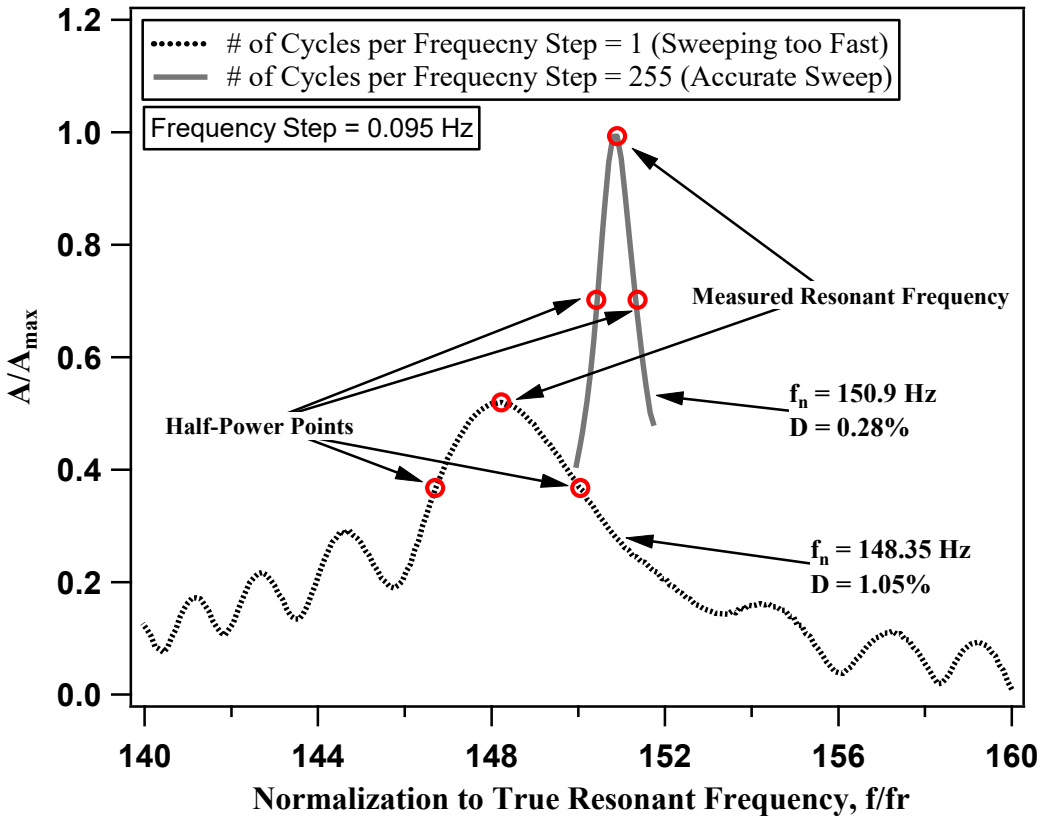

Figure 8.1: An example of two sweeps conducted on the same damped SDOF system, but with two different sweep rates.

8.3 Previous Works Evaluating Sweep-Rates on SDOF Behavior

In order to determine the frequency-domain response of a dynamic system, typically an upgrade or downgrade sine sweep is used. Upgrade sweeps are commonly used in the field of geophysics. Downgrade sweeps are commonly used in the laboratory testing of dynamic systems because some of the systems are expected to have nonlinear dynamic behavior, which can limit the effectiveness of an upgrade sine sweep. Two methods are most commonly used for conducting a frequency sweep to determine the frequency-domain behavior of a dynamic system. The first method is known as a Chirp which is a sinusoidal function that constantly changes frequency with time during the sweep. The second type of sweep is the stepped-sine, where the frequency remains constant for a specific number

of cycles of excitation and the frequency is incrementally changed. When conducting the frequency sweep, sweep rates in the case of the chirps, or size of the frequency step and number of cycles per frequency in the case of the stepped sine, must allow for accurate acquisition of the response curve parameters. Furthermore, in the interest of minimizing testing duration, the sweep rates should be as fast as possible. In this study, both methods are evaluated for maximizing sweep rates and minimizing testing duration while sweeping at rates slow enough to accurately determine the response curve parameters. The Chirp can be configured to change frequency linearly with time or exponentially with time. An equation for a downgrade linear Chirp has the form:

$$f(t) = f_0 + K_s t \tag{8.1}$$

$$x(t) = \sin\left(\varphi_0 + 2\pi\left(f_0 t + \frac{K}{2}t^2\right)\right) \tag{8.2}$$

where f(t) is the excitation frequency as a function of time, f_0 is the initial sinusoidal frequency of the sweep, k_s is the linear chirp rate in Hz/sec, t is time in sec, x(t) is the sweep amplitude, and φ_0 is the initial phase of zero. An exponential chirp has the form:

$$f(t) = f_0 * K^t \tag{8.3}$$

$$x(t) = \sin\left(\varphi_0 + 2\pi f_0\left(\frac{{K_e}^t - 1}{\ln(K_e)}\right)\right) \tag{8.4}$$

where in this case, k_e is the exponential chirp rate in octaves/sec. The stepped-sine sweep method is configured as:

$$f(i) = f_0 + i * f_{step} \tag{8.5}$$

$$x(t) = \sin(2\pi f(i) * t) \tag{8.6}$$

where f(i) is the excitation frequency and incrementally changes based on the counter i, and f_{step} is the frequency step. Examples of a linear Chirp, logarithmic Chirp, and stepped sine sweep are shown in Figure 8.2.

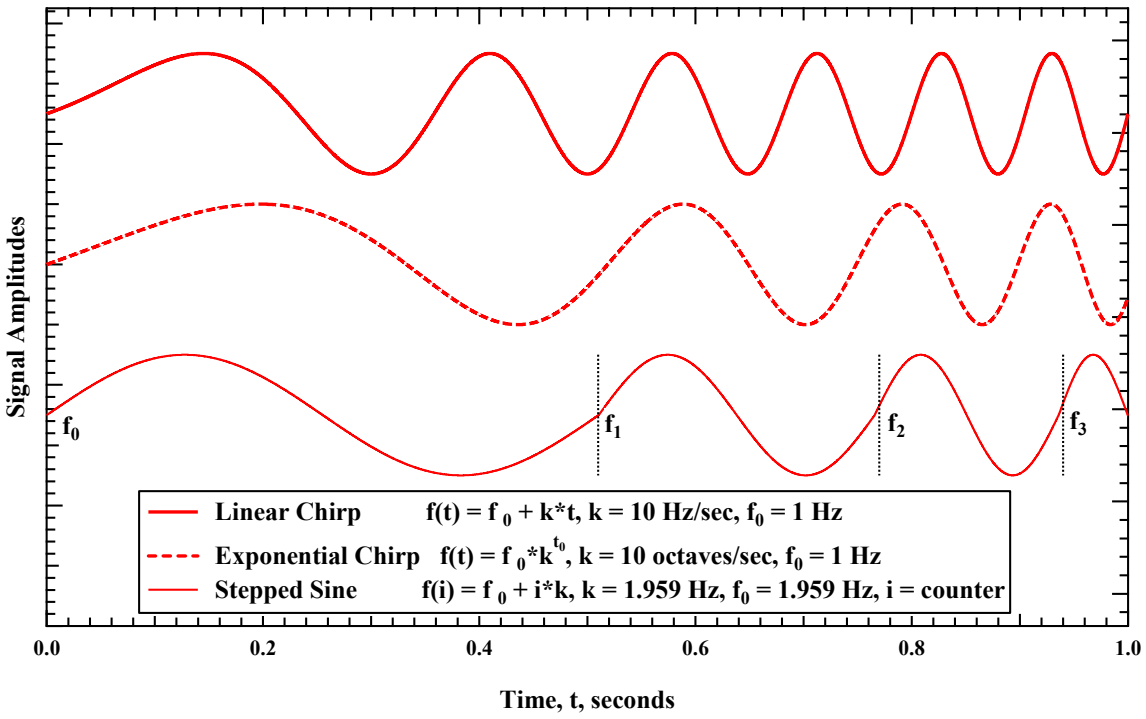

Figure 8.2: Examples of a linear Chirp sweep, logarithmic Chirp sweep, and stepped-sine sweep.

The use of these two types of chirps has been evaluated in previously published studies and the best studies are those of Lollock (2002) and Girard and Bugeat (2004). In both these studies, the sweeping rates of both the linear and exponential chirps were evaluated for their effect on accurately measuring response curve parameters of a single-degree of freedom (SDOF) system. A non-dimensional parameter was developed to relate the sweeping rate of a SDOF system to the ratio of maximum response, resonant frequency, and damping ratio measured to those used in the analysis. Furthermore, the authors developed relationships between the sweeping rates and normalized resonant frequency

error and damping ratio error. They demonstrated that, when sweeping to determine the response curve parameters, the resonant frequency can be determined with minimal sensitivity to the sweep rate whereas the damping ratio is extremely sensitive to the sweeping rate. The non-dimensional parameters in Lollock (2002) and Girard and Bugeat (2004) were developed for linear and exponential sweeps, respectively as:

$$\eta_{\text{linear}} = \frac{Q^2 K_l}{60 f_n^2} \tag{8.7}$$

$$\eta_{\text{exp}} = \frac{Q^2 K_e \ln 2}{60 f_n} \tag{8.8}$$

where, for the first equation, n_{linear} is the non-dimensional parameter for the linear sweep, Q is the quality factor (1/2D), K_l where K is the sweep rate and the subscript l indicates a linear sweep, f_n is the natural frequency, and 60 is included into the denominator to reflect the linear sweep rate in units of Hz per minute. For the second equation, n_{exp} is the non-dimensional parameter for the exponential sweep, K_e where K is the sweep rate and the subscript e indicates an exponential sweep, and 60 is included into the denominator to reflect the exponential sweep rate in units of octaves per minute.

The results of this study were compiled and are shown in figures and expressed as fractions of the maximum steady state response (i.e. ratio of achieving the maximum dynamic response at resonance relative to the theoretical maximum), normalized frequency error (i.e. measured resonant frequency relative to the input damped natural frequency), and ratio of estimated damping to true damping (i.e. damping measured from the response curve relative to that used in the simulation) all compared with the linear or exponential chirp non-dimensional sweep rate parameter. The graphical results of Lollock (2002) and Girard and Bugeat (2004) are shown in Chapter 9.

8.4 EQUIPMENT USED TO EXPERIMENTALLY EVALUATE SWEEP RATE EFFECTS

A computer-controlled resonant column (RC) device was employed in this investigation for dynamically exciting and measuring the response of cylindrical metal and soil specimens. The basic operational principle of the RC test is to vibrate cylindrical specimens in first-mode torsional motion. The RC testing equipment has been developed at The University of Texas at Austin over the past several decades and a large number of RCTS tests (>800) have been performed on cylindrical soil and rock specimens. This equipment is characterized and calibrated using cylindrical metal specimens, some of which were used to fulfill the objective of this study. The testing configuration of a cylindrical specimen in the RC device can be idealized as a fixed-free system. The base of the specimen is fixed and the top is free to rotate in torsion. The top end of the specimen is connected to an electro-magnetic driving system. The driving system supplies harmonic torsional excitation to the top of the specimen at frequencies that range over ~ 0 to 1000 Hz. The excitation system and dynamic response of the cylindrical specimens are equivalent to a single-degree-of-freedom (SDOF) system vibrating in torsion, which is defined as:

$$J_0\ddot{\theta} + C_t\dot{\theta} + k_t\theta = T\,sin(\omega * t) \tag{8.9}$$

where J_0 is the mass polar moment of inertia of the specimen, c_t is the torsional damping coefficient, k_t is the torsional spring constant, T is the torque applied to the specimen, ω is the angular frequency of the torqueing function, t is time, and $\ddot{\theta}$, $\dot{\theta}$, and θ are angular acceleration, angular velocity, and angle of twist, respectively. A photograph of the RC device and a conceptual schematic of the torsional driving system is shown in Figure 8.3.

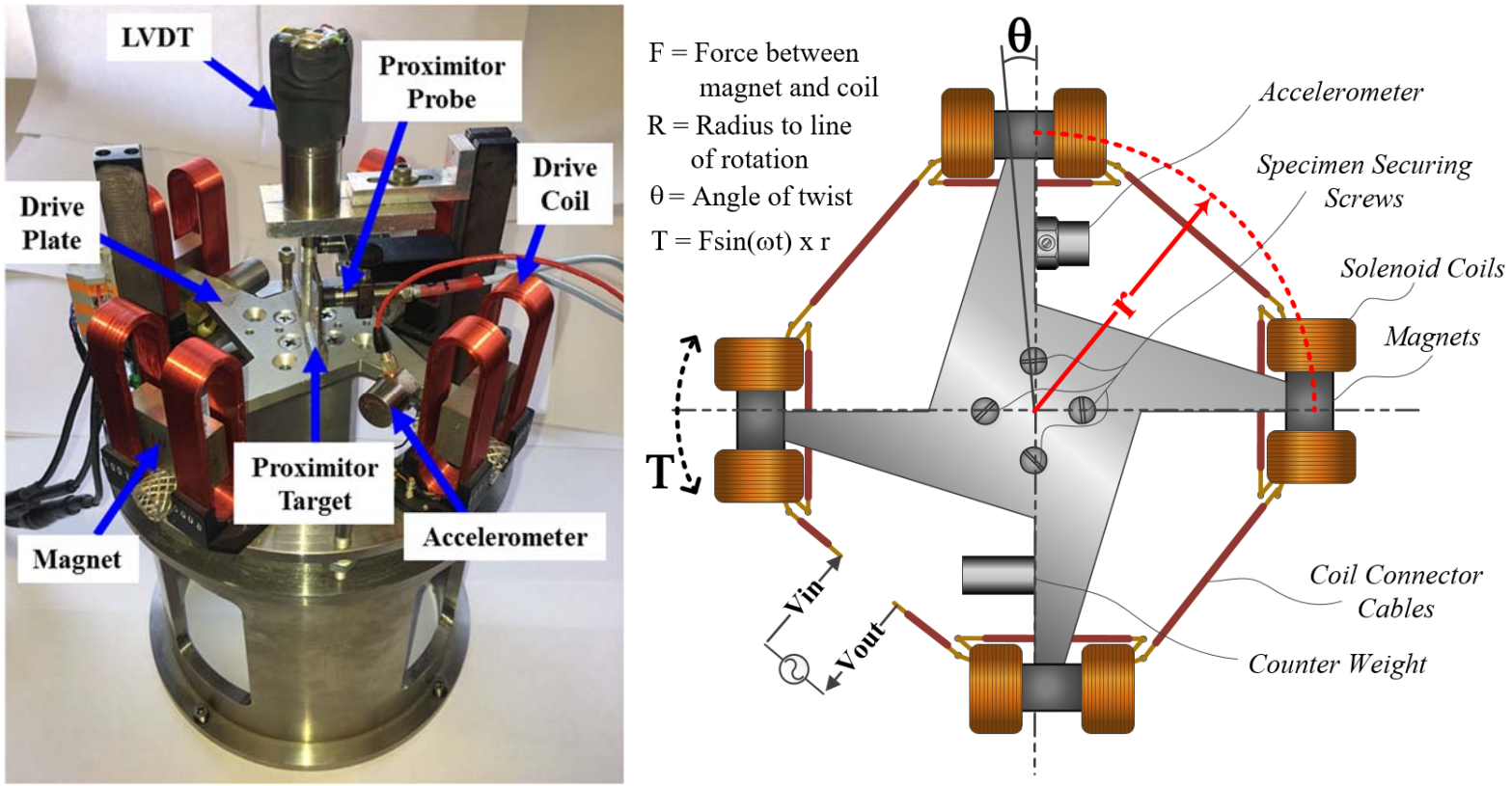

Figure 8.3: Photograph of the Resonant Column device (left) and conceptual schematic of the torsional driving system (right).

The electromagnetic drive system consists of 4 magnets and 8 coils. The drive system is made up of 4 subsystems, each of which is equivalent to an electromagnetic solenoid. Each of the electromagnetic solenoids consist of one permanent magnet and two packed coils of wire. The coils are at both ends of the permanent magnetic coinciding with the magnetic poles. The coils are oriented relative to the permanent magnet to generate magnetic fields parallel to the magnetic field of the permanent magnet. The coils are powered with current that is supplied by a National Instruments (NI) PXI-6251 data acquisition system (DAQ) and, when needed, amplified by a HP 6824A power supply amplifier. This equipment combined with subroutines written in NI LabVIEW allow the excitation of any desired forcing function; however, in this study that forcing function is in the form of a sinusoid with varying frequency. The amplitude of the forcing function is specified in the subroutines in units of voltage, thus the forcing function is supplied to the coils in the form:

$$V_{in} = A * sin(\omega * t) \tag{8.10}$$

and from Ohm's law (Serway and Jewett, 2003):

$$I = V_{in}/Z \tag{8.11}$$

where V_{in} is the voltage sent to the drive coils, A is the voltage amplitude selected in the subroutine, ω is the angular frequency of the forcing function in units of radians per second, t is the time lapse of the excitation in units of seconds, I is the current sent to the drive coils, and Z is the impedance of the electromagnetic drive system. The force-couple generated by the electromagnetic solenoids is a complex problem that would need to be solved using numerical integration and modeling techniques. The force-couples generated by the electromagnetic solenoids are applied to arms of a drive plate that convert this force

into torque applied to the specimen, based on a radius, r from the central axis of the specimen to the radial location of the force-couple. A simplified expression for the torque, T, supplied by one magnet and one drive coil to a specimen is:

$$T = F * r \tag{8.12}$$

Determining the true current supplied to the coils is slightly more complicated than the equation from Ohm's law, due to: (1) inductive impedance in the drive system circuit that is a frequency dependent phenomenon, and (2) back-electromotive force, which is a specific current drop across the coils that is induced by the permanent magnet traveling through the coils at a particular velocity. The second factor creates a force reduction during testing, which is velocity dependent (i.e. frequency dependent) and thus contributes to the damping coefficient, c in the measured SDOF system response. In RC testing, this frequency dependent induced damping is commonly referred to as equipment-generated damping (see Chapter 4). This factor allowed for the range of damping ratios (i.e. 0.19% – 1.51%) used in this study, because the metal specimens tested had a large range of resonant frequencies (i.e. 25.6 Hz – 204.3 Hz), where the equipment-generated damping has the mathematical form $D_{equip} = F_{equip} * f^{-1}$.

8.5 Specimens Tested to Experimentally Evaluate Sweep Rate Effects

In this study, 5 brass metal specimens and one soil specimen subject to 5 different isotropic confining pressures were tested to determine the effect that sweep rates and sweep types have on the sensitivity for determining accurate response curve parameters of a SDOF system. The specimens were tested with decreasing sweep rates until constant response curve parameters were determined. These parameters were then used to simulate the response of equivalent SDOF systems at various sweep rates and sweep types.

As stated previously, the back-electromotive force (equipment-generated damping), created by the electromagnetic solenoids, generates a frequency-dependent reduction in the applied torque during sweeping. The differential effect of this frequency-dependent force reduction is minimal within the sweep range used around the resonant frequency of each specimen, but was large enough for each SDOF system tested to possess a unique damping ratio. These unique damping ratios were confirmed by the results of this study. Geometric properties, mass, equipment-generated damping, equivalent SDOF damping ratio, and resonant frequency of each SDOF system (metal specimens or a soil specimen) tested are tabulated in Table 8.1. A photograph of the metal specimens tested and their specimen numbers are shown in Figure 8.4.

Table 8.1: Geometric and Dynamic Properties of Specimens Tested

Specimen Number	Outside Diameter	Inside Diameter	Height	Weight	RC Equip. Damping	SDOF Damping	Approximate Natural Frequency
	cm	cm	cm	grams	%	%	Hz
1 (Brass Tube)	2.540	2.223	12.65	132.35	0.148	0.190	204.3
2 (Brass Tube)	2.223	2.064	17.68	79.96	0.421	0.463	104.3
6 (Brass Tube)	1.588	1.429	17.68	58.45	0.710	0.752	64.55
9 (Brass Tube)	0.953	0.794	21.45	40.86	1.472	1.514	25.58
13 (Brass Rod)	1.905	0	17.75	429.52	0.239	0.281	150.9
Soil (σc = 0.54 atm)	5.1689	0	10.2810	350.00	0.60	1.42	61.05
Soil (σc = 1.09 atm)	5.1688	0	10.2808	350.00	0.52	1.22	71.60
Soil (σc = 2.18 atm)	5.1687	0	10.2806	350.00	0.45	1.17	83.63
Soil (σc = 4.35 atm)	5.1685	0	10.2802	350.00	0.38	1.07	98.47
Soil (σc = 8.71 atm)	5.1681	0	10.2795	350.00	0.32	1.03	115.7

*Metal Specimen Material Damping is approximately 0.0419%

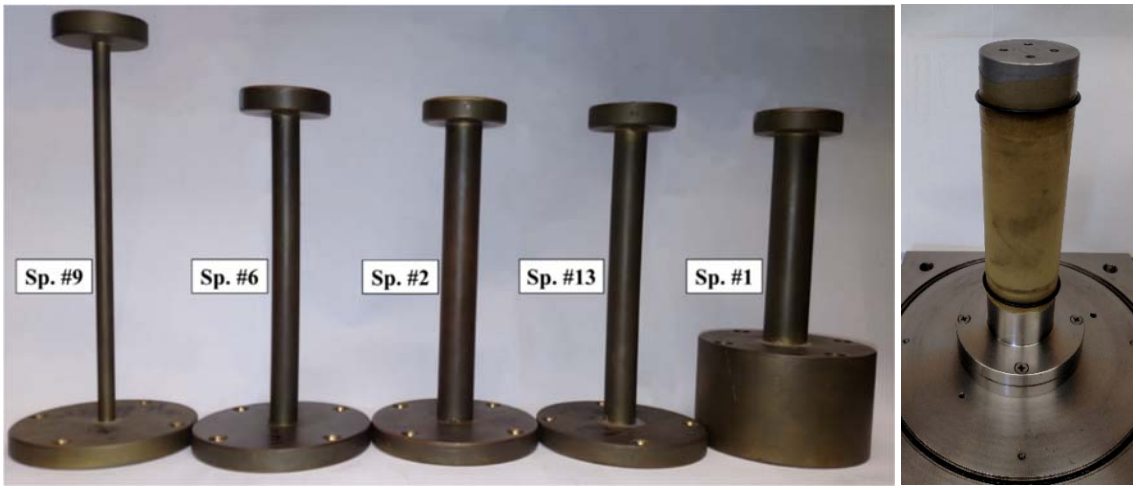

Figure 8.4: Photograph of the metal specimens tested with their specimen numbers marked left of each (left) and a soil specimen (right).

8.6 METHODS

8.6.1 Methods Used to Evaluate the Frequency Response Curve

To begin this investigation, there are two methods used to determine the response curve parameters from the frequency sweep. These include: (1) Using an interpolation method between the local maxima and minima near the half-power points to make a more precise determination of the half-power frequencies, and (2) use of a least-mean squares fitting method that fits the response curve equation to the measured data to iteratively determine the values for the natural frequency and damping ratio. In Lollock (2002), the first method (half-power bandwidth method) was used to determine the sweep rate effects of linear and exponential chirps.

To use the interpolation method, the half-power frequencies are determined by finding the local maximum and minimum amplitudes of the response curve for frequency segments above and below the resonant frequency. These local maxima and minima are recorded points of the response curve that are directly above and below $A_{max}/\sqrt{2}$ and interpolation between these points leads to a more accurate prediction of the half-power

frequencies. If the data points used to populate the measured response curve are too few, this method allows more accurate determination of the half-power frequencies. In the analysis process, the frequency segment below the resonant frequency is evaluated as is and the frequency segment above the resonant frequency can be reversed so that the following equation can be used to evaluate both half-power frequencies:

$$f_{1,2} = f_L + (f_H - f_L) * \left(\frac{(A_i - A_L)}{(A_H - A_L)}\right) \tag{8.13}$$

where $f_{1,2}$ are the half-power frequencies, f_L is the frequency corresponding to the measured amplitude (A_L) below the half-power frequency being interpolated to, f_H is the frequency corresponding to the measured amplitude (A_H) above the half-power frequency being interpolated to, and A_i is the half-power amplitude (i.e. $A_{max}/\sqrt{2}$) from which the half-power frequency is being interpolated to. This method will henceforth be called the half-power interpolation method.

The interpolation method leads to a prediction of the half-power frequencies, f_1 and f_2, that in combination with the measured resonant frequency, f_r, will lead to a calculation of the half-power damping ratio, which is given in the simplified form for low damping ratios (and linear dynamic behavior) as:

$$D_{HP} = \frac{f_2 - f_1}{2 * f_r} \tag{8.14}$$

where D_{HP} is the damping ratio. The least-mean-squares fitting method uses the theoretical response curve for a single-degree-of-freedom (SDOF) system which is given in Richart et al. (1970) as:

$$M = \frac{1}{\sqrt{[1-(\omega/\omega_n)^2]^2 + [2D(\omega/\omega_n)]^2}} \tag{8.15}$$

where the dynamic magnification factor is M, ω is the input frequency, ω_n is the natural circular frequency, and D is the damping ratio. This method will henceforth be called the least-mean-squares fit method. To utilize this equation, the measured response curve is first normalized. In this study, the fitting algorithm was limited to 10,000 iterations and tolerance for the fitting parameters of 1E-8. The example used in the introduction is shown again, in Figure 8.5, with the least-mean-squares best fit response curves plotted for the two sweep cases.

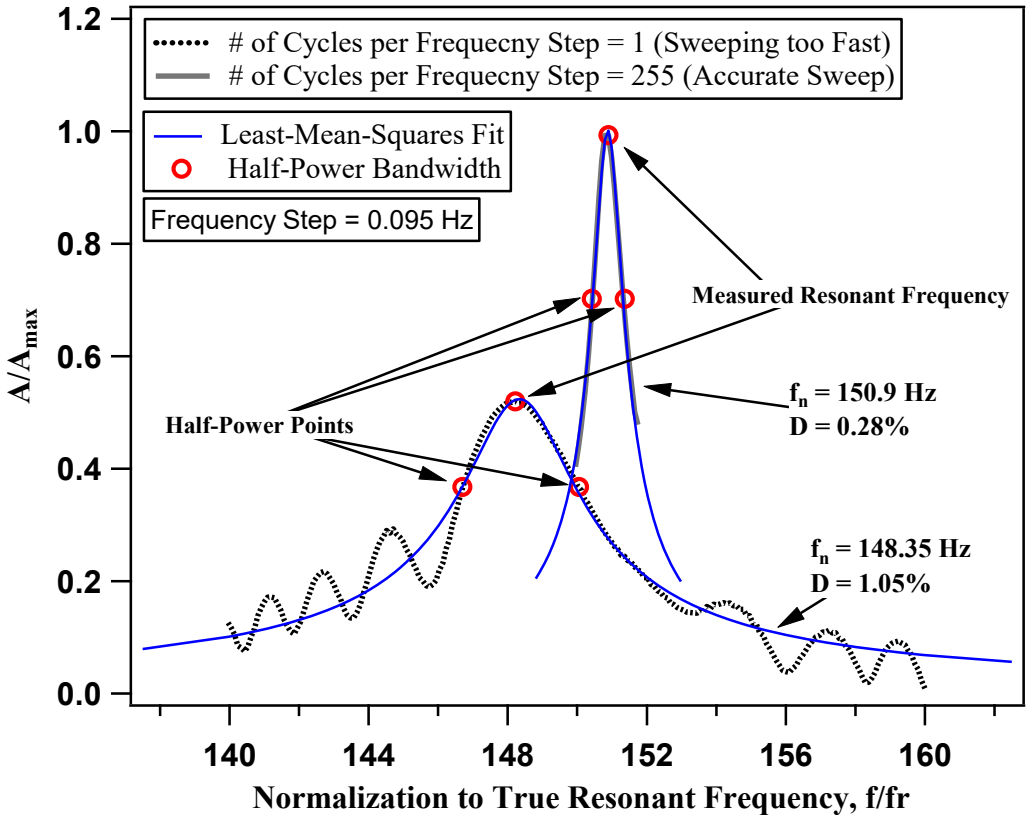

Figure 8.5: An example of two sweeps conducted on the same damped SDOF system, but with two different sweep rates. Results from the Half-Power Method and Least-Mean-Squares-Fit Method are Shown.

8.6.2 Equations Used to Predict Spectral Response from Stepped-Sine Sweeping

The free-vibration response of a linear damped single-degree of freedom system is given from Richart et al. (1970) as:

$$m\ddot{x} + c\dot{x} + kx = 0 \tag{8.16}$$

where m is the mass of the system, c is the damping coefficient, k is the spring constant, and $\ddot{x}$, $\dot{x}$, and x are respectively, acceleration, velocity, and displacement. This equation represents the response of a SDOF system allowed to freely vibrate with viscous damping behavior. The equation for a system with forced vibration with viscous damping behavior is given from Richart et al. (1970) as:

$$\ddot{x}m + c\dot{x} + kx = Q_i \sin(\omega t) \tag{8.17}$$

where Q_i is the amplitude of the cyclic force applied, ω is the angular frequency of excitation, and t is time. This equation was derived in Chopra (2001) into incremental displacement and incremental velocity formulas that can be used to predict the SDOF response to an incrementally changing forcing function. In this study, the amplitude of the forcing function remains constant, but the frequency of forcing function changes in accordance with the sweep rate and sweep type. The key aspect of using the formulas from Chopra (2001) is selecting a small enough incremental change that the forcing function and SDOF response resembles continuous behavior. In this study, the increment size was selected to match the sampling rate used in the sweep tests, which was 10,000 samples per second (about 50 times the highest frequency tested).

From Chopra (2001) the incremental displacement and incremental velocity are:

$$u_{i+1} = Ax_i + Bx_i + CQ_i + DQ_{i+1} \tag{8.18}$$

$$\dot{u}_{i+1} = A'x_i + B'\dot{x}_i + C'Q_i + D'Q_{i+1} \tag{8.19}$$

where u_{i+1} is the preceding incremental displacement, $\dot{u}_{i+1}$ is the preceding incremental velocity, x_i is the current displacement, $\dot{x}_i$ is the current velocity, Q_i is the current input force, and Q_{i+1} is the preceding input force. In Chopra (2001) the coefficients for these recurrence formulas are as follows:

$$A = e^{-D\omega_n\Delta t}\left(\left(\frac{D}{\sqrt{1-D^2}}\right)\sin(\omega_D\Delta t) + \cos(\omega_D\Delta t)\right) \tag{8.20}$$

$$B = e^{-D\omega_n\Delta t}\left(\frac{1}{\omega_D}\sin(\omega_D\Delta t)\right) \tag{8.21}$$

$$C = \frac{1}{k}\left\{\frac{2D}{\omega_D\Delta t} + e^{-D\omega_n\Delta t}\left[\left(\frac{1-2D^2}{\omega_D\Delta t} - \frac{D}{\sqrt{1-D^2}}\right)\sin(\omega_D\Delta t) - \left(1 + \frac{2D}{\omega_n\Delta t}\right)\cos(\omega_D\Delta t)\right]\right\} \tag{8.22}$$

$$D = \frac{1}{k}\left[1 - \frac{2D}{\omega_n\Delta t} + e^{-D\omega_n\Delta t}\left(\frac{2D^2-1}{\omega_D\Delta t}\sin(\omega_D\Delta t) + \frac{2D}{\omega_n\Delta t}\cos(\omega_D\Delta t)\right)\right] \tag{8.23}$$

$$A' = -e^{-D\omega_n\Delta t}\left(\frac{\omega_n}{\sqrt{1-D^2}}\sin(\omega_D\Delta t)\right) \tag{8.24}$$

$$B' = e^{-D\omega_n\Delta t}\left(\cos(\omega_D\Delta t) - \frac{D}{\sqrt{1-D^2}}\sin(\omega_D\Delta t)\right) \tag{8.25}$$

$$C' = \frac{1}{k}\left\{-\frac{1}{\Delta t} + e^{-D\omega_n\Delta t}\left[\left(\frac{\omega_n}{\sqrt{1-D^2}} + \frac{D}{\Delta t\sqrt{1-D^2}}\right)\sin(\omega_D\Delta t) + \frac{1}{\Delta t}\cos(\omega_D\Delta t)\right]\right\} \tag{8.26}$$

$$D' = \frac{1}{k\Delta t}\left[1 - e^{-D\omega_n\Delta t}\left(\frac{D}{\sqrt{1-D^2}}\sin(\omega_D\Delta t) + \cos(\omega_D\Delta t)\right)\right] \tag{8.27}$$

where ω_D is the damped natural frequency based on $\omega_D = \omega_n\sqrt{1-D^2}$.

The differences between the SDOF input parameters (i.e. mass, m, damping coefficient, c, and spring constant, k) of the system simulated and the torsional system tested (i.e. mass polar moment of inertia, J_0, torsional damping coefficient, c_t, and torsional spring constant, k_t, and are unimportant as all of the SDOF response curve parameters (i.e.

amplitude, A, damping ratio, D, and frequency, f_r) are normalized into A/A_{max} and D/D_{min}, and $((f_{peak}-f_D)/f_D)*Q$, where $Q = 1/2D$.

8.6.3 Validation of the Analytical Equations for Predicting the Experimental Stepped-Sine Sweep Response

To begin to validate the simulations that were conducted, using the recurrence formulas in Chopra (2001), three time-domain and ten frequency-domain examples are provided. Each time-domain example shows a normalized time-domain signal recorded from a stepped-sine sweep test on Metal Specimen #13, the sweeps were downgrade that started at 160 Hz, ended at 140 Hz, had a step rate, f_{step}, of 0.095 Hz, and three different cycles per frequency step, C_s, (1, 2, and 3) were used for the three time-domain examples. For the ten frequency-domain examples, sweeps were downgrade that started at 160 Hz, ended at 140 Hz, had a step rate, f_{step}, of 0.095 Hz, and cycles per frequency step, C_s, ranged from 1 to 255. Simulations were conducted with the same sweep rate parameters and are presented as time-domain signal envelopes plotted with the recorded time-domain signals. The three time-domain examples are plotted in Figure 8.8 and the ten frequency-domain examples are plotted in Figure 8.9.

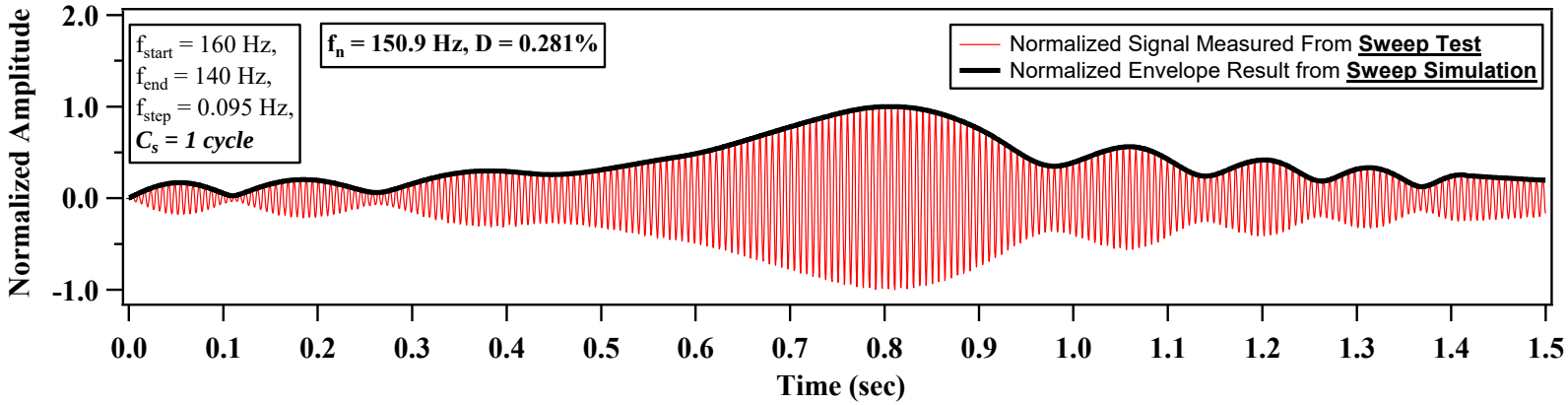

Figure 8.6: Normalized time-domain signals recorded from a stepped-sine sweep tests on Metal Specimen #13, the sweep was a downgrade sweep that started at 160 Hz, ended at 140 Hz, had a step rate, f_{step}, of 0.095 Hz, and cycles per frequency step, C_s, of 1 was used. Both experimental results and theoretical simulations are presented together.

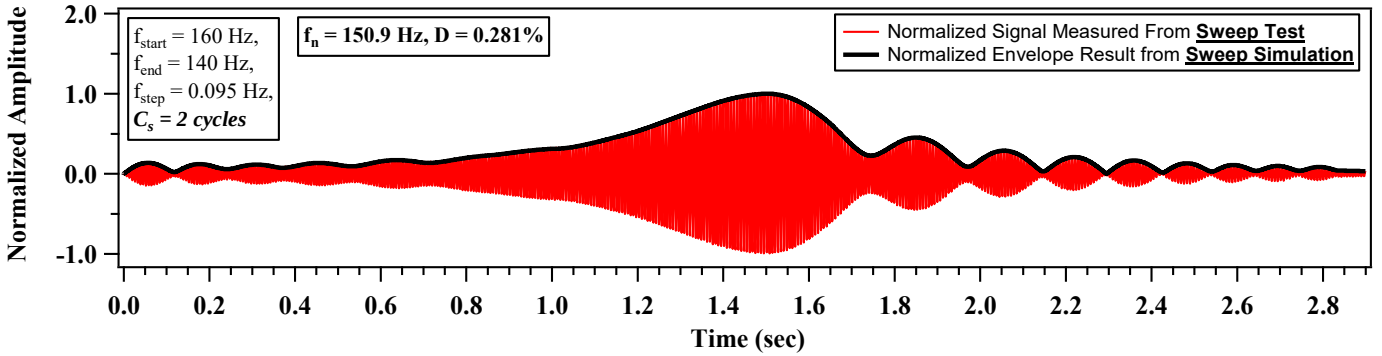

Figure 8.7: Normalized time-domain signals recorded from a stepped-sine sweep tests on Metal Specimen #13, the sweep was a downgrade sweep that started at 160 Hz, ended at 140 Hz, had a step rate, f_{step}, of 0.095 Hz, and cycles per frequency step, C_s, of 2 was used. Both experimental results and theoretical simulations are presented together.

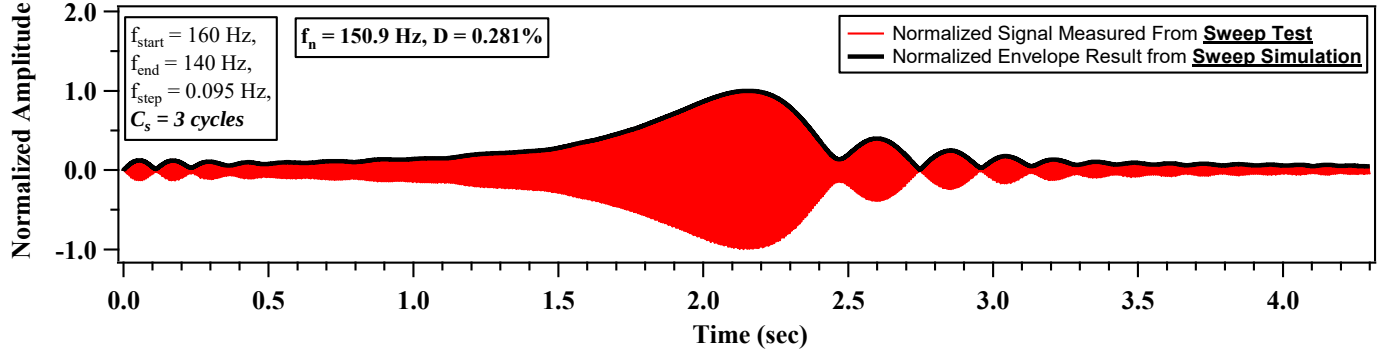

Figure 8.8: Normalized time-domain signals recorded from a stepped-sine sweep tests on Metal Specimen #13, the sweep was a downgrade sweep that started at 160 Hz, ended at 140 Hz, had a step rate, f_{step}, of 0.095 Hz, and cycles per frequency step, C_s, of 3 was used. Both experimental results and theoretical simulations are presented together.

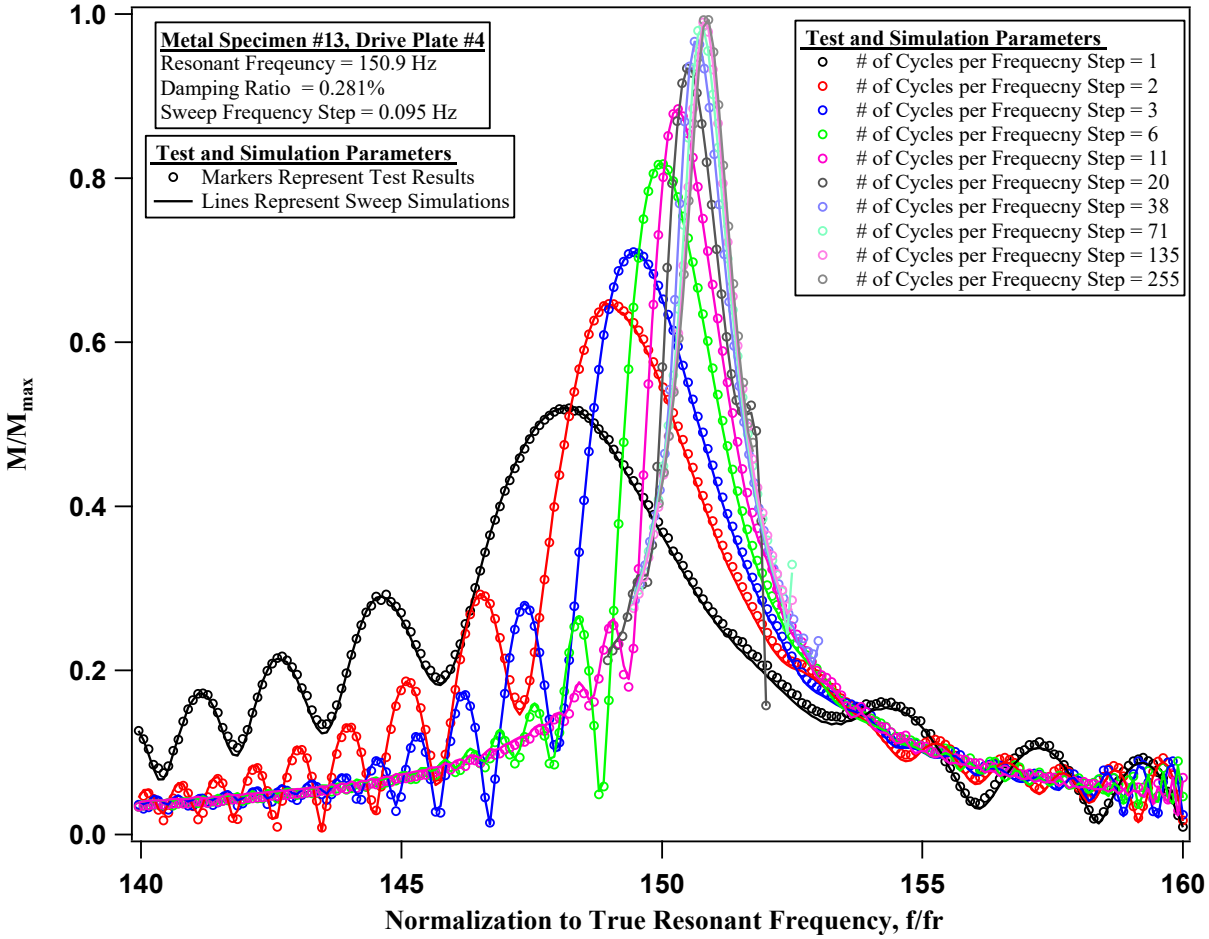

Figure 8.9: Normalized frequency-domain signals recorded from a stepped-sine sweep tests on Metal Specimen #13, the sweep was a downgrade sweep that had a step rate, f_{step}, of 0.095 Hz, and 10 different cycles per frequency step, C_s were used. Both experimental results and theoretical simulations are presented together.

Based on the comparison of the time-domain and frequency-domain data between the experimental and analytical results, the simulations quite accurately model the experimental dynamic behavior.

8.7 Analytical and Experimental Comparisons and Normalization of Sweep Rate Effect

In this sub-section, the analytical estimations of the partial steady-state response, A, and partial damping ratio D, are compared with experimental measurements, which are both relative to the maximum steady state response, A_{max}, and true damping ratio, D_{min}. In each example, first each simulated and measured fraction of steady-state response, A/A_{max}, are assessed, which are based on either the simulated estimation or measured estimation of the steady-state response amplitude compared to that of the simulated or estimated maximum steady sate response amplitude. Second, each simulated and measured ratio of measured damping to true damping, D/D_{min}, are assessed, which are based on either the simulated estimation or measured estimation of the Damping ratio compared to that of the simulated or estimated minimum damping ratio. Third, it is found that the differences that occur due to the number of cycles used per sweep frequency segment can be normalized by step rate, f_{step}, divided by the number of cycles excited at each frequency, C_s, which collapses these curve into a single relationship. Five theoretical simulations and five experimental tests are compared to continue to demonstrate the accuracy of the analytical procedures to model the experimental results.

8.7.1 Comparisons of Analytical and Experimental Results from 5 SDOF Systems and Normalization of Relationships by f_{step}/C_s

In this subsection sweeps on five metal specimens are demonstrated with experimental test results and analytically modeled results. To first demonstrate how the results will be presented, an example of Metal Specimen #13 is shown as Figure 8.10 and Figure 8.11, where the experimental results are shown with markers and each of the simulations are shown as solid lines.

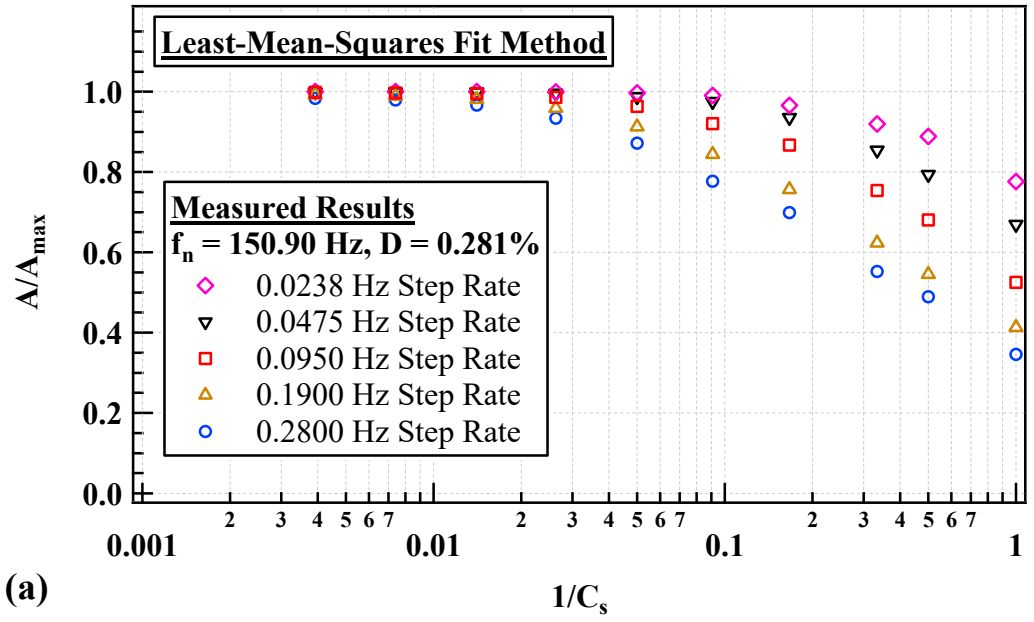

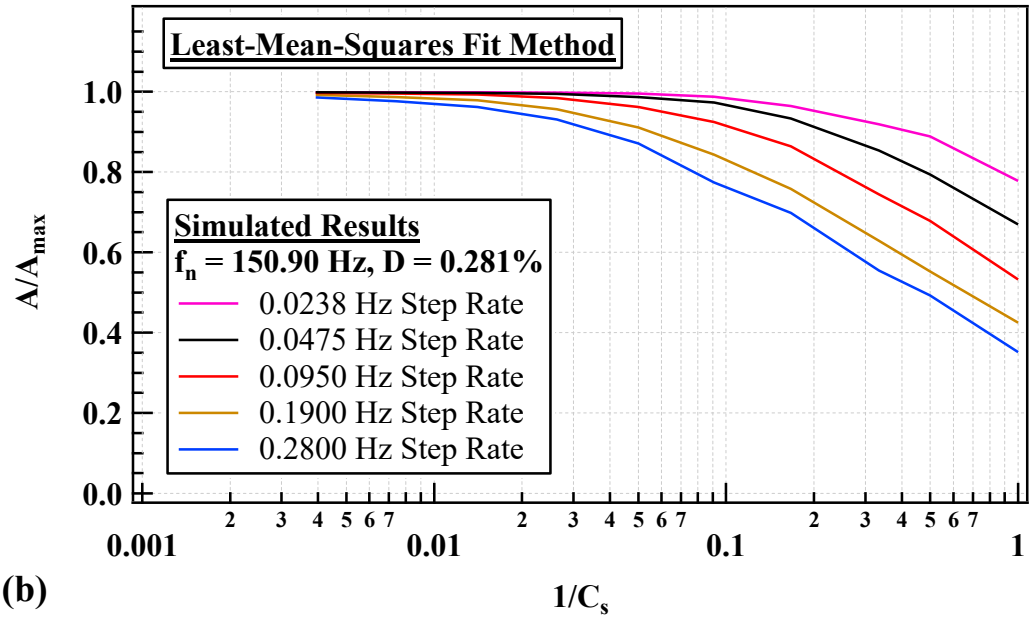

Figure 8.10: (a) Experimental and (b) Numerical Modeling Results Showing the Variation of the Normalized Amplitude Error (A/A_{max}) with the Inverse of the Number of Cycles Per Frequency Step ($1/C_s$) from Frequency Sweep Tests on Metal Specimen #13 that has f_n =150.90 Hz and D = 0.281%.

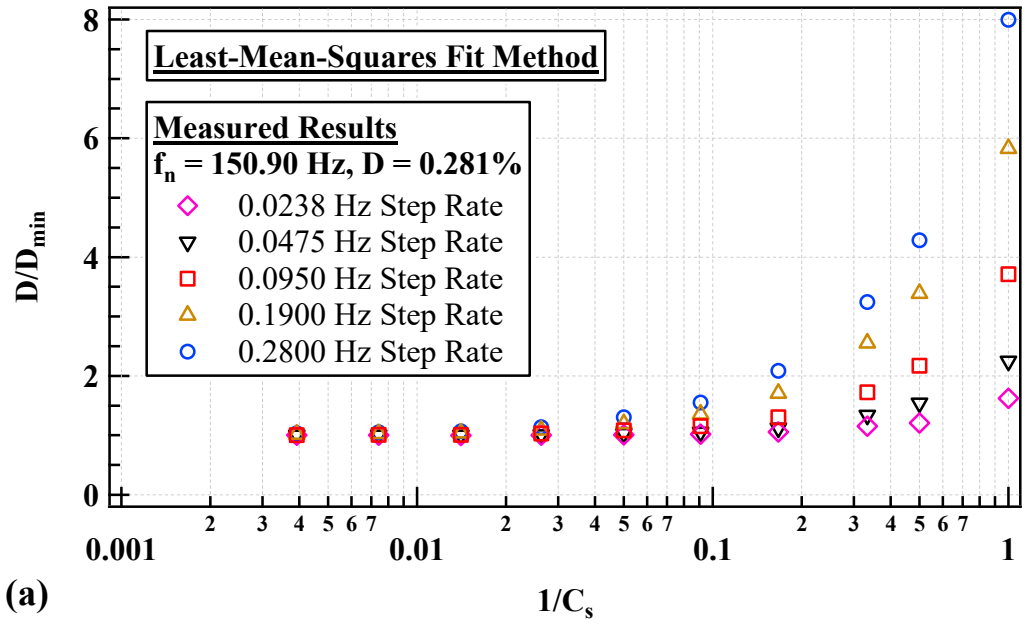

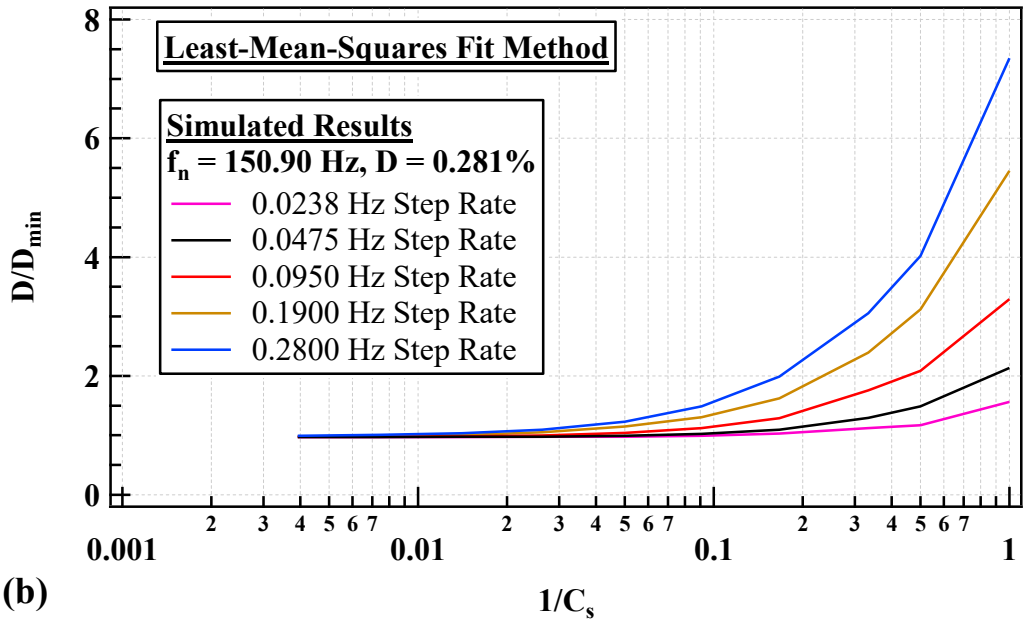

Figure 8.11: (a) Experimental and (b) Numerical Modeling Results Showing the Variation of the Normalized Damping Ratio Error (D/D_{min}) with the Inverse of the Number of Cycles Per Frequency Step ($1/C_s$) from Frequency Sweep Tests on Metal Specimen #1 that has f_n = 204.34 Hz and D = 0.190%.

For each of the five metal specimens either tested experimentally or modeled analytically, four plots are presented for each that contain the following: (1) A/A_{max}-$\log(1/C_s)$, (2) A/A_{max}-$\log(f_{step}/C_s)$, (3) D/D_{min}-$\log(1/C_s)$, and (4) D/D_{min}-$\log(f_{step}/C_s)$. The variation in A/A_{max} or D/D_{min} with $1/C_s$ can be normalized into one relationship by plotting the horizontal axis as f_{step}/C_s. This is possible because each case has a single f_n and single damping ratio. Cases that show normalization with varying f_n and varying D are covered later. In each of the cases presented in this subsection, five different f_{step} are used with 10 different C_s for each f_{step} are used. Sweep rate effect results for the five Metal Specimens are shown in Figure 8.12 through Figure 8.23, the content these figures is shown in Table 8.2.

Table 8.2: Organization of the Results from Frequency Sweep Tests on 5 Metal Specimens That are Shown in Figure 8.12 through Figure 8.23

	MtSp #1	**MtSp #13**	**MtSp #12**	**MtSp #6**	**MtSp #9**
Natural Frequency, f_n (Hz)	204.34	150.90	104.25	64.55	25.58
Damping Ratio, D (%)	0.190	0.281	0.463	0.752	1.514
(a) A/A_{max}-$\log(1/C_s)$ and (b) A/A_{max}-$\log(f_{step}/C_s)$	Figure 8.12	Figure 8.14	Figure 8.16	Figure 8.18	Figure 8.20
(a) D/D_{min}-$\log(1/C_s)$ and (b) D/D_{min}-$\log(f_{step}/C_s)$	Figure 8.13	Figure 8.15	Figure 8.17	Figure 8.19	Figure 8.21
Ratio of f_{peak} to f_r	Figure 8.22 (a)	Figure 8.22 (b)	*Not Shown*	Figure 8.23 (a)	Figure 8.23 (b)

Note: (1) MtSp = Metal Specimen

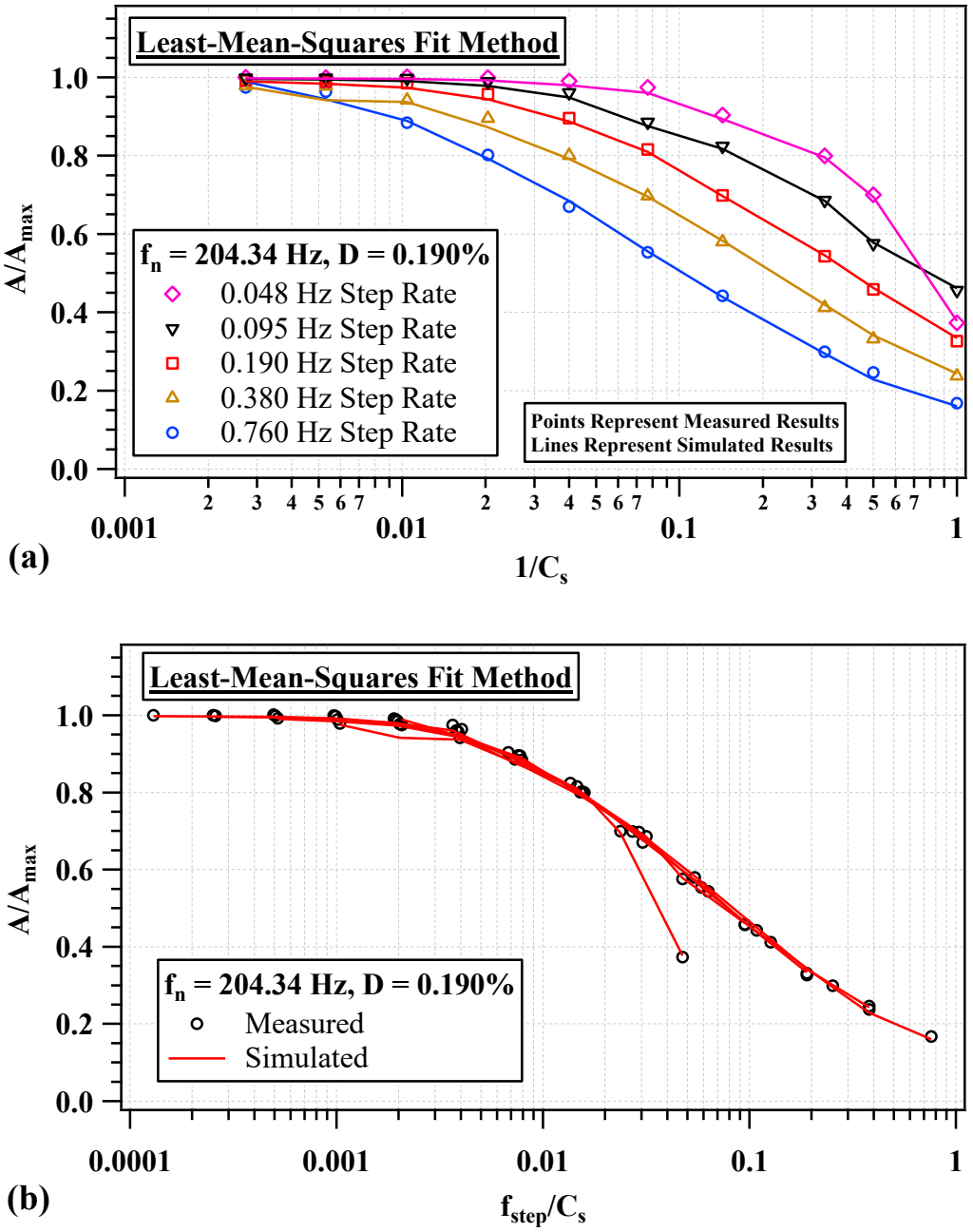

Figure 8.12: Experimental and Numerical Modeling Results Showing the Variation of the Normalized Amplitude Error (A/A_{max}) with (a) the Inverse of the Number of Cycles Per Frequency Step ($1/C_s$) and (b) Frequency Step (f_{step}) Divided by C_s from Frequency Sweep Tests on Metal Specimen #1 that has f_n = 204.34 Hz and D = 0.190%.

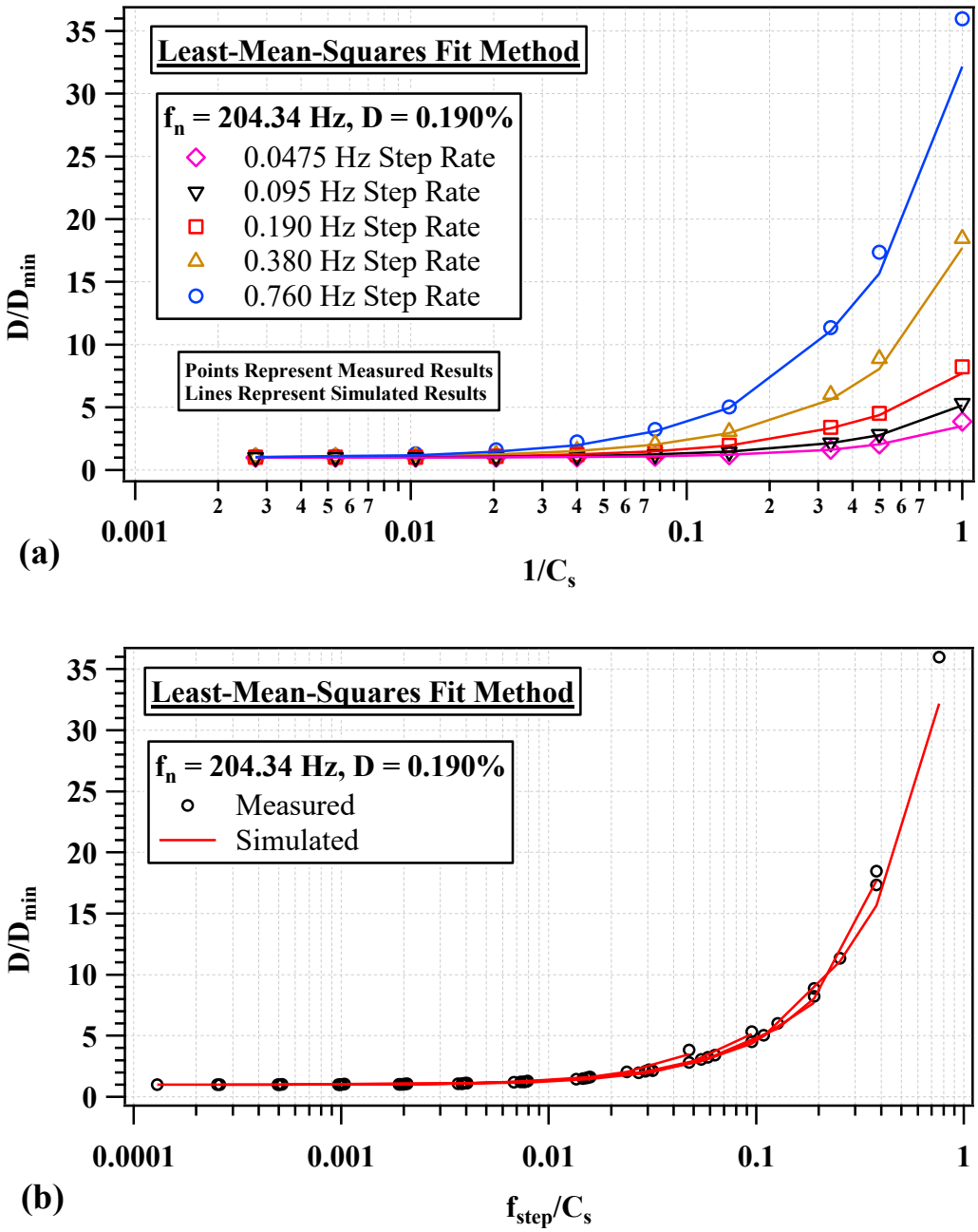

Figure 8.13: Experimental and Numerical Modeling Results Showing the Variation of the Normalized Damping Ratio Error (D/D_{min}) with (a) the Inverse of the Number of Cycles Per Frequency Step ($1/C_s$) and (b) Frequency Step (f_{step}) Divided by C_s from Frequency Sweep Tests on Metal Specimen #1 that has f_n = 204.34 Hz and D = 0.190%.

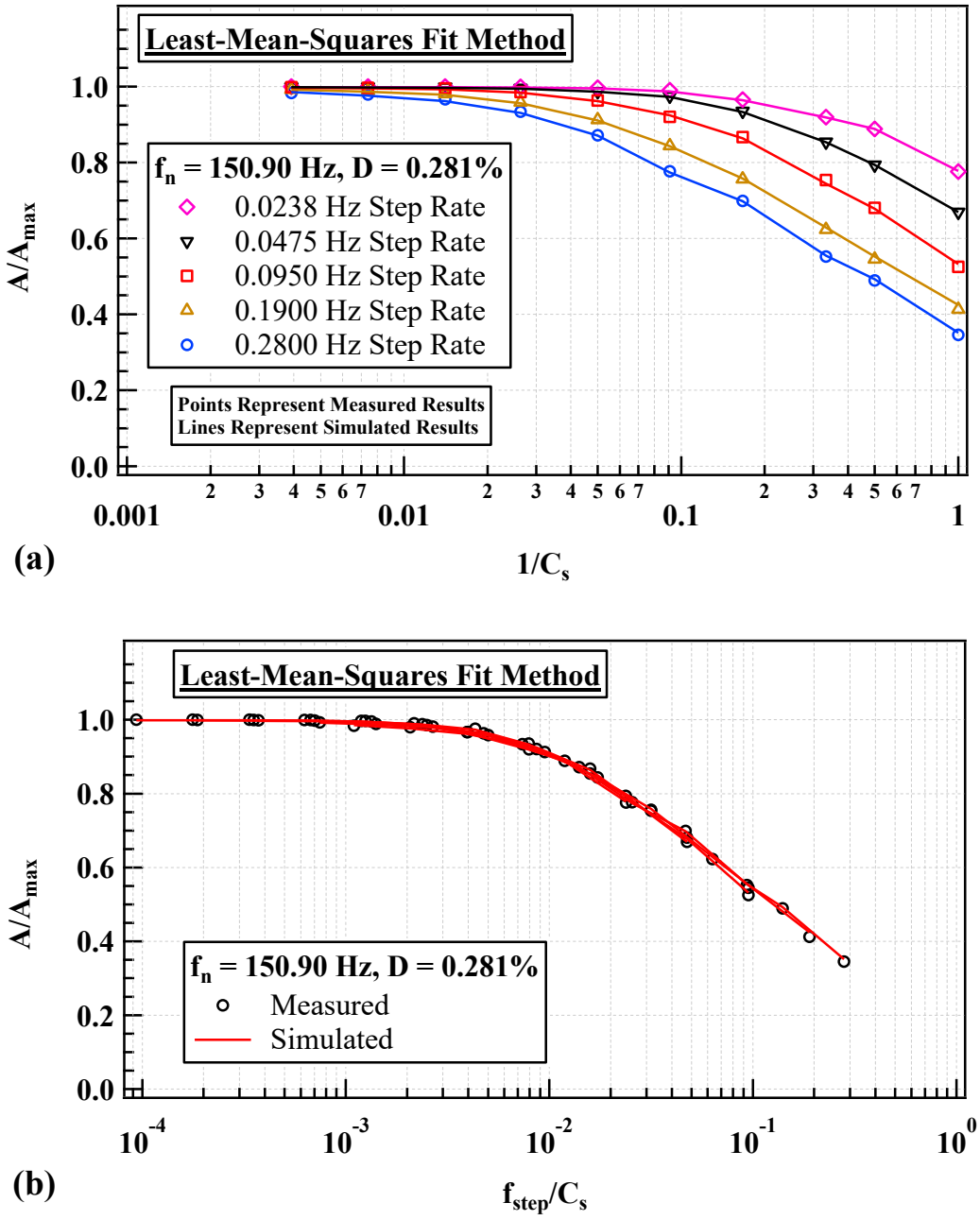

Figure 8.14: Experimental and Numerical Modeling Results Showing the Variation of the Normalized Amplitude Error (A/A_{max}) with (a) the Inverse of the Number of Cycles Per Frequency Step ($1/C_s$) and (b) Frequency Step (f_{step}) Divided by C_s from Frequency Sweep Tests on Metal Specimen #13 that has f_n =150.90 Hz and D = 0.281%.

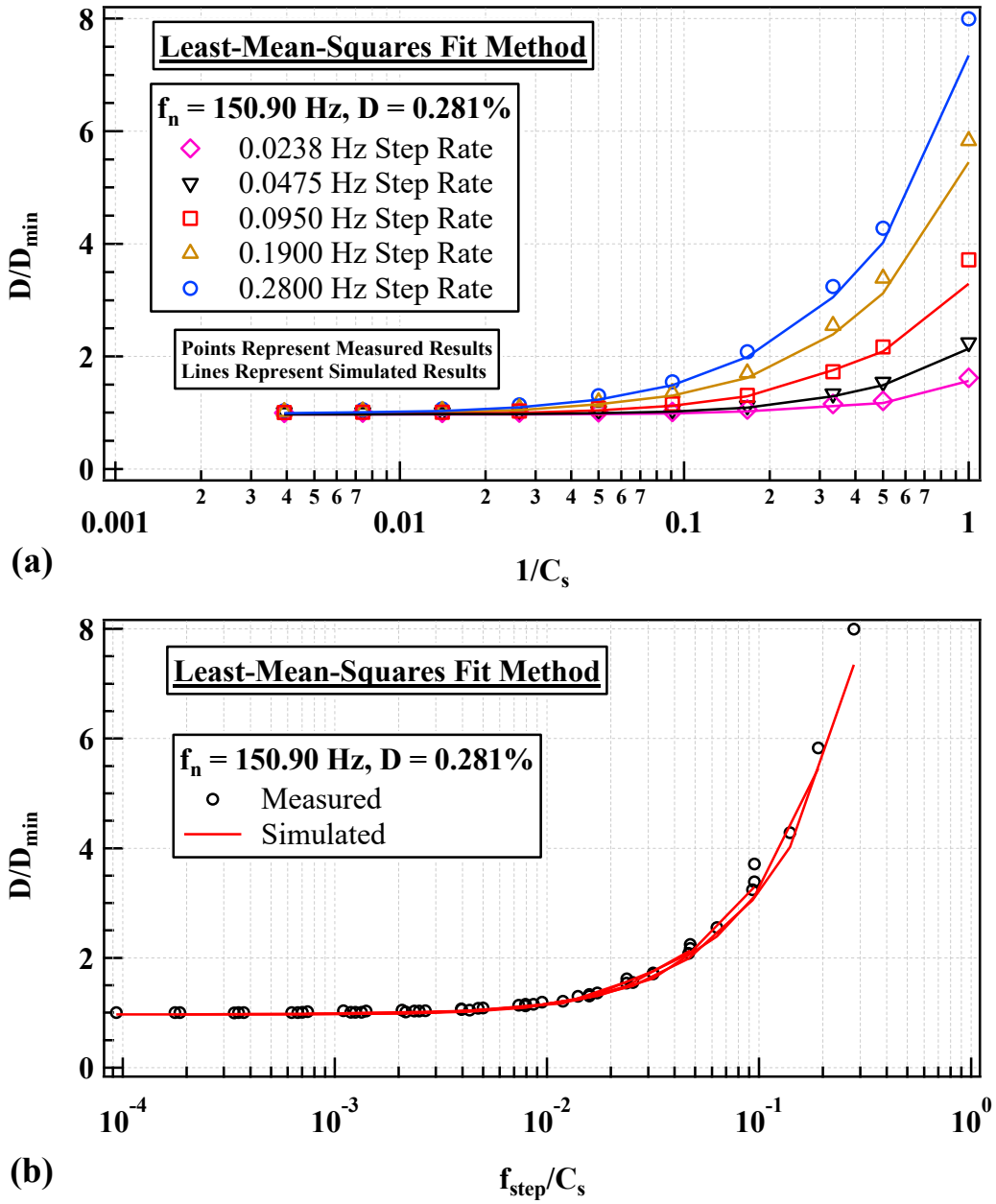

Figure 8.15: Experimental and Numerical Modeling Results Showing the Variation of the Normalized Damping Ratio Error (D/D_{min}) with (a) the Inverse of the Number of Cycles Per Frequency Step ($1/C_s$) and (b) Frequency Step (f_{step}) Divided by C_s from Frequency Sweep Tests on Metal Specimen #13 that has f_n =150.90 Hz and D = 0.281%.

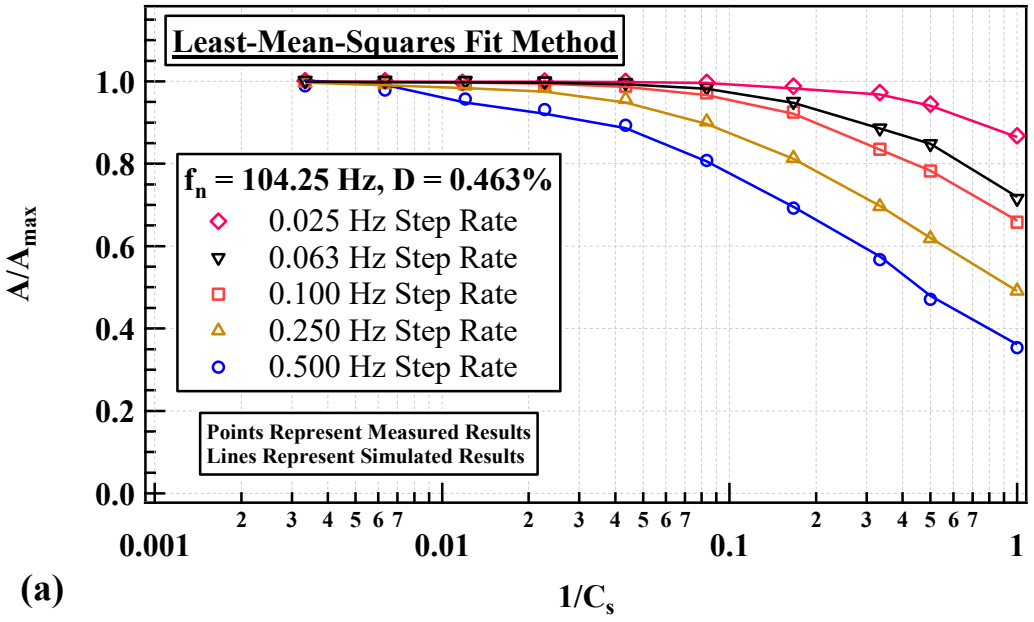

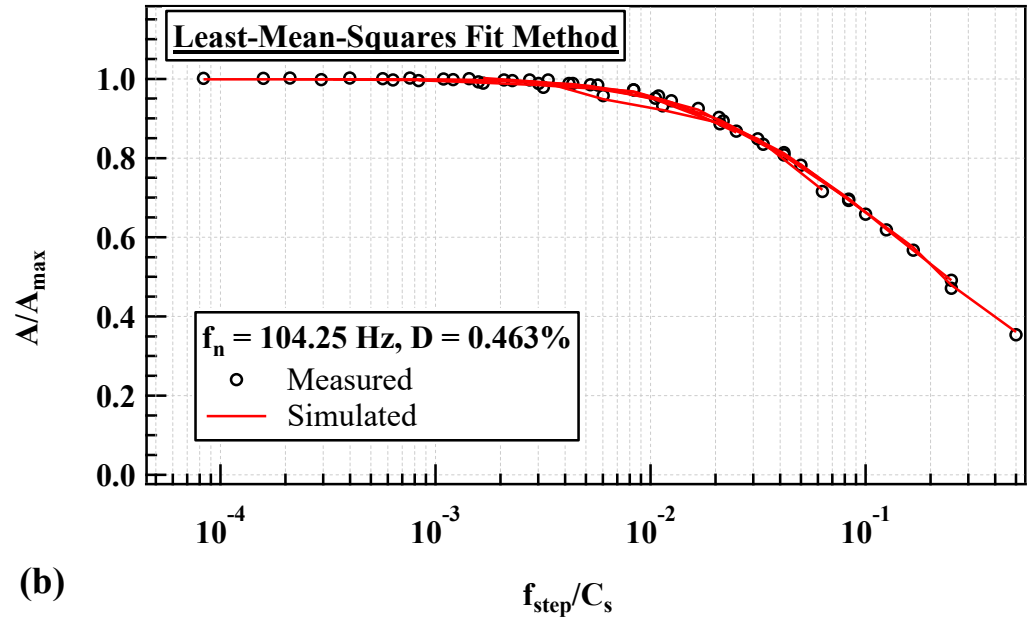

Figure 8.16: Experimental and Numerical Modeling Results Showing the Variation of the Normalized Amplitude Error (A/A_{max}) with (a) the Inverse of the Number of Cycles Per Frequency Step ($1/C_s$) and (b) Frequency Step (f_{step}) Divided by C_s from Frequency Sweep Tests on Metal Specimen #2 that has f_n =104.25 Hz and D = 0.463%.

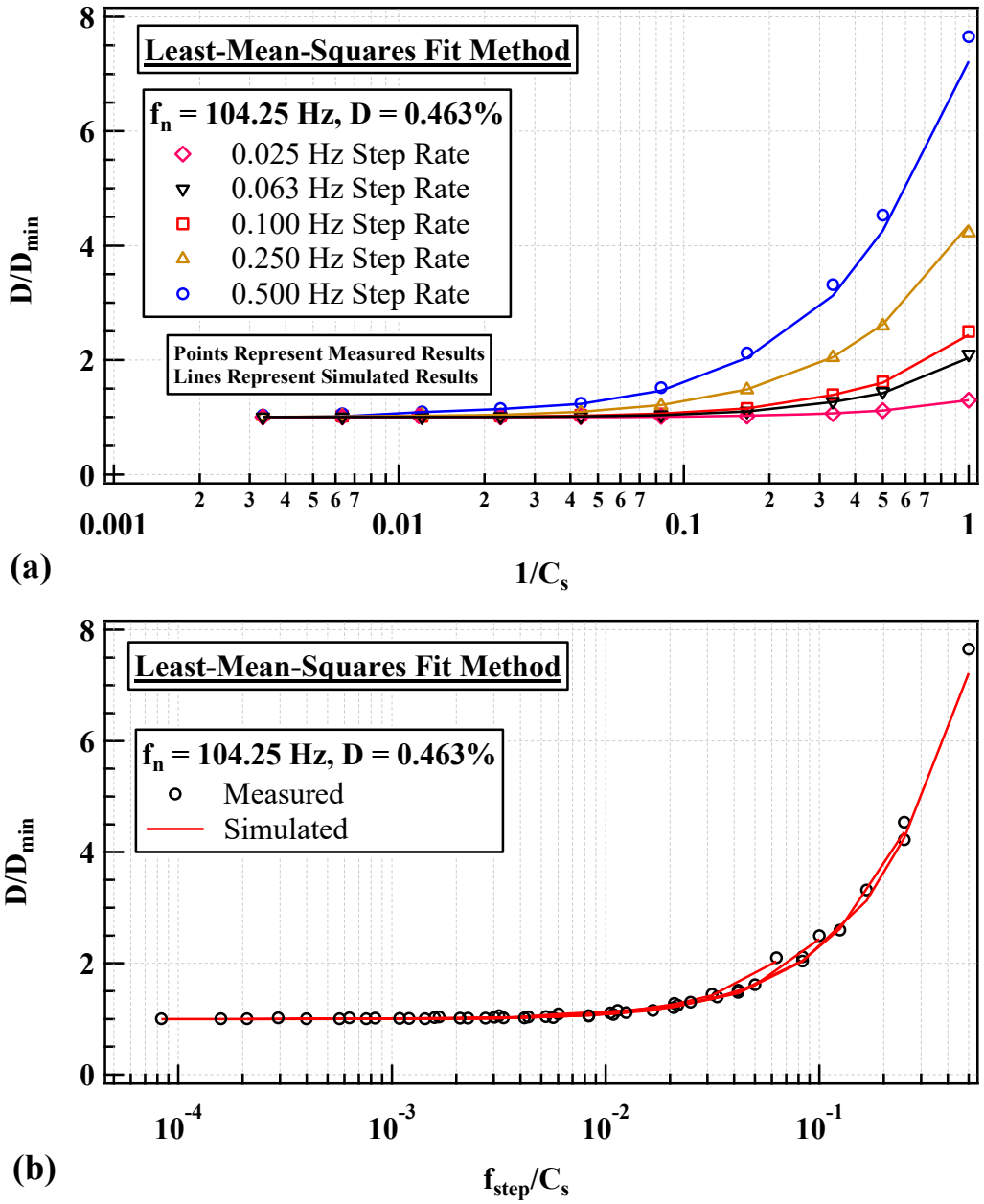

Figure 8.17: Experimental and Numerical Modeling Results Showing the Variation of the Normalized Damping Ratio Error (D/D_{min}) with (a) the Inverse of the Number of Cycles Per Frequency Step ($1/C_s$) and (b) Frequency Step (f_{step}) Divided by C_s from Frequency Sweep Tests on Metal Specimen #2 that has f_n =104.25 Hz and D = 0.463%.

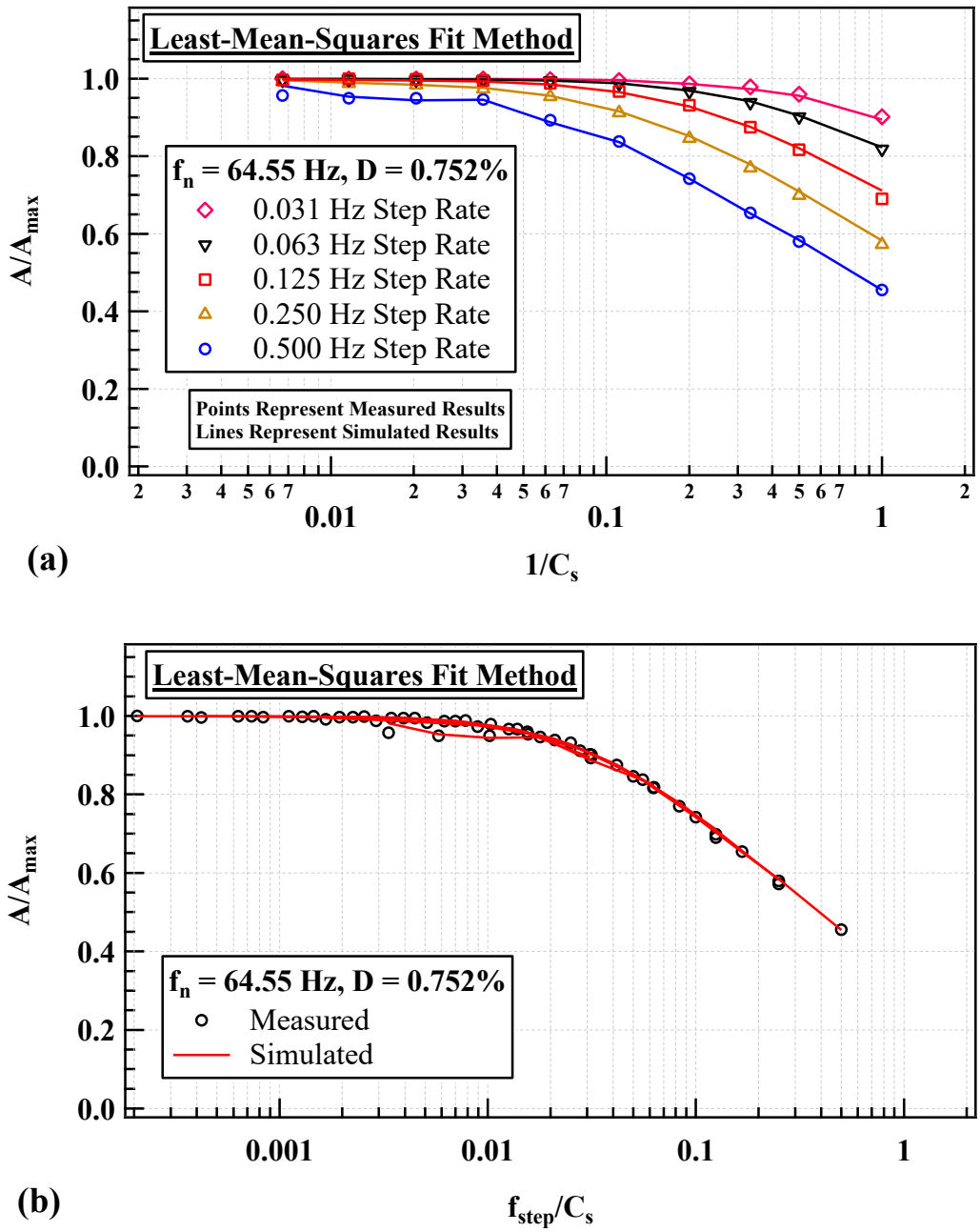

Figure 8.18: Experimental and Numerical Modeling Results Showing the Variation of the Normalized Amplitude Error (A/A_{max}) with (a) the Inverse of the Number of Cycles Per Frequency Step ($1/C_s$) and (b) Frequency Step (f_{step}) Divided by C_s from Frequency Sweep Tests on Metal Specimen #6 that has f_n =64.55 Hz and D = 0.752%.

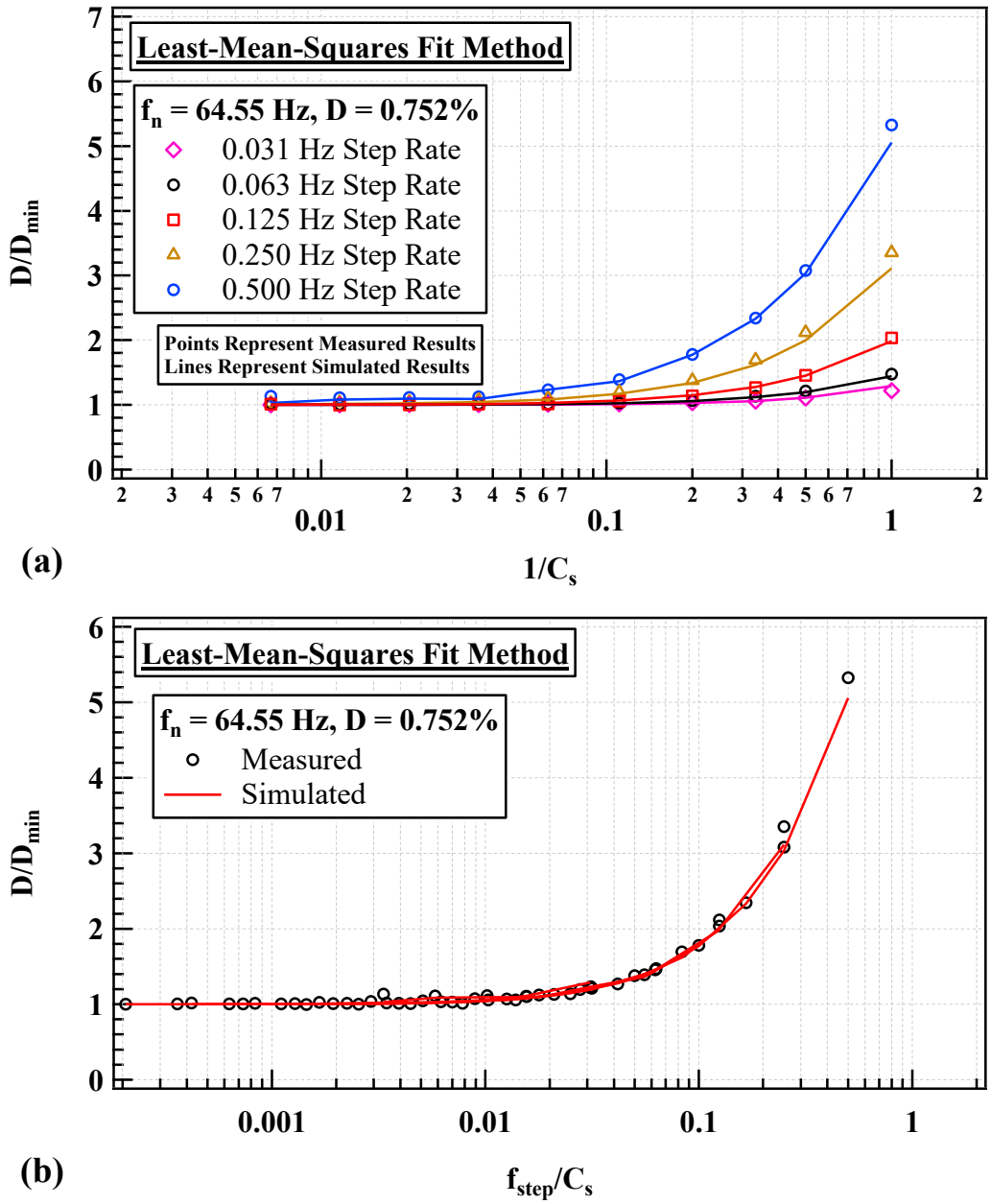

Figure 8.19: Experimental and Numerical Modeling Results Showing the Variation of the Normalized Damping Ratio Error (D/D_{min}) with (a) the Inverse of the Number of Cycles Per Frequency Step ($1/C_s$) and (b) Frequency Step (f_{step}) Divided by C_s from Frequency Sweep Tests on Metal Specimen #6 that has f_n =64.55 Hz and D = 0.752%.

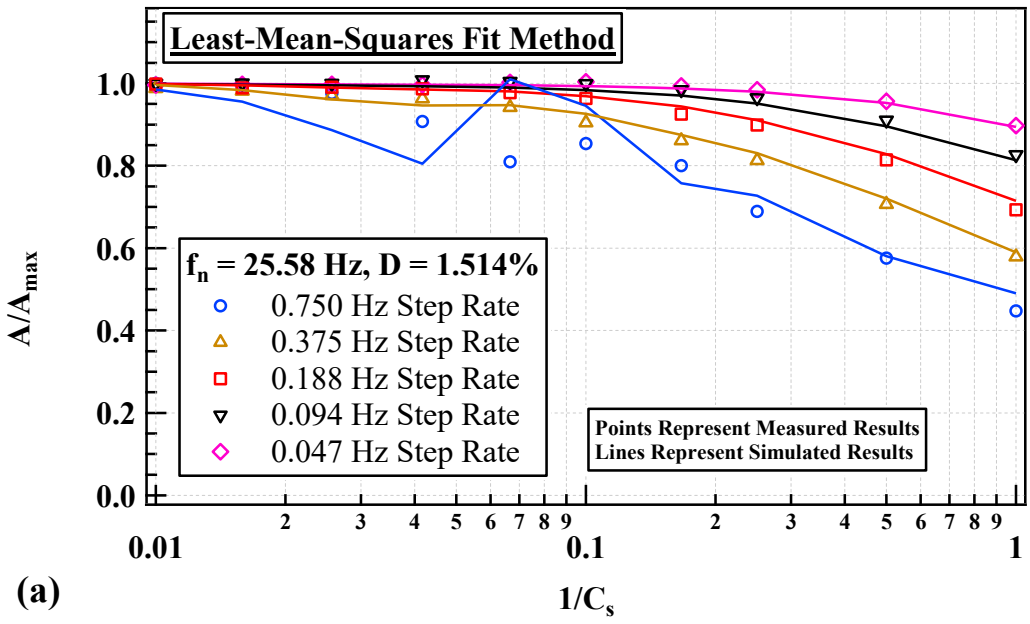

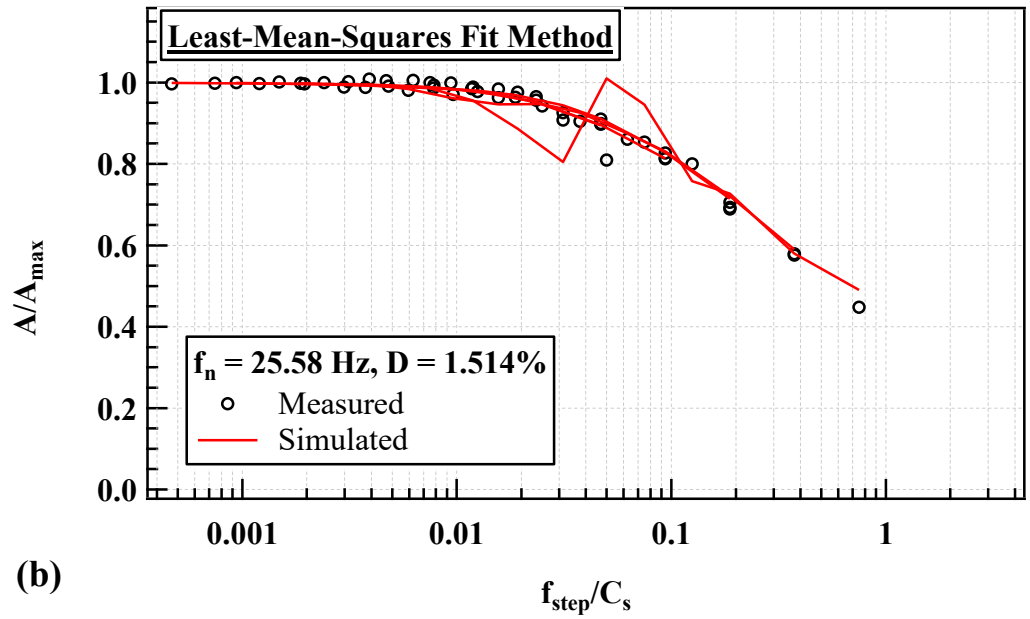

Figure 8.20: Experimental and Numerical Modeling Results Showing the Variation of the Normalized Amplitude Error (A/A_{max}) with (a) the Inverse of the Number of Cycles Per Frequency Step ($1/C_s$) and (b) Frequency Step (f_{step}) Divided by C_s from Frequency Sweep Tests on Metal Specimen #9 that has fn =25.58 Hz and D = 1.514%.

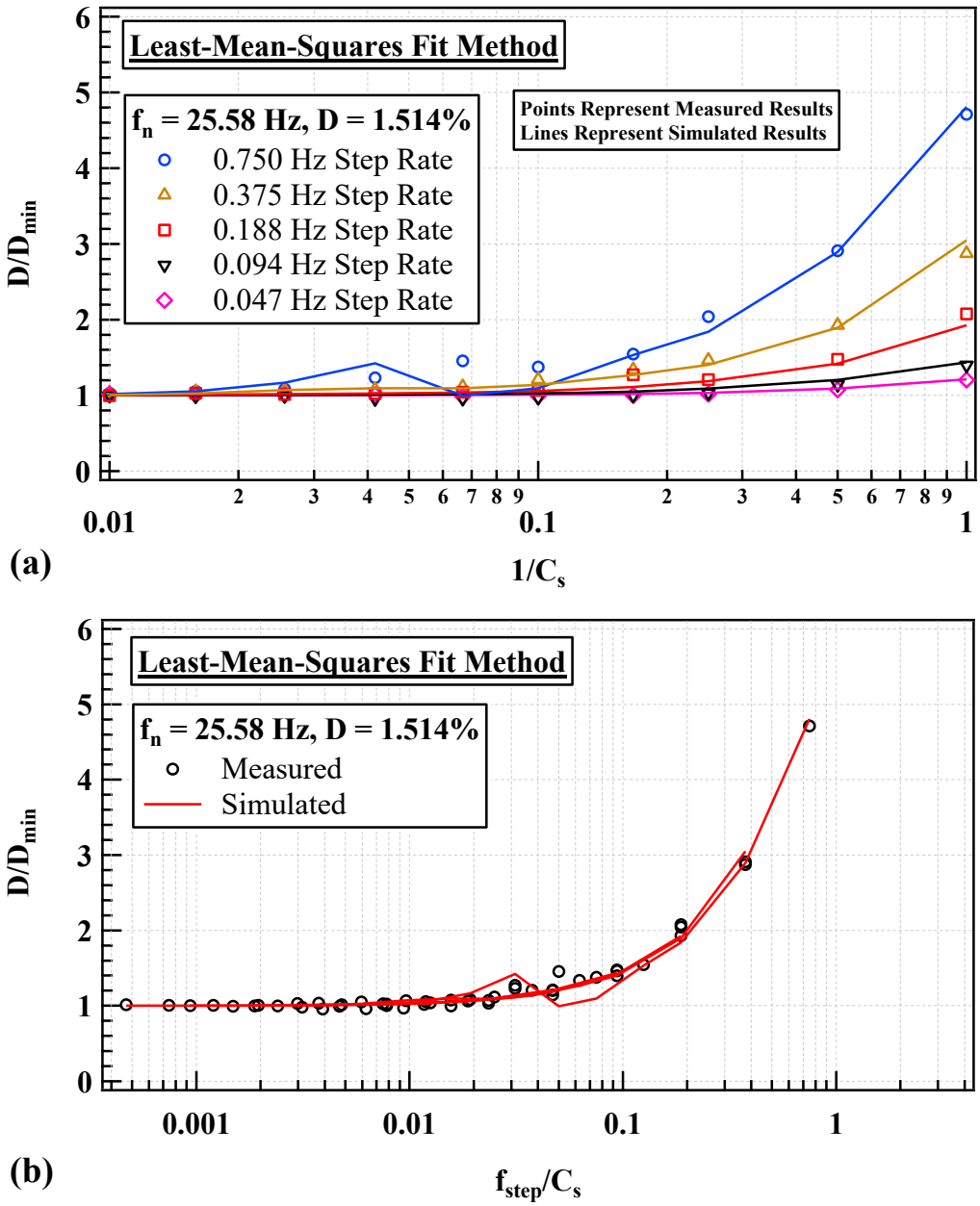

Figure 8.21: Experimental and Numerical Modeling Results Showing the Variation of the Normalized Damping Ratio Error (D/D_{min}) with (a) the Inverse of the Number of Cycles Per Frequency Step ($1/C_s$) and (b) Frequency Step (f_{step}) Divided by C_s from Frequency Sweep Tests on Metal Specimen #9 that has fn =25.58 Hz and D = 1.514%.

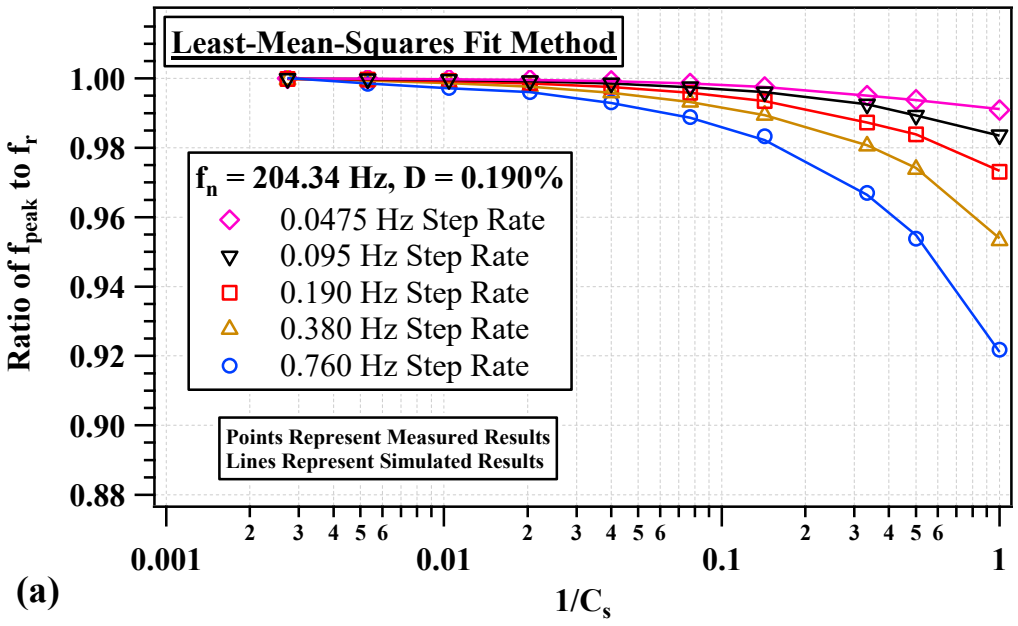

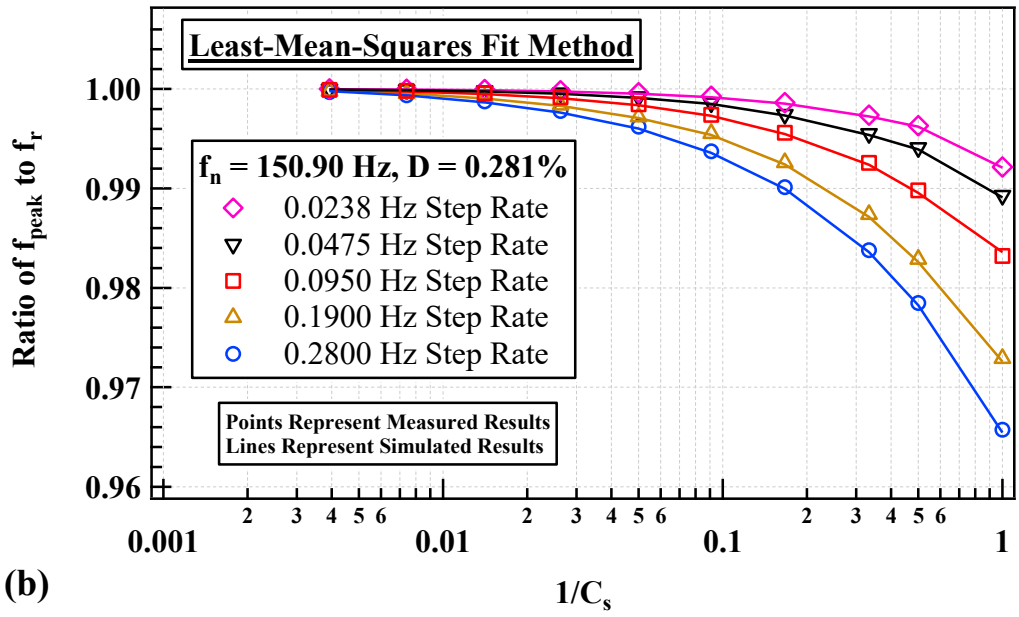

Figure 8.22: Experimental and Numerical Modeling Results Showing the Variation of the Resonant Frequency Error (Ratio of f_{peak} to f_r) with the Inverse of the Number of Cycles Per Frequency Step ($1/C_s$) from Frequency Sweep Tests on (a) Metal Specimen #1 that has f_n = 204.34 Hz and D = 0.190% and (b) Metal Specimen #13 that has f_n =150.90 Hz and D = 0.281%.

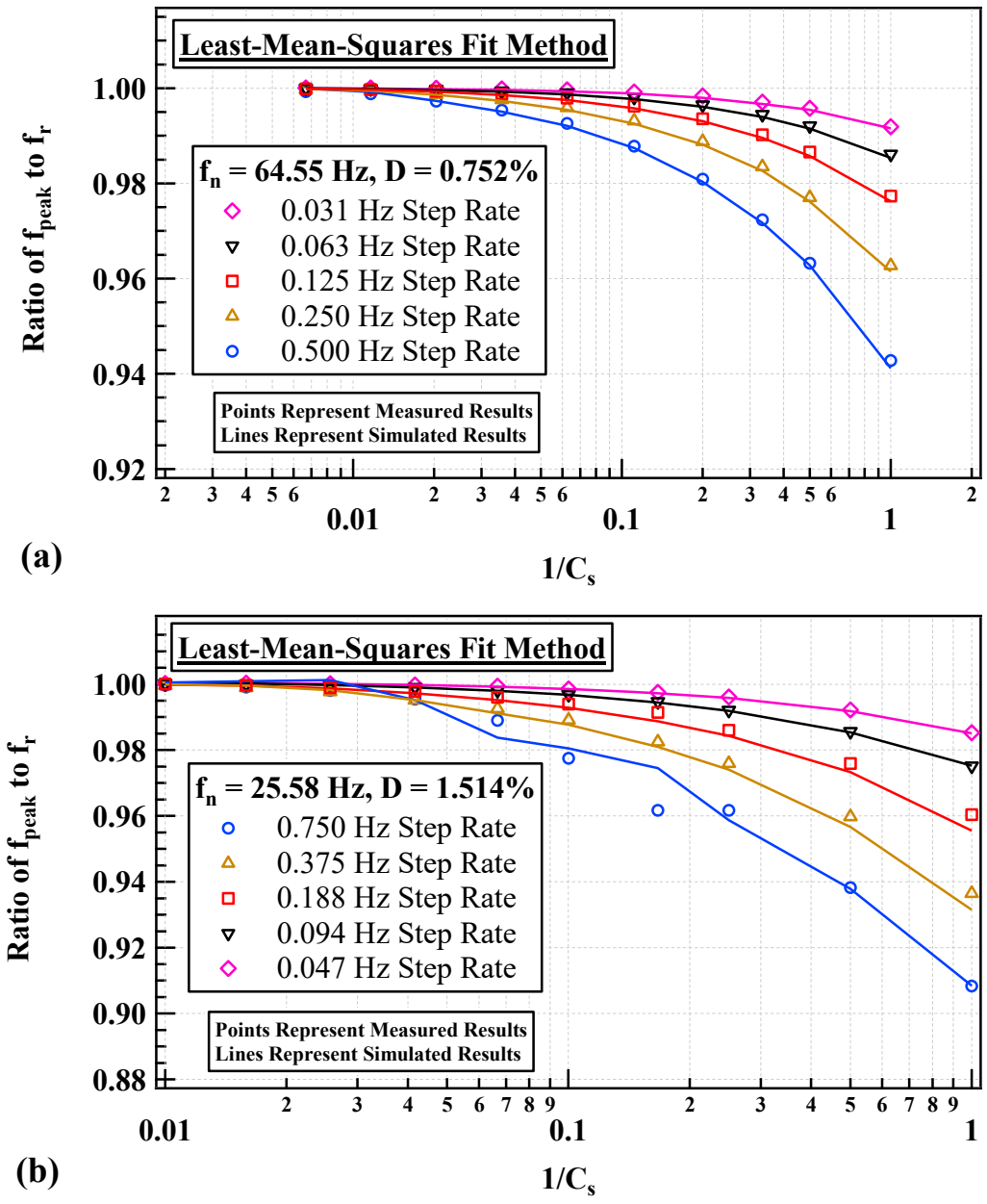

Figure 8.23: Experimental and Numerical Modeling Results Showing the Variation of the Resonant Frequency Error (Ratio of f_{peak} to f_r) with the Inverse of the Number of Cycles Per Frequency Step ($1/C_s$) from Frequency Sweep Tests on (a) Metal Specimen #6 that has f_n =64.55 Hz and D = 0.752% and (b) #13 Metal Specimen #9 that has fn =25.58 Hz and D = 1.514%.

8.7.2 Analytical Examples of Sweep Rate Effect on SDOF System with Varying Natural Frequency and Constant Damping Ratio

In this subsection, simulations are utilized to create cases where the damping ratio, D remains constant, but the natural frequency, f_n is varied. This is done to present a normalization of the sweep rate effects with varying f_n. Simulations were conducted with f_n of 50, 104.3, and 200 Hz, but the D was held constant at 0.416%. For the three f_n modeled numerically, four plots are presented for each that contain the following: (1) A/A_{max}-log(f_{step}/C_s), (2) A/A_{max}-log(f_{step}/C_s)/f_n, (3) D/D_{min}-log(f_{step}/C_s), and (4) D/D_{min}-log(f_{step}/C_s) /f_n. The variation in A/A_{max} or D/D_{min} with f_{step}/C_s can be normalized into one relationship by plotting the horizontal axis as (f_{step}/C_s)/f_n. This is possible because each case has a single D. In each of the cases presented in this subsection, five different f_{step} are used with 10 different C_s for each f_{step} are used. Since the D is constant there less of difference when normalizing the f_n error with the true f_n, the results of the (Ratio of f_{peak} to f_r)-log(f_{step}/C_s) are shown in Figure 8.24. The results of A/A_{max} are shown in Figure 8.26. The results of D/D_{min} are shown in Figure 8.26.

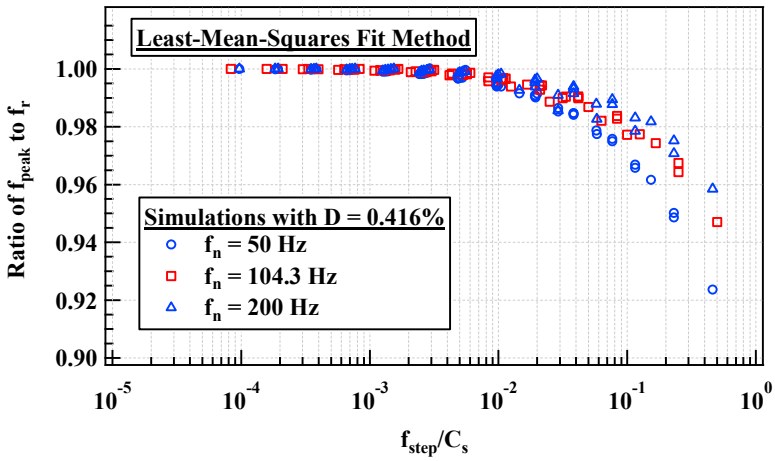

Figure 8.24: Numerical Modeling Results Showing the Variation of the Resonant Frequency Error (Ratio of f_{peak} to f_r) with the Frequency Step (f_{step}) Divided by the Number of Cycles Per Frequency Step (C_s) from Frequency Sweep Simulations of a System with D = 0.416% and f_n of 50, 104.3. and 200 Hz.

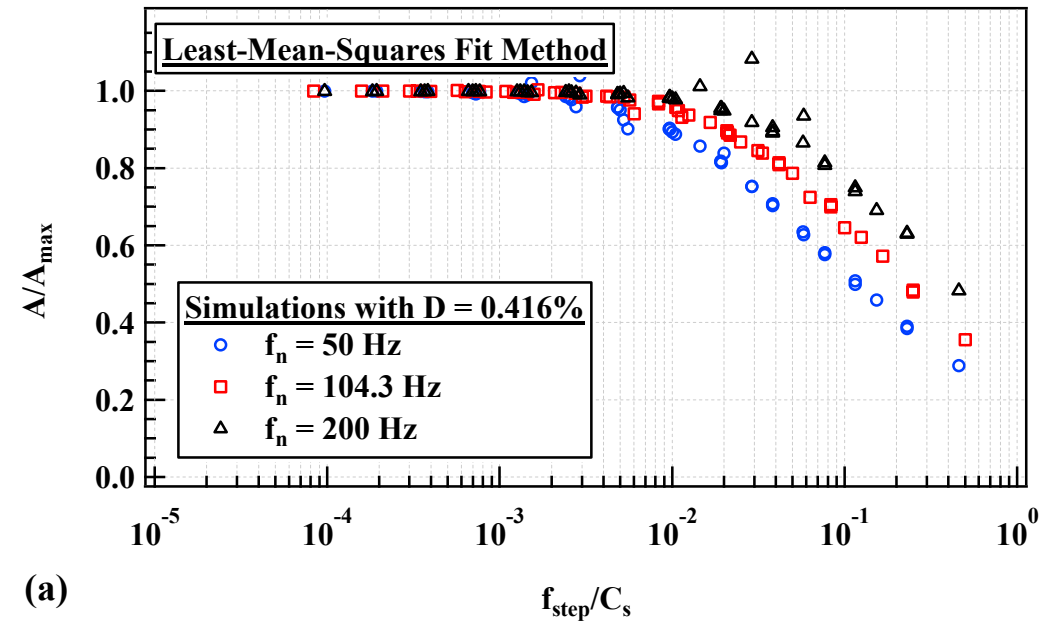

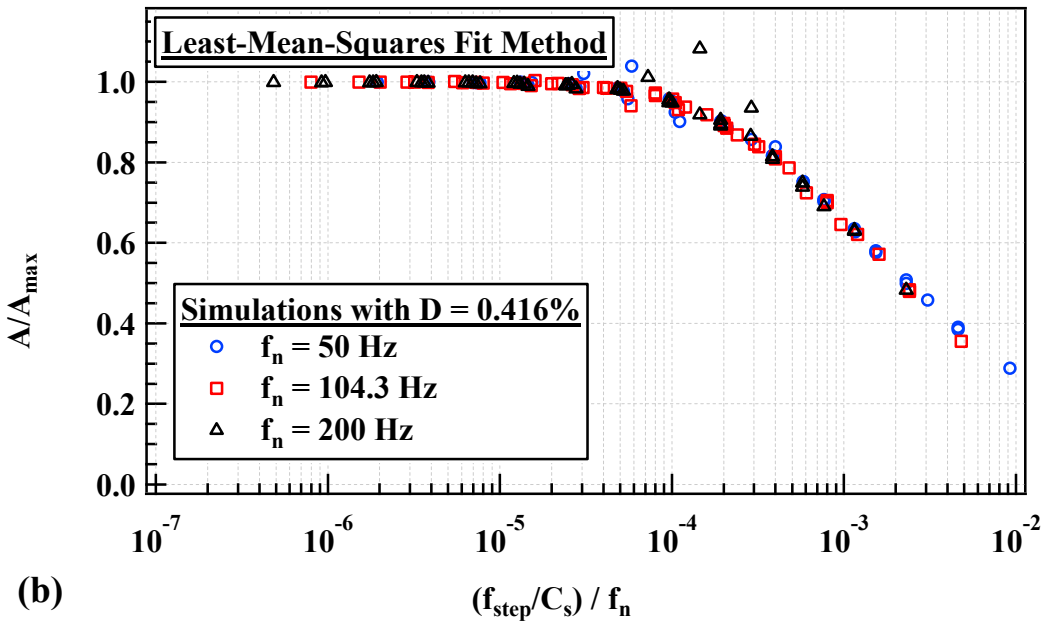

Figure 8.25: Numerical Modeling Results Showing the Variation of the Normalized Amplitude Error (A/A_{max}) with (a) the Frequency Step (f_{step}) Divided by the Number of Cycles Per Frequency Step (C_s) and (b) (f_{step}/C_s) divided by the true natural frequency, f_n from Frequency Sweep Simulations of a System with D = 0.416% and f_n of 50, 104.3. and 200 Hz.

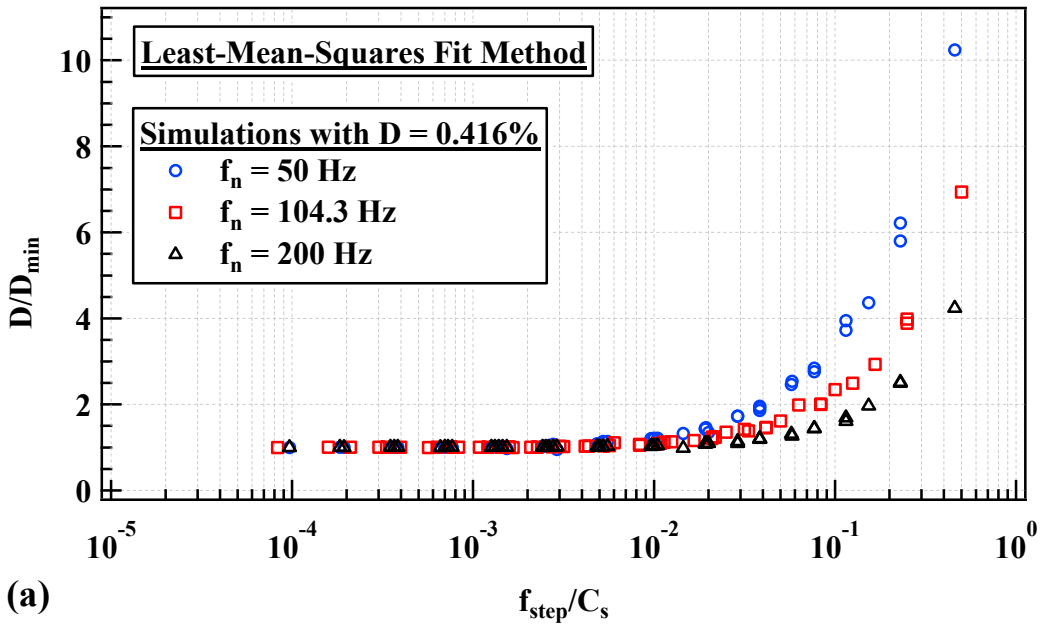

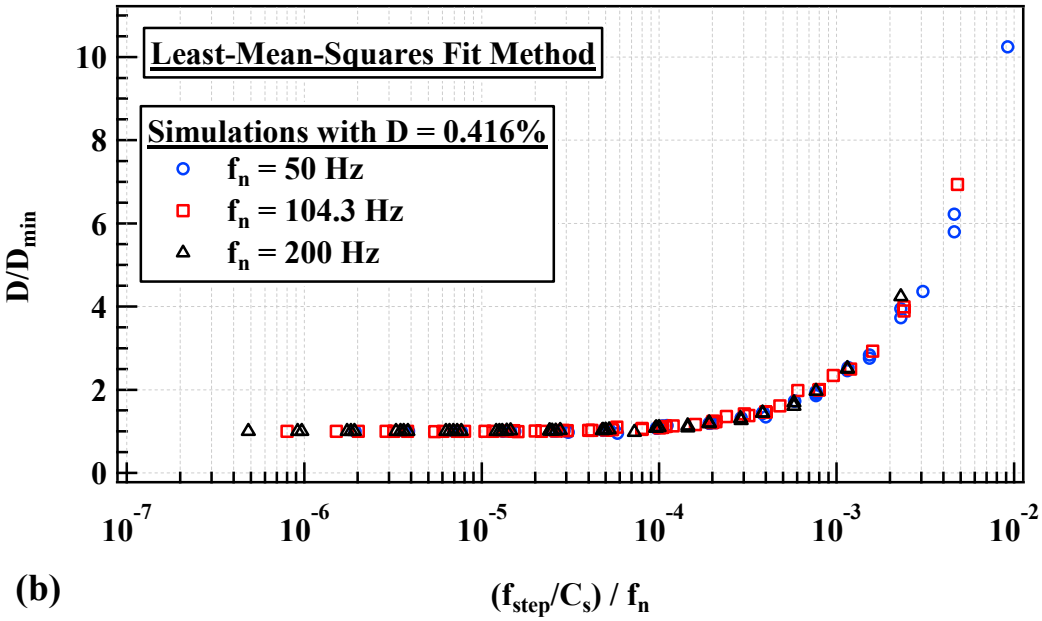

Figure 8.26: Numerical Modeling Results Showing the Variation of the Normalized Damping Ratio Error (A/A_{max}) with (a) the Frequency Step (f_{step}) Divided by the Number of Cycles Per Frequency Step (C_s) and (b) (f_{step}/C_s) divided by the true natural frequency, f_n from Frequency Sweep Simulations of a System with D = 0.416% and f_n of 50, 104.3. and 200 Hz.

8.7.3 Analytical Examples of Sweep Rate Effects SDOF Systems with Constant Natural Frequency and Varying Damping Ratios.

In this subsection, simulations are utilized to create cases where the natural frequency, f_n remains constant, but the damping ratio, D is varied. This is done to present a normalization of the sweep rate effects with varying D. Simulations were conducted for D of 0.1, 0.25, 0.5, 1, 2, 3, and 6%, but the f_n was held constant at 100 Hz. For the seven D modeled numerically, four plots are presented for each that contain the following: (1) A/A_{max}-log($1/C_s$), (2) A/A_{max}-log(f_{step}/C_s) (3) D/D_{min}-log($1/C_s$), and (4) D/D_{min}-log(f_{step}/C_s). The variation in A/A_{max} or D/D_{min} with $1/C_s$ can be normalized into one relationship by plotting the horizontal axis as (f_{step}/C_s). This is possible because each case has a single f_n. Out of the total eight different D that were simulated, only three are shown with the horizontal axis to f_{step}/C_s as seen in Figure 8.27 through Figure 8.32, the content these figures is shown in Table 8.3.

Table 8.3: Organization of the Results from Frequency Sweep Simulations for a System with f_n = 100 Hz and differing D That are Shown in Figure 8.27 through Figure 8.32.

Damping Ratio, D (%)	**0.1**	**0.5**	**2**
(a) A/A_{max}-log($1/C_s$) and (b) A/A_{max}-log(f_{step}/C_s)	Figure 8.27	Figure 8.29	Figure 8.31
(a) D/D_{min}-log($1/C_s$) and (b) D/D_{min}-log(f_{step}/C_s)	Figure 8.28	Figure 8.30	Figure 8.32

Notes: (1) f_n = Natural Frequency and (2) D = Material Damping Ratio

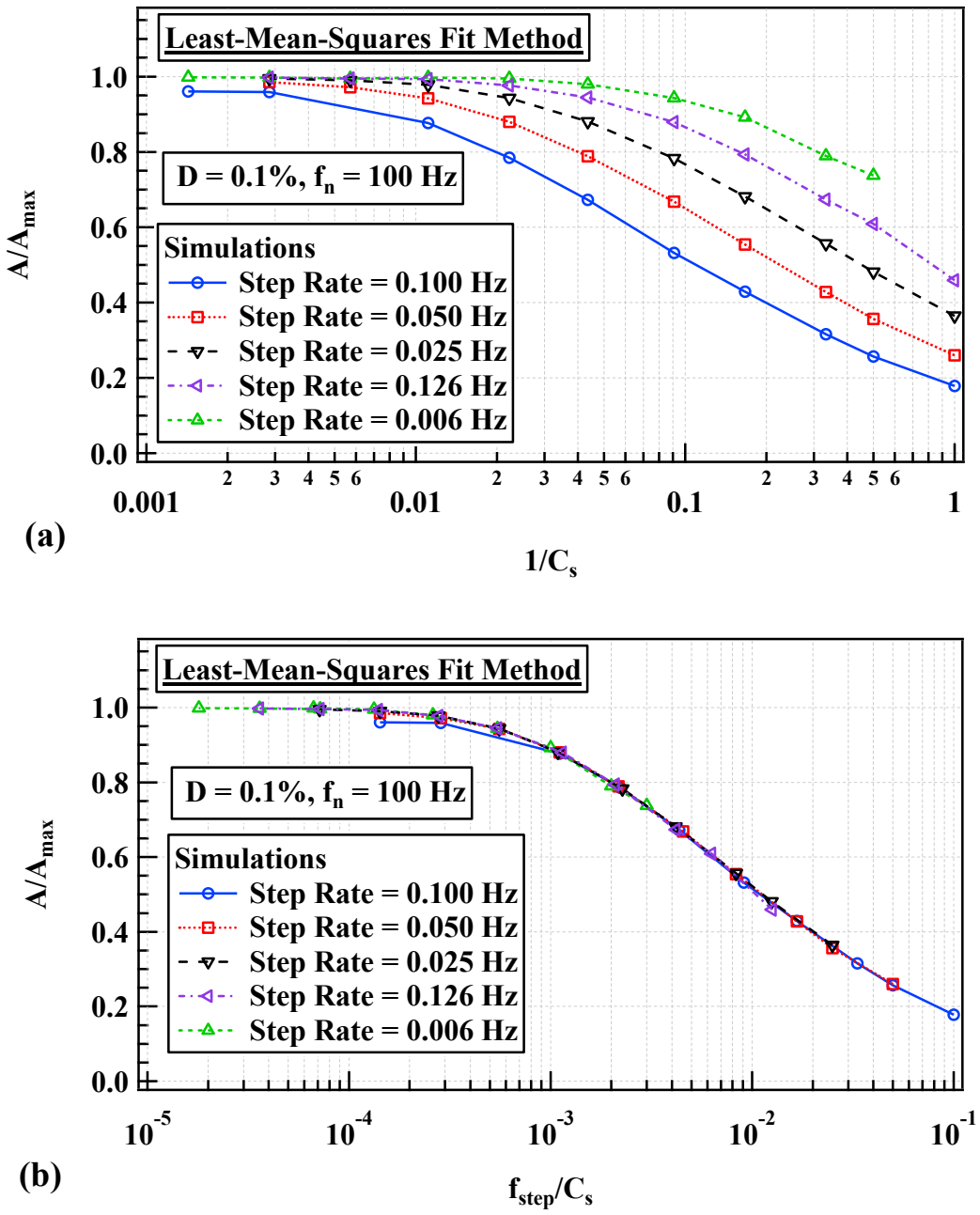

Figure 8.27: Numerical Modeling Results Showing the Variation of the Normalized Amplitude Error (A/A_{max}) with (a) the Inverse of the Number of Cycles Per Frequency Step ($1/C_s$) and (b) Frequency Step (f_{step}) Divided by C_s from Frequency Sweep Simulations of a System with f_n = 100 Hz and **D = 0.1%**.

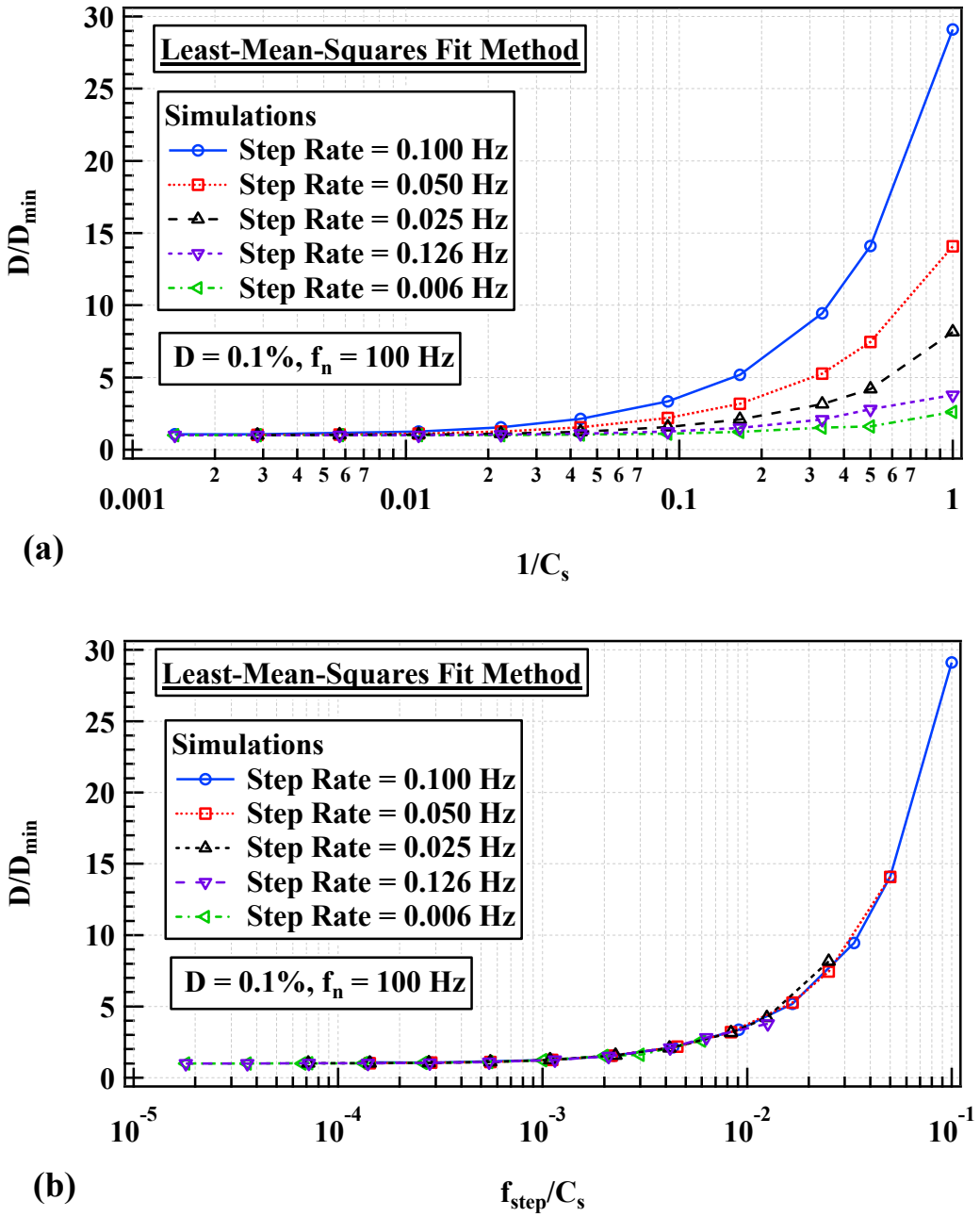

Figure 8.28: Numerical Modeling Results Showing the Variation of the Normalized Damping Ratio Error (D/D_{min}) with (a) the Inverse of the Number of Cycles Per Frequency Step ($1/C_s$) and (b) Frequency Step (f_{step}) Divided by C_s from Frequency Sweep Simulations of a System with f_n = 100 Hz and **D = 0.1%**.

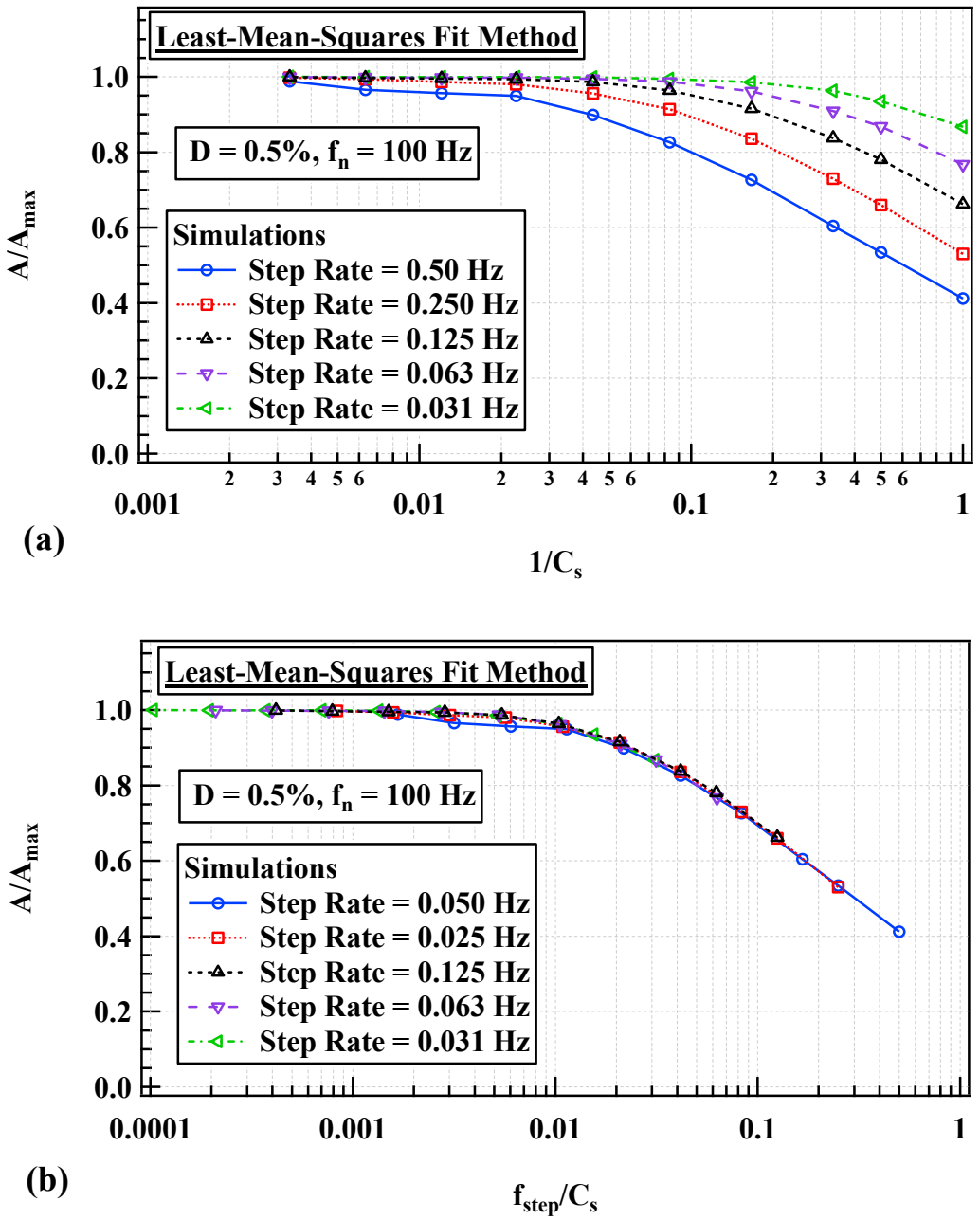

Figure 8.29: Numerical Modeling Results Showing the Variation of the Normalized Amplitude Error (A/A_{max}) with (a) the Inverse of the Number of Cycles Per Frequency Step ($1/C_s$) and (b) Frequency Step (f_{step}) Divided by C_s from Frequency Sweep Simulations of a System with f_n = 100 Hz and **D = 0.5%**.

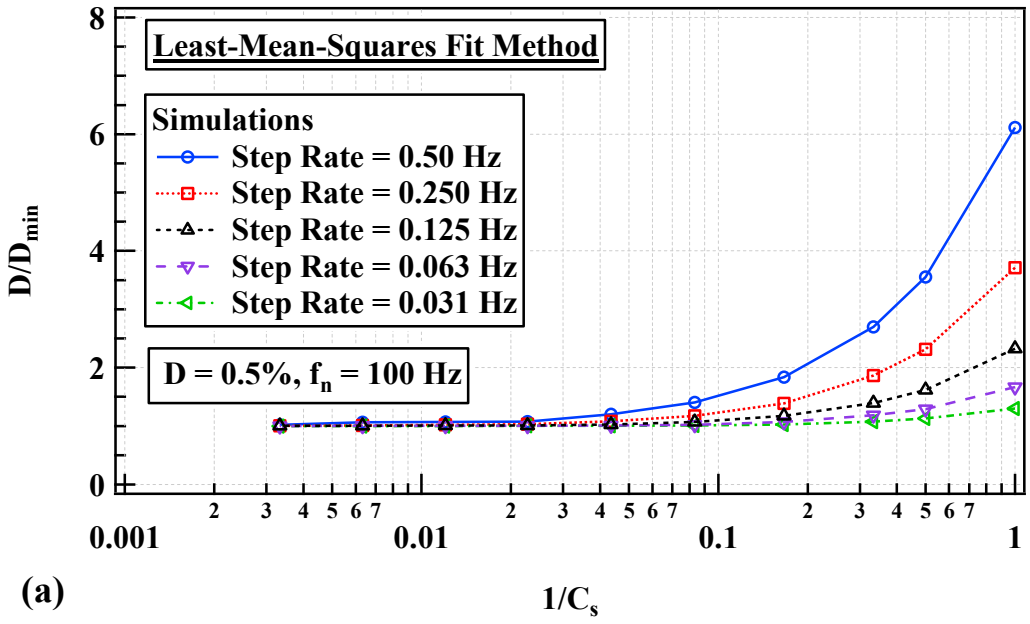

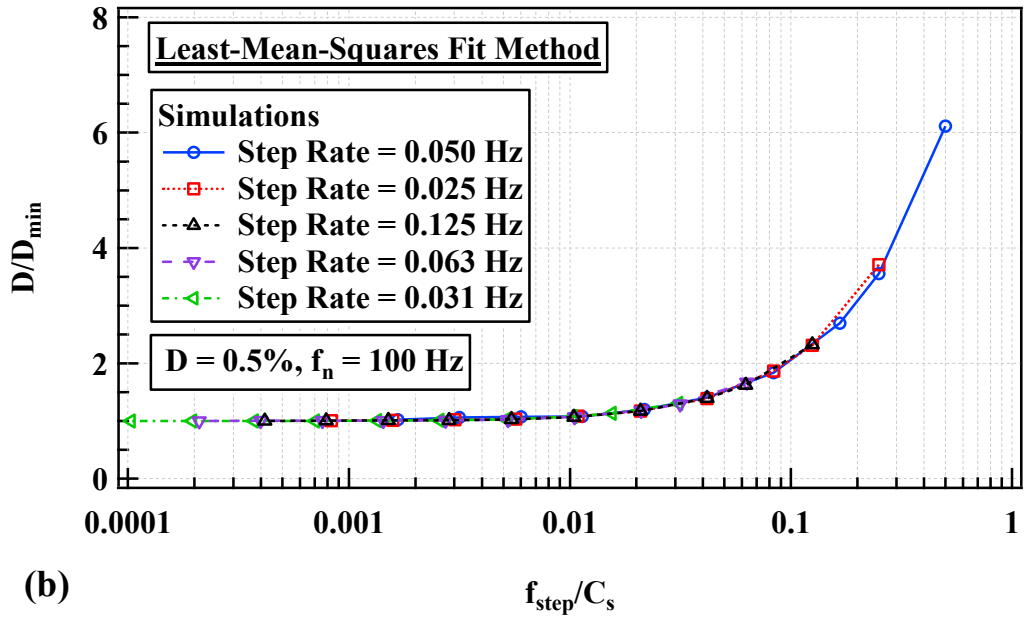

Figure 8.30: Numerical Modeling Results Showing the Variation of the Normalized Damping Ratio Error (D/D_{min}) with (a) the Inverse of the Number of Cycles Per Frequency Step ($1/C_s$) and (b) Frequency Step (f_{step}) Divided by C_s from Frequency Sweep Simulations of a System with f_n = 100 Hz and **D = 0.5%**.

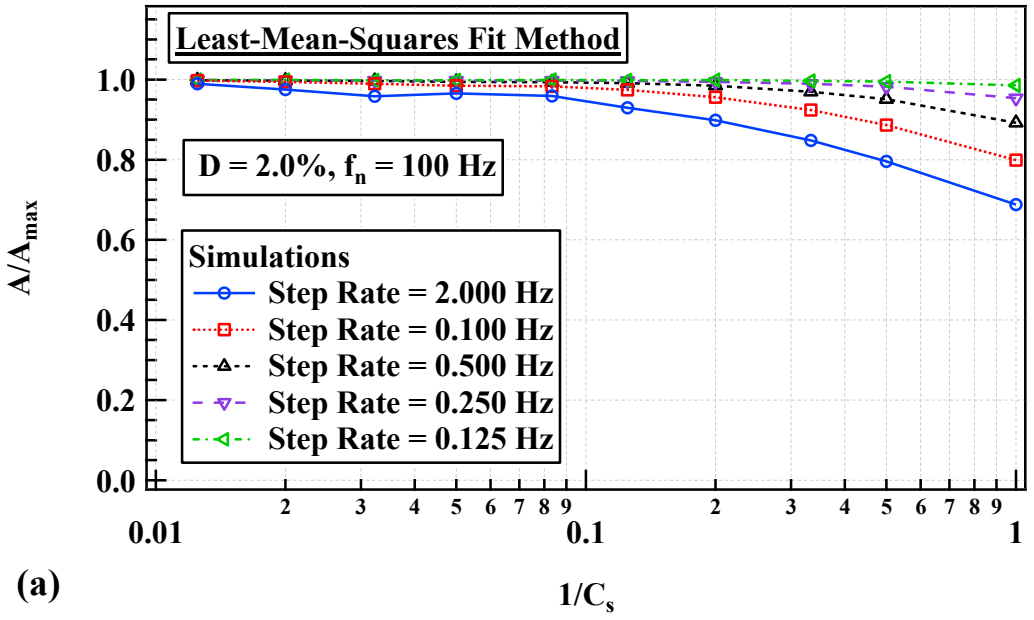

(a)

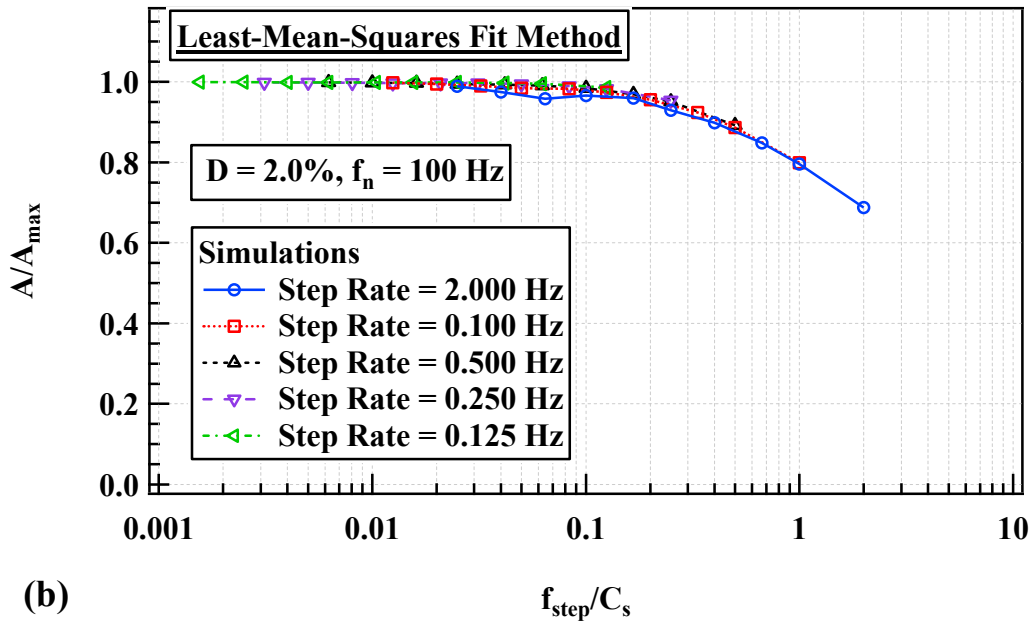

(b)

Figure 8.31: Numerical Modeling Results Showing the Variation of the Normalized Amplitude Error (A/A_{max}) with (a) the Inverse of the Number of Cycles Per Frequency Step ($1/C_s$) and (b) Frequency Step (f_{step}) Divided by C_s from Frequency Sweep Simulations of a System with f_n = 100 Hz and **D = 2.0%**.

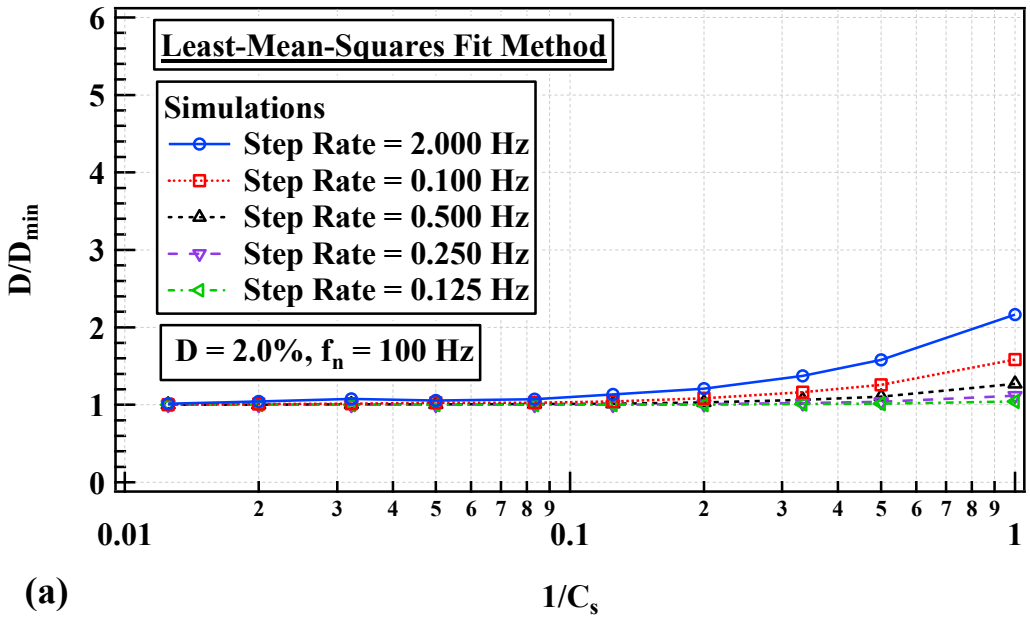

(a)

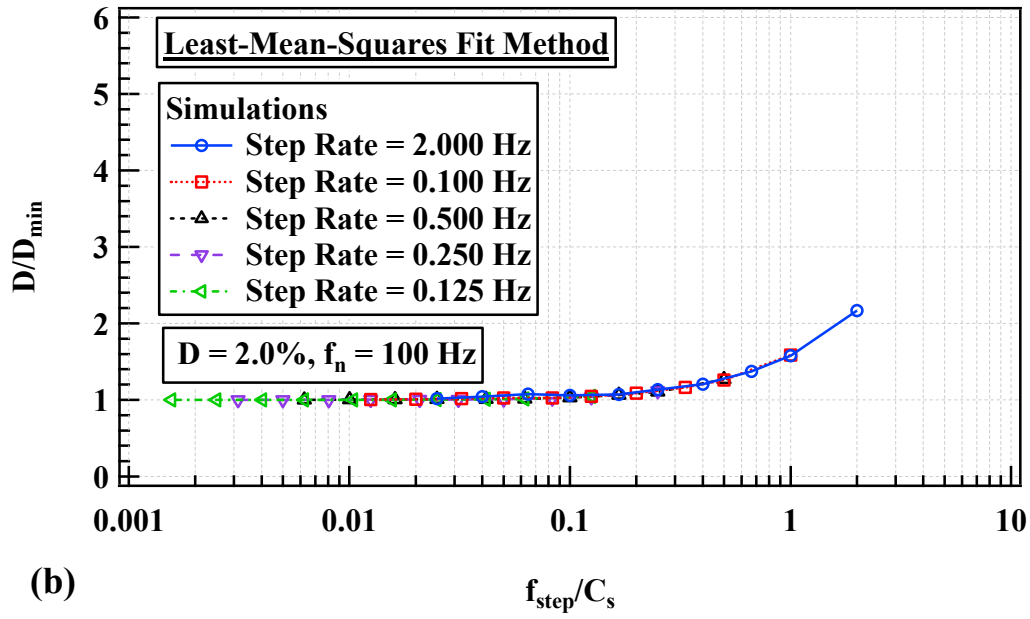

(b)

Figure 8.32: Numerical Modeling Results Showing the Variation of the Normalized Damping Ratio Error (D/D_{min}) with (a) the Inverse of the Number of Cycles Per Frequency Step ($1/C_s$) and (b) Frequency Step (f_{step}) Divided by C_s from Frequency Sweep Simulations of a System with f_n = 100 Hz and **D = 2.0%**.

The seven damping ratios discussed previously are shown together in four plots presented as (1) A/A_{max}-log(f_{step}/C_s), (2) A/A_{max}-log(f_{step}/C_s)/D^2, (3) D/D_{min}-log(f_{step}/C_s), and (4) D/D_{min}-log(f_{step}/C_s)/D^2. The variation in A/A_{max} or D/D_{min} with f_{step}/C_s can be normalized into one relationship by plotting the horizontal axis as (f_{step}/C_s)/D^2. This is possible because each case has a single D. From the frequency sweeps simulated, the results of A/A_{max}-log(f_{step}/C_s) and A/A_{max}-log(f_{step}/C_s)/D^2 are shown in Figure 8.33 and Figure 8.34, respectively. The results of D/D_{min}-log(f_{step}/C_s) and D/D_{min}-log(f_{step}/C_s)/D^2 are shown in Figure 8.35 and Figure 8.36, respectively.

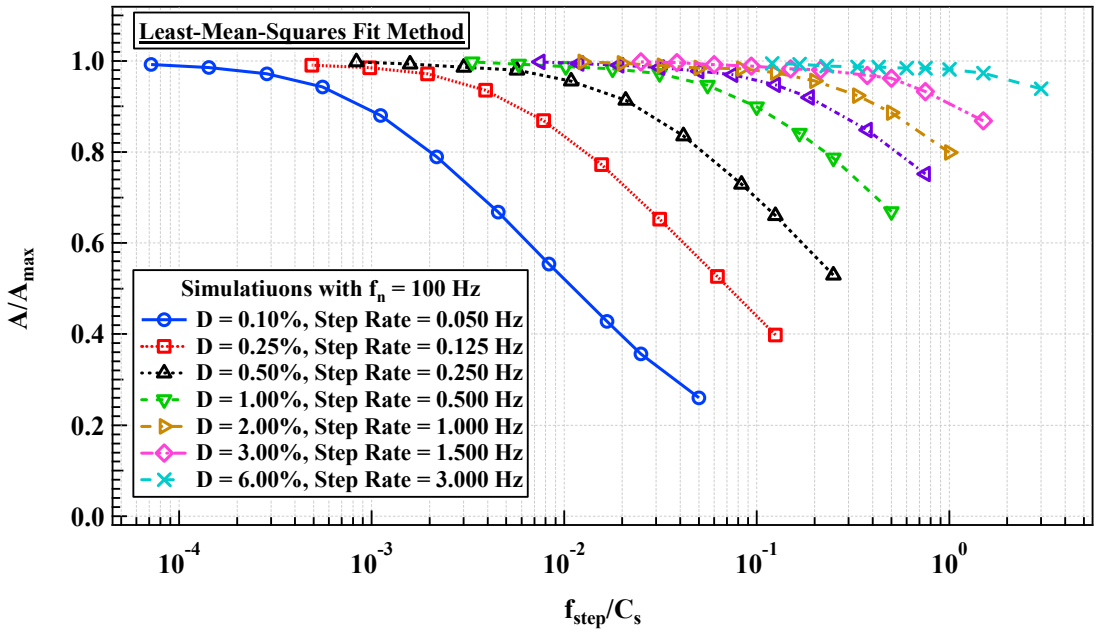

Figure 8.33: Numerical Modeling Results Showing the Variation of the Normalized Amplitude Error (A/A_{max}) with the Frequency Step (f_{step}) Divided by the Number of Cycles Per Frequency Step (C_s) from Frequency Sweep Simulations of a System with f_n = 100 Hz and **D = 0.1, 0.25, 0.5, 1, 2, 3, and 6%**.

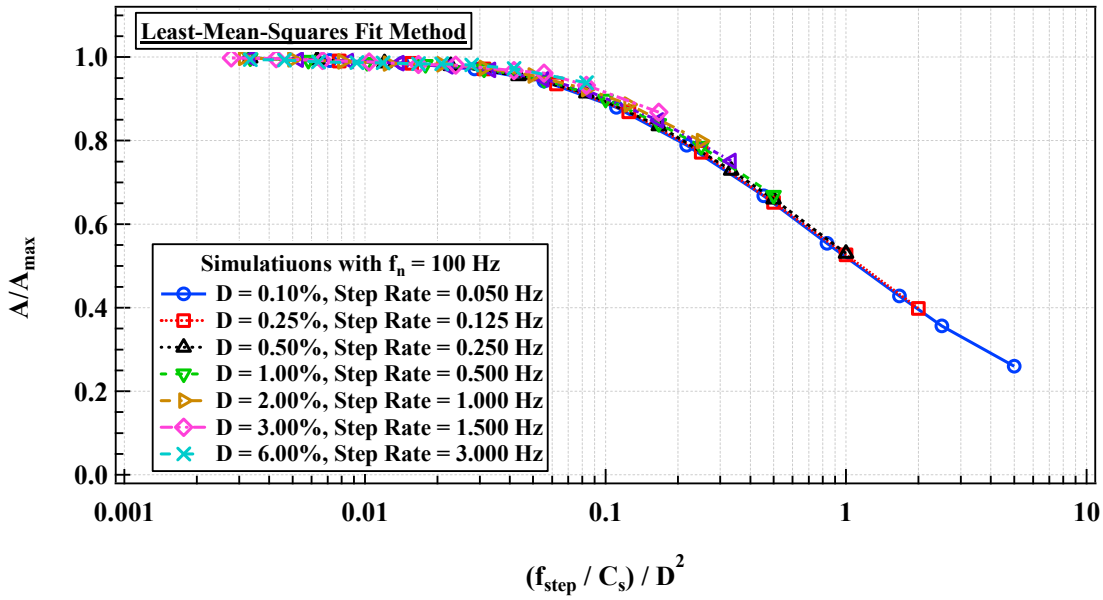

Figure 8.34: Numerical Modeling Results Showing the Variation of the Normalized Amplitude Error (A/A_{max}) with (f_{step}/C_s) divided by D^2 from Frequency Sweep Simulations of a System with f_n = 100 Hz and **D = 0.1, 0.25, 0.5, 1, 2, 3, and 6%**.

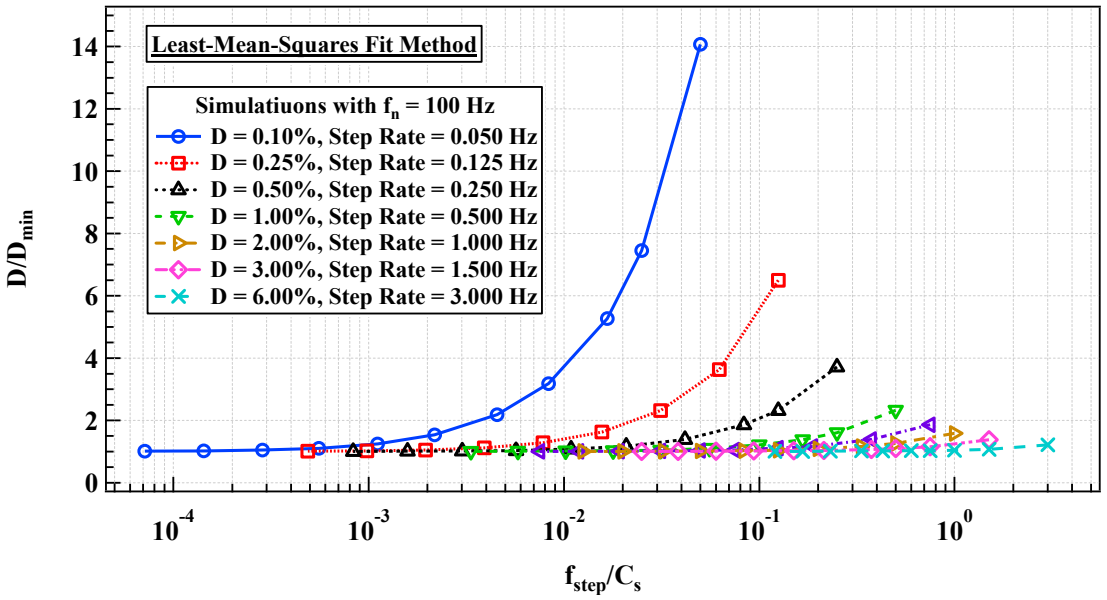

Figure 8.35: Numerical Modeling Results Showing the Variation of the Normalized Damping Ratio Error (D/D_{min}) with the Frequency Step (f_{step}) Divided by the Number of Cycles Per Frequency Step (C_s) from Frequency Sweep Simulations of a System with f_n = 100 Hz and **D = 0.1, 0.25, 0.5, 1, 2, 3, and 6%**.

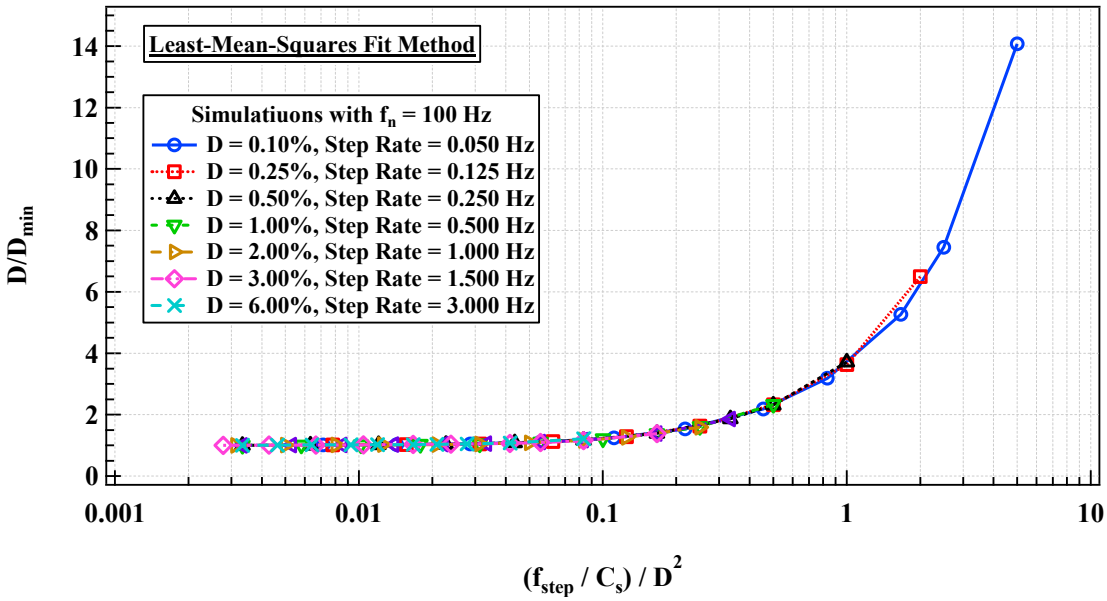

Figure 8.36: Numerical Modeling Results Showing the Variation of the Normalized Damping Ratio Error (D/D_{min}) with (a) the Frequency Step (f_{step}) Divided by the Number of Cycles Per Frequency Step (C_s) and (b) (f_{step}/C_s) divided by D^2 from Frequency Sweep Simulations of a System with f_n = 100 Hz and **D = 0.1, 0.25, 0.5, 1, 2, 3, and 6%**.

8.8 SUMMARY

In this study, the fixed-free resonant column device designed by Prof. Stokoe in the mid 1970's was used to conduct various frequency sweeps on five brass metal specimens and a sand specimen subject to five isotropic confining stresses. The various frequency sweeps were conducted to determine the effect that sweep rates have on the sensitivity for determining accurate response curve of a SDOF system when using a stepped-sine sweep. Analytical simulations were conducted to both validate and compliment the experimental results. The stepped-sine sweep method has been both experimentally and analytically evaluated, and the results are found to normalize to a single relationship for a particular SDOF system. The relationship for a particular SDOF system is found by comparing the normalized amplitude (A/A_{max}) or the normalized damping ratio (D/D_{min}) to the frequency step, f_{step}, divided by the number of cycles, C_S, excited at each frequency. A subsequent

study presented in Chapter 9 outlines an approach for normalizing the sweep rate effect results for any SDOF system by normalizing with a stepped-sine non-dimensional sweep rate parameter (η).

This investigation confirms that the fixed-free resonant column testing device, data control and monitoring system and accompanying software, developed in this dissertation, has the ability to accurately test and measure the fundamental behavior of SDOF systems under various sweep rates for a stepped-sine sweep. Sweep tests on specimens in the fixed-free resonant column device can be precisely simulated using the incremental displacement and incremental velocity equations and coefficients for these recurrence formulas that were presented in Chopra (2001). Finally, application of these formulas apply to a linear system where the SDOF characteristics are constant with strain amplitude, which is does not occur for nonlinear systems.

Chapter 9

Empirical Model for Choosing Sweep Rates When Using a Frequency Sweep in Resonant Column Testing

9.1 INTRODUCTION

Resonant column testing is used to determine the dynamic properties of soil and rock specimens. The dynamic behavior of these materials are determined by exciting cylindrical specimens in torsion in a manner consistent with testing of a damped single-degree-of-freedom system (SDOF). A typical resonant column test is composed of two parts. In the first part, a downgrade frequency sweep is used to determine the resonant frequency, half-power damping ratio, and maximum shear strain amplitude excited during the sweep. The second part begins by exciting the specimen at the resonant frequency determined in part 1. The downgrade sweep is followed by a free-vibration decay test where the specimen is excited at the resonant frequency. After reaching steady-state vibration (i.e. maximum shear strain measured during the downgrade frequency sweep), the excitation is abruptly suspended and the specimen is allowed to freely vibrate. The free-vibration test is used to determine the damped natural frequency and free-vibration damping ratio. Also, the steady-state shear strain amplitude is measured just before the power is abruptly suspended to check that the strain amplitude in the free-vibration decay test matches the peak amplitude at resonance from the downgrade frequency sweep. For this sequence of two-part tests to be accurate, the sweep rate used must be suitable to obtain the correct dynamic characteristics of the specimen in both parts. Sweeping too fast may lead to an incorrect prediction of the dynamic properties from the sweep test and would also result in using the wrong frequency for the free-vibration test.

Configuring sweep rates are different depending on the type of sweep method used. Three common types of frequency sweep methods used for testing SDOF systems are a stepped-sine sweep, a linear chirp, and an exponential chirp. Each of these frequency sweep methods involves incremental or constant changes in frequency during the sweep and can either be upgrade or downgrade. The progression of frequency excited during a linear chirp and a logarithmic chirp vary linearly and nonlinearly with time, respectively. This study investigates the effects that choosing different sweep rates and sweep types has when testing SDOF systems, mainly for the purpose of testing soil and rock specimens in the resonant column device. The sweep types used were downgrade stepped-sine and downgrade linear chirp. The evaluation of sweep rate and sweep type involved experimental tests on metal calibration specimens and one soil specimen, followed by numerical simulations used to model the dynamic behavior as was observed in the experimental tests. The objective of this chapter is to provide a model for choosing adequate sweep rates for properly characterizing a SDOF system after using a rough test for approximate the system characteristics. The application is to expedite the testing process while maximizing accuracy of the testing procedure. Finally, the model proposed has applications in any area of engineering where SDOF systems are being evaluated and where sweep accuracy and testing efficiency are paramount.

9.2 EXAMPLE OF PROPER AND IMPROPER SWEEP RATE

An example of two stepped-sine sweeps conducted on the same damped SDOF system, but with two different sweep rates, is shown in Figure 9.1.

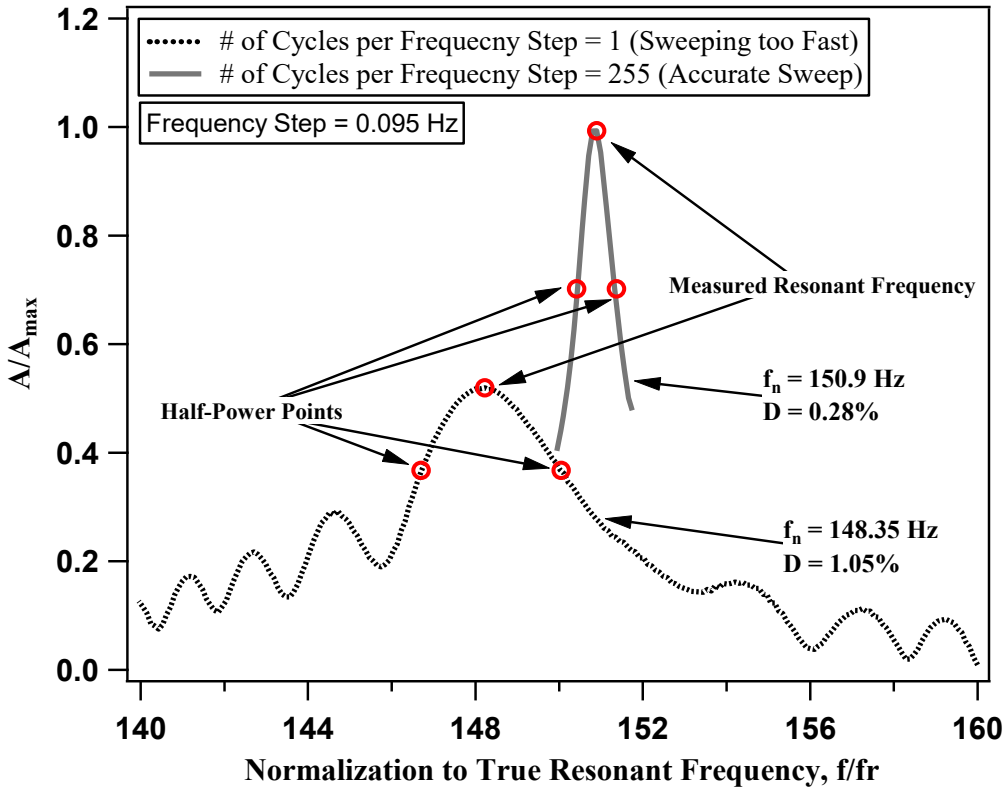

Figure 9.1: An example of two sweeps conducted on the same damped SDOF system, but with two different sweep rates.

In one sweep, the frequency was swept too fast because too few cycles of excitation were used at each frequency step. An adequate number of cycles are needed to obtain a maximum amplitude response at each corresponding excitation frequency. Sweeping too fast also led to high harmonic distortion. In another sweep, the frequency was swept at a suitable step rate to obtain the true dynamic characteristics of the system. This example demonstrates the large range of dynamic behavior that will occur when using sweep rates that are faster than a nominal sweep rate for a particular SDOF system.

9.3 METHODS

9.3.1 Derivation Equating Chirp and Stepped-Sine Sweep Methods

In this investigation, the stepped-sine sweep method is evaluated based on the same criteria shown in the publications Lollock (2002) and Girard and Bugeat (2004), which were provided by the American Institute of Aeronautics and Astronautics and the NASA Astrophysics Data System, respectively. However, analytical and experimental tests are conducted while evaluating additional factors, which include: (1) A frequency step, that is represents the incremental, as opposed to continuous, change in frequency during the sweep; (2) the fixed number of cycles excited at a specific frequency at each frequency step; (3) methods for analyzing the measured and simulated response curves, which include the traditional half-power bandwidth approach and a least-mean-squares fit of the SDOF response curve equation to the results; and (4) empirical models developed from the results that can be used to select an adequate frequency step and excitation cycles per frequency step based on estimates of the natural frequency and damping parameters of a SDOF. Finally, empirical models developed from the results are demonstrated in an example where a rough sweep (high sweep rate or large frequency step in combination with few cycles per step) is used to obtain an estimate of the natural frequency and damping, then a refined sweep is used to accurately obtain the true response curve parameters.

The chirps and stepped-sine input functions used to conduct the frequency sweep are fairly different in mathematical form. However, the non-dimensional sweep parameter, η, and the linear sweep rate, k_l, from Lollock (2002) and Girard and Bugeat (2004), can be equivalently determined for the stepped-sine approach. In Lollock (2002) and Girard and Bugeat (2004), N is defined as the number of cycles between the half-power points defined as:

$$N = \frac{f_n^2}{QK_s} = \frac{2Df_n^2}{K_s} \tag{9.1}$$

where f_n is the natural frequency, Q is the quality factor related to the damping ratio, D, as $Q = 1/2D$, and K_s is the linear sweep rate used in the chirp in Hz/sec. The non-dimensional sweep parameter, η, is given as:

$$\eta = Q/N \tag{9.2}$$

For the stepped-sine approach, the number of cycles between the half-power points is easily determined from the equation for determining half-power damping, which is:

$$D = \frac{f_2 - f_1}{2f_n} = \frac{\Delta f}{2f_n} \text{ and } \Delta f = 2f_n D \tag{9.3}$$

where D is the damping ratio, f_2 and f_1 are the half-power frequencies that correspond to $A_{max}/\sqrt{2}$, and f_n is the natural frequency. For a stepped-sine sweep, the number of cycles between the half-power points is:

$$N = \frac{\Delta f C_s}{f_{step}} \tag{9.4}$$

where C_s is the number of cycles excited at each frequency and f_{step} is the frequency step. From this expression and the expression for linear sweep rate, K_s, from Lollock (2002) and Girard and Bugeat (2004), an equivalent linear sweep rate parameter can be defined for the stepped-sine sweep as:

$$K_s = \frac{f_n^2}{QN} = \frac{2Df_n^2}{N} = \frac{2Df_n^2 \times f_{step}}{\Delta f C_s} = \frac{2Df_n^2 \times f_{step}}{2f_n D \times C_s} = \frac{f_n \times f_{step}}{C_s} \tag{9.5}$$

Then the non-dimensional sweep parameter, η, is found for the stepped-sine sweep as:

$$\eta = \frac{Q}{N} = \frac{1}{2D} \times \frac{K_s}{2Df_n^2} = \frac{1}{2D} \times \frac{1}{2Df_n^2} \times \frac{f_n \times f_{step}}{C_s} = \frac{f_{step}}{C_s} \frac{1}{4f_n D^2} \tag{9.6}$$

9.3.2 Methods Used to Evaluate the Frequency Response Curve

To begin this investigation, there are two methods used to determine the response curve parameters from the frequency sweep. These include: (1) Using an interpolation method between the local maxima and minima near the half-power points to make a more precise determination of the half-power frequencies, and (2) use of a least-mean squares fitting method that fits the response curve equation to the measured data to iteratively determine the values for the natural frequency and damping ratio. In Lollock (2002), the first method (half-power bandwidth method) was used to determine the sweep rate effects of linear and exponential chirps.

To use the interpolation method, the half-power frequencies are determined by finding the local maximum and minimum amplitudes of the response curve for frequency segments above and below the resonant frequency. These local maxima and minima are recorded points of the response curve that are directly above and below $A_{max}/\sqrt{2}$ and interpolation between these points leads to a more accurate prediction of the half-power frequencies. If the data points used to populate the measured response curve are too few, this method allows more accurate determination of the half-power frequencies. In the analysis process, the frequency segment below the resonant frequency is evaluated as is and the frequency segment above the resonant frequency can be reversed so that the following equation can be used to evaluate both half-power frequencies:

$$f_{1,2} = f_L + (f_H - f_L) * \left(\frac{(A_i - A_L)}{(A_H - A_L)}\right) \tag{9.7}$$

where $f_{1,2}$ are the half-power frequencies, f_L is the frequency corresponding to the measured amplitude (A_L) below the half-power frequency being interpolated to, f_H is the frequency corresponding to the measured amplitude (A_H) above the half-power frequency being interpolated to, and A_i is the half-power amplitude (i.e. $A_{max}/\sqrt{2}$) from which the half-

power frequency is being interpolated to. This method will henceforth be called the half-power interpolation method.

The interpolation method leads to a prediction of the half-power frequencies, f_1 and f_2, that in combination with the measured resonant frequency, f_r, will lead to a calculation of the half-power damping ratio, which is given in the simplified form for low damping ratios (and linear dynamic behavior) as:

$$D_{HP} = \frac{f_2 - f_1}{2 * f_r} \tag{9.8}$$

where D_{HP} is the damping ratio. The least-mean-squares fitting method uses the theoretical response curve for a single-degree-of-freedom (SDOF) system which is given in Richart et al. (1970) as:

$$M = \frac{1}{\sqrt{[1-(\omega/\omega_n)^2]^2+[2D(\omega/\omega_n)]^2}} \tag{9.9}$$

where the dynamic magnification factor is M, ω is the input frequency, ω_n is the natural circular frequency, and D is the damping ratio. This method will henceforth be called the least-mean-squares fit method. To utilize this equation, the measured response curve is first normalized. In this study, the fitting algorithm was limited to 10,000 iterations and tolerance for the fitting parameters of 1E-8. The example used in the introduction is shown again, in Figure 8.5, with the least-mean-squares best fit response curves plotted for the two sweep cases.

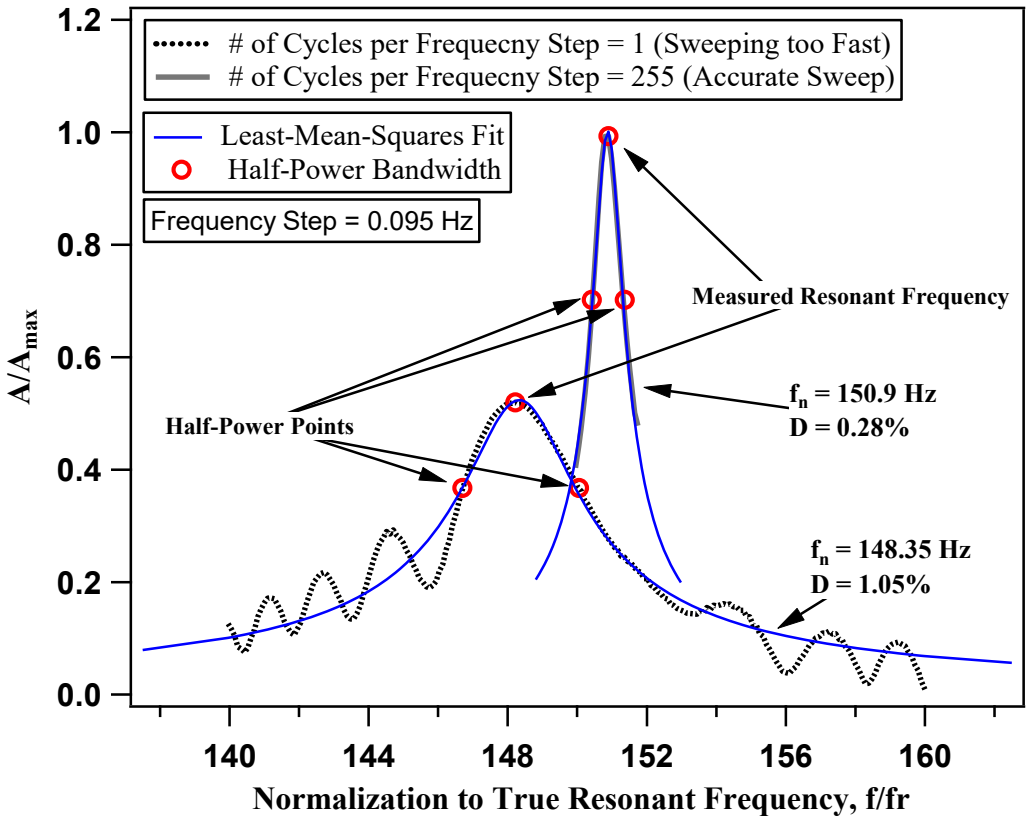

Figure 9.2: An example of two sweeps conducted on the same damped SDOF system, but with two different sweep rates. Results from the Half-Power Method and Least-Mean-Squares-Fit Method are Shown.

9.3.3 Equations Used to Predict Spectral Response from Stepped-Sine Sweeping

The free-vibration response of a linear damped single-degree of freedom system is given from Richart et al. (1970) as:

$$m\ddot{x} + c\dot{x} + kx = 0 \tag{9.10}$$

where m is the mass of the system, c is the damping coefficient, k is the spring constant, and $\ddot{x}$, $\dot{x}$, and x are respectively, acceleration, velocity, and displacement. This equation represents the response of a SDOF system allowed to freely vibrate with viscous damping behavior. The equation for a system with forced vibration with viscous damping behavior is given from Richart et al. (1970) as:

$$\ddot{x}m + c\dot{x} + kx = Q_i \sin(\omega t) \quad (9.11)$$

where Q_i is the amplitude of the cyclic force applied, ω is the angular frequency of excitation, and t is time. This equation was derived in Chopra (2001) into incremental displacement and incremental velocity formulas that can be used to predict the SDOF response to an incrementally changing forcing function. In this study, the amplitude of the forcing function remains constant, but the frequency of forcing function changes in accordance with the sweep rate and sweep type. The key aspect of using the formulas from Chopra (2001) is selecting a small enough incremental change that the forcing function and SDOF response resembles continuous behavior. In this study, the increment size was selected to match the sampling rate used in the sweep tests, which was 10,000 samples per second (about 50 times the highest frequency tested). Equations from Chopra (2001) that were used as methods for evaluating sweep rate effects were shown in Chapter 7.

The differences between the SDOF input parameters (i.e. mass, m, damping coefficient, c, and spring constant, k, of the system simulated and the torsional system tested (i.e. mass polar moment of inertia, J_0, torsional damping coefficient, c_t, and torsional spring constant, k_t) and are unimportant as all of the SDOF response curve parameters (i.e. amplitude, A, damping ratio, D, and frequency, f_r) are normalized into A/A_{max}, D/D_{min}, and $((f_{peak}-f_D)/f_D)*Q$, where Q = 1/2D. The accuracy of the numerical model developed for evaluating sweep-rate effects used in this study has been validated by the experimental test results that were obtained using a resonant column testing device and reported in Chapter 7.

9.4 EXPERIMENTAL AND ANALYTICAL RESULTS CONFIRMING RELATIONSHIPS OF SWEEP RATE EFFECT ON SOIL SPECIMENS

In this sub-section, the analytical estimations of the partial steady-state response, A, and partial damping ratio D, are compared with experimental measurements, which are both relative to the maximum steady state response, A_{max}, and true damping ratio, D_{min}. In each example, first each simulated and measured fraction of steady-state response, A/A_{max}, are assessed, which are based on either the simulated estimation or measured estimation of the steady-state response amplitude compared to that of the simulated or estimated maximum steady sate response amplitude. Second, each simulated and measured ratio of measured damping to true damping, D/D_{min}, are assessed, which are based on either the simulated estimation or measured estimation of the Damping ratio compared to that of the simulated or estimated minimum damping ratio. Third, it is found that the differences that occur due to the number of cycles used per sweep frequency segment can be normalized by step rate, f_{step}, divided by the number of cycles excited at each frequency, C_s, which collapses these curve into a single relationship. Five theoretical simulations and five experimental tests are compared to continue to demonstrate the accuracy of the analytical procedures to model the experimental results.

9.4.1 Comparisons of Analytical and Experimental Results from A Soil Specimen and Normalization of Relationships by f_{step}/C_s

For the soil specimen tested at each of the five confining pressures and tested experimentally or modeled analytically, four plots are presented for each that contain the following: (1) A/A_{max}-$\log(1/C_s)$, (2) A/A_{max}-$\log(f_{step}/C_s)$, (3) D/D_{min}-$\log(1/C_s)$, and (4) D/D_{min}-$\log(f_{step}/C_s)$. The variation in A/A_{max} or D/D_{min} with $1/C_s$ can be normalized into one relationship by plotting the horizontal axis as f_{step}/C_s. This is possible because each case has a single f_n and single damping ratio. Cases that show normalization with varying

f_n and varying D are covered later. In each of the cases presented in this subsection, five different f_{step} are used with 10 different C_s for each f_{step} are used. Sweep rate effect results for the soil specimen tested at five isotropic confining pressures are shown in Figure 9.3 through Figure 9.14, the content these figures is shown in Table 9.1.

Table 9.1: Organization of the Results from Frequency Sweep Tests on the Soil Specimen Tested at Five Isotropic Confining Pressures That are Shown in Figure 9.3 Through Figure 9.14.

Isotropic Confining Pressure, σ'_0 (atm)	**0.54**	**1.09**	**2.18**	**4.35**	**8.71**
Natural Frequency, f_n (Hz)	61.05	71.60	83.63	98.48	115.73
Damping Ratio, D (%)	1.42	1.22	1.17	1.07	1.03
(a) A/A_{max}-log($1/C_s$) and (b) A/A_{max}-log(f_{step}/C_s)	Figure 9.3	Figure 9.5	Figure 9.7	Figure 9.9	Figure 9.11
(a) D/D_{min}-log($1/C_s$) and (b) D/D_{min}-log(f_{step}/C_s)	Figure 9.4	Figure 9.6	Figure 9.8	Figure 9.10	Figure 9.12
Ratio of f_{peak} to f_r	Figure 9.13 (a)	Figure 9.13 (b)	*Not Shown*	Figure 9.14 (a)	Figure 9.14 (b)

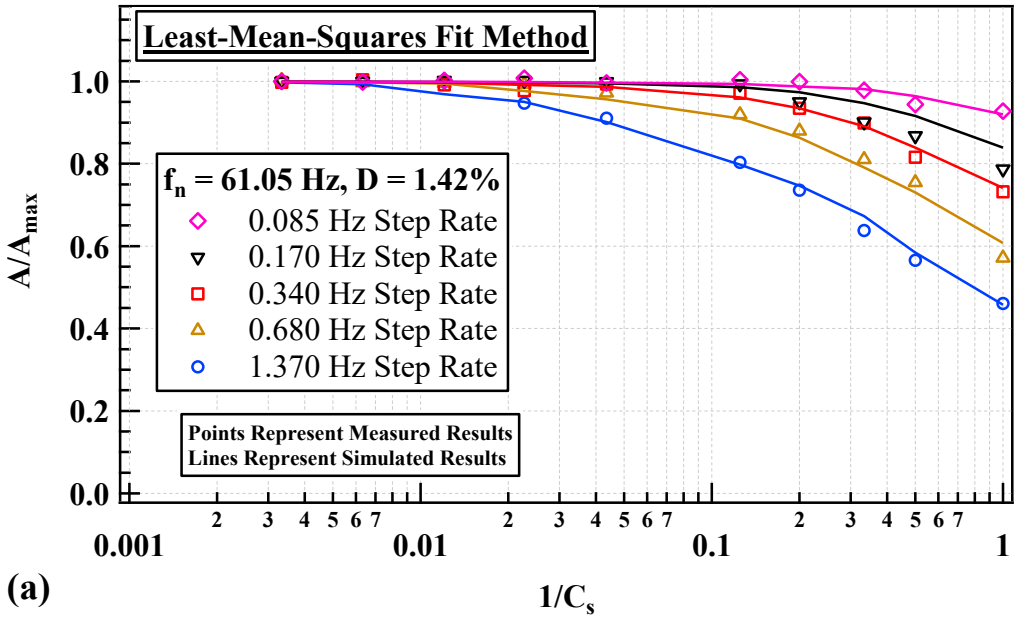

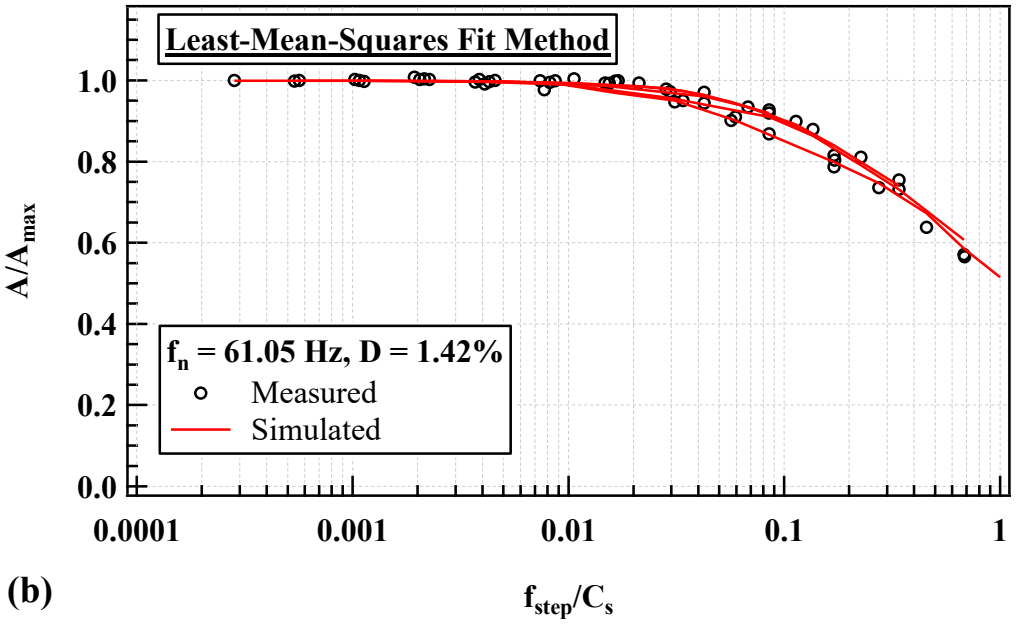

Figure 9.3: Experimental and Numerical Modeling Results Showing the Variation of the Normalized Amplitude Error (A/A_{max}) with (a) the Inverse of the Number of Cycles Per Frequency Step ($1/C_s$) and (b) Frequency Step (f_{step}) Divided by C_s from Frequency Sweep Tests on Soil Specimen at a Confining Pressure of **0.54 atm**, with f_n = 61.05 Hz and D = 1.42%.

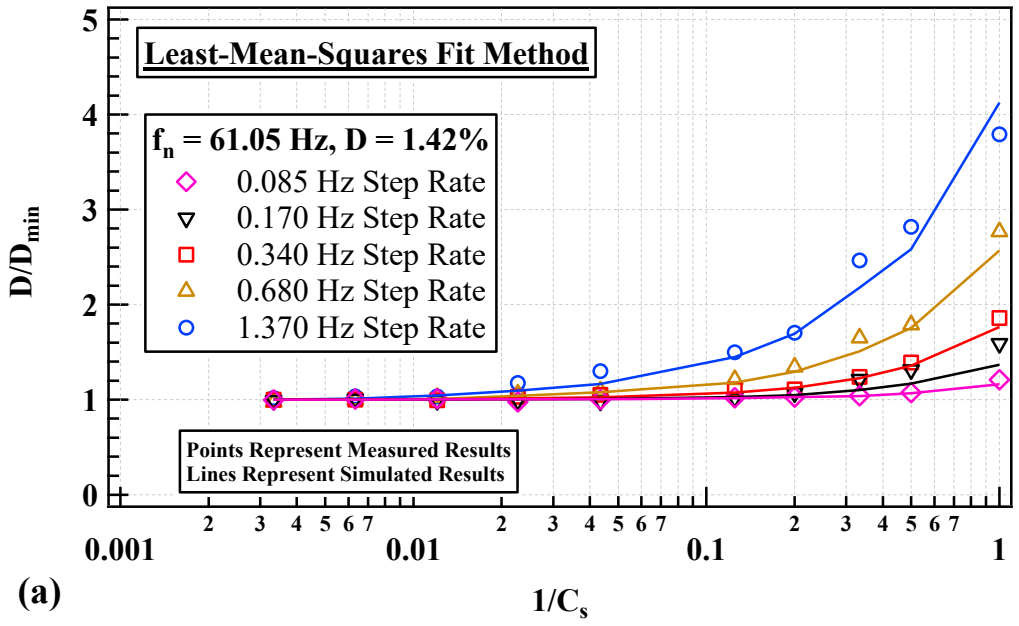

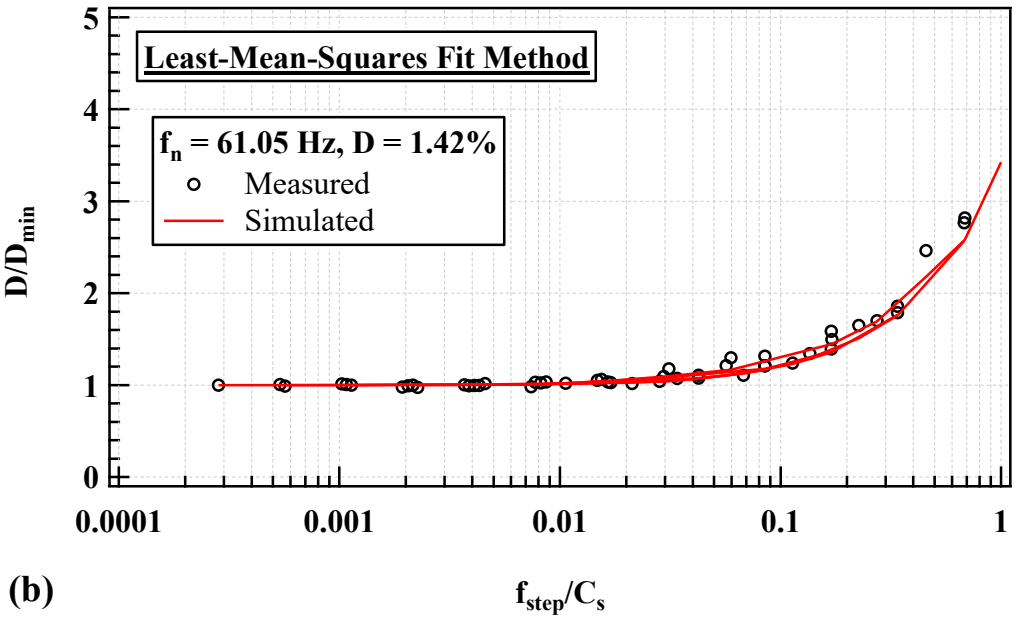

Figure 9.4: Experimental and Numerical Modeling Results Showing the Variation of the Normalized Damping Ratio Error (D/D_{min}) with (a) the Inverse of the Number of Cycles Per Frequency Step ($1/C_s$) and (b) Frequency Step (f_{step}) Divided by C_s from Frequency Sweep Tests on Soil Specimen at a Confining Pressure of **0.54 atm**, with f_n = 61.05 Hz and D = 1.42%.

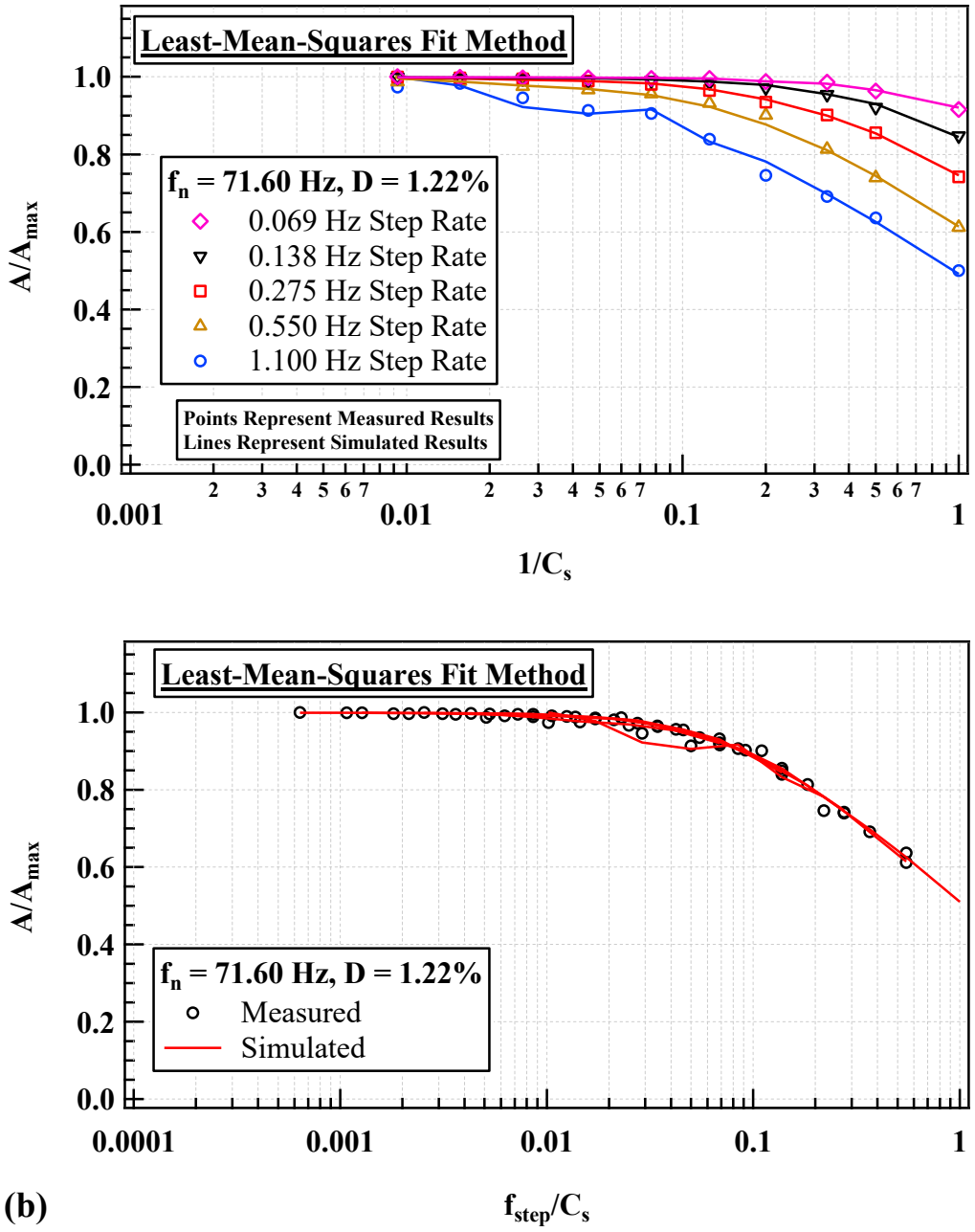

Figure 9.5: Experimental and Numerical Modeling Results Showing the Variation of the Normalized Amplitude Error (A/A_{max}) with (a) the Inverse of the Number of Cycles Per Frequency Step ($1/C_s$) and (b) Frequency Step (f_{step}) Divided by C_s from Frequency Sweep Tests on Soil Specimen at a Confining Pressure of **1.09 atm**, with f_n = 71.6 Hz and D = 1.22%.

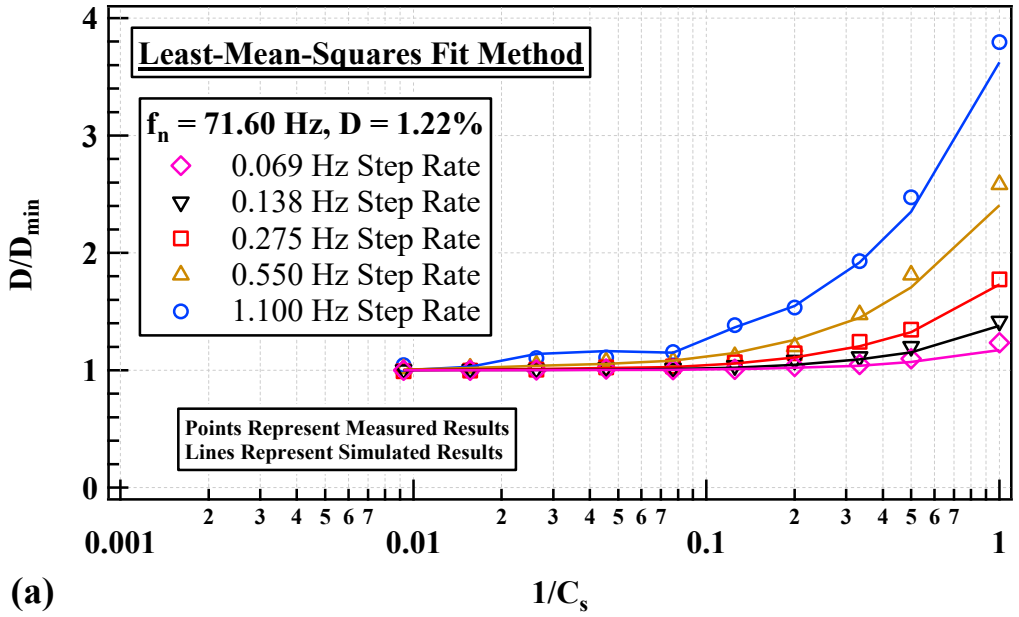

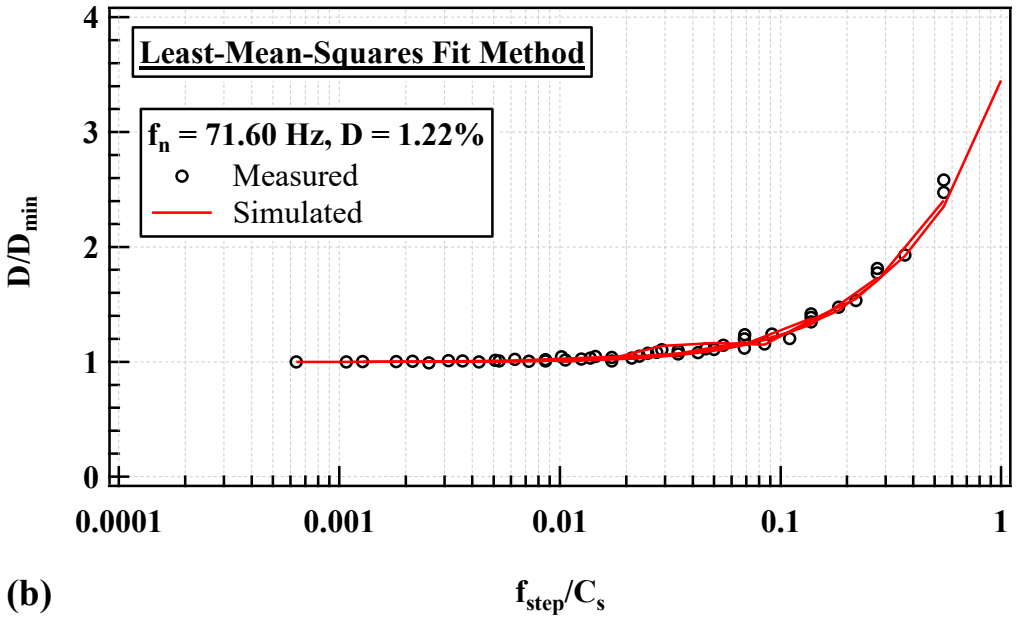

Figure 9.6: Experimental and Numerical Modeling Results Showing the Variation of the Normalized Damping Ratio Error (D/D_{min}) with (a) the Inverse of the Number of Cycles Per Frequency Step ($1/C_s$) and (b) Frequency Step (f_{step}) Divided by C_s from Frequency Sweep Tests on Soil Specimen at a Confining Pressure of **1.09 atm**, with f_n = 71.6 Hz and D = 1.22%.

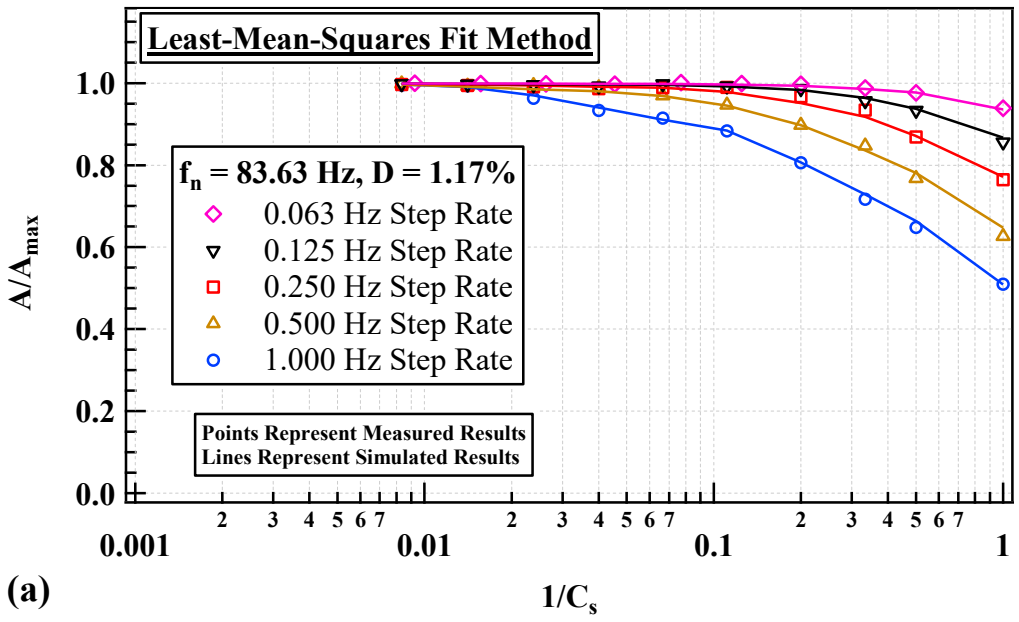

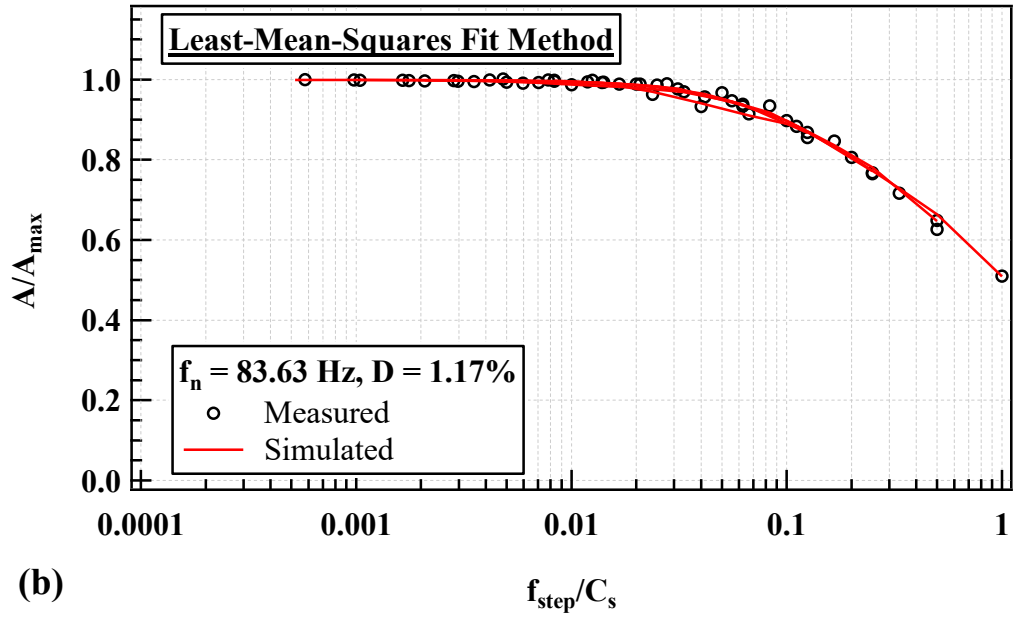

Figure 9.7: Experimental and Numerical Modeling Results Showing the Variation of the Normalized Amplitude Error (A/A_{max}) with (a) the Inverse of the Number of Cycles Per Frequency Step ($1/C_s$) and (b) Frequency Step (f_{step}) Divided by C_s from Frequency Sweep Tests on Soil Specimen at a Confining Pressure of **2.18 atm**, with f_n = 83.63 Hz and D = 1.17%.

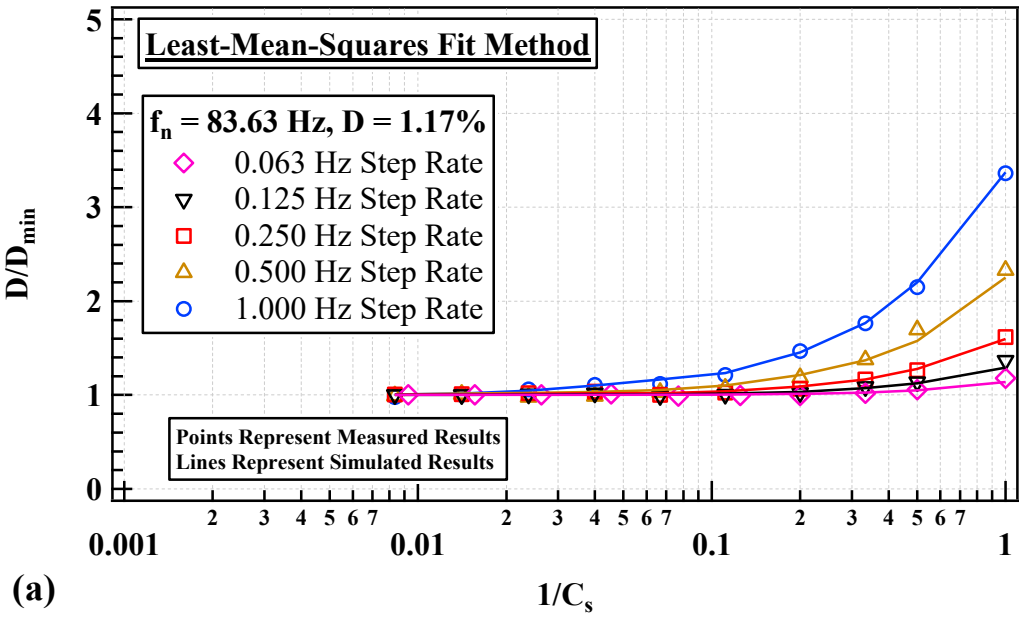

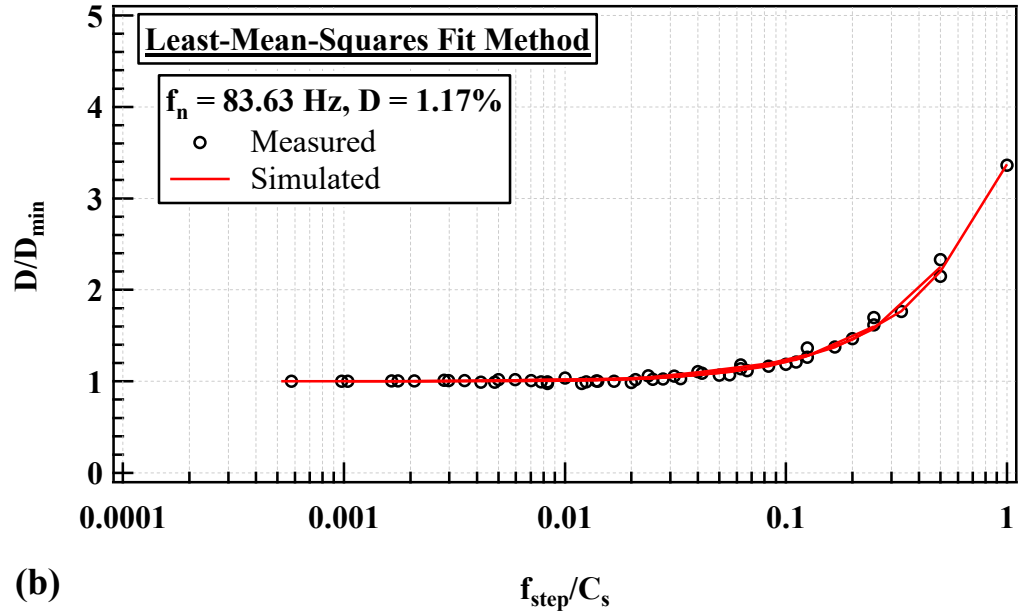

Figure 9.8: Experimental and Numerical Modeling Results Showing the Variation of the Normalized Damping Ratio Error (D/D_{min}) with (a) the Inverse of the Number of Cycles Per Frequency Step ($1/C_s$) and (b) Frequency Step (f_{step}) Divided by C_s from Frequency Sweep Tests on Soil Specimen at a Confining Pressure of **2.18 atm**, with f_n = 83.63 Hz and D = 1.17%.

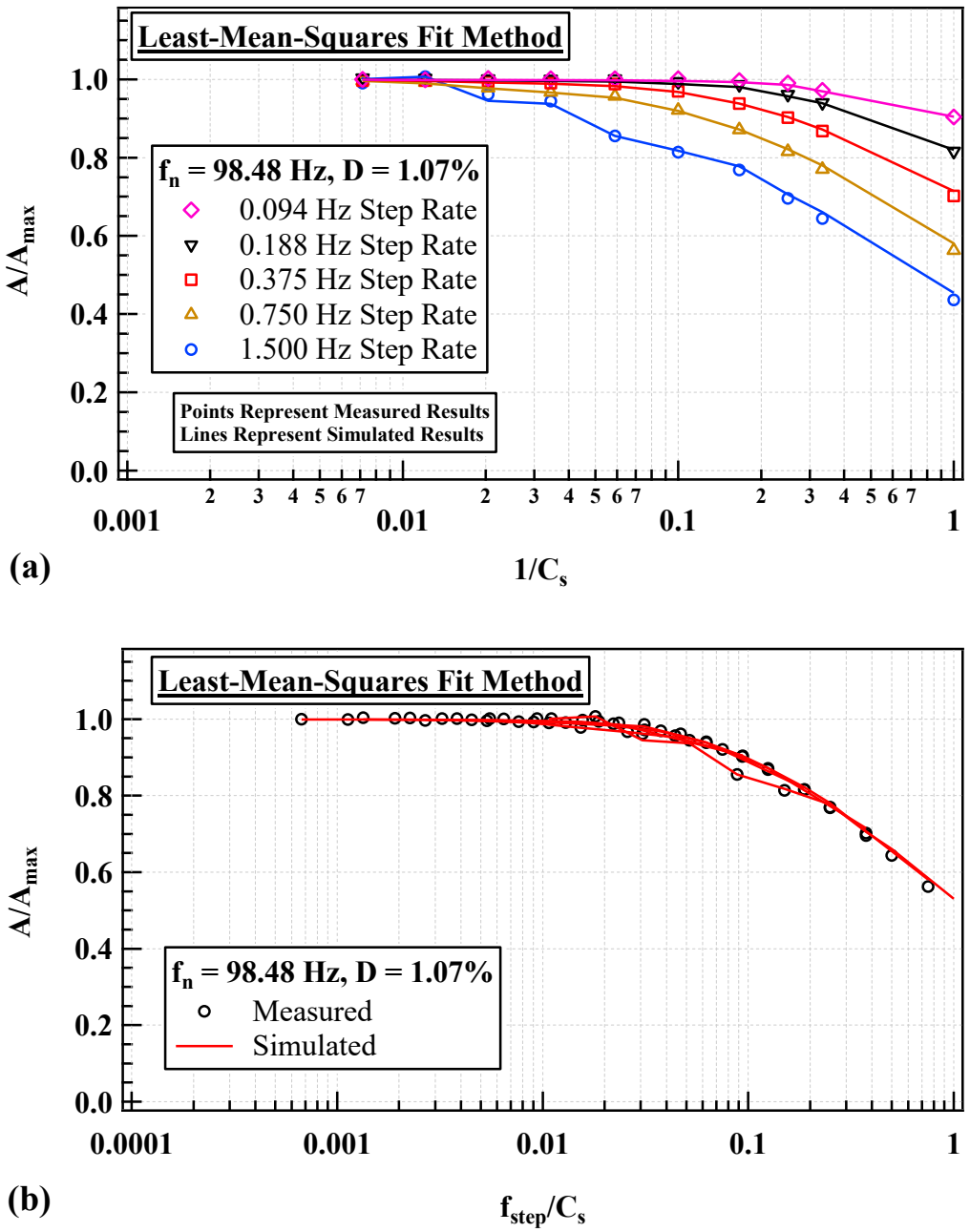

Figure 9.9: Experimental and Numerical Modeling Results Showing the Variation of the Normalized Amplitude Error (A/A_{max}) with (a) the Inverse of the Number of Cycles Per Frequency Step ($1/C_s$) and (b) Frequency Step (f_{step}) Divided by C_s from Frequency Sweep Tests on Soil Specimen at a Confining Pressure of **4.35 atm**, with f_n = 98.48 Hz and D = 1.07%.

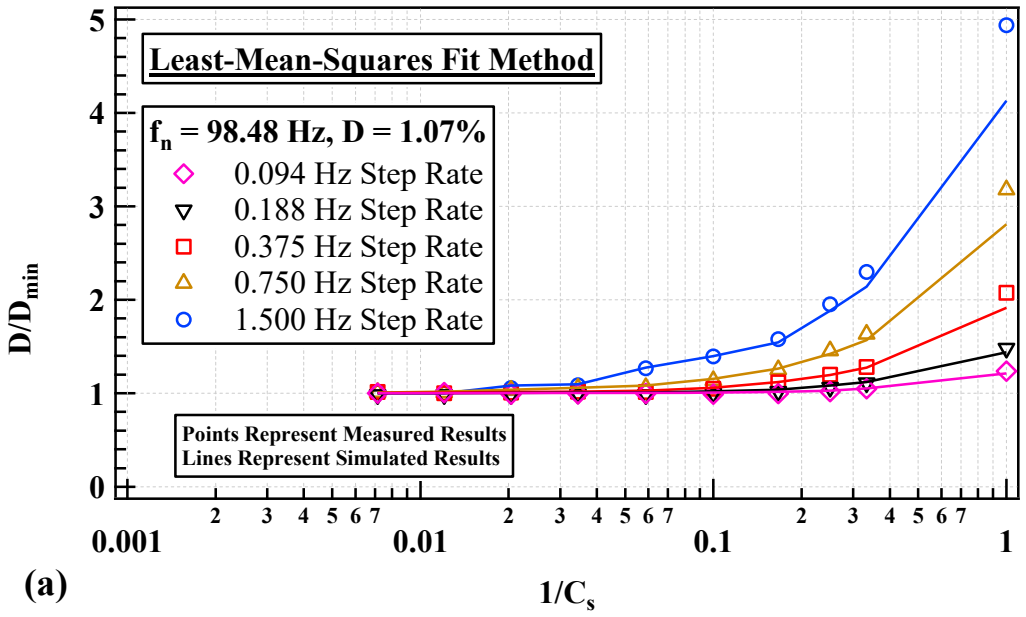

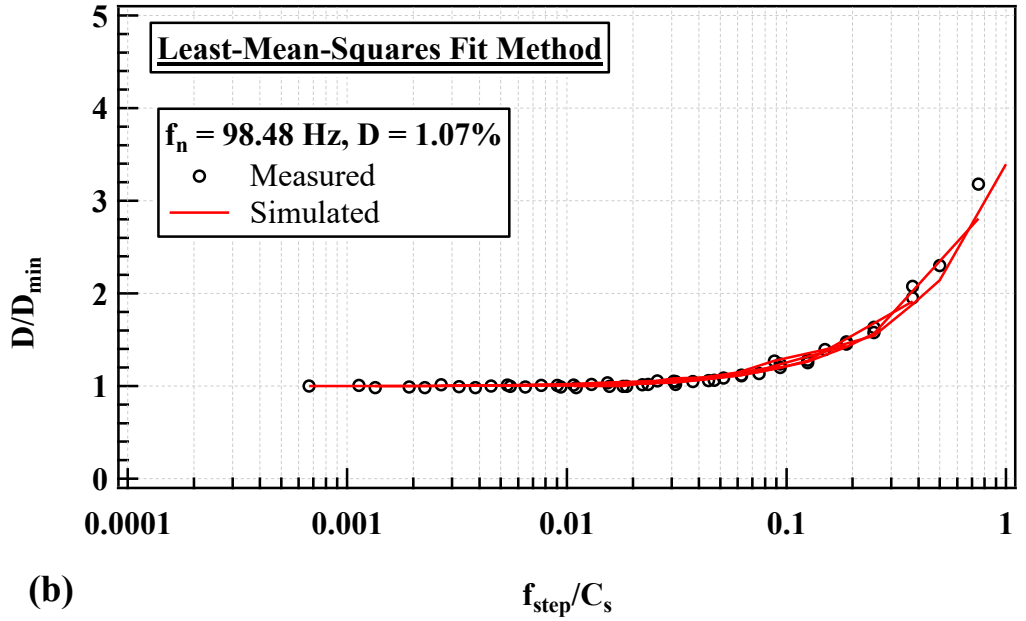

Figure 9.10: Experimental and Numerical Modeling Results Showing the Variation of the Normalized Damping Ratio Error (D/D_{min}) with (a) the Inverse of the Number of Cycles Per Frequency Step ($1/C_s$) and (b) Frequency Step (f_{step}) Divided by C_s from Frequency Sweep Tests on Soil Specimen at a Confining Pressure of **4.35 atm**, with f_n = 83.63 Hz and D = 1.17%.

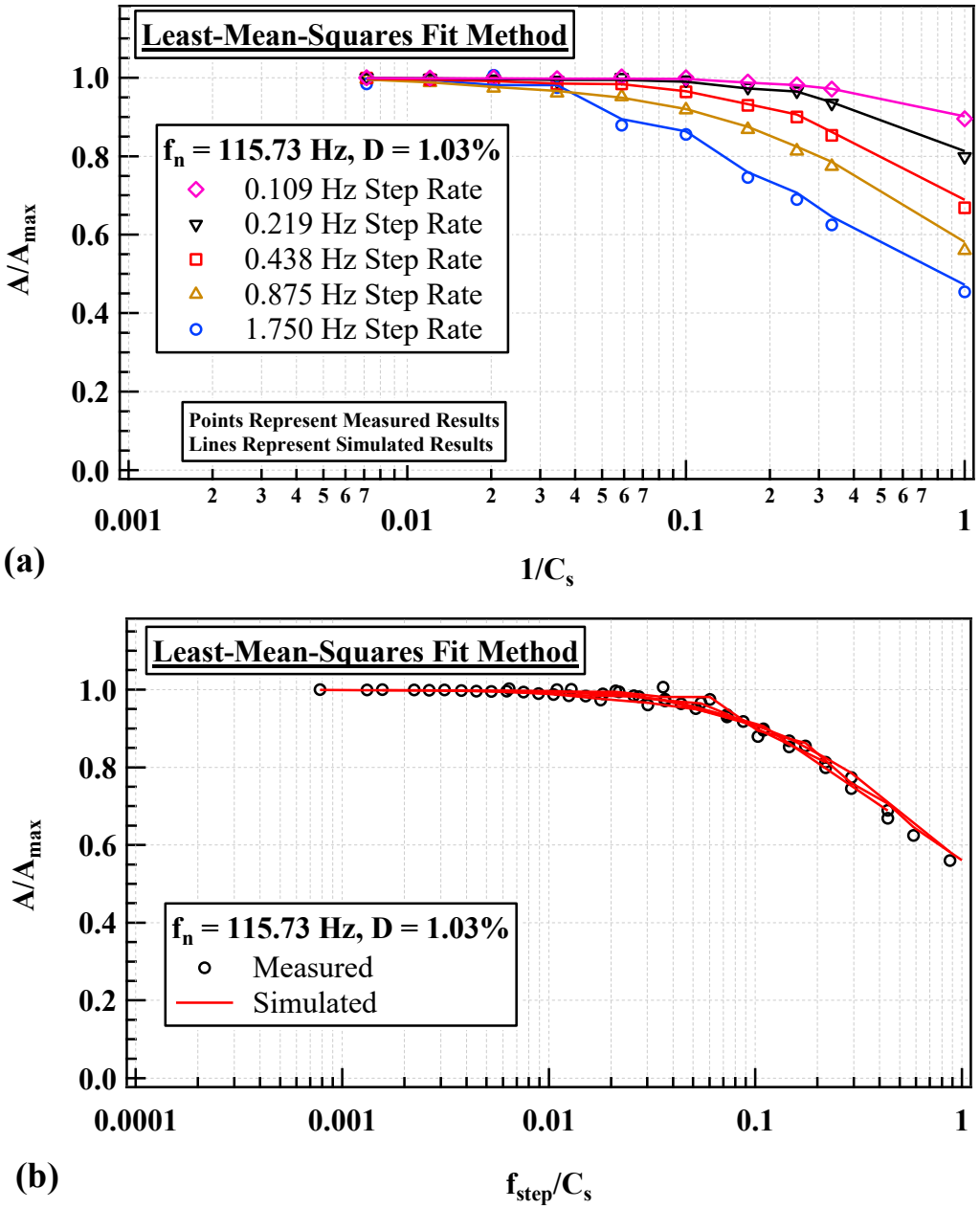

Figure 9.11: Experimental and Numerical Modeling Results Showing the Variation of the Normalized Amplitude Error (A/A_{max}) with (a) the Inverse of the Number of Cycles Per Frequency Step ($1/C_s$) and (b) Frequency Step (f_{step}) Divided by C_s from Frequency Sweep Tests on Soil Specimen at a Confining Pressure of **8.71 atm**, with f_n = 115.73 Hz and D = 1.03%.

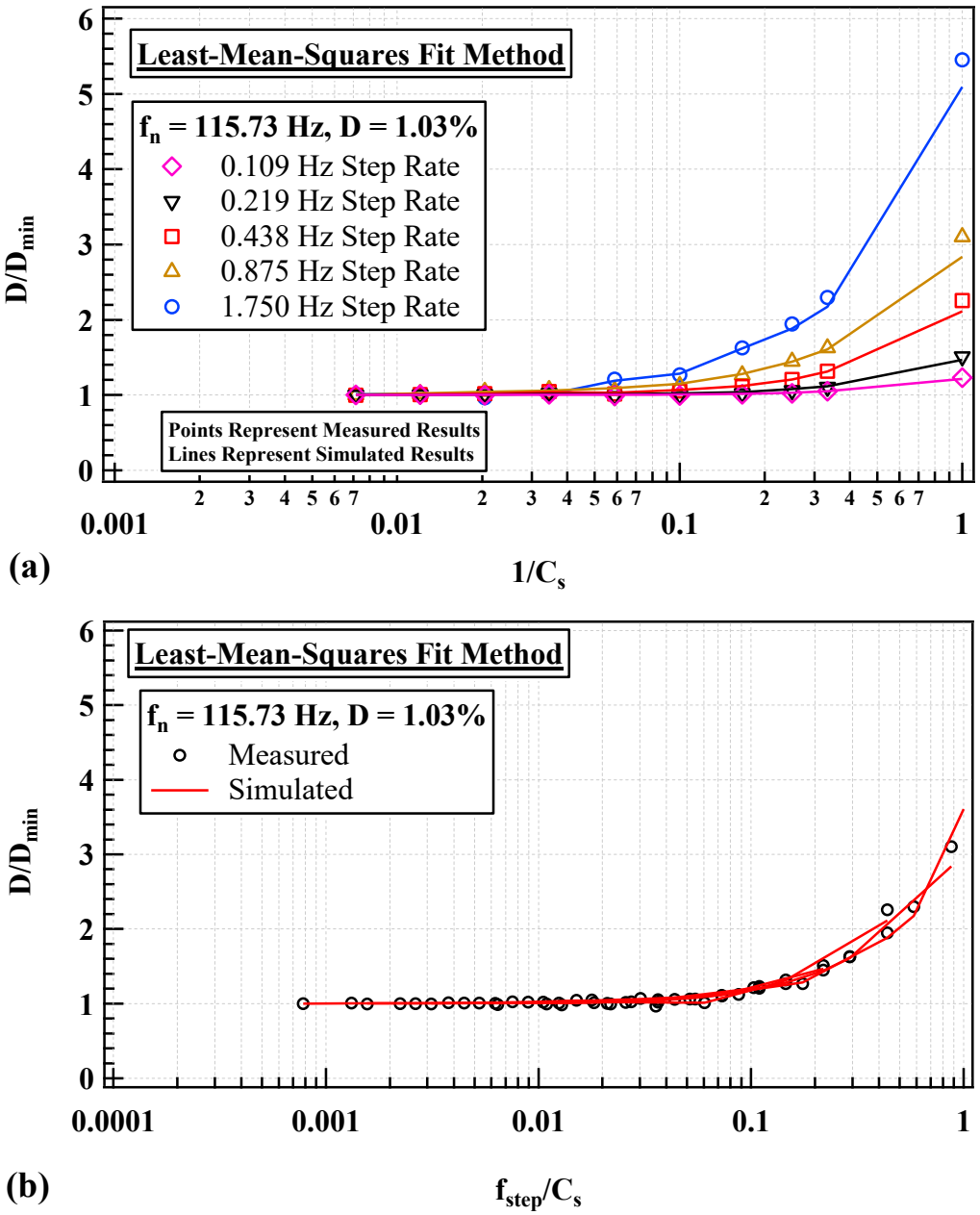

Figure 9.12: Experimental and Numerical Modeling Results Showing the Variation of the Normalized Damping Ratio Error (D/D_{min}) with (a) the Inverse of the Number of Cycles Per Frequency Step ($1/C_s$) and (b) Frequency Step (f_{step}) Divided by C_s from Frequency Sweep Tests on Soil Specimen at a Confining Pressure of **8.71 atm**, with f_n = 115.73 Hz and D = 1.03%.

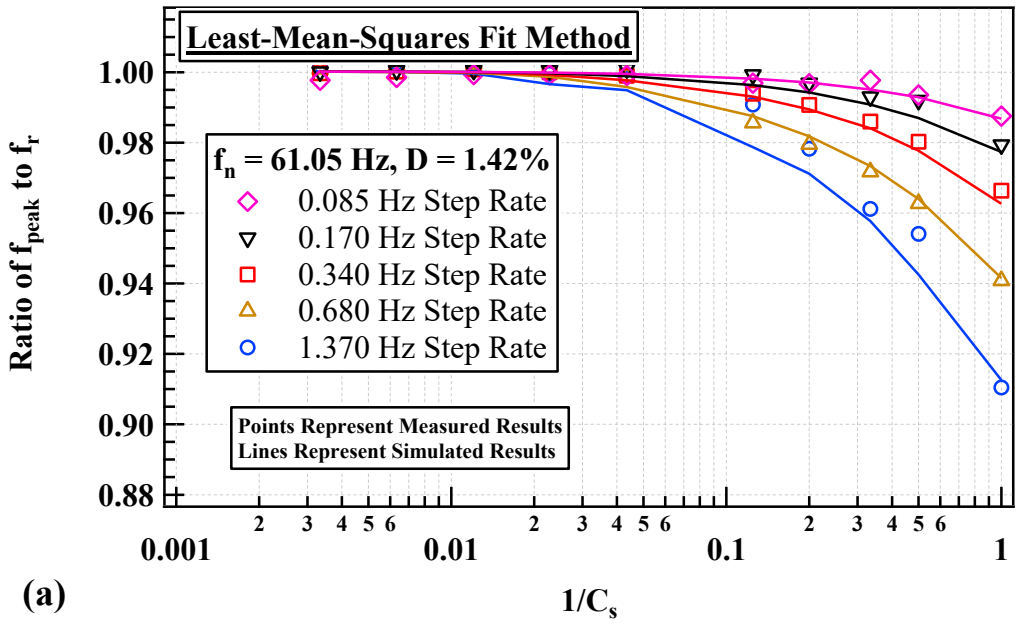

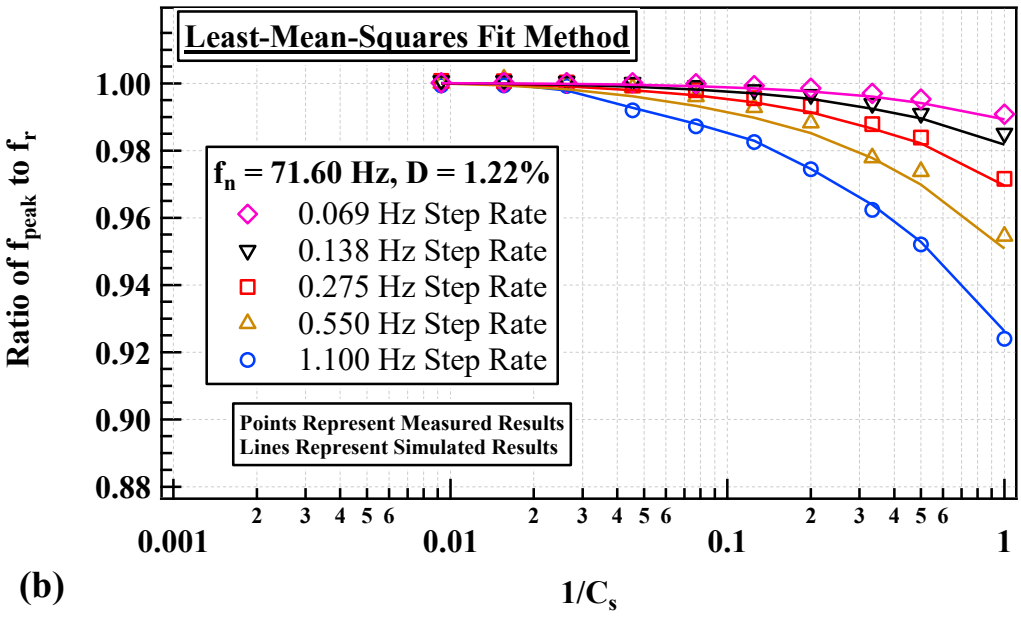

Figure 9.13: Experimental and Numerical Modeling Results Showing the Variation of the Normalized Resonant Frequency Error (Ratio of f_{peak} to f_r) with the Inverse of the Number of Cycles Per Frequency Step ($1/C_s$) from Frequency Sweep Tests on a soil specimen at a confining pressure of (a) **0.54 atm** and (b) **1.09 atm**.

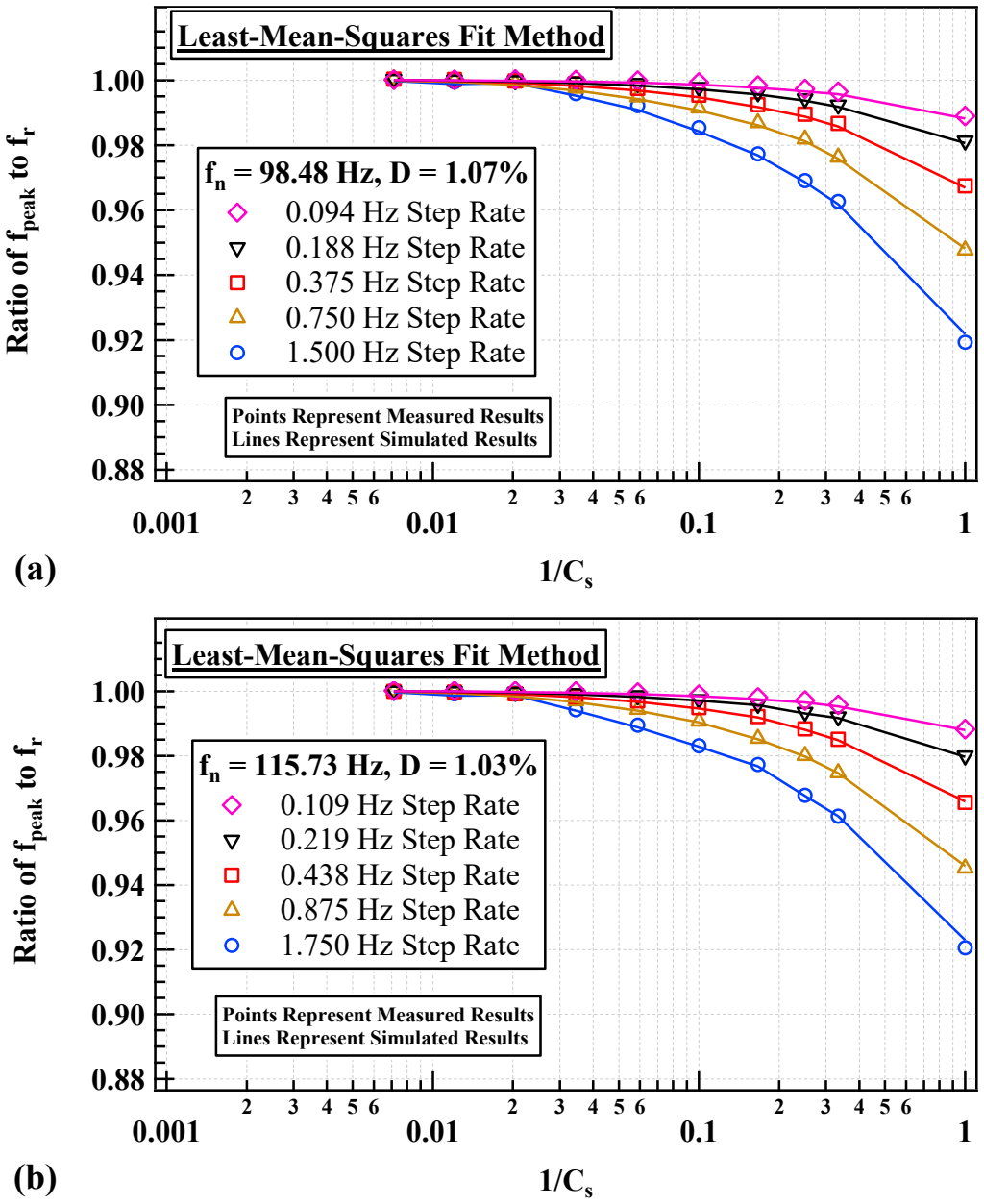

Figure 9.14: Experimental and Numerical Modeling Results Showing the Variation of the Normalized Resonant Frequency Error (Ratio of f_{peak} to f_r) with the Inverse of the Number of Cycles Per Frequency Step ($1/C_s$) from Frequency Sweep Tests on a soil specimen at a confining pressure of (a) **4.35 atm** and (b) **8.71 atm**.

9.4.2 Normalizing Sweep Rate Effects of 5 Metal Specimens and A Soil Specimen at 5 Confining Pressures Using the Non-Dimensional Sweep-Rate Parameter (η)

In this subsection sweep-rate effects from experimental testing and numerical modeling of the five metal specimens and one soil specimen tested at five confining pressures are presented. The results are normalized into one relationship by using the non-dimensional sweep rate parameter, η. The frequency sweep results are obtained using the two methods of analysis, the half-power bandwidth and least-mean-squares fit methods. These methods are plotted separately, but both are compared with the relationship presented in Lollock (2002) and Girard and Bugeat (2004).

Individual sweep rate results for the 5 metal specimens either tested experimentally or modeled analytically were presented in Chapter 8. For each of the five metal specimens either tested experimentally or modeled analytically, four plots are presented for each that contain the following: (1) A/A_{max}-$\log(f_{step}/C_s)$, (2) A/A_{max}-$\log(\eta)$, (3) D/D_{min}-$\log(f_{step}/C_s)$, and (4) D/D_{min}-$\log(\eta)$. The variation in A/A_{max} or D/D_{min} with (f_{step}/C_s) can be normalized into one relationship by plotting the horizontal axis η. In each of the cases presented in this subsection, five different f_{step} are used with 10 different C_s for each f_{step} are used. Sweep rate effect results for the five Metal Specimens are shown in Figure 9.15 and Figure 9.16, the content these figures is shown in Table 9.4.

Table 9.2: Organization of the Results from Frequency Sweep Simulations for the Five Metal Specimens That are Shown in Figure 9.15 and Figure 9.16.

(a) A/A_{max}-$\log(f_{step}/C_s)$ and (b) A/A_{max}-$\log(\eta)$	Figure 9.15
(a) D/D_{min}-$\log(f_{step}/C_s)$ and (b) D/D_{min}-$\log(\eta)$	Figure 9.16

Notes: (1) **η** = Non-Dimensional Sweep Rate Parameter

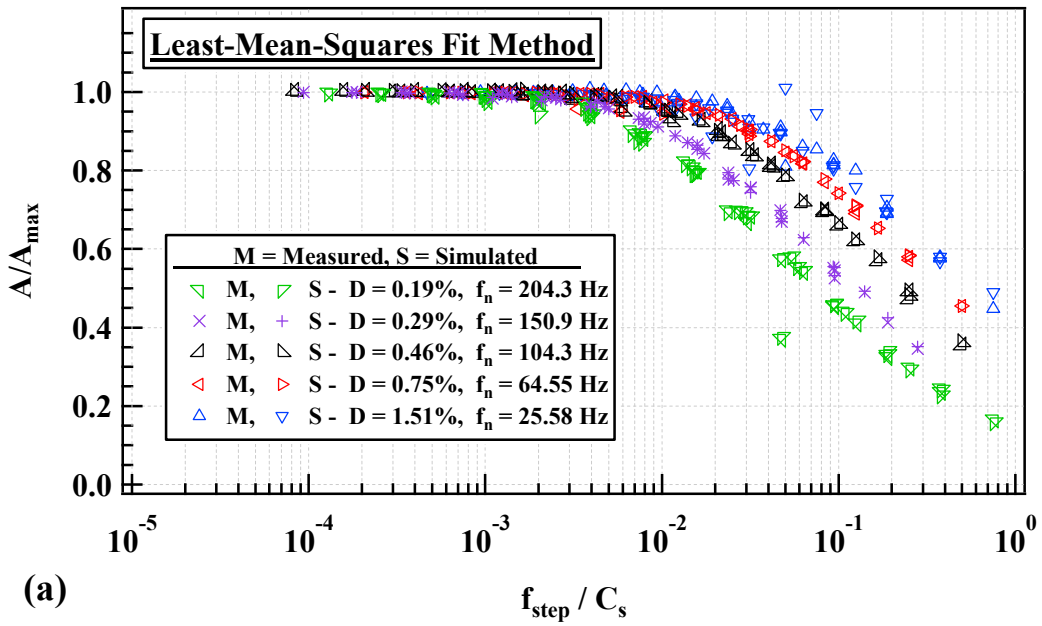

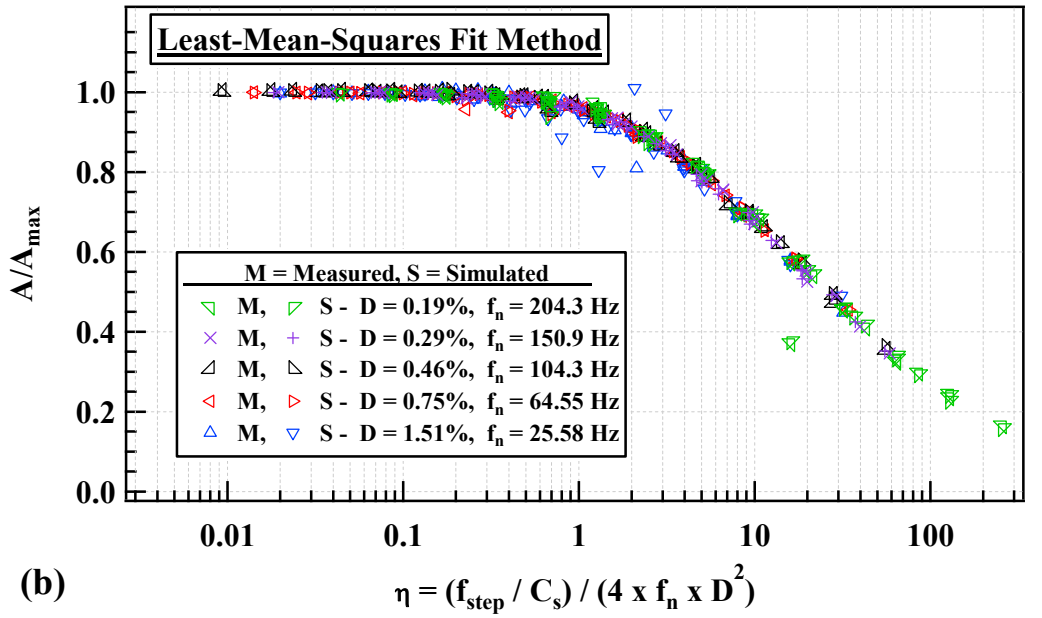

Figure 9.15: Experimental and Numerical Modeling Results Showing the Variation of the Normalized Amplitude Error (A/A_{max}) with (a) (f_{step}/C_s) and (b) The Non-Dimensional Sweep Rate Parameter (η) from Frequency Sweep Tests on five Metal Specimens.

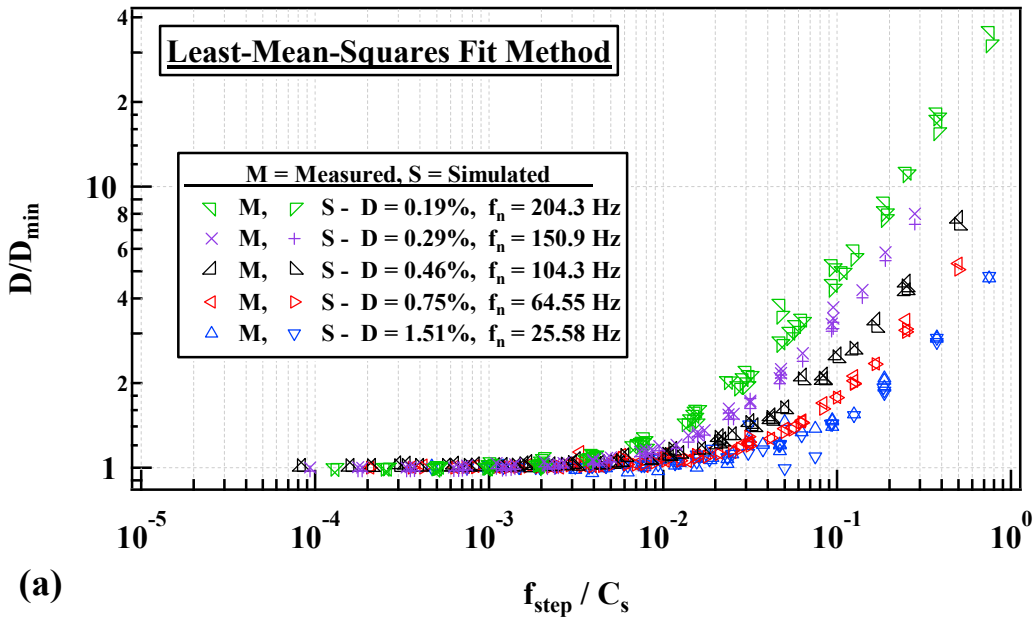

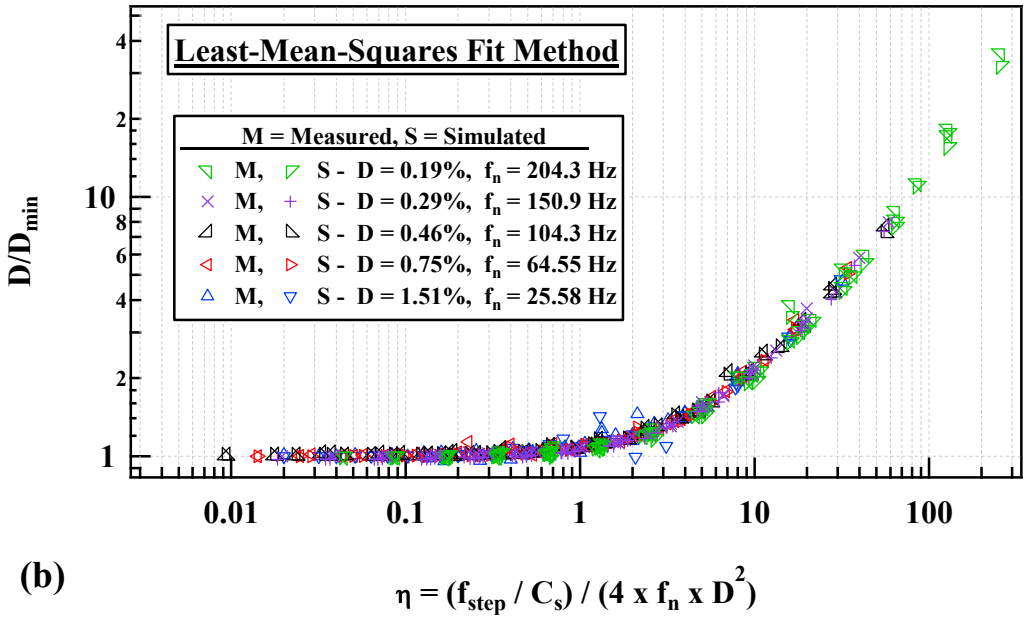

Figure 9.16: Experimental and Numerical Modeling Results Showing the Variation of the Normalized Damping Ratio Error (D/D_{min}) with (a) (f_{step}/C_s) and (b) The Non-Dimensional Sweep Rate Parameter (η) from Frequency Sweep Tests on five Metal Specimens.

For the soil specimen tested at 5 different confining pressures either tested experimentally or modeled analytically, four plots are presented for each that contain the following: A/A_{max}-log(η) for (1) Least-Mean-Squares Fit Method and (2) Half-Power Bandwidth Method and D/D_{min}-log(η) for (1) Least-Mean-Squares Fit Method and (2) Half-Power Bandwidth Method. The four plots show that the relationships can be normalized into one relationship by plotting the horizontal axis as η. Sweep rate effect results for the soil specimen tested at 5 different confining pressures are shown in Figure 9.17 and Figure 9.18.

The frequency sweep results from the 5 metal specimens and one soil specimen tested at 5 confining pressures are presented together as A/A_{max} and D/D_{min} and are normalized by the non-dimensional sweep rate parameter. All of these results are presented for the least-mean-squares fit and half-power bandwidth methods as A/A_{max} and D/D_{min} in Figure 9.17 and Figure 9.18, respectively. With regards to A/A_{max}-log(η), there is much less scattering of the results when using the least-mean-squares fit approach, as seen in Figure 9.17. Similarly, with regards to D/D_{min}-log(η), reduced scattering of the results is also observed for the least-mean-squares fit approach, as seen in Figure 9.18. Furthermore, there is greater accuracy when using the least-mean-squares fit approach for $\eta < 40$, which corresponds to sweep rates that are too fast, but may be used to ascertain a rough estimate of the response curve parameters. Thus, the least-mean-squares fit approach outperforms the half-power bandwidth approach for a majority of the sweep rates that may be used to evaluate a SDOF system. Finally, the scattering of the half-power bandwidth method relative to the least-mean-squares fit method is attributed to the small shear strain ($\gamma <$ 0.0008%) conditions under which specimens in the RC test must be tested. Under low strain conditions, environmental background noise has a significant influence on the efficacy of acquired signals, which is discussed in great detail in Chapter 5.

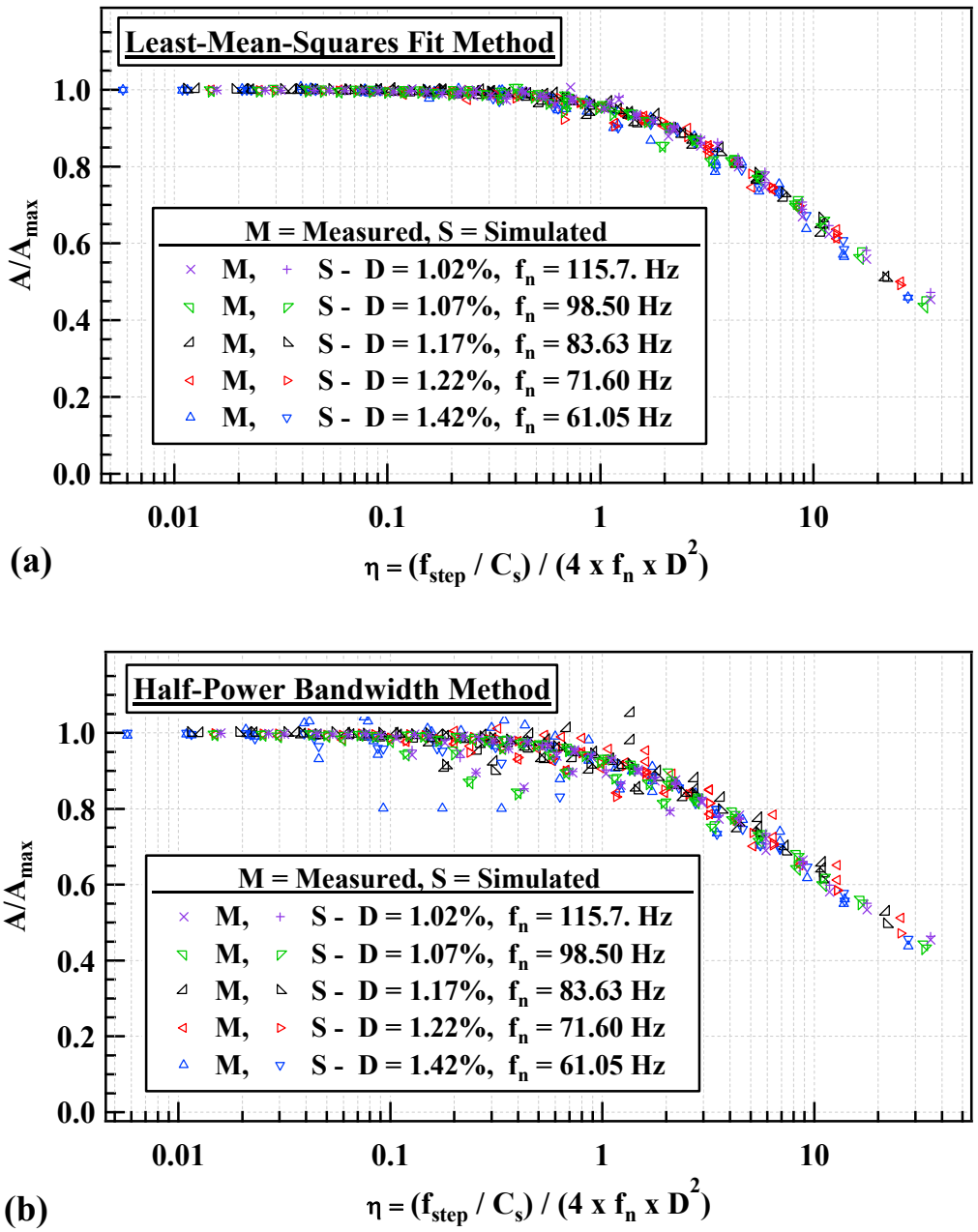

Figure 9.17: Experimental and Numerical Modeling Results Showing the Variation of the Normalized Amplitude Error (A/A_{max}) with The Non-Dimensional Sweep Rate Parameter (η) for (a) The Least-Mean-Squares Fit Method and (b) The Half-Power Bandwidth Method from Frequency Sweep Tests on One Soil Specimen Tested at 5 Different Confining Pressures.

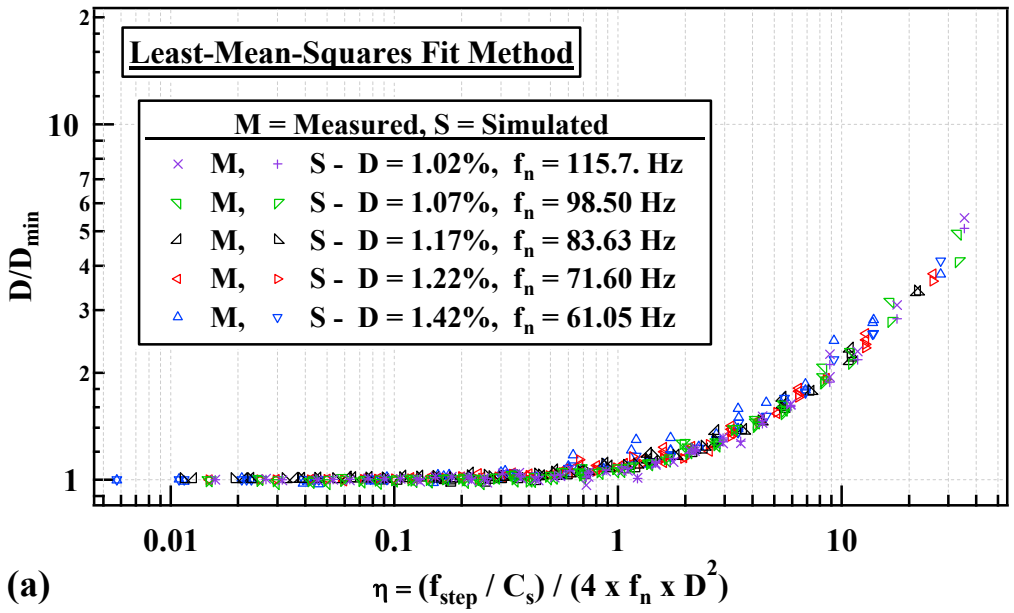

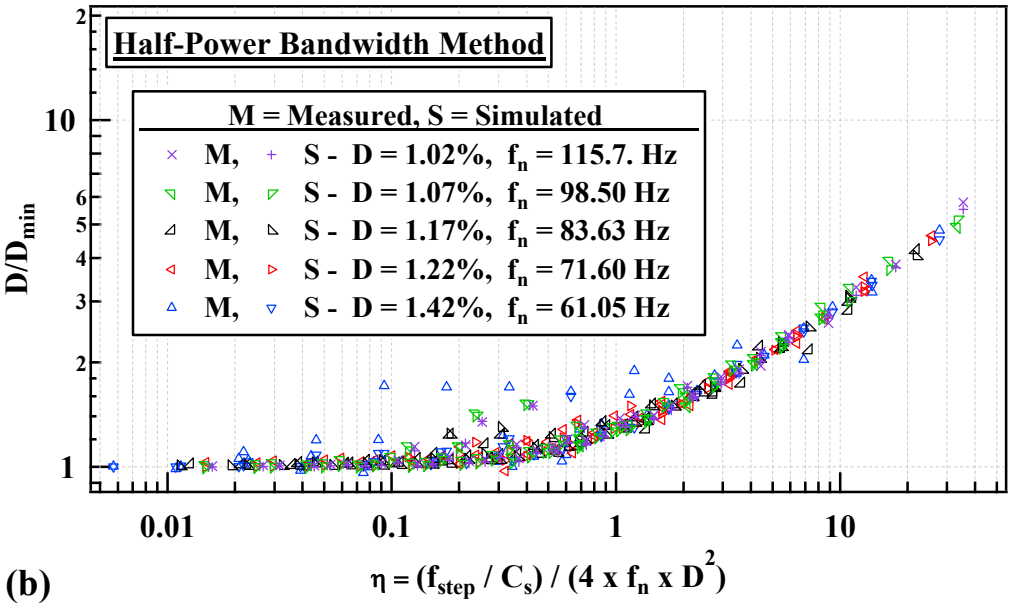

Figure 9.18: Experimental and Numerical Modeling Results Showing the Variation of the Normalized Damping Ratio Error (D/D_{min}) with The Non-Dimensional Sweep Rate Parameter (η) for (a) The Least-Mean-Squares Fit Method and (b) The Half-Power Bandwidth Method from Frequency Sweep Tests on One Soil Specimen Tested at 5 Different Confining Pressures.

9.5 DEVELOPMENT OF EQUATIONS FOR PARAMETERIZING SWEEP RATE EFFECTS ON RESPONSE OF SDOF SYSTEM

The variables needed to normalize the relationships for the sweep rate effects are the frequency step rate, number of excitations per frequency step, true resonant frequency, and true damping ratio. By including each of these variables into the dependent axis, the fraction of maximum steady state response, A/A_{max}, and ratio of estimated damping to true damping, D/D_{min}, can be easily determined. The hyperbolic modified equation developed for determining A/A_{max} is given as:

$$\frac{A}{A_{max}} = \frac{1}{1+\left(\eta/\eta_{ref,a}\right)^{a}} \tag{9.12}$$

$$\eta = \frac{f_{step}}{C_s} \times \frac{1}{4f_n D^2} \tag{9.13}$$

where A is the predicted amplitude response of the system, A_{max} is the maximum amplitude response, η is the non-dimensional sweep parameter for normalization of the horizontal axis, $\eta_{ref,a}$ is the normalization parameter for A/A_{max}, and a is the normalization exponent for A/A_{max}.

Similarly, a modified hyperbolic equation developed for determining D/D_{min}, is given as:

$$\frac{D}{D_{min}} = 1 + \left(\eta/\eta_{ref,b}\right)^{b} \tag{9.14}$$

where D is the predicted damping ratio response of the system, D_{min} is the true damping ratio, η is the non-dimensional sweep parameter for normalization of the horizontal axis, $\eta_{ref,b}$ is the normalization parameter for D/D_{min}, and b is the normalization exponent for D/D_{min}.

Similarly, a modified hyperbolic equation for determining $((f_{peak} - f_D)/f_D) \times Q$, is given as:

$$\frac{f_{peak}-f_r}{f_r} \times Q = \left(\eta/\eta_{ref,c}\right)^c \quad (9.15)$$

where f_{peak} is the true damped natural frequency, f_r is the measured damped natural frequency, $[(f_{peak} - f_r)/f_r] \times Q$ is the normalized frequency error, η is the non-dimensional sweep parameter for normalization of the horizontal axis, $\eta_{ref,c}$ is the normalization parameter for $[(f_{peak} - f_r)/f_r] \times Q$, and *c* is the normalization exponent for $[(f_{peak} - f_r)/f_r] \times Q$. The modified hyperbolic normalization parameters and exponents were determined by using a least-mean-squares fit of the equations to the results. Several outliers were removed to provide a better fit to the majority of the data, which is presented later.

The modified hyperbolic equations are fit to the data presented in the previous section, the frequency sweep results and modified hyperbolic fits are plotted with results from Lollock (2012) and are shown in Figure 9.19 through Figure 9.21, the content these figures is shown in Table 9.4.

Table 9.3: Organization of the Results from Frequency Sweep Tests on the One Soil Specimen Tested at Five Isotropic Confining Pressures and Five Metal Specimens That are Shown in Figure 9.19 through Figure 9.21.

	Least-Mean Squares Fit Method	**Half-Power Bandwidth Method**
A/A_{max}-log(η)	Figure 9.19(a)	Figure 9.19(b)
D/D_{min}-log(η)	Figure 9.20(a)	Figure 9.20(b)
$[(f_{peak} - f_r)/f_r] \times Q$- log(η)	Figure 9.21(a)	Figure 9.21(b)

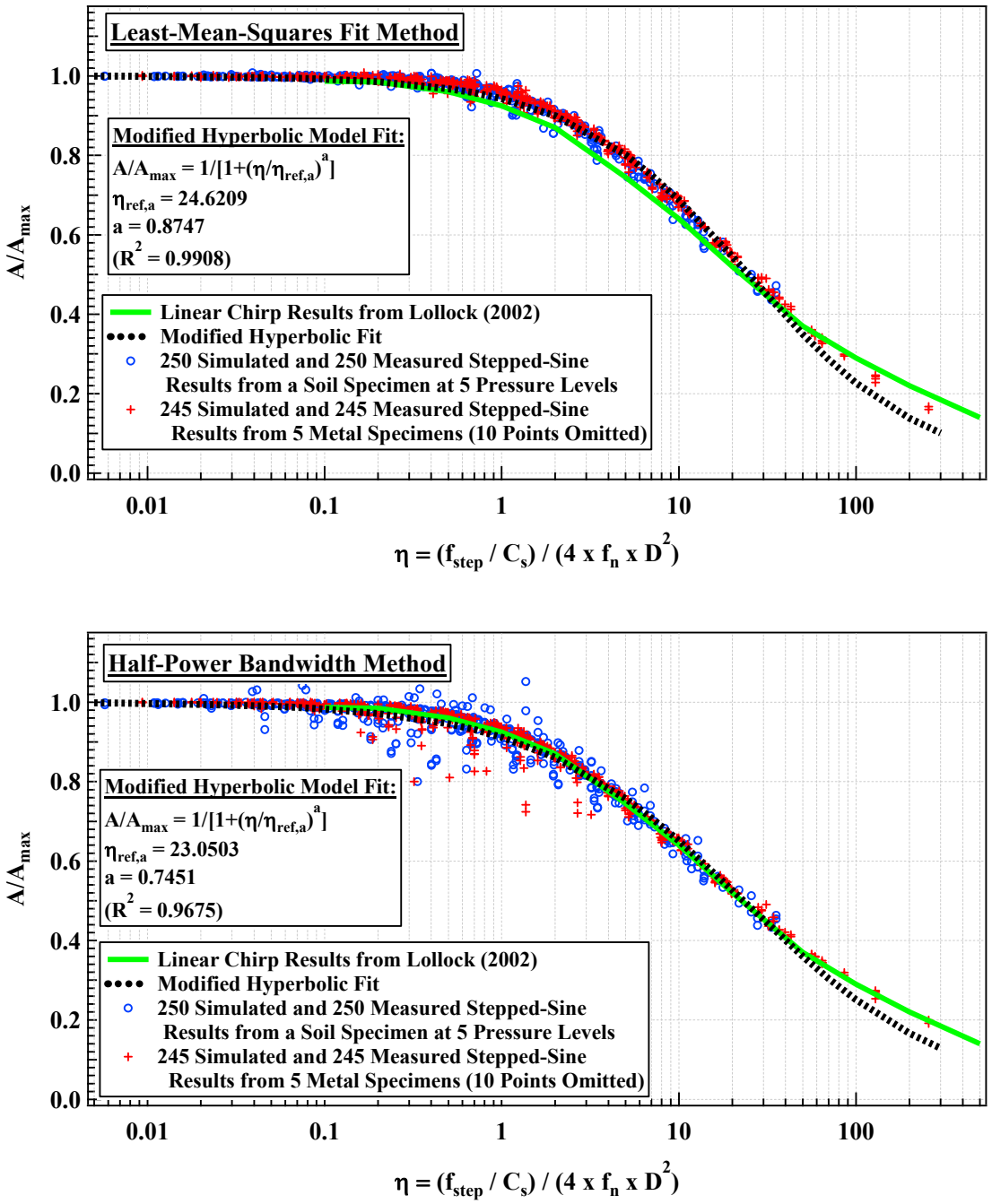

Figure 9.19: Experimental and Numerical Modeling Results Showing the Variation of the Normalized Amplitude Error (A/A_{max}) with The Non-Dimensional Sweep Rate Parameter (η) for (a) The Least-Mean-Squares Fit Method and (b) The Half-Power Bandwidth Method from Frequency Sweep Tests on Five Metal Specimens and One Soil Specimen Tested at 5 Different Confining Pressures.

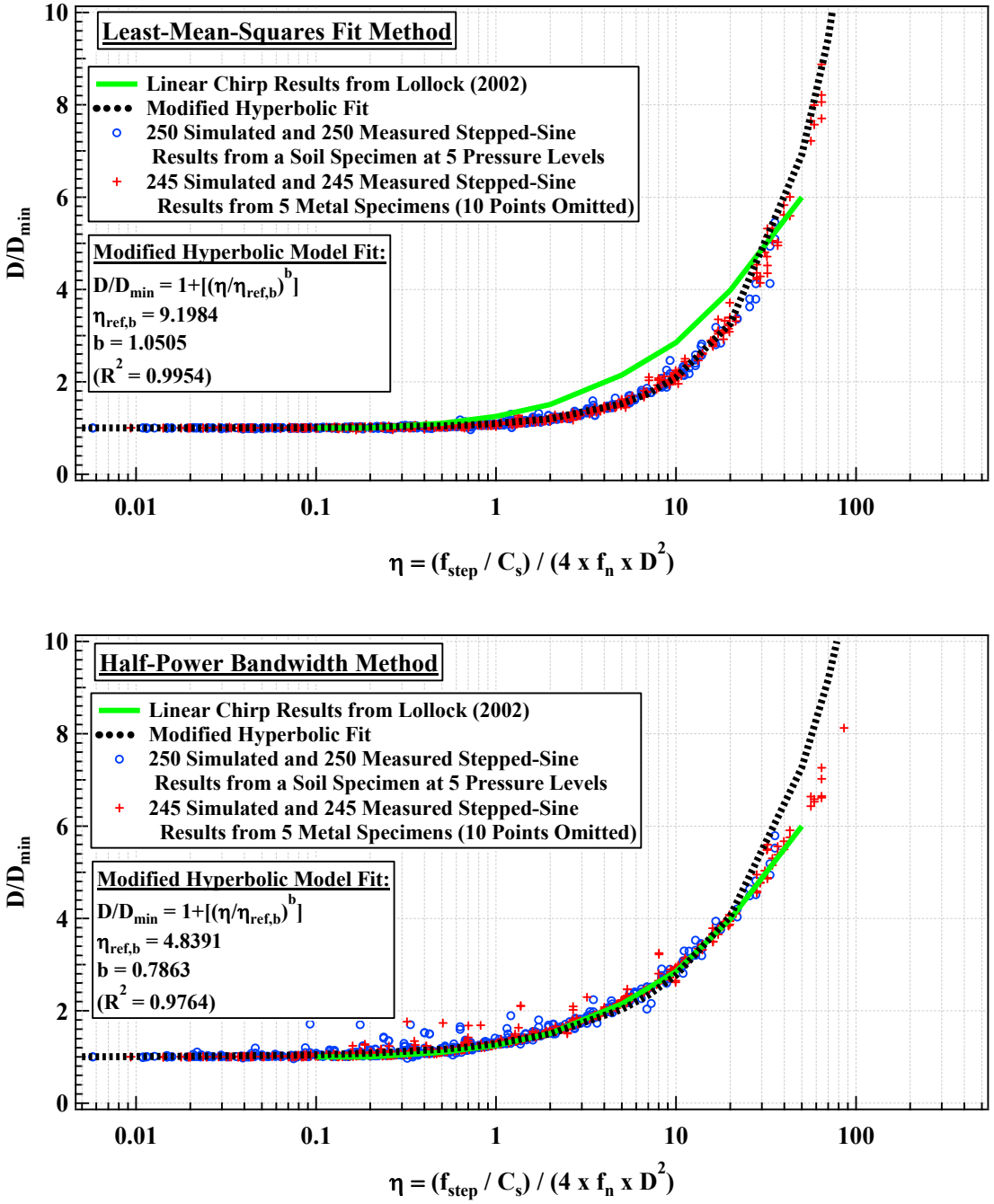

Figure 9.20: Experimental and Numerical Modeling Results Showing the Variation of the Normalized Damping Ratio Error (D/D_{min}) with The Non-Dimensional Sweep Rate Parameter (η) for (a) The Least-Mean-Squares Fit Method and (b) The Half-Power Bandwidth Method from Frequency Sweep Tests on Five Metal Specimens and One Soil Specimen Tested at 5 Different Confining Pressures.

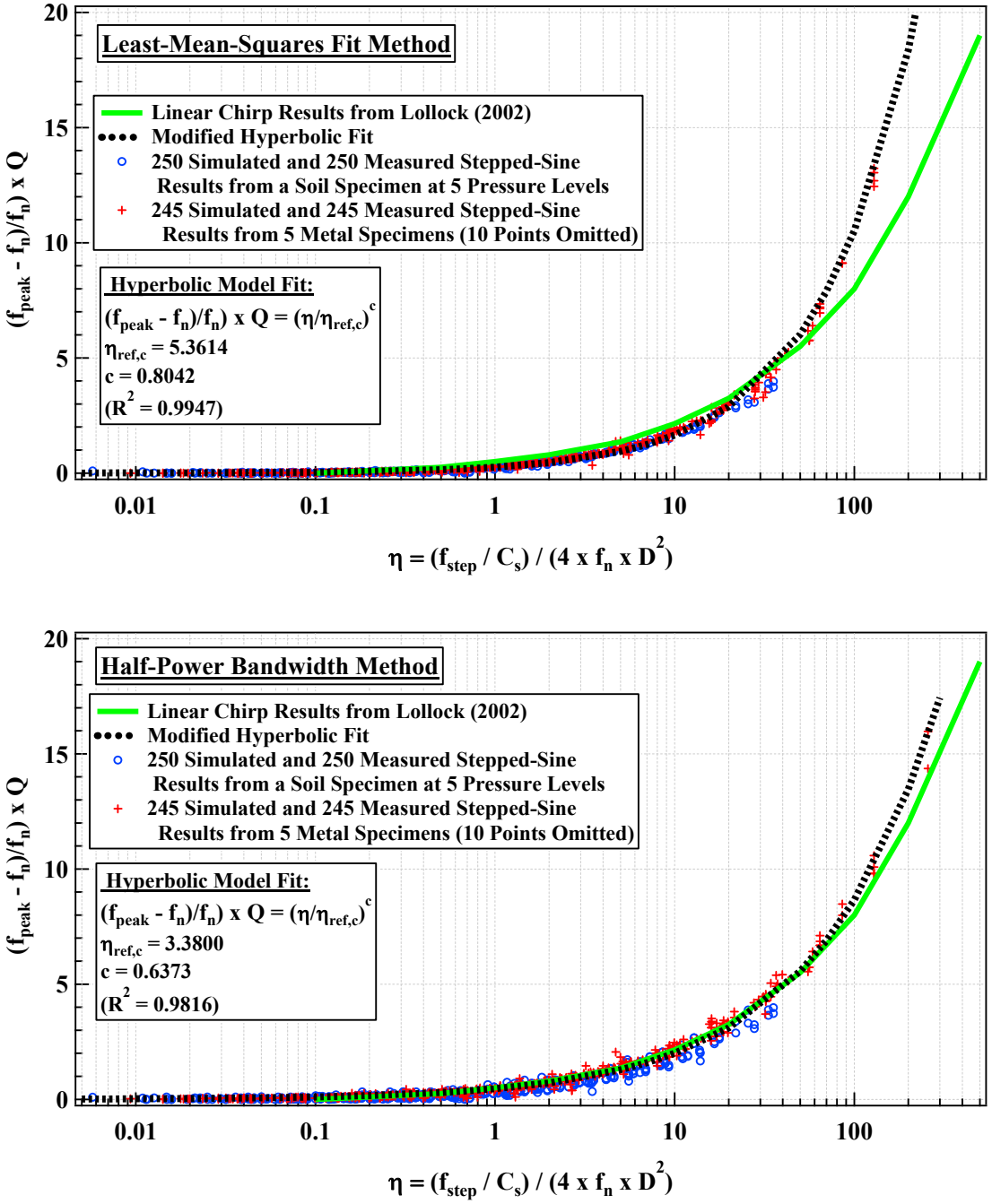

Figure 9.21: Experimental and Numerical Modeling Results Showing the Variation of the Normalized Frequency Error $[(f_{peak}-f_n))/f_n]\times Q$ with The Non-Dimensional Sweep Rate Parameter (η) for (a) The Least-Mean-Squares Fit Method and (b) The Half-Power Bandwidth Method from Frequency Sweep Tests on Five Metal Specimens and One Soil Specimen Tested at 5 Different Confining Pressures

Based on the results presented previously, the normalizations of the measured or simulated amplitude response, damping ratio, and natural frequency by using the non-dimensional sweep rate parameter (η) yield a relationship for the stepped-sine sweep method that is very similar to that presented in Lollock (2002). Two analytical methods were evaluated for predicting the response curve parameters, which included the Least-Mean-Squares Fit method and the Bandwidth Interpolation method as introduced previously. The Bandwidth Interpolation method resulted in a normalized curve that basically matched the curve presented in Lollock (2002). Using the normalized curves the normalization parameters, exponents, and model fit quality are shown in Table 9.4.

Table 9.4: Coefficients, Exponents, and Fit Quality for Modified Hyperbolic Equations.

Method	$\eta_{ref,a}$	a	R^2	$\eta_{ref,b}$	b	R^2	$\eta_{ref,c}$	c	R^2
Bandwidth Interpolation	23.050	0.745	0.968	4.839	0.786	0.976	3.380	0.637	0.982
Least-Mean-Squares Fit	24.621	0.875	0.991	9.198	1.051	0.996	5.361	0.804	0.995

When using the Least-Mean-Squares Fit method, a higher level of accuracy is provided for determining both the maximum response amplitude and the damping ratio. In the results presented previously, the Least-Mean-Squares Fit method resulted in far less outliers when reducing the data to a single curve (i.e. plotting versus η) as compared to the bandwidth interpolation method. Above A/A_{max} of 0.4, the Least-Mean-Squares Fit method was more accurate when predicting the maximum response amplitude. Similarly, below D/D_{min} of 6, the Least-Mean-Squares Fit method was more accurate when predicting the damping ratio. The advantage of this is the ability to more accurately select a sweep rate suitable to the system being tested.

9.6 EXPERIMENTAL AND ANALYTICAL RESULTS CONFIRMING RELATIONSHIPS OF SWEEP RATE EFFECT FROM LINEAR CHIRP SWEEPS ON FIVE METAL SPECIMENS

To confirm that the analytical and experimental methods used in this study match that of Lollock (2002) and Girard and Bugeat (2004). Frequency sweep tests and simulations of the 5 metal specimens using linear chirp sweeps were also conducted. The results from both the least-mean-squares fit and bandwidth interpolation methods show the same relationships as those revealed from the stepped-sine method. Thus, both chirps and stepped-sine sweeps can be reduced to a single relationship using the non-dimensional sweep rate parameter, η, the results of which are shown in Figure 9.22 and Figure 9.24, the content these figures is shown in Table 9.5.

Table 9.5: Organization of the Results from Frequency Sweep Tests Using a Linear Chirp on Five Metal Specimens That are Shown in Figure 9.22 through Figure 9.24.

	Least-Mean Squares Fit Method	**Half-Power Bandwidth Method**
$\mathbf{A/A_{max}\text{-}\log(\eta)}$	Figure 9.22(a)	Figure 9.22(b)
$\mathbf{D/D_{min}\text{-}\log(\eta)}$	Figure 9.23(a)	Figure 9.23(b)
$\mathbf{[(f_{peak} - f_r)/f_r] \times Q\text{-}\log(\eta)}$	Figure 9.24(a)	Figure 9.24(b)

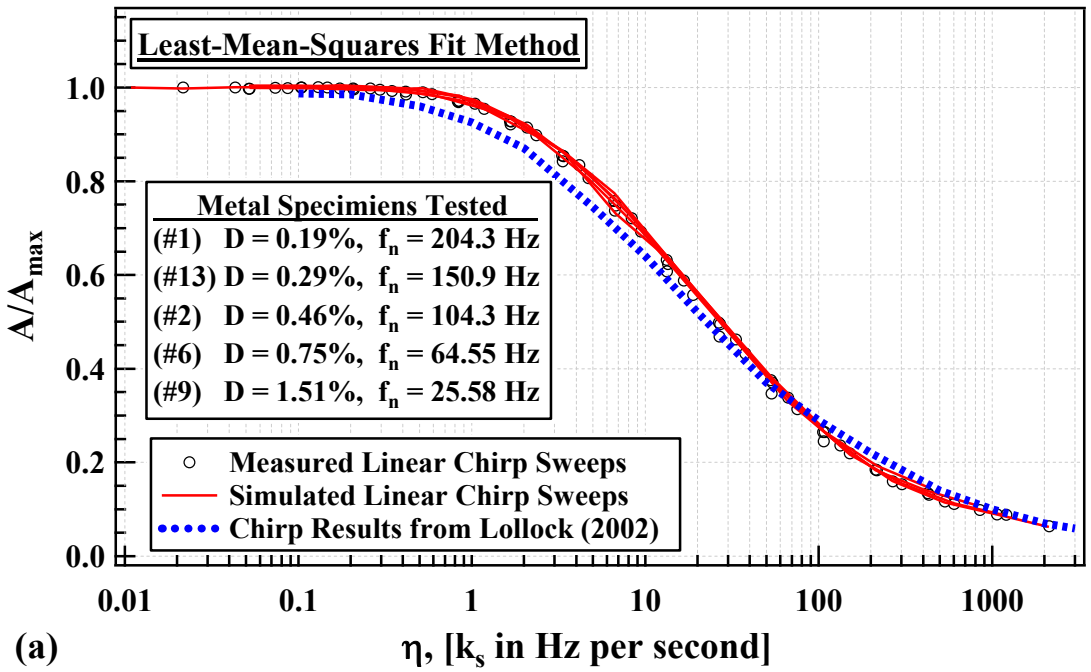

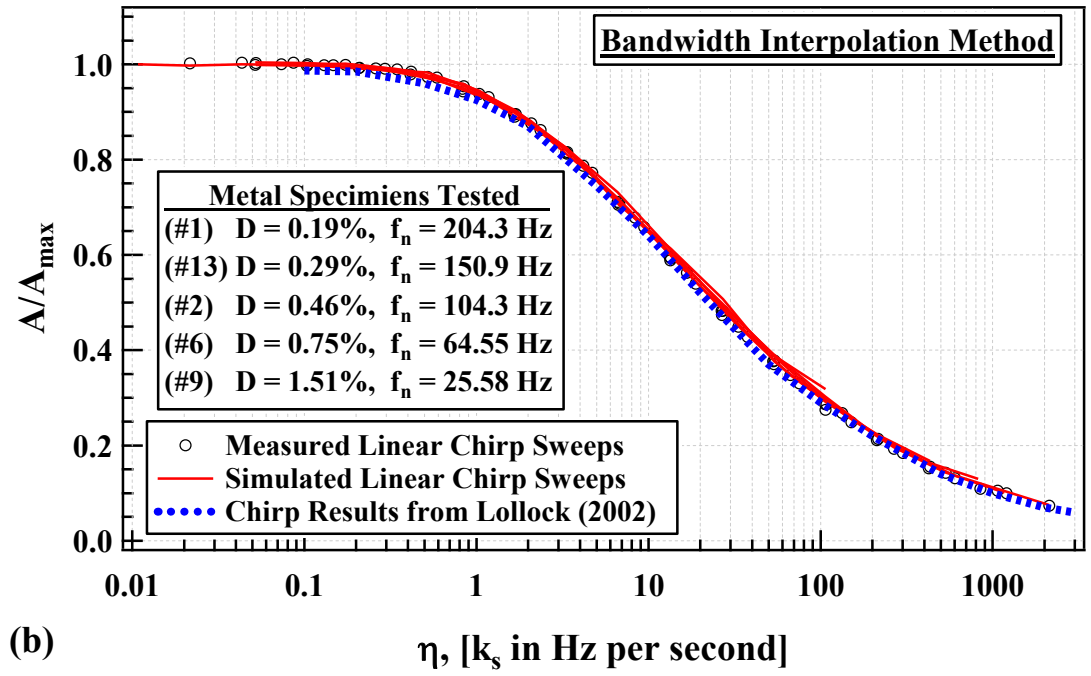

Figure 9.22: Experimental and Numerical Modeling Results Showing the Variation of the Normalized Amplitude Error (A/A_{max}) with The Non-Dimensional Sweep Rate Parameter (η) for (a) The Least-Mean-Squares Fit Method and (b) The Half-Power Bandwidth Method from Frequency Sweep Tests Using a Linear Chirp on Five Metal Specimens.

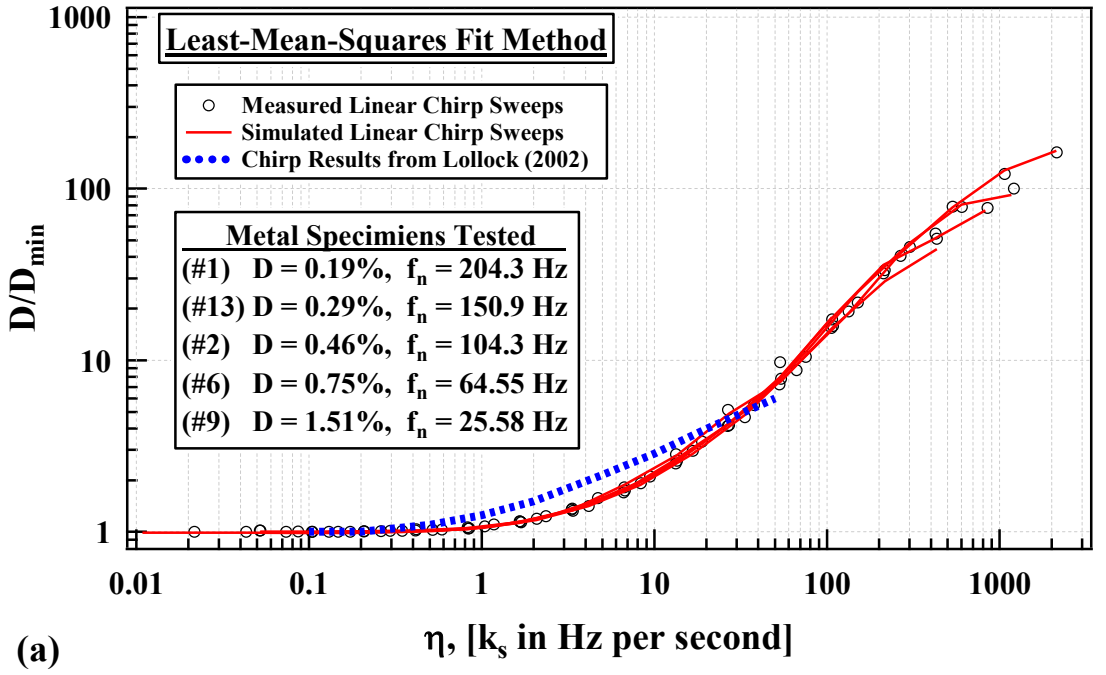

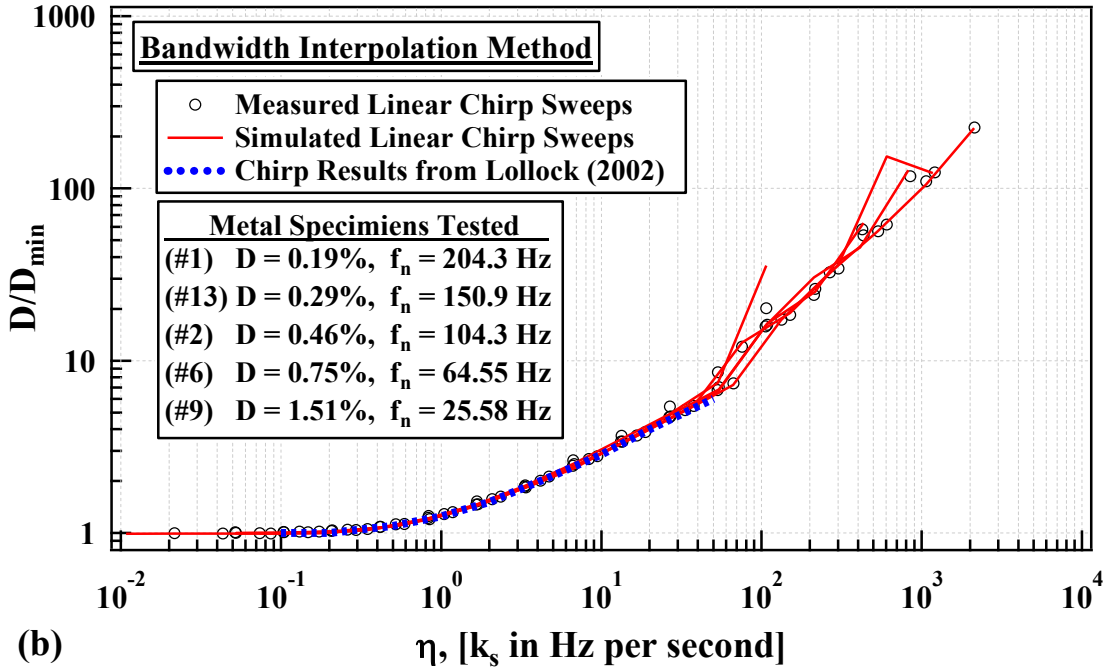

Figure 9.23: Experimental and Numerical Modeling Results Showing the Variation of the Normalized Damping Ratio Error (D/D_{min}) with The Non-Dimensional Sweep Rate Parameter (η) for (a) The Least-Mean-Squares Fit Method and (b) The Half-Power Bandwidth Method from Frequency Sweep Tests Using a Linear Chirp on Five Metal Specimens.

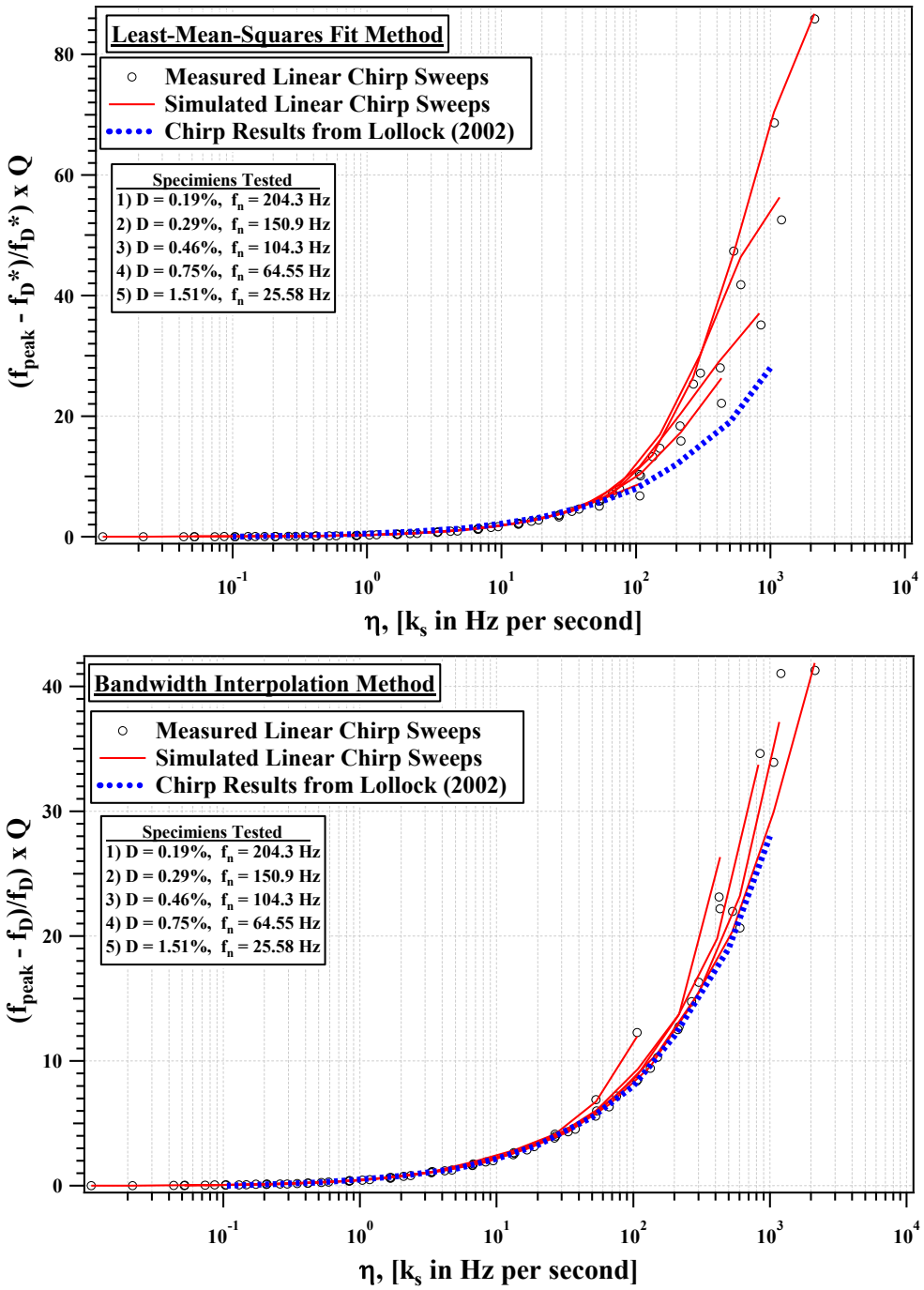

Figure 9.24: Experimental and Numerical Modeling Results Showing the Variation of the Normalized Frequency Error $[(f_{peak} - f_r)/f_r] \times Q$ with The Non-Dimensional Sweep Rate Parameter (η) for (a) The Least-Mean-Squares Fit Method and (b) The Half-Power Bandwidth Method from Frequency Sweep Tests Using a Linear Chirp on Five Metal Specimens.

9.7 EXPERIMENTAL AND ANALYTICAL RESULTS CONFIRMING RELATIONSHIPS OF SWEEP RATE EFFECT FROM LINEAR CHIRP SWEEPS ON A SOIL SPECIMEN TESTED AT FIVE CONFINING PRESSURES

To confirm that the analytical and experimental methods used in this study match that of Lollock (2002) and Girard and Bugeat (2004), experimental tests and simulations of a soil specimen tested at 5 confining pressures using linear chirp sweeps were also conducted. The results from both the least-mean-squares fit and bandwidth interpolation methods show the same relationships as those revealed from the stepped-sine method. Thus, chirps and stepped-sine sweeps can be reduced to a single relationship using the non-dimensional sweep rate parameter, η, the results of which are shown in Figure 9.25 through Figure 9.27, the content these figures is shown in Table 9.6.

Table 9.6: Organization of the Results from Frequency Sweep Tests Using a Linear Chirp on One Soil Specimen Tested at Five Confining Pressures That are Shown in Figure 9.25 through Figure 9.27.

	Least-Mean Squares Fit Method	**Half-Power Bandwidth Method**
A/A_{max}-log(η)	Figure 9.25(a)	Figure 9.25(b)
D/D_{min}-log(η)	Figure 9.26(a)	Figure 9.26(b)
$[(f_{peak} - f_r)/f_r]$ x Q- log(η)	Figure 9.27(a)	Figure 9.27(b)

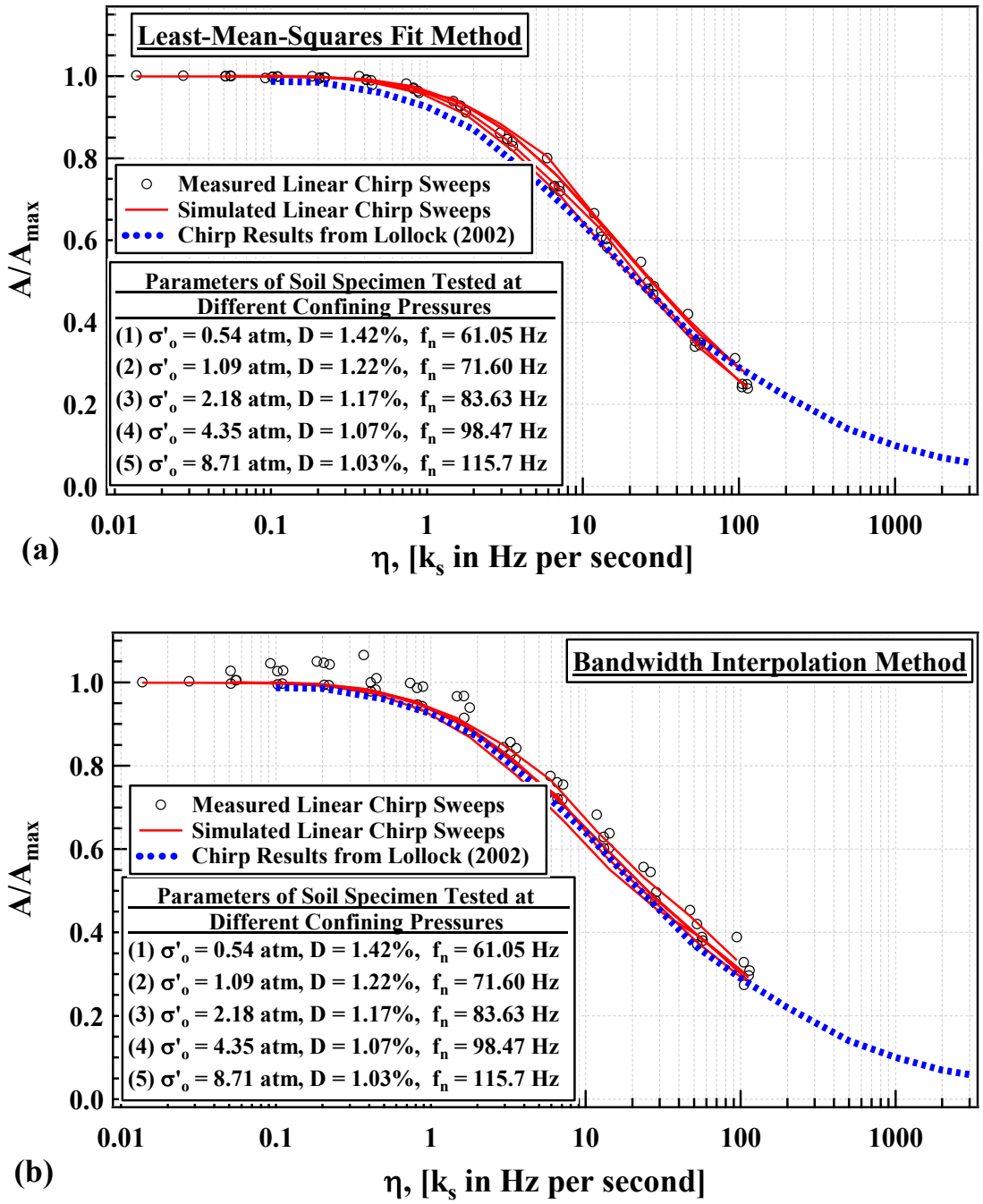

Figure 9.25: Experimental and Numerical Modeling Results Showing the Variation of the Normalized Amplitude Error (A/A_{max}) with The Non-Dimensional Sweep Rate Parameter (η) for (a) The Least-Mean-Squares Fit Method and (b) The Half-Power Bandwidth Method from Frequency Sweep Tests Using a Linear Chirp on One Soil Specimen Tested at Five Confining Pressures.

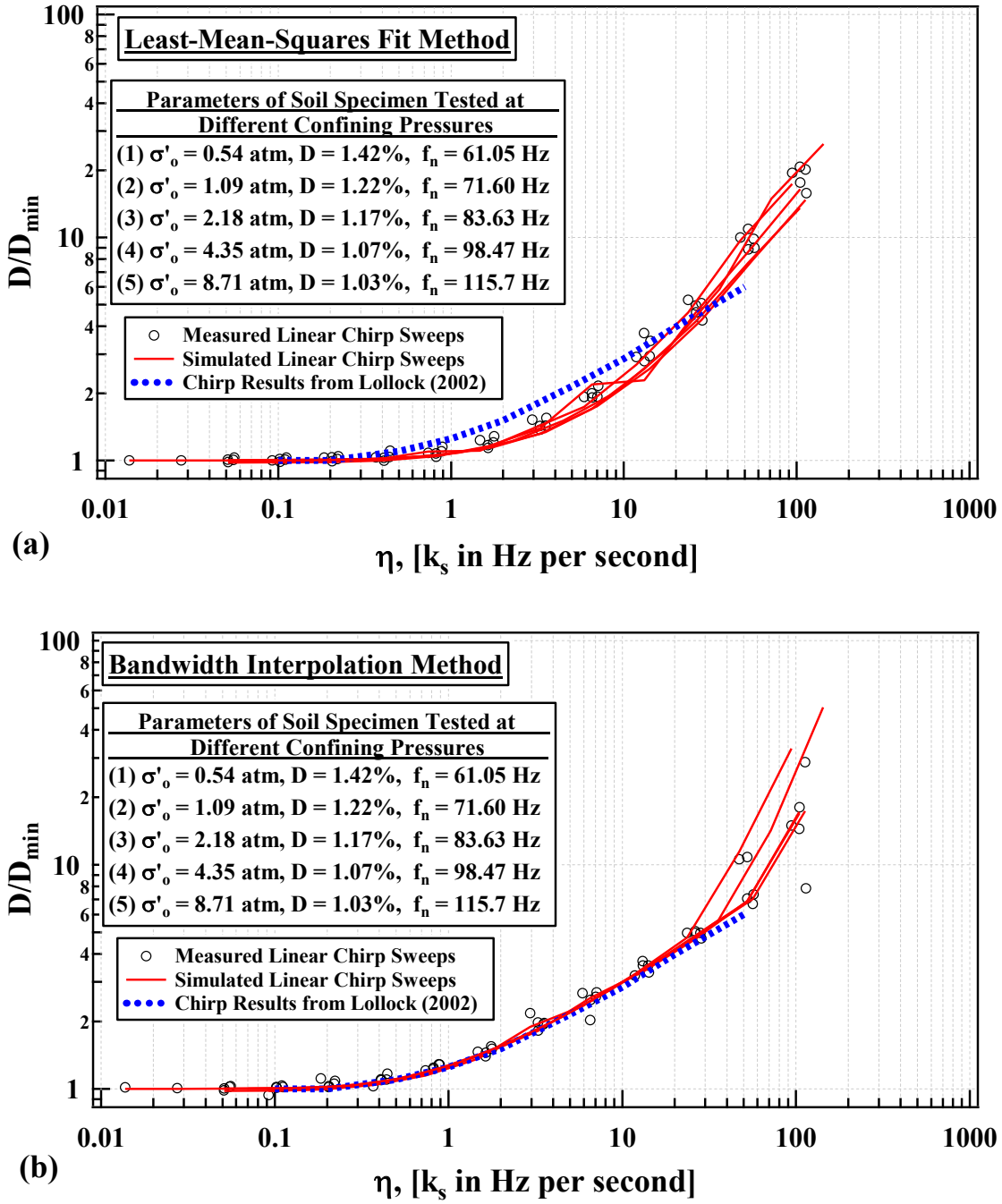

Figure 9.26: Experimental and Numerical Modeling Results Showing the Variation of the Normalized Damping Ratio Error (D/D_{min}) with The Non-Dimensional Sweep Rate Parameter (η) for (a) The Least-Mean-Squares Fit Method and (b) The Half-Power Bandwidth Method from Frequency Sweep Tests Using a Linear Chirp on One Soil Specimen Tested at Five Confining Pressures.

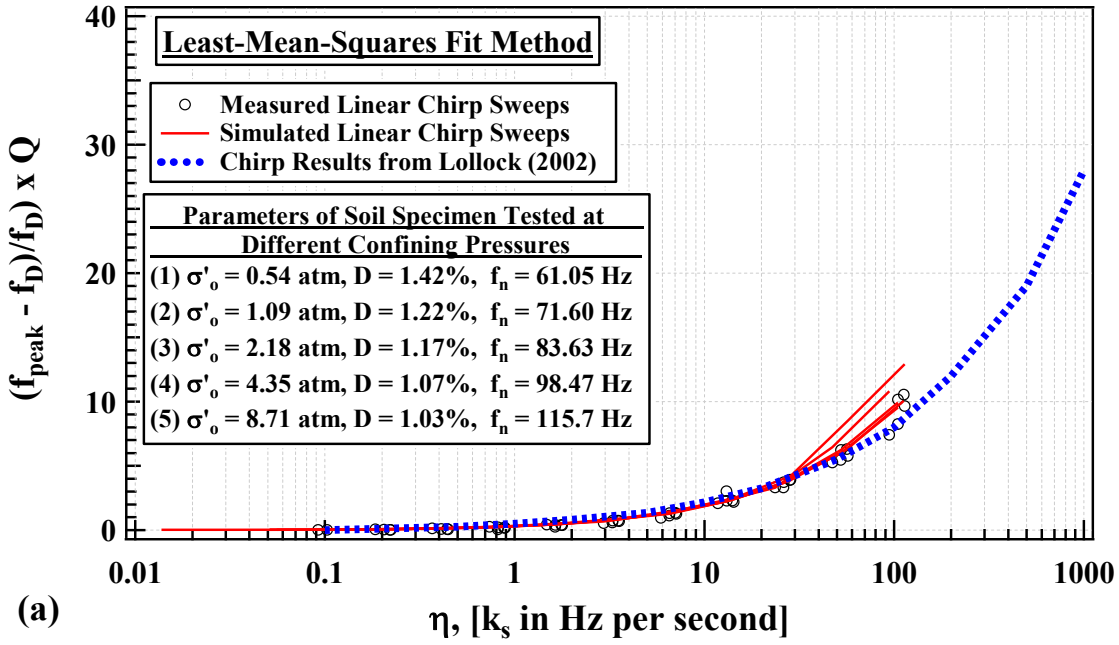

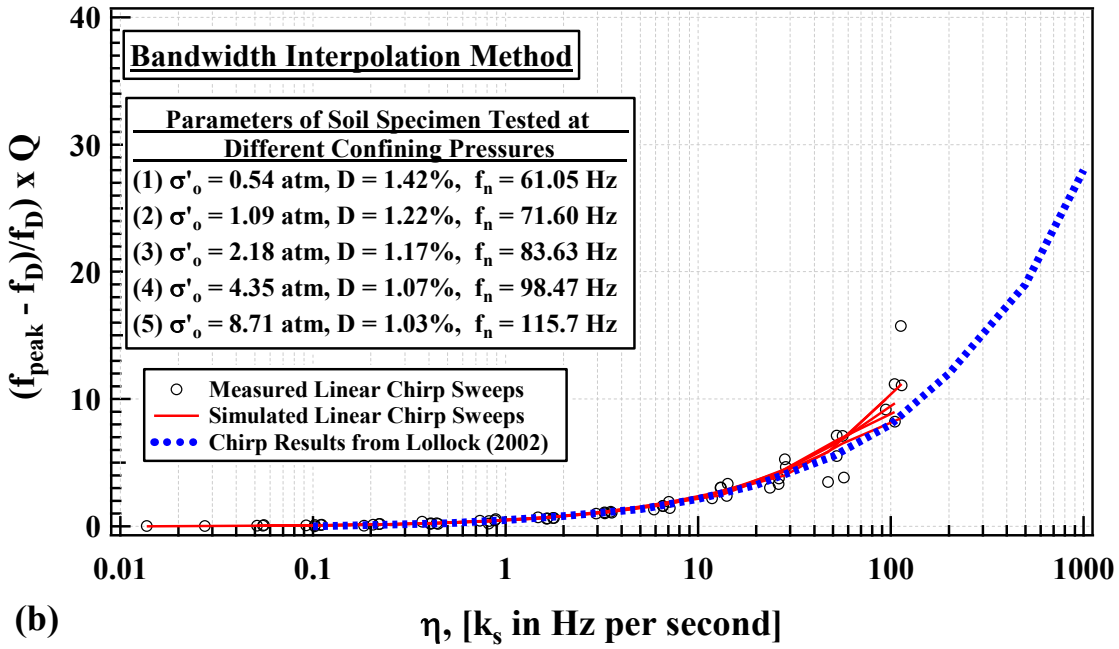

Figure 9.27: Experimental and Numerical Modeling Results Showing the Variation of the Normalized Frequency Error $[(f_{peak} - f_r)/f_r] \times Q$ with The Non-Dimensional Sweep Rate Parameter (η) for (a) The Least-Mean-Squares Fit Method and (b) The Half-Power Bandwidth Method from Frequency Sweep Tests Using a Linear Chirp on One Soil Specimen Tested at Five Confining Pressures.

9.8 APPLICATION OF THE SWEEP RATE EFFECT MODEL

The uses of the sweep rate effect model include selecting sweep rates that will yield an accurate measurements of the response of the a SDOF system being tested while knowing which sweep rates that will minimize the testing time needed to yield accurate measurements. The application of this method applies to the testing of any SDOF system, which includes, but is not limited to, laboratory testing on systems that behave as SDOF systems. The SDOF system in this study is a specimen excited in resonant column testing.

In resonant column this method has two crucial uses. The first is when conducting tests in the linear-elastic strain range of soils, where typically a rough sweep is conducted first and then a finer sweep is used to get accurate response curve properties of the specimen. In this case, a rough sweep provides enough information to use this method to determine the finer sweep rate that will yield accurate measurements of the SDOF system. The second case is when conducting tests in the nonlinear strain range where the dynamic properties are sensitive to the number of cycles used when exciting the system, this method provides faster sweep rates in response to the increase of the material damping ratio at higher shearing strains. Though this method is based on a linear system, this allows a basis for which the number of cycles can be reduced and the frequency step increased. At this time there is no method available that can recommend less cycles per frequency step and larger frequency steps for nonlinear SDOF systems. In any case, since the method is based on a linear system, the cycles per frequency step and size of the frequency step will always be a conservative estimate for what to use to get the accurate nonlinear response curve. Finally, this method will limit an over-conservative excitation of the number of cycles per frequency step and size of the frequency step, which can lead to cyclic degradation of the soil specimen.

This method can also be used for accurately calibrating sensors. Sensors used for dynamic measurements are often calibrated using frequency sweeps and this method allows an easy prediction of the minimum stepped-sine sweep rate needed to conduct an accurate calibration. Some sensors are calibrated through their resonant frequency (e.g. velocity transducers) and this method easily provides optimum sweep rates for calibration of these sensors.

For this section, the implementation of this method on a nonlinear SDOF system is not presented along with a demonstration of its use, because this is covered in other works. However, the implementation of this method for first conducting a rough sweep and then determining the fine sweep rate is explained.

In general, most materials tested in the resonant column device used in this study have resonant frequencies that range from 10 Hz to 200 Hz and damping ratios (at shear strains less than 0.001%) that range from 0.5% to 5%. For the most extreme case of a SDOF with a f_n of 10 Hz and damping ratio of 0.5%, using a f_{step} of 0.25 Hz and C_s of 10 will achieve an A/A_{max} of 0.5 and D/D_{min} of 3.8. This leads to predicted SDOF parameters of f_n = 8.68 Hz and D = 1.9%. Consequently, a larger sweep range will be used when sweeping a second time because the measured damping ratio is higher than the true damping ratio. This will yield very accurate results when a more refined sweep is conducted. Since most materials tested in the resonant column device will have much higher damping ratios at lower natural frequencies, a default sweep rate with f_{step} of 0.25 Hz and C_s of 10 is acceptable for rough sweeps conducted in this device.

Once a rough sweep is conducted, to gain an estimate of the response curve parameters, f_n and D, the hyperbolic equation developed in this study can be reconfigured to select sweep rate parameters that lead to an accurate test of the SDOF system. The reconfigured hyperbolic equation is given as:

$$\frac{f_{step}}{C_s} = 4f_n D^2 \eta_{ref,a} \times 10^{\left[\frac{\log(A_{max}/A-1)}{a}\right]} \quad (9.16)$$

After conducting the rough sweep, conservative inputs should be used in this equation so that an accurate sweep rate is used. The recommended inputs are A/A_{max} = 0.998 and $f_{step} = D * f_r/10$, which aims to populate the response curve with 20 points between the half-power points. Then the corresponding number of cycles per frequency step, C_s is calculated. In general, this leads to a non-dimensional sweep rate parameter, η below 0.1, which is very suitable for accurately testing a SDOF system. The above formulation can also be used for either the damping model or the frequency model.

A demonstration of this method involved a test on a SDOF system with f_n = 150.945 Hz and D = 0.288%. First, a rough sweep with f_{step} of 0.25 Hz and C_s of 10 was used for the frequency sweep. Second, the equations and recommended inputs discussed subsequently were used to conduct a refined frequency sweep. Third, the method was repeated to conduct an even more refined sweep and the results are compared with the results from the second step. The results of this demonstration are shown in

Table 9.7.

Based on the demonstration of the SDOF system with f_n = 150.945 Hz and D = 0.288%, there was minimal improvement of the results from the Recommended Test 1 to the results of the Recommended Test 2. The percent differences in measured f_n, D, and A/A_{max} are well within the degree of accuracy desired and(or) within a general margin of error for the testing equipment.

Table 9.7: A demonstration of this method involved a test on a SDOF system with f_n = 150.945 Hz and D = 0.288%. First, a rough sweep with f_{step} of 0.25 Hz and C_S of 10 was used for the frequency sweep. Second, the equations and recommended inputs discussed subsequently were used to conduct a refined frequency sweep. Third, the method was repeated to conduct an even more refined sweep and the results are compared with the results from the second step.

	$f_{step}^{(1)}$	$C_s^{(1)}$	$f_n^{(2)}$	$A/A_{max}^{(2,4)}$	$D^{(2)}$	$\eta^{(2)}$	$f_{step}^{(3)}$	$C_s^{(3)}$	$\eta^{(3)}$
Initial Test	0.25	10	150.030	0.7928	0.454	4.994	0.0284	40.38	0.057
Test 1	0.028	41	150.937	1.0018	0.289	0.136	0.0181	63.09	0.057
Test 2	0.018	64	150.945	1.0000	0.288	0.056	0.0180	63.28	0.057
% Diff between Tests 1 and 2	-	-	0.0053%	0.183%	0.299%	-	-	-	-

Notes:
1. Inputs used in the frequency sweep.
2. Results of the frequency sweep.
3. Recommended values for preceding frequency sweep.
4. A/A_{max} of 0.998 was targeted for calculation of f_{step} and C_s of the preceding sweep.

9.9 SUMMARY

In this study, the fixed-free resonant column device designed by Prof. Stokoe in the mid 1970's was used to conduct various frequency sweeps on five brass metal specimens and a sand specimen subject to five isotropic confining stresses. The various frequency sweeps were conducted to determine the effect that sweep rates have on the sensitivity for determining accurate response curve of a SDOF system when using a stepped-sine sweep. Analytical simulations were conducted to both validate and compliment the experimental results. The stepped-sine sweep method has been both experimentally and analytically validated and parameterized within this study.

Logarithmic Chirp, Linear Chirp, and Stepped-Sine sweeps reduce to a singular functional relationship based on a non-dimensional sweep rate parameter, η. There is a slight difference in the functional relationship for the three sweep methods, based on the analysis method used to predict the response curve parameters (i.e. half-power method or least-mean-squares fitting method). The half-power bandwidth method evaluated in this study yields essentially the same relationships as to those modeled by Lollock (2002) and Girard and Bugeat (2004). The least-mean-squares fitting method has a similar relationship as the half-power bandwidth method; however, there is an improvement with the fitting method with regards to a reduction in false results (i.e. increased accuracy) and higher prediction potential (i.e. increased precision) when $\eta < 40$. The least-mean-squares fitting method has proven to be a stronger method when sweeping at rates that correspond to $\eta < 40$.

Logarithmic, linear, and stepped-sine sweeps methods are expected to yield the same results when normalizing with the non-dimensional sweep rate parameter developed for each type of sweep. In resonant column tests on soil and soft rock, the maximum amplitude from the sweep is used to determine the shearing strain excited in the specimen,

this study shows that the amplitude from the sweep is less sensitive than damping ratio; however, the sensitivity is at a level that suggests using a suitable sweep rate is crucial for obtaining accurate shearing strain measurements within an acceptable tolerance. This study confirms the same conclusions from Lollock (2002) and Girard and Bugeat (2004), where the resonant frequency and maximum amplitude can be determined with minor sensitivity to the sweep rate whereas the damping ratio is extremely sensitive to the sweeping rate.

This study has shown that sweeping too fast may lead to an incorrect prediction of the dynamic properties from the sweep test and would also result in using the wrong frequency for the free-vibration test. Sweeping at a rate lower than necessary leads to prolonged testing durations. In the case of testing in the nonlinear shear strain range, sweep rates too low may lead to an excessive number of cycles to be excited on a specimen, which can be detrimental. The practical model advanced in this study can be used to select sweep rates that will yield accurate measurements of a SDOF system being tested; in addition, which sweep rates will minimize the testing time needed to yield accurate results. The application of this method applies to the testing of any SDOF system, which includes, but is not limited to, laboratory testing on systems that behave as a SDOF system. This study has proven that accuracy limitations exist due to sweep rate effects and that when conducting resonant column tests, the models advanced in this study should be used to guide proper testing protocols.

Chapter 10

Chronology of a Complete Set of RCTS Tests on One Intact Specimen Covering Raw Data Through to Final Results Showing Time-Dependent, Pressure-Dependent, and Strain-Dependent Behaviors of the Soil

10.1 INTRODUCTION

In the Soil and Rock Dynamics (SRD) Laboratory at the University of Texas at Austin (UT), materials subject to combined RCTS testing are evaluated in a methodical process that involves small-strain ($\gamma < 0.0005\%$) testing at a minimum of five confining pressures and is combined with nonlinear-strain ($\gamma \geq 0.0005\%$) testing at a minimum of two confining pressures. Small-strain testing at each confining pressure is conducted from one hour to one day to determine any time-dependent material behavior (e.g. consolidation). The confinement time depends on the drainage characteristics of the soil, with the shortest times (almost 100 minutes) for granular, non-plastic soils to the longest times (one day) for high-plasticity clays. The purpose of small-strain testing with at least five confining pressures is to develop pressure-dependent relationships of shear modulus, G, shear-wave velocity, V_S, material damping ratio, D, and void ratio, e. These relationships are useful for identifying stress history (e.g. preconsolidation pressure) and provide a model for how the dynamic properties change with increasing confining pressure (i.e. change with depth). The purpose of nonlinear testing is to develop shear strain-dependent relationships of G and D. Two important indices are taken from the shear strain-dependent relationships, the first is the elastic threshold strain, γ_e, which is the strain where the material begins to behave nonlinearly and the second is the reference strain, γ_r, which is the strain where the normalized shear modulus is at 50% (i.e. $G/G_{max} = 0.5$). In general,

as the confining pressure increases the γ_e and γ_r increase. When testing with two or more confining pressures a pressure-dependent expression can also be made with γ_e and γ_r.

In this chapter, some typical time-dependent, pressure-dependent, and strain-dependent results for offshore marine clays are presented. Some of the results presented were developed in conjunction with Kottke et al. (2017). The site was in an area where the mudline was at an elevation of 17 m below the average sea level in the area. The soil specimens tested were sampled from depths of 6.9 to 130 m below the mudline and were extruded in the laboratory just before testing. Each specimen came from intact soil samples that were contained in 7.62-cm diameter, steel Shelby tubes. Reduced results from one of the offshore marine clays will be presented along with examples of signals obtained from some of the small-strain and nonlinear-strain tests. In the Soil and Rock Dynamics (SRD) Laboratory at the University of Texas at Austin (UT), the examples of the signals shown in this chapter were displayed on a flat-screen television in real-time as the RCTS tests were conducted. This real-time display provides means for quality control of the testing process. During each RC or TS test, the display of raw data is used to check that the test is running properly and qualitatively confirm the validity of the test results. Reduced results from one of the offshore marine clays will be presented along with examples of signals obtained from some of the small-strain and nonlinear-strain tests.

10.2 TYPICAL TIME-DEPENDENT AND PRESSURE-DEPENDENT RELATIONSHIPS AT SMALL STRAINS FROM RESONANT COLUMN TESTING OF SOILS

The combined resonant column and torsional shear (RCTS) testing program that is consistently followed for soil specimens consists of small-strain, RC measurements staged at five isotropic confining pressures (σ'_o), typically 0.25, 0.50, 1.0, 2.0, and 4.0 times the in-situ mean effective stress, σ'_m. Small-strain ($\gamma < 0.0005\%$) RC measurements of shear

wave velocity, V_S, shear modulus, G_{max}, and material damping ratio, D_{min}, are performed at each pressure for anywhere from a few hours to one day. The confinement time depends on the drainage characteristics of the soil, with the shortest times (almost 100 minutes) for granular, non-plastic soils to the longest times (one day) for high-plasticity clays.

For the highest confining pressure tested (441 kPa) for the Offshore Marine Clay Specimen A, each of the response curves measured from a frequency sweep during the timed tests are plotted along with the variation in G with time, as shown in Figure 10.1. The response curves are observed to shift to higher frequencies as the time after the confining pressure was changed increases. In addition, the least-mean-squares fitting method as discussed in Chapter 5 is shown to bypass the background noise present near 60 Hz. Free-vibration decay tests were conducted subsequent to each of the frequency sweep tests, but is not shown herein. The presentation of the data in Figure 10.1 shows how the dynamic behavior of a specimen with moderate-to-high plasticity changes significantly with time after the confining pressure is increased due to consolidation. The software developed in conjunction with this dissertation is programmed to track and adapt to the dynamic behavior that changes after changing the confining pressure, which can be seen by the symmetry of each response curve relative to the resonant frequency that existed during that test. Following the timed test for this Offshore Marine Clay specimen, nonlinear TS tests were conducted followed by nonlinear RC tests.

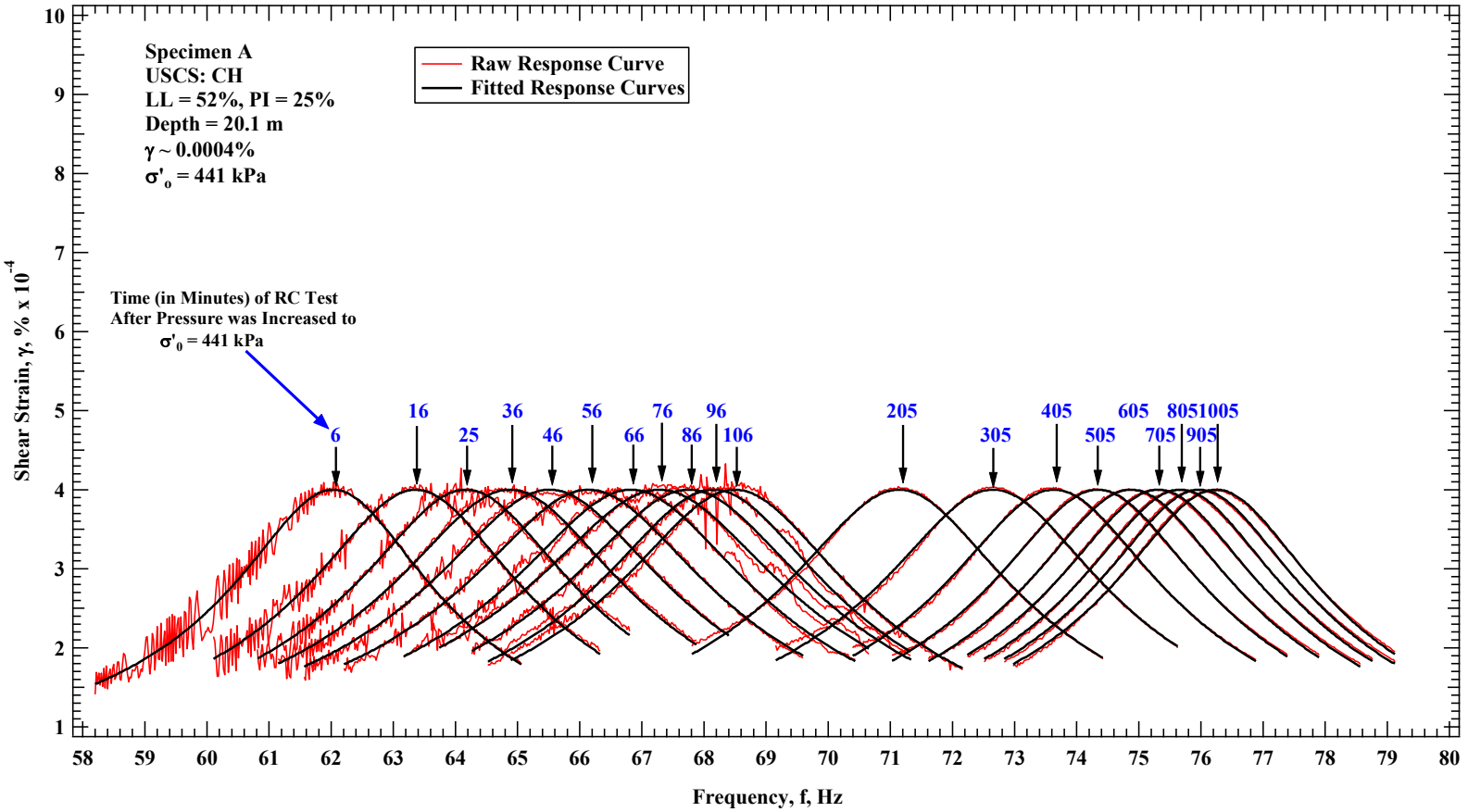

Figure 10.1: Frequency Response Curves Measured During Increasing Confinement Times at a Constant Cell Pressure for the Offshore Marine Clay Specimen A.

The small-strain results for an offshore marine clay (Specimen A) shows the variation in V_S, G_{max}, and D_{min} with time as presented in Figure 10.2 through Figure 10.4. The void ratio, e, of a specimen is also estimated at each RC measurement time, an example of these results is shown in Figure 10.5. The dynamic properties change significantly with time, which is expected for soils with plasticity. The dynamic behavior at the higher three of the five confining pressures show a more rapid change with time, which reflects the confining pressures that are above the in-situ mean effective stress. The points at the end of the timed tests are used to develop the pressure-dependent results. The variations of small-strain Vs, G_{max}, D_{min}, and e with increasing isotropic confining pressure are presented in Figure 10.6 through Figure 10.9, respectively. The relationship of Vs, G_{max}, and e with isotropic confining pressure show two trends that intersect at a specific isotropic confining pressure. This intersection is generally representative of the in-situ mean effective stress that separates over-consolidated (OC) and normally-consolidated (NC) behavior that occurs during the test. In general, D_{min} has been observed to be a less sensitive parameter when comparing OC to NC behavior in RCTS testing. The organization of Figure 10.2 through Figure 10.9 is shown in Table 10.1.

Table 10.1: Typical Time-Dependent and Pressure-Dependent Relationships at Small Strains from Resonant Column Testing of Soils That are Shown in Figure 10.2 through Figure 10.9.

	Plotted as:			**Plotted as:**
V_S-log(Time)	Figure 10.2		**V_S-log(σ'_0)**	Figure 10.6
G-log(Time)	Figure 10.3		**G-log(σ'_0)**	Figure 10.7
D-log(Time)	Figure 10.4		**D-log(σ'_0)**	Figure 10.8
e-log(Time)	Figure 10.5		**e-log(σ'_0)**	Figure 10.9

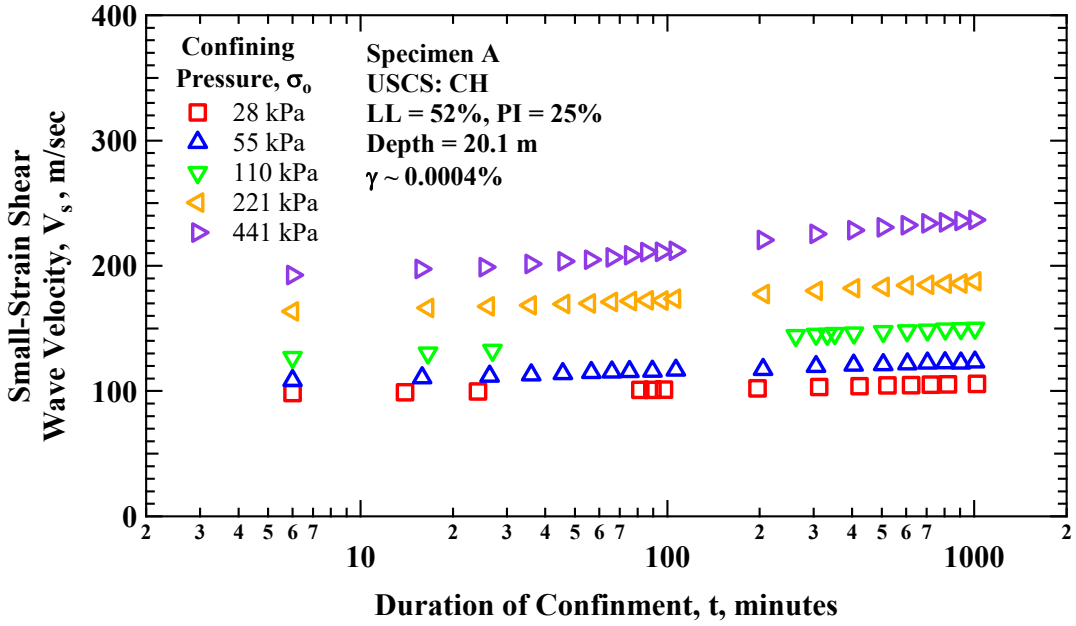

Figure 10.2: Variation in Small-Strain Shear Wave Velocity with Magnitude and Duration of Isotropic Confining Pressure from Resonant Column Testing of Specimen A.

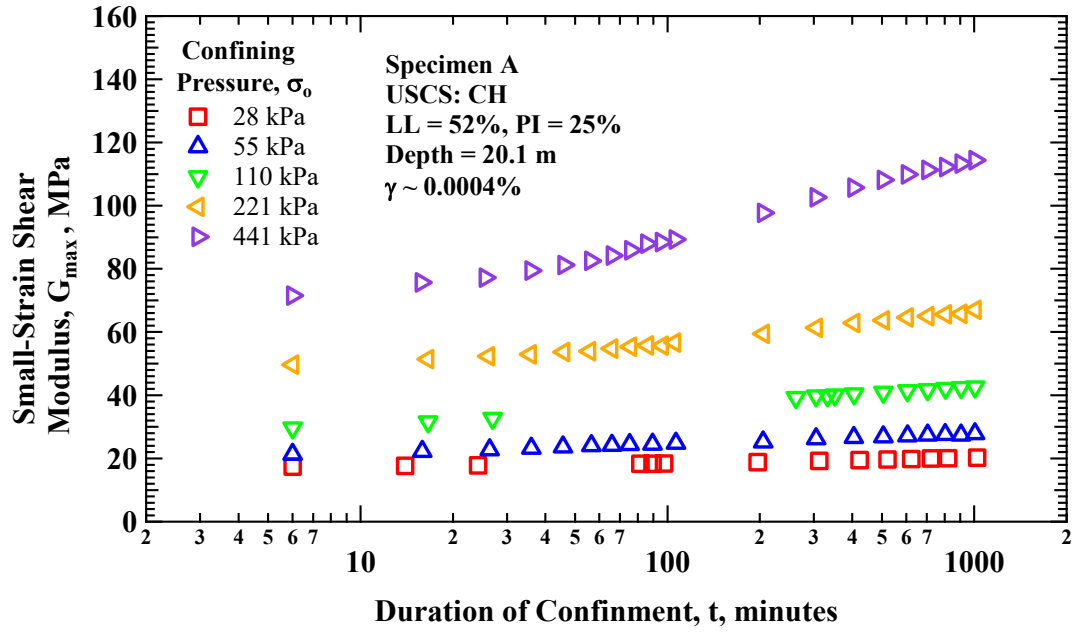

Figure 10.3: Variation in Small-Strain Shear Modulus with Magnitude and Duration of Isotropic Confining Pressure from Resonant Column Testing of Specimen A.

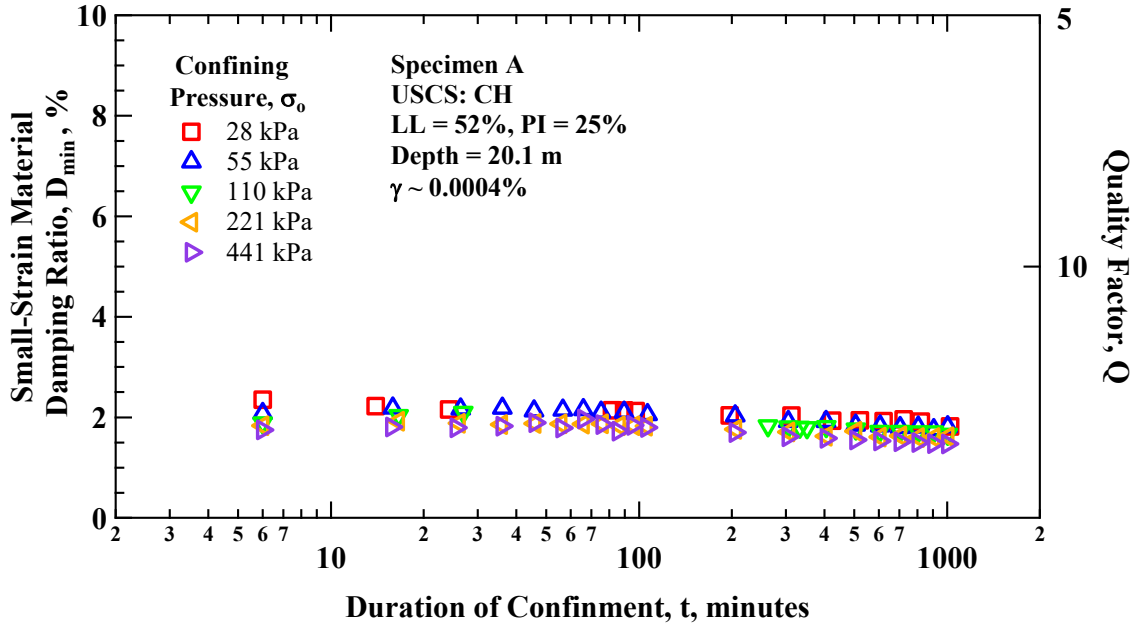

Figure 10.4: Variation in Small-Strain Material Damping Ratio with Magnitude and Duration of Isotropic Confining Pressure from Resonant Column Testing of Specimen A.

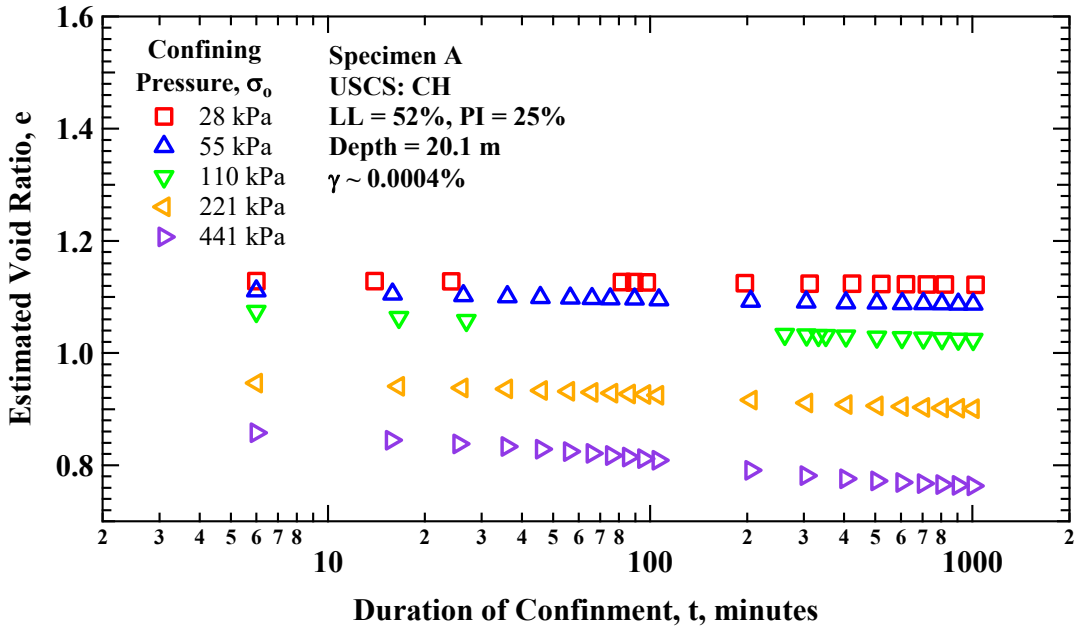

Figure 10.5: Variation in Small-Strain Estimated Void Ratio with Magnitude and Duration of Isotropic Confining Pressure from Resonant Column Testing of Specimen A.

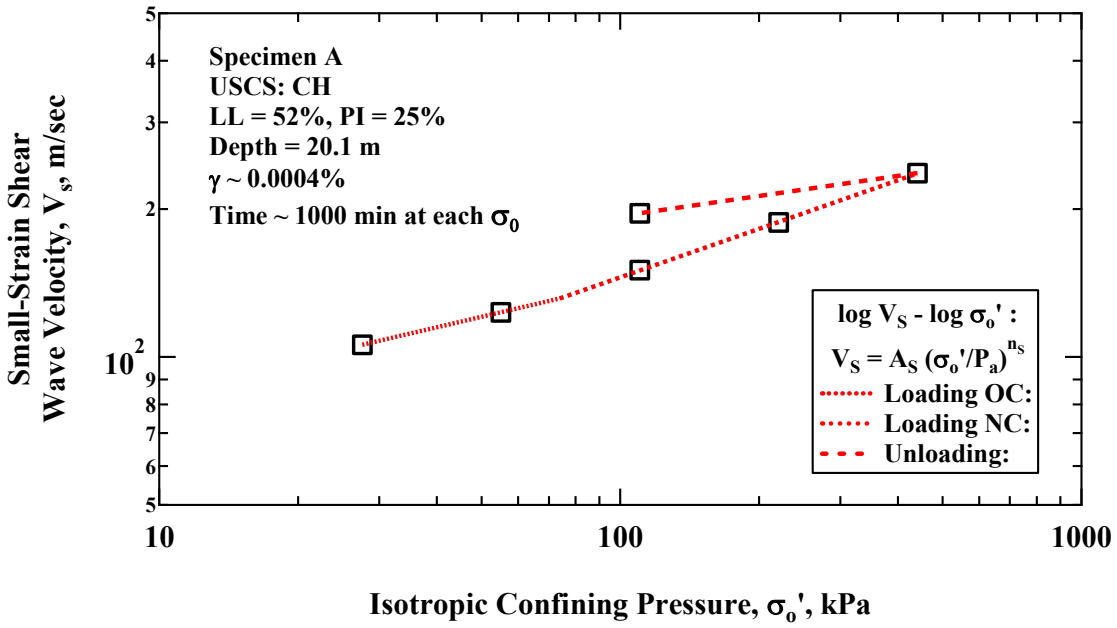

Figure 10.6: Variation in Small-Strain Shear Modulus with Magnitude and Duration of Isotropic Confining Pressure from Resonant Column Testing of Specimen D.

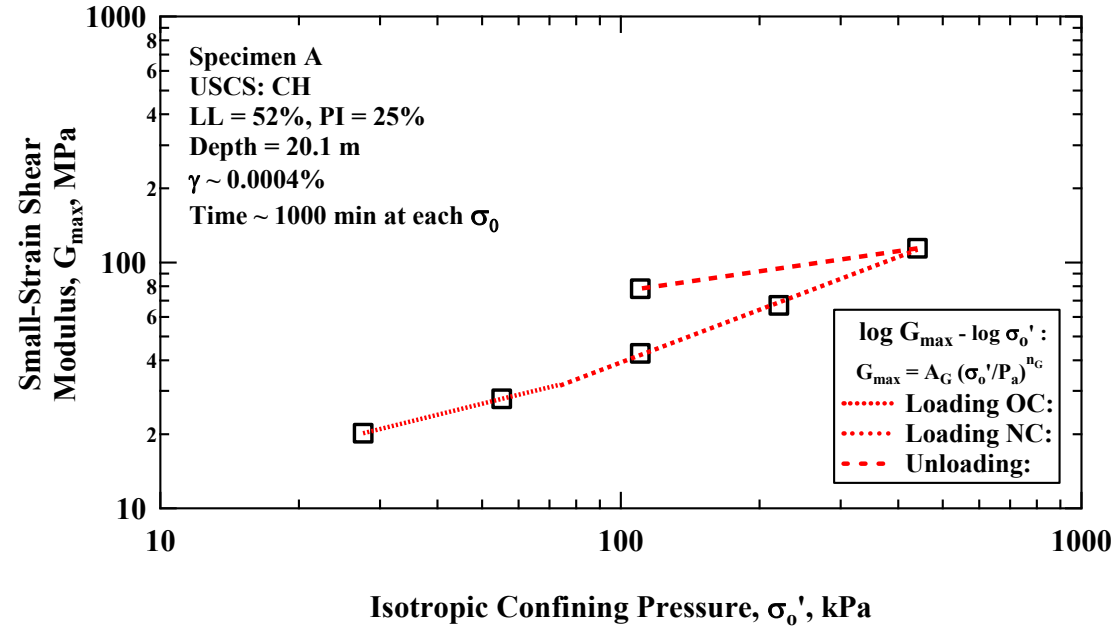

Figure 10.7: Variation in Small-Strain Shear Wave Velocity with Magnitude and Duration of Isotropic Confining Pressure from Resonant Column Testing of Specimen D.

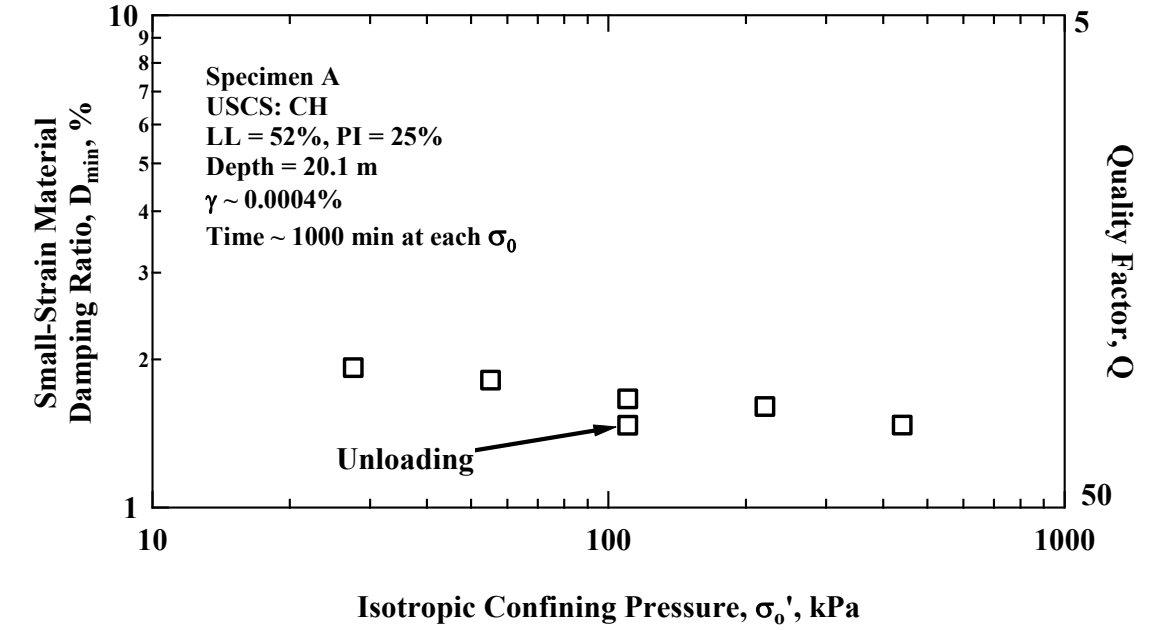

Figure 10.8: Variation in Small-Strain Material Damping Ratio with Magnitude and Duration of Isotropic Confining Pressure from Resonant Column Testing of Specimen D.

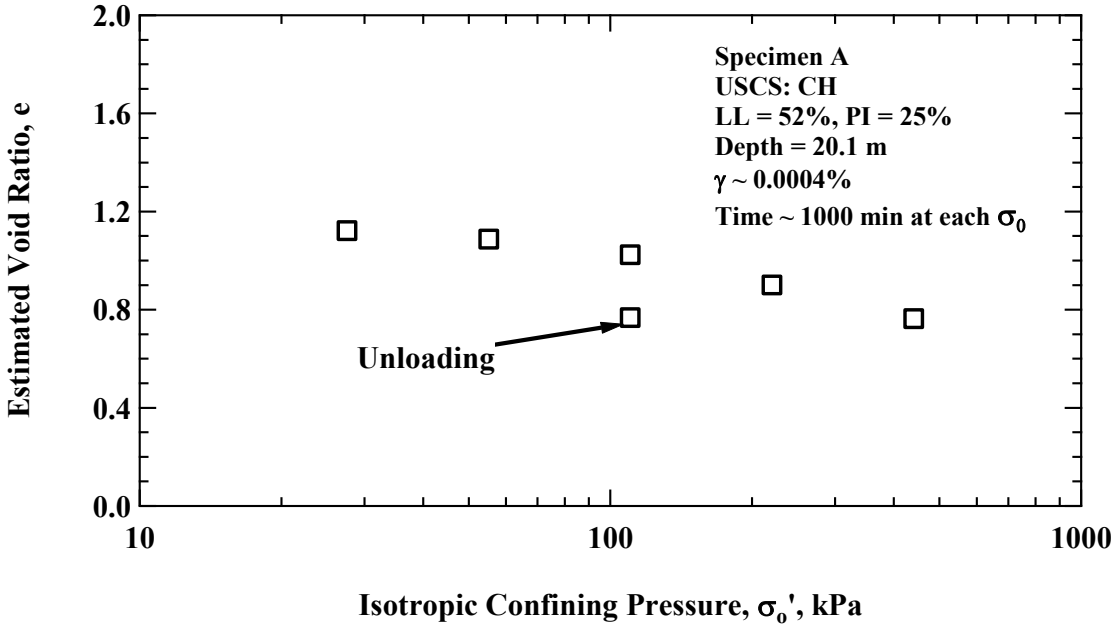

Figure 10.9: Variation in Small-Strain Estimated Void Ratio with Magnitude and Duration of Isotropic Confining Pressure from Resonant Column Testing of Specimen D.

10.3 TYPICAL STRAIN-DEPENDENT RELATIONSHIPS FROM RESONANT COLUMN AND TORSIONAL SHEAR TESTING OF SOILS

Generally, at confining pressures of 1.0 and 4.0 times σ'_m, higher-strain RC measurements of shear modulus, G, and material damping ratio, D, are also conducted. The higher-strain tests include measurements into the nonlinear range. For the offshore marine clay (Specimen A), confining pressures, σ'_0 of 0.5, 1.0, 2.0, and 4.0 were used and examples of the results from these tests in terms of G-logγ, G/G_{max}-logγ, and D-logγ are presented in Figure 10.10 (a), (b), and (c), respectively. As shown in Figure 10.10 (a), when the σ'_0 increases the shear modulus at all strains is much higher as expected. As seen in Figure 10.10 (b), as the σ'_0 increases, the shear strain amplitude increases for the same G/G_{max}. Thus, the elastic threshold and reference strain increases with increasing σ'_0. A similar relationship can be seen in Figure 10.10 (c) where the change in material damping ratio with shear strain is slightly less sensitive as the σ'_0 increases.

Cyclic torsional shear (TS) tests into the nonlinear strain range are combined with the higher-strain RC measurements of G and D to investigate the effects of frequency and number of cycles of loading on the dynamic properties. The TS measurements are performed in the low-frequency range of 0.1 to 5 Hz. The comparison of the variation in G, G/G_{max}, and D with γ at one σ'_o of 441 kPa from combined RCTS testing of the offshore marine clay (Specimen A) is shown in Figure 10.11 (a), (b), and (c), respectively. The G/G_{max}-logγ and D-logγ compare well between the RC and TS tests, which indicates that there was minimal effect of frequency and number of cycles of loading on the dynamic properties. This subsection shows some examples of the typical results that are obtained from RCTS testing. The subsequent section presents the signal data that is obtained from each RC or TS test and goes into detail about dynamic behavior that is not traditionally available or presented from RCTS testing results.

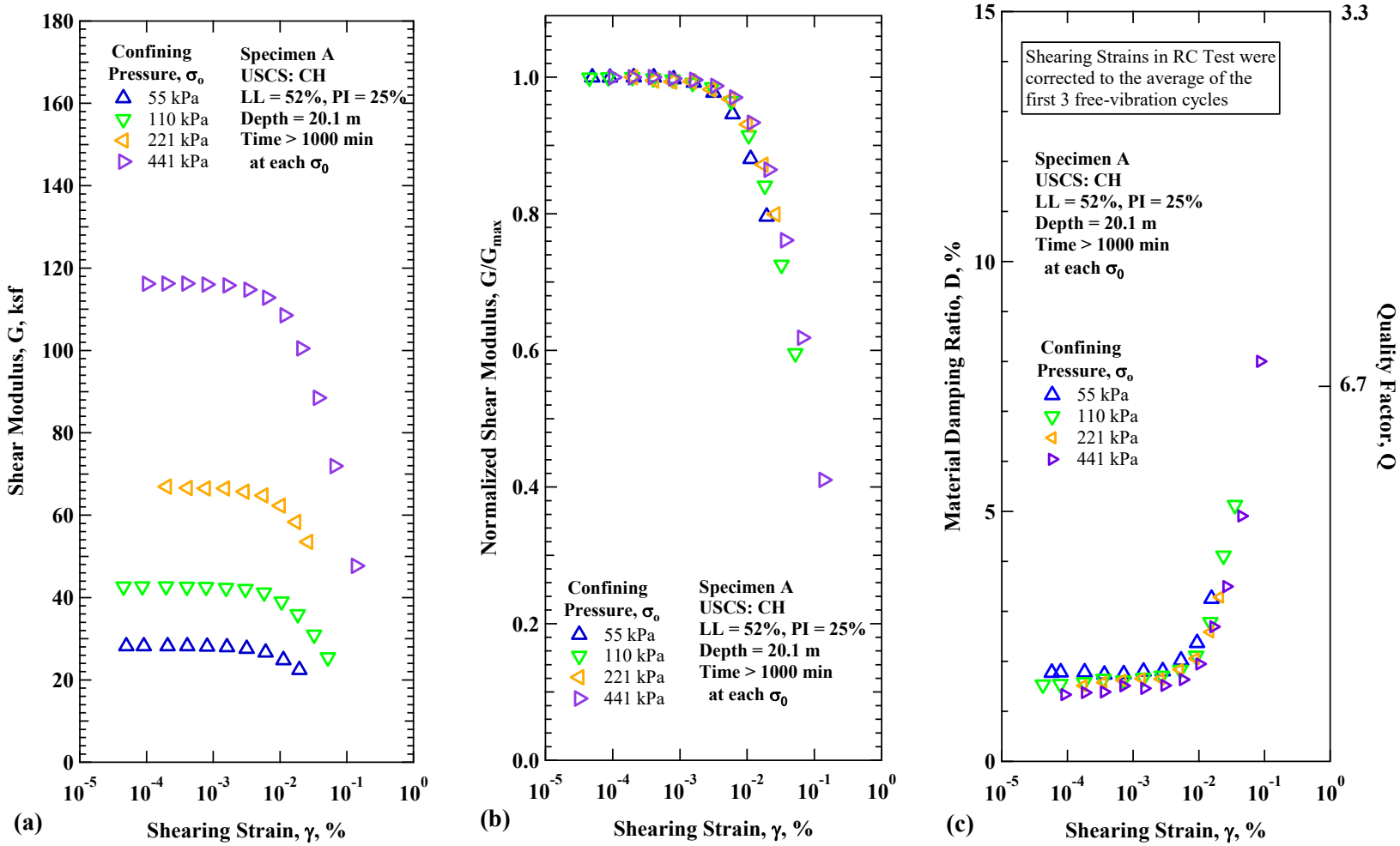

Figure 10.10: Variation in (a) Shear Modulus, (b) Normalized Shear Modulus, and (c) Material Damping Ratio with Shearing Strain at Different Isotropic Confining Pressures from Resonant Column Testing of Specimen A.

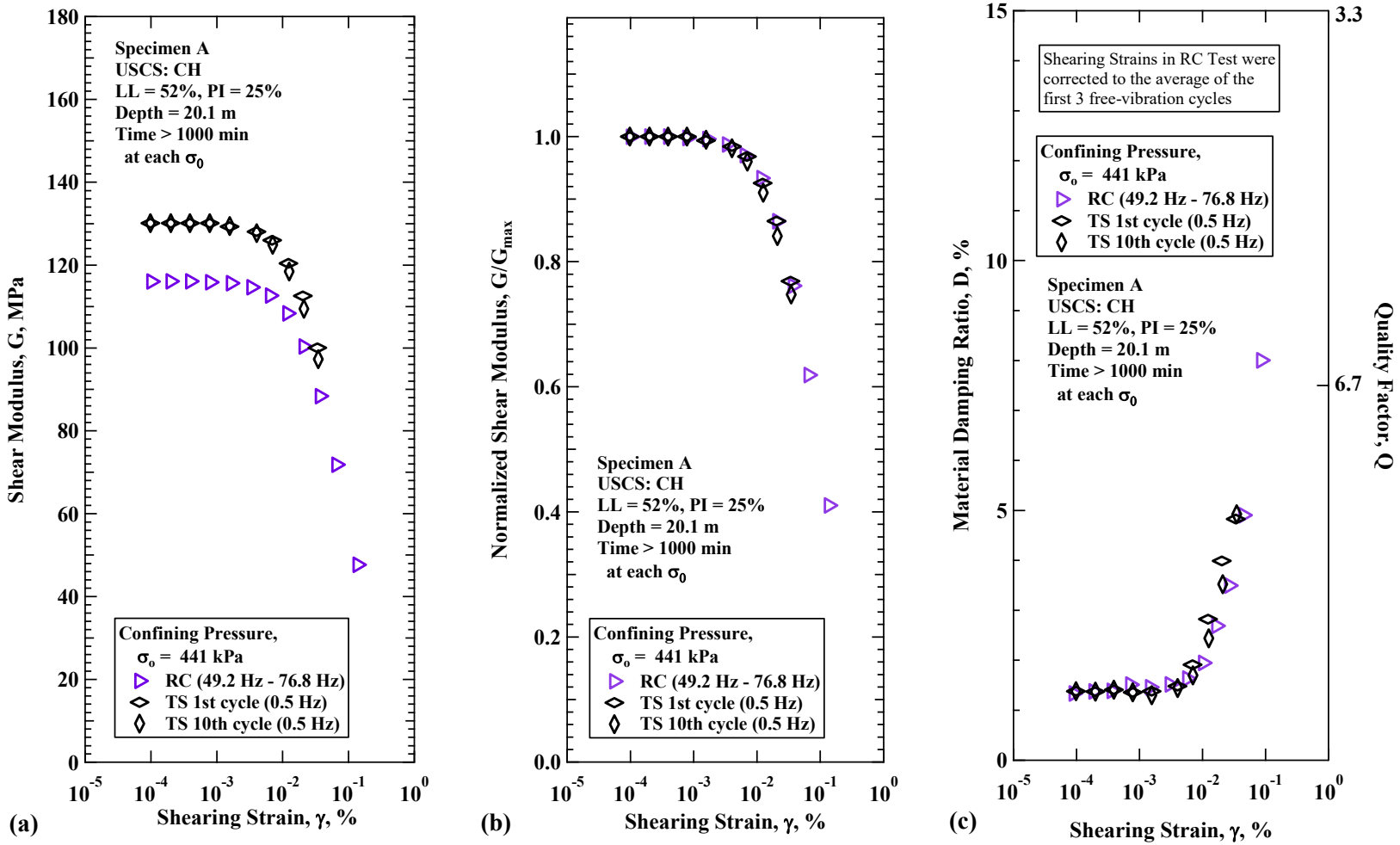

Figure 10.11: Comparison of the Variation in (a) Shear Modulus, (b) Normalized Shear Modulus, and (c) Material Damping Ratio with Shearing Strain at a Isotropic Confining Pressure of 64 psi (9.2 ksf = 441 kPa) from Combined RCTS Testing of Specimen A (Offshore Marine Clay from 20.1 m).`

10.4 SIGNAL DATA FROM TS TESTS AND NONLINEAR CYCLIC BEHAVIOR DETERMINED BY TS TESTING

The preceding subsection shows some examples of the typical time-dependent, pressure-dependent, and strain-dependent dynamics properties that are obtained from typical RCTS testing procedures in the SRD lab at UT. This section presents some examples of the signals that accompany the reduced results from RC and TS tests. Concurrently, some examples are shown that go into detail about dynamic behavior that is not traditionally available or presented from RCTS testing results.

Following the timed tests for this Offshore Marine Clay specimen, nonlinear TS tests were conducted and the signal data for each TS test is presented herein. The variation in shear modulus, G, with shear strain, γ, is presented along with some of the hysteresis loops measured, as shown in Figure 10.12. The hysteresis loops shown in Figure 10.12 are in terms of applied shear stress, τ, versus γ. Both the scales for τ and γ are doubled in each subplot from left to right to account for the increasing order of magnitude of shear strain in the TS test. The slope of the hysteresis loop decreases in each subplot from left to right, which represents the decreasing G, which is shown in the main plot with G-logγ. Within each subplot, the tip of the hysteresis loop is shown and displays that there is no effect of friction as the shear strain responds to the applied peak stress. Frictional effects can occur with other geotechnical laboratory tests, such as the cyclic triaxial (CTX) test, where friction between the piston and the cell enters into the results. The effect of friction is seen as a flattened peak at the maximum applied shear stress, where the strain remains constant (i.e. flat), but the shear stress continues as the frictional resistance between the piston and cell is measured.

The variation in hysteretic damping ratio, D, with γ is presented along with some of the hysteresis loops measured, as shown in Figure 10.13. Both the scales for τ and γ are

doubled in each subplot from left to right to account for the increasing order of magnitude of shear strain in the TS test. The area of the hysteresis loop increases in each subplot from left to right, which represents the increasing D as is shown in the main plot with D-logγ. Within each subplot, the tip of the hysteresis loop is shown and displays that the loop becomes wider near the peak, which is representative of the increasing hysteretic damping ratio with increasing shear strain. The following section presents nonlinear response curves and free-vibration decay curves from the RC tests that were conducted subsequent to the TS tests presented thus far.

Nonlinear TS tests are conducted before nonlinear RC tests for two key reasons. First, there are only 10 cycles excited, at each strain level during a TS test. Depending on the dynamic characteristics of the system (i.e. f_r and D), several hundred to over a couple thousand cycles are excited during an RC test. Exciting a large number of cycles at higher levels of strain can lead to either cyclic degradation or densification. Since the number of excitation cycles are far less during a TS test, the cumulative effects due to cycling is far less exacerbated. The second reason for conducting TS tests before RC tests pertains to the torque limitations of the RCTS device. In the RC test, the dynamic response of the system can lead to reaching shear strains several times greater than those reached in the TS test. Reaching higher strains in the RC test relative to the TS test is dependent on the viscous material damping ratio of the system, i.e. dynamic amplification of the system at resonance. The dynamic response magnification factor, M, is equal to 1/2D. For example, if the material damping ratio is 5%, the dynamic magnification in the RC test is 10 times that of the TS test. Similarly, if the material damping ratio is 20%, the dynamic magnification in the RC test is 2.5 times that of the TS test. Therefore, when the level of torque that can be generated is limited, the RC test reaches higher strains because of the dynamic amplification of the system at resonance.

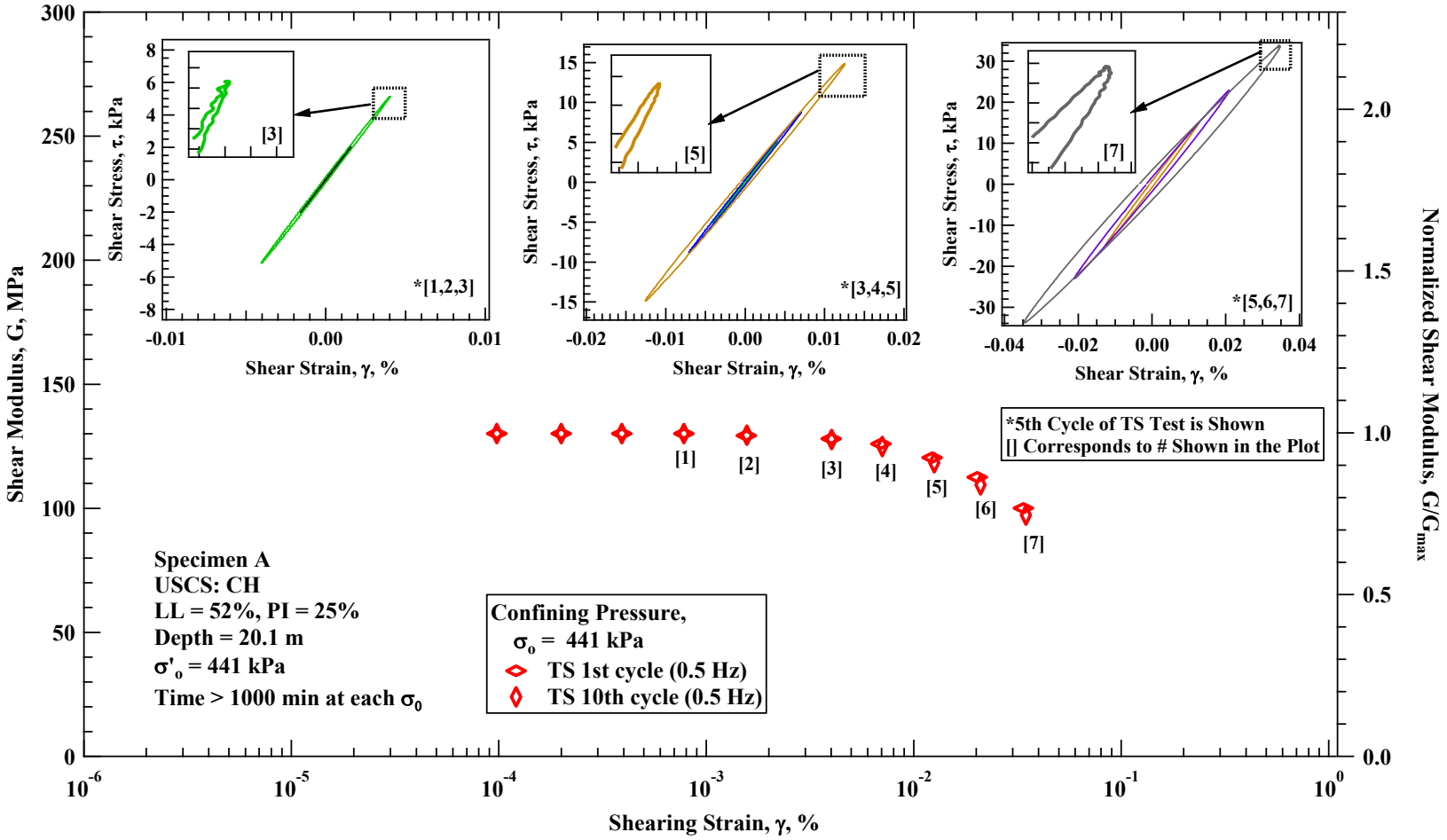

Figure 10.12: Variation in Shear Modulus with Shear Strain Presented Along with Some of the Hysteresis Loops Measured for the Offshore Marine Clay Specimen A at a Isotropic Confining Pressure of 441 kPa; measurements performed by TS Testing.

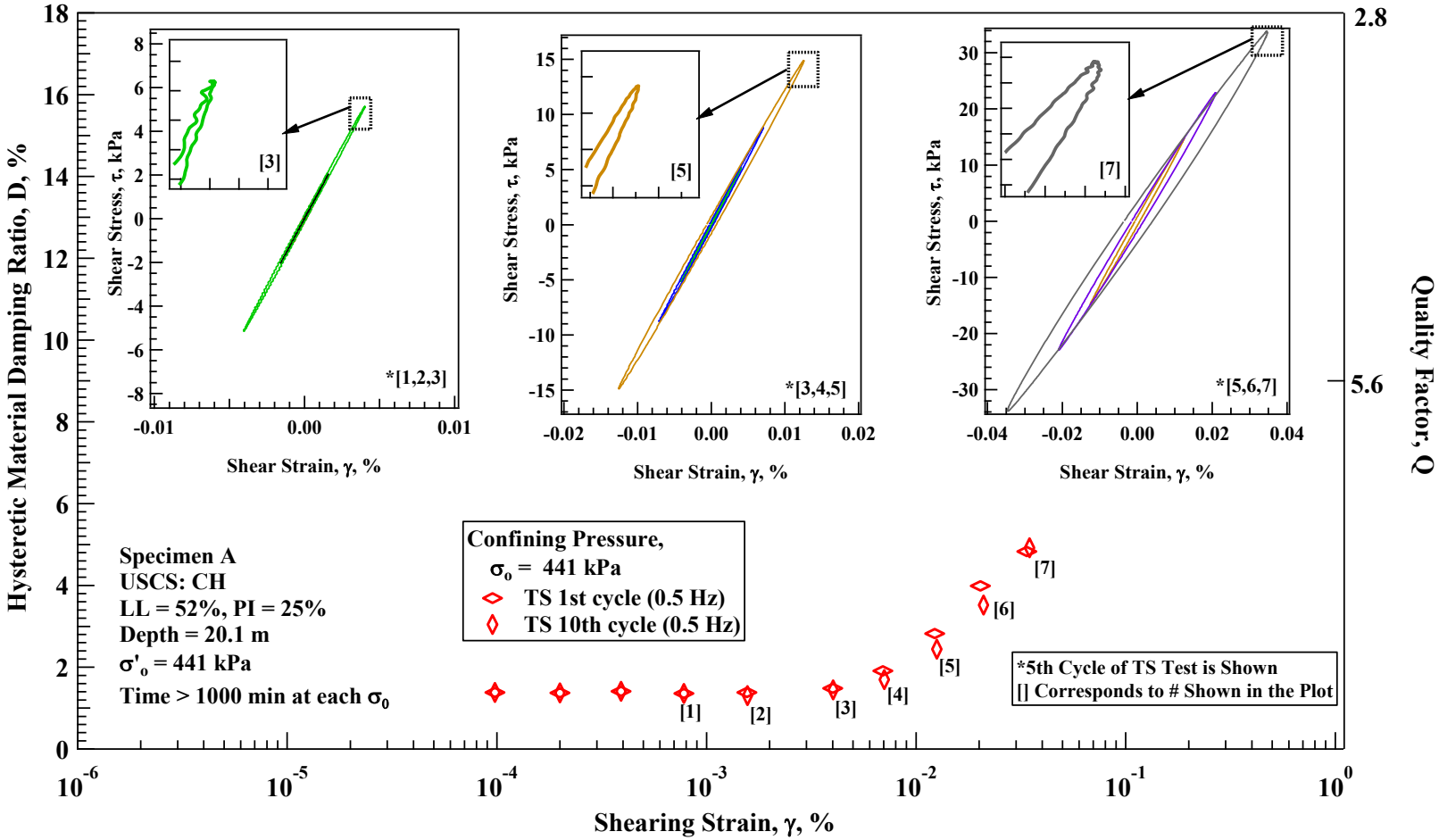

Figure 10.13: Variation in Material Damping Ratio with Shear Strain Presented Along with Some of the Hysteresis Loops Measured for the Offshore Marine Clay Specimen A at a Isotropic Confining Pressure of 441 kPa; measurements performed by TS Testing.

10.5 SIGNAL DATA FROM RC TESTS AND NONLINEAR CYCLIC BEHAVIOR DETERMINED BY RC TESTING

Following the TS tests for this Offshore Marine Clay specimen, nonlinear RC tests were conducted and the signal data for each RC test is presented herein. The response curves are presented with the reduced shear modulus results and the free-vibration response curves are presented with the reduced material damping ratio results. The variation in shear modulus, G, with shear strain, γ, is presented along with some of the response curves measured, as shown in Figure 10.14. The response curves shown in Figure 10.14 are in terms of shear strain, γ, versus excitation frequency, f. The maximum value of γ for the vertical scale is multiplied by a factor of 6.5 in each subplot from left to right to account for the increasing order of magnitude of shear strain excited in the frequency sweep. The minimum f for the horizontal scale is decreased in each subplot from left to right to accommodate the larger range of excitation frequencies required in the frequency sweep to evaluate the nonlinear response curves. The magnitude of the response curves increase in each subplot from left to right, which represents the decreasing G as is shown in the main plot with G-logγ. The response curves widen with increasing shear strain, which represents the increasing material damping ratio with shear strain. The response curves tilt towards lower frequencies and become increasingly non-symmetric with increasing shear strain, which represents the increasing nonlinear dynamic behavior with increasing shear strain.

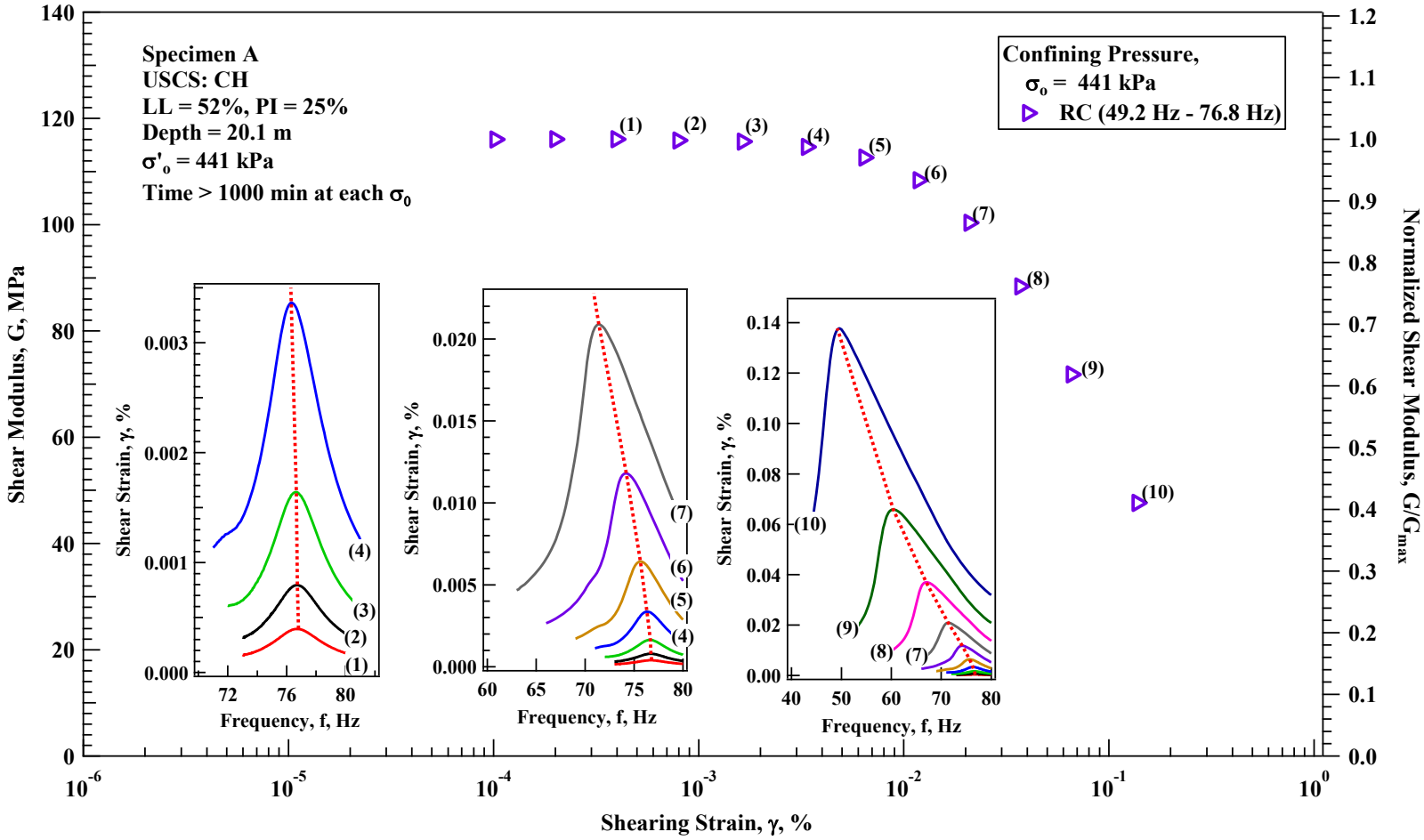

Figure 10.14: Variation in Shear Modulus with Shear Strain Presented with Some of the Response Curves Measured From Frequency Sweep Tests on Offshore Marine Clay Specimen A at a Isotropic Confining Pressure of 441 kPa.

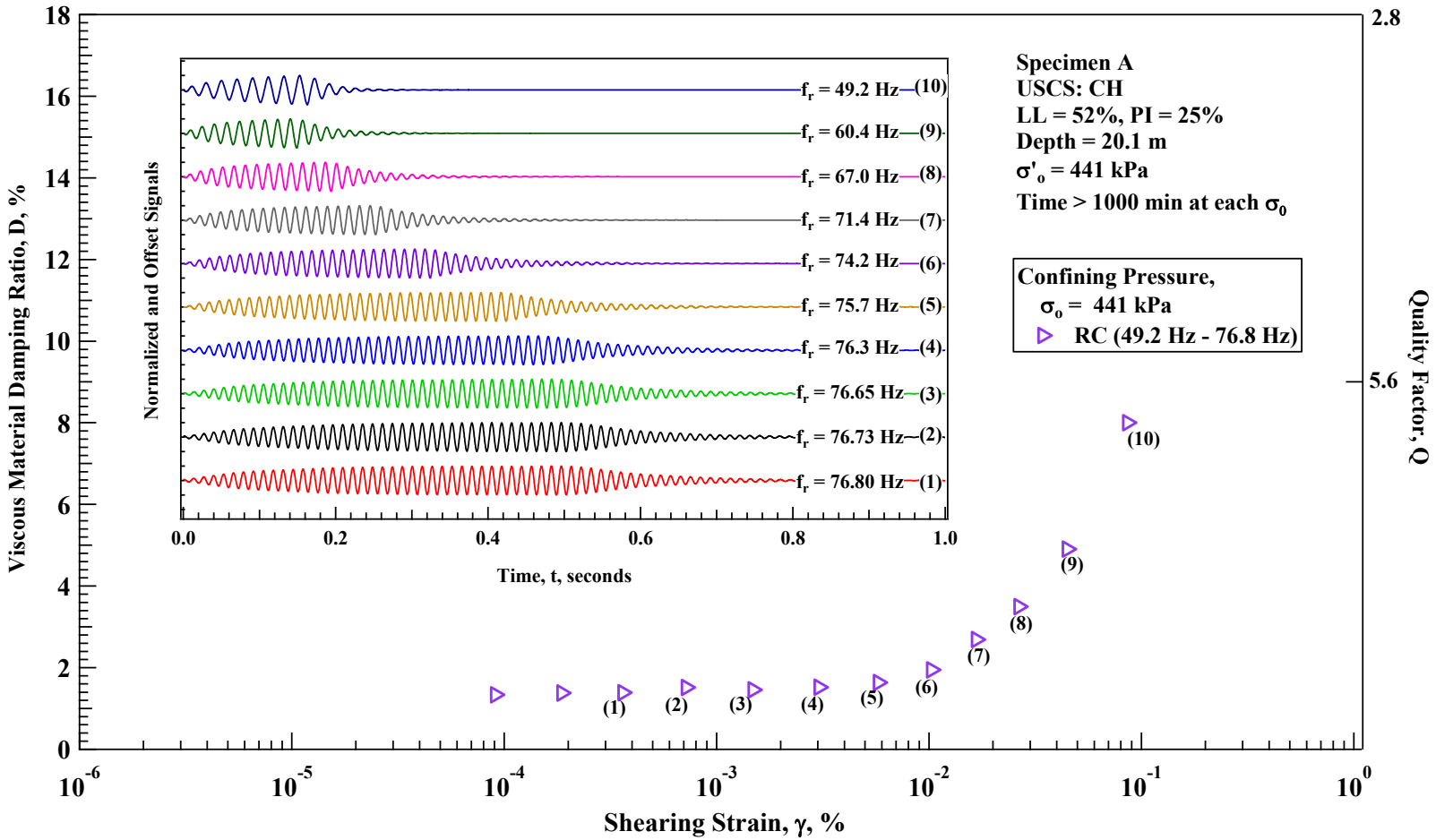

Figure 10.15: Variation in Material Damping Ratio with Shear Strain Presented Along with Some of the Free-Vibration Decay Curves Measured for the Offshore Marine Clay Specimen A at a Isotropic Confining Pressure of 441 kPa.

The variation in viscous material damping ratio, D, with γ is presented along with some of the free-vibration decay waveforms measured, as shown in Figure 10.15. Each of the free-vibration decay waveforms are normalized and are offset in the order of increasing material damping ratio. The number of cycles required to reach steady-state vibration and subsequent cycles of free-vibration decrease as shearing strain increases, which represents the increasing material damping ratio. In addition, the resonant frequency (used for forced-vibration) and damped natural frequency (that occurs during free-vibration) decrease, which corresponds to the decreasing resonant frequency as shown in Figure 10.14.

The preceding segments of this subsection presents the nonlinear behavior of an Offshore Marine Clay in both RC and TS tests. In the TS tests, hysteresis loops were presented with the reduced G-logγ and D-logγ results over the full range of shear strains excited during the test. In the RC tests response curves and free-vibration decay curves were presented with the reduced G-logγ and D-logγ results over the full range of shear strains excited during the test, respectively. The RC and TS tests are considerably different based the theoretical underpinning of each test. However, despite the difference in the testing methodologies, as was shown earlier in this subsection, these two tests compare well. The reduced results of these tests are compared together along with the signal data obtained from each test. The G-logγ and D-logγ results for both RC and TS tests are presented together in Figure 10.16 and Figure 10.17, respectively. The following subsection focuses on additional geometric behavior (i.e. contraction and dilation behavior) that occurs during the frequency sweep testes when nonlinear shear strains are excited.

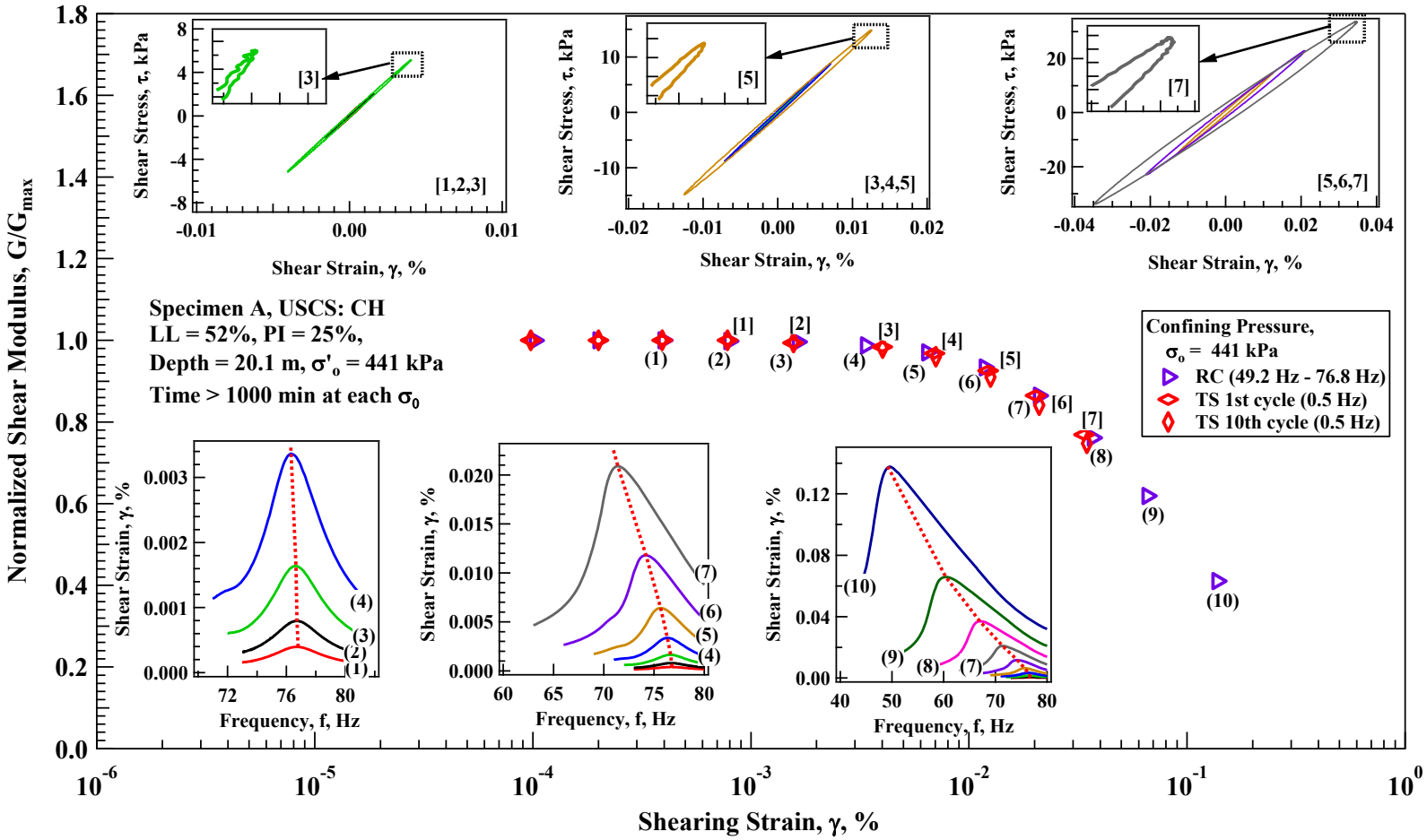

Figure 10.16: Variation in Shear Modulus with Shear Strain Presented Along with Some of the Response Curves Measured for the Offshore Marine Clay Specimen A at a Isotropic Confining Pressure of 441 kPa.

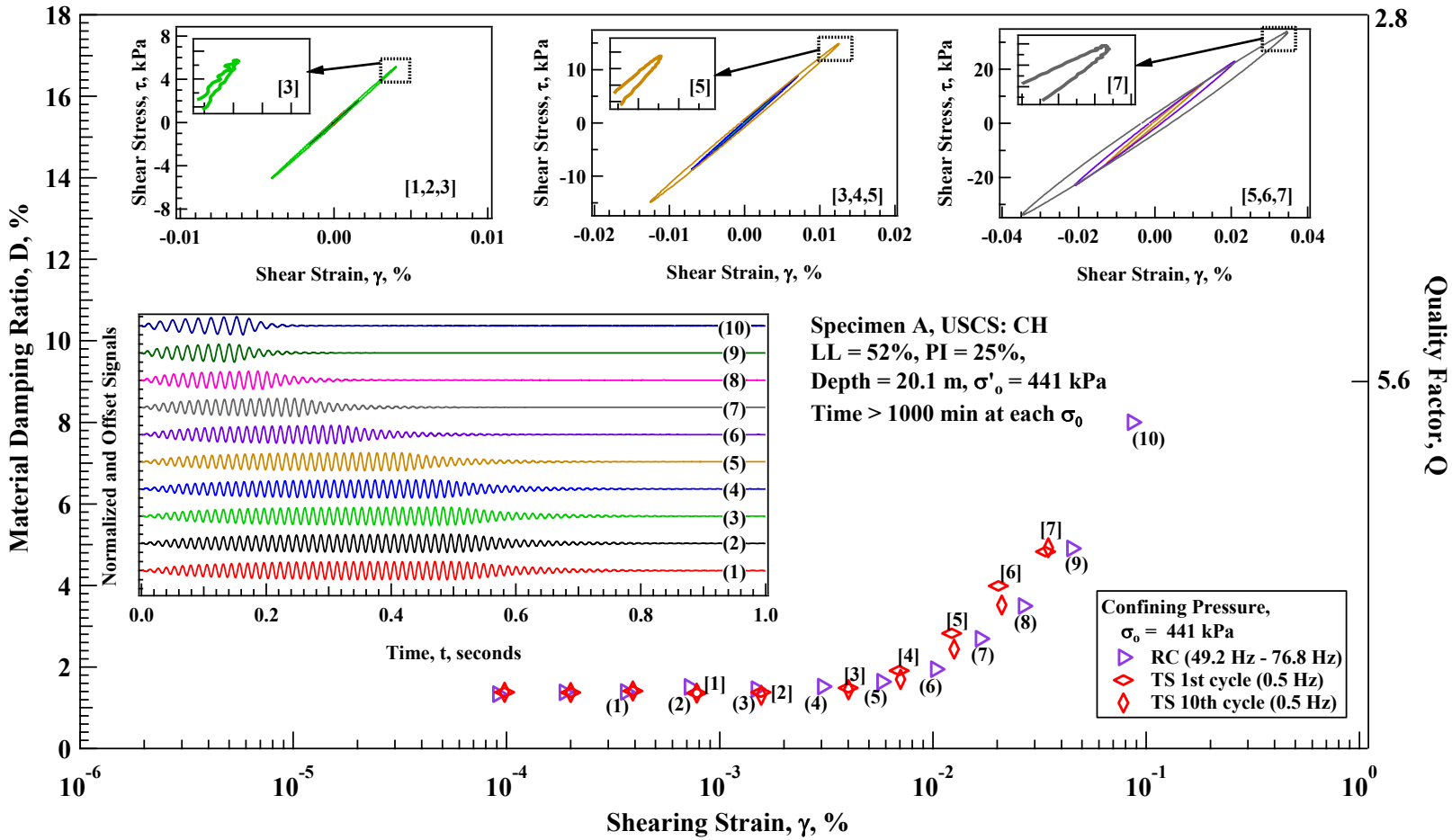

Figure 10.17: Variation in Material Damping Ratio with Shear Strain Presented Along with Some of the Free-Vibration Decay Curves Measured for the Offshore Marine Clay Specimen A at a Isotropic Confining Pressure of 441 kPa.

10.6 SUMMARY

In the Soil and Rock Dynamics (SRD) Laboratory at the University of Texas at Austin (UT), materials subjected to combined RCTS testing are evaluated in a methodical process that involves small-strain ($\gamma < 0.0005\%$) testing at a minimum of five confining pressures in an increasing pressure sequence combined with nonlinear-strain ($\gamma \geq 0.0005\%$) testing at a minimum of two confining pressures as a part of the increasing pressure sequence. Typically, the nonlinear-strain testing is performed at confining pressures of 1.0 and 4.0 times σ'_m. In this chapter, typical pressure-dependent and strain-dependent results for an offshore marine clay are presented. The examples of the signals shown in this chapter were displayed on a flat-screen television in real-time as the RCTS tests were conducted. The real-time display provides a means of quality control in real-time during the testing process. The real-time displays of raw data allows the operator to check that the test is running properly and qualitatively confirm the validity of the test results.

In traditional RCTS testing systems, the ability to save signal results from each RC or TS test was not available due to computer memory limitations. Signals could only be reduced to tabulated results and the signals were then overwritten by subsequent tests. With the steep advance in computer power and memory availability, saving signals from each test is no longer an issue. This database allows for more advanced analysis of the dynamic behavior of soils as is discussed in the preceding chapters.

Chapter 11

Potential for Improved Understanding of Material Behavior by Height Change Measurements During Cyclic and Resonant Torsional Testing

11.1 INTRODUCTION

In traditional RCTS testing systems, the ability to save signal results from each RC or TS test was not available due to computer memory limitations. Signals could only be reduced to tabulated results and the signals were then overwritten by subsequent tests. With the steep advance in computer power and memory availability, saving signals from each test is no longer an issue. The software developed in conjunction with this dissertation stores results from each RC and TS test conducted. During the development of this dissertation, a cache of results has been stored for over 100 specimens that have been tested over the past 4 years. This database allows for more advanced analysis of the dynamic behavior of soils. The purpose of presenting the signals that correspond with the small-strain and nonlinear-strain test results is to provide a more detailed and informative perspective into the dynamic behavior of soils during RC testing. The more detailed perspective presented in this chapter prefaces the subsequent chapter where nonlinear behavior in the RC tests is quantitatively examined and modeled.

11.2 ADDITIONAL ASPECTS OF NONLINEAR BEHAVIOR DURING RC TESTING

Traditionally the reduced results from the frequency sweep and free-vibration tests were considered. In this subsection additional plots are presented that shown the signals acquired during the RC tests along with the reduced data. The examples in this subsection are shown for another Offshore Marine Clay, which includes results from Specimen B that was sampled from a depth of 46 m. The variation in normalized shear modulus with shear

strain and some of the response curves measured for the Offshore Marine Clay Specimen B at a isotropic confining pressure of 992 kPa are shown in Figure 11.1 (a) and (b), respectively. The variation in material damping ratio with shear strain and some of the free-vibration decay curves measured for the Offshore Marine Clay Specimen B at a isotropic confining pressure of 992 kPa are shown in Figure 11.2 (a) and (b), respectively.

As discussed previously, the characteristics of the test signals represent the reduced results with regards to the frequency sweep signals and free-vibration decay signals. The resonant frequency of the response curves decreases with increasing shear strain, γ, which represents the decreasing shear modulus, G, with increasing γ as shown in Figure 11.1. The response curves widen with increasing γ, which represents the increasing material damping ratio, D, with γ. The response curves tilt towards lower frequencies and become increasingly non-symmetric with increasing shear strain, which represents the increasing nonlinear dynamic behavior with increasing shear strain. The variation in D with γ is presented along with some of the free-vibration decay waveforms measured, as shown in Figure 11.2. The number of cycles required to reach steady-state vibration and subsequent cycles of free-vibration decrease as shearing strain increases, which represents the increasing material damping ratio. In addition, the resonant frequency (used for forced-vibration) and damped natural frequency (that occurs during free-vibration) decrease, which corresponds to the decreasing resonant frequency.

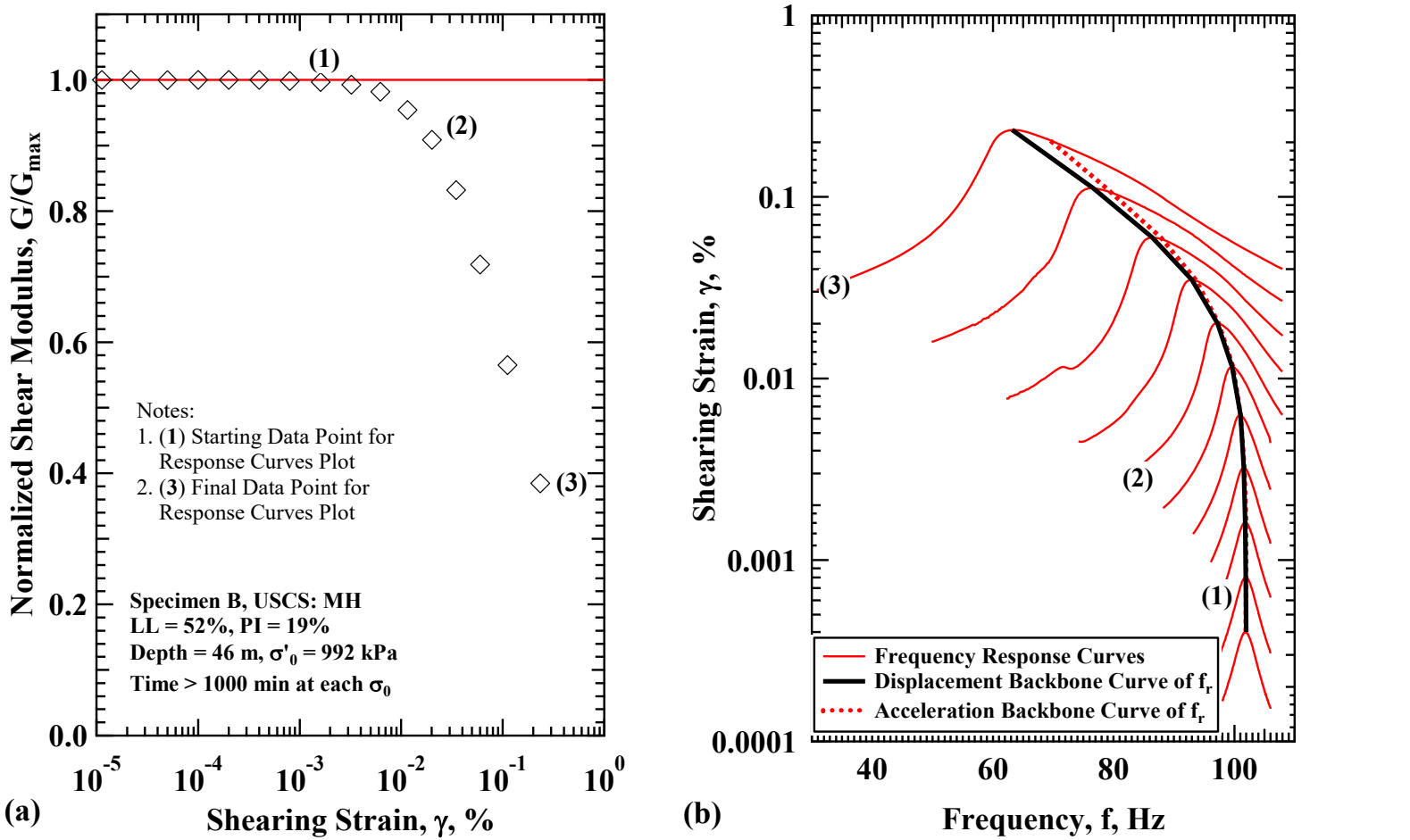

Figure 11.1: (a) Variation in Normalized Shear Modulus with Shear Strain and (b) Some of the Response Curves Measured for the Offshore Marine Clay Specimen B at a Isotropic Confining Pressure of 992 kPa.

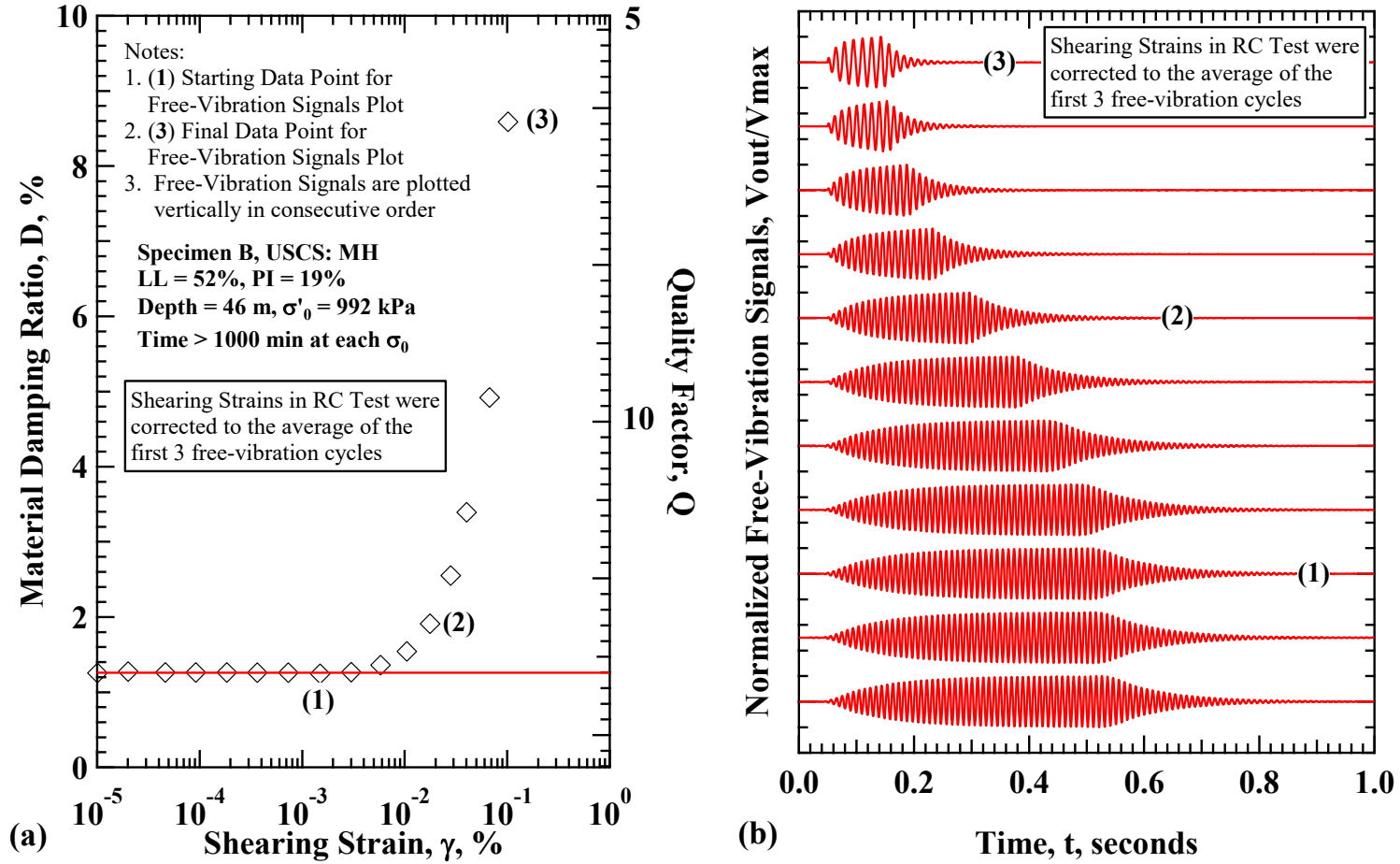

Figure 11.2: (a) Variation in Material Damping Ratio with Shear Strain and (b) Some of the Free-Vibration Decay Curves Measured for the Offshore Marine Clay Specimen B at a Isotropic Confining Pressure of 992 kPa.

In the new system developed in conjunction with this dissertation, the LVDT is excited and measured during the frequency sweep tests. Thus the height is measured during the frequency sweep tests and has been found to change during the sweep depending on the soil type, sequence of confining pressure applied, and level of shear strain amplitude excited during the test. The height changes measured during the frequency sweep test are presented along with the response curves measured during the frequency sweep for the Offshore Marine Clay Specimen B at a isotropic confining pressure of 992 kPa is shown in Figure 11.3. The height change that occurs during the frequency sweep increases as the shear strain amplitude increases. This behavior shows that, in addition to the nonlinearity observed in the test signals and reduced results, there is a geometric response of the soil that is dependent on the level of shear strain excited during the test.

In Figure 11.3, the sequence of the confining pressure applied corresponds to a normally consolidated (NC) state because the pressure applied is the first occurrence of this level of pressure to be applied to this sample. Contractive behavior with increasing shear strain is observed, which agrees with the traditional understanding in geotechnical engineering where contractive behavior occurs when straining a NC clay (Holtz, Kovacs, and Sheahan 2011). The proportion of height change that occurs during the frequency sweep test increases as the level of shearing strain excited during the test increases. Thus the contractive behavior becomes more pronounced at higher shear strains, which is expected when straining a NC clay. The geometric response to shear strain during the frequency sweep adds an additional characteristic that defines a threshold of shear strain where the specimen exhibits, not only nonlinear dynamic behavior but, plastic behavior. Some slight gaps between in the height measurements are observed which are attributed to the free-vibration decay tests that are conducted subsequent to each frequency sweep test.

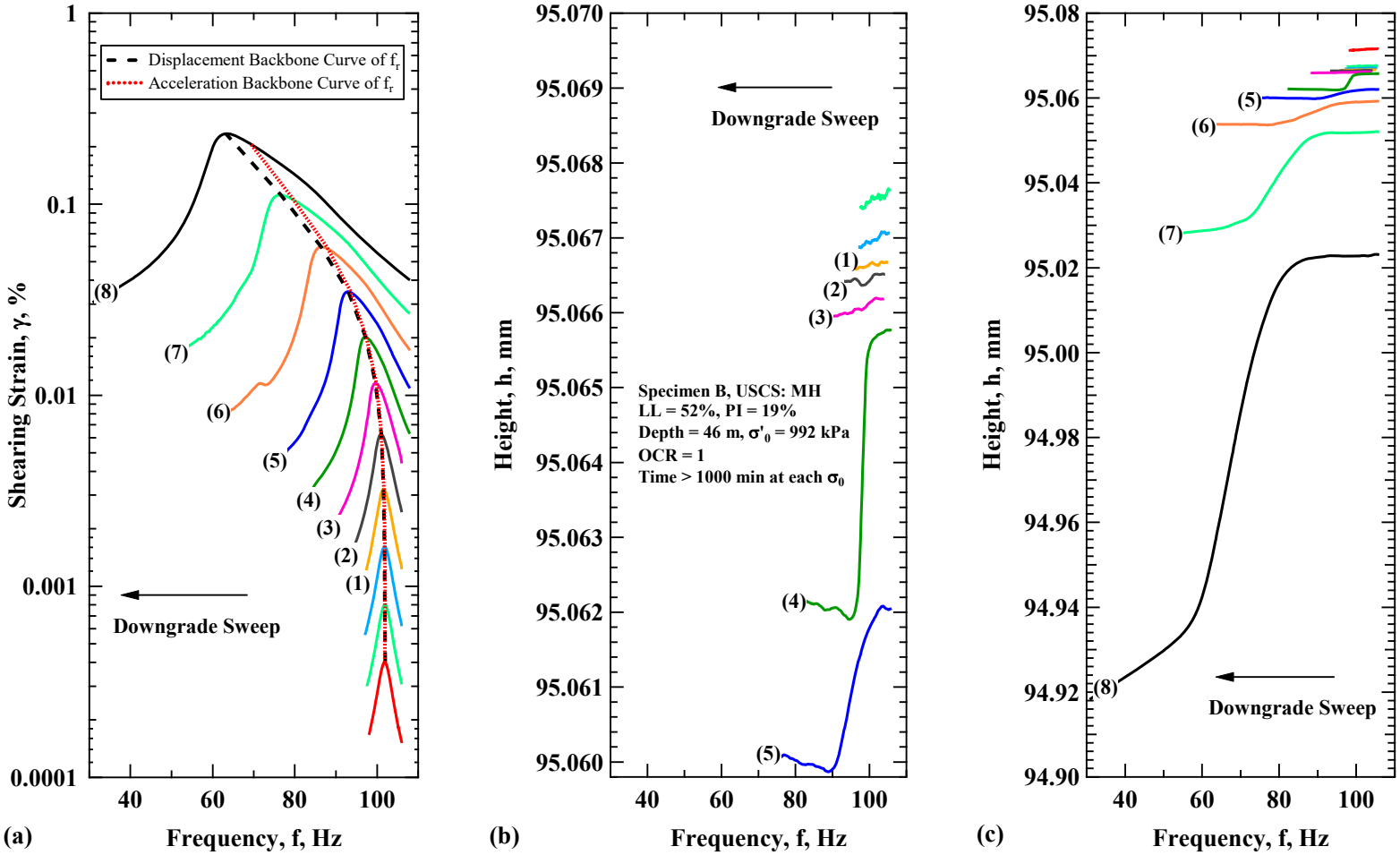

Figure 11.3: (a) Some of the Response Curves Measured, (b) Height Change Measurements During Frequency Sweep at Lower Shear Strains, and (c) Height Change Measurements During Frequency Sweep at Higher Shear Strains for the Offshore Marine Clay Specimen B at a Isotropic Confining Pressure of 992 kPa (OCR =1).

The change in height during the frequency sweep can be used to estimate the volumetric distortion that occurs during the frequency sweep test with increasing shear strain. It is important to note that the volumetric distortion occurs in response to a pure shear condition excited in the RC test and is not forced as is done in other geotechnical engineering laboratory tests. Thus, the volumetric distortion observed herein is the natural response of the soil sample to a pure shear strain condition. Some of the response curves measured are presented with corresponding height change measurements at higher shear strains, and estimated volume change at higher shear strains during frequency sweep tests for the Offshore Marine Clay Specimen B at a isotropic confining pressure of 992 kPa is shown in Figure 11.4 (a), (b), and (c), respectively.

The change in volume is assumed to occur in proportion to the change in height that occurs during the frequency sweep test. It is important to note that the change is volume in an estimate and that the change in volume relative to the change in height measured may not be reflected herein to a perfect degree of accuracy. However, when observing both height change and estimated volume change, the geometric response of the sample to shear strains resembles NC clay behavior and is an agreement with the traditional understanding in geotechnical engineering for a NC clay.

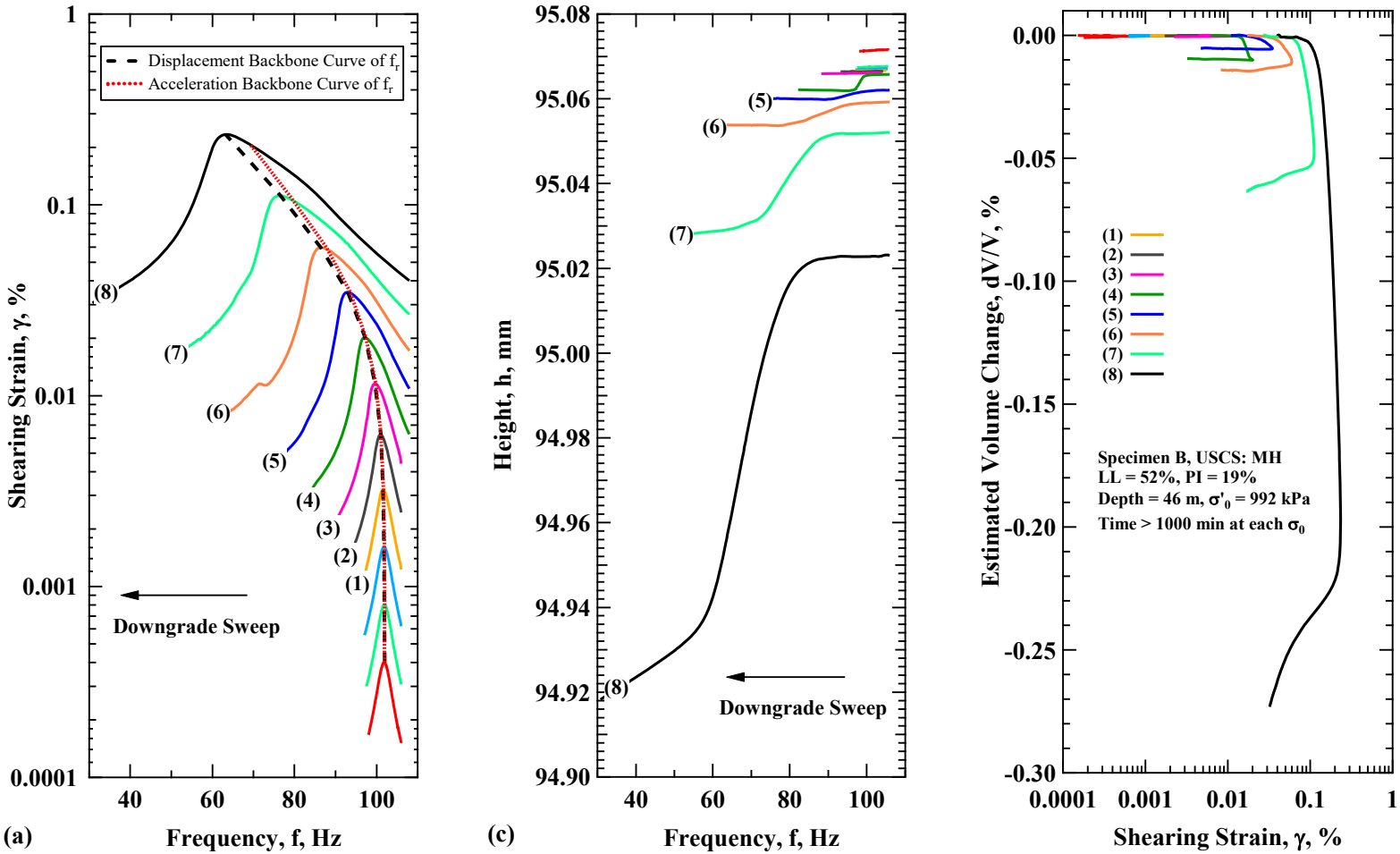

Figure 11.4: (a) Some of the Response Curves Measured, (b) Height Change Measurements During Frequency Sweep at Higher Shear Strains, and (c) Estimated Volume Change During Frequency Sweep at Higher Shear Strains for the Offshore Marine Clay Specimen B at a Isotropic Confining Pressure of 992 kPa (OCR = 1).

To complement the assertion that fundamental geotechnical soil behavior is observed during the RC tests, the Offshore Marine Clay Specimen B was unloaded and tested in a similar manner that has been shown thus far. The specimen was unloaded to 248 kPa resulting in an over-consolidation ratio (OCR) of 4. Similar to what was presented previously, the variation in normalized shear modulus with shear strain and some of the response curves measured for the Offshore Marine Clay Specimen B at an unloading isotropic confining pressure of 248 kPa are shown in Figure 11.5 (a) and (b), respectively. Concurrently, the variation in material damping ratio with shear strain and some of the free-vibration decay curves measured for the Offshore Marine Clay Specimen B at an unloading isotropic confining pressure of 248 kPa are shown in Figure 11.6 (a) and (b), respectively. As discussed previously, the characteristics of the test signals represent the reduced results with regards to the frequency sweep signals and free-vibration decay signals.

Some of the response curves measured are presented with corresponding height change measurements at higher shear strains and estimated volume change at higher shear strains during frequency sweep tests for the Offshore Marine Clay Specimen B at an unloading isotropic confining pressure of 248 kPa are shown in Figure 11.7 (a), (b), and (c), respectively. In Figure 11.7, the sequence of the confining pressure applied corresponds to an over-consolidated (OC) state because the pressure applied is after unloading to a lower level of pressure. Dilative behavior with increasing shear strain is observed, which agrees with the traditional understanding in geotechnical engineering where dilative behavior occurs when straining an OC clay (Holtz, Kovacs, and Sheahan 2011). When observing both height change and estimated volume change, the geometric response of the sample to shear strains resembles OC clay behavior.

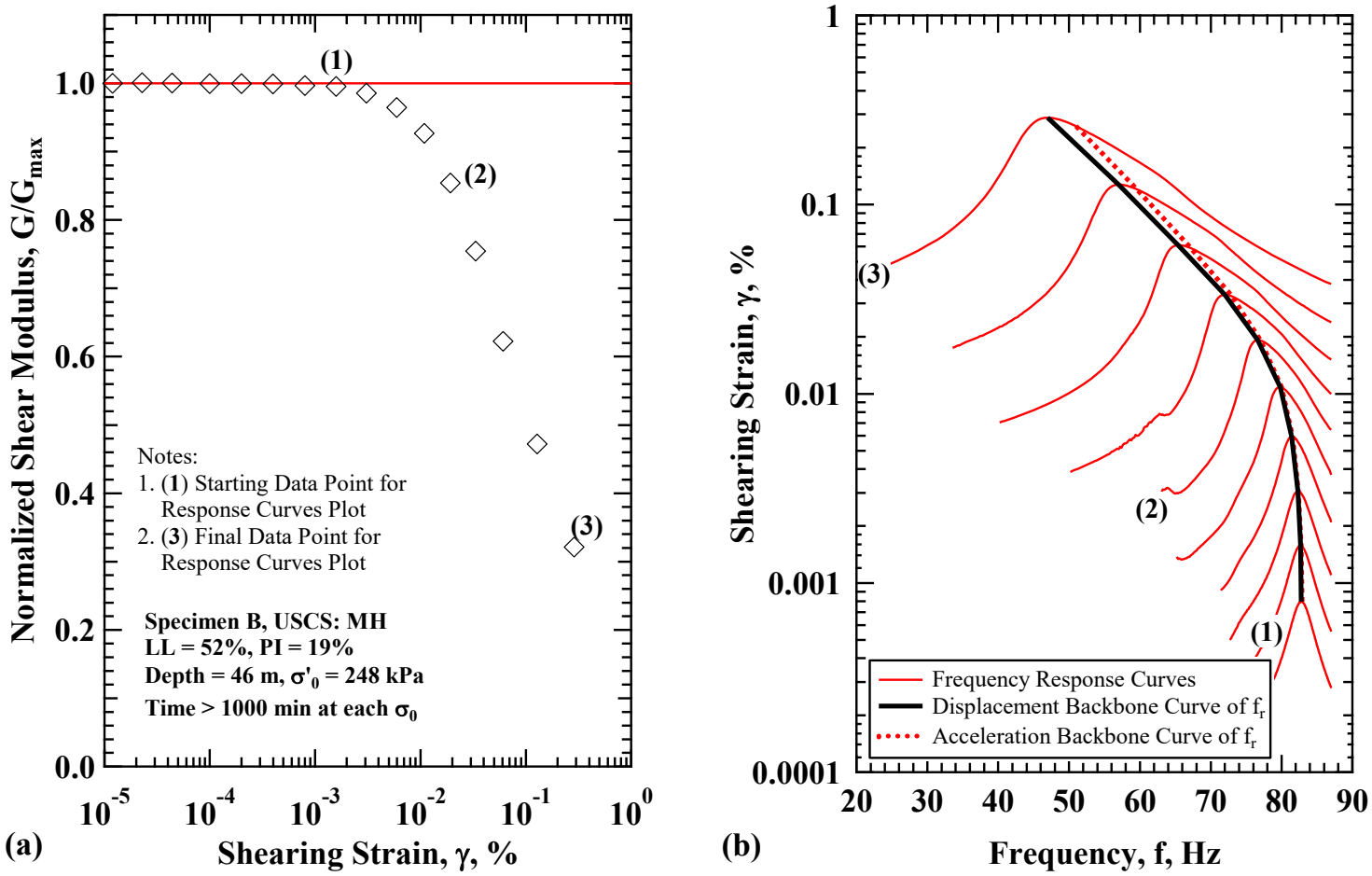

Figure 11.5: (a) Variation in Normalized Shear Modulus with Shear Strain and (b) Some of the Response Curves Measured for the Offshore Marine Clay Specimen B at an Unloading Isotropic Confining Pressure of 248 kPa.

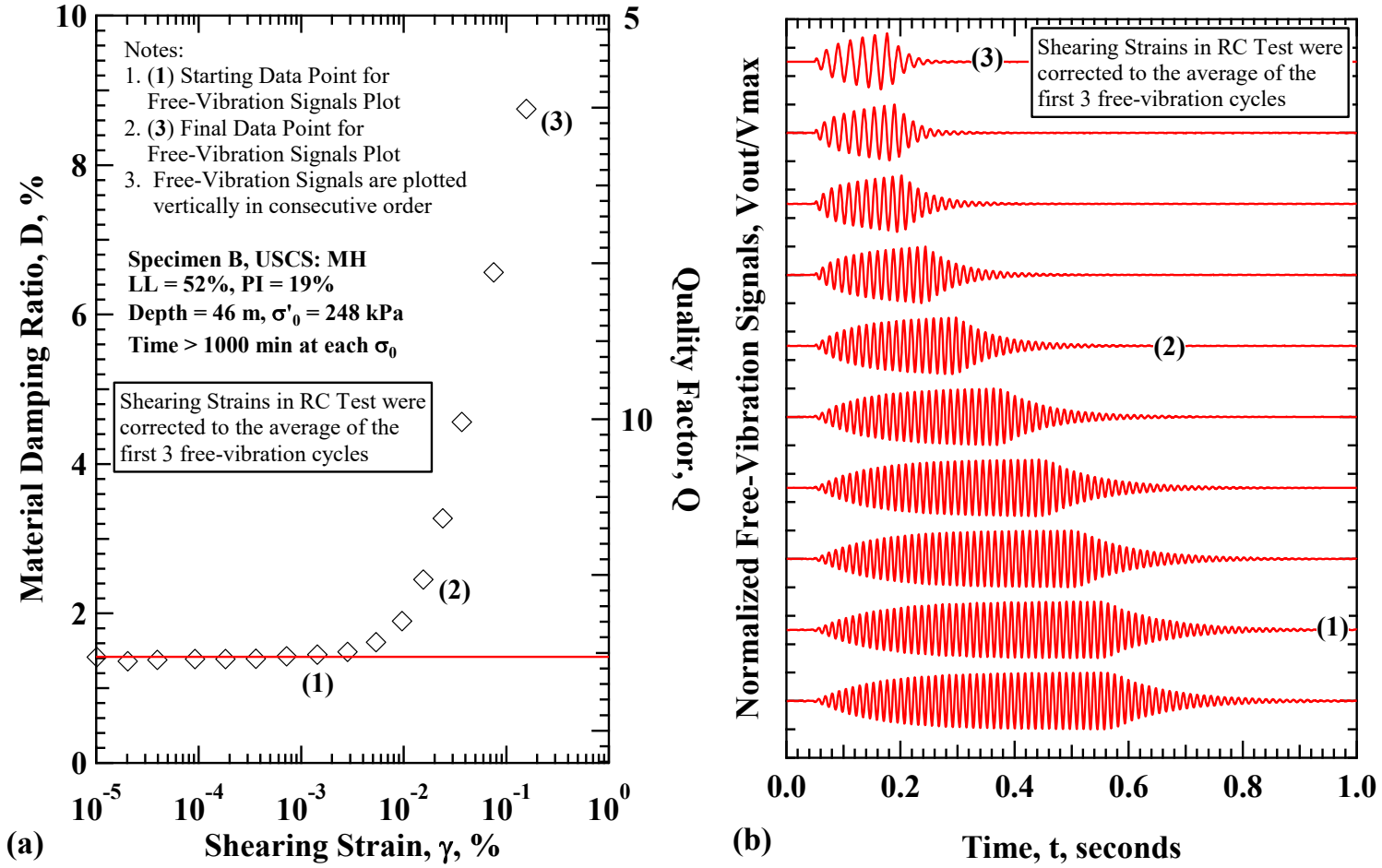

Figure 11.6: (a) Variation in Material Damping Ratio with Shear Strain and (b) Some of the Free-Vibration Decay Curves Measured for the Offshore Marine Clay Specimen B at an Unloading Isotropic Confining Pressure of 248 kPa.

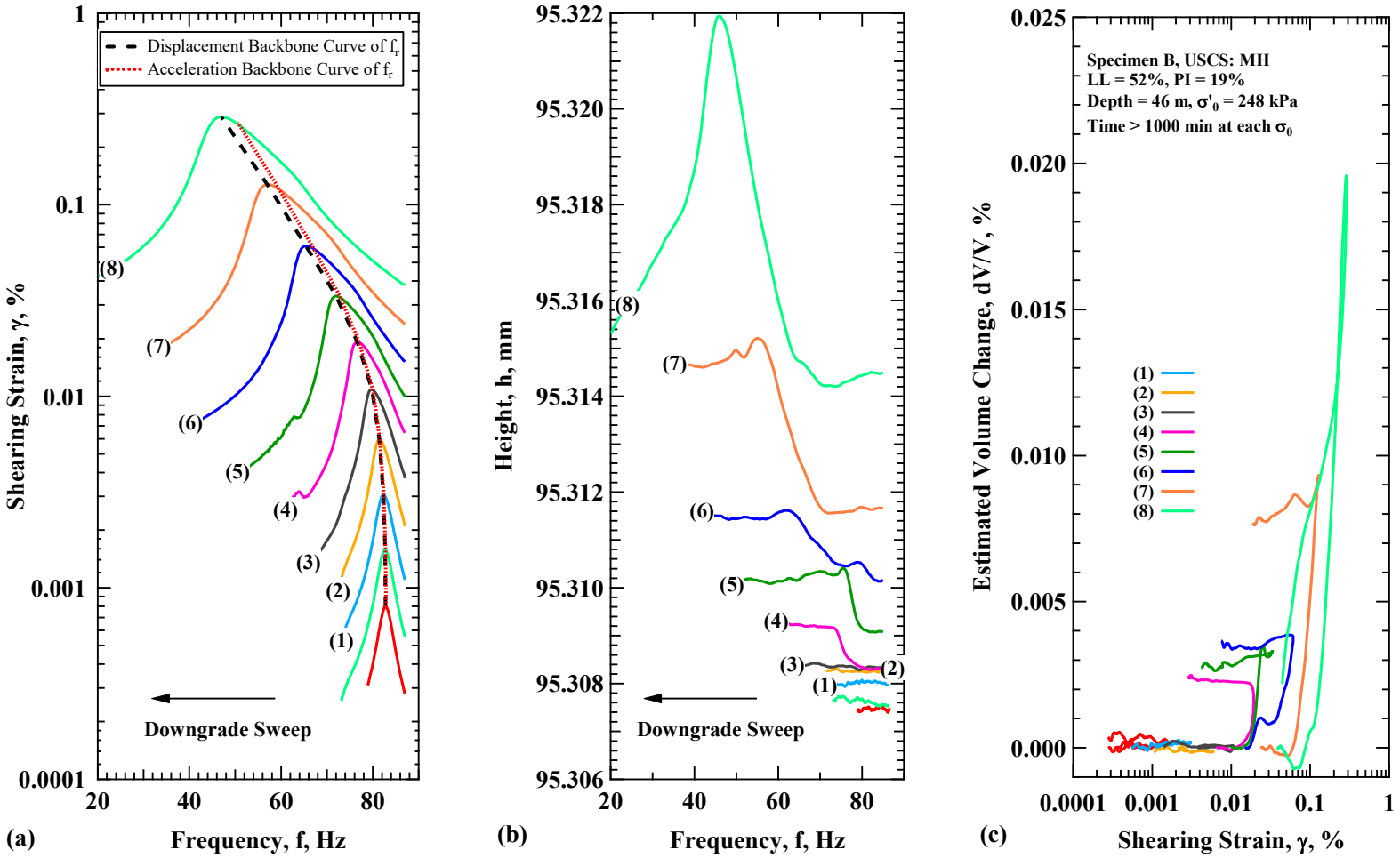

Figure 11.7: (a) Some of the Response Curves Measured, (b) Height Change Measurements During Frequency Sweep at Higher Shear Strains, and (c) Estimated Volume Change During Frequency Sweep at Higher Shear Strains for the Offshore Marine Clay Specimen B at an Unloading Isotropic Confining Pressure of 248 kPa (OCR = 4).

In general, dilative behavior occurs with increasing shear strain. In Figure 11.7, the final frequency sweep test shows dilative behavior with increasing shear strain until passing the resonant frequency, after which the change in volume beings to decrease. However, the net volume change still reflects dilative behavior. This behavior may either represent a nonlinear elastic response, where the height change rebounds as unloading of shear strain occurs during the frequency sweep or that the dilative behavior is overcome and contractive behavior ensues due to the repetitive straining that occurs due to sequential frequency sweep tests. Conclusions to the aberrant behavior during the final frequency sweep cannot be asserted; however, the complex behavior presented herein is worth taking note when attempting to further understand the dynamic or moderate strain response of soils. Though not presented herein, the geometric behavior of the Offshore Marine Clays was consistent for each of the samples tested, where the geometric response to shear strain is in agreement with the traditional understanding of the response of NC and OC clays to strain.

11.3 SUMMARY

The data presented in this chapter provides an original perspective on the nonlinear dynamic behavior from RCTS tests and a glimpse at dilative and contractive behavior of materials that occurs during the pure shear straining that excited during the RC tests. From the frequency sweep tests, the change in volume was estimated based on the height change measured and was assumed to occur in proportion to the change in height. When one of the offshore marine clay samples was under normally-consolidated (NC) conditions, the estimated volume change in response to shear strain was contractive, which resembles NC clay behavior. When one of the offshore marine clay samples was under over-consolidated (OC) conditions, the estimated volume change in response to shear strain was dilative,

which resembles OC clay behavior. When the offshore marine clay samples were at NC and OC conditions the samples responded to shear strain in a manner that was contractive and dilative, respectively, which is in agreement with the traditional understanding in geotechnical engineering for a NC and OC clays.

The proportion of height change that occurs during the frequency sweep test increases as the level of shearing strain excited during the test increases. Thus the contractive or dilative behavior becomes more pronounced at higher shear strains, which is expected when straining soils below critical state strains. The geometric response to shear strain during the frequency sweep adds an additional characteristic that defines a threshold of shear strain where the specimen exhibits, not only nonlinear dynamic behavior but, plastic behavior. Though not presented herein, the geometric behavior of the Offshore Marine Clays was consistent for each of the samples tested, where the geometric response to shear strain is in agreement with the traditional understanding of the response of NC and OC clays to strain.

The purpose of presenting the signals that correspond with the small-strain and nonlinear-strain test results is to provide a more detailed and informative perspective into the dynamic behavior of soils during RC testing. The more detailed perspective presented in this chapter prefaces the subsequent chapter, where more advanced analysis of nonlinear dynamic behavior is discussed. Two examples of more advanced analysis include, but are not limited to, developing nonlinear models for non-symmetry of the response curve or evaluating the variation of the damped natural frequency and shear modulus with strain during nonlinear free-vibration decay.

Chapter 12

Modeling Components of the Torque Motor Used in the Traditional RCTS Device and Experimental Comparisons

12.1 INTRODUCTION

A computer-controlled combined resonant column (RC) and torsional shear (TS) device is the focus of this investigation. The RCTS device can be idealized as a fixed-free system with the fixed and the top is free to rotate in torsional motion. The top of the specimen is connected to an electromagnetic driving system. In typical RCTS testing, the electromagnetic driving system consists of 4 permanent magnets and 8 specially configured coils. The driving system is configured to allow for specific levels of torque to be applied to the specimen based on the amperage sent to the coils. The magnetic force between the permanent magnet and the coils positioned on either side of the magnet, acts as a balanced magnetic solenoid. In this study, experimental testing and numerical modeling are conducted to understand the characteristics of the electromagnetic torque motor in the traditional RCTS device.

12.2 TRADITIONAL RCTS ELECTROMAGNETIC SOLENOIDS AND TORSIONAL SYSTEM

A computer-controlled combined resonant column (RC) and torsional shear (TS) device is the equipment that is the focus of this investigation. The basic operational principle of the RC test is to vibrate cylindrical specimens in first-mode torsional motion. In the TS test, the specimen is excited in cyclic torsion at frequencies low enough to avoid inertial effects of the testing system and dynamic amplification of the specimen. The RCTS testing equipment has been developed at The University of Texas at Austin over the past several decades and a large number of RCTS tests (>1000) have been performed on

cylindrical soil and rock specimens. This equipment is characterized and calibrated using cylindrical metal specimens, some of which were used to verify the objective of this study. The testing configuration of a cylindrical specimen in the RCTS device can be idealized as a fixed-free system. The base of the specimen is fixed and the top is free to rotate in torsion. The top end of the specimen is connected to an electromagnetic driving system. The driving system supplies harmonic torsional excitation to the top of the specimen at frequencies that range over 0 to 1000 Hz. In the RC test, the excitation system and dynamic response of the cylindrical specimens are equivalent to a single-degree-of-freedom (SDOF) system vibrating in torsion, which is defined as:

$$J_0\ddot{\theta} + C_t\dot{\theta} + k_t\theta = \tau \sin(\omega * t) \tag{12.1}$$

where J_0 is the mass polar moment of inertia of the specimen, C_t is the torsional damping coefficient, k_t is the torsional spring constant, τ is the torque applied to the specimen, ω is the angular frequency of the torqueing function, t is time, and $\ddot{\theta}$, $\dot{\theta}$, and θ are torsional acceleration, torsional velocity, and angle of twist, respectively. In the RC sweep test, the exact magnitude of the cyclic torsion input into the cylindrical specimen is not typically needed because the shear strain response of the system is measured and the resonant frequency determined from a frequency sweep is used to determine the shear modulus. In the TS test, low frequency cyclic torsion is applied to the cylindrical specimen and though the shear strain is measured, the torque and shear stress applied to the specimen is needed to determine the shear modulus. Determination of shearing stress in the torsional shear test is based on the theory of elasticity for circular or tubular rods in pure torsion. Assuming that pure torque, T, is applied to the top of the specimen. The torque can be calculated from:

$$T = \frac{\tau}{r} \cdot \frac{\pi}{2} \cdot r^4 = \frac{\tau}{r} \cdot J_p \tag{12.2}$$

where τ is the shearing stress, r is the radius of the specimen, and J_p is the area polar moment of inertia of the specimen. The equation to calculate the applied shear stress is given as:

$$\tau = r \cdot \frac{T}{J_p} \tag{12.3}$$

In the TS test, the electromagnetic driving system is calibrated to determine the torque driven based on the voltage sent to the drive system. The shearing strain, γ, is then calculated from:

$$\gamma = \frac{r * \theta}{l} \tag{12.4}$$

where θ is the angle of rotation in the plane of the electromagnetic driving system and l is the height of the specimen. A photograph of the RC device and conceptual schematic of the torsional driving system is shown in Figure 8.3.

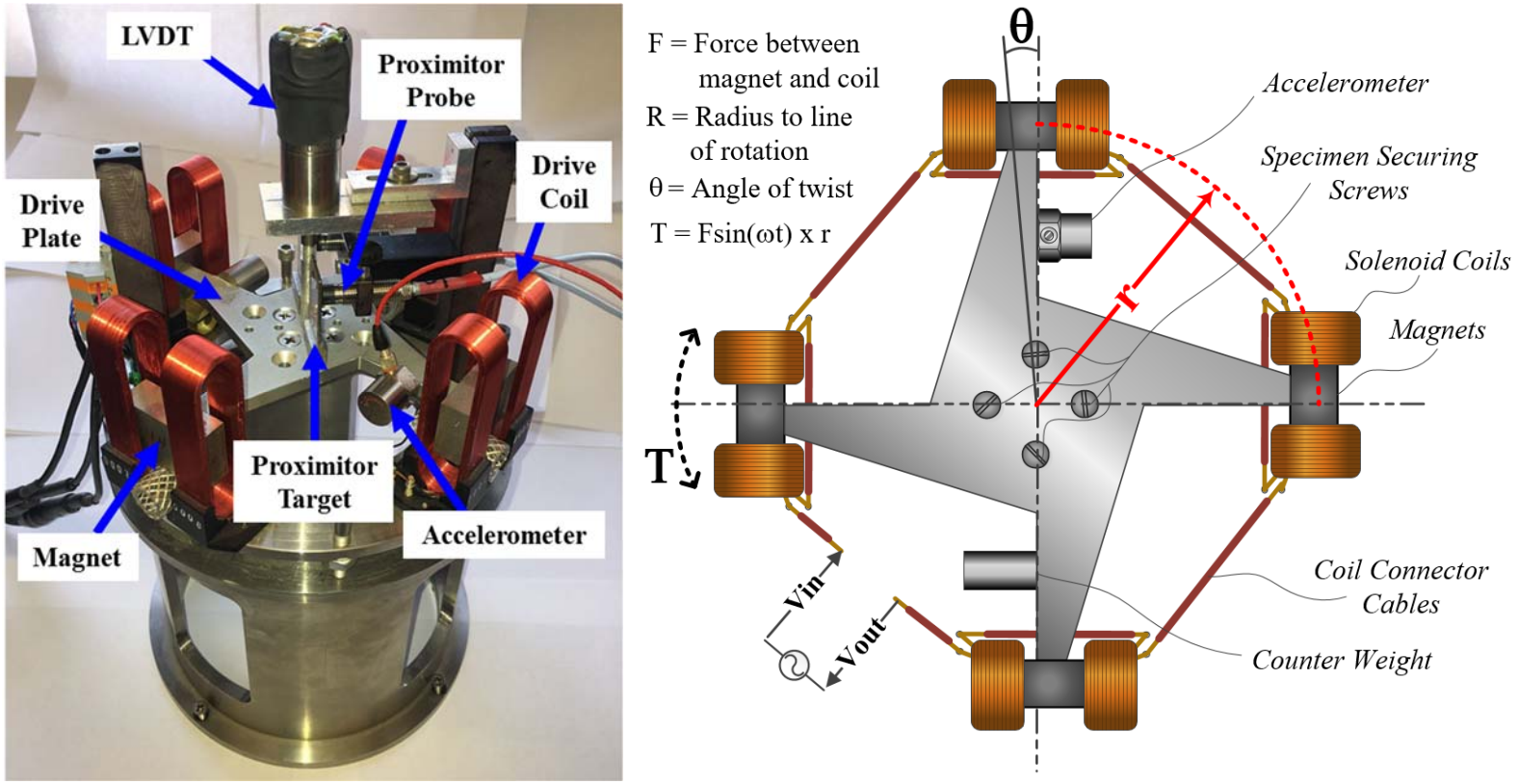

Figure 12.1: Photograph of the Combined Resonant Column and Torsional Shear device (left) and conceptual schematic of the torsional driving system (right).

The electromagnetic drive system consists of 4 magnets and 8 coils. The drive system is made up of 4 subsystems, each of which is equivalent to an electromagnetic solenoid. Each of the electromagnetic solenoids consist of one permanent magnet and two packed coils of wire, the coils are at both ends of the permanent magnetic coinciding with the magnetic poles. The coils are oriented relative to the permanent magnet to generate magnetic fields parallel to the magnetic field of the permanent magnet. The coils are powered with current that is supplied by a National Instruments (NI) PXI-6251 data acquisition system (DAQ) and, when needed, amplified by a HP 6824A power supply amplifier. This equipment combined with subroutines written in NI LabVIEW allow the configuration of any desired forcing function; however, in this study that forcing function is in the form of a sinusoid with varying frequency. The amplitude of the forcing function is specified in the subroutines in units of voltage, thus the forcing function is supplied to the coils in the form:

$$V_{in} = A\sin(\omega * t) \tag{12.5}$$

and from Ohm's law (Serway and Jewett, 2003)

$$I = V_{in}/Z \tag{12.6}$$

where V_{in} is the voltage sent to the drive coils, A is the voltage amplitude selected in the subroutine, ω is the angular frequency of the forcing function in units of radians per second, t is the time lapse of the excitation in units of seconds, I is the current sent to the drive coils, and Z is the impedance of the electromagnetic drive system. The force-couple generated by the electromagnetic solenoids is a complex problem that would need to be solved using numerical integration and modeling techniques, but for simplicity the magnetic field can be conceptualized using the equation:

$$B_{coil} \approx \mu_0 \frac{N}{L} I \tag{12.7}$$

where B_{coil} is the magnetic field generated by the drive coil, μ_0 is the vacuum magnetic permeability, L is the length of the drive coil, and I is the current (Schimpf 2013). A simplified expression of the force couple between the magnet and the drive coil is:

$$F \approx \frac{(B_{coil} \times B_{magnet}) A_{core}}{2\mu_0} \tag{12.8}$$

where F is the force couple, B_{magnet} magnetic field strength of the permanent magnet, and A_{core} is the area of the magnet. The force-couples generated by the electromagnetic solenoids are applied to arms of a drive plate that convert this force into torque applied to the specimen, based on a radius, r from the central axis of the specimen to the radial location of the force-couple between the magnet and the packed coils. A simplified expression for the torque, T, supplied by one magnet and one packed coil is:

$$T = F * r \tag{12.9}$$

Determining the true current supplied to the coils is slightly more complicated than the equation from Ohm's law, due to: (1) inductive impedance in the drive system circuit that is a frequency dependent phenomenon, and (2) back-electromotive force, which is a specific current drop across the coils that is induced by the permanent magnet traveling through the coils at a particular velocity. The second factor creates a force reduction during testing, which is velocity dependent (i.e. frequency dependent) and thus contributes to the damping coefficient, c in the measured SDOF system response. In RC testing, this frequency dependent induced damping is commonly referred to as equipment-generated damping and is corrected in a well-documented calibration procedure.

12.3 NUMERICAL METHODS FOR PREDICTING FORCE-DISPLACEMENT RELATIONSHIPS FOR A LINEAR SOLENOID

12.3.1 Previous Work

The method for predicting the force interaction between a permanent magnet and a coil of wire can become quite complicated based on the number of winds of the coils and geometry of the both the coil configuration and the magnet. The method for modeling the force interaction of the coils and permanent magnets in the RCTS test are developed based on a model presented in Robertson et al. (2012). Their model involved using a numerical integrative method that modeled the interaction between cylindrical coils and a cylindrical permanent magnet. In their study, several methods were presented to model the solenoid, which were: (1) a filament method where each individual wind of the packed coil is considered and the permanent magnet is modeled as a series of coils, i.e. the coils and magnet are modeled as individual current loops, and (2) a shell method where the each radial wind of the coils were modeled as a shell and the permanent magnet as one shell, i.e. the coils are modeled as concentric surface current densities and the magnet as a cylindrical surface current density. A figure from Robertson et al. (2012) is shown as Figure 12.2 to graphically depict the concept of the filament and shell methods. The method later used to model the interaction of the coils and the magnets in the RCTS device is the filament method and thus will be the only method discussed further. The filament method was more appropriate for model adaptation to the complex geometry of the coils used in the RCTS device.

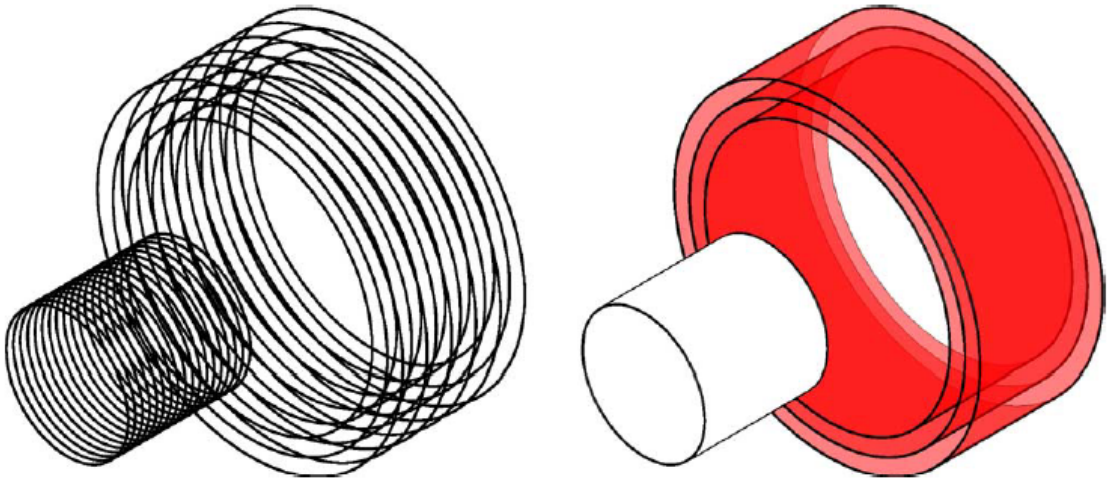

Figure 12.2: Figure from Robertson et al. (2012) illustrating the solenoid modeling concepts of the filament (left) and sell (right) methods for predicting the force of a cylindrical electromagnetic solenoid.

The force interaction between cylindrical coils and a cylindrical permanent magnet depend on the geometry of the coils and the magnet, the distance between each coil and each segment of the magnet, the current in the coils, and the magnetic strength of the permanent magnet. The integrative method involves discretizing the problem into individual coil segments and individual segments of coils used to represent the permanent magnet. The coils are defined by the number of turns radially as Nr and the number of turns axially as Nz. Thus the total number of turns is N = Nr x Nz and it is assumed that each coil is uniformly positioned radially and axially. The inner radius of the coil is defined as r_C, the outer radius of the coil is defined as R_C, and the length of the coil is defined as l_C. The radius of the permanent magnet is defined as R_m and the length of the magnet as l_m. The axial displacement between the center of the coils and the center of the magnet is a distance z. A schematic cross-section was recreated from Robertson et al. (2012) and shows the geometry of the coils and magnet in Figure 12.3. The open air space between the magnet and the coils is shown in Figure 12.3 as r_g.

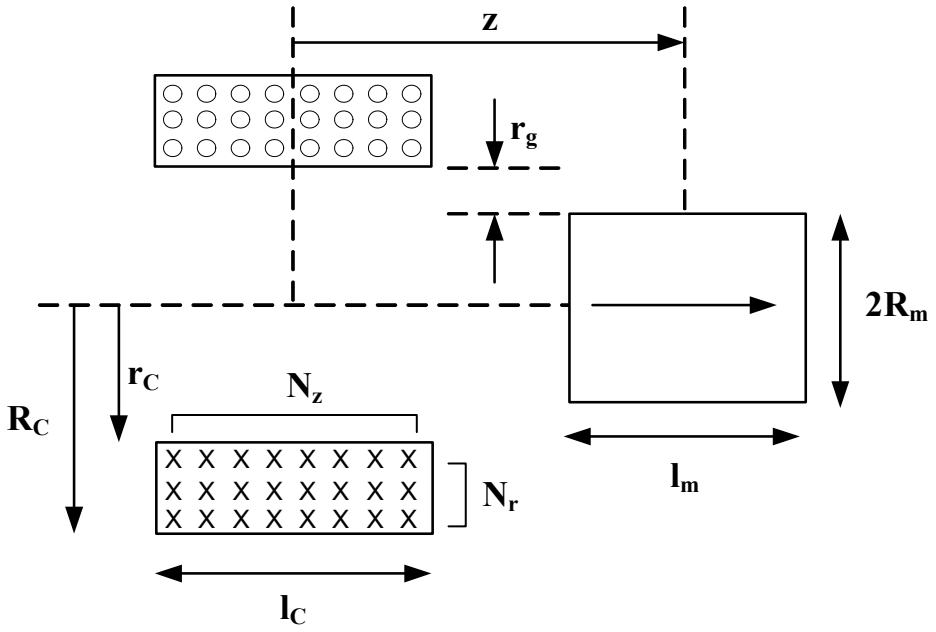

Figure 12.3: Recreated figure from Robertson et al. (2012) of a solenoid configuration of a cylindrical permanent magnet and cylindrical coil of wire.

Using the filament method, the magnetic strength and geometry of the permanent magnet can be modeled as a set of coiled wires, as shown in for filament method in Figure 12.2. The coil and magnet are modeled as discrete elements (i.e. a single turn of wire) and the total force interaction between the magnet and coil is summed through superposition of each combination of elements (Robertson et al. 2012). The force interaction between two coaxial loops (one combination of discrete elements) carrying currents I_1 and I_2 respectively, the axial force between them are given in Shiri and Shoulaie (2009) as:

$$F_f(r_1, r_2, z) = \mu_0 I_1 I_2 z \sqrt{\frac{m}{4r_1 r_2}} \times \left[K(m) - \frac{m/2-1}{m-1} E(m)\right] \tag{12.10}$$

$$m = \frac{4r_1 r_2}{[r_1+r_2]^2+z^2} \tag{12.11}$$

where r_1 and r_2 are the coil radii and z is the axial distance between them. The functions K(m) and E(m) are the complete first and second elliptical integrals, respectively, with

respect to parameter m. Using the previous formula, the total force interaction between the magnet and coil is summed through superposition as given in Robertson et al. (2012) by:

$$F_{z_1} = \sum_{n_m=1}^{N_m} \sum_{n_r=1}^{N_r} \sum_{n_z=1}^{N_z} F_f\left(r(n_r), R_m, z + L(n_m, n_z)\right) \tag{12.12}$$

$$r(n_r) = R_C + \frac{n_r - 1}{N_r - 1}[R_C - r_c] \tag{12.13}$$

$$L(n_m, n_z) = -\frac{1}{2}[l_m + l_c] + \frac{n_z - 1}{N_z - 1} l_c + \frac{n_m - 1}{N_m - 1} l_m \tag{12.14}$$

where R_m is the magnetic radius, r_c and R_c and the inner and outer coil radii, l_m and l_c are the magnet and coil lengths, z is the axial distance between their centers, N_r and N_z are the number of turns in the thin coil. The current carried by the outer coils, I_1, is the same as the current that is intended; however, the current used in the coils that model the magnet is related to an equivalent surface density with current per turn of $I_2 = B_r l_m/[N_m \mu_0]$ and permanent magnet strength B_r. The magnet must be modeled using a sufficient number of turns N_m so that the solution converges to a consistent value. The total force equation is related to the individual force equation where r_1 is $r(n_r)$ and is the radial distance to a single loop from the central axis, r_2 is R_m, z is the axial distance between the centers of the magnet and coils, and $L(n_m, n_z)$ accounts for the distance between a specific turn in the coils and turn in the permanent magnet filament. The elliptical integral gives the solution for the interaction, based on geometry, between two coaxial loops without having to radially discretize the loops. This greatly increases the speed at which the total force interaction can be computed.

12.3.2 Initial Development of Numerical Model in LabVIEW Based on Robertson et al. (2012)

As is used for the software written for operating the RCTS device and National Instruments data acquisition system and for many of the numerical models and simulations in this dissertation, LabVIEW was also used to model the force interaction of magnetic solenoids. The equations presented from Robertson et al. (2012) were programmed in LabVIEW as shown in Figure 12.5.

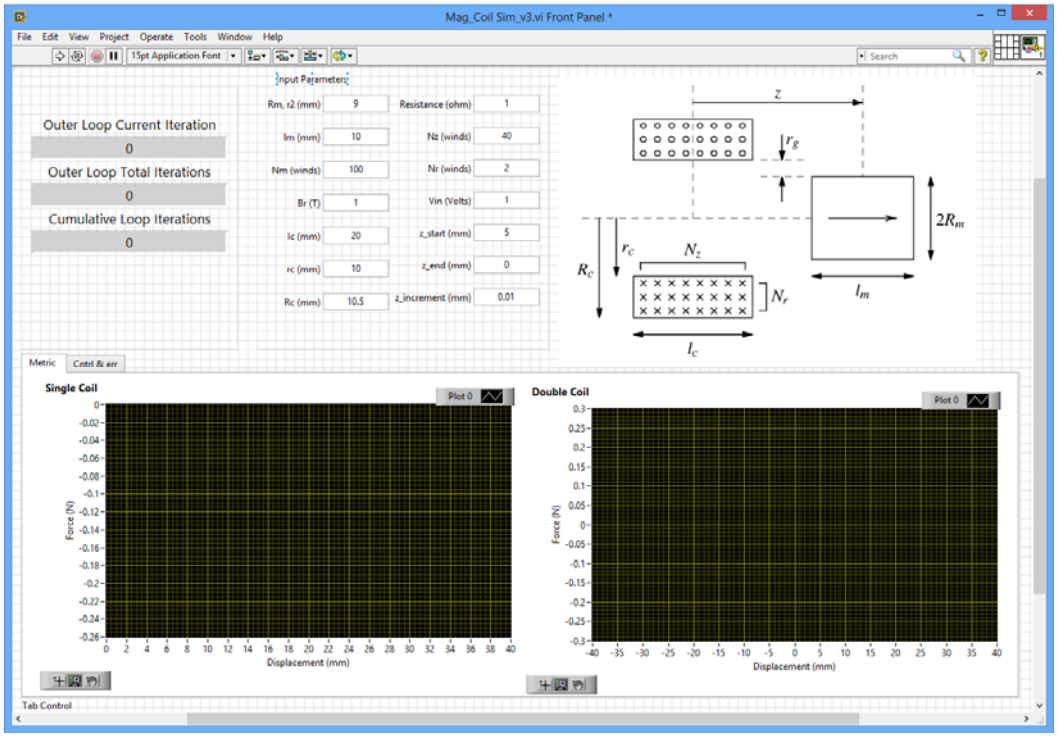

Figure 12.4: Front Panel of Program Used to Simulate the Force of a Cylindrical Electromagnetic Solenoid.

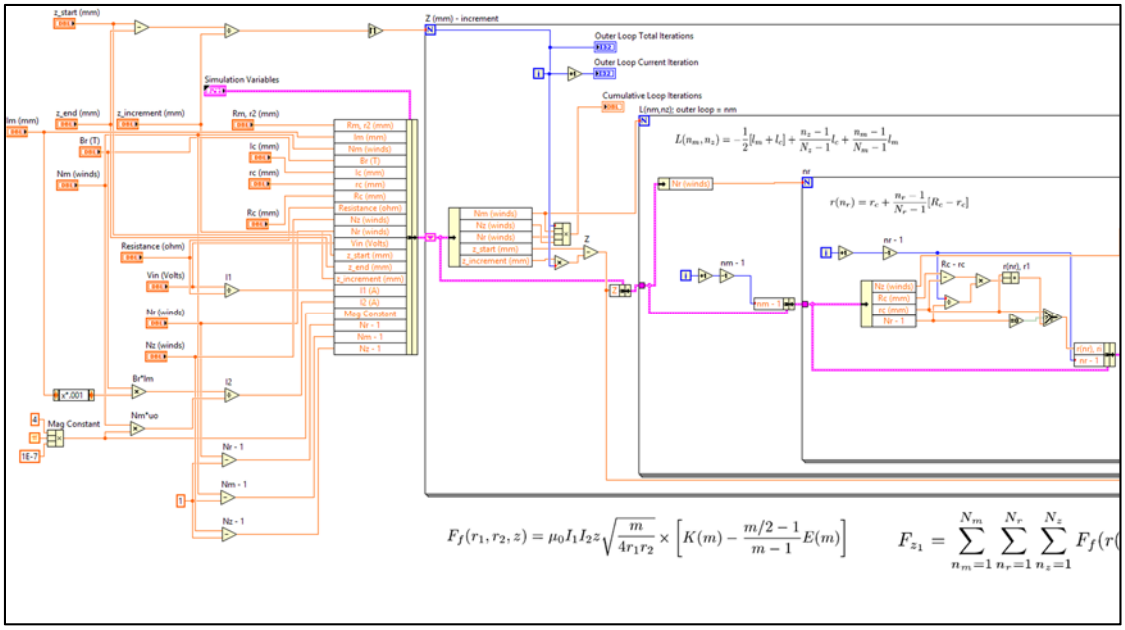

(a) Screenshot of the Left Side of the Block Diagram

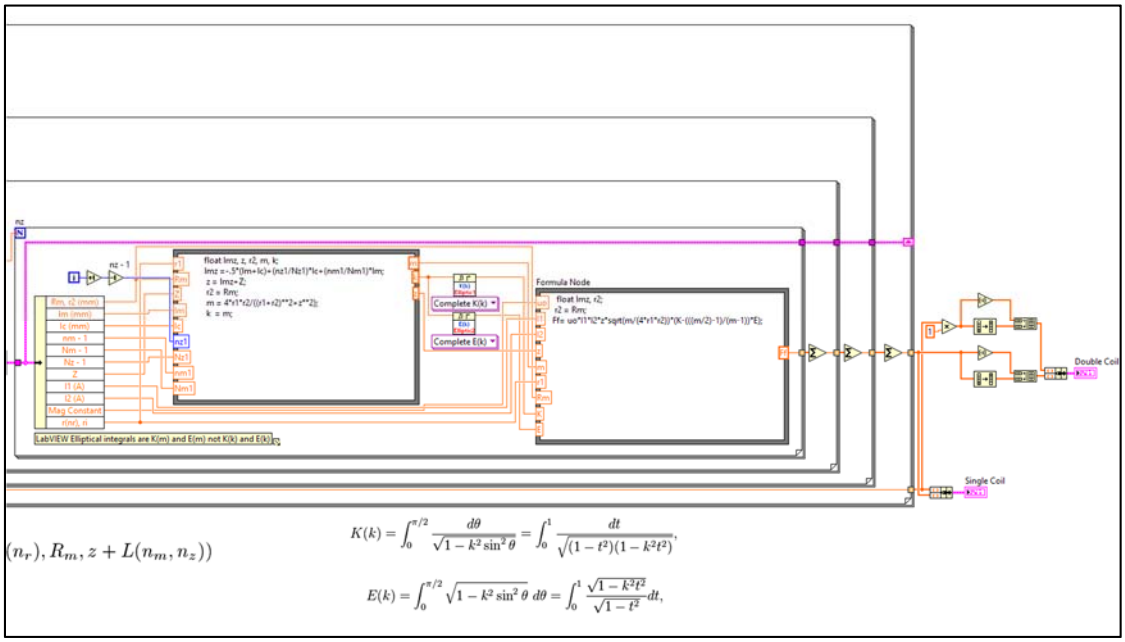

(b) Screenshot of the Right Side of the Block Diagram

Figure 12.5: Block diagram of LabVIEW Program Written to Simulate the Force of a Cylindrical Electromagnetic Solenoid.

In Robertson et al. (2012), two examples where given where the force-displacement relationship of a magnetic solenoid was simulated using several methods presented in their paper. The model developed in LabVIEW for this study is validated by simulating the force-displacement relationships of the same two examples. The input parameters for the two examples are shown in Table 12.1. A comparison of the results from the LabVIEW model created for this study and the results presented in Robertson et al. (2012) are shown Figure 12.6. The LabVIEW model was based on the filament method presented in Robertson et al. (2012) and as seen in Figure 12.6, the LabVIEW model is validated for the filament method.

Table 12.1: Input Parameters for the Two Examples Presented in Robertson et al. (2012) and Simulated by the LabVIEW Model Created for This Study.

Parameter	Symbol	Example 1	Example 2
Magnetic radius	R_m	9 mm	9 mm
Magnet length	l_m	10 mm	10 mm
Magnet 'turns'	N_m	100	100
Magnetic remanence	B_r	1 T	1 T
Coil inner radius	r_c	10 mm	10 mm
Coil thickness	R_c - r_c	0.5 mm	5 mm
Coil length	l_c	20 mm	20 mm
Coil axial turns	N_z	40	20
Coil current	I	1 A	1 A
Coil radial turns	N_r	1	5

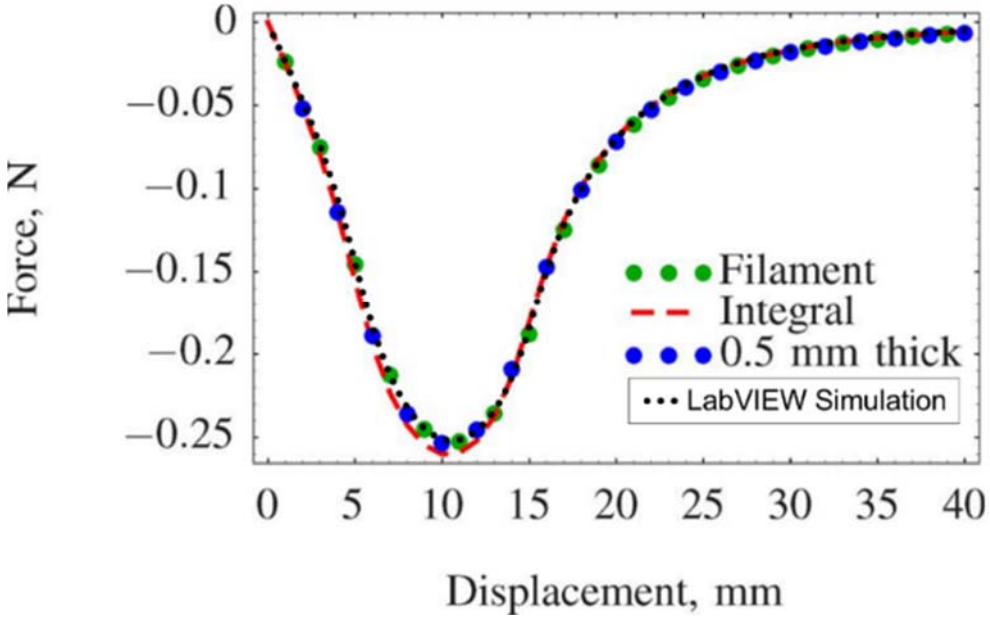

(a) Example 1

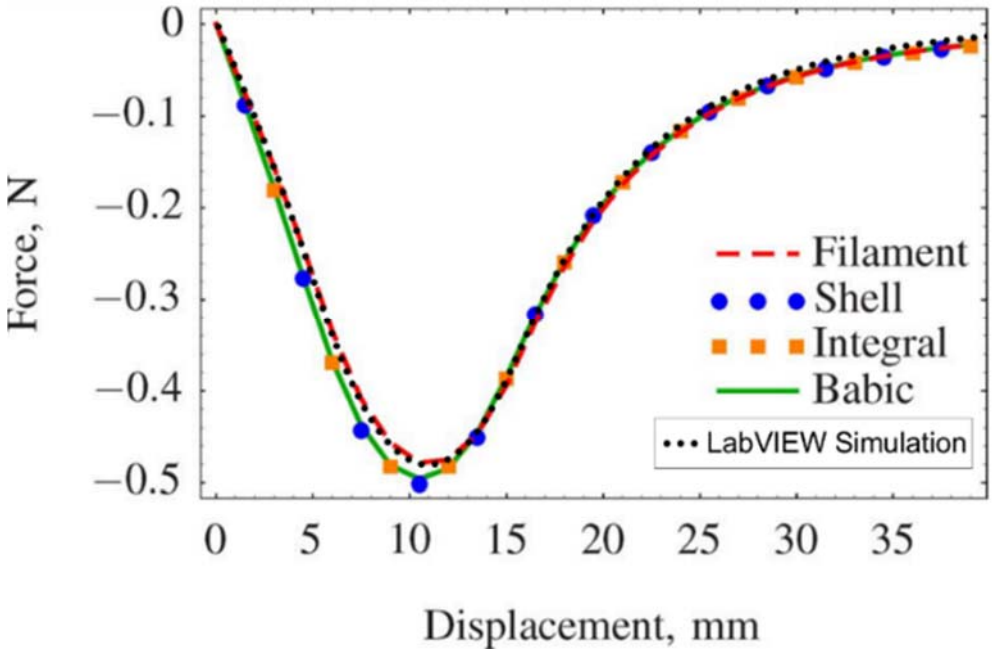

(b) Eample 2

Figure 12.6: Two Examples with Parameters Shown in Table 12.1 are Presented from Robertson et al. (2012) and Simulated by the LabVIEW Model Created for This Study are Compared, Where The LabVIEW Model Created for This Study is Based on the Filament Method from Robertson et al. (2012) and is Shown to Exactly Agree with Their Filament Model Results.

12.4 DEVELOPMENT OF NUMERICAL MODEL TO PREDICT THE BEHAVIOR OF TRADITIONAL RCTS SOLENOIDS

In the RCTS device, the geometry of the solenoids that make up the electromagnetic drive system are much more complicated than the cylindrical solenoid model created based on Robertson et al. (2012). Therefore, a few more steps are taken to create a model that can model for force-displacement relationships of the solenoids used in the RCTS device. The key aspects that differentiate the cylindrical solenoid design and the RCTS solenoids are: (1) In the RCTS device the magnets are rectangular and tall in the vertical direction, this is done so that the magnet can be placed as far as possible from the center of rotation of the RCTS device so as to maximize the moment arm for creating torque while fitting within the confining chamber manufactured for soil testing; (2) the coils are elongated in the vertical direction (with an approximate ¾ in. gap between the magnet and the coil), but are in close proximity to the magnet in the lateral direction (with an approximate 0.05 in. gap between the magnet and the coil), this is done to allow vertical movement for specimens that undergo significant consolidation (i.e. clayey materials) under increasing isotropic confining stresses while maintaining close proximity to the coils (laterally) to maintain higher magnetic force coupling; and (3) As the drive plate of the RCTS device rotates and the permanent magnets rotate, the magnetic vector of the permanent magnet rotate out of axial axis that the coils and the magnet initially share, thus a slight reduction occurs in the magnetic force couple. The model discussed in this subsection addresses the complexities of the first two points.

To model the non-cylindrical solenoids used in the RCTS device, some additional parameters are defined for the geometry of the solenoid. These parameters are presented in Figure 12.7.

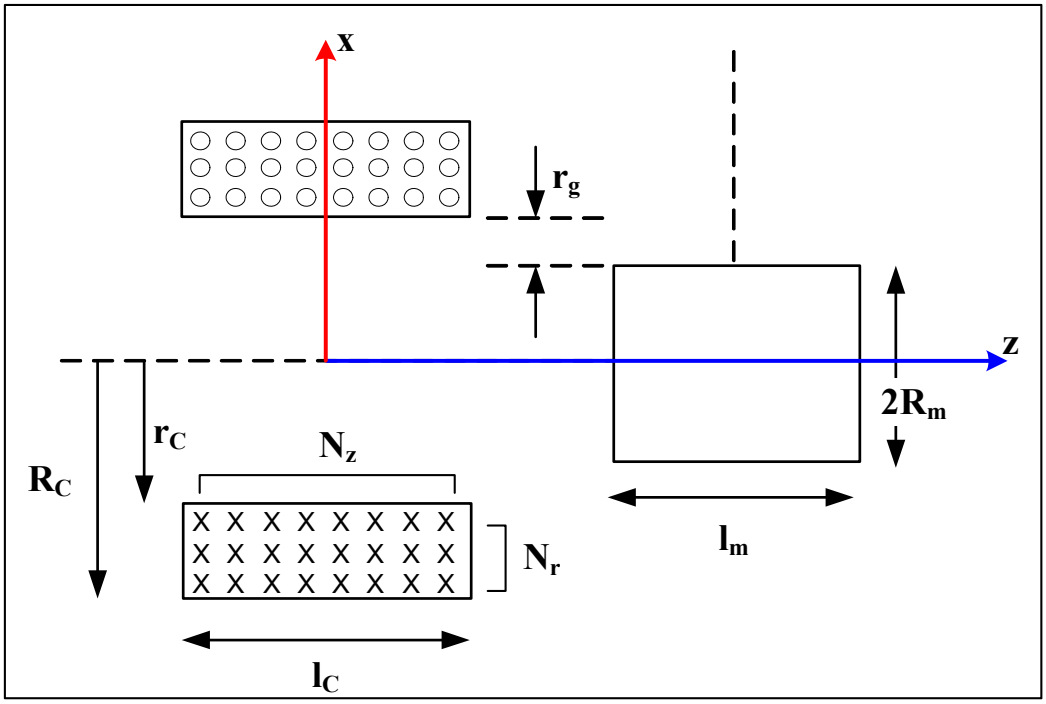

(a) Plane View

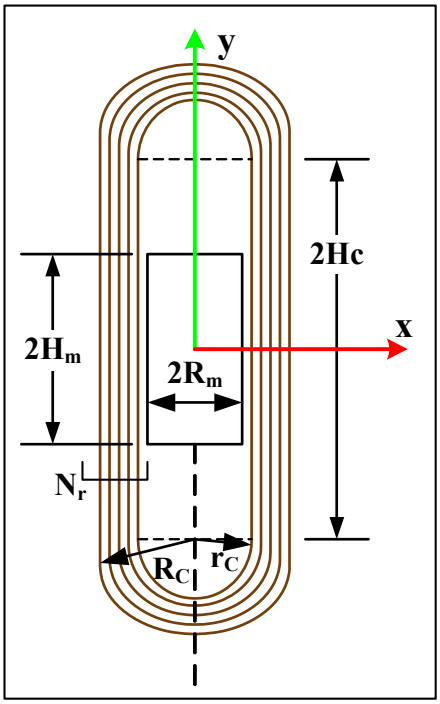

(b) Crosssectional View

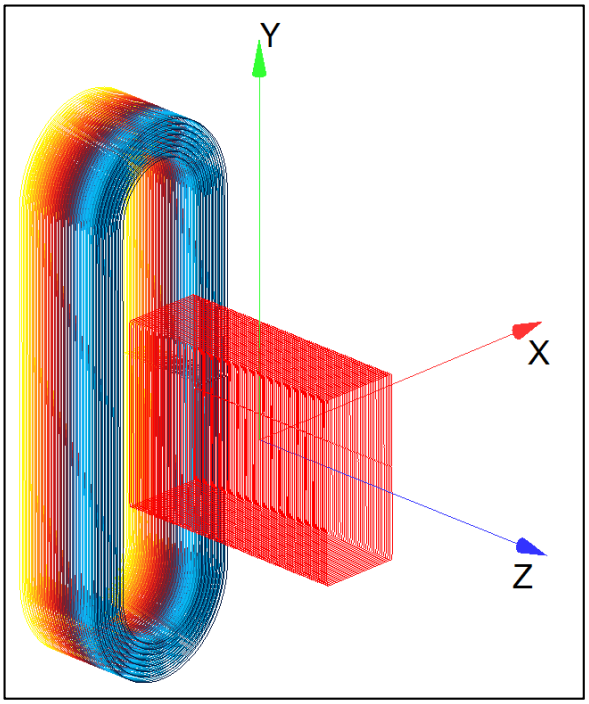

(c) 3-Dimensional Perseectiove

Figure 12.7: Traditional RCTS Solenoid with Dimensional Parameters Shown.

Unlike the model used for cylindrical solenoids, complete elliptical integrals cannot be used to simplify and expedite the computational process, which is due to the complex geometry of the coils used in the RCTS drive system. Before discussing the use of incomplete elliptical integrals, equations are created to define the geometry of the magnets and coils along the z axis (i.e. the axis shared by the magnetic poles of the magnet and packed coils). A single coil, that contributes to modeling the permanent magnet as numerous concentric coils, is discretized radially by angle and is given in Cartesian coordinates (eventually converted to polar coordinates) as:

$$\alpha = \tan^{-1}\frac{H_m}{R_m} \tag{12.15}$$

$$x_m = \begin{matrix} \theta \le \alpha \\ \theta \le \pi - \alpha \\ \theta \le \pi + \alpha \\ \theta \le 2\pi - \alpha \end{matrix} \begin{Bmatrix} R_m \\ H_m/\tan\theta \\ -R_m \\ -H_m/\tan\theta \end{Bmatrix} \tag{12.16}$$

$$y_m = \begin{matrix} \theta \le \alpha \\ \theta \le \pi - \alpha \\ \theta \le \pi + \alpha \\ \theta \le 2\pi - \alpha \end{matrix} \begin{Bmatrix} R_m/\tan\theta \\ H_m/2 \\ -R_m/\tan\theta \\ -H_m/2 \end{Bmatrix} \tag{12.17}$$

$$r_m = \sqrt{x_m^2 + y_m^2} \tag{12.18}$$

where H_m is ½ height of the magnet, R_m is ½ the width of the magnet, x_m is the horizontal Cartesian coordinate of the magnet coil, y_m is the vertical Cartesian coordinate of the magnet coil, and r_m is the radial distance to the magnetic coil at an angle θ. The purpose of discretizing the coils, that define the magnet, in in polar coordinates is so that the geometry of the outer coils can be simultaneously discretized using the same angle θ. The geometry of the outer coils on a plane orthogonal to the z axis is defined in two segments. First, where the wires making up the coil are straight (that run along the sides of the magnet) and

second, where the wires are curved (at the top and bottom below the ends of the rectangular magnet). The radial distance of the coil at any point along the arc is given by:

$$\alpha = \tan^{-1}\frac{H_c}{r_c} \tag{12.19}$$

$$R_{c,r} = \begin{matrix}\theta \le \pi \\ \theta > \pi\end{matrix}\begin{Bmatrix} r_{c,r} * \sin\left[\frac{\pi}{2} + \theta - \sin^{-1}\left(\left(\frac{H_c}{r_{c,i}}\right) * \cos\theta\right)\right] / \cos\theta \\ -r_{c,r} * \sin\left[\frac{\pi}{2} + \theta - \sin^{-1}\left(\left(\frac{H_c}{r_{c,i}}\right) * \cos\theta - \pi\right)\right] / \cos\theta - \pi \end{Bmatrix} \tag{12.20}$$

$$x_{c,r} = \begin{matrix}\theta \le \alpha \\ \theta \le \pi - \alpha \\ \theta \le \pi + \alpha \\ \theta \le 2\pi - \alpha\end{matrix}\begin{Bmatrix} r_{c,r} \\ R_{c,r} * \cos\theta \\ -r_{c,i} \\ R_{c,r} * \cos\theta \end{Bmatrix} \tag{12.21}$$

$$y_{c,r} = \begin{matrix}\theta \le \alpha \\ \theta \le \pi - \alpha \\ \theta \le \pi + \alpha \\ \theta \le 2\pi - \alpha \\ \theta = \pi/2 \\ \theta = 3\,\pi/2\end{matrix}\begin{Bmatrix} r_{c,r}\tan\theta \\ R_{c,r} * \sin\theta \\ -r_{c,r}\tan\theta \\ R_{c,r} * \sin\theta \\ H_c + r_{c,r} \\ -(H_c + r_{c,r}) \end{Bmatrix} \tag{12.22}$$

substituting $y_{c,r}$ where $\theta = \pi/2, 3\pi/2$, then $R_{c,r}$ is reassigned as:

$$R_{c,r} = \sqrt{x_{c,r}^2 + y_{c,r}^2} \tag{12.23}$$

where $x_{c,r}$ is the horizontal Cartesian coordinate of the outer coil n_r, $y_{c,r}$ is the vertical Cartesian coordinate of the outer coil n_r, $r_{c,r}$ is the local radius of the upper or lower circular portions of coil r (based on n_r), and $R_{c,r}$ is the radial distance to the coil r (or coil n_r) based on an angle θ. After discretizing the polar components of the magnet and coil loops, the geometry can be simply defined by arrays containing r_m, $R_{c,r}$, and the discretization angle θ_i. This simplified geometry is defined in Figure 12.8.

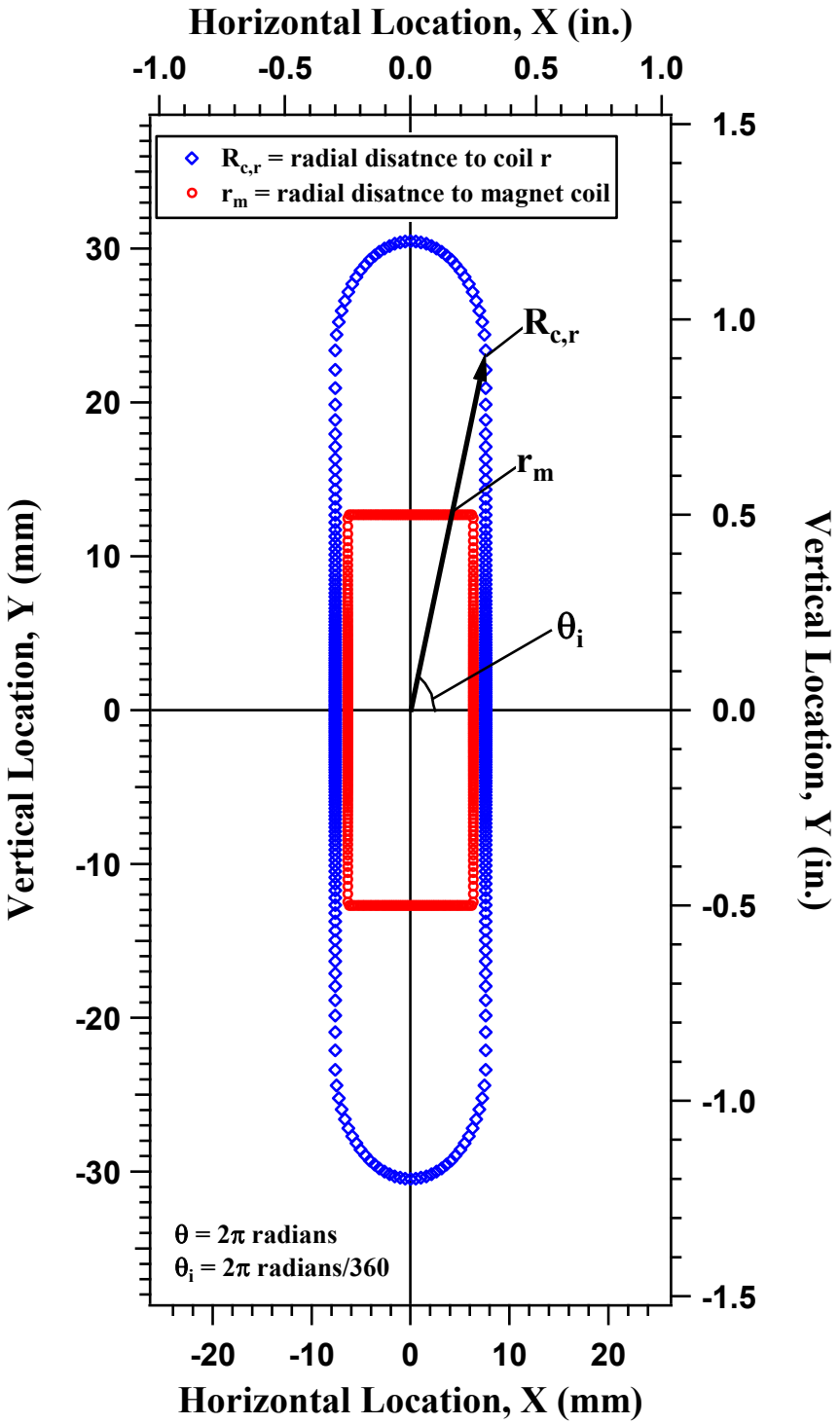

Figure 12.8: Example of Discretizing Both the Magnet and Coil Loops based on the Discretization angle θ_i.

The simplified geometry is used to create elements that are simultaneously discretized by the same angle θ_i for simplicity when simulating the force-displacement relationships of the RCTS solenoid. Reusing the formula from Robertson et al. (2012), the total linear force interaction between an RCTS magnet and coil is summed through superposition and is given by:

$$F_f(r_1, r_2, z) = \mu_0 I_1 I_2 z \sqrt{\frac{m}{4r_1 r_2}} \times \left[K(m) - \frac{m/2-1}{m-1} E(m)\right] \tag{12.24}$$

$$m = \frac{4r_1 r_2}{[r_1+r_2]^2+z^2} \tag{12.25}$$

$$F_{z_1} = \sum_{n_m=1}^{N_m} \sum_{n_r=1}^{N_r} \sum_{n_z=1}^{N_z} F_f\left(r(n_r), R_m, z + L(n_m, n_z)\right) \tag{12.26}$$

$$r(n_r) = R_C + \frac{n_r-1}{N_r-1}[R_C - r_c] \tag{12.27}$$

$$L(n_m, n_z) = -\frac{1}{2}[l_m + l_c] + \frac{n_z-1}{N_z-1} l_c + \frac{n_m-1}{N_m-1} l_m \tag{12.28}$$

where, in the $r(n_r)$ formulation, R_c is replaced by $R_{c,r}$ as defined above, $R_c - r_c$ is the thickness of the RCTS solenoid coil pack, R_m is replaced by r_m as defined above, and the remaining variables remain the same.

The complete elliptical integrals used in Robertson et al. (2012) are reconfigured as incomplete elliptical integrals whose base equations are:

$$K(m) = \int_0^\theta \frac{d\theta}{\sqrt{1-m*\sin^2\theta}} \tag{12.29}$$

$$E(m) = \int_0^\theta \sqrt{1 - m * \sin^2\theta}\, d\theta \tag{12.30}$$

where the integral is defined from 0 to $\theta=2\pi$, and $d\theta$ is based on the discretization angle of the magnet-coil geometry (e.g. given as $2\pi/360$ as presented in Figure 12.8). In this case,

the modulus, m, used in the elliptical integral is not constant but is defined by the geometry provided for the RCTS solenoid where:

$$m_{RCTS} = \frac{4r_1 r_2}{[r_1+r_2]^2+z^2} \tag{12.31}$$

where r_1 is $r(n_r)$ reassigned previously as $R_{c,r}$, which is the radial distance from the central axis (z) to a single loop and r_2 reassigned as R_m, both are defined at the discretization angle θ_i. Therefore, the integral calculation of the force-displacement calculation for the RCTS solenoid is similar to the simulations in Robertson et al. (2012); however, the RCTS geometry is discretized by $d\theta$ and sums to Nr x Nz x N_m x θ iterations.

12.4.1 Measurements of Solenoid Force-Displacement Relationships

To calibrate the numerical model used in this study, an experimental setup was used to test different packed coil configurations and magnetic strengths. An experimental setup was configured to position a permanent magnet at a specific distance from a packed coil of wire. The line of the poles of the permanent magnet were placed to match the magnetic poles generated by the coils (i.e. visualized using the thumb rule). The distance was measured as the distance from the center of the coils to the center of the permanent magnet. When the center of the magnet is position at the center of the coils, the force-couple is 0 because the magnetic flux through the magnet balances equal and opposite to the magnetic flux created by the coils. The experimental setup consisted of the coils mounted to an aluminum (nonmagnetic) arm that was fastened to an aluminum base plate. The base plate was placed on a Sartorius MSE8202S laboratory scale used to measure vertical load measured in metric units of grams. The center of the coils coincides with the center of the base plate in order to translate the vertical load between the magnet and the coil axially into the scale without generating moments. The axial distance between the center of the permanent magnet and the coils was determined using a L.S. Starrett Co. 763 Micrometer.

The micrometer was also used to control the axial distance between the magnet and coils. An Agilent E3620A DC power supply was used to supply current to the coils generating the cumulative packed coil magnetic flux. Four different coil magnet configurations were tested and numerically modeled, the parameters of these configurations are shown in Table 12.2. The schematic shown in Figure 12.3 provides an illustration of this experiment as well as a perspective for the numerical simulations. Two photographs of the experimental setup are shown in Figure 12.9.

Table 12.2: Parameters for Experimental Tests and Numerical Simulations.

Configuration:		1	2	3	4
Coil					
Nr	Winds	8	1	8	8
Nz	Winds	34	34	34	20
lc	(in.)	0.6	1.2	0.6	0.35
rc	(in.)	0.3	0.3	0.3	0.3
Rc	(in.)	0.5	0.335	0.5	0.5
2Hc	(in.)	2	2	2	1.5
Resistance	(Ohm)	5.95	0.27	5.95	3.1
Wd	(in.)	0.01	0.035	0.01	0.01
Magnet					
lm	(in.)	1.5	1.5	1.5	1.5
2Rm	(in.)	0.463	0.463	0.5	0.5
2Hm	(in.)	2	2	1	1

In each experiment and simulation, three different current levels were supplied to the packed coils. The experimental and numerical results are presented together and are provided in Figure 12.9 to Figure 12.13.

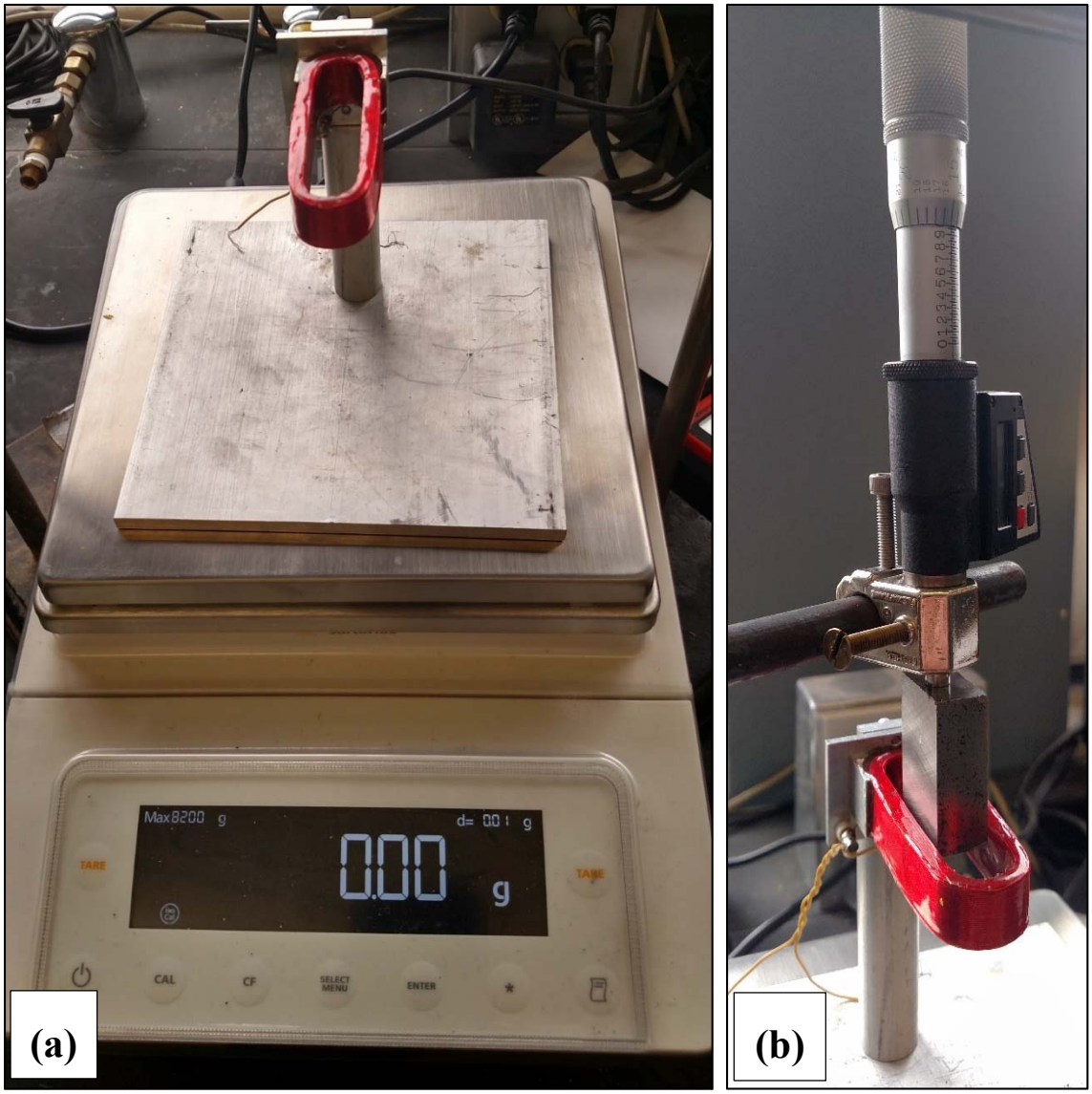

Figure 12.9: (a) Coil Mounting Plate and Scale Used for Measuring the Generated Magnetic Force and (b) Micrometer with Magnet Mounted.

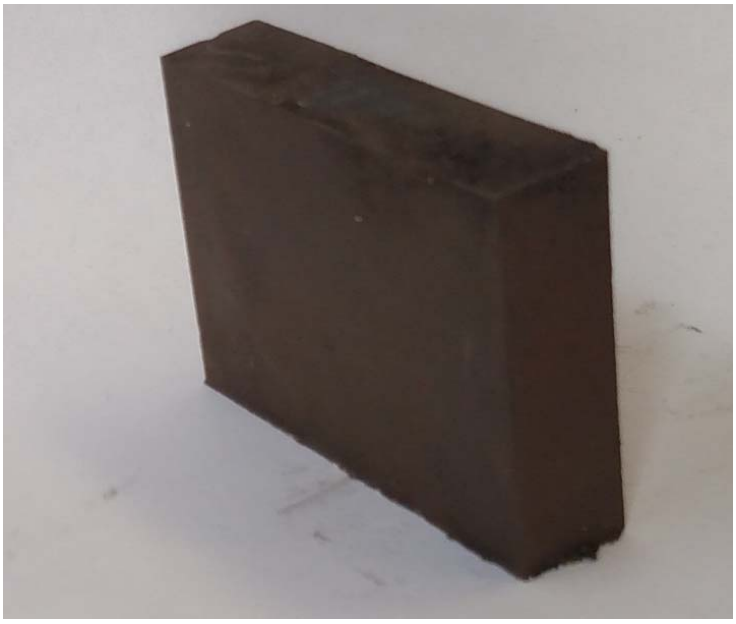

(a) Picture of 2 x 1 x 0.46 -in. Magnet

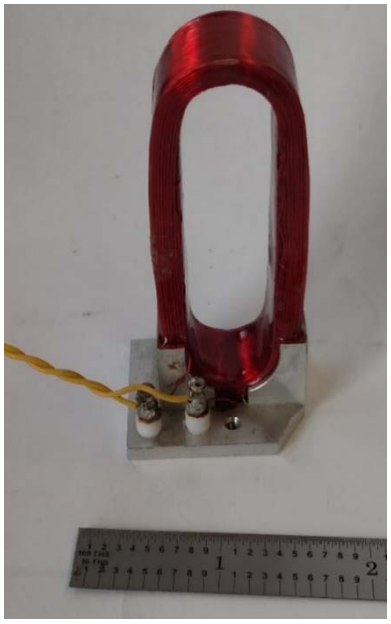

(b) 0.6-in. Wound Coil

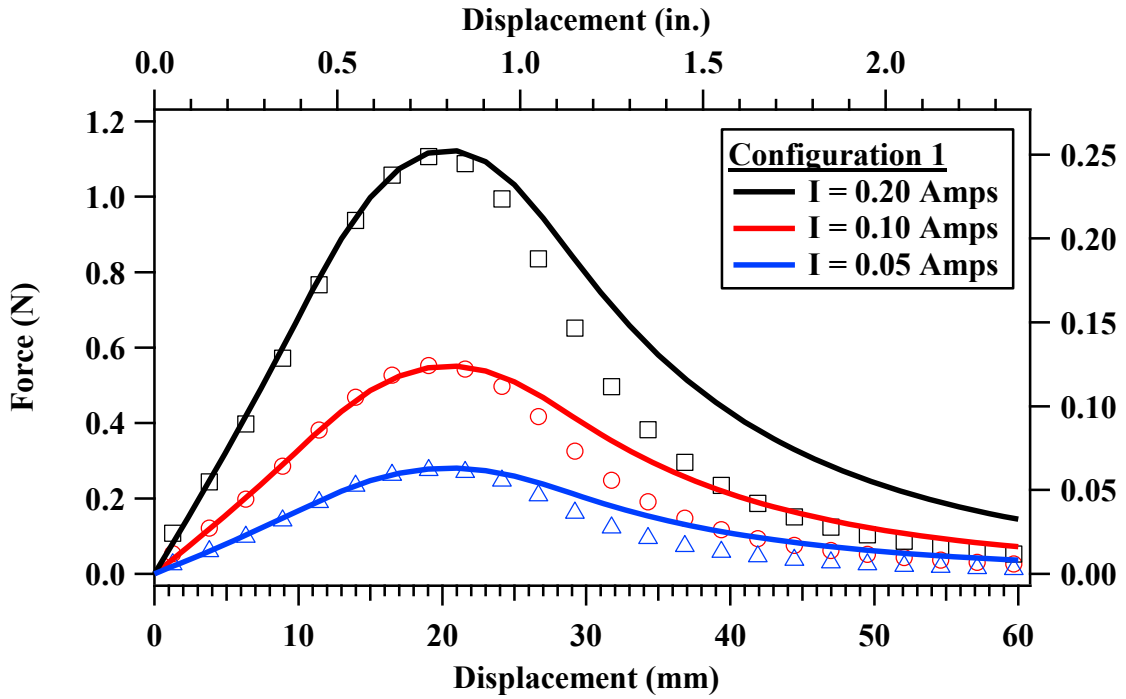

(c) Variation in Force with Displacement for Numerical and Experimental Results

Figure 12.10: (a) Pictures of the Magnet, (b) Wound Coils, and (c) Numerical and Experimental Results for the Force Generated Between the Magnet and the Coils; Based on the Distance from the Center of the Coils to the Center of the Magnet for 3 Levels of Current for Configuration #1.

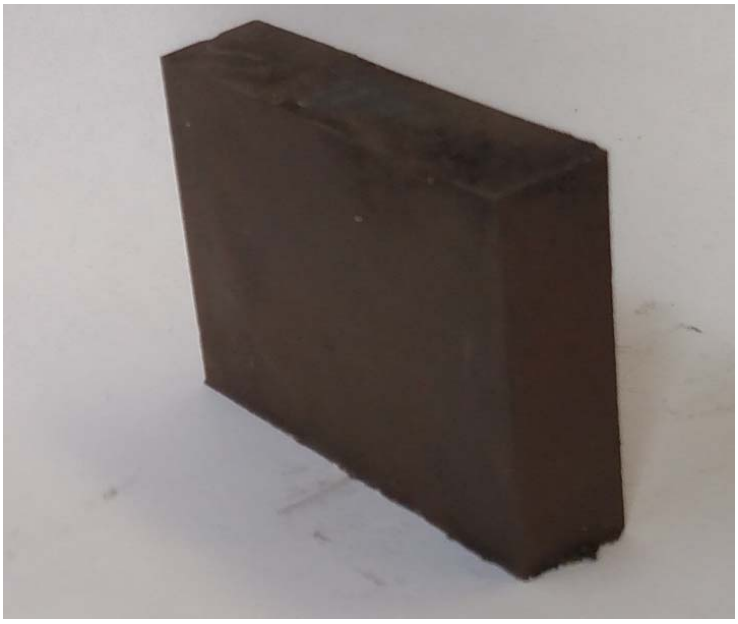

(a) Picture of 2 x 0.46 x 1 -in. Magnet

(b) 1.2-in. Wound Coil

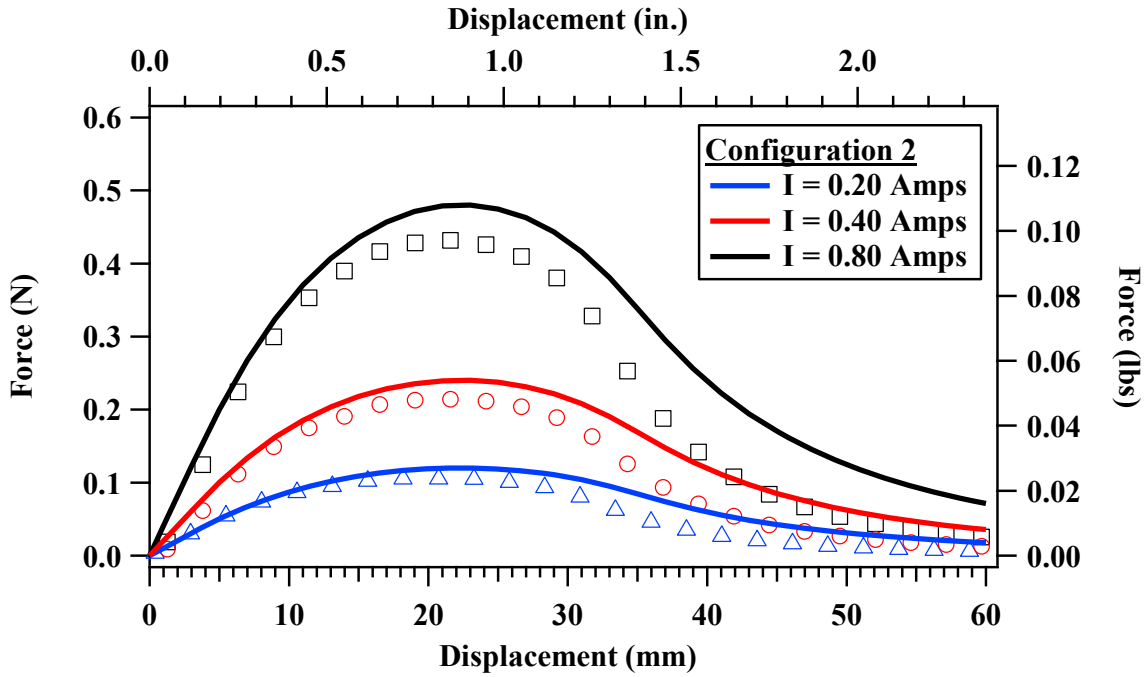

(c) Variation in Force with Displacement for Numerical and Experimental Results

Figure 12.11: (a) Pictures of the Magnet, (b) Wound Coils, and (c) Numerical and Experimental Results for the Force Generated Between the Magnet and the Coils; Based on the Distance from the Center of the Coils to the Center of the Magnet for 3 Levels of Current for Configuration #2.

(a) Picture of 1.5 x 0.5 x 1 -in. Magnet

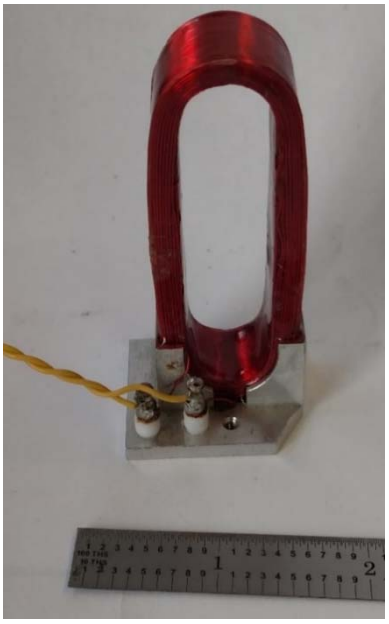

(b) 0.6-in. Wound Coil

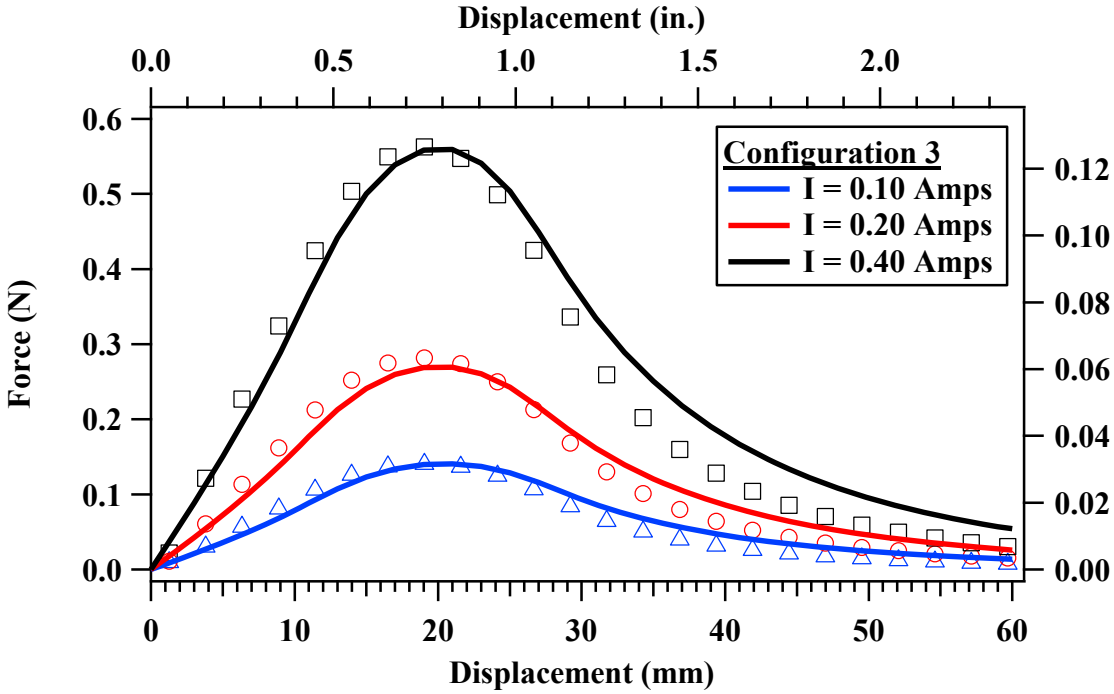

(c) Variation in Force with Displacement for Numerical and Experimental Results

Figure 12.12: (a) Pictures of the Magnet, (b) Wound Coils, and (c) Numerical and Experimental Results for the Force Generated Between the Magnet and the Coils; Based on the Distance from the Center of the Coils to the Center of the Magnet for 3 Levels of Current for Configuration #3.

(a) Picture of 1.5 x 0.5 x 1 -in. Magnet

(b) 0.6-in. Wound Coil

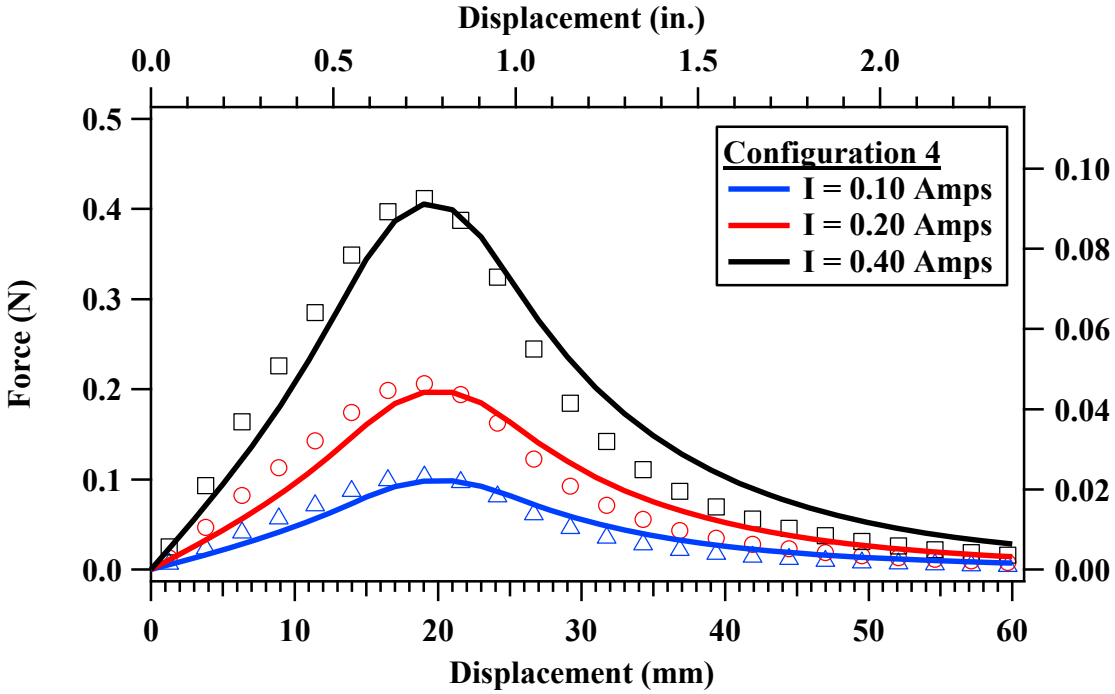

(c) Variation in Force with Displacement for Numerical and Experimental Results

Figure 12.13: (a) Pictures of the Magnet, (b) Wound Coils, and (c) Numerical and Experimental Results for the Force Generated Between the Magnet and the Coils; Based on the Distance from the Center of the Coils to the Center of the Magnet for 3 Levels of Current for Configuration #4.

Some differences between the experimental and numerical results are seen and are discussed herein. In general, the numerical results yields higher forces between the magnet and packed coils at axial distances that are greater than 25 mm. This can be attributed to the imperfections in the coil-magnet setup in the experimental method, which are otherwise perfect in the numerical simulation. When a new RCTS solenoid geometry is advanced later in this chapter, these differences have the potential to lead to an overall reduction of the solenoid force couple, but this is of minor consequence in the composite scheme of the new design.

12.4.2 Validation of Numerical Model and Experimental Setup using a TS Calibration Procedure

To validate the numerical model and experimental setup, a procedure used to calibrate the TS test in the traditional RCTS device is presented and compared with calculations from the model and experiments. The TS calibration procedure involves using a metal specimen that has known dimensions and mass. The specimen is first evaluated using the resonant column (RC) test for determining the resonant frequency and material damping ratio. These results are used to calculate the torsional stiffness constant of the metal specimen. In the TS calibration procedure, sinusoidal excitation is supplied to the drive coils at several voltage amplitudes to generate corresponding levels of torque to the metal specimen. The torsional angle of rotation at the top of the specimen is measured and the torsional stiffness constant, determined from the RC test, is used to determine the torque corresponding to the voltage amplitude supplied. The torque versus excitation voltage is used to determine a torque calibration factor for the drive plate given in units of ft-lbs/V. The calibrated torque calibration factor is compared with a theoretical torque calibration factor determined from the numerical model and experimental setup of the magnetic solenoids used in the RCTS device.

First, the calculations conducted to determine the torsional stiffness constant are provided. The natural frequency from the RC test is given as:

$$\omega_n = \frac{\omega_r}{\sqrt{1-2D^2}} \tag{12.32}$$

where ω_n is the natural frequency, ω_r is the resonant frequency determined from the RC test, and D is the material damping ratio from the RC test. The stiffness constant is based on the mass polar moment of inertia of the metal specimen and the drive plate used to excite the specimen in torsion. The mass polar moment of inertial of the drive plate, I_{DP}, is determined in a separate calibration procedure and the mass polar moment of the metal specimen includes the stem of the specimen and the top disk-like attachment cap. The mass polar moment of the stem, I_0, is given as:

$$I_0 = m * (r_i^2 + r_o^2) \tag{12.33}$$

where r_i and r_o are the inner and outer radii of the calibration specimen, respectively. The mass polar moment of the attachment cap is simply:

$$I_{TC} = m * r^2 \tag{12.34}$$

where the mass is known to be uniformly distributed with the radius of the top cap. The torsional stiffness constant, k_t, as discussed in the introduction of this chapter, can be defined as:

$$k_t = \omega_n^2 * (I_{tot}) = \omega_n^2 * (I_{DP} + I_0 + I_{TC}) \tag{12.35}$$

where I_{tot} is the summation of I_{DP} and I_0. The k_t is given in terms of ft-lbs/rad. In the torque calibration procedure, the sinusoidal excitation is supplied at a low frequency of 1 Hz to avoid dynamic response of the specimen as well as inertial effects that occur with

increasing frequency. The torque applied is determined from the measured angle of rotation, θ, resulting from the voltage amplitude supplied. The torque, T, applied, for a particular voltage amplitude, is determined as:

$$T = k_t * \theta \tag{12.36}$$

The torque calibration factor, $K_{t,cal}$, for this singular instance is determined by dividing the calculated T corresponding to the excitation voltage supplied, which is given as:

$$K_{t,cal} = \frac{T_i}{V_i} \tag{12.37}$$

where T_i is the torque corresponding to the voltage amplitude V_i. Thus, the $K_{t,cal}$ is given in ft-lbs/V. In the torque calibration procedure, several voltage amplitudes are supplied and several levels of torque are calculated. $K_{t,cal}$ is determined using a linear least-mean-squares fit to the calculated torque versus the voltage amplitude supplied.

An example of the results from this calibration are provided for UT Drive Plate #5 and Metal Specimen #2. The properties of the drive plate and metal specimen used in this calibration procedure are listed in Table 12.3.

Table 12.3: Properties of Calibrated Drive Plate and Metal Calibration Specimen.

Drive Plate #5

	Symbol	Units	Value
Calibrated Mass Polar Moment of Inertia	I_{DP}	ft-lb/sec^2	6.77806E-06

Metal Specimen #2

	Symbol	Units	Value
Outer Radius	r_o	cm	1.11
Inside Radius	r_i	cm	1.03
Mass	m	g	79.96
Resonant Frequency	ω_r	rad/sec	669.6
Material Damping Ratio	D	%	0.42
Natural Frequency	ω_n	rad/sec	669.7
Torsional Stiffness Constant	k_t	ft-lb/V	998.0

The torque calibration factor, $K_{t,cal}$, for a 2016 calibration of UT Drive Plate #5 and Metal Specimen #2 was 0.0161 ft-lbs/V for an excitation frequency of 1 Hz.

Now this calibration factor is compared with the results of the numerical model and experimental setup for a single solenoid used in the RCTS device. The typical solenoid configuration used in the traditional RCTS device was presented previously as Configuration #3. Both experimental and numerical results revealed that this solenoid configuration yields a force-couple at an optimum displacement (i.e. where maximum force occurs), based on the current supplied, of 1.41 Newton (N) per Amperage (A). For a single packed coil, this can be converted to force versus DC voltage amplitude, based on the resistance of the packed coil, which was approximately 6 ohms. Therefore, the force per voltage amplitude (using Ohm's law) is 0.235 N/V. The next step is to convert the force output per voltage amplitude to torque per voltage amplitude. The numerical model and experimental setup are for a single solenoid pair and the RCTS device has 8 solenoid parings that apply the force-couple in terms of toque based on the radius from the center of rotation. In addition, the resistance of the single solenoid pairing is also multiplied by 8

to account for all of the coils in the traditional RCTS device. Thus, the theoretical torque calibration factor is determined by:

$$K_{T,theory} = \frac{8*rF}{I*8R} \tag{12.38}$$

where $K_{T,\ theory}$ is the theoretical force constant based on a single coil in the numerical model and experimental setup, r is the radial distance of the force-couple from the center of rotation of 3.25 in., I is the current supplied to the packed coil, and R is the resistance of the packed coil. In the numerator, the product of the force and the radius are multiplied by 8 to represent the 8 coils in the RCTS device; however, the resistance of a single packed coil is also multiplied by 8 and thus the number of coils cancels out in the force constant calculation. From the force per voltage amplitude given previously and the formulation given above, the theoretical torque calibration factor is 0.0143 ft-lb/V. This value is similar to the 0.0161 ft-lbs/V for the UT Drive Plate #5 and Metal Specimen #2 calibration. The minor difference in the numerical values is attributed to the magnets in UT Drive Plate #5 possessing greater magnetic strength than the one modeled and experimentally tested and UT Drive Plate #5 may have less resistance than the packed coil that was experimented with. In summary, the numerical model and experimental setup are shown to adequately model the torque characteristics of the RCTS devices with an absolute difference of 0.0018 ft-lbs/V, which is otherwise negligible for this comparison.

12.5 NUMERICAL MODEL FOR TRADITIONAL RCTS DEVICE

The numerical model for modeling the entire drive plate of the traditional RCTS device is similar to the model for a single packed coil with some adjustments. There are two key differences between the numerical model and experimental setup and the RCTS device. First, in the RCTS device, the magnets are situated adjacent and between two

packed coils. This is done to double the force output and balance the force-displacement relationship, also this configuration extends the range where the force-displacement behavior is linear. Second, as the drive plate rotates, the magnetic poles of the magnets rotate out of plane with the magnetic poles of the packed coils. This results in a reduction of the force vector that is proportional to the angle of rotation of the drive plate. In this subsection, the force-displacement relationship for a magnet paired with two coils is shown in combination with the numerical model that incorporates rotation of the drive plate.

In the RCTS device, the magnets are situated adjacent and between two packed coils. The magnets are situated between adjacent coils so that, in the initial position, the force-displacement relationships for each adjacent coil and magnet are near the maximum. When rotating from the initial position, the magnet approaches one coil and the force-couple begins to reduce. As the magnet moves away from the other coil, the force-couple increases. This occurs for about 1 degree of rotation or 1 mm of displacement of the magnet from the initial position. After 1 degree of rotation the force-couple decreases in either case. This configuration extends the range where the force-displacement behavior is linear. A visual rendering of this configuration is shown in Figure 12.14.

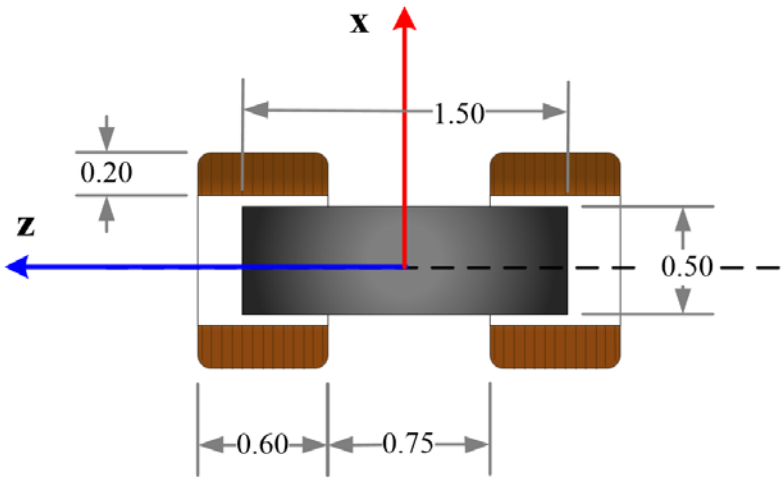

Figure 12.14: Conceptual Mid-Height Cross-Section of a Coil-Magnet-Coil Solenoid in the Traditional RCTS Device Design.

The traditional RCTS device configuration only allows for a maximum of 2.5 degrees of rotation of the drive plate or about 4 mm of axial displacement of the magnet. After the drive plate rotates 2.5 degrees, but in most cases less, the magnet rotates into and contacts the coils. However, the force-displacement relationship, permitted and as modeled, is plotted far past this to visualize the behavior as though the magnet could occupy the same space as the coils. The displacement of the force couples from the single coil experiments are converted into degree of rotation as would occur in the RCTS device and are shown in Figure 12.15. However, in an actual RCTS test the coupled coil-magnet-coil solenoid would generate a force that is 2 times greater than the average relationship shown in Figure 12.15.

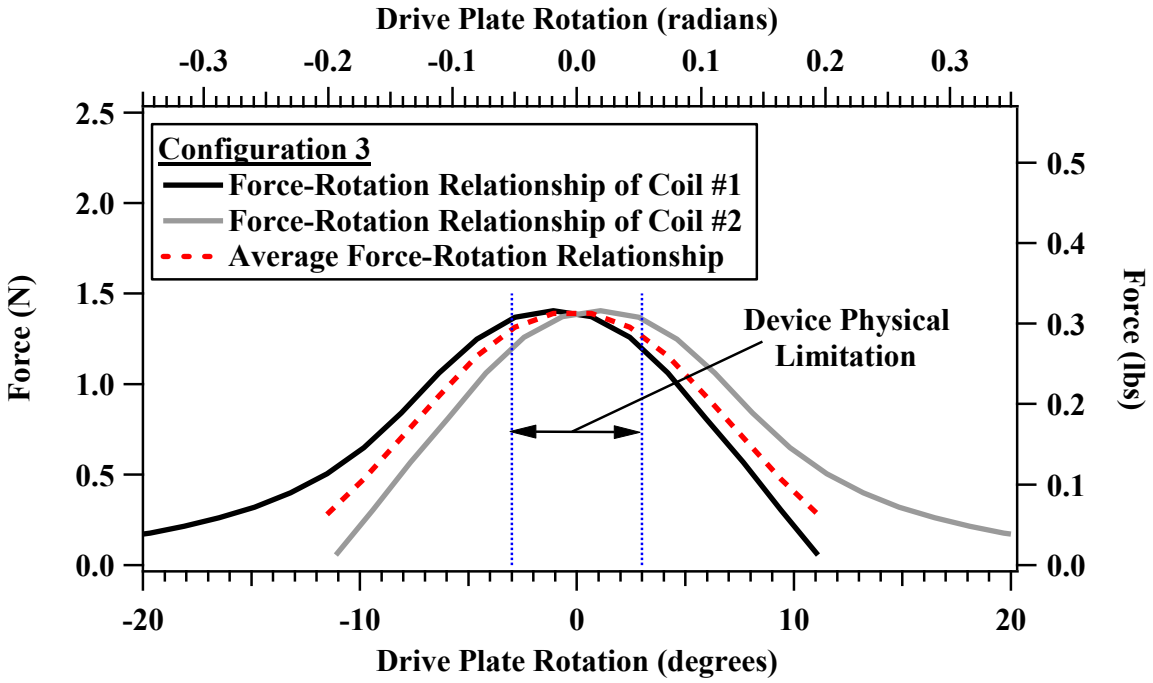

Figure 12.15: Force-Rotation Relationship of Traditional RCTS Device Design.

The numerical model calculates the force-displacement relationship as though the magnet is traveling linearly through the coils, but the force vector is reduced based on the angle that the magnet rotates away from the axis of the coils (i.e. force times cosine of the

angle of rotation). The force-displacement relationships from the experimental results and the numerical model developed herein are converted into torque and are plotted with the horizontal axis in terms of angle of rotation as torque-rotation relationships, shown in Figure 12.16.

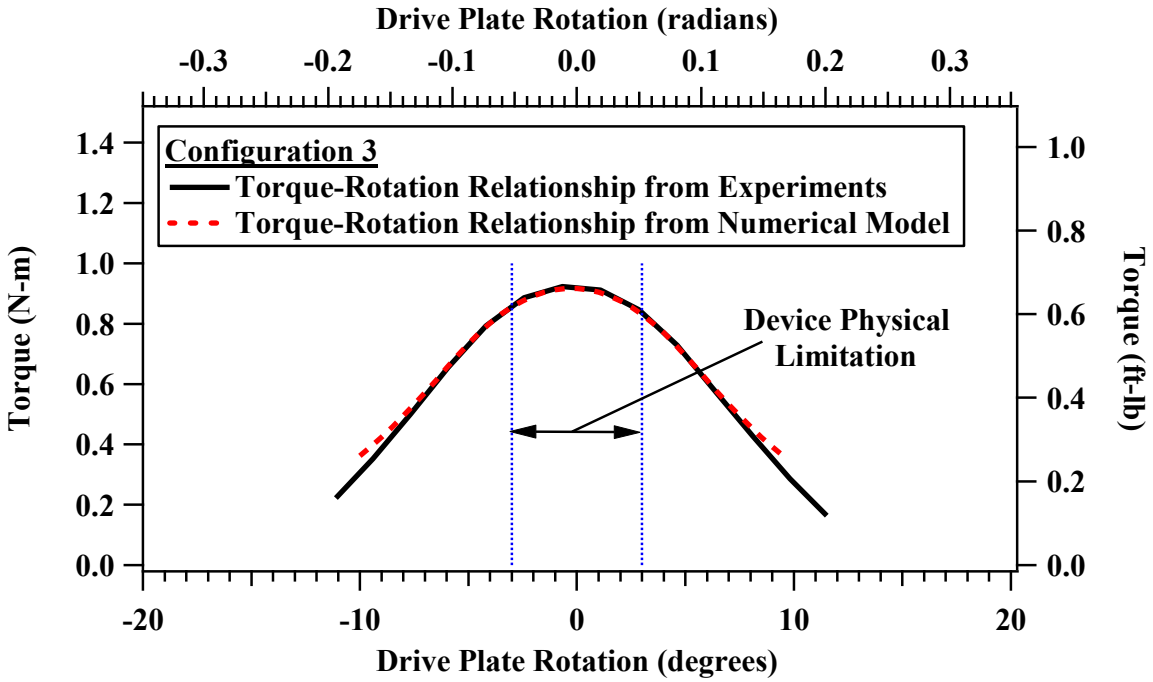

Figure 12.16: Torque-Rotation Relationship of Traditional RCTS Device Design Calculated from Experiments on a Magnet-Coil Pair and Predicted from the Numerical Model Developed Herein.

Both of the experimental and numerical model results for predicting the torque-rotation relationships are in good agreement and show that the numerical model is suitable for predicting the torque-rotation relationship of the drive plate. Thus, the model can be used to further to develop a more powerful solenoid system to enhance the capacity of the RCTS device.

12.6 SUMMARY

In typical RCTS testing, the electromagnetic driving system consists of 4 permanent magnets and 8 specially configured coils of wire. The driving system is configured to permit specific levels of torque to be applied based on the amperage sent to the packed coils. The driving system is configured to allow for specific levels of torque to be applied to the specimen based on the amperage sent to the coils. The magnetic force between the permanent magnet and the coils positioned on either side of the magnet, acts as a balanced magnetic solenoid. In this study, experimental testing and numerical modeling were conducted to understand the characteristics of the electromagnetic torque motor in the traditional RCTS device. Results from the experimental testing and numerical modeling for predicting the torque-rotation relationships are in good agreement and show that the numerical model is suitable for predicting the torque-rotation relationship of the drive plate. Thus, the model can be used to further to develop a more powerful solenoid system to enhance the capacity of the RCTS device, which is discussed in the next chapter.

Chapter 13

Development of Higher Capacity RCTS Device to Reach Higher Levels of Shearing Strain

13.1 INTRODUCTION

In this chapter, numerical modeling is conducted to facilitate the design of an electromagnetic driving system in the RCTS equipment that will provide: (1) higher levels of torque that can be applied to a soil specimen, (2) further travel of the magnetics within the solenoids to allow for greater angle of rotation of the driving system, which will allow for higher shearing strains to be applied to the specimen, (3) greater area around the magnetic to minimize the potential for contact between the magnets and the coils during testing, and (4) lower impedance in the solenoid circuits that enhances the capability of the electronic equipment used to control the driving system.

The extent of the traditional RCTS test has been limited by the amount of toque that can be generated by the driving system and the angle of rotation allowed by the driving system before magnet-coil contact. The amount of toque applied is limited by the electronic equipment used to supply current to the coils and angle of rotation is limited by the geometry of the coils and the initial position of the magnet between the two adjacent coils. These limitations translate into limited shearing strains that can be excited by the equipment. For stiffer materials, which incorporates materials tested at high confining stresses (i.e. > 1atm), the electronic equipment is unable to supply high enough currents to the coils that would achieve higher force output and thus higher shearing strains. Furthermore, if high current (i.e. > 2 amps) is used, then the amount of heat generated, potential for demagnetization of the permanent magnets, and risk of electrical shock to the operator become a major concern. The geometry of the magnets and the coils limit the

angle of rotation of the drive system thereby limiting the shearing strains exited during the test to no more than 0.5%. In this investigation, a new electromagnetic driving system is designed to maximize the capability of the electronic equipment that supplies current to the driving system while reducing the potential of overheating the driving system and eliminate the risk of electrical shock to the operator. The geometry of the magnets and the coils are reconfigured to allow a greater angle of rotation of the drive system that can allow shearing strains up 4% (i.e. for a 2 in. diameter specimen). This new device allows for soil testing that can test soil from the linear-elastic shearing strain range (e.g. < 0.0005%), and in many cases, to shear strains that begin to fail some soils (e.g. > 1%). A device and control and monitoring system that can accurately map 8 orders of magnitude of shear strain (i.e. 10^{-6} % to 1% or higher) was developed and is presented in this chapter. Some additional modifications to the sensors used to measure dynamics behavior are recommended along with potential limitations of a higher capacity RCTS device.

13.2 DEVELOPMENT OF NEW, HIGHER-POWERED, ELECTROMAGNETIC SOLENOIDS AND TORSIONAL SYSTEM

The design of a new electromagnetic drive system aims at increasing the force capacity of the device and the degree of rotation possible. The increase in force is achieved by increasing the number of coils in each solenoid while limiting the resistance of the packed coils. The increase in angle of rotation possible is achieved by placing the coils further from the initial position of the magnets. The initial magnetic poles of the magnet are offset from the magnetic poles of the packed coils. As the drive plate rotates, the magnet poles of the permeant magnets and the coils come closer into parallel magnetic alignment. The angle of rotation was targeted at 10 degrees, which would bring most soils into a shearing strain range that would induce failure (i.e. ~ 4%). Several steps were taken to

adjust the numerical model from the traditional RCTS design to account for the offset of the packed coils and the rotation of the magnets during operation of the RCTS device. This subsection goes into detail about the steps taken to advance a numerical model that can predict and help design a new RCTS drive system that can test soils to a level of shear strain not before reached in RCTS devices.

The numerical model developed in Chapter 12 is adjusted for a more complex geometry of the coils. The more complex geometry of the coils is needed to enhance torque capacity and angle of rotation of the drive system. This is done by offsetting the angle of the coils relative to the initial position of the permanent magnet. Several configurations were evaluated to determine an angle offset and size of the packed coils that enhances the maximum force output, allows for high angle of rotation, and that can fit the current RCTS device physical boundaries. A 2D conceptual schematic of this configuration is shown in Figure 13.1. A 3D conceptual schematic of this configuration is shown in Figure 13.2.

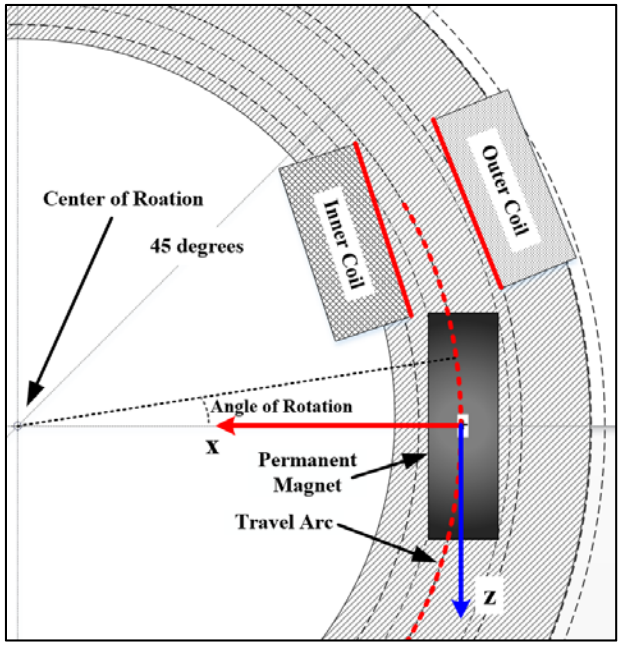

Figure 13.1: 2D Conceptual Schematic of a Magnet, the Anticipated Travel Arc of the Magnet, and a Cross-Section of the Coils of Wire; Where the Coil and Magnet Elements are Illustrated Relative to the Center of Rotation.

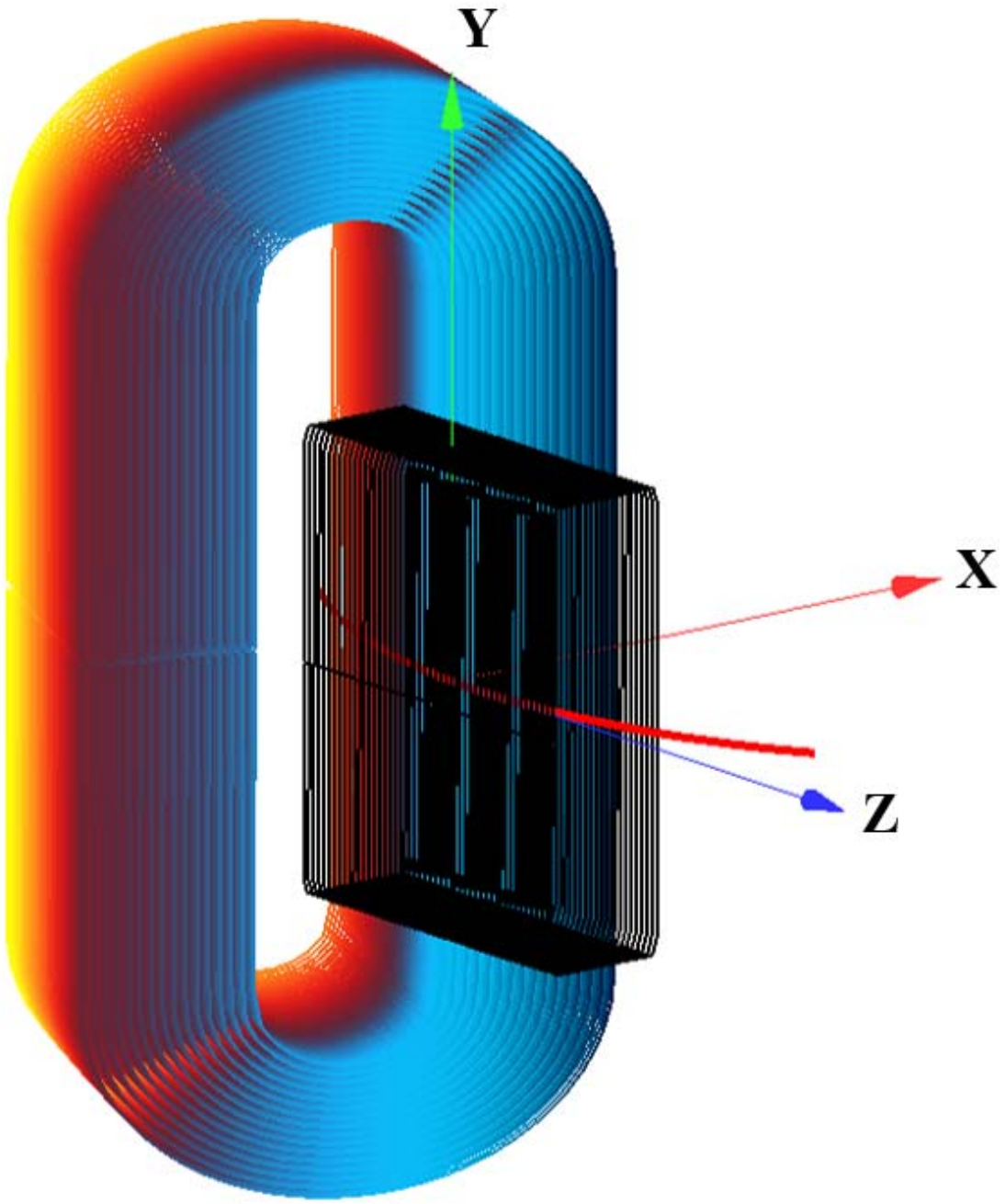

Figure 13.2: 3D Conceptual Schematic of a Magnet, the Anticipated Travel Arc of the Magnet, and the Coils of Wire.

The numerical model was constructed by first creating a coordinate system for the location for the magnet and the location of the coils. The coils were modeled by defining boundary lines on which the inner and outer segments of the coils could be based. These line segments are called the inner and outer coil line segments and are subsequently shown in red in Figure 13.1. In the X-Z plane, the lines for the inner and outer coil were based on the center of rotation and defined in Cartesian coordinates as z = mx + b. Each line is defined with starting and ending coordinates, X_1, Z_1 and X_2, Z_2, respectively. The linear parameters are based on the center of rotation and starting and ending points, an example is given for the outer coil as:

$$m_{coil,out} = \frac{(Z_2 - Z_1)}{(X_2 - X_1)} \tag{13.1}$$

$$b_{coil,out} = Z_2 - X_2 * m_{coil,out} \tag{13.2}$$

Angles for the start and finish of these lines are based on the center of rotation and starting and ending points, an example for the starting and ending angles of the outer coil is given as:

$$\theta_{start} = \tan^{-1}(Z_1/X_1) \tag{13.3}$$

$$\theta_{end} = \tan^{-1}(Z_2/X_2) \tag{13.4}$$

The lines are discretized into angle segments based on the number of axial winds Nz, i.e. $d\theta = (\theta_{end} - \theta_{start})/Nz$. For each $d\theta$, the points along the line of the inner coils is given by:

$$X_{n_z,i} = \frac{b_{coil,out}}{\tan(d\theta) - m_{coil,out}} \tag{13.5}$$

$$Z_{n_z,i} = m_{coil,out} * X_{n_z} + b_{coil,out} \tag{13.6}$$

where the subscript n_z is the counter in the numerical model that accounts for a single wind out of the total N_z winds. The coordinates for the inner and outer coil line segments are labeled as (X_o,Z_o) and (X_i,Z_i), respectively. Thus, a mean can be established as the center between these segments as:

$$X_{n_z} = (X_o + X_i)/2 \tag{13.7}$$

$$Z_{n_z} = (Z_o + Z_i)/2 \tag{13.8}$$

The angle of a single wind of the packed coils relative to the Z-axis is defined as:

$$\theta_{coil} = \tan^{-1}\left(\frac{1}{(b_{coil,out}+b_{coil,in})/2}\right) \tag{13.9}$$

where θ_{coil} is the angle of a single coil relative to the z axis and $b_{coil,in}$ is the slope of the line defining the inner segment of the coils. As shown in Figure 13.1, the line segments that define the inner and outer geometry of the coils are not parallel, but rather they approach each other, which indicates the average radius of each wind degreases as the angle from the initial position of the magnet increases. Thus the average distance between the coils and the magnet decrease as the magnet rotates into the coils. This helps to maintain a more consistent force-displacement relationship as the magnet rotates into the coils. Consequently, this design makes defining the model geometry more complicated than what has been detailed thus far. However, the diminishing coil cannot be too extreme because this would reduce the overall force-couple of a single coil wind.

The radius of each coil is based on the line segments defined previously, which is shown to change with each coil. A geometry of each coil is first defined using the formulations presented for the traditional RCTS device geometry in Cartesian coordinates as $x_{,cr}$ and $y_{c,r}$. To convert these coordinates into a 3-dimensional geometry, θ_{coil} is used to

develop a new set of coordinates. $y_{c,r}$ remains the same and a new value for the X coordinate is defined as:

$$X_{c,n_z} = X_{n_z} + x_{c,r} \tag{13.10}$$

where X_{c,n_z} is the X coordinate of a single point along the coil. The Z coordinate is defined as:

$$Z_{c,n_z} = X_{c,n_z} * \tan(-\theta_{coil}) + Z_{n_z} \tag{13.11}$$

where Z_{c,n_z} is the Z coordinate of a single point along the coil and a negative sign is placed in front of θ_{coil} because the coil is tilted to the left of the Z axis. Altogether, the Cartesian coordinates of a single point along a coil is ($X_{c,n_z}, Y_{c,r}, Z_{c,n_z}$). This 3-dimensional geometry is useful for visualization purposes, as was used for Figure 13.2, but a more simplified approach is used in the numerical model for defining the force-rotation relationship between the magnet and the coil.

In the numerical model used for the traditional RCTS device design, the coils were discretized into polar components of the magnet and coil loops, the geometry was defined by arrays containing r_m, $R_{c,r}$, and the discretization angle θ_i. This simplified geometry was shown in Figure 12.8. The updated numerical model used the same method, but these values were defined for each coil (i.e. for each n_z). However, the force between a single loop of the magnet and single loop of the coil is reduced based on the cosine of the angle between the loop of the magnet and loop of the coil. The angle of the magnet used was relative to the Z axis and was the same as the angle of rotation of the magnet. The angle, α, between the magnetic axis of the magnet and the magnetic axis of the coils is defined as:

$$\alpha = \theta_{coil} - \varphi \tag{13.12}$$

where φ is the angle of rotation of the drive plate. A conceptual schematic of the magnet at an angle of rotation of 5 degrees is shown in Figure 13.3. Thus, the force at a particular rotation of the drive plate is found using the axial distance between the centers of the magnets and the coils as was done previously, but multiplied by the cosine of φ, which is given as:

$$F_{\varphi} = F * \cos\alpha \tag{13.13}$$

where F_{φ} is the force between the magnet and the coils at an angle of rotation, φ, of the drive plate.

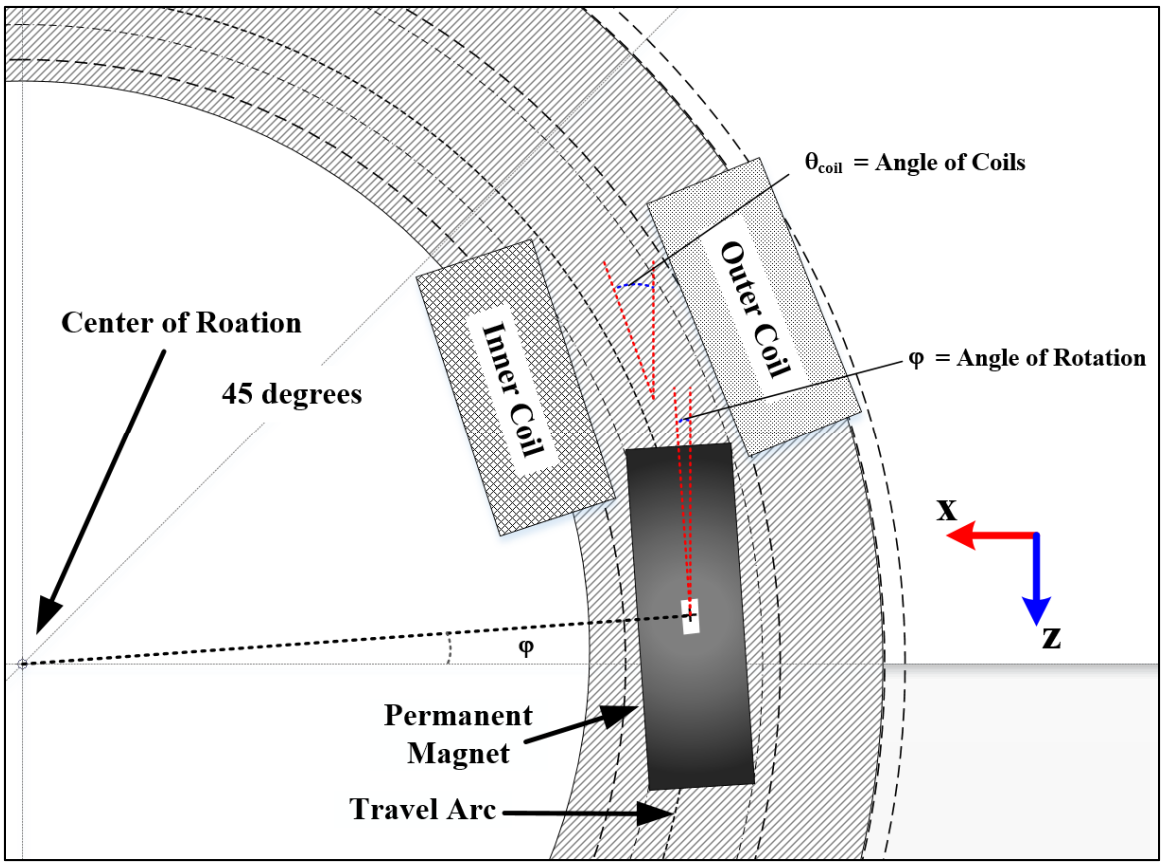

Figure 13.3: Conceptual schematic of the magnet at an angle of rotation of 5 degrees with annotations for angle of rotation of the drive plate (i.e. angle of the magnet poles of the permanent magnet) and offset angle packed coils (i.e. magnetic poles generated by the packed coils).

13.3 COMPARISONS OF THE POWER AND MOVEMENT OF THE NEW AND TRADITIONAL TORSIONAL SYSTEMS

Several design concepts were evaluated to determine the one that would have the best performance and allow for easy implementation into the equipment currently used in the Soil and Rock Dynamics Laboratory at the University of Texas at Austin. The goal of a particular design concept was to meet certain criteria, which included: (1) Maximum force output to test soils to higher shear strains that become very stiff at higher confining pressures; (2) maximize allowable angle of rotation to test soils to high shear strains when the force output is not the limiting factor; (3) maximize force output and angle of rotation while determining a configuration that fits and allows easy implementation with the equipment currently available in the soil and rock dynamics laboratory; and (4) a sensor configuration that allows easy setup and operation of the RCTS device and corresponding tests.

There were over 10 designs evaluated, but only one was chosen that is best suitable for comparison and implementation. The final design maximizes the force output because: (1) The magnet used in the design is twice as powerful as the traditional design; (2) the new design uses 592 winds per packed coil, whereas the traditional design uses 256 winds per packed coil; (3) The new design has 16 winds radially per packed coil compared with 8 winds per packed coil in the traditional design, where the new design greatly increases the force output for each increment of rotation; and (4) the type of wire chosen in the new design is 3.5 times greater than the diameter of the wire used in the traditional design, which greatly reduces the resistance in the coils thereby economizing the use of the amplifier supplying the current to the coils.

The final design maximizes the angle of rotation because the packed-coil magnetic axes are angled away from the initial orientation of the poles of the magnet. Furthermore,

the average radius of each axial coil (i.e. n_m) is larger near the initial position of the magnet and decreases further away from the magnets. The adjustment of these two geometric features allow the magnet to rotate up to 10 degrees of rotation without contacting the coils, which occurs by 2.5 degrees of rotation in the traditional design. Since the new coil design takes up more space, the radius from the center of rotation to the axis of the force-couple between the magnets and the coils is slightly less than the traditional design. The radius of torque application of the new design is 2.95 in. compared with the 3.25 in. in the traditional design.

For the traditional design, there were coils on either side of a permanent magnet so that both could simultaneously generate force. As the magnet rotates towards one magnet the force increases and as the magnet rotates away from the other magnet the force decreases. In the traditional design, the force lost as the magnet rotates away from one coil is made up by approaching the other. In theory, at a certain angles of rotation, the overall force would decrease as the magnet passed an optimum distance between the coil and magnet centers. In the traditional design, the angle of rotation is physically limited before this can occur. In the new design, the possible angle of rotation allows this optimum distance between the coil and magnet centers to be passed. This was allowed in the design so that a larger angle of rotation could be physically possible in the device. Even with this decrease in force due to large angle of rotation, the new design maintains a far greater torque capacity than the traditional design. The force-rotation and torque-rotation relationships for the traditional design and a new Design #8 are shown in Figure 13.4. Three-dimensional conceptual images of the full 8 coil-magnet-coil configurations for the traditional and new Design #8 are shown in Figure 13.5 and Figure 13.6, respectively. Three-dimensional conceptual images of the traditional and new Design #8 are shown together in Figure 13.7.

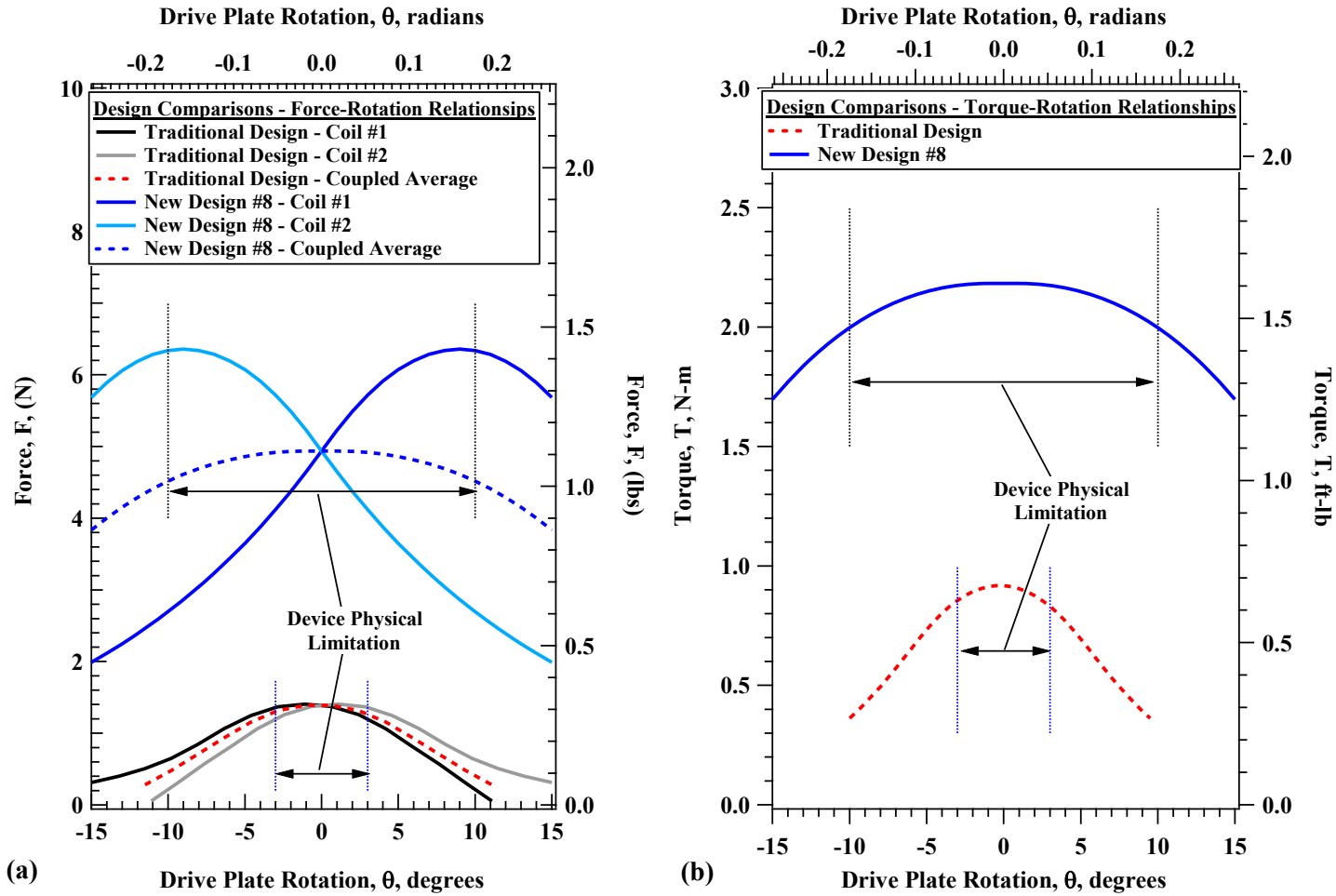

Figure 13.4: Comparisons of the Variation of (a) Force-Rotation and (b) Torque-Rotation Relationships with Drive Plate Angle of Rotation for of a Single Coil-Magnet-Coil Pair In the Traditional Design and New Design #8.

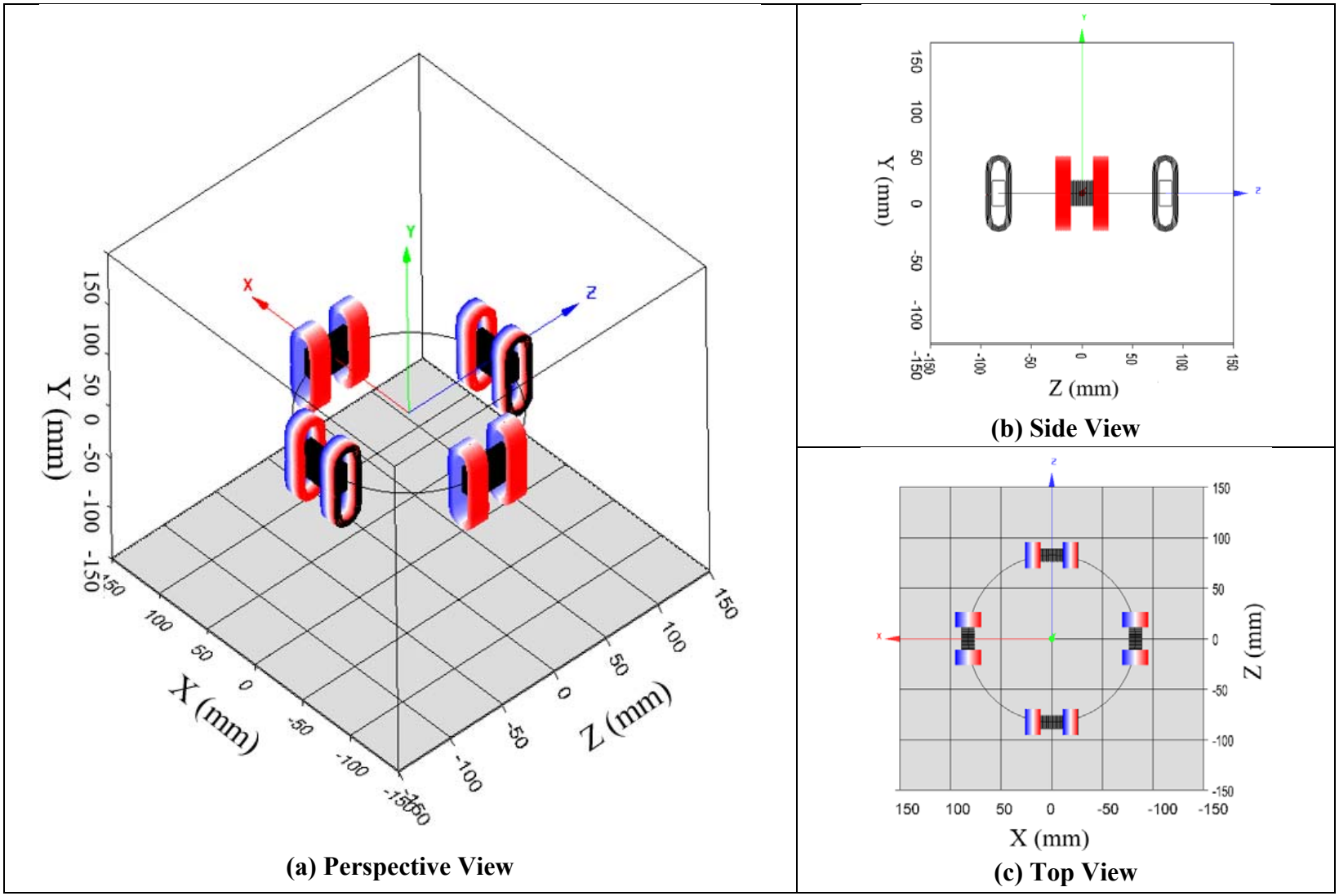

Figure 13.5: Three-Dimensional Perspectives of Traditions RCTS Device Design.

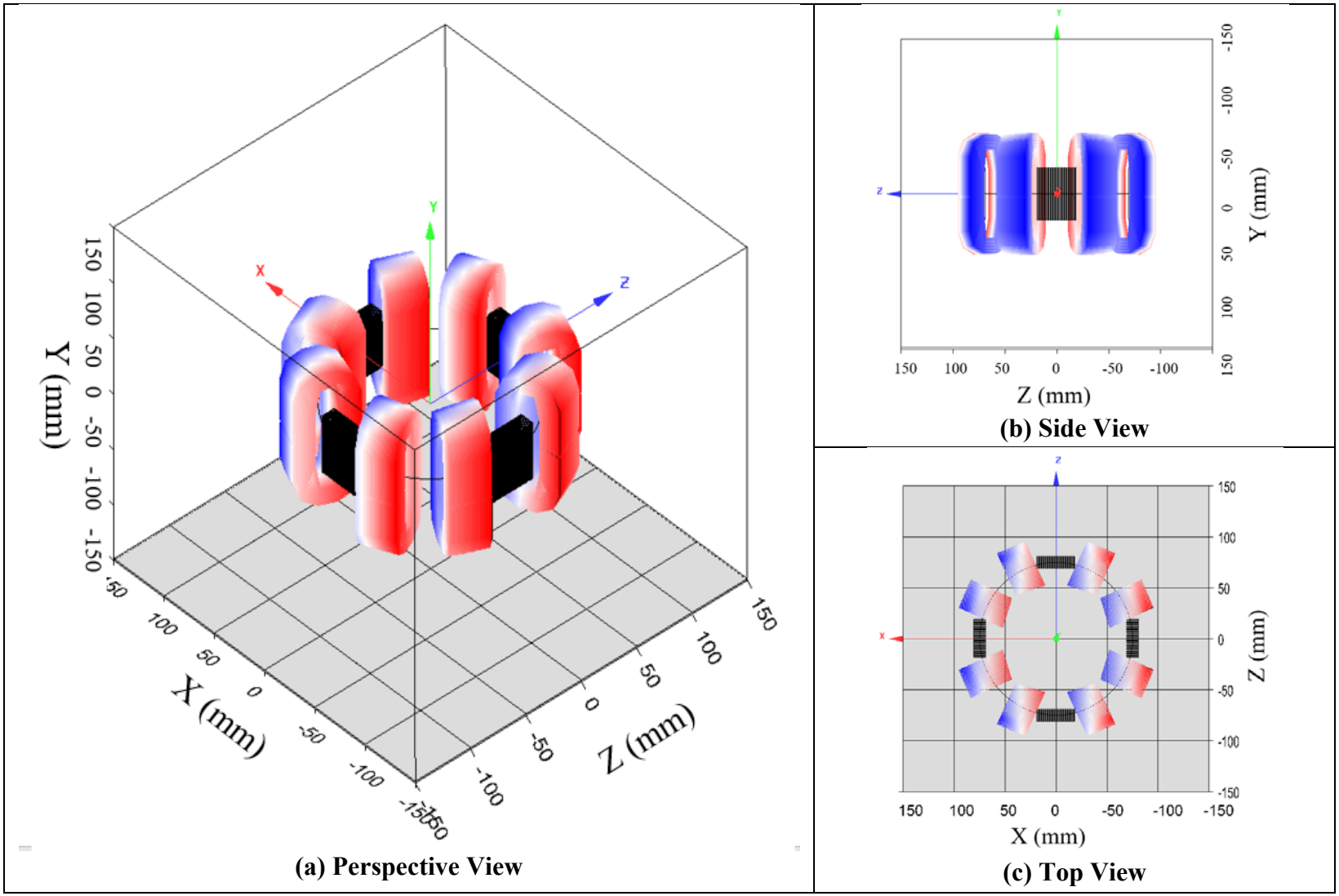

Figure 13.6: Three-Dimensional Perspectives of RCTS Device New Design #8.

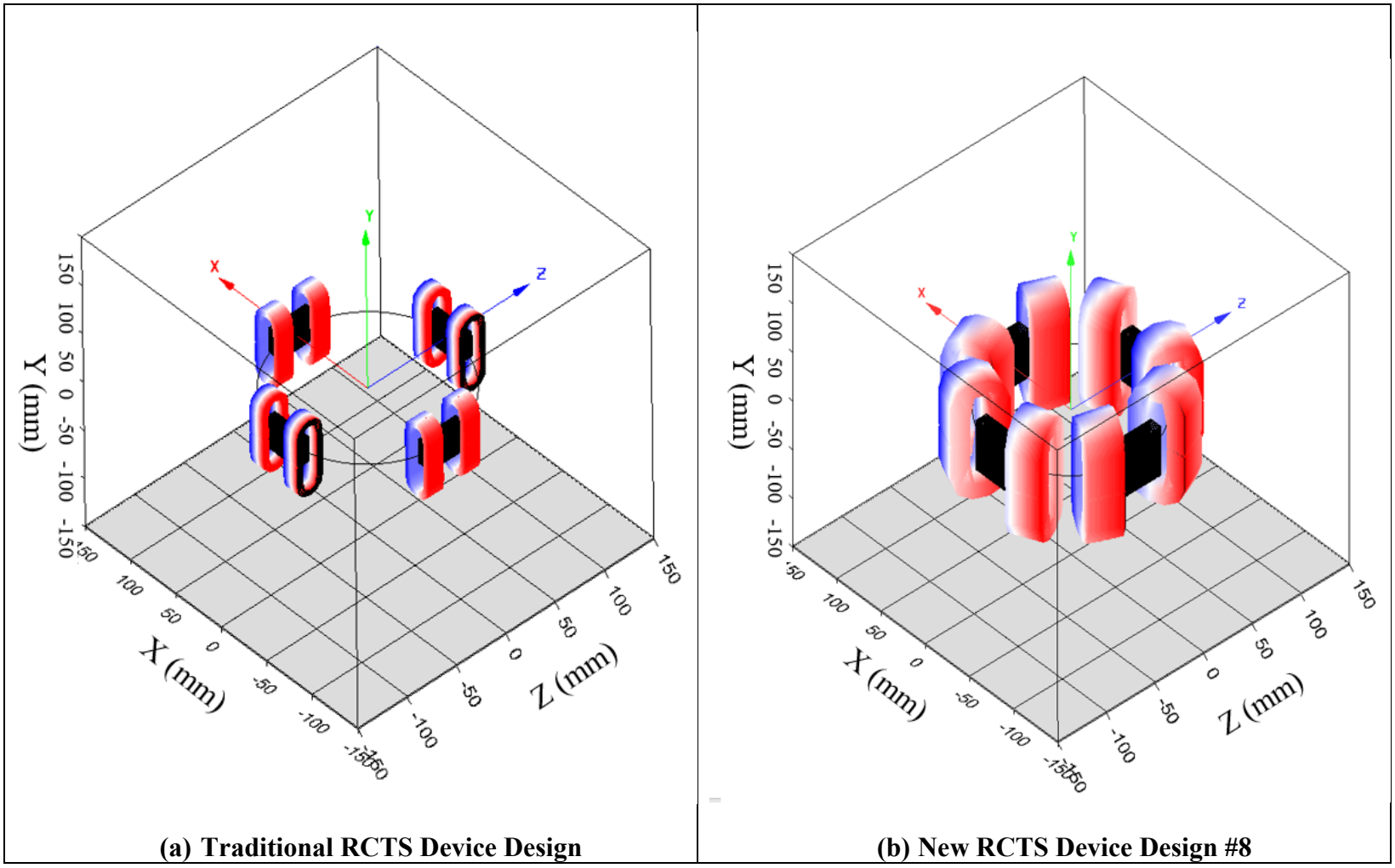

(a) Traditional RCTS Device Design **(b) New RCTS Device Design #8**

Figure 13.7: Three-Dimensional Perspective Views of (a) Traditional RCTS Device Design and (b) New RCTS Device Design #8.

13.4 MODELING OF THE CAPABILITIES OF THE TRADITIONAL AND NEW RCTS SYSTEMS TO TEST SPECIMENS OF DIFFERING STIFFNESSES

Based on previous models for the dynamic behavior of soils from Menq (2003), a comparison between the traditional and new RCTS designs can be theorized. Models from Menq (2003) are used to compare the potential performance of each design. The soil models from Menq (2003) are for modulus reduction relationships for dense sands and dense gravels. For low shear strains ($\gamma < 0.001\%$), the mean-effective stress (σ'_0) versus shear wave velocity (V_S) relationship (log σ'_0 - V_S) is defined as:

$$V_S = A_S \left(\frac{\sigma'_0}{P_a}\right)^{n_S} \tag{13.14}$$

where, based on the power model used, A_S is the model coefficient, n_S is the model exponent, and P_a is the reference atmospheric pressure used to normalize the mean-effective stress parameter. This formulation can be approximated to determine the power model for shear modulus, G, where A_S is converted to A_G by $A_G = A_S^2 * \rho$, where ρ is the soil density and A_G is the shear modulus power model coefficient. In general, and typically for sands and gravels, $n_G = 2 \times n_S$. This formulation is used to define the low shear strain behavior with regards to mean-effective stress.

The nonlinear dynamic behavior of soil is modeled using the modified hyperbolic model discussed in Darindeli (2001) and Menq (2003) as:

$$\frac{G}{G_{max}} = \frac{1}{1+(\gamma/\gamma_{ref})^a} \tag{13.15}$$

where G_{max} is the shear modulus in the low shear strain range defined by the power model, γ is the shearing strain, γ_{ref} is the reference shearing strain corresponding to a G/G_{max} of 0.5, and a is the modified hyperbolic model exponent. The hyperbolic model parameters

are sensitive to mean-effective stress and coefficient of uniformity, C_u for coarse-grained soils (i.e. sand and gravel). The hyperbolic model parameters are defined in Menq (2003) as

$$\gamma_{ref} = 0.12 * C_u^{-0.6} * \sigma^{0.5*C_u^{-0.15}} \quad (13.16)$$

$$a = 0.86 + 0.1 * \log \sigma \quad (13.17)$$

where in this formulation σ is in units of atmospheres. These parameters for dense sand and gravel are presented from Menq (2003) in Table 13.1.

Table 13.1: Power model shear wave velocity parameters for sand and gravel presented in Menq (2003) with assumed density added as 110 pcf.

Menq (2003)

	Sand	Gravel
C_u	2.5	35
A_S (fps)	837	1025
n_S	0.261	0.331
Total Density (pcf)	110	110

The prediction for the capabilities of the traditional and new RCTS solenoid designs are presented in terms of the potential testing limitations for G/G_{max} and shearing strain in the TS test, RC test with 5% damping, and RC test with 20% damping. The RC test G/G_{max} and shearing strain plots are simply based on the dynamic amplification expected based on the damping ratios chosen (i.e. 5% and 20%). The dynamic amplifications are relative to the force output determined for the TS test and an determined as

$$M_{max} = \frac{1}{2D*\sqrt{1-2D^2}} \quad (13.18)$$

where M_{max} is the amplification factor. In an actual RC test, the damping ratio is slightly higher due to the presence of equipment-generated damping; however, this correction is small for the damping ratios used (i.e. 5% and 10%) and is thus ignored for the device capacities that are presented. Basically, as the damping ratio increases the dynamic amplification decreases and the capacity of the RC test tends to become limited as the TS test would.

These capabilities are simulated with increasing confining pressure. The predictions consist of two segments where: (1) the confining pressure is low enough where the soil has a low enough shear modulus that the specimen can be strained, in shear, to the maximum shearing strain possible based on the maximum angle of rotation capable of the design, and (2) the maximum torque is limited by the electromagnetics of the solenoids and the electronic capacity of the amplifier and the drive system circuit. The remaining plots in this subsection are based on the two predicted segments subsequently mentioned. A plot is provided that includes annotations for these two segments and the remaining plots do not include these annotations. An example plot of the G/G_{max} and shearing strain capacities of the traditional RCTS device design are shown for a dense sand from Menq (2003) for the TS test, which is shown as Figure 13.8.

The G/G_{max} and shearing strain capacities of the traditional RCTS device design are shown for a dense sand from Menq (2003) in Figure 13.9. The G/G_{max} and shearing strain capacities of the new RCTS device Design #8 are shown for a dense sand from Menq (2003) in Figure 13.10. The G/G_{max} and shearing strain capacities in the TS test for the traditional design and new Design #8 are compared in Figure 13.11.

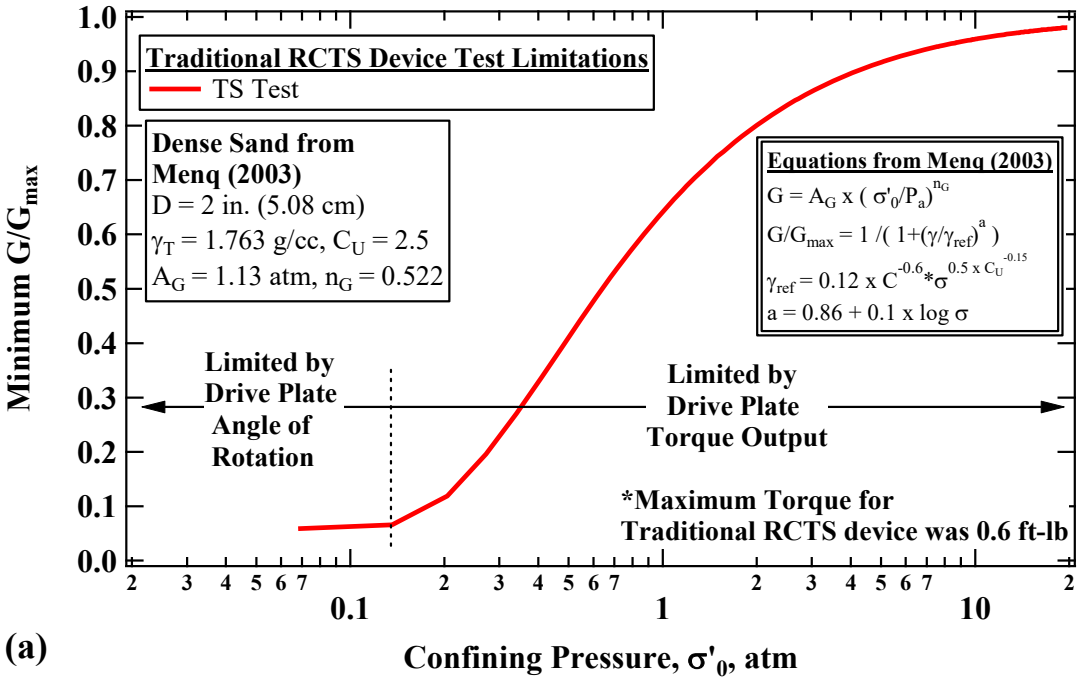

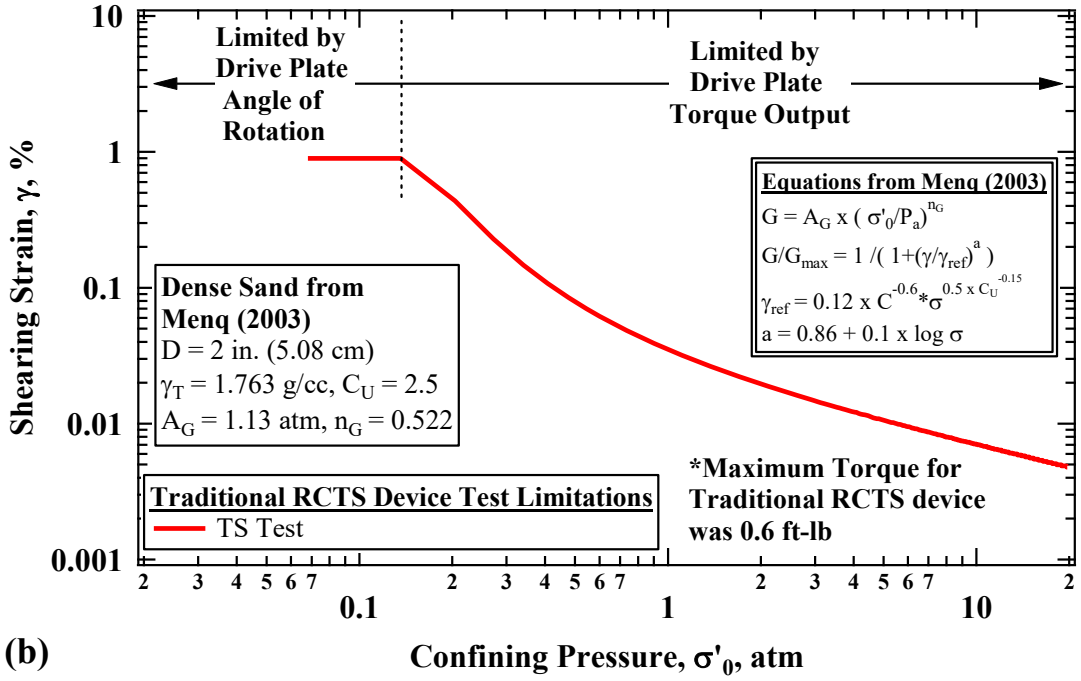

Figure 13.8: Modeled Variation in (a) Minimum G/G_{max} and (b) Maximum Shearing Strain Capacities with Confining Pressure of the Traditional RCTS Device Design of a Dense Sand from Menq (2003).

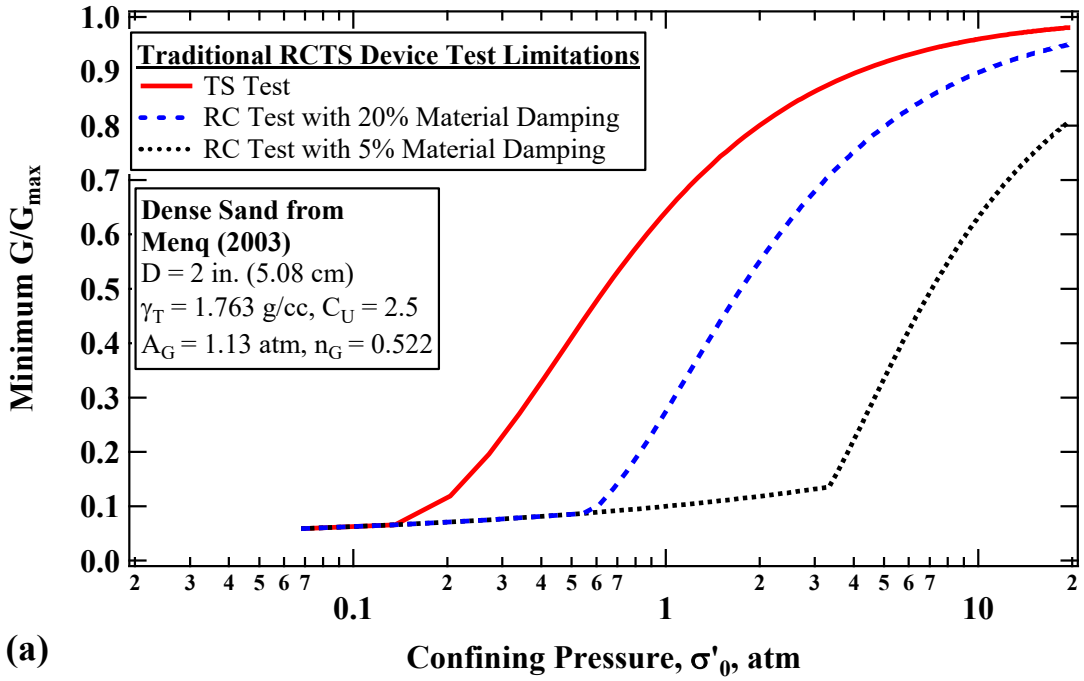

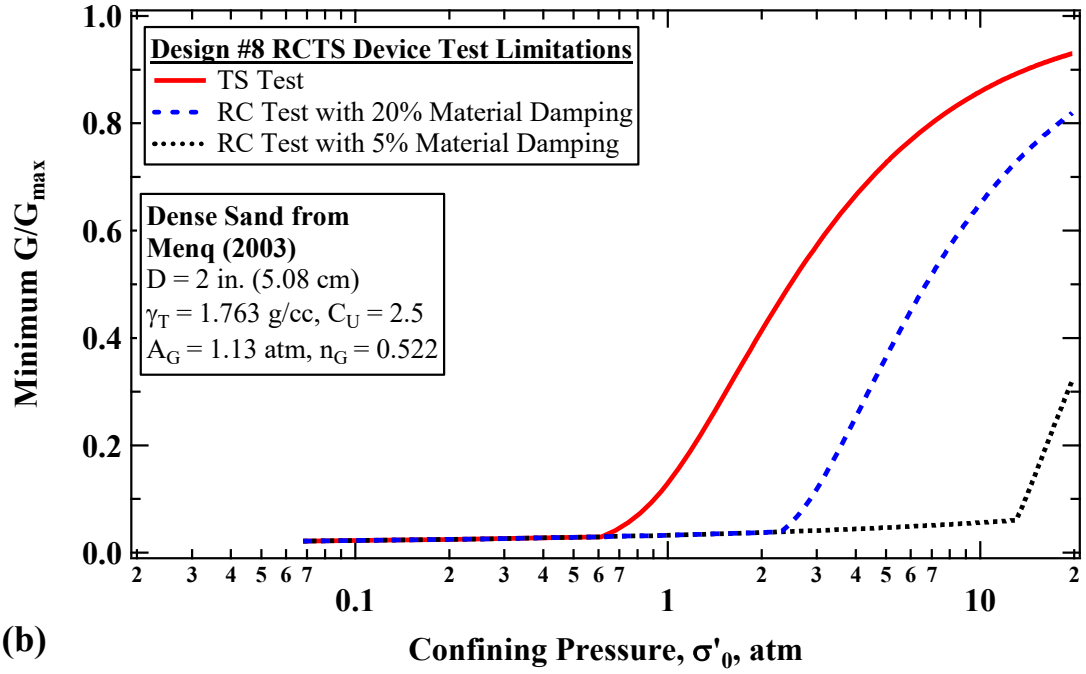

Figure 13.9: (a) G/G_{max} and (b) Shearing Strain Capacities of the Traditional RCTS Device Design of a Dense Sand from Menq (2003).

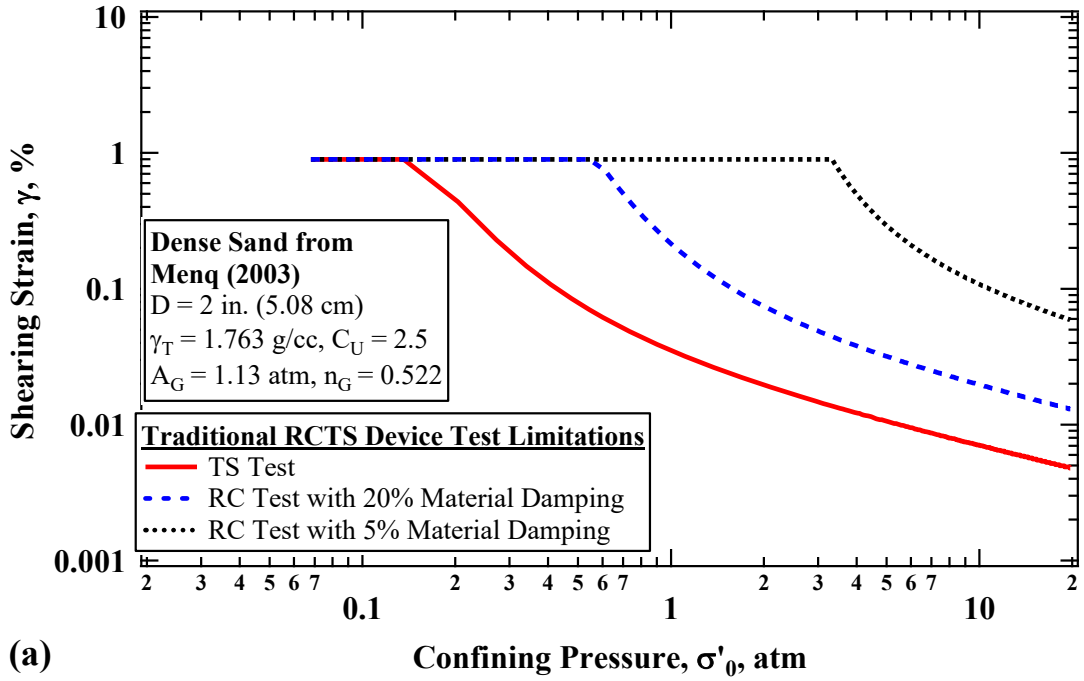

(a)

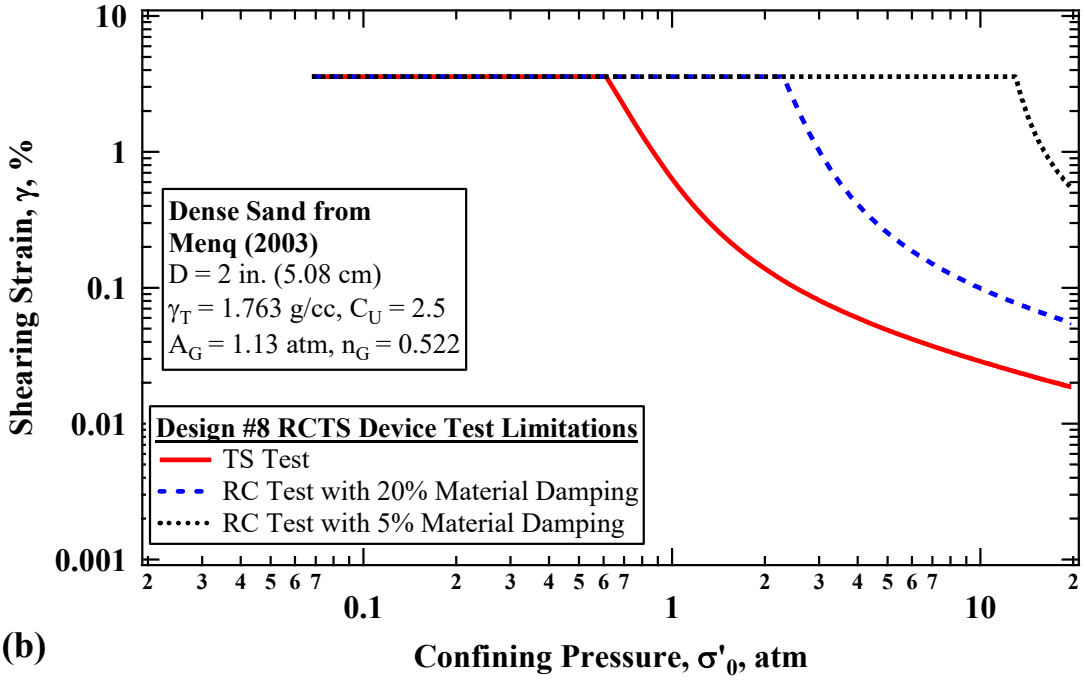

(b)

Figure 13.10: G/G_{max} and shearing strain capacities of the new RCTS device Design #8 for a dense sand from Menq (2003).

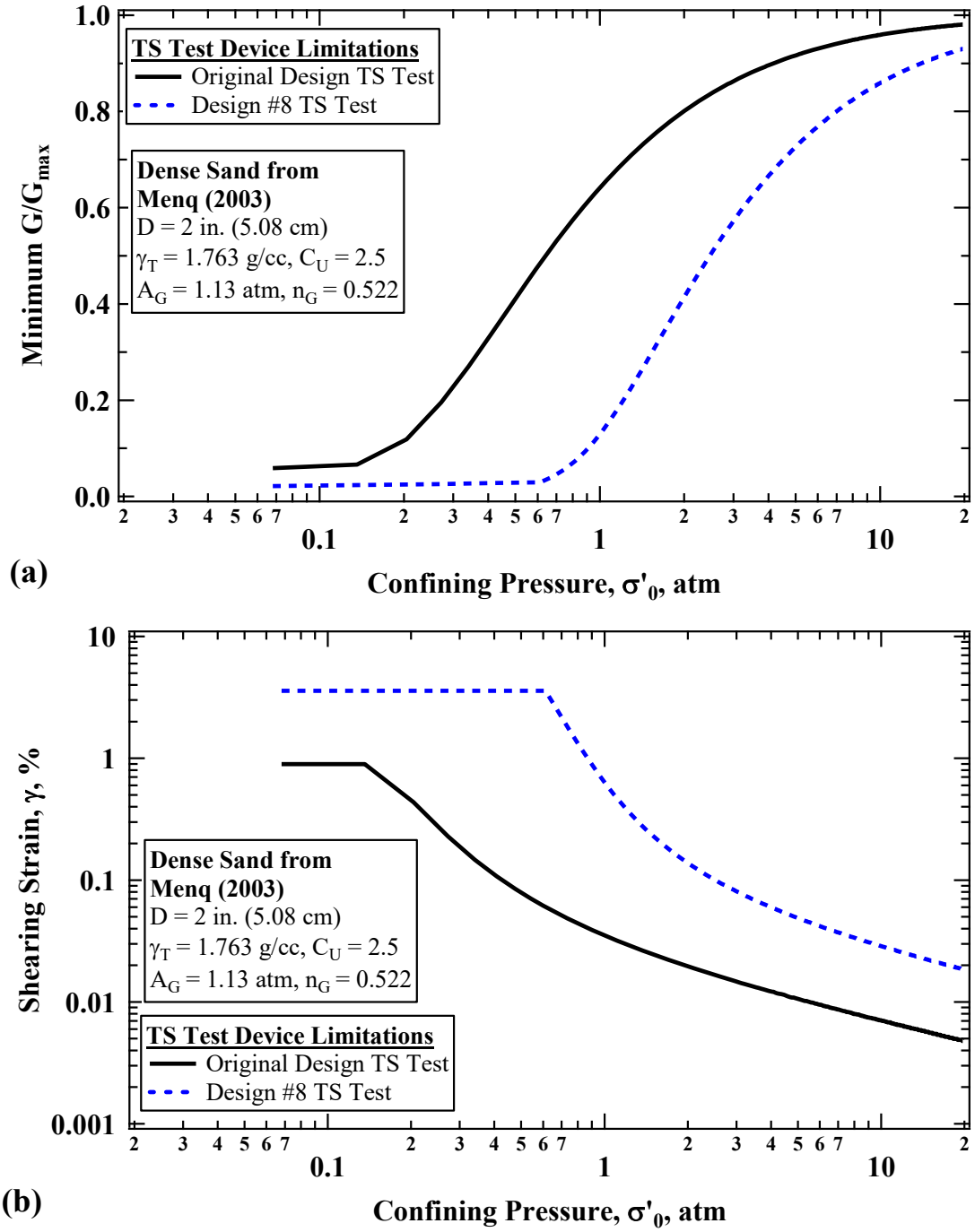

Figure 13.11: G/G_{max} and shearing strain capacities in the TS test for the traditional design and new Design #8.

The maximum torque output of the RCTS device that was subsequently presented was based on the amplifier used, which is a HP 6824A DC Power Supply Amplifier. A photograph of this unit is shown in Figure 13.12. This unit is capable of amplifying DC or AC signals up to 50 volts (~60 volts at higher frequencies) and up to 1.2 amps. Most modern high voltage/current units only allow preprogramed signals from the unit itself. The capability of the HP 6824A DC Power Supply Amplifier is crucial to RCTS testing where very specific input signals are used. Two additional HP 6824A DC Power Supply Amplifiers were purchased at the University of Texas at Austin Soil and Rock Dynamics Laboratory. To increase the maximum torque output of the RCTS device, two of these units can be connected in parallel, which will double the maximum torque output. The G/G_{max} and shearing strain capacities of the new RCTS device Design #8 are shown for a dense sand from Menq (2003), with the doubled maximum torque output provided by connecting two HP 6824A DC Power Supply Amplifiers in parallel, is shown in Figure 13.13.

Figure 13.12: Photograph of HP 6824A DC Power Supply Amplifier used in RCTS Testing at UT Austin.

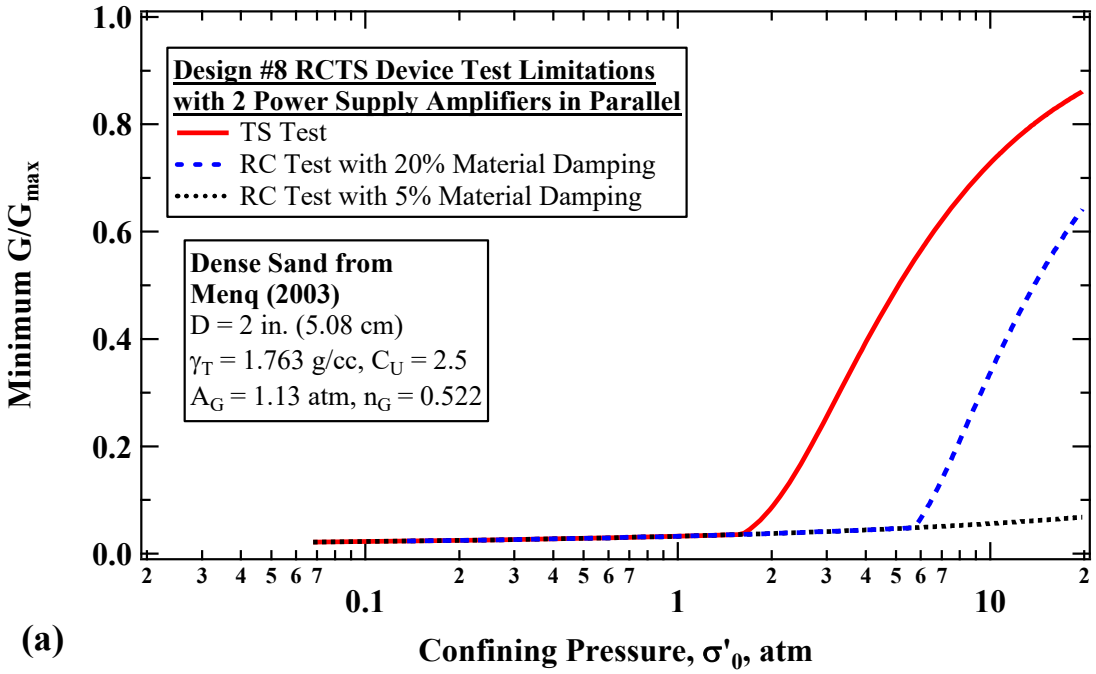

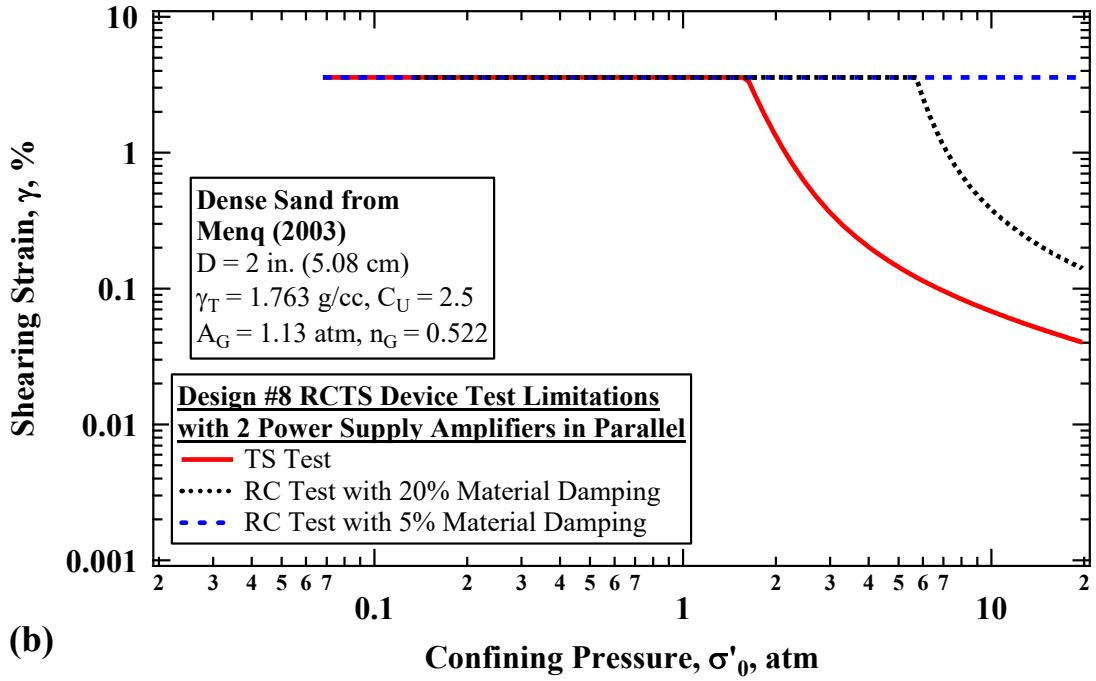

Figure 13.13: G/G_{max} and shearing strain capacities of the new RCTS device Design #8 for a dense sand from Menq (2003) with 2 HP 6824A DC Power Supply Amplifier connected in parallel.

13.5 CONCERNS IN THE RCTS TESTS WHEN REACHING HIGH SHEAR STRAINS

In both the RC and TS tests, certain nonlinear behaviors occur at high shear strains that can be of significant concern, especially with the new device design that can reach shear strains that are at a level of failure for some soils. In the RC test, at high levels of strain, numerous cycles are excited during the stepped sine sweep that can lead to significant cyclic degradation of the specimen and can limit the theoretical soundness of the test. In some cases a resonant frequency may seize to exist as the specimen is continually degraded by the cumulative number of cycles excited in the sweep. In the TS test, at high levels of strain, the specimen may not deform in pure torsion, but rather bending can occur or a combination of both bending and torsion. The capacity of the traditional RCTS device design and traditional data acquisition system rarely provided opportunities to evaluate high nonlinear behavior in the RC or TS tests. In the new RCTS device Design #8, these phenomenon may be much more prevalent. In the preceding subsection, further design considerations are discussed that may aid in the functionality of the RC test and proper measurement of highly nonlinear behavior in the TS test.

13.6 DESIGN FOR NEW DRIVE PLATE GEOMETRY AND SENSOR PLACEMENT

The new RCTS device Design #8 takes up the space that would normally be partially inhabited by the accelerometer and accelerometer counter balance weight. A new configuration of sensors are proposed that eliminate the need for the accelerometer and accelerometer counter balance. The use of 4 proximitor probes is considered and there are several benefits to this configuration: (1) eliminating the accelerometer and accelerometer counter balance weight reduce the drive plate mass polar moment of inertia and would thereby lead to higher specimen resonant frequencies in the RC test; (2) eliminating the accelerometer and accelerometer counter balance weight allow for easier calculation and

calibration of the drive plate mass polar moment of inertia; (3) the configuration of the 4 sensors allow for a complete evaluation of the torsional and/or bending action during the RC and TS tests, where the bending action can be corrected when evaluating the true torsional component that is the focus of the tests; (4) the level of noise captured with the proximitor signals tends to increase with excitation frequency; however, the combined analysis of the 4 sensors would greatly reduce the effects of background noise; and (5) even though more noise may be present at higher frequencies with the use of proximitor sensors, the next-generation data acquisition system designed in this dissertation still allows for a thorough establishment of the linear-elastic shear strain range regardless of the tests that would occur at the higher frequencies.

13.6.1 New Sensor Selection and Placement

The new RCTS device Design #8 allows for drive plate rotation up to a maximum of 10 degrees of rotation. The current proximitor probes used are the Bently Nevada 3300 XL 8 mm Proximity Transducer System. The linear calibration displacement range of these transducers is 0.01 in. to 0.1 in. With the same positioning of the traditional proximitors at 0.71 in., from the center of rotation, the expected displacement at a drive plate angle of rotation of 10 degrees, the proximitor target is expected to displace 0.13 in. Thus, the current proximitor probes used are not sufficient for making accurate displacement measurements throughout this range of rotation. Therefore, probes from the Bently Nevada 3300 XL 11 mm Proximity Transducer System are proposed. The linear calibration displacement range of these transducers is 0.02 in. to 0.2 in. With the same positioning of the traditional proximitors at 0.71 in. from the center of rotation, and if the initial position of the probes from the targets is 0.13 in, then all of the potential rotation angles of the drive plate can be measured. For the near 10 degree angle of rotation that can potentially occur, nonlinear calibration behavior may occur with the new proposed probes and would either

invalidate the test results when these angles of rotation or would need to be calibrated for. The proposed proximitor target and sensor configuration is illustrated in a conceptual schematic shown in Figure 13.14.

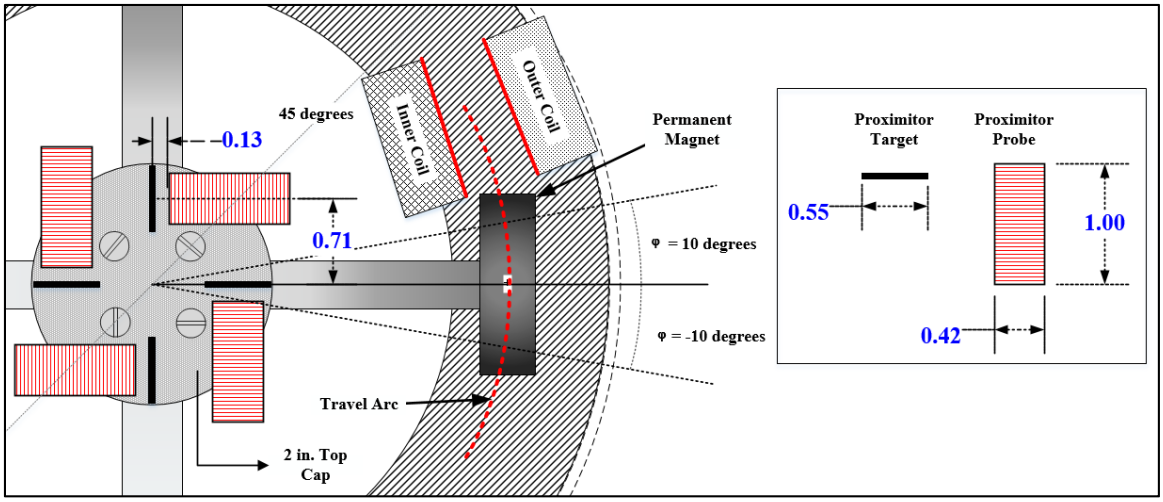

Figure 13.14: Conceptual Schematic of Proposed Proximitor Target and Sensor Configuration.

13.6.2 Data Acquisition Equipment Proposed with New Sensor Selection and Placement

In the next-generation data acquisition equipment previously designed for the traditional RCTS device, most of the needs are already met in order to acquire signals from the new RCTS device Design #8. However, two additional proximitor acquisition channels are required. For the new 4 proximitor transducer configuration, the NI PXI-4461 is a logical addition to the NI PXI-1033 chassis used to house the DAQ equipment subsequently used for the studies conducted in this dissertation. This device has 24 bit resolution and a 42 V range to acquire and process signals from each of the newly proposed proximitor transducers. In addition, the NI PXI-4461 is equipped with programmable anti-aliasing and AC coupling which will greatly enhance noise reduction and increased resolution of the acquired signals.

13.7 SUMMARY

The new design of the RCTS device presented in this chapter possesses the capability to test soils from the elastic strain range (< 0.0003%) to the nonlinear-plastic shear strain range (> 1%). A geotechnical engineering laboratory test that can accurately map the large shear strain range of soil behavior from 10^{-6} % to 1% without complications of frictional forces induced by the equipment does not currently exist. This range is achieved using a combination of geotechnical laboratory tests, that include, but are not limited to, traditional combined resonant column and torsional shear (RCTS, 10^{-4} % to 0.5%), cyclic triaxial (CTX, 0.001% to 2%), and cyclic simple shear (CSS, 0.5% to 2). A device that can accurately map 8 orders of magnitude of shear strain (i.e. 10^{-6} % to 1% or higher) was modeled to estimate its performance and was presented in this chapter. Some additional modifications to the sensors used to measure dynamics behavior were recommended along with potential limitations of a higher capacity RCTS device.

The new device designed herein has the capability to test soils over a range of shearing stresses and strains that provide meaningful results to most realms of geotechnical engineering involved with the mechanical characteristics of soils. This new geotechnical laboratory testing device would also have great importance to geotechnical engineers concerned with an area of research that involves the evaluation of soil liquefaction. The traditional RCTS device is limited in its ability to excite shearing strains that generate significant pore pressures that are of interest and cannot excite shear strains that can bring soil to complete failure due to soil liquefaction. The new RCTS device is capable of testing soil in a manner can generate pore pressures that would lead to specimen failure.

Chapter 14

Summary, Conclusions, and Recommendations

14.1 SUMMARY

In Chapter 2, background is provided detailing combined resonant column and torsional shear (RCTS) equipment. The theories used to develop testing procedures for this device are discussed, with the focus around evaluating the deformational characteristics (shear modulus and material damping in shear) of soil and rock specimens. The theoretical basis behind both the RC and TS tests is presented along with the new control and monitoring equipment that was developed in conjunction with this dissertation. The overall RC test consists of two individual parts, a frequency sweep test and a free-vibration decay test. The first part involves a frequency sweep to determine the resonant frequency, f_r and half-power damping ratio, D_{HP}. The second part involves excitation at resonance until reaching steady-state vibration and then stopping the power to allow a free-vibration decay, where the free-vibration decay is evaluated to determine the damped natural frequency, f_D and the damping ratio from free-vibration decay, D_{FV}.

In Chapter 3, the details surrounding the construction of the new control and monitoring equipment for the RCTS device is discussed. Development of the new equipment consisted of selecting and configuring modules housed in a National Instruments (NI) PXI-1033 Chassis. These modules and the NI PXI-1033 Chassis were combined with some additional enhancements built in-house to increase RCTS testing efficiency and simultaneous, real-time, and highly accurate monitoring during RCTS testing. These capabilities and combinations of components essentially eliminate the need for peripheral equipment allowing a “single unit” system for control and monitoring of at least two RCTS devices.

In Chapter 4, an investigative approach was undertaken to further the understanding of the operational characteristics of the RCTS device. An experimental evaluation of the electronic characteristics of the coils was conducted and the results were compared with traditional calibration procedures used to provide a correction factor for these electronic characteristics. More specifically, an electronic phase delay is responsible for a greater value of hysteretic damping ratio that is measured during TS testing (i.e. TS equipment generated damping). This equipment-generated damping is determined ("calibrated") by testing a metal specimen, which has a negligible level (< 0.03%) of hysteretic damping. An experimental evaluation of the equipment-generated damping in the RC test was conducted. This evaluation involved using a relay switch that was connected between the control system and the RCTS device (i.e. coils), which allowed the circuit to be disconnected during testing. When conducting a free-vibration decay test after reaching steady-state, the electronic circuit can be flipped to open which eliminates back-generated electromotive-force (EMF) (i.e. equipment generated damping in RC testing). The method of opening the relay and allowing free-vibration decay to occur without the influence of back-generated EMF was conducted for 10 metal specimens with different resonant frequencies to develop a relationship for the variation of back-generated EMF with frequency. Results from tests on the metal specimens were also used to determine an equipment-generated damping coefficient, which is normally expressed as a frequency-dependent equipment-generated damping ratio. The damping coefficient from RC tests on the metal specimens were compared with an independent experimental setup involving a single magnet, single coil, and electrodynamic shaker.

In Chapter 5, modern digital data processing methods were developed to enhance measurements taken during RC testing at small shear strains ($\gamma < 0.0005\%$). A method known as the wavelet integration method is discussed that is used to enhance the accuracy

of the measurements taken during the frequency-sweep portion of the RC test. Measurement accuracy was further enhanced by taking the results from the frequency sweep and using a least-mean-squares fitting method. This method involved fitting the response curve equation for a single-degree-of-freedom (SDOF) system to the experimental results from the frequency sweep. A combination of methods were used to enhance the accuracy of the measurements taken during the free-vibration decay part of the RC test. These methods included signal stacking, targeted notch filtering, Butterworth filtering, and using a part of the Hilbert Transform method.

In Chapter 6, analytical evaluations of the methods of analysis used in the resonant column test at small strains were conducted to determine the most accurate methods. More specifically, these methods were evaluated for their effectiveness in reducing the influence of environmental background noise. These analytical evaluations involved using a random-number generator to simulate Gaussian-distributed random noise and combining the noise with theoretically created signals that represent results from the frequency sweep or free-vibration decay parts of the RC test. For the frequency sweep test, the wavelet integration method and a root-mean squares method were evaluated for the level of accuracy that each method has for measuring the resonant frequency and half-power damping ratio. For the free-vibration decay test, the percentage of the free-vibration decay to use in evaluating the damping ratio when specific levels of background noise are present was studied.

In Chapter 7, an experimental evaluation of the methods of analysis used in the torsional shear test at small strains was conducted to determine the most accurate methods. The methods apply mainly to measurements acquired at low shearing strains where the impact of background noise can range from detrimental to completely prohibitive. Four digital signal processing methods were evaluated. These methods include: (1) determining the maximum values of the shearing stress and shearing strain from the time records to

determine shear modulus and using the traditional area integration method to determine the hysteretic damping ratio; (2) calculating the root-mean-squares (RMS) amplitudes and taking the quotient of the shearing stress and shearing strain to determine shear modulus and using the traditional area integration method to determine the hysteretic damping ratio; (3) use of a least-mean squares fitting method that fits a linear trend to the measured hysteresis loop to iteratively determine the slope of the hysteresis loop, which is combined with the traditional area integration method to determine the hysteretic damping ratio; and (4) using the wavelet integration method, where the magnitude response, between the shear stress and the shear strain, is the shear modulus and the phase shift measured between the shear stress and shear strain is used to simulate a hysteresis loop from which the traditional area integration method is used to determine the hysteretic damping ratio.

In Chapter 8, experimental testing and numerical modeling were used to evaluate the effects that frequency sweep rate has on the shape of the response curve determined when using a stepped-sine sweep. Sweep rates were based on two parameters: (1) the incremental frequency step, f_{step}, and (2) the number of cycles excited at each of the frequency increments, C_S. The experimental evaluation of sweep rate involved testing 5 metal specimens and one soil specimen subjected to 5 confining pressures. Numerical simulations were conducted in conjunction with each experimental test using incremental displacement and incremental velocity equations and coefficients for these recurrence formulas that were presented in Chopra (2001). Results from the numerical simulations and experimental tests were compared together and presented as the variation in amplitude error, damping ratio error, and resonant frequency error in relation to the components of the sweep rate (i.e. f_{step} and C_S) and the dynamic characteristics (i.e. f_r and D) of the system.

In Chapter 9, an empirical model for choosing sweep rates when using a frequency sweep in the resonant column test was developed. A non-dimensional sweep rate parameter

was derived for a stepped-sine sweep that is functionally the same as the non-dimensional sweep rate parameter for a linear chirp or logarithmic chirp presented in Lollock (2002) and Girard and Bugeat (2004). The dependent variables for amplitude error, damping ratio error, and resonant frequency error all collapse into individual relationships when the independent variable is expressed by the non-dimensional sweep rate parameter. Thus, an empirical model was developed to mathematically describe the variation in amplitude error, damping ratio error, and resonant frequency error with the non-dimensional sweep rate parameter. Finally, an example of how the empirical model can be implemented is presented in Chapter 9.

In Chapter 10, the chronology of a complete set of RCTS tests on one intact specimen is presented. The chronology covers the collection of raw data acquired during testing through to final results showing time-dependent, pressure-dependent, and strain-dependent behaviors of the soil. The comparison of the raw data obtained from RCTS testing compared with the results that are calculated from the raw signals provide a more detailed perspective of soil behavior during RCTS testing.

In Chapter 11, the potential for an improved understanding of material behavior by measuring height-change during cyclic and resonant torsional testing is discussed. After implementation of the new control and monitoring system, height-change measurements are recorded during RC and TS testing. These measurements are saved and stored along with the traditional measurements discussed in Chapter 10. Both increases and decreases in height change were measured during RCTS testing and generally correlate with normally consolidated (NC) or Overconsolidated (OC) conditions. Finally, the new control and monitoring system started in 2013 combined with the customized software has allowed a data repository to grow and is discussed herein.

In Chapter 12, modeling and experimental evaluations of the torque motor used in the traditional RCTS device were conducted. The numerical model was written in LabVIEW for circular coils and circular magnets based on a study by Robertson (2012). The model was tailored to the actual geometry of the rectangular magnets and elongated coils used in the traditional RCTS device. The numerical model was validated experimentally. The experimental setup was configured to position a permanent magnet at a specific distance from a coil of wire. Direct current (DC) was sent thorough the coils and the magnetic force was measured for each increment of distance between the center of the magnet and the center of the coil. The experimentally determined force-displacement relationship was determined for four configurations involving different coils and different magnets These force-displacement relationships agreed with numerical simulations for each of the configurations. The numerical model was further adapted to model torque-rotation relationship of the torque motor used in the RCTS device. Another experimental approach, where the RCTS device was used to evaluate the level of torque applied to a metal specimen, was used to validate the numerical model.

In Chapter 13, the numerical models developed in Chapter 12 was adapted to evaluate different coil positions and different coil and permanent magnet strengths with the objective of designing a higher capacity RCTS device. Configurations were evaluated that would allow higher power, more space between magnets and coils, and higher angles of rotation of the drive plate to be reached. An optimum design was found and the potential capabilities of this this new design are compared with the traditional design. The comparisons were done by predicting the shear strain and modulus reduction behavior of a soil specimen modeled from constitutive relationships provided in Menq (2003).

14.2 CONCLUSIONS

In Chapter 3, enhancements were added to the new control and monitoring systems that were discussed in Chapter 2. These enhancements include AC coupling circuits and voltage divider circuits that were designed specifically to meet the data acquisition needs of the new RCTS control and monitoring system. The enhancements were fabricated in-house permit RCTS testing to be conducted at lower shearing strains and with more precision and accuracy than achieved in past systems.

In previously built RCTS testing systems, different motion sensors were used for the RC test and the TS test. An accelerometer was used in RC testing and a pair of proximitors were exclusively used in TS testing. In the new control and monitoring system, acquisition capabilities were added for acquiring the pair of proximitor signals and additional accelerometer signal during RC testing. This new capability reduces the influence of background noise, enhances quality control during testing, and provides several signals that can be used to determine how closely the theoretical and measured torsional motions agree.

In Chapter 4, the electromagnetic and electronic characteristics of the RCTS device are evaluated to provide a more advanced understanding of equipment-generated damping in the RC and TS tests, respectively. Equipment-generated damping in the RC test was found to be purely frequency-dependent and best represented by a viscous damping coefficient. The traditional calibration procedures used to for equipment-generated damping in the RC test were found to be efficient and adequate to correct for equipment-generated damping when testing soils. The adequacy of the traditional calibration procedures used to for equipment-generated damping in the RC test was confirmed by using an open-relay method that allowed for determining the true value of equipment-generated damping versus frequency without including the small level of damping

contributed by the metal specimen. Based on the comparison from the original and open-relay calibration methods, there is little difference between the methods. The original method overestimates equipment-generated damping by 0.28% to 0.83% (depending on the drive plate), which is generally negligible during RC testing. However, when testing materials with material damping ratios below 0.1%, this slight overestimation should be considered.

The electronic characteristics of the drive coil setup is shown in Chapter 4 to be responsible for a phase shift between the voltage sent to the coils by the control system and the actual current within the coils that generates torque. This electronic phase shift appears as hysteretic damping in the TS test and is described as equipment-generated damping that occurs in the TS test. Hysteretic damping determined from experimental tests on a metal specimen were shown to match hysteretic damping simulated using the phase shift introduced by the electronic characteristics of the drive coil setup. Thus, TS equipment-generated damping is purely a result of the electronic characteristics of the testing device. The traditional calibration procedure was shown to be easier than and as accurate as the more tedious approach of evaluating the electronic characteristics of the coils.

In Chapter 5, signal processing techniques are developed and experimentally evaluated for enhancing small-strain measurements during the resonant column test. The time-domain digital signal subroutine called the wavelet integration method is highly proficient at reducing the influence of background noise during the frequency sweep test. Following the frequency sweep test, the least-mean-squares approach is far more accurate than the half-power bandwidth approach for calculating the response curve characteristics (i.e. f_r, D, & γ) from the frequency sweep. The robustness of the wavelet integration approach in combination with the least-mean-squares fit approach has been found to

improve measurement accuracy to the extent that reliable measurements of f_r and D_{HP} can be made at shear strains below 10^{-6} %.

As discussed in Chapter 5, signals from free-vibration decay tests are processed in four steps and then analyzed to make accurate measurements of the damped natural frequency and the material damping ratio. The processes are: (1) signal stacking, (2) targeted notch filtering, (3) bandpass Butterworth filtering, and (3) using the Hilbert Transform method. In combination, these processes have been found to consistently make accurate measurements of f_D and D_{FV} at shear strains as low as 10^{-6} %.

In Chapter 6, analytical evaluations of the methods of analysis used in the resonant column test at small strains were conducted to determine the most accurate methods. For the frequency sweep part of the RC test, the wavelet integration approach in combination with a least-mean-squares fit of the response curve was found to me the most accurate approach. Statistical parameters were determined that can be used to quantify experimental error of methods used in the frequency sweep part of the RC test based on the assumption of Gaussian-distributed background noise. For the free-vibration decay part of the RC test, the accuracy of measurements were evaluated based on the percentage of the free-vibration decay envelope used for analysis versus the signal-to-noise ratio (SNR). Statistical parameters were determined and used to develop a relationship of variation in the maximum measurement accuracy with percentage of the free-vibration decay envelope used for analysis based on the SNR. The statistical parameters can also be used to quantify experimental error of methods used in the free-vibration decay part of the RC test based on the assumption of Gaussian-distributed background noise.

In Chapter 7, experimental evaluation of the methods of analysis used in the torsional shear test at small strains was conducted to determine the most accurate methods. The wavelet integration method is more robust than other methods that were evaluated.

When comparing shear modulus and material damping ratio measurements in the TS tests, the hysteretic damping ratio is more sensitive to background noise. Therefore, the measurements of the hysteretic damping ratio is improved more by signal stacking, digital filtering, and the wavelet integration method. In general, the wavelet integration is found to be the most stable method.

In Chapter 8, experimental testing and numerical modeling are used to evaluate the effects of frequency sweep rate when using a stepped-sine sweep in resonant column testing. This study was conducted for linear SDOF systems only. This investigation confirms that the fixed-free resonant column testing device, data control and monitoring system and accompanying software, developed in this dissertation, has the ability to accurately test and measure the fundamental behavior of SDOF systems under various sweep rates for a stepped-sine sweep. Sweep tests on specimens in the fixed-free resonant column device can be precisely simulated using the incremental displacement and incremental velocity equations and coefficients for these recurrence formulas that were presented in Chopra (2001). The application of these formulas apply to a linear system where the SDOF characteristics are constant with strain amplitude, which is does not occur for nonlinear systems. These equations could be further adapted to nonlinear systems if a sufficient nonlinear strain-dependent model is incorporated.

In Chapter 9, an empirical model for choosing sweep rates when using a frequency sweep in resonant column testing is developed. This study shows that sweeping too fast may lead to an incorrect prediction of the dynamic properties from the sweep test and would also result in using the wrong frequency for the free-vibration test. Sweeping at a rate lower than necessary leads to prolonged testing durations. In the case of testing in the nonlinear shear strain range, sweep rates that are too slow may lead to an excessive number of cycles being applied to the specimen, which can be detrimental. The empirical model

advanced in this study can be used to select sweep rates that will yield accurate measurements of a SDOF system being tested. In addition, the sweep rates will minimize the testing time needed to yield accurate results are recommended. This study has proven that accuracy limitations exist due to sweep rate effects and that when conducting resonant column tests, the models advanced in this study should be used to guide proper testing protocols.

In Chapter 10, the observations that can be made from the raw signals measured during the test correspond to and the resulting dynamic behavior that is calculated from the raw signals. More specifically, explicit characteristics of the signals are understood to represent certain dynamic characteristic such as the resonant frequency, damping ratio, and nonlinearity. The raw signals are presented in real-time during testing and help to increase testing quality control and advance the understanding of dynamic soil behavior through experimental observation. Furthermore, this chronology of results further validates an objective of this dissertation, which was to enhance the ability to take accurate measurements at small shear strains and at lot confining pressure. This chronology includes accurate results taken from both small shear strains and low confining pressure.

In Chapter 11, the amount of height change that occurs during the frequency sweep test increases as the level of shearing strain increases for shearing strains above the cyclic threshold strain. Thus the contractive or dilative behavior becomes more pronounced at moderate to higher shear strains. More studies are required to investigate this behavior and how it is affected by the threshold strain at which height change begins to occur.

In Chapter 12, the experimental testing and numerical modeling were conducted to understand the characteristics of the electromagnetic torque motor in the traditional RCTS device. Results from the experimental testing and numerical modeling for predicting the torque-rotation relationships are in good agreement and show that the numerical model is

suitable for predicting the torque-rotation relationship of the drive plate. Thus, the model can be used to further to develop a more powerful solenoid system to enhance the capacity of the RCTS device.

In Chapter 13, a higher capacity RCTS device was designed based on the numerical model from Chapter 12, but was further tailored to simulate more complex coil geometries and higher degrees of rotation. The design presented in Chapter 13 possesses the capability to test soils from below the elastic strain range (< 0.0003%) to the nonlinear-plastic shear strain range (> 1%). The new device designed in this dissertation has the capability to test soils over a range of shearing stresses and strains that is the working strain for most practical design purposes. The new device would have the potential to provide meaningful results to most realms of geotechnical engineering involved with the mechanical characteristics of soils. This new geotechnical laboratory testing device would also have great importance to geotechnical engineers concerned with an area of research that involves the evaluation of soil liquefaction.

14.3 RECOMMENDATIONS FOR FUTURE WORK

1. The databank of test results can be used to further develop nonlinear dynamic models from the results stored from frequency sweep tests. Currently, in the nonlinear shear strain range (~ $\gamma > 0.0008\%$), only the resonant frequency, f_r, and peak strain amplitude, γ, are used for developing the modulus reduction curve (G/G_{max}-logγ). Nonlinear dynamic models can incorporate the shear strain response amplitudes at all of the other frequencies that are excited during the test, which will more fully map the G/G_{max}-logγ relationship. Furthermore, the relationship of the variation of material damping ratio, D with γ can also be evaluated (D-logγ).
2. Further development of nonlinear dynamic models can be done using the results stored from the free-vibration decay tests. Currently, in the nonlinear shear strain range, only the first 3 cycles of decay are used to develop the D-logγ relationship. Since γ is decreasing during free-vibration decay, the changing logarithmic decrement with decreasing γ can be used to develop the D-logγ relationship from a single free-vibration decay test. Furthermore, as the γ is decreasing, the damped natural frequency, f_D is increasing. The increasing f_D can be used to develop the G/G_{max}-logγ relationship from a single free-vibration decay test.
3. Additional proximitors or another type of sensor can be added to measure lateral deformation that occurs simultaneous to the height change that occurs during RC and TS testing as was shown in Chapter 11. Volume change that occurs during RC or TS testing at higher shear strains can be more accurately measured with the combination of highly sensitive vertical and lateral deformation measurements.
4. Modeling of the nonlinear soil behavior in RC and TS tests can also incorporate the degradation effects, as a function of γ, by acquiring height-change, dH and volume-change, dV measurements. These empirical models can also include the number of

cycles of torsion excited on a specimen. Sensitive measurements of dV from moderate-to-high shear strains ($0.001\% < \gamma < 1\%$) that is generated by pure shear loading from RC and TS testing, in combination with the number of torsional loading cycles, has the potential for identifying and modeling fundamental characteristics of soil behavior at moderate-to-high shear strains.

5. With more advanced nonlinear soil models that incorporate dV and the effect of the number of cycles excited in torsion, a parametric evaluation of various soil types (e.g. LL, PI, Cu, e, etc.), preparation conditions (γ_d, S_r, w, etc.), and confining conditions (σ_3 and/or σ_1) can be performed. The results of the parametric evaluation may lead to a constitutive soil model that describes the torsional and volumetric deformational characteristics (γ & dV), effect of the number of cycles excited in torsion, and frequency of excitation based on soil types and in-situ conditions from moderate-to-high shear strains ($0.001\% < \gamma < 1\%$).
6. Construction of a higher-capacity RCTS device can be used to test soils over a much larger shear strain range than traditional geotechnical laboratory tests as discussed in Chapter 13.
7. The RCTS device and testing chamber can be configured to allow for back-pressure saturation of samples. The control and monitoring system can be equipped with pore-pressure transducers to measure the generation of pore-pressures as moderate to higher strains are excited in the RCTS device. This type of analysis is recommended for the TS test, where the number of cycles of excitation and the shear strain amplitude can be more easily controlled. Furthermore, the complexities of the nonlinear dynamics of system that dictate the results in the RC test are not present in the TS test.

Appendix A

LabVIEW Based RCTS Program User's Guide

A.1 INTRODUCTION

With the significant advances of technology, the capabilities for digitization and processing of signals and vibrations have profoundly grown. These advances using modern systems have allowed what once were theories and hypotheses to now be programmed and executed, where traditional equipment would have been limiting or too costly. The combined resonant column and torsional shear (RCTS) equipment and experimental processes are a well-documented form of testing soil and rock that is a theoretically sound process for obtaining stiffness, material damping characteristics over a wide in shearing strains as well as wide ranged in other important parameters. However, the ability to expand beyond the basic fundamentals of the test has been limited to the previous generation of analog signal processing equipment. A new generation of RCTS equipment and experimental processes has been developed using modern signal digitization and processing equipment, which is accompanied by a constructed user interface that provides convenient test parameter selection and timely progression though the steps of the RCTS test. The new collection of subroutines and user interfaces has been developed in the LabVIEW 2014 programming environment provided by National Instruments of Austin, Texas. The objective of this portion of the report is to provide a guide to users for navigating the developed interfaces and executing the steps of the RCTS test.

A.2 RCTS TEST INPUT REQUIREMENTS

A.2.1 Introduction

The RCTS test has numerous input parameters that must first be measured and entered into the RCTS subroutine platform in order for the testing methods to execute properly. In addition to hard copy documentation, several input menus are provided for users to input their specimen measurements and for required calculations to be conducted and stored digitally.

A.2.2 Start-Up Window

At the beginning the RCTS test the user is provided a “Start Up Window” where the steps of the RCTS test can be executed and review of data can be accessed. The “Start Up Window” can be accessed using the following methods:

(1) Follow the file path (C:\RCTS Tests\LabView Programs\Main Program\Start up Window_v2), or

(2) Use “search” in Windows Explorer and type in “Start-Up Window_v2”.

The opened interface “Start-Up Window” is provided as the RCTS-Test user home screen. This user home screen is shown in Figure A.1.

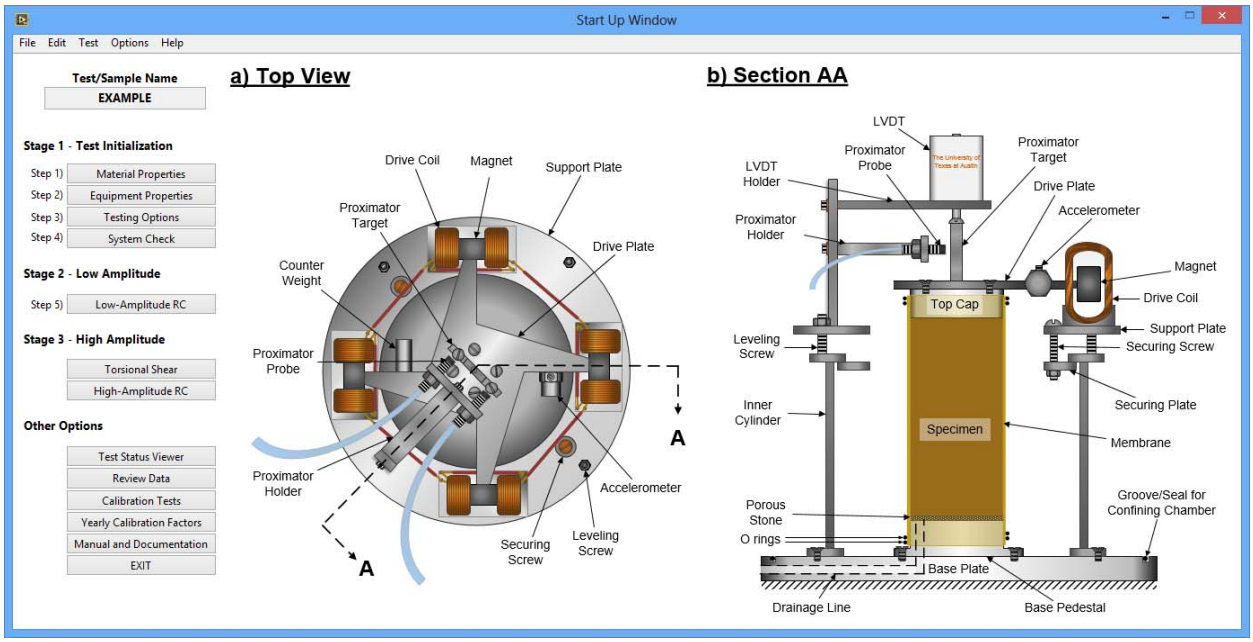

Figure A.1: The “Start-Up Window” for the RCTS-Test user

A.2.3 Specimen Test Results Folder Naming, Saving, and Re-Opening

The first step in the RCTS test is defining a file folder name within which specimen data and test results are saved and can later be accessed. Upon opening the “Start Up Window” the “File” menu can be accessed to create a “New Test” file folder, open a previous-test file folder “Open Test File”, or the settings of a previous file folder can be saved under a new name “Save File Under New Name” as shown in Figure A.2.

Once either “New Test” file folder, “Open Test File”, or “Save File Under New Name” has been selected, the user is asked to select “Metal Specimen”, “Soil Specimen”, or “Cancel”. If “New Test” is selected, after selecting “Metal Specimen” or “Soil Specimen”, the “Test File Name” prompt appears for the user to enter the name of the specimen, which is the folder name where all specimen properties, settings, and results will be saved. The “Metal Specimen” or “Soil Specimen” selection will specify the results folder under which the specimen folder will be saved. The “Choose Specimen Type” and “Test File Name” menus are shown in Figure A.3.

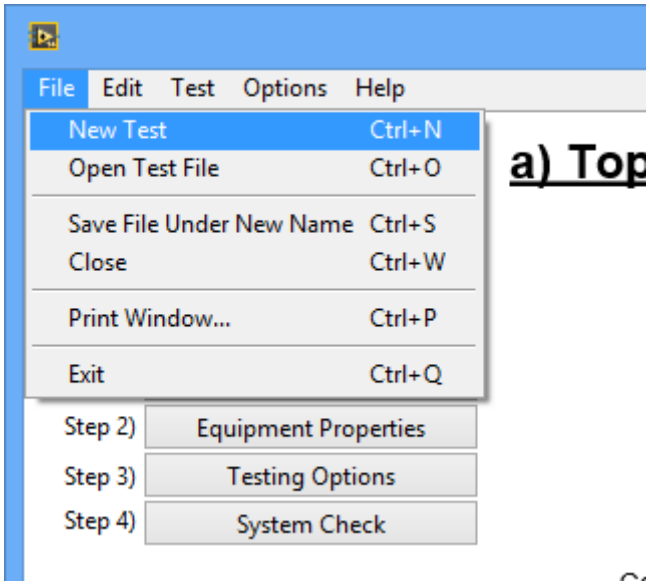

Figure A.2: "File" drop-down menu for selecting defining a file folder name for saving and accessing specimen data and test results

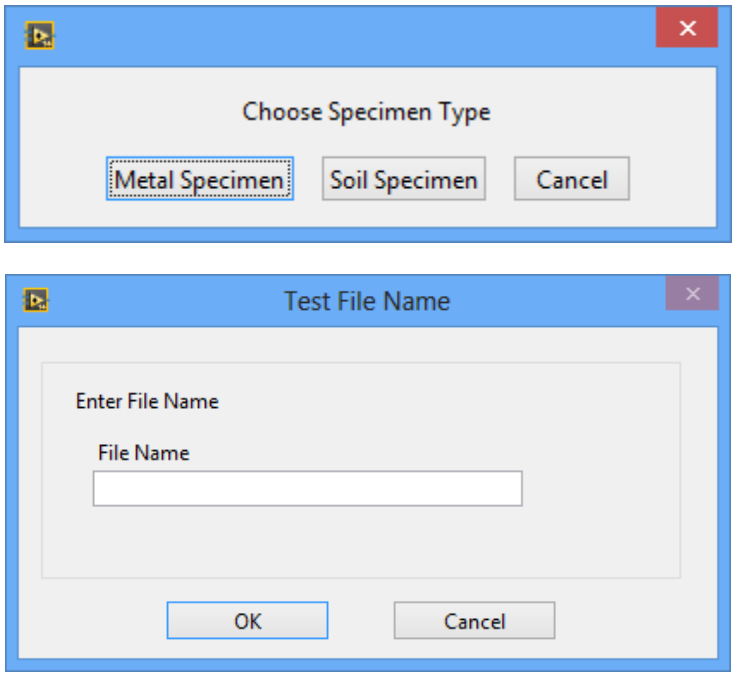

Figure A.3: "Choose Specimen Type" and "Test File Name" menus

A.2.4 "Step (1)" Material Properties

In the RCTS test, accurately measuring specimen dimensions and material phase properties are crucial for obtaining dynamic behavior of the material during testing. When testing a calibration/metal specimen, the "Material Properties" menu button is disabled as the Metal Specimen material properties are predetermined. Specimen observations, measurements, and composition are recorded using procedural checklists prior to accessing the menu for inputting the specimen properties. After a thorough assessment has been conducted, the "Material Properties" menu can be accessed to input the nominal dimensional and compositional quantities of the specimen. The executed computerized calculations can be verified with the. This menu must be accessed and completed before proceeding to the next step in the RCTS test process. A diagram of the "Material Properties" menu is provided in Figure A.4.

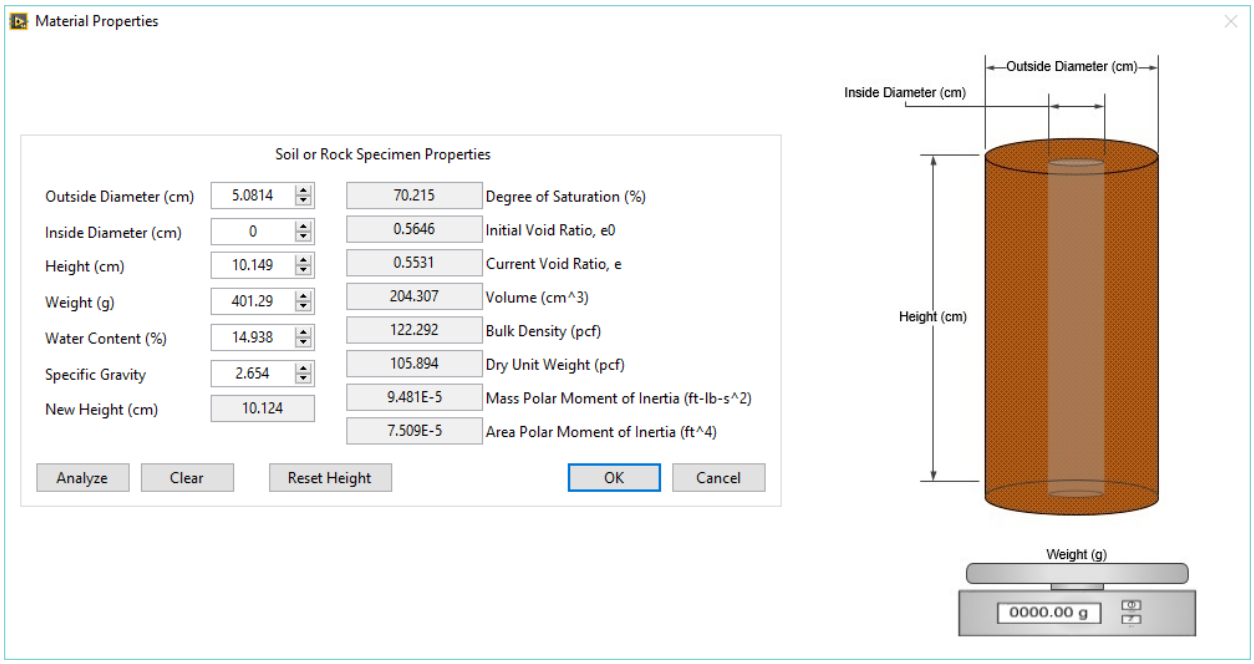

Figure A.4: "Material Properties" menu for entering nominal dimensional and compositional quantities of a soil or rock specimen

In the “Material Properties” menu, the specimen dimensions for either a solid or hollow specimen are entered. If a solid specimen is being tested, then the “Inside Diameter (cm)” is zero. After the additional properties are entered (i.e., weight, water content, and specific gravity), the “Analyze” button is pressed to calculate the phase properties of the specimen. The “Clear” button will clear all numeric inputs and specimen phase results. During RCTS testing, the height of the specimen can change from consolidation due to increase in confining pressure or deformation due to high amplitude RCTS sequences. The “New Height (cm)” numeric indicator will display the new height of the specimen after RCTS tests have been conducted or will need to be reset (“Reset Height”) if the specimen properties are being initialized. This “New Height (cm)” numeric indicator can also be reset to the “Height (cm)” entered by pressing the “Reset Height” button. The user must double check the calculated values to verify that the specimen dimensional and compositional quantities have been entered correctly. Click “OK” to proceed or “Cancel” to return to the “Start-Up Window”.

A.2.5 “Step (2)” Equipment Properties

The equipment properties are the values that are part of the yearly internal RCTS calibrations that allow precise testing and acquisition of specimen material properties. The “Equipment Properties” menu provides the user with a selection of the equipment calibrated for RCTS testing. This menu must be accessed and completed before proceeding to the next step in the RCTS testing process. The menu consists of thirteen selections that include the following:

- “(1) Test Status” is no longer a configurable option and is unimportant to the testing procedure.

- “(2) Cell No.” to select the cell in which the specimen is to be tested. This selection will switch between cables connected to either RCTS cell wired to the RCTS testing system in use.
- “(3) Drive Plate No.” to select the calibrated drive plate that is mounted on the top cap pf the specimen in the RCTS test cell.
- “(4) Accelerometer #1” to select the calibrated accelerometer that is mounted on the drive plate and is being used to measure the specimen behavior during the RCTS test. A “Charge Amp. Range” drop-down menu is provided adjacent to the “4) Accelerometer #1” menu where the charge amplifier range can be selected.
- “(5) Accelerometer #2” to select the second calibrated accelerometer sensor that is mounted on the drive plate and is being used to measure the specimen behavior during the RCTS test. A “Charge Amp. Range” drop-down menu is provided adjacent to the “5) Accelerometer #2” menu where the charge amplifier range can be selected. Note: if no secondary accelerometer is attached, select “None” in the drop down menu.
- “(6) LVDT No.” to select the calibrated LVDT sensor that is mounted on the cell and is used to continually measure the specimen height during RCTS testing.
- “(7) Proximitor Set (select Y)” to select the calibrated set of proximitors that are mounted to the support plate. Note: to select a proximitor pair, select the first proximitor labeled in the pair which is denoted with a Y.
- “(8) Top Cap” to select the calibrated top cap that is mounted between the specimen and drive plate. Note: if a “Metal Specimen” was initialized or selected in the “Start Up Window”, this option will not be available and a menu “Metal Specimen No.” will be available to select the serial number of the metal specimen being used.

- “(9) Confining Pressure (psi)” to select the confining pressure that has been manually applied to the specimen. Note: this value must be changed each time the confining pressure applied to the specimen is being manually changed during testing. This option serves as record keeping when the testing results are saved to the output files. When testing a metal specimen this menu is arbitrary. When the pressure value is changed, new file naming conventions will be used for the results that are saved during RCTS testing.
- “(10) Loading/Unloading” to select whether the test is in the loading, unloading, or reloading process. This selection serves as record keeping that will be entered into the log of the test results “RC Test”. When this value is changed, folders containing the signals saved from RCTS testing will have the same name that is selected from this menu.
- “(11) Calibration Factors” to select the calibration factors determined for the “New System” or the “Old System”. The “New System”: refers to the calibration factors that have been determined for the system that this document is written for. Note: The “Old System” calibration factors can only be used for Drive Plates #4 and #5.
- “(12) Anisotropic Test” to select whether the test being conducted will involve application of anisotropic or isotropic stress states. Selecting “No” enables calculation routines that are applicable for applying isotropic stress states (i.e., air pressure) to a specimen. Selecting “Yes” enables calculation routines that are applicable for applying anisotropic stress states to a specimen. Note: The anisotropic calculation routines are reserved for research purposes and are not generally used for typical projects.

- "(13) Power Amplifier" to select the amplifier configured in the RCTS testing system. In general the HP 6824A is used. A "Self-Input" option is available where the user can input a predetermined amplification factor.

Click "OK" to process the user inputs or click "Cancel" to eliminate the user selections and return to the "Start Up Window". Diagrams of the "Equipment Properties" menus for either soil/rock or metal specimens are provided in Figure A.5.

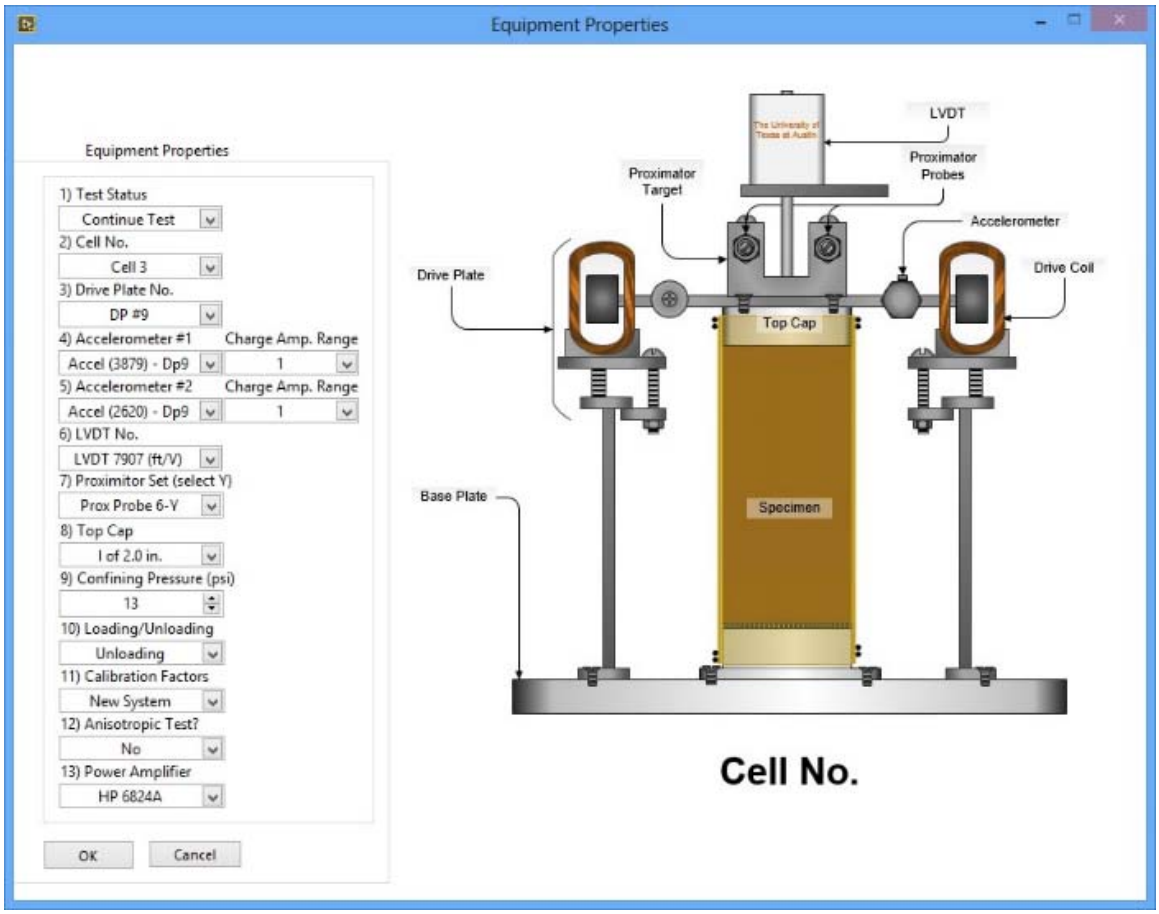

Figure A.5: "Equipment Properties" menu for entering characteristics of the RCTS system. Menu for soil.

A.2.6 "Step (3)" Testing Options

The "Testing Options and Features" menu provides various features to the user that enable for more advanced testing aspects to be available during the RCTS testing process. The "Testing Options and Features" is separated into several groups that are presented in Figure A.6, which shows the menu.

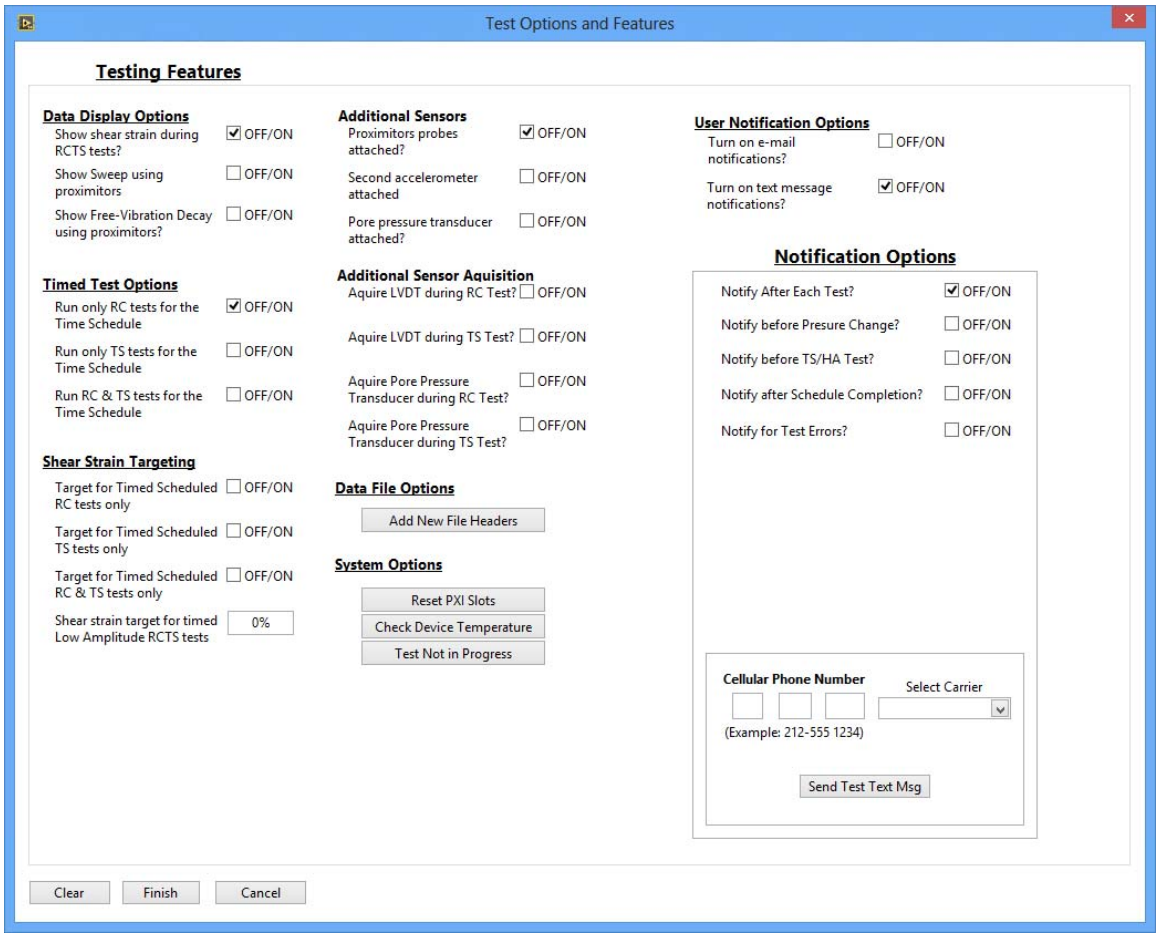

Figure A.6: "Testing Options and Features" menu.

A.2.6.1 Data Display Options

These options enable plotting of additional sensors configured in the RCTS testing system. "Show shear strain during RCTS tests?" is a default configuration and cannot be

changed. “Show Sweep using proximitors” can be selected to show the shear strain response curve determined from the proximitors. “Show Free-Vibration Decay using proximitors” is not currently an active feature.

A.2.6.2 Timed Test Options

“Run only RC tests for the Time Schedule” is the only active feature in this group. The remaining options are for research purposes for when both RC and TS tests are used to track the time dependent properties of the specimen being tested.

A.2.6.3 Shear Strain Targeting

“Target for Timed Scheduled RC Tests” is the only active feature in this group. The remaining options are for research purposes for when both RC and TS tests are used to track the time dependent properties of the specimen being tested. In each of the cases, the “Shear strain target for timed low-amplitude RCTS tests” value can be entered so that a specific shear strain level is targeted when timed tests are being conducted. This option should be deselected when conduction high-amplitude tests.

A.2.6.4 Additional Sensors

The check boxes in this group can be selected “Checked” to activate these sensors during RCTS testing.

A.2.6.5 Additional Sensor Acquisition

The check boxes in this group can be selected “Checked” to enable visibility and saving of these sensors during RCTS tests.

A.2.6.6 Data File Options

This feature is used to place headers between sets of data that resembles a change in loading condition or between timed tests and high-amplitude or TS tests. Changing this

option is at the user's discretion, but is highly recommended for partitioning the data sets as well as the folders under which the signals collected during RCTS testing are saved. When clicking the "Add New File Headers" button, a separate menu is opened to view the header attributes that will be used to compose the new file header. In the "Add File Header to Files" menu, the "Change Header" button can be pressed, which will open the "Equipment Properties Menu", where the "Confining Pressure (psi)" and "Loading/Unloading" values can be changed and the "Header Attributes" will be updated. An example of the header is shown in the "Header Example" table, which is shown in Figure A.7. Any previously recorded RC or TS results are shown in the "RC Table" and "TS Table", respectively. Clicking the "Add Header Separator" button will add headers to both the RC and TS data files. If "Accept" is clicked, any changes will be saved and if "Cancel" is clicked, any changes will be discarded.

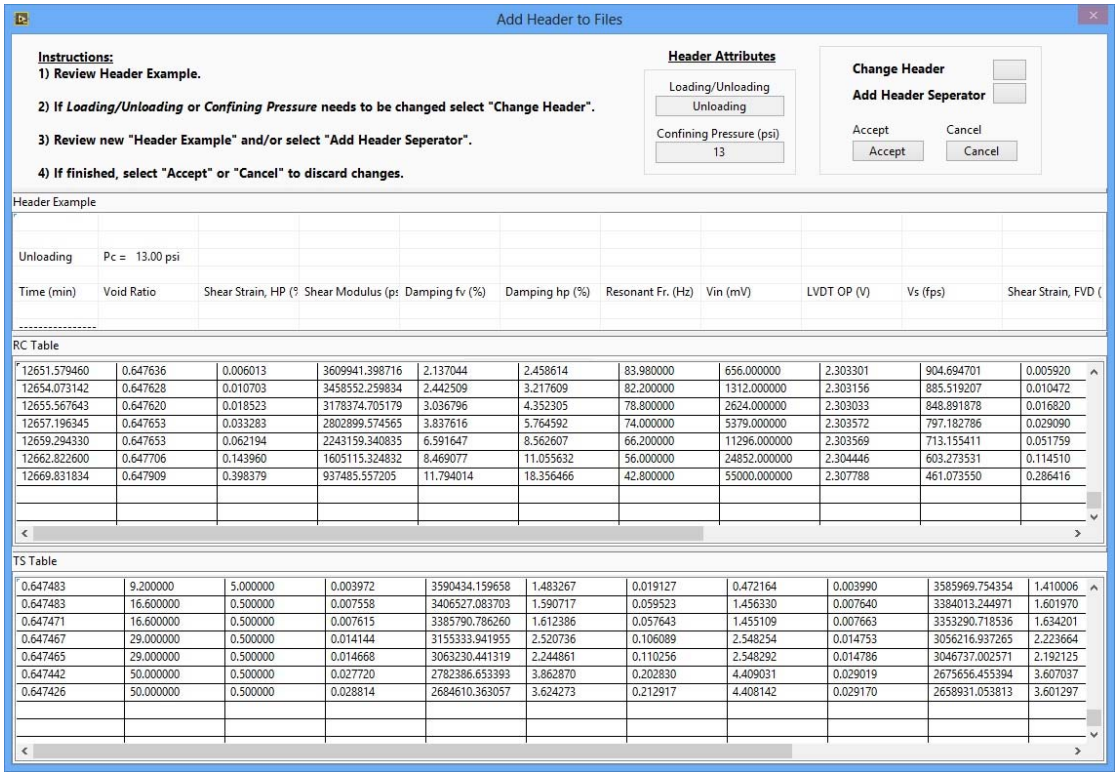

Figure A.7: "Add File Header to Files" menu.

A.2.6.7 System Options

If the data acquisition system is not responding or if an error occurred during an RCTS test, the "Reset PXI Slots" can be clicked to reset the NI PXI system. The "Check Device Temperature" button is clicked to view the current operating temperatures of two of the NI PXI data acquisition slots. A separate screen will open to show the current NI PXI data acquisition slot temperatures and the temperatures recorded during their calibration. The operating temperatures shown should not deviate more than ±10˚C from their calibration temperatures. This feature automatically closes after 1 min. An example of this feature is shown in Figure A.8.

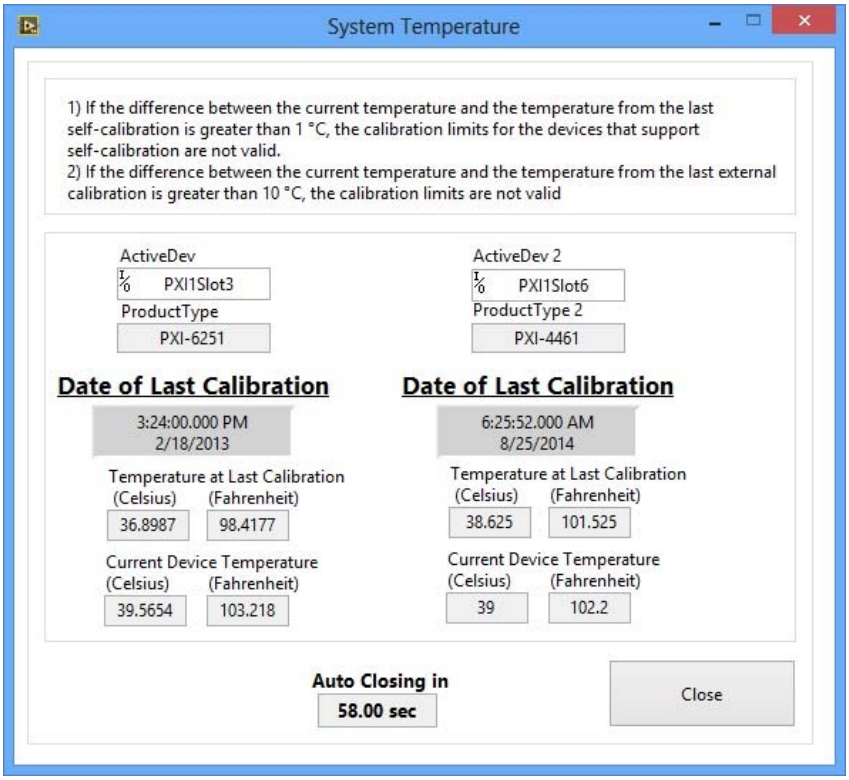

Figure A.8: System Temperature reading.

During RCTS testing, a safety function is enabled that prohibits access to certain testing menus while a test is running. In the case of an error occurring during an RCTS test,

this function may remain enabled, even if the test is closed. The “Test Not in Progress” button temporarily disables this feature.

A.2.6.8 User Notification Options

The items in this group provide the user with a notification system that will contact the user when an error occurs during RCTS testing or when certain testing sequences are complete. Currently, the only active feature is the Test Message notifications to notify the user is there is an error in the test or once an RC or TS test is completed. To activate this feature, the user will check the “Notify After Each Test?” box and enter their cellular phone number and their cellular phone carrier. The “Send Test Text Msg.” is clicked to test that this feature is functioning.

A.2.7 “Step (4)” System Check

During cell assembly or when changing the confining pressure, a system check is needed to ascertain the linear-elastic dynamic behavior of the specimen for conducting further RCTS tests. In the “System Check” menu there are options such as “LVDT Voltage” to acquire the position of the specimen as measured by the LVDT, “Pressure Transducers” to check the values of the electronic pressure transducers if they are attached, “Proximitor Status” to check the output voltages and background noise levels of the proximitors, and “Rough Sweep” to access the menu for conducting a frequency sweep on the specimen to determine the half-power range and resonant frequency of the current specimen.

This menu must be accessed and completed before proceeding to the next step in the RCTS test process. A diagram of the “System Check” menu is provided in Figure A.9.

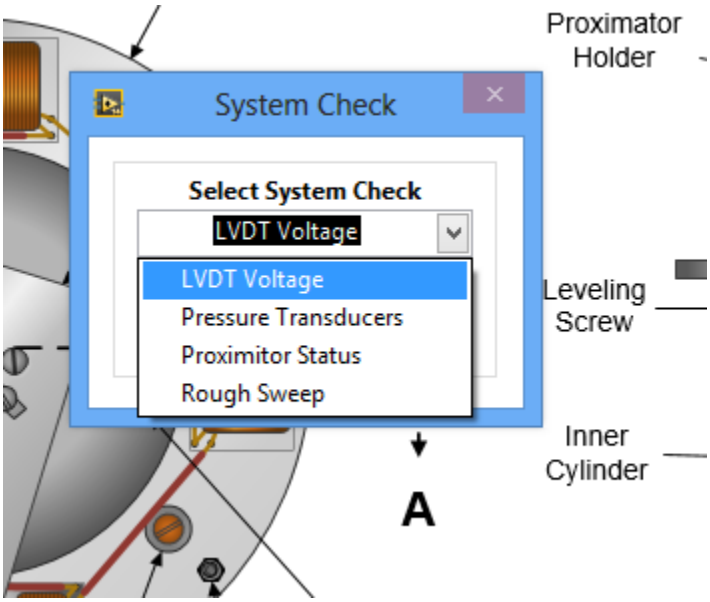

Figure A.9*:* "System Check" menu.

A.2.7.1 LVDT Status

Under the "System Check" menu, when selecting "LVDT Voltage" an additional menu is available where either an "LVDT Acquisition Window" can be accessed or the "LVDT Reference Voltage" can be determined. The menu for these options is presented as Figure A.10.

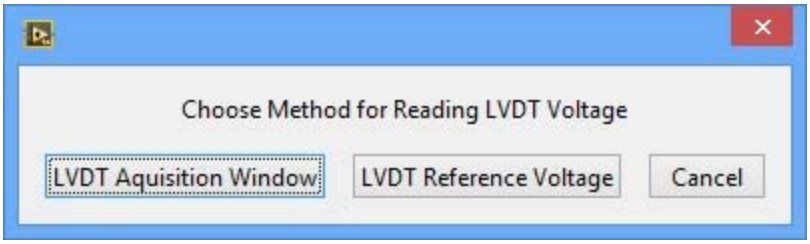

Figure A.10*:* Method for reading and setting acquired LVDT values.

The "LVDT Acquisition Window" for taking one reading or timed readings for determining specimen movement after adjusting the test cell (e.g. changing confining pressure, mounting the confining chamber, etc.). The timed readings provides the user with an option to acquire LVDT readings for testing intervals of 2.5-180 seconds (up to 3

minutes) and durations from 10 to 7200 seconds (up to 2 hours). The “LVDT Acquisition Window” is shown as Figure A.11.

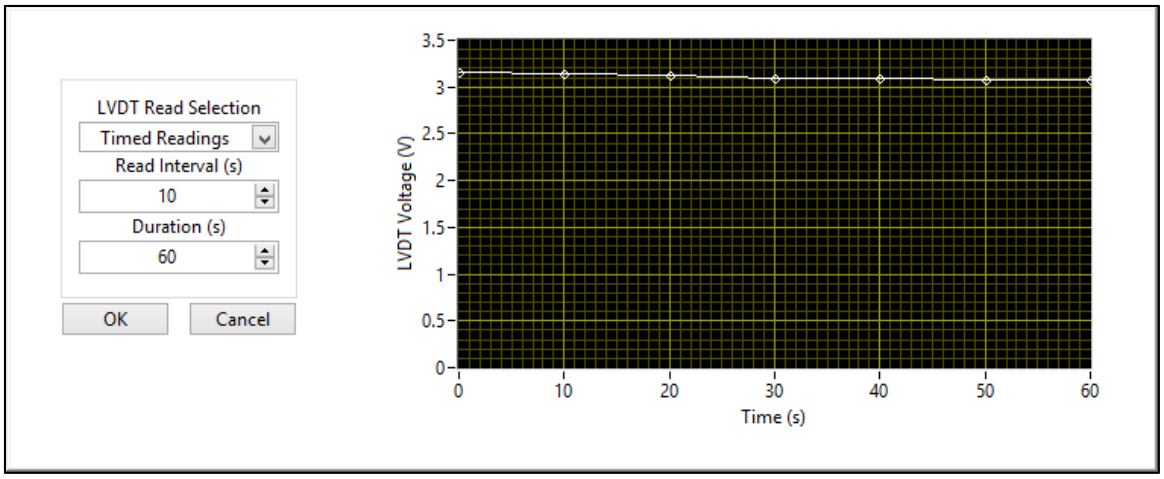

Figure A.11: “LVDT Acquisition Window”

The LVDT reference voltage is used to determine the initial LVDT reading that corresponds to the initial height of the specimen. Subsequent LVDT readings taken during RCTS testing are used to determine change in specimen height. When initializing the LVDT reference voltage, a warning menu will appear to make sure the user intends this course of action. The subsequent menu allows the user “Acquire” the LVDT reference voltage, which will conduct an LVDT reading to establish the LVDT reference voltage, “Self-Input” the LVDT reference voltage, which allows the user to manually enter the value of the LVDT reference voltage, or “Cancel” to exit this process. If “Self-Input” is selected, a “Prompt User for Input” dialog box will appear where the user can enter the LVDT reference voltage. These dialog boxes are shown in Figure A.12.

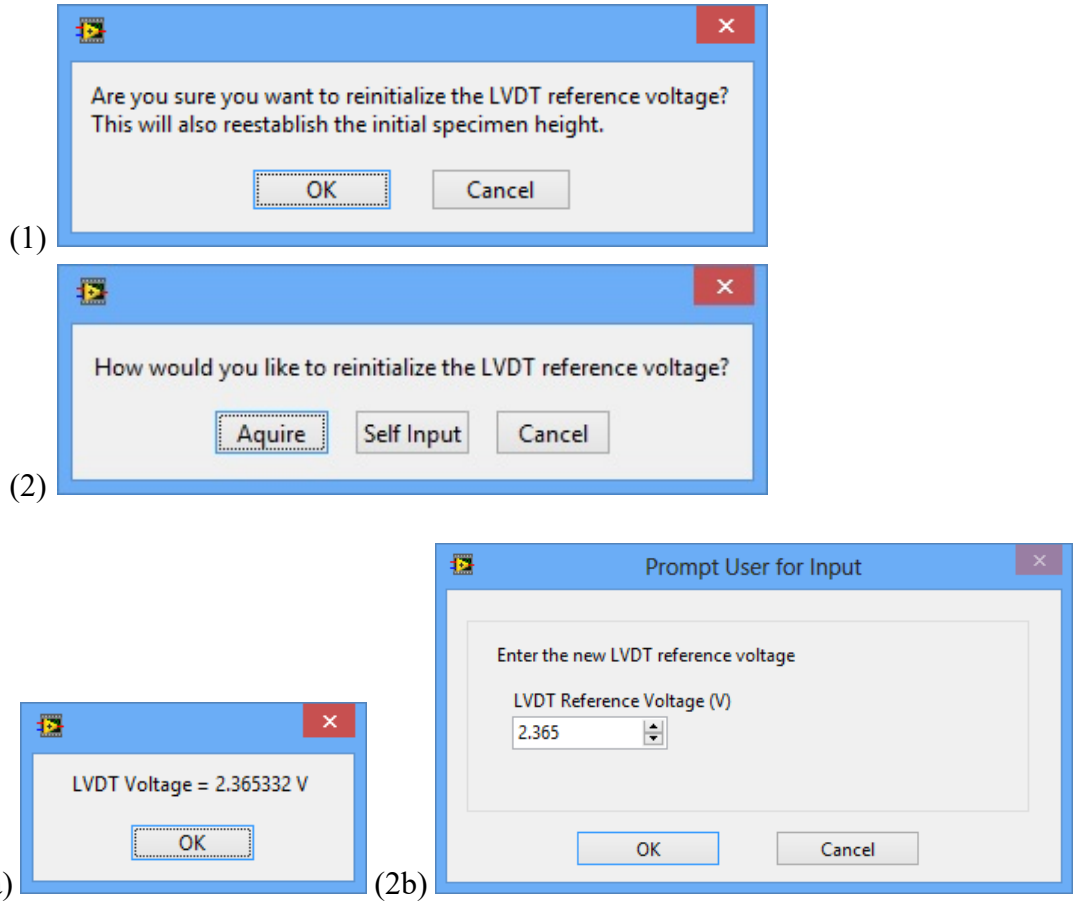

Figure A.12: Menu progression for establishing the reference LVDT voltage.

A.2.7.2 Status of Pressure Transducers

When selecting "Pressure Transducers", a window opens where constant pressure transducer readings are displayed. The "Cell 3" or "Cell 4" buttons are selected when no pressure is applied to the system to set the initial DC offsets recorded by the transducers. "Stop" is clicked to exit this window. If no pressure transducers are configured for the testing then this option can be ignored. An example of this window is shown in Figure A.13.

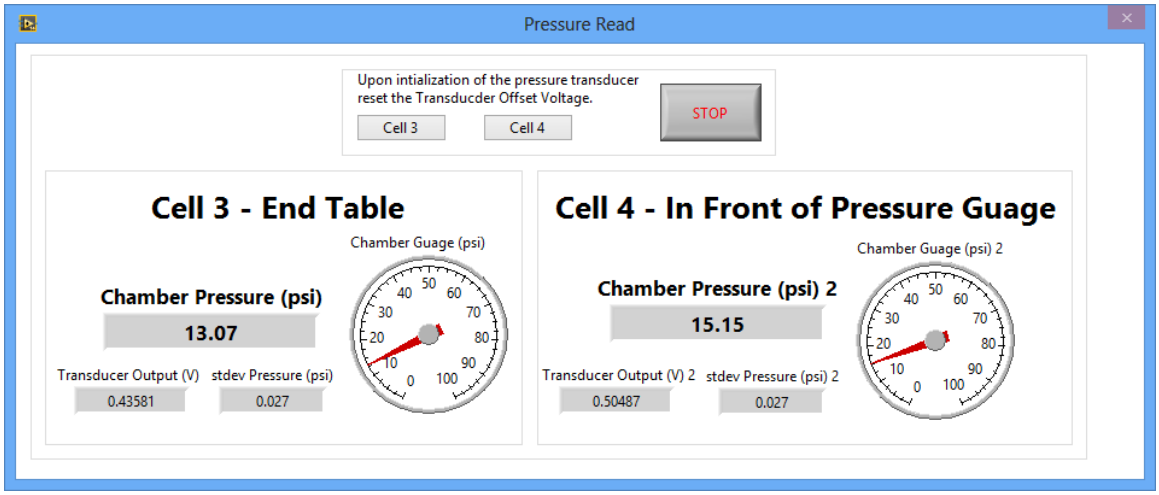

Figure A.13: Pressure transducer readings window.

A.2.7.3 Status of Proximitors:

"Proximitor Status" is selected to check the output voltages and background noise levels of the proximitors. An example of this window is shown in Figure A.14.

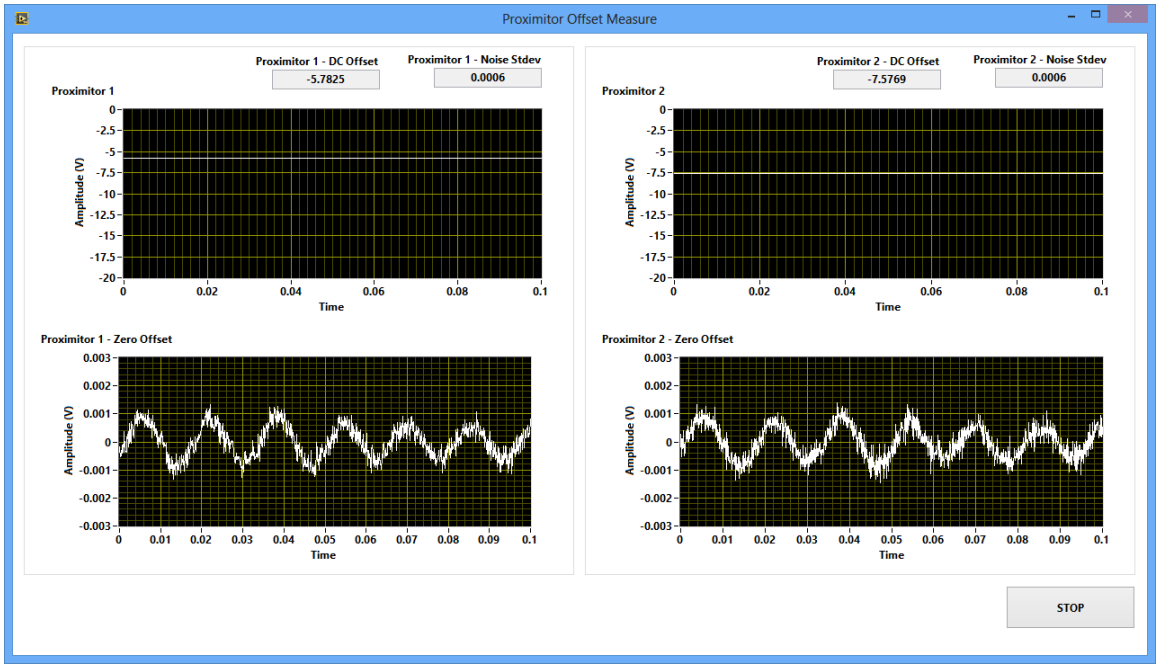

Figure A.14: Proximitor output window.

A.2.7.4 Status of Specimen and Test Setup:

Readdressing the "System Check" menu (Figure A.9), the "Rough Sweep" option is available to determine the linear-elastic dynamic properties of the specimen. When conducting the rough sweep, the user must recognize the resonant frequency and the half-power range so that these inputs can be used for further RCTS testing. Based on the confining pressure applied and the type of material being tested, the user must perceive the range of frequencies that might comprise the resonant frequency of the specimen. If this is not intuitively known, a broad range can be chosen and is provided with a default stepped-sine sweep function that applies 15 cycles per frequency and steps at 0.1 Hz, 0.25 Hz, or 0.8 Hz increments. Whether the bandwidth containing the resonant frequency is known or a wide sweep is conducted, the "Rough Sweep" subroutine should allow the user to determine the resonant frequency of the specimen in a timely manner. A diagram of the input menu for the "Rough Sweep" subroutine is provided in Figure A.15.

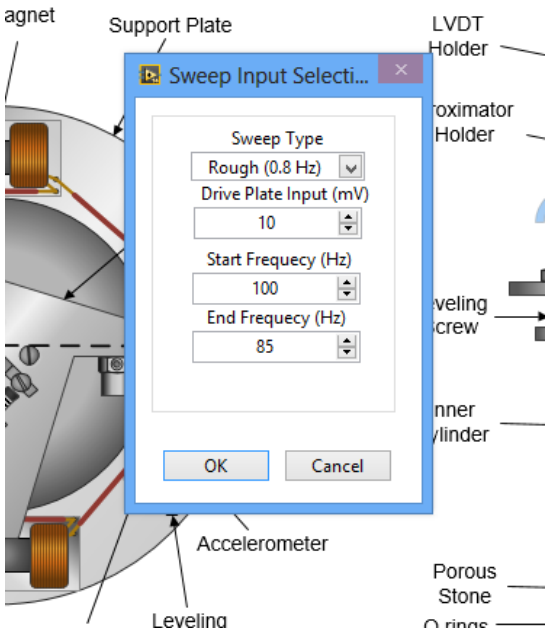

Figure A.15: Input menu for the "Rough Sweep" routine. Example includes gravel at 51 psi confining pressure.

The “Sweep Type” menu provides the use with the option to select a “Rough” sweep or “Fine” sweep. Though both options are available, a “Rough” sweep is recommended for system checking. The details of the stepped-sine sweep function used for the “Rough” or “Fine” sweep are discussed in Keene (2017). The “Drive Plate Input (mV)” entered should be in an input voltage range that is understood to be in the linear-elastic range when testing soil or rock specimens. An appropriate input voltage must be selected that would not induce non-linear elastic or plastic deformational behavior in the specimen as such loading does not yield proper results for system checking. This range is typically 1 to 15 mV for clay, 5 to 30 mV for sand, and 10 mV to 150 mV for soft rock. A diagram of a response curve after a rough stepped-sine sweep on a gravel specimen at 18 psi confining pressure is shown in Figure A.16. Typically, for determining the resonant frequency and half-power range, a higher “Start Frequency (Hz) and lower “End Frequency (Hz)” are chosen (i.e. a downgrade sweep), which is preferred for laboratory specimen testing.

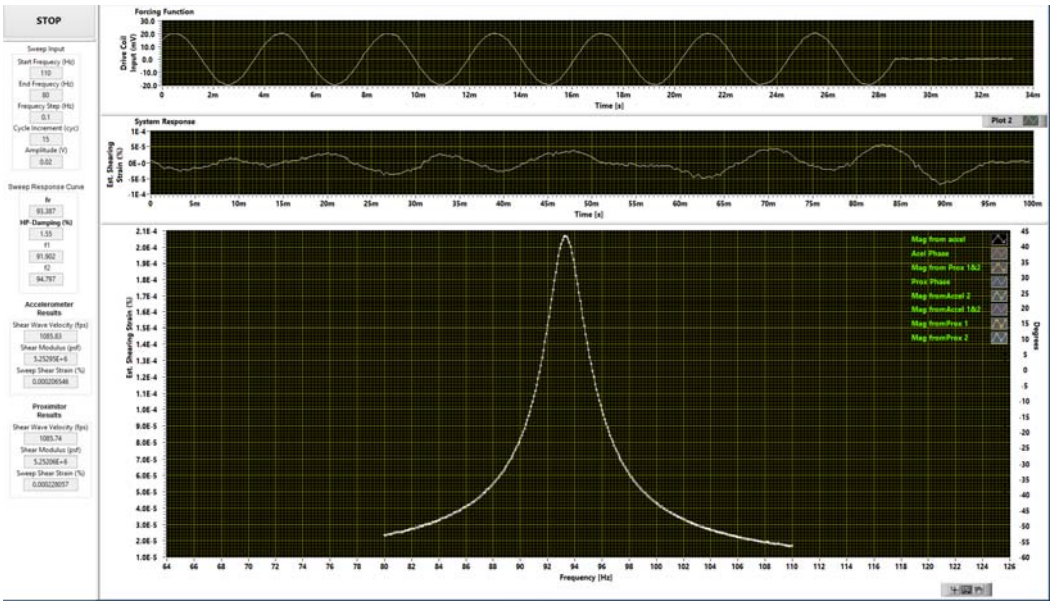

Figure A.16: Diagram of a response curve after a stepped-sine sweep for a sand at 51 psi confining pressure.

Approximations for half-power damping, shear wave velocity, shear modulus, and shear strain are calculated and shown in the left side-bar for verification purposes. The "System Check" sweep test is used to find the range of frequencies to sweep in order to determine the half-power range and resonant frequency.

A.3 RESONANT COLUMN (RC) TEST

A.3.1 Introduction

The resonant column (RC) test consists of two tests that are used to determine the dynamic characteristics of a soil or rock specimen. The sine sweep test is used to find the resonant frequency and half-power damping of a test specimen and is followed by a forced/free-vibration test for determining the damping ratio of a specimen from free-vibration decay. The purpose of the low-amplitude resonant column (LARC) is to run both the sine sweep and forced/free vibration tests in the linear-elastic strain range and determine mechanical properties of the specimen without causing permanent strain in the specimen. The high-amplitude resonant column (HARC) test is used to incrementally increase the strain excited to the specimen and measure the nonlinear change in specimen dynamic properties (i.e. shear modulus, shear wave velocity, and half-power and free-vibration damping).

A.3.2 "Step (5)" Low-Amplitude RC (LARC)

A.3.2.1 LARC Input Menu

Once the initial system input properties are configured and dynamic characteristics of the specimen are known, the "Low-Amplitude RC" subroutine can be employed. The function of this subroutine is adaptable to either run at timed intervals to obtain time dependent change in stiffness (e.g. after change in confining pressure) or to assess both

response curve and free-vibration decay characteristics of the specimen in the linear-elastic strain range. The user menu for the LARC test can be seen in Figure A.17.

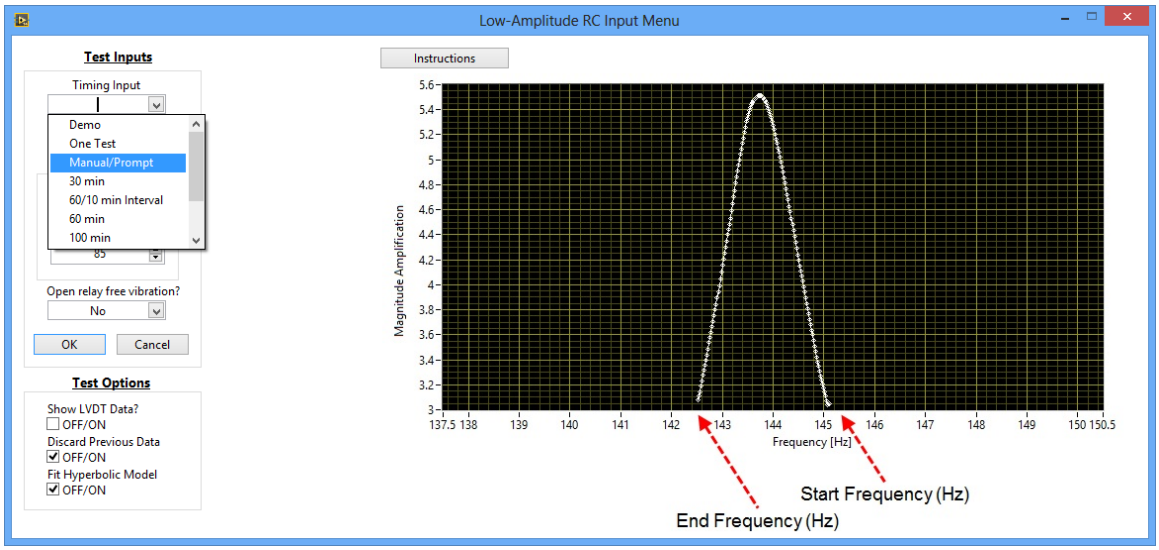

Figure A.17: Input window for the LARC test.

Under the “Timing Input” drop-down menu there are options for conducting “One Test”, “30 min”, “60 min”, “100 min”, “1000 min”, and “Self-Input”. The timing input selection is chosen by the user, but the recommended selection is one test or 30 minutes for rock, 30-100 minutes for sand, and 100-1000 minutes for clay. The recording intervals involve tests being conducting as fast as possible up to 40 minutes, after 40 minutes the tests will commence every 10 minutes, and after 100 minutes each preceding tests will commence at 100 minute intervals. Other options are available to test at 10 min intervals for tests that run up to 60 min, 100 min, or 1000 min in duration. A diagram of the available testing schedules is shown as Figure A.18.

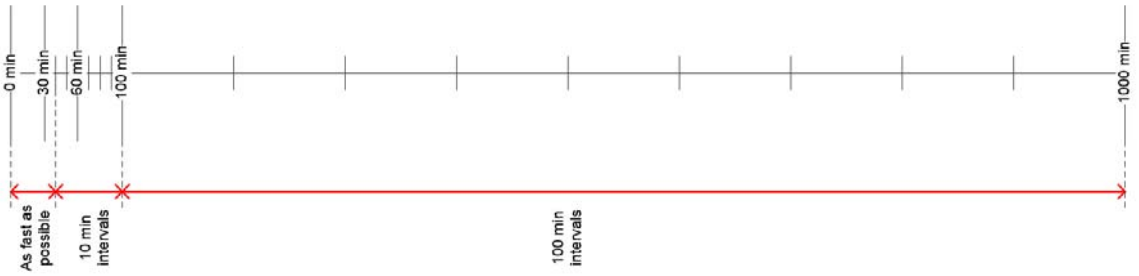

Figure A.18: Timeline of available testing schedules.

The "One Test" option is selected to conduct one test or is recommended to check the functionality of the sweep and force/free-vibration tests. For a manual testing schedule, "Self-Input" is selected and successive tests at the same or differing excitation voltages is entered. These two options are shown as part of the main LARC input menu in Figure A.19.

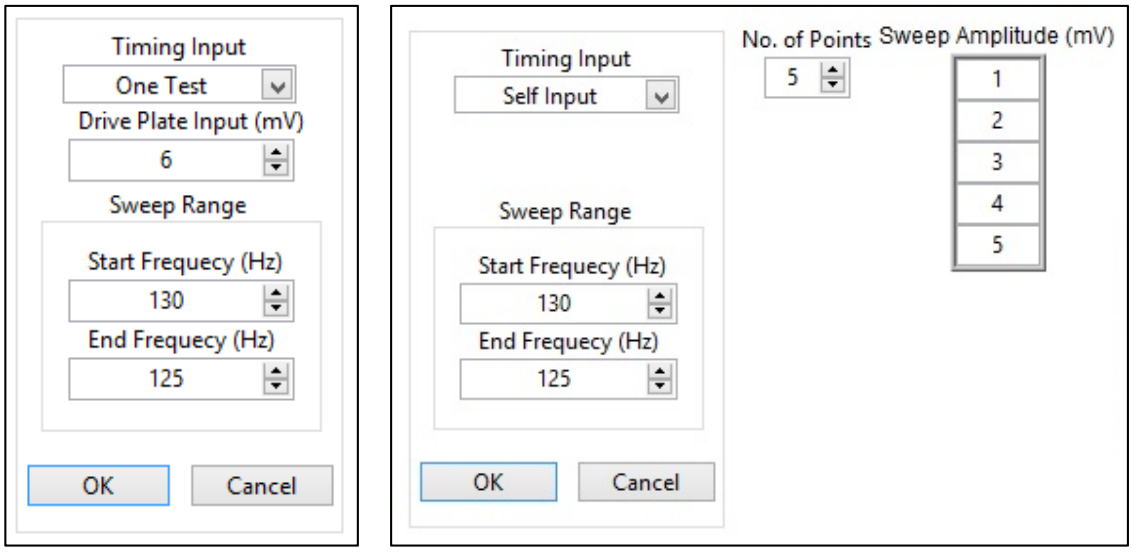

Figure A.19: "One Test" (left) and "Self-Input" (right) options of the main LARC input menu.

The "Demo" option is available to conduct an expedited Low-Amplitude RC test where only one rough sweep is conducted followed by the free-vibration decay test. The "Demo" option is primarily used for providing a system demonstration. The "Manual/Prompt" is used when beginning a High-Amplitude RC testing sequence. This

option is started from the Low-Amplitude menu to use testing features that provide a more accurate analysis of the dynamic behavior of the specimen at very low shearing strains.

The “Show LVDT Data” option will acquire LVDT readings taken during the test and plot them as a function or frequency. This option is not valuable during the Low-Amplitude test because the shear strains excited during the test are in the linear-elastic strain range and neither dilation nor contraction of the specimen is expected during the test. “Discard Previous Data” is selected to discard previous data that would be plotted in the “RCTS – Graphing” plot, which is discussed later. “Fit Hyperbolic Model” is not currently an available feature.

Once the proper input values are entered and “OK” is pressed, the LARC test will commence. If there are any errors or discrepancies in specimen or system values being sent to the RC Test subroutine, the user will be notified. The “Manual/Prompt” feature will enable a menu to appear after each RC test where the input amplitude and sweep range can be adjusted.

A.3.2.2 LARC Test

The first subtest performed is the stepped-sine sweep. The subroutine will start by running a rough sweep based on the start and end frequencies entered by the user. After a rough sweep is conducted, the subroutine will find an approximate value for the resonant frequency and calculate values for damping. These values are used to redefine a range of frequencies over which to conduct a fine sweep. The fine sweep excites more cycles at each step frequency and has smaller frequency step increments than the rough sweep. A screenshot of the RC Test during the sine sweep is shown in Figure A.20.

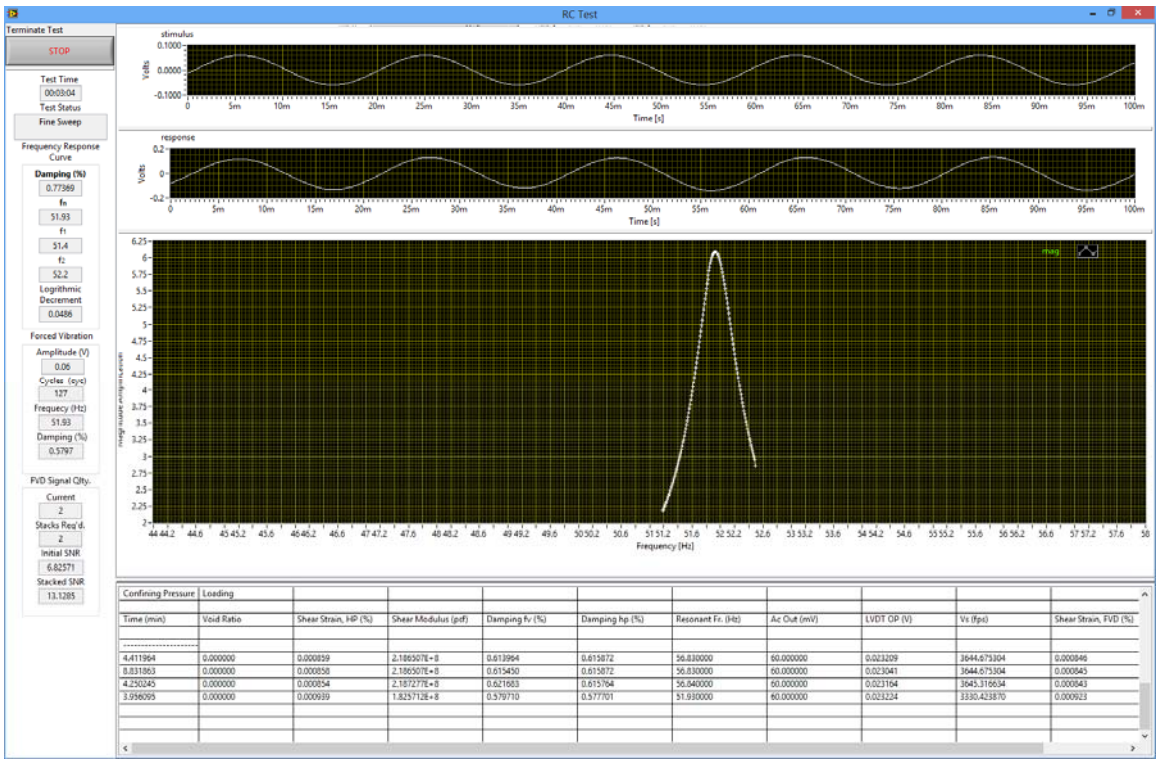

Figure A.20: Screenshot of the RC Test during the sine sweep.

Once the results of the fine sweep are collected, the subroutine will use these parameters to execute the forced/free-vibration test. The resonant frequency and damping are used to determine the number of cycles for forcing vibration from rest to 99.5% steady-state vibration. During forced excitation of the predetermined number of cycles and during free-vibration decay, the system records specimen behavior. The free-vibration decay of the specimen is analyzed to determine free-vibration damping. A screenshot of the RC Test during the free-vibration is shown in Figure A.21.

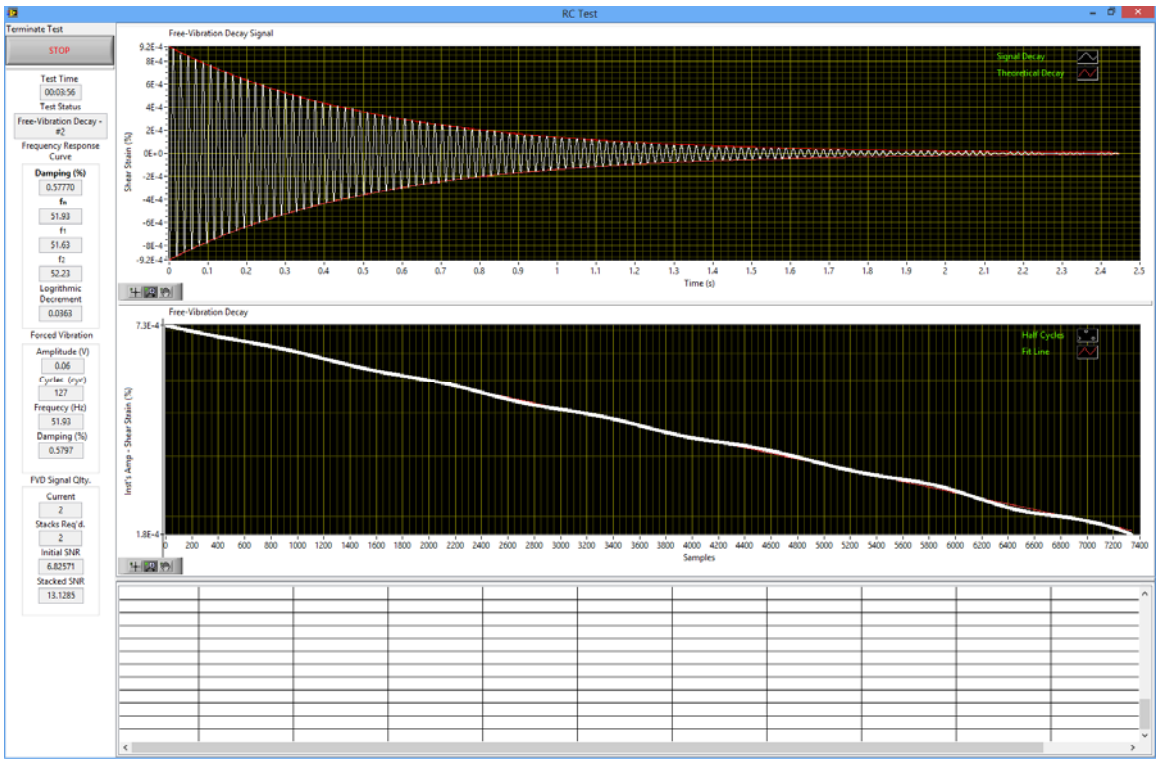

Figure A.21: A screenshot of the RC Test during the free-vibration.

A.3.2.3 LARC Test Progression: Signal Stacking for Free-Vibration Decay

The purpose of the LARC test is to determine the linear-elastic dynamic characteristics of the specimen. To ensure that these dynamic characteristics (i.e., resonant frequency, half-power damping, and free-vibration decay damping) are obtained in the linear-elastic range, the lowest excitation voltage is preferred. When inputting very low excitation voltages, obtaining these parameters becomes more difficult due to presence of background noise; especially for measuring free-vibration decay damping. At low excitation voltages the response signal from the accelerometer contains high levels of background noise. For the purpose of obtaining accurate results for free-vibration damping, a method of signal stacking is executed to eliminate noise from the true signal result. The method of signal stacking relies on a statistical calculation that determines the number of signals that must be stacked to ensure a sufficient signal-to-noise ratio. This ensures that

the stacked signal is suitable for analysis and for calculating the dynamic characteristics of the system. The number of signals to be stacked are limited to 20 so that an unreasonable number of tests are not repeated and to maintain an appropriate testing duration.

A.3.2.4 LARC Test Progression: Graphing and Test Progression

In the "Low-Amplitude RC Input Menu", under the "Timing Input" drop-down menu, if any of the timed setting or "Self-Input" is selected the RC Test subroutine will plot the results of each test. For LARC testing the shear modulus and damping versus time at the end of each test are plotted. A screen shot of the "RCTS Graphing" window is shown in Figure A.22.

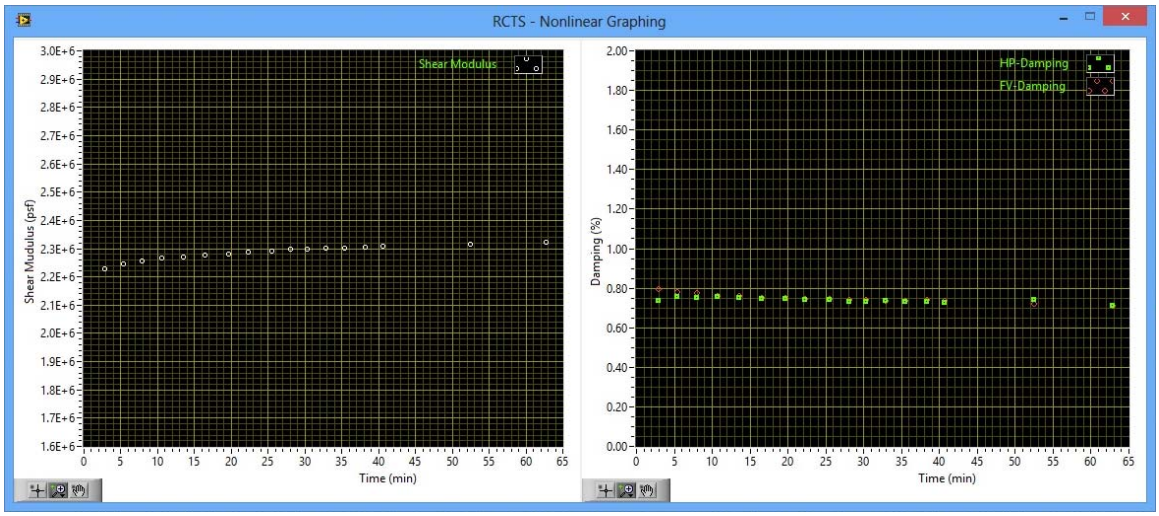

Figure A.22: Display of test progression with shear modulus is shown in the left plot and material damping ratio is shown in the right plot, both plots are shown with time on the independent axis.

If "Manual/Prompt" was selected in the menu before the Low-Amplitude RC test a menu appears after each RC test (see Figure A.23) where the input amplitude and sweep range can be adjusted. After each test, a new sweep range is recommended based on the half-power damping that was determined from the previous test. When reaching higher

shearing strains (i.e., close to or beyond the linear-elastic threshold), the test can be switched to the "High-Amplitude" test used the "Switch Test to?" drop down menu. A reasonable time to switch the test from the Low-Amplitude to the High-Amplitude test is when the number of signals stacked in the free-vibration decay tests is equal to 1.

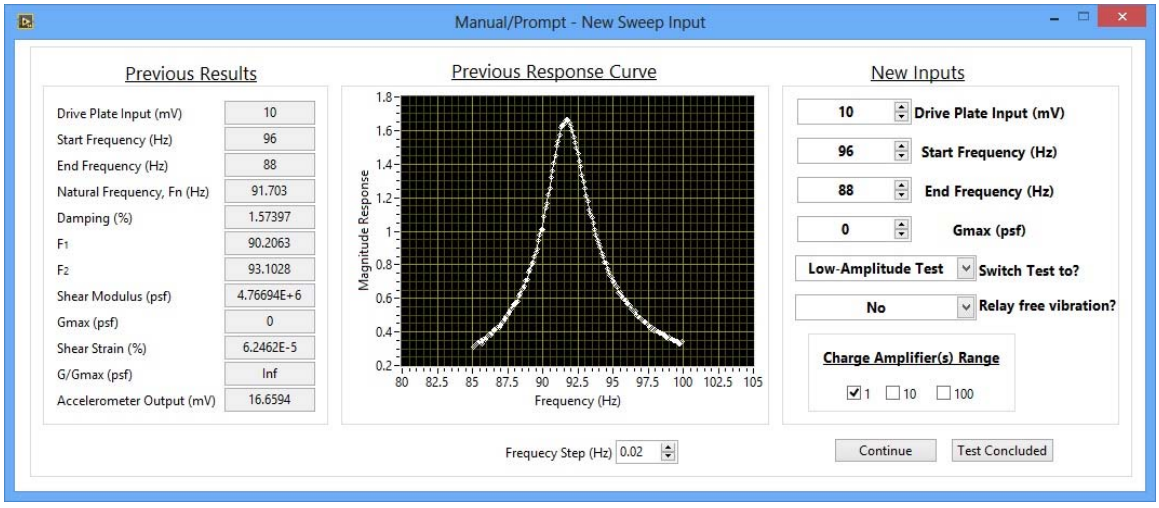

Figure A.23: "Manual/Prompt" menu.

A.3.3 High-Amplitude RC (HARC)

A.3.3.1 HARC Input Menu

Once LARC testing is conducted and linear-elastic dynamic characteristics of the specimen are known, the "High-Amplitude RC" subroutine can be employed. The purpose of this test is to first determine G_{max} (i.e., the modulus in the linear elastic range) and then to incrementally increase the excitation voltage of each successive test to measure the nonlinear elastic or plastic dynamic behavior of the specimen. The function of this subroutine is adaptable to allow the user to automatically conduct the HARC test, conduct the HARC test with prompting between each successive test, or to input a set range of excitation voltages. The user menu for the HARC test can be seen in Figure A.24.

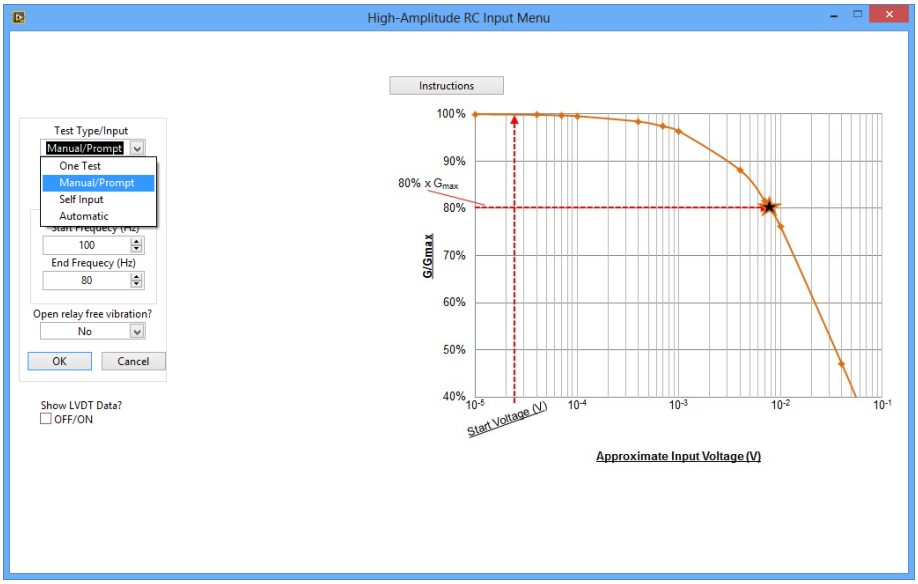

Figure A.24: Input window for the HARC test.

In the "High-Amplitude RC Input Menu" the "Start Frequency (Hz)" and "End Frequency (Hz)" are entered in a similar manner as the LARC Test. The sweep range for starting the HARC test can be taken from the system check results or from the last LARC test conducted. The remaining test parameters can be entered via the following steps:

A.3.3.2 "Test Type/Input" to select the testing regime:

- "One Test" is selected and the sweep range and "Drive Input Voltage (mV)" can then be entered for a single test to be conducted.
- "Manual/Prompt" is selected and the sweep range and "Drive Input Voltage (mV)" are entered for the first test. After the first and each subsequent test are concluded, the user will be prompted to select a new excitation voltage, charge amplifier range, and new sweep range.
- "Self-Input" is selected and the user is provided with an array to enter a self-determined array of input voltages.

- "Automatic" is a feature that is meant for research purposes and is not currently deployable for non-research related purposes.

The respective menu features for "One Test", "Manual/Prompt", "Self-Input", and "Automatic" are shown in Figure A.25.

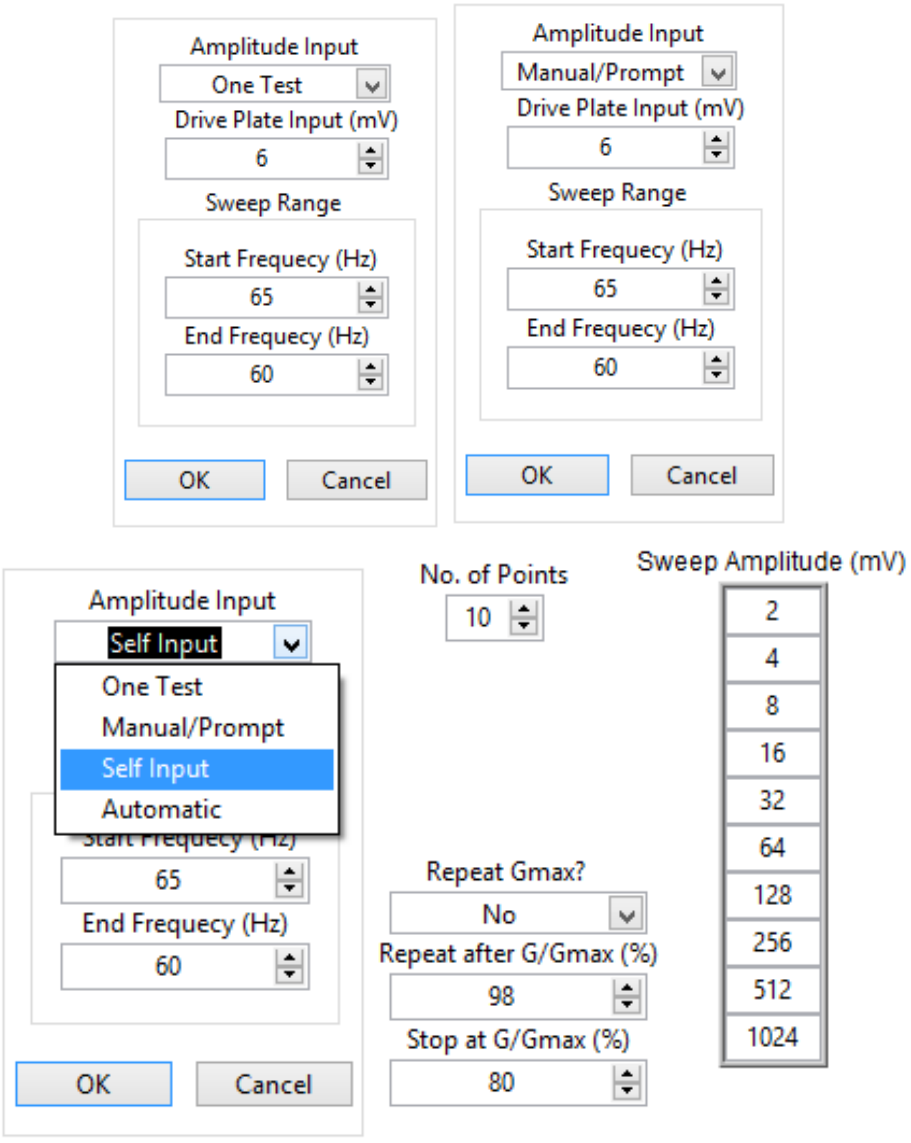

Figure A.25: Menu features for Amplitude Input options of "One Test" (top-left), "Manual/Prompt" (top-right), and "Self-Input" (bottom).

A.3.3.3 Additional Discussion for HARC input menu

For the "Manual/Prompt" *Test Type/Input* selection, the test will execute the sweep range and "Drive Input Voltage (mV)" entered and a prompt will appear after each sweep and free vibration test. The prompts will appear in sequential order as "Select Next Task" to submit new test inputs or conclude the test. The "Manual/Prompt" menu is shown in Figure A.26.

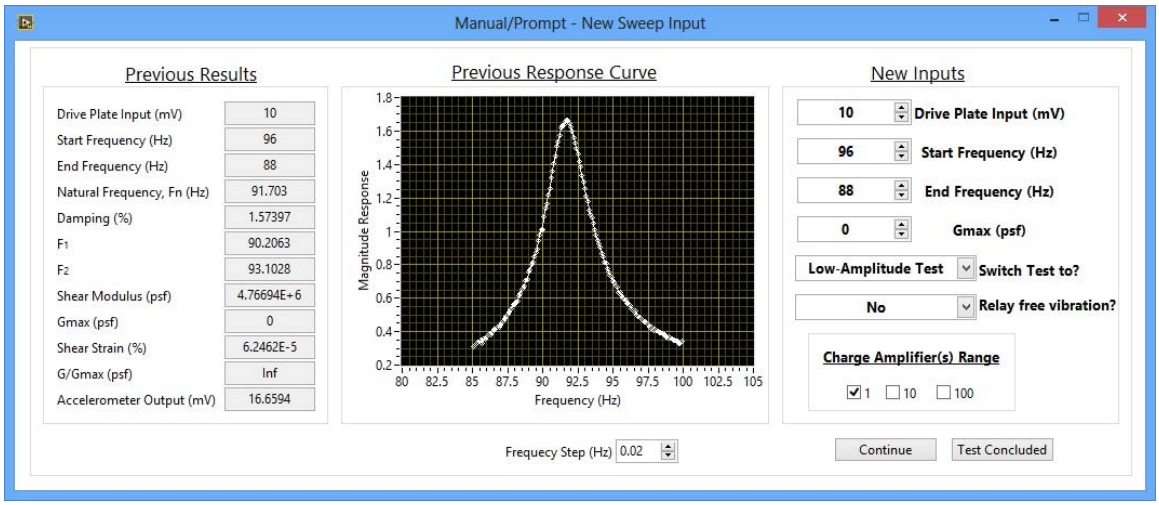

Figure A.26: "Manual/Prompt" to select new excitation voltage, charge amplifier range, and new sweep range.

A.3.4 HARC Test

The HARC test runs in the same manner as the LARC test accept the progression of the subroutine depends on the input menu selection and the nonlinear behavior of the specimen. The stepped-sine sweep and free-vibration decay tests run similar as during the LARC test; however, several aspects of each successive test adapts with the changing dynamic behavior of the specimen.

A.3.4.1 The changing conditions of the test are the following:

- After acquiring the resonant frequency of each test, the end frequency of the subsequent rough sweep test is 10 Hz higher or lower than the preceding

resonant frequency depending on the direction of the sweep. This is to ensure that as the excitation voltage increases the rough sweep test will sweep over the entire half-power range of the specimen with the increased excitation voltage.

- At the beginning of the HARC sequence, while the excitation voltage is low and corresponding response signal is noisier, signal stacking will occur as needed for adequate signal resolution and mechanical property determination. As the excitation voltage is incrementally increased during the test, the quality of the response signal increases and the required signal stacks will be 1; which occurs before the linear-elastic threshold is exceeded.

A.3.5 HARC Test Progression and Repetition

A.3.5.1 Graphing of Test Progression

In the "High-Amplitude RC Input Menu", under the *Test Type/Input* drop-down menu, if any of the options are selected other than "One Test" the RC Test subroutine will plot the results of each test. For HARC testing G/G_{max} and damping versus Shear Strain at the end of each test are plotted. A screen shot of the "RCTS Graphing" window is shown in Figure A.27.

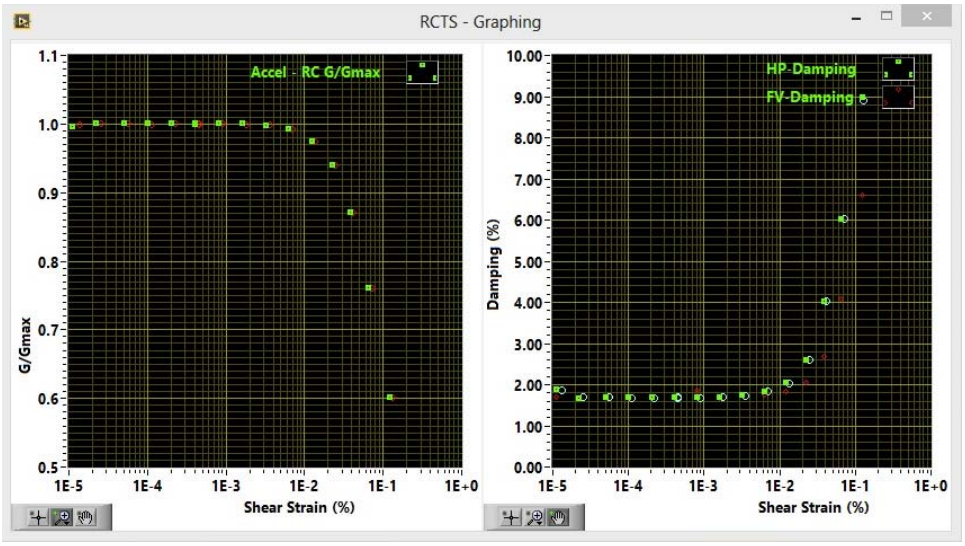

Figure A.27: Display of test progression with G/G_{max} (left) and damping (right) versus shear strain.

A.4 TORSIONAL SHEAR (TS) TEST

A.4.1 Introduction

The torsional shear (TS) test consists of several excitation voltages and frequencies to determine the dynamic characteristics of a system. The TS test is used to incrementally increase the shear strain excited on the specimen and measure the nonlinear change in specimen mechanical properties (i.e. shear modulus and hysteretic damping). While the shear strain is increased in subsequent tests, the excitation frequency is also varied to determine the dynamic response of the specimen with respect to the excitation frequency. Much of the nonlinear mechanical characteristics of a material can be determined by the tests used in the torsional shear procedure and serve as a compliment to the resonant column procedure.

A.4.2 TS Input Menu

Once LARC testing is conducted and linear-elastic dynamic characteristics of the specimen are known, the "TS Test" subroutine can be employed. The purpose of this test

is to incrementally increase the excitation voltage of each successive test and measure the shear strain based on the torque applied to the specimen and the corresponding nonlinear shear modulus and hysteretic damping behavior of the specimen. The function of this subroutine is adaptable to allow the user to automatically conduct the TS test, conduct the TS with a predetermined array of excitation voltages, or to self-input a set range of excitation voltages. Theory behind the shear strain based on torque applied and corresponding nonlinear shear modulus and hysteretic damping behavior of the specimen can be reviewed in Keene (2017). The user menu for the "TS Test" can be seen in Figure A.28.

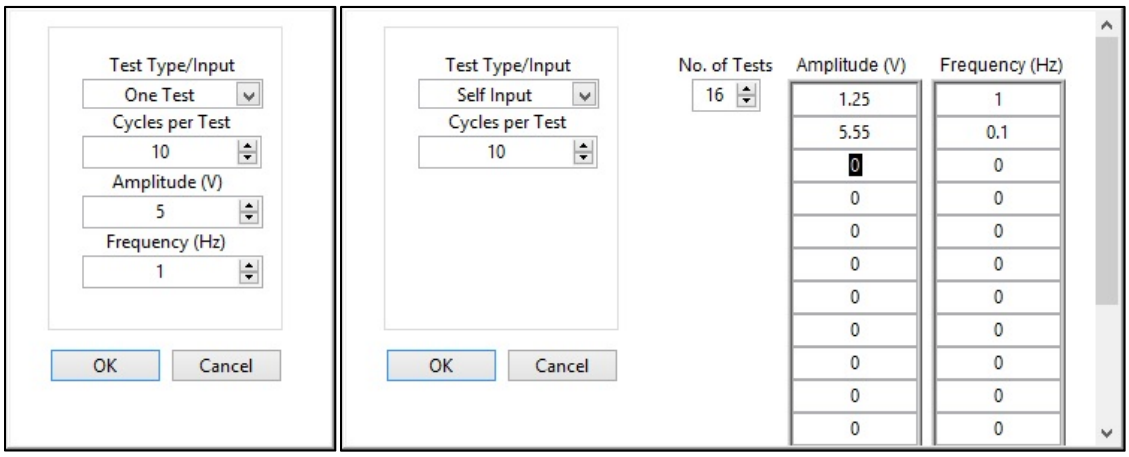

Figure A.28: Input window menu for the "TS Test".

A.4.2.1 "Test Type/Input" to select the testing regime:

- "One Test" is selected and the "Cycles per Test", "Amplitude (V)", and "Frequency (Hz)" can then be entered for a single test to be conducted.
- "Standard Sequence" is selected and the "No. of Tests" and predetermined array of amplitudes and frequencies can then be entered for a single test to be conducted. When selecting this feature, a "Test Continuation" window

is displayed after each sequence of TS tests are completed. This window allows the user to add additional TS tests to the testing sequence.

- "Automatic" is selected and a sequenced test progression schema is executed and will conclude after a G/G_{max} threshold has passed. This option is currently only available for research purposes.
- "Self-Input" is selected and the user is provided with an array to enter a self-determined array of excitation voltages and input frequencies.

A.4.3 TS Test

In the TS test, the specimen behavior and quality of the results can be observed in real time during the test. After each sequence of the test is executed, the results of the test will be populated into a table in the "TS Test" window. The TS testing window is shown in Figure A.29.

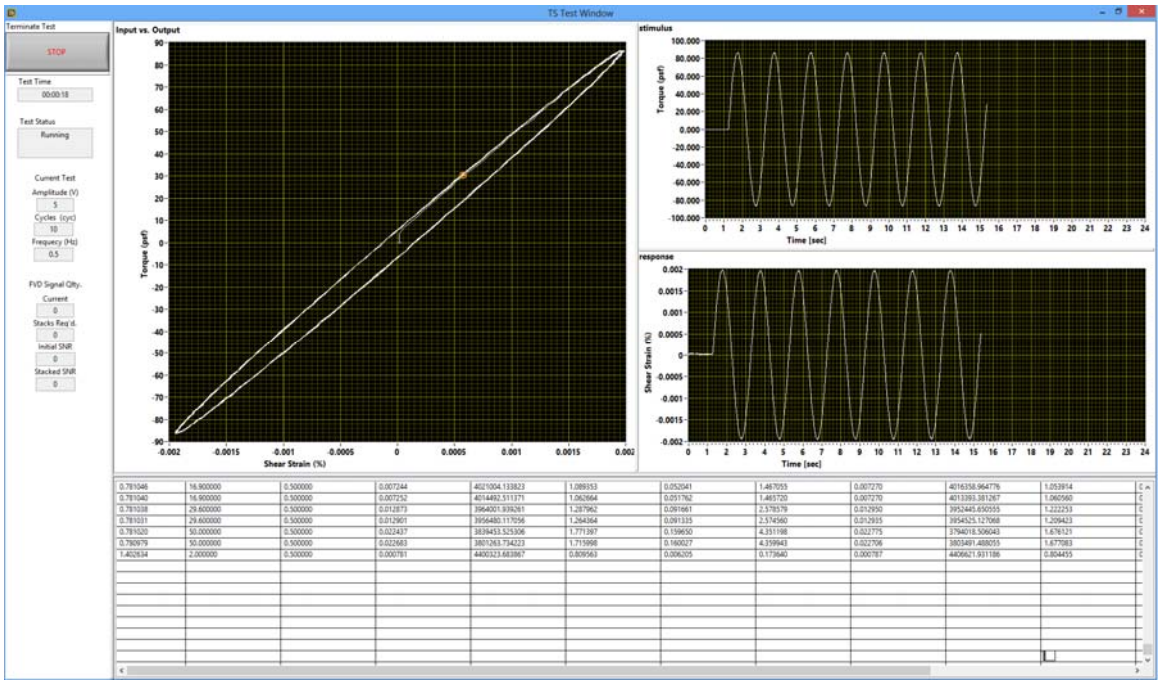

Figure A.29: TS testing window.

When selecting this “Self-Input” from the initial TS test input window, a “Test Continuation” window is displayed after each sequence of TS tests are completed. This window allows the user to add additional TS tests to the testing sequence. An example of this window is shown in Figure A.30.

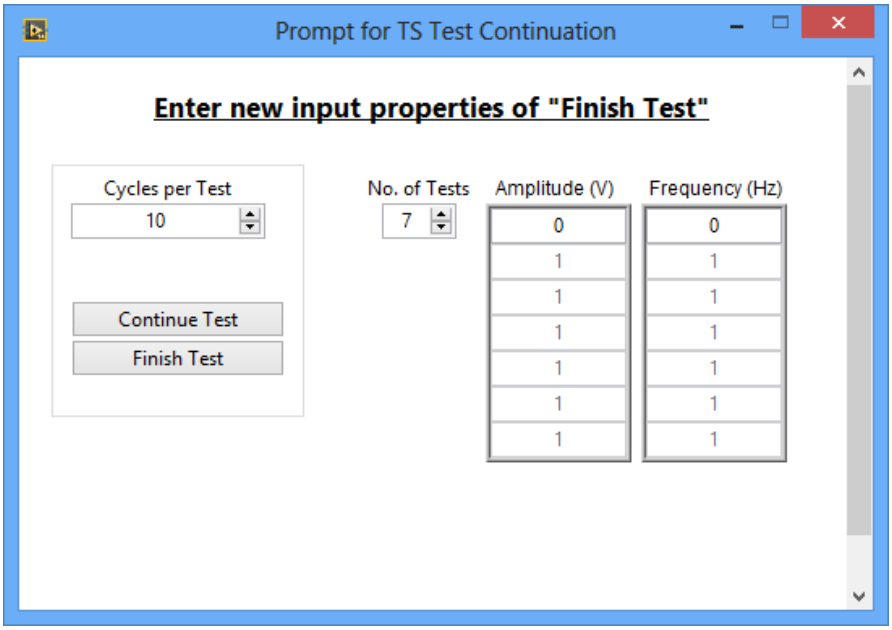

Figure A.30: “Prompt for Test Continuation” window.

Appendix B

Hollow Specimen Construction and Calculations

B.1 Sample Equipment and Schematics

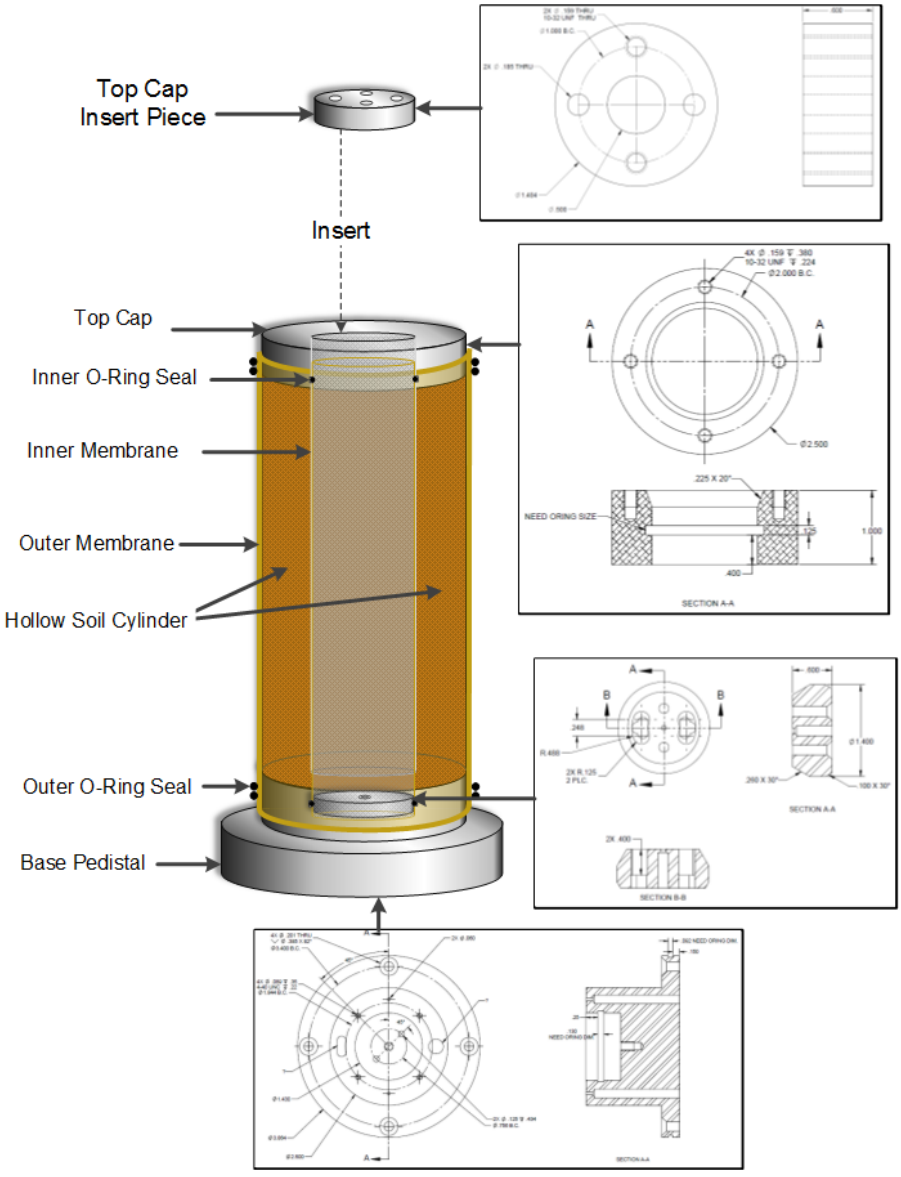

Figure B.1: Diagram of Hollow Cylindrical Specimen with Schematics of Parts that Make up the Pedestal and Top Cap.

B.2 PHOTOGRAPHS OF SPECIMEN CONSTRUCTION

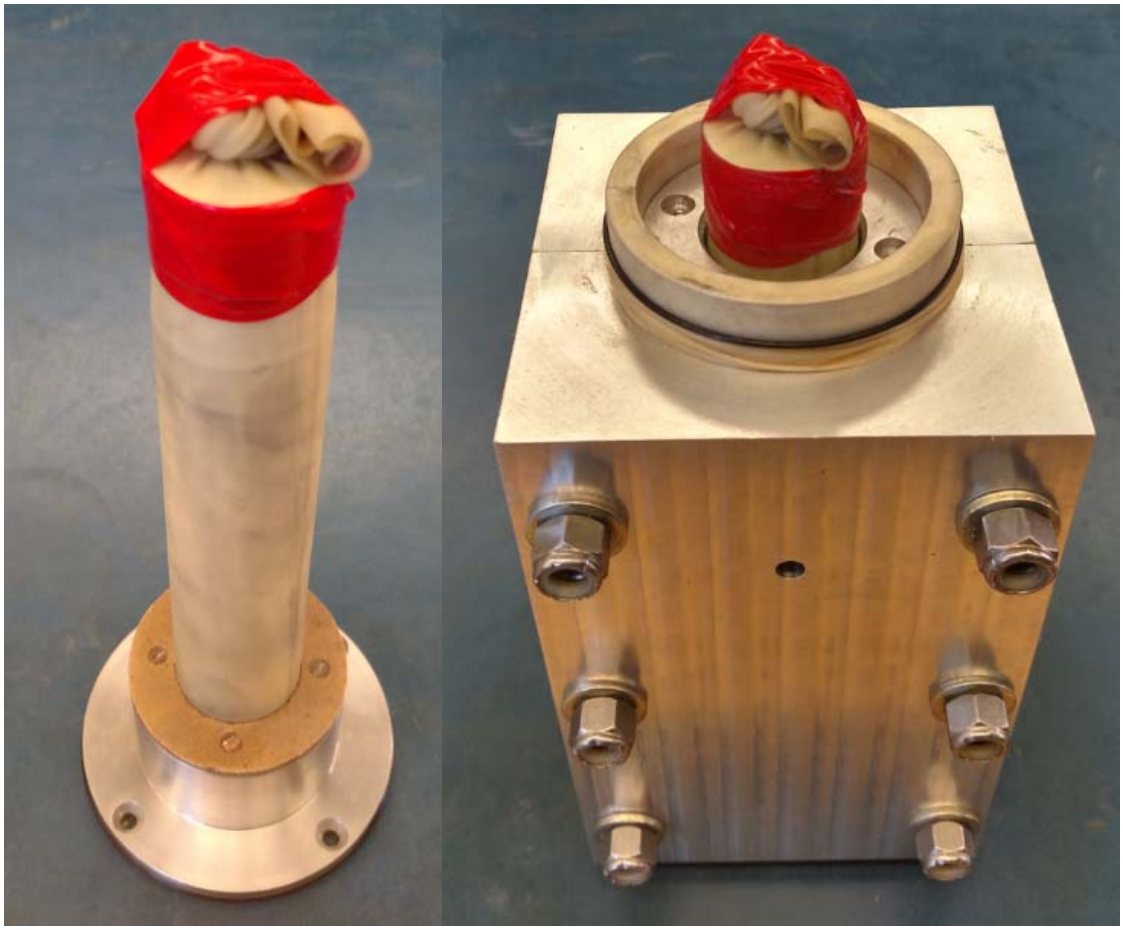

Figure B.2: (left) Inner Mold and Inner Membrane Before Hollow Specimen Construction and (right) Outer Mold, Membrane, and Top Cap After Specimen Construction.

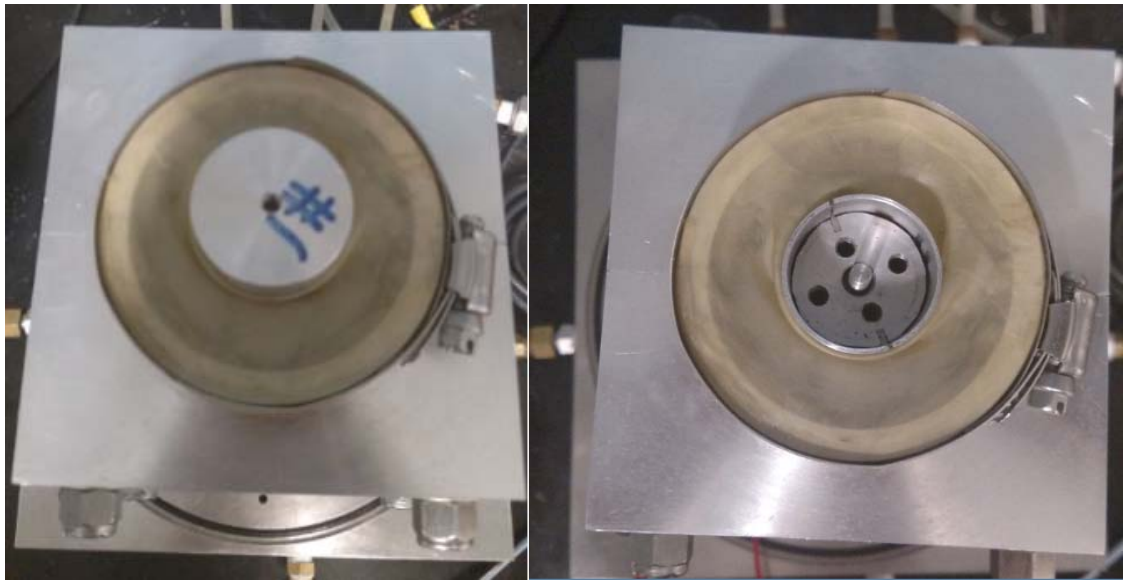

Figure B.3: (left) Inner membrane Secured Over Top Cap During Removal of Inner Mold and (right) Removal of Inner Mold in Progress. *Specimen is Held Under a Vacuum.

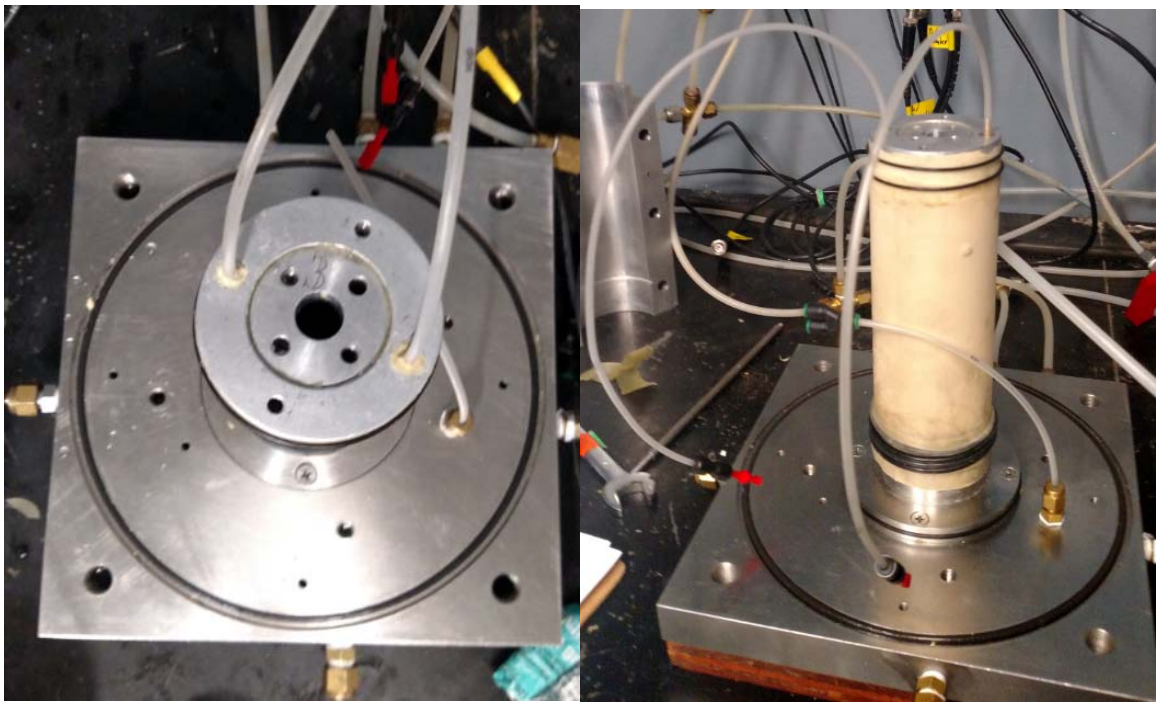

Figure B.4: (left) Configuration of Inner and Outer Top Caps after Removal of Inner and Outer Molds and (right) Specimen After Removal of Inner and Outer Mold with Lines Attached for Backpressure Saturation. *Specimen is Held Under a Vacuum.

B.3 CALCULATION OF HOLLOW SPECIMEN DIMENSIONS DURING RCTS TESTING

(a) Dry Unit Weight, γ_d, pcf:

$$\gamma_d = \frac{\text{Dry Weight of Sample}}{\text{Volume of Sample}} \tag{B.1}$$

$$\gamma_d = \frac{\frac{W_{tsamo}}{(1+W_{csamo})}}{\text{Volume of Sample}} \tag{B.2}$$

(b) Void Ratio, e_0:

$$e_0 = \frac{G_S \times \gamma_w}{\gamma_d} - 1 \tag{B.3}$$

(c) Degree of Saturation, Srsamo, %:

$$S_{rsamo} = \frac{W_{csamo} \times G_S}{e_0} \tag{B.4}$$

(d) Volume of Sample (Volo):

$$V_{olo} = (D_{outo}^2 - D_{ino}^2) \times \pi/4 \times H_{tsamo} \tag{B.5}$$

(e) Dry Weight of Sample (Wtctry):

$$W_{tdry} = W_{tsamo}/(1 + W_{csamo}) \tag{B.6}$$

(f) Volume of Solid (Vsolid):

$$V_{solid} = W_{tdry}/(G_S \times \gamma_w) \tag{B.7}$$

Hand Calculations after initial confinement time:

(a) Length of Sample (H_t):

$$H_t = H_{tsamo} - (V_{lvdt} - V_{lvdto}) \times F_{lvdt} \quad (B.8)$$

(b) Inner Diameter of Sample (D_{in}): (assuming isotropic strain for isotropic confinement)

$$D_{in} = D_{ino} \times (H_{tsamo}/H_t) \quad (B.9)$$

(b) Outer Diameter of Sample (D_{out}): (assuming isotropic strain for isotropic confinement)

$$D_{out} = D_{outo} \times (H_t/H_{tsamo}) \quad (B.10)$$

(c) Volume of Sample (Volume):

$$Volume = D_{out}^2 \times \pi/4 \times H_t \quad (B.11)$$

(d) Total Weight of Sample (Weight) (assuming S_r remains constant):

$$Weight = W_{tsamo} - \left((V_{olo} - Volume) \times S_{rsamo} \times \gamma_w\right) \quad (B.12)$$

(e) Void Ratio(e):

$$e = (Volume - V_{solid})/V_{solid} \quad (B.13)$$

(f) Shear Wave Velocity (Vs):

Mass Polar Moment of Inertia of Sample (I):

$$I = Weight \times (D_{out}^2 + D_{in}^2)/(8 \times g) \quad (B.14)$$

(g) Mass Polar Moment of Inertia of Drive Plate and Top Cap(I_0):

$$I_0 = D_P + T_C \quad (B.15)$$

$$I/I_0 = \quad (B.16)$$

Solving for P from equation $I/I_0 = \beta \times \tan\beta$

$\beta \approx 0.4538296$

β(rad)	β×tanβ
0.453	0.22050249
0.4535	0.22102642
0.45356	0.22108934
0.45362	0.22115227
0.45368	0.22121522
0.45374	0.22127817
0.4538	0.22134113
0.45386	0.22140411
0.45392	0.22146710

Since $\beta = \omega_n \times H_t / V_S$ and for Small Damping Ratios, $f_n \approx f_r$

(f) Area Polar Moment of Inertia, Jp

$$J_p = \pi \times (D_{out}^4 - D_{in}^4)/32 \qquad \text{(B.17)}$$

B.4 SHEARING STRAIN CALCULATION FROM NI (1987)

From Ni (1987), the strain linearly increases from zero where r = 0 to a maximum of $r_0*\theta_{max}/l$ at $r = r_0$, where r_0 is the radius of the soil column. Since shearing strain varies within the soil column, some equivalent shearing stain, γ_{eq}, must be chosen so that the shearing strain can be expresses as:

$$\gamma_{eq} = \frac{r_{eq}\theta_{max}}{l} \quad \text{(B.18)}$$

where r_{eq} is the equivalent radius [$=2*(r_0^3 - r_i^3)/(3*(r_0^2 - r_i^2))$], and r_i is the inside radius.

$$\gamma(r) = \frac{r*\theta_{max}}{l} \quad \text{(B.19)}$$

where r is the radius, θ_{max} is the is the maximum angle of rotation.

B.5 SHEARING STRESS

B.5.1 Equations From Ni (1987)

In the torsional simple shear test, the stress-strain hysteresis loop is measured. The shear modulus corresponds to the slope of a line through the end points of the hysteresis loop. The secant shear modulus is calculated from the following relationship:

$$G = \tau/\gamma \quad \text{(B.20)}$$

Since shear modulus is based on the torsional stress-strain hysteresis loop, the shear stress and shearing strain should be defined by the applied torque and measure twist. Determination of shearing stress is based on the theory of elasticity for circular or tubular bar in pure torsion. Assume that pure torque, T, is applied to the top of the soil column. The shearing stress varies linearly varied across the radius. The average torsional shear stress, on a cross section of a specimen τ_{avg}, is defined as:

$$\tau_{avg} = S/A \tag{B.21}$$

where A is the net area of the cross section of the specimen, i.e. $A = \pi (r_0^2 - r_i^2)$, and r_0 and r_i are the outside and inside radius of a hollow specimen, respectively. S is the total magnitude of shearing stress. Therefore, S can be calculated as:

$$S = \int_{r_i}^{r_0} \tau_r (2\pi\, r)\, dr \tag{B.22}$$

where τ_r is the shearing stress at a distance r from the axis of specimen, i.e. $\tau_r = \tau_m\, r/r_0$, where τ_m is the maximum shearing stress at $r = r_0$. On the other hand, the torque, T, can be calculated from:

$$T = \int_{r_i}^{r_0} \tau_r (2\pi\, r) r\, dr = \frac{\tau_m}{r} J \tag{B.23}$$

where J is the area polar moment of inertia, which is equal to $\pi (r_0^4 - r_i^4)/2$. From the equation above, τ_m can be expressed as:

$$\tau_m = r_0 \cdot \frac{T}{J} \tag{B.24}$$

Substituting this and τ_r into the equation for the total magnitude of shearing stress (S), one can write the equation for τ_{avg} as:

$$\tau_{avg} = \frac{2}{3} \frac{r_0^3 - r_i^3}{r_0^2 - r_i^2} \frac{T}{J} \tag{B.25}$$

or

$$\tau_{avg} = r_{eq} \cdot \frac{T}{J} \tag{B.26}$$

where r_{eq} is defined as the equivalent radius. It can be seen in the equation above that the value or r_{eq} is 2/3 of r_0 for a solid specimen and $2/3 * (r_0^3 - r_i^3)/ (r_0^2 - r_i^2)$ for hollow

specimens. In practice, r_{eq} is defined as the average of the inside and outside radii for hollow specimens. As an example, the difference between simplified r_{eq} and exact r_{eq} for the case where r_0 = 1.2 in. and r_i = 0.7 in. is 2.6%.

B.5.2 Equivalent Radius from Chen and Stokoe (1979)

In terms of equivalent radius, the strain range of most importance in the resonant column test is 0.01 to 0.1 percent (below this level, strain has little effect on modulus). In this strain range an equivalent radius of 0.85 times the outside radius, a, represents a good value. However, the average radius, ρ_{av}, of the hollow sample (one half of the inner and outer radii) is typically assumed to represent the effective radius in practice. For the sample size used herein, ρ_{av}/a equals 0.79 instead of 0.85. Therefore, the shearing strain which is assumed to correspond to the measured modulus is slightly greater that than presently used.

Appendix C

Anisotropic Loading Device

C.1 TEXT FROM ALLEN AND STOKOE (1992)

Instead of pushing downward on the sample top cap, a system was developed where the additional axial load is applied by pulling down on the top cap. This is accomplished by utilizing the thin central rod which extends downward from the top cap, through the sample, ad out the bottom of the confining chamber. The thin rod is a mild steel rod with a diameter of 1/16 in. (0.159 cm) and a length of 13.5 in. (34.3 cm). The top of the rod is rigidly attached to the top cap and is somewhat restrained against rotation with an O-ring seal at the bottom of the sample as shown in Figure 2.7. Below the O-ring seal, the rod extends through the base pedestal, base plate, and table top on which the system is mounted.

C.2 DIAGRAMS AND PHOTOS FOR ANISOTROPIC LOADING DEVICE

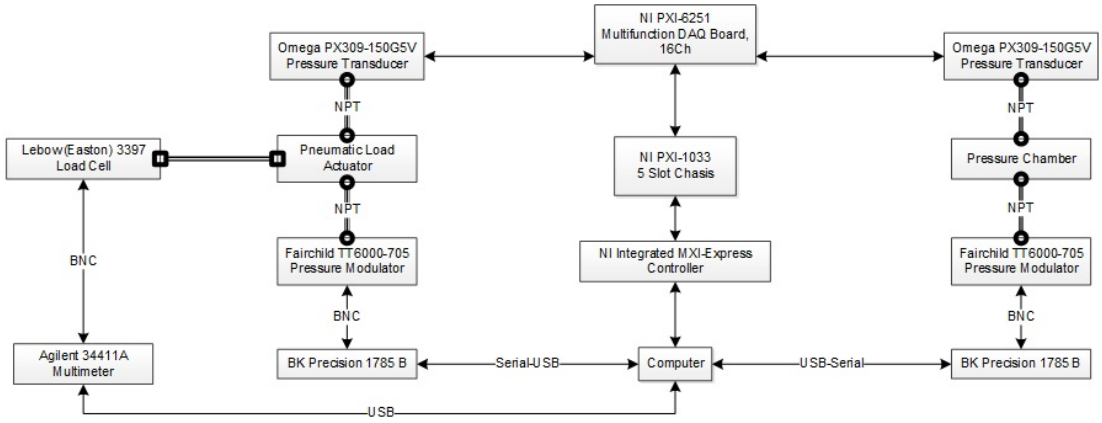

Figure B.5: Connection Diagram for the Components Used In Monitoring and Controlling Anisotropic Stress Testing

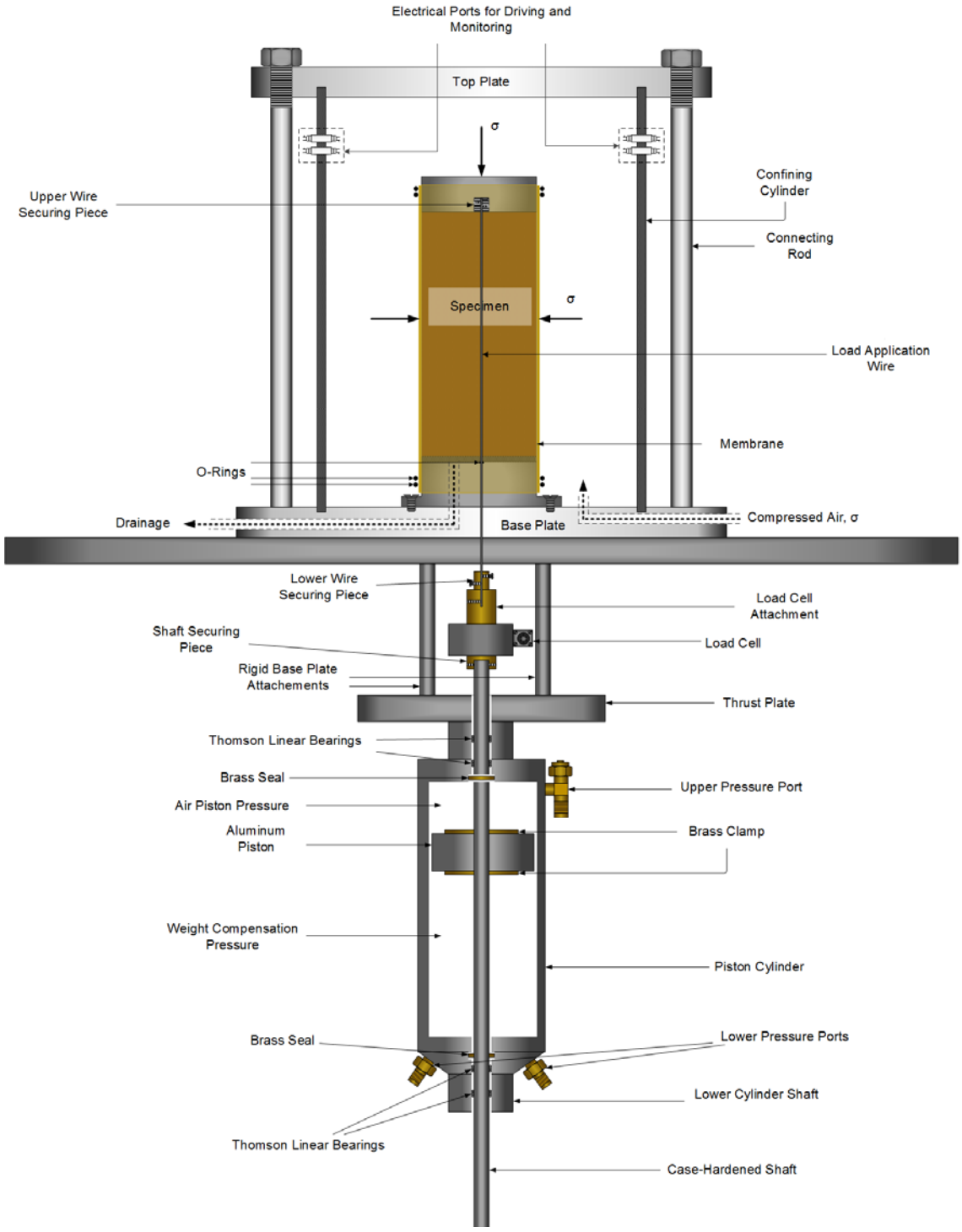

Figure B.6: Schematic Diagram of the Components Used In Monitoring and Controlling Anisotropic Stress Testing

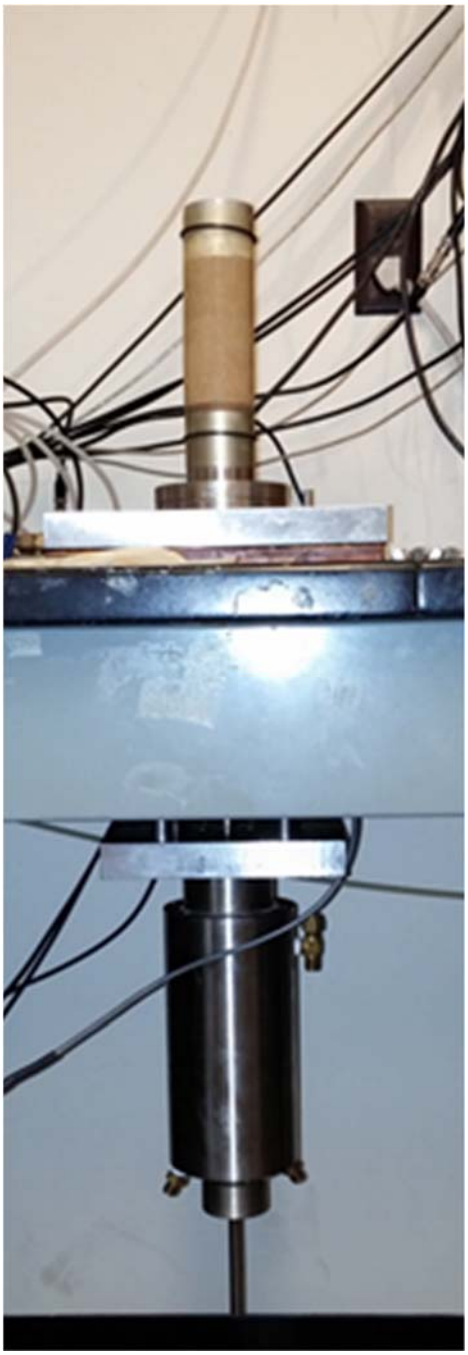

Figure B.7: (left) Photo of Anisotropic Loading Setup while Specimen is Held Under A Vacuum Before (right) Setup with RCTS Device and Chamber Secured in Place.

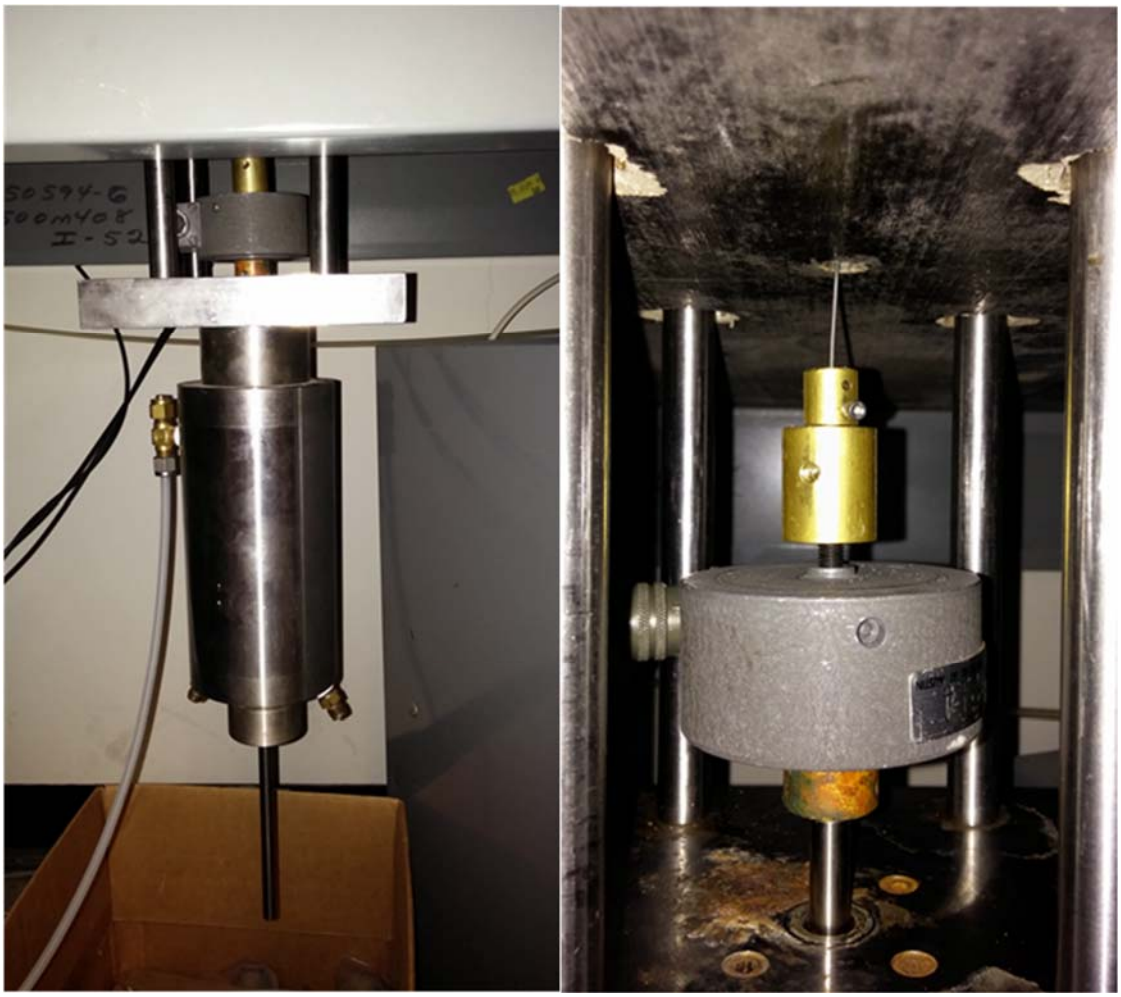

Figure B.8: (left) Photo of Anisotropic Loading Setup Pneumatic Actuator and (right) Configuration of Load Cell and Central Loading Wire.

C.3 EQUATIONS AND CALCULATIONS FOR ANISOTROPIC LOADING DEVICE

C.3.1 Initial Calculations for Estimating Changes in Specimen Dimensions:

1. Initial Volume of Sample (V_o):

$$V_o = D_{outo}^2 \times \pi/4 \times H_{tsamo} \quad (C.1)$$

2. Length of Sample (H_t):

$$H_t = H_{tsamo} - (V_{lvdt} - V_{lvdto}) \times F_{lvdt} \quad (C.2)$$

3. Axial Strain (ε_a):

$$\varepsilon_a = \frac{H_{tsamo} - H_t}{H_{tsamo}} \quad (C.3)$$

C.3.2 Iterative Calculations for Estimating Changes in Specimen Dimensions

1. Start Loop by setting D_{out} to the previously calculated value of the specimen diameter, $D_{out,old}$:

2. Setting the New Diameter

$$D_{out} = D_{out,old} \quad (C.4)$$

3. Volume of Sample (V):

$$V = D_{out}^2 \times \pi/4 \times H_t \quad (C.5)$$

4. Deviator Stress (σ_d):

$$\sigma_d = \frac{L}{D_{out}^2 \times \pi/4} \quad (C.6)$$

5. Principal Effective Stress (σ_1):

$$\sigma_1 = \sigma_d + \sigma_3 \quad (C.7)$$

6. Radial Stress (σ_r):

$$\sigma_r = \frac{\sigma_d}{3} + \sigma_3 \quad (C.8)$$

7. Axial Stress (σ_r):

$$\sigma_a = \frac{\sigma_d}{2} + \sigma_r \quad (C.9)$$

8. Shear Stress (σ_r):

$$q = \left(\frac{\sigma_1 - \sigma_3}{2} = \frac{\sigma_d}{2}\right) = \sigma_a - \sigma_r \quad (C.10)$$

9. Radial Strain (ε_r):

Assume Poisson's ratio of 0.25-0.4 depending on the material or 0.495 if the specimen in saturated. If p-wave piezo-ceramic emitters are used then a precise Poisson's ratio can be determined.

$$\varepsilon_r = \frac{(1-\nu)\times\sigma_r + \nu\times\sigma_a}{2G(1+\nu)} \quad (C.11)$$

10. Volumetric Strain (ε_p):

$$\varepsilon_p = \varepsilon_a + 2 \times \varepsilon_r = \frac{V_0 - V}{V_0} \quad (C.12)$$

11. Outer Diameter of Sample (D_{out}): (assuming anisotropic strain for anisotropic confinement)

$$D_{out} = \left[\frac{V_0\times[1-(\varepsilon_a+2\times\varepsilon_r)]}{\pi/4\times H_t}\right]^{1/2} \quad (C.13)$$

12. End of Loop, set $D_{out,new}$ to equal D_{out}, repeat until $\left|D_{out,old} - D_{out,new}\right| < 0.01$

C.3.3 Continued calculations for estimated shear behavior

1. Volume of Sample (Volume):

$$\text{Volume} = D_{out}^2 \times \pi/4 \times H_t \quad \text{(C.14)}$$

2. Total Weight of Sample (Weight) (assuming Sr remains constant):

$$\text{Weight} = W_{tsamo} - \left((V_{olo} - \text{Volume}) \times S_{rsamo} \times \gamma_w\right) \quad \text{(C.15)}$$

3. Void Ratio(e):

$$e = (\text{Volume} - V_{solid})/V_{solid} \quad \text{(C.16)}$$

4. Shear Wave Velocity (Vs):

(a) Mass Polar Moment of Inertia of Sample (I):

$$I = \text{Weight} \times D_{out}^2/(8 \times g) \quad \text{(C.17)}$$

(b) Mass Polar Moment of Inertia of Drive Plate and Top Cap(I_0):

$$I_0 = D_P + T_C \quad \text{(C.18)}$$

(c) Solve for β from equation $I/I_0 = \beta \times \tan\beta$,

Since $\beta = \omega_n \times H_t / V_S$ and for Small Damping Ratios, $f_n \approx f_r$

$$V_S = (2 \times \pi \times f_r) \times H_t/\beta \quad \text{(C.19)}$$

5. Shear Modulus (G):

$$G = \rho \times V_S^2 \quad \text{(C.20)}$$

Appendix D

Limitations of the Half-Power Bandwidth Interpolation Method

Before determining a similar sweep rate parameter for a stepped sine sweep method, as developed in the aforementioned studies by Lollock (2002) and Girard and Bugeat (2004), the limitation of the method involving interpolation of the half-power points is first evaluated. As determined in Lollock (2002) and Girard and Bugeat (2004), the measurement of the resonant frequency is relatively insensitive to the sweep rate; however, a theoretical minimum sweep rate is established as:

$$Step_{min} = 2 * f_n * D/100\% \quad \text{(D.1)}$$

where $Step_{min}$ is the minimum frequency step required in units of Hz, f_n is the input natural frequency, and D is the damping ratio in percent. This equation basically provides a step rate that is required to populate the response curve with the minimum data points required to utilize this methods; i.e. 3 points, one near the resonant frequency and two below the half-power amplitudes to allow interpolation between the highest amplitude point and the two below the half-power amplitudes. This criterion does not provide an accurate determination of the response curve parameters, but serves as a constraint on the analysis procedures. The importance of establishing the limits of this method becomes valuable for developing a fruitful understanding of the effects that the sweep rate has on determining the response curve parameters discussed later on in this section.

The interpolation method was evaluated based on damping ratios well above and below those measured in the resonant column test for both the brass calibration specimens and soils or rock materials that are tested in the device. The method was evaluated for damping ratios from 0.01% to 20% damping ratios. Few soils or rock materials exhibit

damping ratios around or below 0.01% and damping ratios approaching 20% are more characteristic of a nonlinear dynamic strain range for natural geologic materials, which are outside of the scope of using linear SDOF system equations. Nonlinear dynamic response is covered in other sections. Metal specimens used for calibration of the RCTS device may have damping ratios near 0.01%. However, the RCTC device used in this study has equipment-generated damping, based on the electromagnetic response of the drive system, which adds damping to the response curve. As discussed in subsequent sections, there are corrections for equipment-generated damping, but for this analysis, the additional damping aids in economizing the experimental evaluation of sweep rate. Finally, the half-power method is limited to measuring lower damping ratios and cannot be used accurately for higher damping ratios.

In the analysis of the interpolation method, the range of frequencies used were approximately $0.5*Step_{min}$, as defined earlier, to $0.5*Step_{min}*10^{-6}$. This range of frequencies was subdivided into 54 frequency step rates at each log cycle within the frequency range. Thus, for each damping ratio used to simulate a response curve, 54 different frequency step rates were used and the interpolation method was used to predict the resonant frequency, maximum amplitude, and material damping ratio. The damping ratios used in this analysis are 0.01%, 0.05%, 0.1%, 0.5%, 1%, 5%, 10%, and 20%.

The prediction of the resonant frequency and maximum amplitude was relatively insensitive to sweep rate and when starting at a frequency step rate below $Step_{min}$ these two parameters are easily found. The damping ratio is, however, very sensitive to the number of data points (i.e. step rate) that populate the response curve. To present the results of this parametric evaluation in one plot, the percent difference between the input damping ratio and the analytically measured damping ratio versus the normalized frequency step to minimum frequency step were determined by:

$$D_{\%\,diff} = \frac{(D_{input} - D_{result,i})}{D_{nput}} \quad \text{(D.2)}$$

$$Normalized\ Frequency\ Step = Step_i / Step_{min} \quad \text{(D.3)}$$

where D_{input} is the damping ratio value used to create the simulated response curve in units of percent, $D_{result,i}$ is the analytically determined damping ratio at a specific $Step_i$, $Step_i$ is the frequency step rate used to create a specific number of points populating the response curve given in units of Hz, and $Step_{min}$ is the minimum step rate required to create a response curve as defined earlier. The results are shown in Figure D.1.

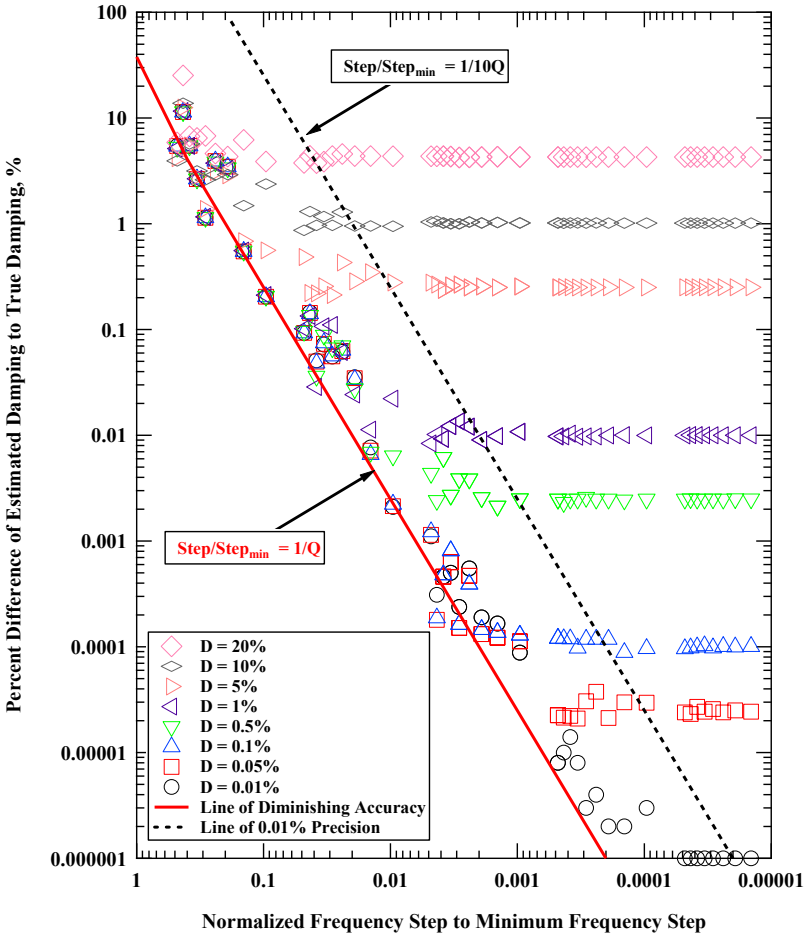

Figure D.1: Variation in Percent Difference Between Estimated and True Damping Ratio with Normalized Frequency Step to Minimum Frequency Step.

Two key aspects can be observed from the analytical results, the first is that there are two noticeable thresholds where the accuracy is diminishes with increasing frequency step rate (line of diminishing accuracy) and where using successively smaller step rates does not improve the precision (line of 0.01% precision) of the interpolation method. These two lines can be conveniently defined using the quality factor, Q =1/2D, where the line of diminishing accuracy has a $Step/Step_{min}$ of 1/Q and the line of 0.01% precision has a $Step/Step_{min}$ of 1/10Q. The second is that as damping ratio increases the minimum ratio of estimated damping to true damping increases; this is because as the damping ratio becomes larger the difference between the resonant frequency and the natural frequency becomes larger. This shortcoming is due to the half-power method and is not limited to the interpolation method. Nevertheless, the expected degree of error of the half-power method is the same as the minimum ratio of estimated damping to true damping. The percent difference can be quantified using the input damping ratio and the difference between the resonant frequency and the natural frequency, which is given as:

$$\%difference = \frac{(f_n - f_n\sqrt{1-2D^2})}{f_n} \times 100\% \tag{D.4}$$

To conclude the analysis, the following equation recommends a step rate based on the damping ratio of the system being tested when using the interpolation method. The minimum step rate will allow for enough points to populate the response curve that the interpolation method will be expected to have repeatable precision within 0.01%.

The equation for recommended step rate is:

$$Step_{rec} = \frac{1}{10Q} = \frac{2*D/100\%}{10} \tag{D.5}$$

where $Step_{rec}$ is the recommended step rate, Q is the quality factor, and D is the damping ratio in units of percent.

Appendix E

LVDT Resolution and Variability

The LVDT sensors are Columbia LVDT SH-200-SxR. The LVDT program sends a signal excitation of 4.77 RMS Volts at 500 Hz from a NI PXI-4461 output channel and sensor signal received on a NI PXI-6251 input channel. Signal excitation and acquisition channels are set to +/- 10 V range setting. Over 1000 repeated LVDT measurement trials the standard deviation of these recordings was +/- 0.000086553 V. These LVDTs typically have a calibration factor of approximately 0.0045 ft/V, thus the statistical variation from the LVDT measurements is +/- $4.674*10^{-6}$ in. The measurement of height during RCTS testing using the LVDT has a high degree of accuracy. Therefore, very small changes of specimen height can be measured during RCTS testing.

Appendix F

Excitation Cycles in the Free-Vibration Decay Test

F.1 Excitation Cycles Required to Reach Stead-State Vibration

A typical resonant column test is composed of two parts. In the first part, a downgrade frequency sweep is used to determine the resonant frequency, half-power damping ratio, and maximum shear strain amplitude excited during the sweep. The second part begins by exciting the specimen at the resonant frequency determined in part 1. The downgrade sweep is followed by a free-vibration decay test where the specimen is excited at the resonant frequency. After reaching steady-state vibration (i.e. maximum shear strain measured during the downgrade frequency sweep), the excitation is abruptly suspended and the specimen is allowed to freely vibrate. The free-vibration test is used to determine the damped natural frequency and free-vibration damping ratio. Also, the steady-state shear strain amplitude is measured just before the power is abruptly suspended to check that the strain amplitude in the free-vibration decay test matches the peak amplitude at resonance from the downgrade frequency sweep. The number of cycles needed to reach steady-state vibration is dependent on the material damping ratio of the system.

Using the characteristic obtained from the frequency sweep, the resonant frequency and material damping ratio are used in the free-vibration decay test as the frequency of excitation and to determine the number of cycles to reach steady-state vibration. Based on a linear SDOF system, the number of cycles to reach steady-state when exciting at the resonant frequency, is theoretically the same as cycles of free vibration decay at the damped natural frequency. Hence, the envelope for forced-vibration is the inverse of the envelope for free-vibration. The equations reduced from SDOF theory and some examples are shown herein.

F.1.1 Number of Cycles to Reach Steady-State Vibration

The number of cycles needed to achieve a defined percent of steady-state vibration, with $\omega = \omega_r$, is taken from Chopra (2001) and defined as:

$$\frac{|u_j|}{u_0} = 1 - e^{-2\pi \cdot D \cdot j} \qquad \text{(F.1)}$$

where u_j is the absolute value of the amplitude at cycle j, u_0 is the steady-state amplitude, j is the number of input cycles, and D is the material damping ratio. Example calculations are performed to show the number of cycles needed to reach steady state for different damping ratios as seen in Figure F.1.

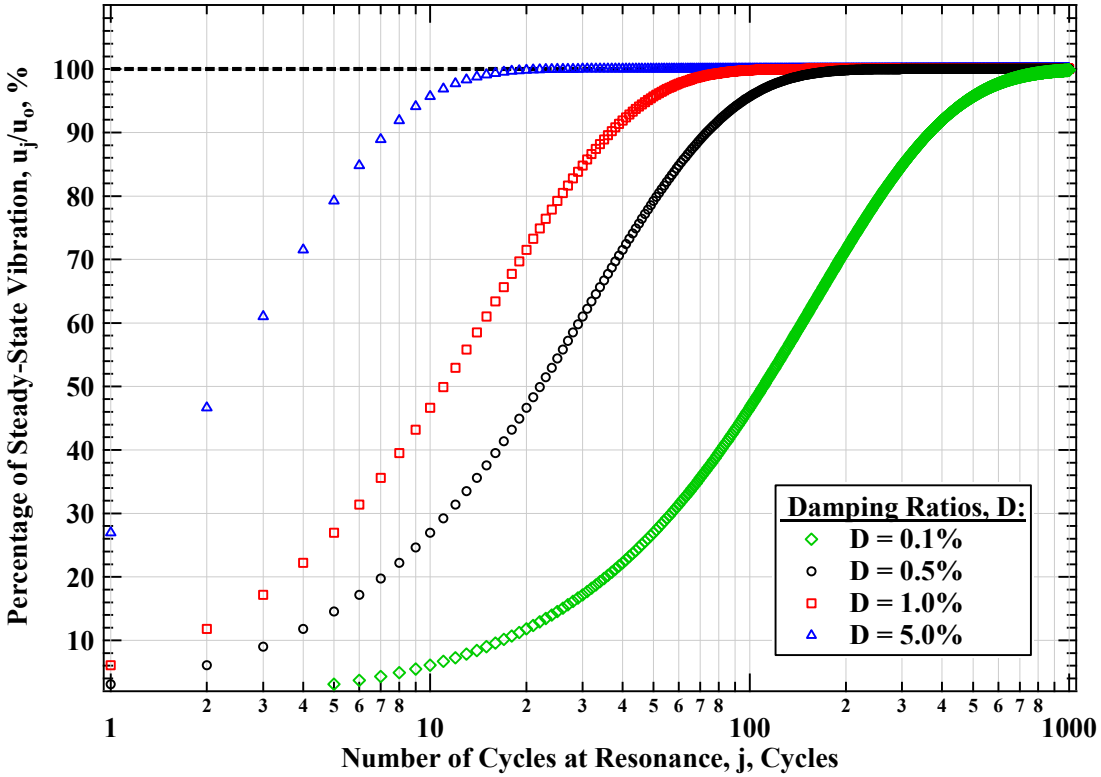

Figure F.1: Variation in the Percentage of Steady-State Vibration Reached with the Number of Cycles of Forced Vibration at the Resonant Frequency Based on Damping Ratios of 0.1, 0.5, 1, and 5%.

As seen Figure F.1, more cycles are required to reach steady state with lower damping ratios, which coincides with the many cycles of free-vibration that occur in materials with low damping ratios (i.e. long duration for ringing of a bell). In the free-vibration test, 100% dynamic amplification or steady-state conditions can take many cycles at lower damping ratios, which generally occur at lower strains during RC testing. For example, Metal Specimen #13 has a resonant frequency around 150 Hz and the combined specimen and equipment-generated damping ratio is approximately 0.33%. For these dynamic characteristics, reaching 99.99% of steady-state vibration would take 3 seconds and thus free-vibration decay would take at least an additional 3 seconds. An additional second is added to take readings of background noise that was present and to process the signals from the free-vibration decay test. As discussed in Chapter 5, signal stacking is used when the level of background noise is significant. The system is limited from repeating more than 20 free-vibration decay tests for signal stacking purposes. Therefore, based on the dynamic characteristics of this system, repeating the test 20 times would take 140 seconds (2.33 minutes), which would be in additional to the time that passed during the frequency sweep test. Therefore, unnecessarily long testing durations can be traded with a marginal degree of accuracy. The software is programmed to target 99.5% of steady-state vibration to expedite testing durations.

When conducting nonlinear testing, typically an overestimate of the material damping ratio is obtained from the frequency sweep relative to the free-vibration decay damping ratio. Thus, an underestimate of the number of cycles needed to reach steady state will occur when using damping ratios obtained from the frequency sweep. To account for the potential underestimate in the number of cycles required to reach steady-state vibration, when nonlinear tests are conducted, the percentage of steady-state targeted is set to 99.75% and 5 additional excitation cycles are added. For practical purposes, increasing the

percentage of steady-state targeted to 99.75% and adding 5 cycles is sufficient to account potential underestimate in the number of cycles required to reach steady-state vibration. To validate this assertion, peak shear strains from frequency sweep tests are compared with peak shear strains from free-vibration decay tests, where the number of cycles required to reach steady state were based on the material damping ratio obtained from the frequency sweep test. Peak shear strains from frequency sweep tests are compared with peak shear strains from free-vibration decay tests are presented in Figure F.2. The shear strain results presented come from an intact Sandy Fat Clay (CH) specimen retrieved from a depth of 4.77 m with LL = 79% and PI = 55% tested at a confining pressure of 0.54 atm.

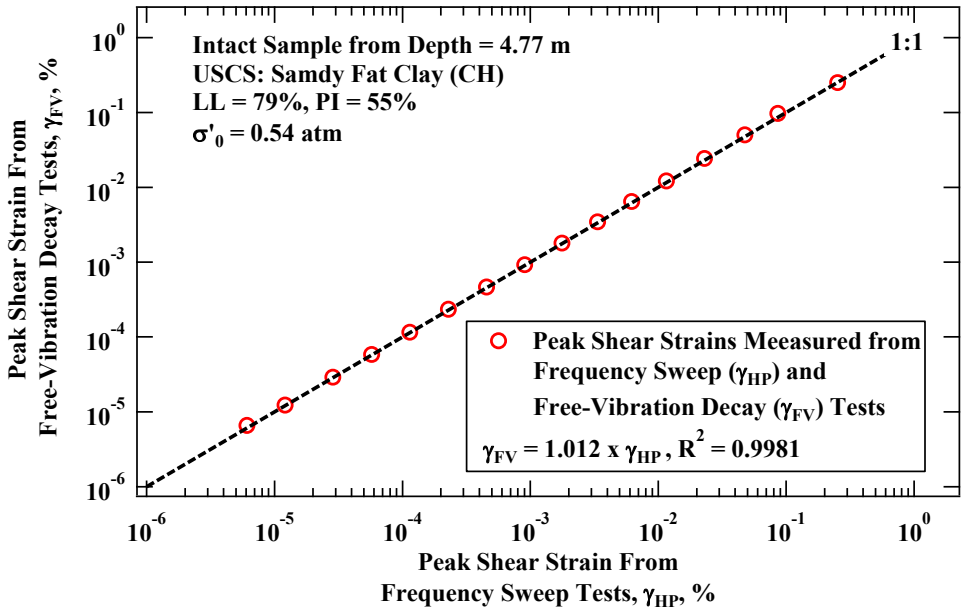

Figure F.2: Results of Low and High amplitude RC tests on washed mortar sand (Sample# AKK_003) at 18 psi confining stress.

Good agreement is found between frequency sweep and forced vibration shear strains excited in low and high amplitude tests. These tests were also based on use of the resonant frequency and damping measured in the frequency sweep for selecting number of cycles to 99.5% of steady state in forced vibration.

References

Chen, A.T.F. and Stokoe, K.H., II (1979), "Interpretation of Strain Dependent Modulus and Damping from Torsional Soil Tests," Report No. USGS-GD-79-002, NTIS No. PB-298479, U.S. Geological Survey.

Chopra, A. K. (2012). *Dynamics of structures: Theory and applications to earthquake engineering* (4th ed.). Upper Saddle River, N.J: Prentice Hall.

Darendeli, M.B. (2001). *Development of a New Family of Normalized Modulus Reduction and Material Damping Curves*. PhD Dissertation, Department of Civil, Arcitectural and Environmental Engineering, University of Texas, Austin.

Feldman, M. (2011). *Hilbert Transform Applications in Mechanical Vibrations*. John Wiley & Sons, Ltd. England.

Gilbert, R.B. (2014). *Decision, Risk, and Reliability*. Couse Notes for CE 387T for Spring 2014, University of Texas at Austin.

Girard, A. and Bugeat, L.P. (2004). *Effect of Sine Sweep Rate on Modal Parameter Identification*. Proceedings of the 5th International Symposium on Environmental Testing for Space Programs. June 15-17, 2004. Noordwijk, The Netherlands (ESA SP-558, August 2004).

Holtz, R.D., Kovacs, W.D., and Sheahan, T.C. (2011). *An Introduction to Geotechnical Engineering Second Addition*. Pearson Education, Inc. Upper Saddle River, New Jersey.

Isenhower, W.M. (1979). *Torsional Simple Shear/Resonant Column Properties of San Francisco Bay Mud*. Geotechnical Engineering Thesis GT 80-1, University of Texas.

Kim, D.S. (1991). *Deformational Characteristics of Soils at Small to Intermediate Strains from Cyclic Tests*. Ph.D. Dissertation, The University of Texas at Austin.

Kottke, A.R., Keene, A.K., Wang, Y., Shin, B., Stokoe, K.H., and Lewis, M.R. (2017). *In-Situ and Laboratory Measured Dynamic Properties of a Marine Clay*. ASCE Geotechnical Frontiers, Orlando, Florida.

Lodde, P.F. (1982). *Shear Moduli and Material Damping of San Francisco Bay Mud*. M.S. Thesis, The University of Texas at Austin.

Lollock, J. A. (2002). *The Effect of Swept Sinusoidal Excitation On The Response Of A Single-Degree-Of-Freedom Oscillator*. American Institute of Aeronautics and Astronautics.

Mayne, P. (2014). *Geocharacterization by In-Situ Testing (with emphasis on CPT, CPTu, and SCPTu in site exploration)*. Georgia Tech Professional Education GT Global Learning Center, June 03-04.

Menq, J. and Rix G.J. (2003). *Reduction of Equipment-Generated Damping in Resonant Column Measurements*. *Géotechnique* 53, No. 5, 503-512.

Menq, F.Y. (2003). *Dynamic Properties of Sandy and Gravelly Soils*. PhD Dissertation, Department of Civil, Arcitectural and Environmental Engineering, University of Texas, Austin.

Ni, S.H. (1987). *Dynamic Properties of Sand Under True Triaxial Stress States from Resonant Column/Torsional Shear Tests*. Ph.D. Dissertation, The University of Texas at Austin.

Richart, F.E. Jr., Hall, J.R. Jr., and Woods, R.D. (1970). *Vibrations of Soils and Foundations*. Prentice-Hall, Inc., Englewood Cliffs, New Jersey.

Robertson, W., Cazzolato, B., and Zander, A. (2012). *Axial Force Between a Thick Coil and a Cylindrical Permeant Magnet: Optimizing the Geometry of an Electromagnetic Actuator*. IEEE Transactions On Magnetics, Vol. 48, No. 9, September 2012.

Santamarina, J.C., and Fratta, D. (2005). Discrete Signals and Inverse Problems An Introduction for Engineers and Scientists. *John Wiley & Sons, Ltd*. England.

Sasanakul, I. (2005). *Development of an Electromagnetic and Mechanical Model for a Resonant Column and Torsional Shear Testing Device for Soils*. PhD Dissertation, Department of Civil and Environmental Engineering, Utah State University.

Schimpf, P.H. (2013). *A Detailed Explanation of Solenoid Force*. International Journal on Recent Trends in Engineering and Technology, Vol. 8, No. 2, January 2013.

Serway, R. A., and Jewett, J. W. (2003). *Physics for Scientists and Engineers (6th ed.)*. Pacific Grove, California; London; Brooks/Cole.

Shiri, A. and Shoulaie A. (2009). *A New Methodology for Magnetic Force Calculations Between Planar Spiral Coils*. Progress in Electromagnetics Research. Vol. 95, pp. 39–57, 2009.

Stokoe, K.H., Choi, W.K., Jeon, S.Y., and Lee, J.J. (2006). *Test Procedures and Calibration Documentation Associated with The RCTS and URC Tests at The University of Texas at Austin*. Geotechnical Engineering Report GR06-04, Geotechnical Engineering Center of the Civil Engineering Department of The University of Texas at Austin.

Stokoe, K.H., Keene, A.K., Shin, B., and Wang, Y. (2016). *Technical Procedures Associated with The Combined Resonant Column And Torsional Shear (RCTS) Tests Of Soil And Rock Samples at The University Of Texas At Austin*. Geotechnical Engineering Report GR16-05, Geotechnical Engineering Center of the Civil Engineering Department of The University of Texas at Austin.

Wilson, C.R. (2013). *Geophysical Data Processing Essentials*. Couse Notes for GEO 325K, 383D, 365N, 384R, Academic Year 2013-2014, University of Texas at Austin.